Organisation des Nations Unies pour l'éducation, la science et la culture
منظمة الأمم المتحدة للتربية و العلم و الثقافة

Commission nationale algérienne pour l'éducation, la science et la culture
اللجنة الوطنية الجزائرية للتربية و العلم و الثقافة

ISSH2' 2017 Proceedings

2017 ISSH2

الندوة الدولية الثانية حول الهيدروجين المستدام

The 2nd International Symposium on Sustainable Hydrogen

Le 2ème Symposium International sur l'Hydrogène Durable

26 - 27 **November** 2017

Algiers, Algeria

ISBN : 978-9931-9366-1-9

Organisation des Nations Unies pour l'éducation, la science et la culture
منظمة الأمم المتحدة للتربية و العلم و الثقافة

Commission nationale algérienne pour l'éducation, la science et la culture
اللجنة الوطنية الجزائرية للتربية و العلم و الثقافة

ISSH2' 2017 Proceedings

2017 ISSH2

الندوة الدولية الثانية حول الهيدروجين المستدام

The 2nd International Symposium on Sustainable Hydrogen

Le 2ème Symposium International sur l'Hydrogène Durable

26 - 27 **November** 2017 **Algiers, Algeria**

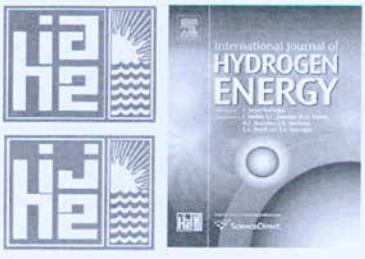

Printed by Flash Color

ACKNOWLEDGEMENT

The organizers acknowledge the financial support of the UNESCO Algerian National Commission for Education, Science and Culture.

Organisation
des Nations Unies
pour l'éducation
la science et la culture
منظمة الامم المتحدة
للتربية والعلم والثقافة

Commission nationale
algérienne
pour l'éducation
la science et la culture
اللجنة الوطنية
للتربية والعلم والثقافة

COMMITEES

SYMPOSIUM HONORARY CHAIRMAN
Nouredine Yassaa, CDER, Algiers, Algeria

SYMPOSIUM CHAIRMAN
Abdallah Khellaf, CDER, Algiers, Algeria

SCIENTIFIC COMMITTEE

Noureddine YASSAA	CDER, Algiers, Algeria
Bilge ALBAYRAK CEPER	Erciyes Univ. Turkey
Jordi LLORCA PIQUE	Universitat Politècnica de Catalunya, Spain
Kamel HALOUANI	Sfax Univ, Sfax, Tunisia
Abdallah KHELLAF	CDER, Algiers, Algeria
Rachida RIHANI	USTHB, Algiers, Algeria
Rafika BOUDERIES	CDER. Algiers. Algeria
Toufik AZIB	ESTACA'LAB. Paris, France
Ouahiba GUERRI	CDER, Algiers, Algeria
Salah HANINI	Medea Univ. Medea, Algéria
Khaled IMESSAD	CDER, Algiers, Algeria
Farid KHOUCHA	EMP, Algiers, Algeria
Achour MAHRANE	UDES, Algiers, Algeria
Fethia AMROUCHE	CDER. Algiers, Algeria
Abla CHAKER	Constantine Univ. Algeria
Hammou TEBIBEL	CDER, Algiers, Algeria
Rabah DIZENE	USTHB, Algiers, Algeria
Mohamed KHERAT	CDER, Algiers, Algeria
Omar EL KEDIM	U.T. de Belfort-Montbéliard, Belfort, France
Ilyès NOUICER	CDER, Algiers, Algeria
Abdesslem DJERDIR	U.T. de Belfort-Montbéliard, Belfort, France
Sabah MENIA	CDER, Algiers, Algeria
Amel BOUDJEMAA	CRAPC, Tipaza, Algeria
Ali MALEK	CDER, Algiers, Algeria
Amine Boudghene STAMBOULI	USTO, Oran, Algeria
Nourdine KABOUCHE	CDER, Algiers, Algeria
Fouzi TABET	DBFZ, Leipzig, Germany
Fatiha LASSOUANE	CDER, Algiers, Algeria
Ahmed BENZAOUI	USTHB, Algiers, Algeria
Fares MEZIANE	CDER, Algiers, Algeria
Farouk CHELLALI	Djelfa Univ. Algeria
Abdenour MENAA	CDER, Algiers, Algeria
Lotfi ZIANI	USTHB, Algiers, Algeria
Mounia BELACEL	CDER, Algiers, Algeria
Lamia HAMDI	USTHB, Algiers, Algeria
Bachira ABADA	CDER, Algiers, Algeria

ORGANIZING COMMITEE

The Symposium is organized by the Hydrogen- Renewable Energy Division at the Renewable Energy Development Center (CDER).

Rafika BOUDRIES
Fethia AMROUCHE
Nourdine KABOUCHE
Lamia HAMDI
Mohamed KHERAT
Fatiha LASSOUANE
Sabah MENIA
Fares MEZIANE
Sabrina ZITOUNI
Mounia BELACEL
Ilyès NOUICER
Bachira ABADA
Mohamed KEDAID
Mohamed MEDJOUTI
Sabiha DJOUAB
Zouhir MOUHOUB
Youcef MOHAMMEDI
Rafik MEDJEBOUR
Hammou TEBIBEL

Preface

Energy is the prime mover of economic development and social change. It is important to the degree that the level of a country development is indicated by its level of energy consumption. At the world level, with the fast growing economy, the improvement of quality of life and the exploding world population, the energy needs are increasing exponentially.

Energy sources have evolved and this evolution has given new impetus to social, technological and economic progresses. However, despite these unquestionable progresses, the actual energy resources are sources of concerns. The ever-increasing demand for energy is putting a lot of pressure on their limited reserves, raising the fear of shortage and depletion in the not too far future. Moreover, the production, the transport and the use of the actual energy sources have serious negative effects on the environment. Finally, the actual energy sources, by their centralized nature, are not suitable for remote areas such as islands in the middle of oceans and oases in the middle of deserts. It has been reported that the rational use of energy has not curbed the energy demand nor reduced the negative impacts on the environment.

In light of the conventional energy sources risk of shortage and depletion and the deepening of the pollution problem, resort to sustainable development is becoming a necessity.

This has led to the active development of alternative sources of energy. An energy evolution or an energy transition is underway. Many events are leading in that direction. For example, with COP 21 agreement and commitment to reduce the temperature increase to less than to 2°C, the transition from a fossil-based energy sources to sustainable and clean energy sources has to take place.

Renewable energy sources, being clean and inexhaustible, are under development as an alternative and eventually as a substitute to the depleting and polluting conventional energy sources. Actually, the share of renewable energy at the world level is around 20 % and it is in full expansion.

However, renewable energy sources suffer from intrinsic drawbacks. They are not only intermittent but are also of dilute character. This raises the issue of the disparity in energy supply and demand. The need for their transformation into a form of energy of high density that can be transported over long distances and stored over long periods is necessary.

Hydrogen is the best contender. Produced from renewable sources, it is clean and sustainable. It can also be used in mobile as well as stationary applications.

Moreover, with the energy transition, the extensive use of renewable energy sources has led to energy management problems. To deal with this problem, use of hydrogen as a storage medium or an intermediary product allows a smooth energy transition. In this sense, the

Power-to- Gas process where the electricity of renewable energy is transformed into hydrogen helps not only avoid energy waste but also balance the offer and demand.

The 2017 International Symposium on Sustainable Hydrogen (ISSH2'2017) that is going to be held in Algiers in November 26-27, 2017, is addressing some of the issues raised by the introduction of hydrogen as a sustainable energy vector and fuel.

The aim of this symposium is to provide a platform for exchange of technical information on the state of the art in the field, the disseminations of the new developments in the technologies of production, the storage and the use of hydrogen as an energy vector and the indications of the future directions and the priorities in hydrogen applications. It is also aimed at enabling discussion on the gained experiences, the provided opportunities, the encountered hurdles and the actions to undertake to ensure sustainable development.

This symposium proceedings book contains the refereed extended abstracts of most of the contributions that are going to be presented at the symposium ISSH2'2017. No distinction is made in these proceedings between oral or poster presentations.

In the name of the organizing committee, I would like to acknowledge the financial support of the UNESCO Algerian National Commission. We would like also to thank the International Association for Hydrogen Energy for their endorsement.

We would like to thank the participants for their contributions to the symposium and to the proceedings. We would also like to express our appreciation to the experts who have accepted our invitations to give plenary sessions. Special thanks go to Roger Sierens, professor at the University of Gent (laboratory of Transport Technology, Belgium) and John W. Sheffield, professor of Engineering Technology, Purdue University (USA) and IAHE executive Vice President.

The International Symposium on Sustainable Hydrogen (ISSH2) chairman
A. Khellaf, Ph.D.

Table of Contents

Existing and Future Options for Transport and Distribution of Renewable Hydrogen

John W. Sheffield, PhD

Professor of Engineering Technology
Executive Vice President, International Association for Hydrogen Energy
Senior Associate Editor, International Journal of Hydrogen Energy
Purdue University – USA

EXTENDED ABSTRACT

A review of existing and future options for the transport and distribution of renewable hydrogen provides insight into implementation strategies for Power-to-Gas (P2G) technology which uses renewable electricity to produce hydrogen. Specifically, variable renewable energy sources from wind and solar power are expected to meet an increasing share of the overall demand of electricity consumption. Thus, high variable renewable energy source penetration scenarios generally will require a combination of strategies to maintain electric power-grid reliability. The P2G storage technology offers the advantage of storing electricity in a multi-purpose energy carrier, hydrogen, for example can be used as fuel for transportation and also can be injected in the existing natural gas pipeline networks for transport and distribution. The common element of P2G is the electrolyser. The P2G technology offers different energy application "pathways" shown in Fig. 1 [1] that can be implemented gradually and incrementally, making efficient use of the power generation mix.

The P2G energy application "pathways" are as follows:

1. Power-to-Hydrogen-to-Natural Gas End-users via Hydrogen Enriched Natural Gas (P2HENG)
2. Power-to-Renewable Hydrogen enriched petroleum fuel (P2RHpetrol)
3. Power-to-Power (P2P)
4. Power-to-Gas as Seasonal Energy Storage-to-Electricity (P2Gses2E)
5. Power-to-Zero Emission Vehicle (P2zeV)
6. Power-to-Seasonal Storage for Vehicle (P2ssV)
7. Power-to-Renewable Natural Gas (RNG) to Pipeline via "Methanation" (P2RNG2pipeline)
8. Power to Renewable Natural Gas (RNG) to Seasonal Storage (P2RNG2ss)

Corresponding author email: jsheffie@Purdue.edu

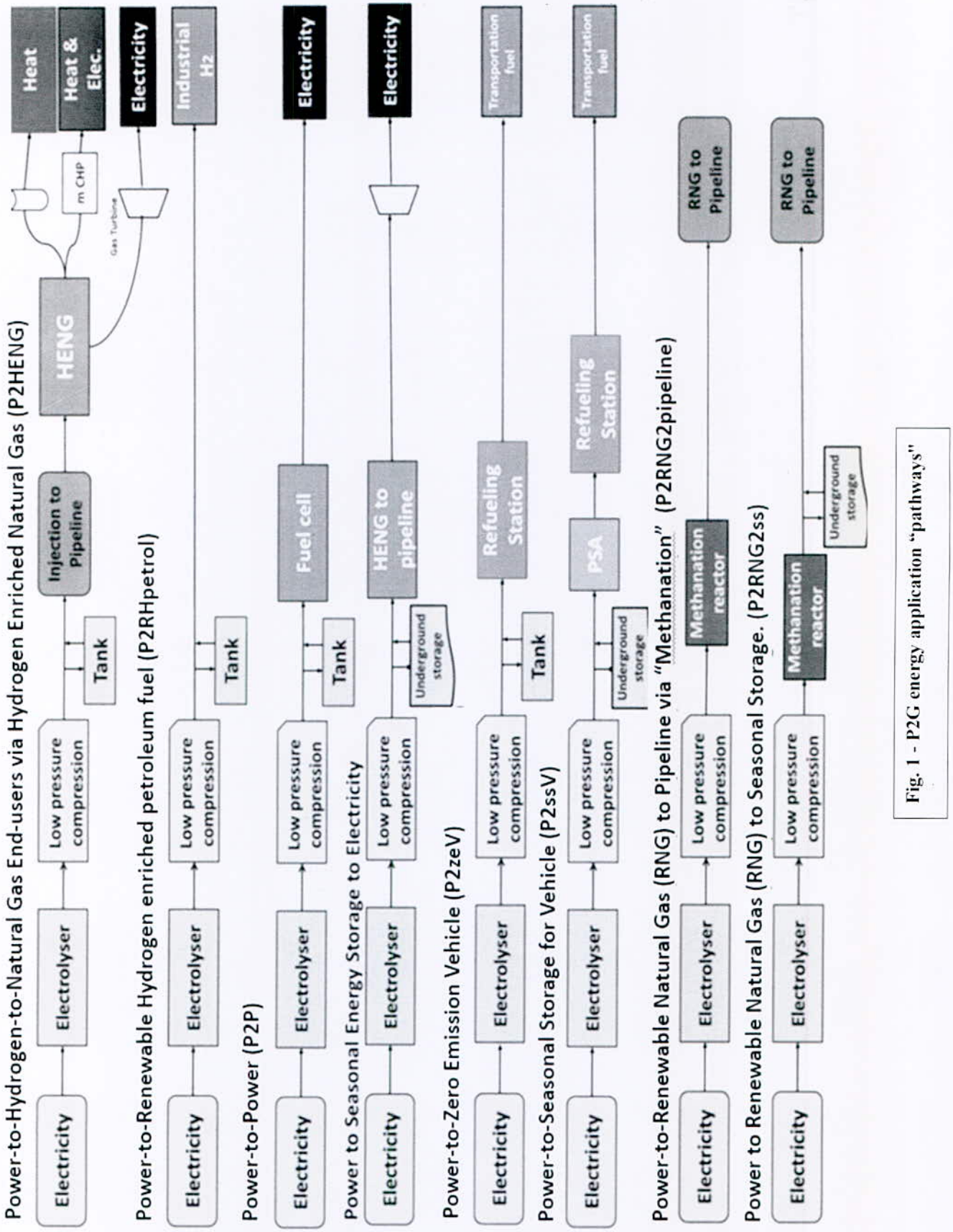

Fig. 1 - P2G energy application "pathways"

Corresponding author email: jsheffie@Purdue.edu

P2G ENERGY APPLICATION PATHWAY #1 [1]:

Power to Hydrogen to Natural Gas End-Users Pipeline Blending:

- ***Power to Hydrogen Enriched Natural Gas* (P2HENG)**

Hydrogen generated from excess electric power including renewable energies can be injected to natural gas pipelines to decarbonize natural gas via direct blending to make hydrogen-enriched natural gas (HENG). The electrolytic hydrogen which is produced by this method can be injected into the natural gas transportation or distribution pipelines, up to the certain limits. This limitation which is based on the fraction of the hydrogen allowable in the natural gas can be in the range of 5 to 20% for different applications. Note that even with these concentrations, there is a need to build and install many electrolysers. Moreover, hydrogen storage tanks are required as a buffer to balance the supply and demand of hydrogen. Since a part of grid electricity is from intermittent renewable energy, and due to the natural gas demand profile, there is need for energy storage systems. The optimum capacity of the storage systems is a challenging problem. Research results suggest that although considering the hydrogen storage systems' added complexity and more cost to the power-to-gas systems, they increase the performance of the whole system.

- **Key Technologies:** electrolyser, low-pressure compression, storage systems, transmission and distribution pipelines.
- **Qualitative Benefits:** This pathway requires minimal incremental investment and can address the immediate need for energy storage.
- **Technology Limitations and Outstanding Questions:** The allowable fraction of hydrogen in natural gas pipelines has several limitations. There are different key issues related to blending hydrogen into natural gas pipelines such as its effect on the (1) end-user systems, (2) safety and risk associated with blending hydrogen into natural gas, (3) durability of pipeline materials and leakage of hydrogen from pipelines.

1. **Effect on the end-user systems:** The effect of hydrogen blending into natural gas for end-user appliances namely, furnaces, boilers, and power generators depends on various factors including the natural gas composition, type of appliances or engine and their age. Acceptable limit for end-user application range between 5% and 20% of hydrogen, noting that higher hydrogen concentration may result in higher cost. Compression stations and compressed natural gas (CNG) tanks have a limitation of approximately 2% hydrogen concentration, while dried, compressed blended hydrogen permits up to 20% in natural gas for dispensing to CNG vehicles are favorable due to higher performance. Current installed gas turbines have a limitation of 1%, but hydrogen concentrations up to 5–15% can be attained with new adjustments and upgraded systems. Hydrogen content in gas engines is 2%, however, higher concentrations (up to 10%) are possible with simple control system upgrades.
2. **Safety and risk associated to blending hydrogen into natural gas:** Safety and risk analysis are two important issues that should be considered when blending hydrogen into natural gas pipelines that depend on the hydrogen concentration, pipeline types and material, as well as failure mode conditions. The main concern regarding the risk of blending hydrogen into natural gas pipelines is the possibility of ignition. Research indicate that natural gas systems enjoy a lower risk of severe accidents than large-scale power plants such as coal and nuclear, however, they pose a higher risk than renewable systems such as solar PV and wind. Moreover, the risk associated with the transmission and distribution pipelines may be different, for instance, the distribution systems should be reassessed for the severity of the explosion, when near urban areas. Research indicate that up to 20% of the hydrogen in a pipeline results in a minor increased ignition risk and in a case of natural gas leakage that results in explosion, there is a minor increase in the severity of the explosion. Certainly in the initial stages of implementation (and for many years) concentrations in the natural gas system will be well below 2%, and thus represent no significant risk increase over natural gas itself.
3. **Durability of pipeline materials:** The material of pipelines may degrade faster when hydrogen is blended into natural gas, especially at a higher pressure and higher concentrations of hydrogen. This can be an issue for blending high concentrations of hydrogen into transmission pipelines, while at the distribution level, hydrogen is not a major concern for the steel pipelines. Many materials such as ductile iron, cast, as well as polyethylene which are used for the distribution pipeline are compatible with hydrogen. Research indicate that fatigue and hydrogen embrittlement do not happen for concentrations up to a maximum of 10% hydrogen in natural gas for any type of material, thus once again in the initial stages of implementation no increase significant risks are anticipated. Leakage of hydrogen from pipelines: Hydrogen is lighter than methane and can leak from pipeline fittings. The permeation rate of hydrogen is 4

Corresponding author email: jsheffie@Purdue.edu

to 5 times faster than methane and it can permeate more from walls rather than joints. However, research indicates that up to 20% hydrogen in natural gas is needed in order to have the same order of the leakage.

REFERENCES

[1] Azadeh Maroufmashat and Michael Fowler "Transition of Future Energy System Infrastructure; through Power-to-Gas Pathways" by - Energies 10(8):1089 · July 2017

AUTHOR PROFILE

John W. Sheffield joined Purdue University in January 2015. He holds the title of Professor Emeritus of Mechanical and Aerospace Engineering from Missouri University of Science and Technology. Dr. Sheffield has a broad base of experience in energy technologies. He has served as one of the founding associate directors at the United Nations Industrial Development Organization - International Centre for Hydrogen Energy Technologies (UNIDO-ICHET) during their first two years of operation in 2005-2006.

He also served as the Associate Director of the National University Transportation Center at Missouri S&T. For more than thirty years, he has served as an editor of the International Journal of Hydrogen Energy. In August 2014, he completed a two-year assignment as a principal consultant at DNV GL - Energy supporting the evaluation, measurement and verification of energy efficiency programs and the response to the U.S. DOE Uniform Methods Project Protocol review of compressed air systems.

In August 2015, he completed a 7-week National Science Foundation Innovation Corps program as an industrial mentor for a potential startup company based on the manufacturing of bio-inspired bipolar plates for PEM fuel cells.

Corresponding author email: jsheffie@Purdue.edu

Hydrogen is Still the Fuel of the Future for IC Engines

Prof. dr. ir. Roger Sierens, Laboratory of Transport Technology, Ghent University, Belgium

ABSTRACT :

Hydrogen as a fuel in internal combustion engines (ICE's) is still a solution for the near future to realize zero CO2 emissions for traffic applications in spite of the competition with electrical vehicles and fuel cells. And the hydrogen fueled IC engine is ready for that competition. IC engines will not disappear in the next decades. The advantages and disadvantages are given briefly. Load control strategies for high power output and high efficiencies are discussed. Certainly for rotary (Wankel) engines hydrogen has its benefits. Recently the interest is mainly on direct injection hydrogen IC engines. But the storage and production of hydrogen and to build the necessary infrastructure, are the real shortcomings in the general use of hydrogen in IC engines. Finally a comparison with methanol is made and the use of hydrogen as a mixture fuel and as a storage medium is shown.

Keywords : hydrogen, IC engines, efficiency, power output, methanol, bi-fuel systems

I. Introduction

Hydrogen-fueled internal combustion engines (H2ICEs) are an affordable, practical and efficient technology to introduce the use of hydrogen as an energy carrier. They are practical as they offer fuel flexibility, furthermore the specific properties of hydrogen (wide flammability limits, high flame speeds) enable a dedicated H2ICE to reach high efficiencies, bettering hydrocarbon-fueled ICEs and approaching fuel cell efficiencies [1].

The easiest way to introduce H2ICE vehicles is through converting engines to bi-fuel operation by mounting a port fuel injection (PFI) system for hydrogen. However, for naturally aspirated engines this implies a large power penalty due to loss in volumetric efficiency and occurrence of abnormal combustion [2].

This presentation reports measurements on a single cylinder hydrogen PFI engine equipped with an exhaust gas recirculation (EGR) system and a supercharging set-up. The measurements were aimed at increasing the power output to gasoline engine levels or higher, while maximizing efficiency and minimizing emissions. Two strategies were tested: one using stoichiometric mixtures, with or without EGR, where a three way catalyst (TWC) was relied upon for aftertreatment of oxides of nitrogen (NOX); and a second one using lean mixtures limiting engine-out NOX emissions so that after treatment was not needed [3],[4].

Hydrogen is a versatile fuel that enables high efficiencies and low emissions of NOX (oxides of nitrogen) throughout the load range. However, there are lasting issues concerning its storage and distribution. Liquid methanol is more compatible with the existing fueling and distribution infrastructure and is easily stored in a vehicle. In addition, methanol can be synthesized from a wide variety of sources, including renewably produced hydrogen in combination with atmospheric CO2 [5], [6]. But before the possibilities of direct injection of hydrogen will be discussed and afterwards the use of hydrogen as a mixture fuel and as a storage medium.

II. Advantages and Disadvantages of Hydrogen as a Fuel for IC Engines

Figure 1 gives the flammability limits for different fuels at normal temperature and pressure (NTP).

As can be seen, the flammability limits (= possible mixture compositions for ignition and flame propagation) are very wide for hydrogen (between 4 and 75% hydrogen in the mixture) compared to gasoline (between 1 and 7.6%). This means that the load of the engine can be controlled by the air to fuel ratio, as for diesel engines. Nearly all the time the engine can be run with a wide open throttle, resulting in a higher efficiency.

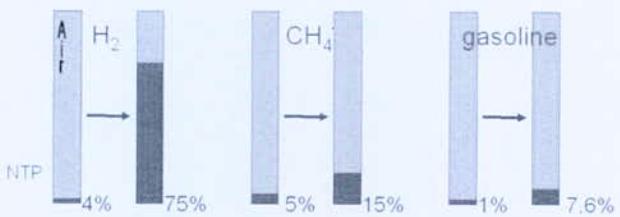

Figure 1. Flammability limits for air with hydrogen (H_2), air with natural gas (methane = CH_4) and air with gasoline

A second advantage of hydrogen for SI engines is the high burning velocity. For near-stoichiometric mixtures (near $\lambda = 1/\varphi = 1$) the combustion is almost a constant-volume combustion, which increases the (thermodynamic) efficiency. Also the properties of lean hydrogen flames will cause flame acceleration due to cellularity and no turbulence enhancing methods have to be used (swirl ports, etc.). Again this increases the efficiency of the engine.

Furthermore, hydrogen has a high octane number and the compression ratio of the engine can be increased. This, of

course, increases the efficiency. Finally the emissions of a hydrogen engine are very clean, only the noxious component NOX is emitted.

H2ICEs employing direct injection (DI) offer the highest potential in terms of power output, efficiency and emissions (see IV). The advantages of PFI compared to DI include a lower fuel system cost, the possibility of retrofitting engines and the widest choice in hydrogen storage technology (as only relatively low injection pressures are needed, compared to e.g. late DI). However, the low density of hydrogen implies a loss in power compared to, e.g., gasoline, due to the resulting lower volumetric energy density. At stoichiometric operation, hydrogen takes up about 30 vol % of the mixture, resulting in a theoretical power density decrease of 14% relative to gasoline.

With external mixture formation, backfire can be another factor limiting the power density. Backfire is the uncontrolled ignition of fresh mixture during the intake stroke, and is caused by the wide flammability limits, low required ignition energy and small quenching distance of hydrogen-air flames. Backfire can be a limit to the maximum richness of the mixture, with richer mixtures resulting in higher combustion and thus component temperatures which can lead to backfire. Thus, if backfire prevents the engine from running stoichiometric, this results in an additional power density decrease.

This has led to a number of different operating strategies for hydrogen PFI engines (see Section III). The wide flammability limits of hydrogen enable (very) lean burn operation, and load control by using a variable equivalence ratio and keeping the throttle wide open (WOT). Such a strategy is beneficial for the engine efficiency as it avoids pumping losses.

When people refers to Internal Combustion (IC) engines, this means nearly always reciprocating engines. But the rotary Wankel engine has real benefits for the use of hydrogen. With the high flame speed of hydrogen the flame will reach the far corner of the leading chamber (no unburned fuel as for a gasoline version). The hydrogen can be injected after the inlet port is closed (less change on backfire). Many studies have been done worldwide, Mazda of course, at the university of Canterbury, New Zealand and also at the Renewable Energy Development Center in Algiers [7],[8].

III. Load Control Strategies for Hydrogen

For atmospheric operation, limiting the air-to-fuel equivalence ratio to 2 results in a low power density, of the order of 50% relative to gasoline. Thus, strategies have been proposed using stoichiometric operation and relying on a three way catalyst (TWC) to reduce NOX emissions to acceptable levels. As mentioned above, at $\lambda = 1$ the power density at atmospheric operation is then limited to 86% relative to gasoline.

Increasing the power density to gasoline levels or higher can thus be done in two ways: either staying lean enough to avoid NOX formation and using supercharging; or using supercharging at $\lambda = 1$ with a TWC to limit tailpipe NOX. In the latter case, care must be taken to avoid abnormal combustion: supercharging increases pressures and temperatures and thus increases the likelihood of combustion anomalies. Diluting the charge with exhaust gas recirculation (EGR) is a possibility to decrease temperatures while still allowing stoichiometric operation.

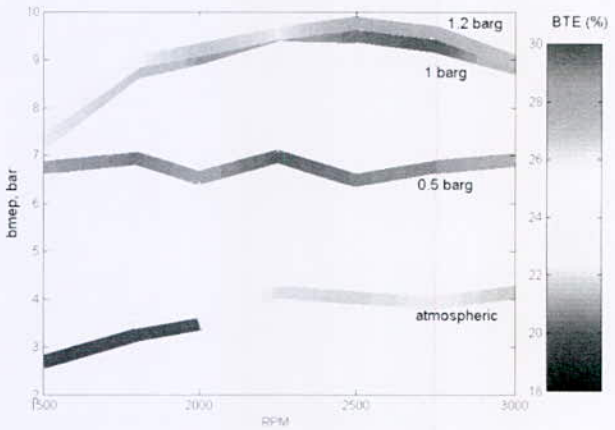

Figure 2. Net bmep and brake thermal efficiency (BTE) versus engine speed, as a function of charging pressure, for lean burn operation (engine-out NOX $\leq$ 100 ppm)

Lean-burn supercharged operation offers the possibility to obtain similar and even higher power output than conventional gasoline engines, with higher efficiencies and without any need for after treatment (Figure 2).

Stoichiometric operation offers the possibility to generate even more power when supercharging (Figure 3). The TWC can be activated if the exhaust temperature is above 500 °C but EGR is still needed to control the NOX formation. At low charging pressures, more EGR is needed than at high charging pressures due to insufficient exhaust temperature (especially at low RPM). At high charging pressures and low RPM, no EGR is required. Increasing the engine speed at high pressure on the other hand necessitates the use of EGR to stay below the tailpipe NOX limit.

The overall obtained brake thermal efficiency is lower than for supercharged lean-burn operation at a similar net power output. Higher power outputs could be reached if the engine withstands the high cylinder pressures, but results in lower efficiencies, see Figure 3.

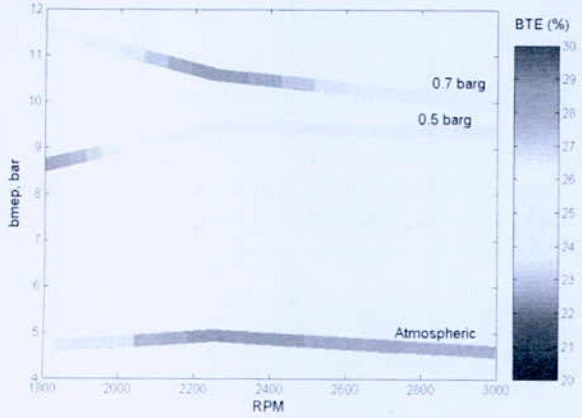

Figure 3. Net bmep and brake thermal efficiency (BTE) versus engine speed, as a function of charging pressure, for stoichiometric operation + TWC + EGR (tailpipe $NO_X \leq 100$ ppm)

It is concluded that supercharged lean-burn operation is the best option to obtain similar or even higher power output than a gasoline engine, with the advantage of higher efficiencies, the absence of an EGR-circuit and no need for aftertreatment. However, a NSR catalyst could be helpful for reducing the NOX-emissions so higher power output could be reached using $\lambda = 2$ at high charging pressure and engine speed, thus not having to operate at a leaner mixture which was necessary in the experiments reported here.

IV. DIRECT INJECTION OF HYDROGEN

Typically hydrogen direct injection is performed after the intake valves are closed to avoid displacement of intake air (reduced power) and backfiring. Hydrogen direct injection poses challenges due to injector leakage and durability [9]. Avoiding leakage of hydrogen at pressures in the range of 10 MPa with the injector nozzle exposed to combustion temperatures and pressures is everything but trivial. It is estimated that the injector tip of a hydrogen injector can easily reach 300 °C–400 °C.

Furthermore, hydrogen injectors for late direct injection and multiple injection applications are required to have a control range of up to 1 : 16 (ratio of minimum to maximum amount of fuel that can be delivered by a single injection) at minimum injection durations around 0.1 ms while operating at a complete absence of lubrication [10]. Life times of 200 hours are reported for current injector prototypes with a short term target to extend the durability to 1000 hours which would allow for multicylinder demonstrations. A longer term goal of 20 000 hours with a production-oriented design has also been targeted.

Hydrogen direct injection mixture formation systems can be classified based by injection strategy, injection pressure and number of injection pulses. Fig. 4 illustrates the most common hydrogen direct injection strategies graphically. Also the position of the injector is important [11].

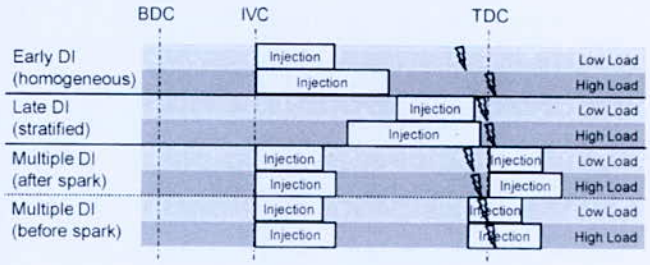

Figure 4. Schematic of H2 DI strategies

Early injection refers to strategies with start of injection (SOI) shortly after intake valve closing typically resulting in fairly homogeneous mixtures at spark timing. The required injection pressures for early injection are in the range of 0.5–2 MPa.

On the other hand, late injection against higher in-cylinder pressure at the end of the compression stroke requires higher injection pressures of up to 10 MPa and typically results in rather stratified mixtures. Finally, multiple injection strategies with pulses during the compression as well as the combustion phase require injection pressures between 10 and 30 MPa.

The mixture stratification that results from a late injection strategy can be exploited to improve the typical tradeoff between efficiency on the one hand and NOX emissions on the other hand.

V. METHANOL

Liquid alcohols, such as methanol, are largely compatible with the existing fueling and distribution infrastructure and are easily stored in a vehicle. Methanol can be produced from a wide variety of renewable sources (e.g. gasification of wood, agricultural by-products and municipal waste) and alternative fossil fuel based feed stocks (e.g. coal and natural gas).

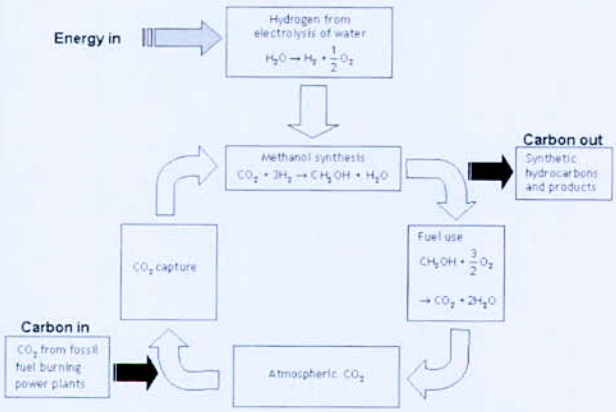

Figure 5. Production of methanol by captured $C0_2$

A number of works have even proposed a sustainable closed-carbon cycle where methanol is synthesized from renewable hydrogen and atmospheric CO2, thus forming a liquid hydrogen carrier (Figure 5). Light alcohols can be used in low-cost ICEs with only minor adjustments. Unlike many other alternative fuels, they have the potential to increase the engine performance and efficiency over that achievable with gasoline.

VI. HYDROGEN AS A MIXTURE FUEL (AND FUEL FLEXIBLE)

Some disadvantages of hydrogen can be partly solved by blends of hydrogen with a hydrocarbon fuel. Many combinations have been tested such as with natural gas (methane) [12], gasoline [13], ethanol and methanol, biogases and even diesel fuel [14]. This can be done as a real blend or or as an enrichment technique.

Mainly hydrogen-natural gas blends (HCNG) have been proposed as an alternative which can improve fuel economy and emissions of lean-burn natural gas engines since it has wider flammability limit and faster burning speed. And it could play a role of technical bridge for hydrogen era. For example the Indian government has chosen this direction.

Hydrogen-enriched natural gas mixtures are commonly named "Hythane" (a registered trademark of Hydrogen Consultants Inc.). Already at the end of the 90's extensive tests were done at the University of Gent on HCNG mixtures with variable proportions [12].

Next to this, ICEs have the interesting advantage of being fuel-flexible: they can be set up to allow the combustion of different fuels within the same engine. Inevitably this leads to compromises in the engine design, but having the option of switching to another fuel is a distinct benefit, especially for introducing a new fuel such as hydrogen into the market.

VII. HYDROGEN AS A STORAGE MEDIUM

Hydrogen is a means to chemically store energy. It can be used to buffer energy in a society increasingly relying on renewable but intermittent energy or as an energy vector for sustainable transportation [15],[16].

One of the options for converting intermittent renewable energy to storable energy, at times when energy supply exceeds demand, is to electrolyze water to hydrogen. However, hydrogen's potential as an energy storage medium for buffering renewable energy was not the main reason for the start of research on hydrogen vehicles. Work on hydrogen as an energy carrier for transport started for three other reasons. One is the reversible cycle, second is the diversity of energy sources that can be used to produce one and the same energy carrier, hydrogen.

Third is the possibility of achieving (near-) zero tailpipe emissions from hydrogen-fueled vehicles, eliminating or strongly reducing noxious emissions.

Hydrogen does offer a number of advantages compared to chemical storage of electricity in batteries (for road transport).

The first are the practical aspects: hydrogen has a far superior energy storage density than batteries, thus enabling much larger driving ranges, and refueling times are quite comparable to what we are used to today. A second advantage lies in the chemical sustainability and availability of chemical elements, as opposed to batteries.

VIII. CONCLUSIONS

The internal combustion engine is a sustainable power source. Hydrogen has high potentials as fuel for SI engines, mainly very high efficiencies and nearly negligible noxious and CO2 emissions. But the storage on a vehicle and the infrastructure to build a hydrogen economy are real disadvantages

Recent research activities with hydrogen direct injection suggest that peak engine efficiencies around 45% are achievable.

The three main reasons for a hydrogen economy to be so desirable consider that a) a reversible cycle can be established, with hydrogen made from water and turning back into water when used; b) a variety of (renewable) sources can be used to make hydrogen, and c) the conversion of hydrogen into other forms of energy results in (near-) zero emissions.

Although further development for hydrogen internal combustion engines is needed in several areas including development of injection equipment that meets automotive durability requirements, as well as assessment of efficiency potential of advanced mixture formation concepts on multicylinder engines

Due to lack of space for this abstract, experimental results on hydrogen direct injection, comparison with methanol and hydrogen fuel blends will be shown at the presentation.

REFERENCES

[1] S. Verhelst and T. Wallner, "Hydrogen-fueled internal combustion engines", *Progress in Energy and Combustion Science*, doi:10.1016/j.pecs.2009.08.001, 2009.

[2] S. Verhelst, R. Sierens, S. Verstraeten, "A critical review of experimental research on hydrogen fueled SI engines", SAE Technical Paper 2006-01-0430 (2006). Also in SAE 2006 Transactions, Journal of Engines, pp. 264-274.

[3] S. Verhelst, P. Maesschalck, N. Rombaut, and R. Sierens, "Increasing the power output of hydrogen internal combustion engines by means of supercharging and exhaust gas recirculation", *Int J Hydrogen Energy* **34**:4406-4412, 2009.

[4] A.M. Nande, S. Szwaja, J.D. Naber, "Impact of EGR on Combustion Processes in a Hydrogen Fueled SI Engine", SAE Technical Paper 2008-01-1039, 2008 .

[5] R.J. Pearson, J.W.G. Turner, and A.J. Peck, "Gasoline-ethanol-methanol tri-fuel vehicle development and its role in expediting sustainable

organic fuels for transport", presented at IMechE Low Carbon Vehicles Conference, London, UK, 2009.

[6] T. Wallner and R. Frazee, "Study of Regulated and Non-Regulated Emissions from Combustion of Gasoline, Alcohol Fuels and their Blends in a DI-SI Engine", SAE paper no. 2010-01-1571, 2010.

[7] "Overview of Mazda hydrogen vehicles", presented at the DOE Hydrogen and Fuel Cell Technical Advisory Committee (HTAC)

[8] F. Amrouche, P. Erickson, J. Park, S. Varnhagen, "Extending the lean operation limit of a gasoline Wankel rotary engine using hydrogen enrichment", Int. J. Hydrogen Energy, 41 (32), 14261-14271, 2016.

[9] S Verhelst, "Recent progress in the use of hydrogen as a fuel for internal combustion engines", Int. J Hydrogen Energy, 39, 1071-1085, 2014.

[10] S. Verhelst, T. Wallner, H. Eichlseder, , K. Naganuma, F. Gerbig, B. Boyer and S.Tanno, "Elelctricity Powering Combustion Engines", Proceedings of the IEEE, Vol. 100, n° 2, Febr. 2012.

[11] M.H. Zulhafli, M.R. Mansor, "The effect of injector position on direct injetion hydrogen engine conditions", Journal of Eng. Science and Technology, June (2015), 55-61.

[12] R. Sierens, E. Rosseel, "Variable composition hydrogen/natural gas mixtures for increased engine efficiency and decreased emissions", Journal of Engineering for gas turbines and power, Transactions of the ASME, January 2000, Vol. 122, p. 135-140.

[13] N.S. Gandhi et all., "Gasoline-hydrogen operated SI engine and its performances analysis", Int. Journal of Research in Eng. And Technology, Vol. 04, issue 02, Febr. 2015.

[14] C. Dhanasekaran, G. Mohankumar, "Hydrogen as a fuel in direct injection diesel engine", Journal of Inst. Of Engineers (India), ser C (2016), 97:157.

[15] "Hydrogen as a storage medium – facilating increased integration of RES", European Commission, SETIS (Strategic Energy Technologies Information System), August 2015.

[16] J. Töpler, "Hydrogen as energy-storage-medium and fuel – a strong partner of renewable energies", Renew. Energy Environ. Sustain., 1 (2016), 31.

AUTHOR PROFILE

Roger Sierens is professor at the University of Gent, Belgium and previous chairman of the department of Flow, Heat and Combustion Mechanics and director of the Laboratory of Transport Technology.

He obtained several awards: Dugald Clerk Prize (Inst. of Mechanical Engineers, England), Erskine Fellowship (New Zealand), I.Akerman Prize (Atlas Copco), Professor Onorific (Romania), Outstanding Scientific achievement award by the Int. Association for Hydrogen Energy, Dr.HC university of Havana (CUJAE) and published nearly 200 international papers on IC engines.

Evaluation de la Production d'Hydrogène par deux Technologies Photovoltaïques

N. Kabouche*, F. Meziane, I. Nouicer and R. Bouderies

Centre de Développement des Energies Renouvelables, (CDER), B.P. 62, Route de l'Observatoire, 16340, Bouzaréah, Alger, Algérie.

Résumé—**Le but de ce travail est d'évaluer la production d'hydrogène en utilisant deux technologies photovoltaïques. La première technologie consiste en un système photovoltaïque à base de module monocristallin (cellule à simple jonction). La seconde technologie consiste en un système photovoltaïque à haute concentration à base de cellules triple jonction. La puissance nominale choisie pour chaque système étudier est de 5.2 kW. Comme le second système nécessite une poursuite du rayonnement direct, et pour avoir une comparaison équitable un traqueur à deux axes est considéré pour les deux cas. En raison de quelques paramètres (un coefficient de concentration inférieur à 500, le rendement optique des lentilles et la conversion du rayonnement direct seulement), la production d'hydrogène par le second système était 25.8% moins que celle du premier.**

Mots-clés—Electrolyseur alcalin, Rayonnement solaire global, Rayonnement solaire direct, Photovoltaïque, Concentrateur photovoltaïque,

I. INTRODUCTION

Les problèmes environnementaux causés par les sources d'énergies fossiles ainsi que leur épuisement ont élargi l'utilisation des sources d'énergies propres et renouvelables. Cependant, l'intermittence de ces sources, sur et sous-production, nécessitent des systèmes de stockage adéquats. Pour cette raison, plusieurs procédés de stockage (mécanique, électrochimique, chimiques, etc.) de l'énergie excédentaire existent. Ces systèmes de stockage sont inévitables pour combler l'écart de temps entre la production et la consommation d'énergie. La conversion de l'excès de l'énergie en gaz "*Power to gas*", hydrogène ou méthane, prend une place importante dans la transition énergétique mondiale. L'excès de l'électricité est injecté dans un électrolyseur pour produire de l'oxygène et du dihydrogène. Le gaz, hydrogène, produit peut être stocké à haute pression, injecté dans le réseau du gaz naturel, utilisé comme carburant dans des moteurs ou converti en électricité via des piles à combustibles. La solution "*Power to gas*" peut être utilisée pour stocké l'excès d'énergie ou même convertir complètement cette énergie renouvelable en gaz, ainsi de nombreuses installations pilotes existent [1].

Le stockage de l'excès d'électricité produite à partir de l'énergie solaire seule ou combinée avec d'autres sources renouvelables est largement utilisé [1]. En effet, l'énergie solaire peut être convertie en énergie thermique puis en électricité via les centrales solaires thermodynamiques à concentration ou directement en électricité via les modules photovoltaïques (PV). La combinaison de la concentration solaire, lentilles et miroirs, et des cellules PV à triple jonction a conduit à la technologie photovoltaïque à concentration (CPV). Comparé à la technologie PV classique la technologie CPV présente plusieurs avantages comme la captation d'un large spectre solaire, un meilleur rendement ainsi que l'utilisation de matériaux moins onéreux [2].

Dans ce travail on évalue le taux de production d'hydrogène dans un site Algérien en utilisant les deux technologies, 16 modules PV monocristallin et 10 modules CPV à lentilles, couplé à 4 cellules d'électrolyse alcaline connectées en série et d'une puissance maximale d'environ 5 kW. Le logiciel SAM "*System Advisor Model*" a été utilisé pour déterminer l'énergie produite par ces deux systèmes.

II. DESCRIPTION DU SYSTEME ET DU SITE

Les deux systèmes étudiés se composent d'une source d'énergie (PV ou CPV) d'environ 5.2 kW, d'un traqueur double axe (l'un des principaux composants du système CPV, pour le PV il est utilisé pour avoir une comparaison équitable), d'un électrolyseur alcalin de quatre cellules (0.25 m^2 par cellule). Un dispositif MPPT (*Maximum Power Point Tracking*) ainsi qu'un convertisseur DCDC entre le CPV ou le PV et l'électrolyseur sont considérés. Le module PV étudié est le *SolarWolrld SW 325 XL mono* de 325 Wc, le module CPV est le *Arima CPV G1* de 520 Wc et un coefficient de concentration de 476X (voir tableau II).

1. Site et Données Météorologiques

Le site d'étude, Bechar (31.6°N, -2.23°E, 772m), est situé dans le sud-ouest de l'Algérie. Bechar est caractérisé par un climat continental, chaud en été et froid en hiver avec des précipitations fluctuantes. Le choix de ce site, parmi 23 sites répartis sur le territoire Algérien, est à cause de son meilleur gisement solaire selon Meteonorm. En fait, en considérant simultanément, le rayonnement solaire global et le rayonnement solaire direct, le site de Béchar était à la première place, légèrement meilleur que les sites d'In Aminas et de Tamanrasset. Sur la Fig. 1, sont reportées les données journalières pendant un an du rayonnement solaire direct et du rayonnement global pour une poursuite à double axes. Ces données sont calculées à l'aide du logiciel *SAM* et des données de Meteonorm.

*Corresponding author email: n.kabouche@cder.dz

Ainsi le rayonnement annuel capté par un traqueur double axe est d'environ 16.5MW/m² pour le global et environ 12 MW/m² pour le direct.

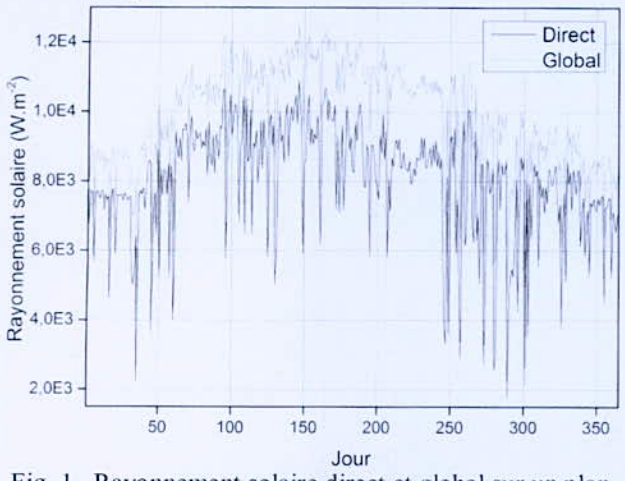

Fig. 1. Rayonnement solaire direct et global sur un plan avec une poursuite double axes

2. *Electrolyseur Alcalin*

Vue sa simplicité et son coût réduit l'électrolyse alcaline est largement utilisée pour la production d'hydrogène à l'échelle industrielle. Cependant, sa pression de fonctionnement et sa densité de courant sont limitées [5]. Le passage d'un courant électrique continu de l'anode à la cathode, séparées par un électrolyte aqueux, permet la décomposition de l'eau en hydrogène et en oxygène. La réaction globale est décrite dans l'équation (1) :

$$H_2O(l) + Energie \rightarrow H_2(g) + 1/2\,O_2(g) \quad (1)$$

La tension électrique minimale, V_{rev}, nécessaire pour le démarrage de cette réaction est donnée par l'équation de Gibbs (2) :

$$V_{rev} = \Delta G_{nn}/nF = 1.229V \quad (2)$$

En prenant les surtensions d'activation et ohmique en considération augmentent la tension électrique requise pour l'électrolyse de l'eau devient :

$$V = V_{rev} + V_{act} + V_{ohm} \quad (3)$$

Ainsi la caractéristique V-I d'une cellule d'électrolyse alcaline en fonction de la température est donnée par Ulleberg [3] par :

$$V = V_{rev} + \frac{r_1 + r_2 t}{A} I_E + \left(S_1 + S_2 T + S_3 T^2\right) \log\left[\frac{t_1 + t_2/T + t_3/T^2}{A} I_E + 1\right] \quad (4)$$

TABLEAU I
PARAMETRES DU MODELE D'ELECTROLYSEUR [4]

Symbole	Valeur	Symbole	Valeur
V_{rev} (V)	1.229	S_2 (V°C^{-2})	-1.606 10^{-5}
r_1 (Ωm²)	7.331 10^{-5}	A (m²)	0.25
r_2 (Ωm²/°C)	-1.107 10^{-7}	t_1 (m²/A)	1.599 10^{-2}
S_1 (V)	0.1586	t_2 (m² °C/A)	-1.302
S_2 (V/°C)	1.378 10^{-3}	t_3 (m² °C²/A)	421.3

Le taux de production d'hydrogène est donné en fonction du courant traversant la cellule d'électrolyse, I_E, et le rendement Faradique, n_F, par :

$$\dot{n}_{H2} = \frac{n_F . N_c . I_E}{n.F} \quad (5)$$

Avec N_c, n, F sont respectivement le nombre de cellule d'électrolyse, le nombre d'électrons nécessaire pour l'électrolyse d'une molécule d'eau et la constante de Faraday (A.s. mol^{-1}).

3. *Système Photovoltaïque*

SAM propose cinq modèles pour la modélisation du module PV. Nous avons choisi le modèle de performance CEC (*California Energy Commission*). Il s'agit d'une implémentation du modèle à six paramètres [6], qui est une extension du modèle à cinq paramètres [7]. La température de fonctionnement de la cellule PV est déterminée à l'aide du NOCT (température de fonctionnement nominale de la cellule) [8]. Les paramètres du module PV choisi sont reportés dans le tableau II.

4. *Système Photovoltaïque à concentration*

La technologie CPV vise à réduire le matériau semi-conducteur des cellules PV par des dispositifs optiques économiques. Ces dispositifs permettent de concentrer la lumière sur des cellules PV petites et très efficaces. Les systèmes CPV présentent des avantages (une haute efficacité à des températures élevées, des surfaces de cellules PV réduites…) et des inconvénients (complexité de la fabrication, nécessitent un rayonnement direct, utilisation des cellules multi-jonction chères…) [2]. Selon le dispositif optique ou le type de concentrateur on distingue les CPV à lentilles Fresnel, les CPV paraboliques, les CPV cylindro paraboliques, les CPV hyperboloïdes. Les lentilles de Fresnel, avec leurs faibles coûts, volumes, et poids sont largement utilisées [9]. Les paramètres du module CPV choisi sont reportés dans le tableau II.

*Corresponding author email: n.kabouche@cder.dz

TABLEAU II
CARACTERISTIQUES DES MODULES PV ET CPV

Paramètre	PV	CPV
Nombre de cellule	72	144
Pm @STC (Wc)	325	520
V_{oc} (V)	46.1	445
I_{sc} (A)	9.48	1.465
V_m (V)	37	390
I_m (A)	8.84	1.333
Surface (m^2)	1.587	2.755
Type de cellule	Mono cristallin	3 Jonctions

5. *Dimensionnement des systèmes*

La puissance électrique de N_C cellules PV est donnée par l'équation (6).

$$P = N_C . I_C . V_C \tag{6}$$

Avec I_C, V_C sont le courant et la tension d'une cellule.

I_C peut être donné par le modèle à une diode que ce soit pour la cellule PV ou CPV, dans le second cas il faut prendre l'effet de la concentration en considération.

Ainsi la puissance au point de puissance maximum est donnée par :

$$P_{mppt} = \eta_{mppt} N_C . I_{mppt} . V_{mppt} \tag{7}$$

Le nombre de cellules d'électrolyse (N_{CE}), taille de l'électrolyseur, prisent en série est donné donc comme :

$$N_C = \frac{\eta_{DCDC} . P_{max}}{I_{E\,max} . V_{E\,max}} \tag{8}$$

η_{DCDC}, P_{max}, I_{Emax}, V_{Emax} sont respectivement le rendement du convertisseur DCDC, la puissance maximale du générateur, 5.2 kW, et les valeurs maximales de la tension et du courant d'une cellule d'électrolyse 1,8 V et 750 A [3], [4].

III. RESULTATS

1. *Systèmes PV et CPV*

L'énergie journalière produite par les deux systèmes, PV et CPV, est représentée sur Fig. 2. L'énergie annuelle produite par le système PV est de 15732.1 kWh et une moyenne journalière de 43.14 kWh. L'énergie annuelle produite par le système CPV est de 11349.4 kWh (légèrement supérieur à la production d'un système PV incliné à la latitude de Bechar qui est de 11282.3 kWh/an) et une moyenne journalière de 31.11 kWh. La figure montre que le système PV produit toujours plus d'énergie que le système CPV. Cette différence est due au fait que le traqueur à deux axes capte le maximum de rayonnement global qui est toujours supérieur au rayonnement direct ainsi qu'aux différentes pertes qui caractérisent les modules CPV.

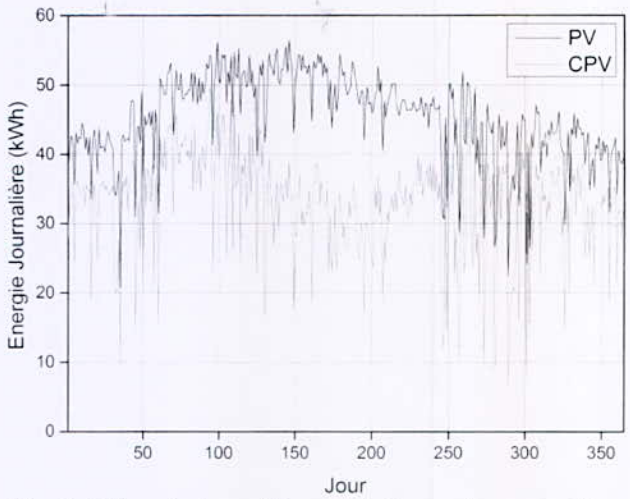

Fig. 2. L'énergie journalière produite par chaque système

2. *Production d'hydrogène*

Le taux de production, journalier et mensuel, d'hydrogène par les deux systèmes est représenté respectivement sur Fig. 3 et Fig. 4. Pour le système PV la production d'hydrogène est presque stable et au-dessus de la moyenne annuelle au printemps et à l'été. Par contre, pour le système CPV la variabilité de la production d'hydrogène est forte le long de l'année, elle dépasse la moyenne annuelle dans le printemps, au mois d'aout et au mois de novembre. Dans les deux cas la production d'hydrogène est minimale au tour de l'hiver. La variabilité dans le cas du CPV par rapport au PV est due à la variabilité du rayonnement direct sensible aux aérosols et à l'humidité de l'air.

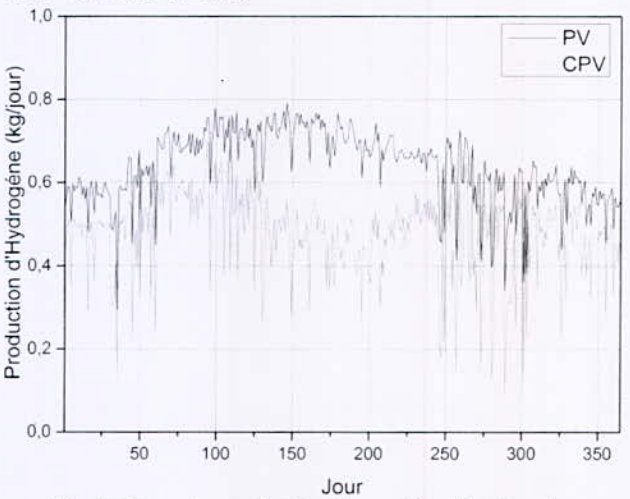

Fig. 3. Taux de production journalier d'hydrogène

La production annuelle d'hydrogène est estimée à 233.84 kg dans le cas du PV et de 173.54 kg dans le cas du CPV, soit 25.78% en moins, malgré une surface de module 8.46% supérieure pour le CPV. Cette différence est due au fait que les modules CPV n'exploitent que le rayonnement direct qui est de 18.63% moins que le rayonnement global exploité par les modules PV, un coefficient de concentration de 476X et un rendement

*Corresponding author email: n.kabouche@cder.dz

optique de 72.5%. Le rendement optique est un facteur qui caractérise les pertes optique dues aux lentilles Fresnel (absorption et dispersion de certaines longueurs d'onde), il est toujours inférieur à 100%.

Cependant, comme le montre Fig. 5, un rendement optique de 90% permet une augmentation de 19.4% de l'énergie annuelle produite par les modules CPV. De plus un taux de concentration de 800X permet un accroissement de 40.5% dans l'énergie annuelle des modules CPV soit 23855,6 kWh. Le second cas est pratiquement accessible puisque des modules à un taux de concentration de 1000X existent.

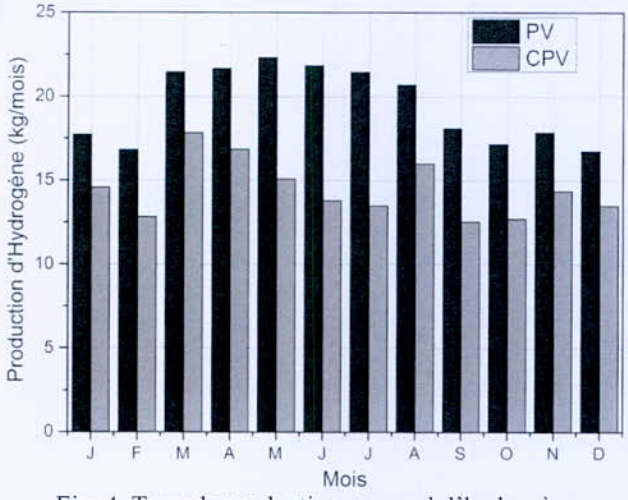

Fig. 4. Taux de production mensuel d'hydrogène

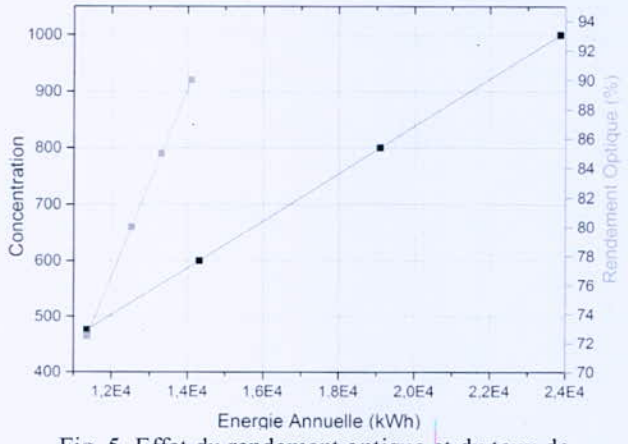

Fig. 5. Effet du rendement optique et du taux de concentration sur l'énergie annuelle du CPV

IV. CONCLUSION

Dans ce travail nous nous sommes intéressés à l'évaluation de production d'hydrogène par deux technologies photovoltaïques, mono cristallin PV classique et multi jonctions à haute concentration HCPV, dans un site Algérien bien choisi. Le logiciel libre SAM (*system Adivisor Model*) développé par NREL est utilisé pour évaluer l'énergie produite par ces deux technologies, deux systèmes de 5.2 kWc chacun. Comme le HCPV nécessite un traqueur à deux axes et afin d'avoir une comparaison juste le même traqueur est considéré pour le PV.

Les résultats ont montré que le système PV produit annuellement 25.78% d'hydrogène plus que le système HCPV à cause d'une exploitation d'une seule partie de rayonnement (le direct seulement), un faible rendement optique de lentille et un taux concentration inferieur à 500X. Il a été trouvé que pour concurrencer le système PV un rendement optique et/ou un taux de concentration plus élevés sont inévitables. En effet il faut un taux de concentration supérieur à 650X. Comme perspective une étude comparative avec d'autres sites ainsi que l'étude d'un système de stockage peuvent être effectuées. De plus, afin d'une validation expérimentale de ces résultats de simulation une mise en place d'un prototype est nécessaire.

REFERENCES

[1] G. Gahleitner, "Hydrogen from renewable electricity : An international review of power-to-gas pilot plants for stationary applications," Int. J. Hydrogen Energy, vol. 38, no. 5, pp. 2039–2061, 2012.

[2] C. Renno and F. Petito, "Design and modeling of a concentrating photovoltaic thermal (CPV/T) system for a domestic application," Energy Build., vol. 62, pp. 392–402, 2013.

[3] Ø. Ulleberg, "Stand-alone power systems for the future: optimal design, operation and control of solar-hydrogen energy systems," University of Science and Technology Trondheim, 1998.

[4] M. Burhan, K. Jon, E. Chua, and K. Choon, "Sunlight to hydrogen conversion : Design optimization and energy management of concentrated photovoltaic (CPV-Hydrogen) system using micro genetic algorithm," vol. 99, 2016.

[5] R. Boudries, "Techno-economic study of hydrogen production using CSP technology," Int. J. Hydrogen Energy, pp. 1–12, 2017.

[6] A. P. Dobos, "An Improved Coefficient Calculator for the California Energy Commission 6 Parameter Photovoltaic Module Model," J. Sol. Energy Eng., vol. 134, no. 2, 2012.

[7] W. De Soto, S. A. Klein, and W. A. Beckman, "Improvement and validation of a model for photovoltaic array performance," Sol. Energy, vol. 80, pp. 78–88, 2006.

[8] J. A. Duffie and W. A. Beckman, Solar Engineering of Thermal Processes, John Wiley. 1991.

[9] M. Khamooshi, H. Salati, F. Egelioglu, A. H. Faghiri, J. Tarabishi, and S. Babadi, "A Review of Solar Photovoltaic Concentrators," Int. J. Photoenergy, vol. 2014, 2014.

*Corresponding author email: n.kabouche@cder.dz

First Principle Study of Hydrazine Borane and Its Alkali Metal Derivatives for Hydrogen Storage

Y. Bouhadda[1*], K. Benyelloul[1], A. Aichouche[2], B. Bentria[2]

[1]Unité de Recherche Appliquée en Energies Renouvelables, URAER, Centre de Développement des énergies Renouvelables, CDER, 47133 Ghardaïa, Algeria.

[2]Laboratoire de physique des matériaux, Amar Telidji University of Laghouat, BP 37G, Laghouat 03000, Algeria

Abstract—**we investigated the crystal structure and electronic of hydrazine of the alkali metal derivatives of hydrazine borane, i.e. sodium hydrazinidoborane $NaN_2H_3BH_3$ and potassium hydrazinidoborane $KN_2H_3BH_3$, using first-principle methods based on density functional theory with generalized gradient approximation. The computed equilibrium lattice constants are in excellent agreement with the available experimental and theoretical data. The calculated density of state indicated that $N_2H_4BH_3$ has a wide band gap with a value equal to 5.78 eV. Also, $KN_2H_3BH_3$ and $NaN_2H_3BH_3$ have a wide band gap: 4.36 eV and 4.35 eV respectively. These materials can be considered as an insulator. This indicated that the substitution of one hydrogen atom from hydrazine borane by alkali atom Na or K could reduce the gap between conduction band and valence band. The alkali (K and Na) atoms contributed less to the DOS of $NaN_2H_3BH_3$ and $KN_2H_3BH_3$ respectively. To our best of knowledge, there are no previous experimental or theoretical works on the gap energy of $NaN_2H_3BH_3$ and $KN_2H_3BH_3$. We hope our work could provide a useful reference for future study.**

Key words—Hydrogen storage, hydrazine borane, DFT, gap energy, density of states.

I. INTRODUCTION

Hydrogen seems to be the perfect candidate as a clean energy carrier (for both mobile and stationary applications) replacing fossil fuels [1]. However, the widespread use of hydrogen as fuel requires the development of a safe, reliable and cheap method for its transportation and storage. The storage of hydrogen-based material hydride, also known as storage in solid form, is very safe. It also offers significant improvements in terms of weight and costs [1].

Among many criteria for perfect solid hydrogen storage material, good hydrogen sorption kinetics and light weight has always been the main defies to be surmounted. Some boron- and nitrogen-containing materials are attractive hydrogen-dense compounds because they can satisfy the above criteria (sorption kinetics and light weight). Among them, Ammonia borane, NH_3BH_3, which has a hydrogen capacity of 19.6 wt.%, exceeding that of gasoline, has made itself an attractive candidate for chemical hydrogen storage applications [2], but the hydrogen release from solid Ammonia borane is not fast enough and includes the reaction byproduct borazine, which can damage a fuel cell.

Another candidate is $N_2H_4BH_3$ (hydrazine borane, HB) solid with 15.4 wt% hydrogen capacity, which can release 5.8 wt% H_2 at 140 °C in 12 min [3] and can yield 11 wt% H_2 at 150 °C in less than an hour after mixing with LiH, has attracted more attention and has been experimentally studied as one novel B-N-based material for hydrogen storage through different routes, such as thermal decomposition, hydrolysis, etc… [4-8]. This material can be easily prepared from a reaction of dihydrazine sulfate with sodium borohydride [3].

However, the decomposition of $N_2H_4BH_3$ is an exothermic process, and its dehydrogenation is accompanied by emission of N_2H_4 and NH_3 which can damage a fuel cell. But, Hydrazine Borane has not been eliminated as a candidate solid-state chemical hydrogen storage material because it can be chemically modified towards formation of derivatives [3].

Improving this kind of material for practical and reliable uses requires an understanding of the fundamental physical phenomenon such as electronic interaction between atoms, vibration and phonons ...etc. Besides that, no experimental or theoretical data about electronic structure and chemical bond nature of hydrazine borane and its alkali metal derivatives are available. They have a significant role in determining various material properties such as phase transition, thermodynamic stability, transport and thermal properties.

In this work, we investigated the crystal structure and electronic of hydrazine of the alkali metal derivatives of hydrazine borane, i.e. sodium hydrazinidoborane $NaN_2H_3BH_3$ and potassium hydrazinidoborane $KN_2H_3BH_3$, using first-principle methods based on density functional theory with generalized gradient approximation.

II. THEORETICAL METHODS

In this study, all the computations have been done using the ABINIT code [9] based on pseudopotentials and planewaves in density functional theory (DFT) [10]. We used as exchange and correlation energy the generalized gradient approximation (GGA-PBE) [11]. Fritz–Haber–Institute GGA pseudopotentials [12] are used to represent the electronic atomic. An energy cut-off of 70 Hartree and a 6x6x6 grid for k-point were used after a carefully tests

*Corresponding author email: bouhadda@yahoo.com

of the convergence of our calculations with respect to the plane-wave cut-off and k-point mesh

III. RESULTS AND DISCUSSION

1. Crystal structure

$N_2H_4BH_3$ has an orthorhombic structure with the space group Pbcn (No 60) [13]. It has 80 atoms and contains one occupation sites of each atom (*8d*) (with 8 formula unit of HB). Also, $NaN_2H_3BH_3$ has a monoclinic structure with the space group P2_1/c (N° 14; β=115.17°) [13]. It has 40 atoms and contains one occupation sites of each atom (*4e*) (with 4 formula unit of NaHB). While, $KN_2H_3BH_3$ has a monoclinic structure with the space group P2_1 (N° 4; β=108.28°) [13]. It has 20 atoms and contains one occupation sites of each atom (*2a*) (with 2 formula unit of KHB).

To generate one hydrazine borane (HB) molecule, each hydrazine unit N_2H_4 is connected terminally to one BH_3 group which is locating in one side of the N-N bond. It can be considered as a derivative of ammonia borane where the NH_3 moiety is substituted by N_2H_4.

In same description, each hydrazine unit NaN_2H_3 (/KN_2H_3) connected terminally to one BH_3 group to generate one $NaN_2H_3BH_3$ (/$KN_2H_3BH_3$) molecule, with the BH_3 groups locating in one side of the N-N bond. It can be considered as a derivative of HB where NaN_2H_3 (/KN_2H_3) substitutes the N_2H_4 moiety.

We did a crystal geometry optimization and we relaxed the atomic positions; this relaxation lowered the total energy. The final structure obtained within the PBE GGA approximations is given for HB, NaHB and KHB respectively. The deviation from the experiment [13] is less than 0.75%. Also our results are more accurate than the theoretical calculations of Quin et al [2] for HB using the projector augmented wave (PAW) with the generalized gradient approximation (GGA) [2]. However, no theoretical studies performed on the crystal structure of NaHB and KHB have found to compare with our present study.

2. Electronic structure

The electronic structure is investigated to understand the bonding properties of hydrides and further reveal the mechanism about structural stability. We have plotted the total and the partial density of states (PDOS) of HB, NaHB and KHB each atom in Fig. 1, Fig. 2, Fig. 3, Fig. 4, Fig. 5 and Fig. 6 respectively. The calculated DOS (Fig. 1) indicated that $N_2H_4BH_3$ has a wide band gap with a value equal to 5.78 eV little greater than the calculated gap reported by Quian et al. [2]. Also, $KN_2H_3BH_3$ (Fig.2) and $NaN_2H_3BH_3$ (Fig.3) have a wide band gap: 4.36 eV and 4.35 eV respectively. These materials can be considered as an insulator. This indicated that the substitution of one hydrogen atom from HB by alkali atom Na or K could reduce the gap between conduction band and valence band. Our calculated band gaps are equal or smaller than the reel gap, due to the well-known band-gap underestimation in density functional theory calculations [1].

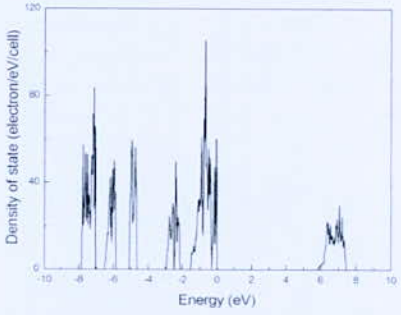

Fig. 1. The calculated total electronic density of states (DOS) for HB solid. The Fermi level is set at zero energy

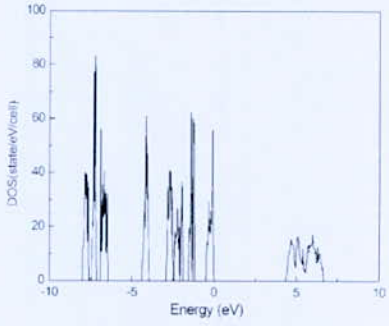

Fig. 2. The DOS for KHB solid. The Fermi level is set at zero energy

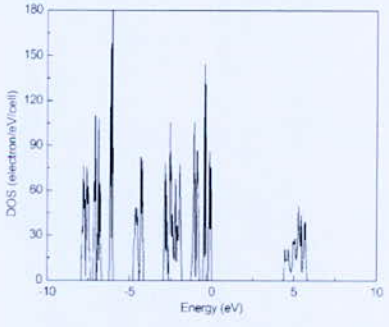

Fig. 3. The DOS for NaHB solid. The Fermi level is set at zero energy

To our best of knowledge, there are no previous experimental or theoretical works on the gap energy of NaHB and KHB. Fig.4 shows the calculated partial DOS, for HB in the solid state. It can be seen that the total DOS of HB consists of two well-separated regions: the region above 5.7 eV (conduction band) and the region below 0eV (region of valence band). This latter is also separated into two regions: the region from -2 eV to 0 eV (top of the valence band) and the region below -2 eV (lower energy region of valence band). The PDOS (fig. 4) shows that the

*Corresponding author email: bouhadda@yahoo.com

electronic density of states close to the Fermi level (between -2 and 0 eV) is mainly dominated by the B p-states, N p-states (especially the N2 atom) and hydrogen atoms associated with B atom (H1, H2 and H3). However, in the region below -2 eV, is mainly dominated by the N p-states and the hydrogen atoms associated with the two N atoms (H4, H5, H6 and H7). The strong sp hybridization between B and H (connected to B) and between N and H (connected N) in the valence band causes the strong bonding occurring between B and H (B) and between N and H (N). According to these observations the chemical bonding in NH2 and BH3 are covalent.

Fig.5 shows the calculated partial DOS respectively, for NaHB in the solid state. We note that the total DOS of NaHB consists of two regions: the region above 4.36 eV (conduction band) and the region below 0eV (region of valence band). This latter is also separated into three regions. Fig.6 shows the calculated partial DOS respectively, for KHB in the solid state. It can be seen that the total DOS of KHB consists of two well-separated regions: the region above 4.35 eV (conduction band) and the region below 0eV (region of valence band). This latter is separated into four regions. The alkali (K and Na) atoms contributed less to the DOS of NaHB and KHB respectively.

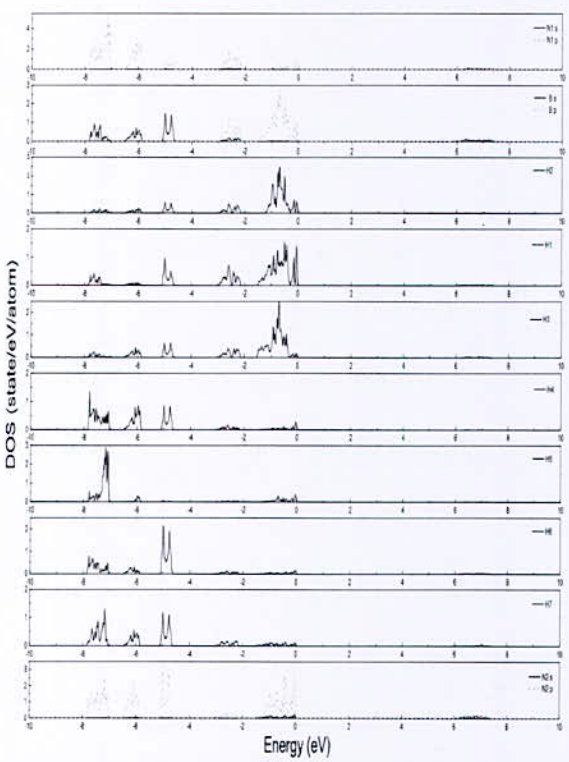

Fig. 4. The calculated partial electronic density of states (PDOS) for HB. The Fermi level is set at zero energy; s-state and p-state contributions are distinguished with black continue and red dashed line respectively

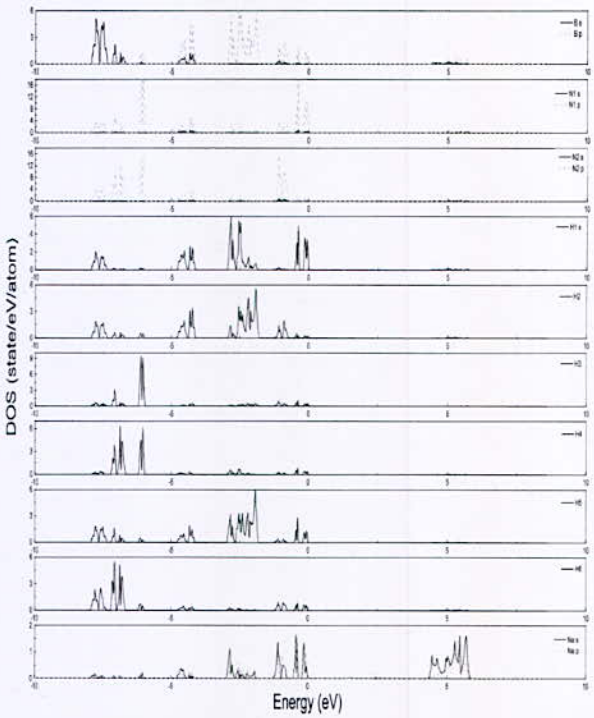

Fig. 5. The calculated PDOS for NaHB. The Fermi level is set at zero energy; s-state and p-state contributions are distinguished with black continue and red dashed line respectively

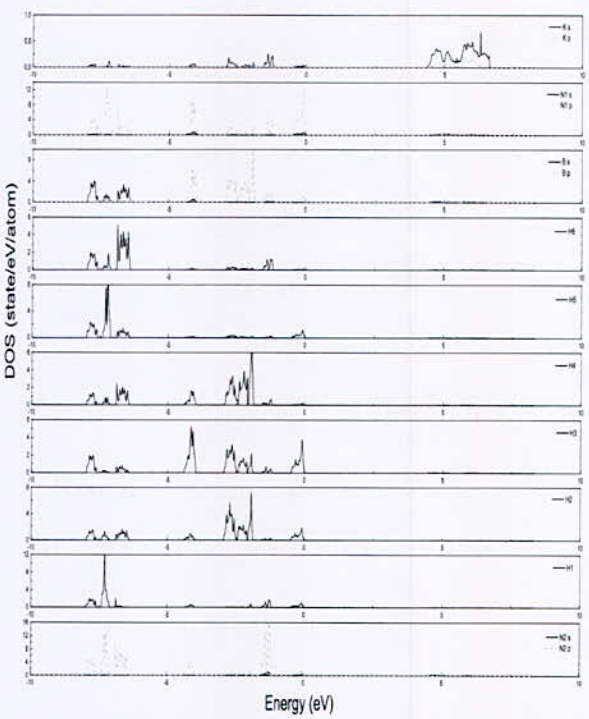

Fig. 6. The calculated PDOS for KHB. The Fermi level is set at zero energy; s-state and p-state contributions are distinguished with black continue and red dashed line respectively

*Corresponding author email: bouhadda@yahoo.com

IV. CONCLUSION

Based on the first principles calculations, we have investigated the crystal structure and electronic properties of hydrazine borane ($N_2H_4BH_3$) and its derivative ($NaN_2H_3BH_3$ and $KN_2H_3BH_3$) using the norm-conserving pseudo-potentials and plane waves (PP-PW) within the general gradient approximation (GGA).

The computed equilibrium lattice constants are in excellent agreement with the available experimental and theoretical data. However, no theoretical studies performed on the crystal structure of NaHB and KHB have found to compare with our present study.

The calculated density of state indicated that $N_2H_4BH_3$ has a wide band gap with a value equal to 5.78 eV. Also, $KN_2H_3BH_3$ and $NaN_2H_3BH_3$ have a wide band gap: 4.36 eV and 4.35 eV respectively. These materials can be considered as an insulator. This indicated that the substitution of one hydrogen atom from HB by alkali atom Na or K could reduce the gap between conduction band and valence band. To our best of knowledge, there are no previous experimental or theoretical works on the gap energy of NaHB and KHB. We hope our work could provide a useful reference for future study.

REFERENCES

[1] Y. bouhadda, N. fenineche, Y. Boudouma, A. bentabet, "Ab initio calculations study of the electronic, optical and thermodynamic properties of NaMgH 3, for hydrogen storage" *J. Physics Chem. Solids*, vol. 71, pp. 1264–1268, 2010.

[2] T. Umegaki, J. Yan, X. Zhang, H. Shioyama, N. Kuriyama, Q. Xu, "Boron- and nitrogen-based chemical hydrogen storage materials", *Int. J. Hydrogen Energy*, vol. 34, pp. 2303–2311, 2009.

[3] T. Hügle, M. F. Kühnel, D. Lentz, "Hydrazine borane: a promising hydrogen storage material", *J. Am. Chem. Soc.*, Vol. 131, pp. 7444-7446, 2009.

[4] A. Staubitz, A. P. M. Robertson, I. Manners, "Ammonia-borane and related compounds as dihydrogen sources", *Chem. Rev.*, vol. 110, pp. 4079-124, 2010.

[5] T. Hugle, M. Hartl, D. Lentz, "The route to a feasible hydrogen-storage material: MOFs versus ammonia borane", *Chem. Eur. J.*, vol.17, pp. 10184-10207, 2011.

[6] R. Moury, G. Moussa, U.B. Demirci, J. Hannauer, S. Bernard, E. Petit, A. van der Lee, P. Miele, "Hydrazine borane: synthesis, characterization, and application prospects in chemical hydrogen storage", *Phys. Chem. Chem. Phys.*, vol 14, pp. 1768-1777, 2012.

[7] J. Hannauer, O. Akdim, U. B. Demirci, C. Geantet, J. M. Herrmann, P. Miele, Q. Xu, "High-extent dehydrogenation of hydrazine borane $N_2H_4BH_3$ by hydrolysis of BH_3 and decomposition of N_2H_4", *Energy Environ. Sci.*, vol. 4, pp. 3355-3358, 2011.

[8] S. Karahan, M. Zahmakiran, S. Ozkar, "Catalytic hydrolysis of hydrazine borane for chemical hydrogen storage: highly efficient and fast hydrogen generation system at room temperature", *Int. J. Hydrogen Energy*, vol. 36, pp. 4958-66, 2011.

[9] X. Gonze, J. M. Beuken, R. Caracas, F. Detraux, M. Fuchs, G. M. Rignanese, L. Sindic, M. Verstraete, G. Zerah, F. Jollet, M. Torrent, A. Roy, M. Mikami, Ph. Gohsez, J.Y. Raty, D.C. Allan, "First principles computation of material properties: the ABINIT software project", *Comput. Mater. Sci*, vol. 25, pp. 478-492, (2002).

[10] W. Kohn, L. J. Sham, "Self-consistent equations including exchange and correlation effects", *Phys. Rev. A*, vol. 140, pp. 1133-1138, 1965.

[11] J.P. Perdew, K. Burke, M. Ernzerhof, "Generalized gradient approximation made simple", *Phys. Rev. Lett.*, vol. 77, pp. 3865-3868, 1996.

[12] M. Fuchs, M. Scheffler, "Ab initio pseudopotentials for electronic structure calculations of poly-atomic systems using density-functional theory", *Comput. Phys. Commun.*, vol. 119, pp. 67-98, 1999.

[13] H. Wu, W. Zhou, F. E. Pinkerton, T. J. Udovic, T. Yildirim, J. J. Rush, "Metal hydrazinoborane $LiN_2H_3BH_3$ and $LiN_2H_3BH_3{\cdot}2N_2H_4BH_3$: crystal structures and high-extent dehydrogenation", *Energy Environ. Sci.*, vol. 5, pp. 7531-7535, 2012.

*Corresponding author email: bouhadda@yahoo.com

Optimization Study of the Produced Electric Power by SOFCs

Y. Sahli[1*], B. Zitouni[2] and H. Ben Moussa[3]

[1*]Unité de Recherche en Energies Renouvelables en Milieu Saharien, URERMS, Centre de Développement des Energies Renouvelables, CDER 01000, Adrar, Algérie.
[2]Institut des Sciences Vétérinaires et des Sciences Agronomiques, Université Batna 1, Algérie.
[3]Département de Mécanique, Faculté de Technologie, Université Batna 2, Algérie.

Abstract—**The object of this work is the thermodynamic study of the solid oxide fuel cell; a particular attention is given to maximizing the produced power density by a single cell. In this study, the SOFC real potential is defined by the Nernst potential and the over-potentials due to the activation polarizations of the chemical reactions in the anode and the cathode, the losses due to the specie concentration in these two electrodes (anode and cathode), and the Ohmic losses caused by the Joule's effect in the electrolyte and the two electrodes. The obtained results show that the SOFC power density is proportional to the variations of the operating temperature and the oxygen concentration in the oxidizer; conversely, it is inversely proportional to the evolutions of the fuel humidification and the thicknesses of the electrolyte.**

Key words—SOFC, Thermodynamic, Power density, and Optimization.

I. INTRODUCTION

Fuel cell is one of clean energy production vectors. SOFC is one of the fuel cell family that is characterized by a high overall efficiency (90%), a solid electrolyte and a high operating temperature (600-1050°C). The high overall efficiency and operating capability of various fuels of the SOFCs gave a very good status between the renewable energies family. Current development research of SOFCs is focused on maximizing the energy produced by cells or fuel cell systems and reducing the high operating temperature that affecting the cell components, in several ways and in various disciplines to improve the lifetime of this technology.

Several studies are carried out on this subject. The energetic production optimization of SOFCs has been conducted by several researchers in this domain using several optimization methods. The most widely used methods can be divided into three categories: deterministic, meta-heuristic and stochastic methods. [1].

Wen et al [2] have realized a numerical simulation in the microstructure level for optimized the electrical power of single SOFC cell using a deterministic method. Goyal et al [3] have used a deterministic method to optimize the SOFC-PEM system power generation.

*Corresponding author email: sahli.sofc@gmail.com

Cheddie [4] has presented a thermo-economic study that based to a stochastic method to obtain the energy production minimum cost of an indirectly coupled SOFC. Francois et al [5] have proposed a real-time optimization according to a stochastic method to optimize SOFC electrical efficiency.

Moller et al [6] have used a genetic algorithm that based to a meta-heuristic method for optimization of several operating parameters of the coupled system (SOFC-GT). Shi et al [7] have study the microstructure optimization by a meta-heuristic method to obtain the electrodes optimum porosity (pore size and porosity distribution) to maximize the cell output power.

In this work, we present a thermodynamic study of the solid oxide fuel cell, while paying special attention to the maximizing the power density produced by the SOFC fuel cell bay a graphical method that uses the SOFC physical and dimensional parameters (operating temperature, species concentrations and electrolyte thickness).

II. PHYSICAL MODEL

SOFC stack tension (V) is defined by the following equation:

$$V = E_{Nernst} - Losses \tag{1}$$

E_{Nernst} is the Nernst potential, which represents the maximum potential of the SOFC; it is given by the Nernst equation [8]:

$$E_{Nernst} = \frac{R.T}{n.F} ln(k) + \frac{R.T}{n.F}\left[ln\left(\frac{P_{H_2} . P^{0.5}{}_{O_2}}{P_{H_2O}} \right)\right] \tag{2}$$

R is the gas constant, T is the operating temperature, n is the transfer electrons number , F is the Faraday number, P_i is the partial pressure of each specie i, P_{ref} is the reference pressure and k is a constant defines by the following equation [8]:

$$k = A.e^{\frac{-E}{R.T}} \tag{3}$$

Where A is a constant and E is the potential produced under standard conditions, its constants are defined by 0.00144 and -246 KJ/mol respectively. [8].

The losses defined by equation (1) include three types of tension losses; activations, concentrations and ohmic.

1. Ohmic losses

These tension losses are due to the resistance phenomenon. Ohmic loss in each SOFC constituent element is given by the product of the current density (i) and the electrical resistance (r). Equation (4). [9].

$$\eta_{ohm} = i.r \tag{4}$$

Where (r) is the ratio of the thickness of each component of the cell heart (e) and its electrical conductivity (σ). Equation (5). [9].

$$r = \frac{e}{\sigma} \tag{5}$$

2. Activation losses

These tension losses are due to the chemical reaction activation in both electrodes. Equation (6). [10].

$$\eta_{Act,j} = \frac{R.T}{\alpha.n.F}.\sinh^{-1}\left(\frac{i}{2.i_{0,j}}\right), j = anode, cathode \tag{6}$$

Where (α) is the charge transfer coefficient and (i_{0j}) is the exchange current density of each electrode, it is given by Equation (7). [10].

$$i_{0,j} = k_j.\exp\left(-\frac{E_j}{R.T}\right), j = anode, cathode \tag{7}$$

3. Concentration losses

These losses are due to the inability of the system to maintain the initial concentrations. Equation (8). [11].

$$\eta_{conc,j} = -\frac{R.T}{n.F}.\ln\left(1-\frac{i}{i_{l,j}}\right), j = anode, cathode \tag{4}$$

Where (j_{Lj}) is the limit current of the anode and of the cathode, it is given for these two electrodes respectively by 2.99 x 10^4 and 2.16 x 10^4.

III. RESULTS AND DISCUSSION

The obtained results are presented according to three parts, in the first; we present the impact of operating temperature and current density on the power density. For the second part, we shows the influence of the oxygen concentration and the moisture content according to the different current densities on the power density. Finally, the third part exposes the effect of the electrolyte thickness and the current density on the power density delivered by SOFC.

Fig. 1 shows the effect of the operating temperature and the current density on the power density of a supported electrolyte SOFC, the building materials are (N_iYSZ) for the anode, LSM) for the cathode and (YSZ) for the electrolyte, the cell heart elements thicknesses are identical to 100mm for the electrodes and 50mm for the electrolyte. The fuel is humidified hydrogen (XH2O = 0.05), and the oxidizer is air (XO2 = 0.21) is the oxidizer, the supply pressure is common for these both gases (1 bar).

Fig. 1 shows that all lose types are inversely proportional to the operating temperature, this conduct to a potential and power density proportional to the operating temperature.

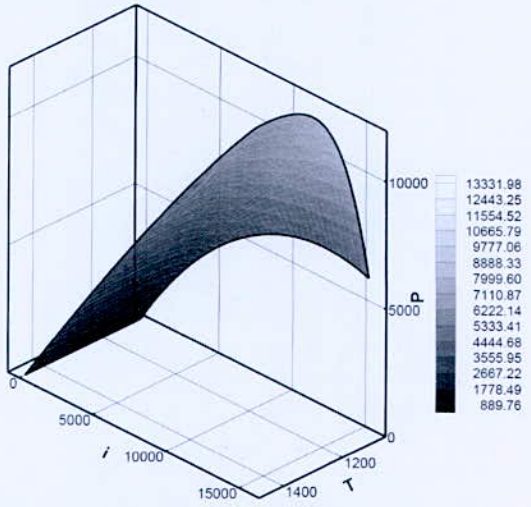

Fig. 1. Power density evolution according to the operating temperature and current density

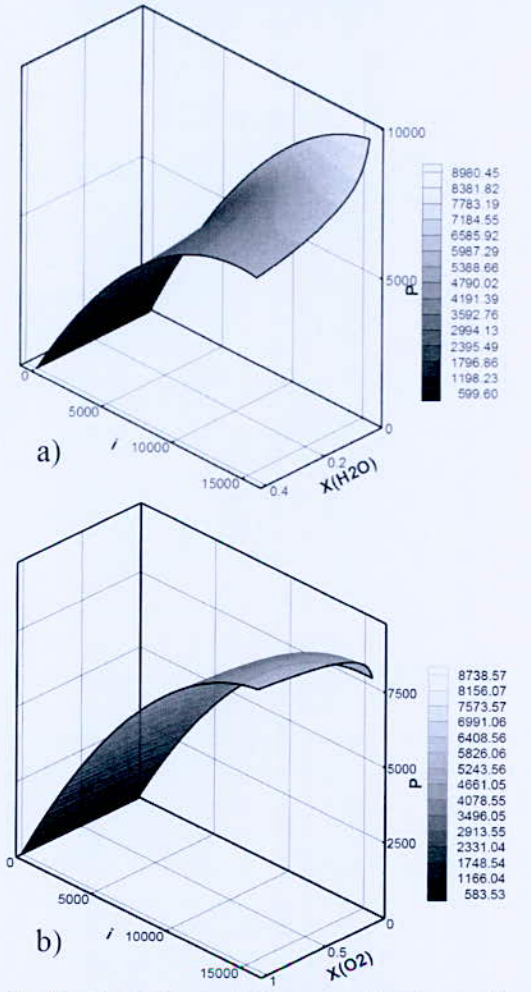

Fig. 2. Power density evolution according to species concentrations and current density. (a) Water concentration in the fuel, (b) Oxygen concentration in the oxidizer

*Corresponding author email: sahli.sofc@gmail.com

Fig. 2 shows the effect of the hydrogen water content and the oxidizer oxygen concentration on the power density of a supported electrolyte SOFC, the building materials are (NiYSZ) for the anode, LSM) for the cathode and (YSZ) for the electrolyte, the cell heart elements thicknesses are identical to 100mm for the electrodes and 50mm for the electrolyte. The supply pressure is common for these both gases (1 bar). The SOFC operating temperature is 1073 k.

Fig. 2 shows that the power density of the solid oxide fuel cell is inversely proportional to the fuel humidification rate.

Fig. 2 shows that the power density of the solid oxide fuel cell is inversely proportional to the fuel humidification rate. The SOFC real potential is proportional to the oxygen concentration rate in the oxidizer. The SOFC power density is also proportional to the oxygen concentration in the oxidizer.

Fig. 3 shows the effect of the electrolyte thickness and the current density on the power density of a supported electrolyte SOFC, the building materials are (NiYSZ) for the anode, LSM) for the cathode and (YSZ) for the electrolyte, the thicknesses of the anode and cathode are of 100mm .The fuel is humidified hydrogen (XH2O = 0.05), and the oxidizer is air (XO2 = 0.21) is the oxidizer. The supply pressure is common for these both gases (1 bar). The SOFC operating temperature is 1073 k.

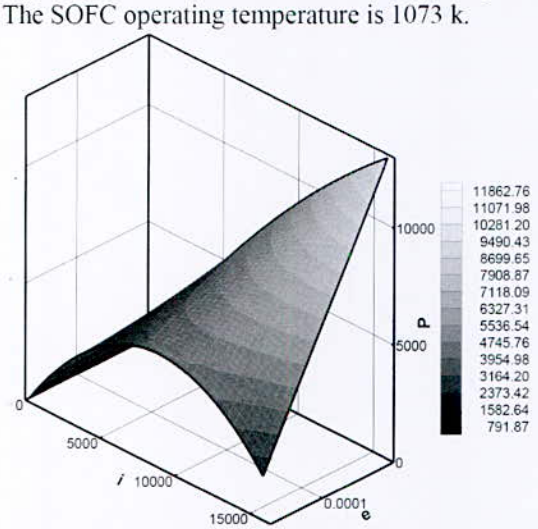

Fig. 3. Power density evolution according to the electrolyte thickness and current density

Fig. 3, shows that the SOFC power density is inversely proportional to the electrolyte thickness.

IV. CONCLUSION

The oxide solid fuel cell is an electrochemical device that converts the chemical energy of a reaction to the thermal and electrical energies. In the present study, an optimization study of the produced electric power by SOFCs is presented. A program in FORTRAN language that is based on the thermodynamic model equations has been developed locally. According to analysis of the obtained result, it appears that the realized code can be used as a design tool to the optimization of the produced electric power by SOFCs. The main obtained results in this work are:

-The SOFC power density is proportional to the operating temperature and the oxygen concentration in the oxidizer.

-The SOFC power density is inversely proportional to the fuel humidification and the electrolyte thickness.

REFERENCES

[1] F. Ramadhani, M.A. Hussain, H. Mokhlis, S. Hajimolana, "Optimization strategies for Solid Oxide Fuel Cell (SOFC) application: A literature survey," Renewable Sustainable Energy Rev., vol. 76, pp. A460–A480, 2017.

[2] H. Wen, J.C. Ordonez, J.V.C. Vargas, "Single solid oxide fuel cell modeling and optimization," J. Power Sources, vol. 196, pp. A7519–A7532, 2011.

[3] A. Goyal, U. Diwekar, "Multi-objective optimization for hybrid fuel cells power System design," J. Chem. Inf. Model., vol. 53, pp. A1689–A1709, 2001.

[4] D.F.Cheddie, "Thermo-economic optimization of an indirectly coupled solid oxide fuel cell/gas turbine hybrid power plant," Int. J. Hydrog. Energy, vol. 36, pp. A1702–A1709, 2011.

[5] G. François, S. Costello, D. Bonvin, "Application of real-time optimization methods to energy systems in the presence of uncertainties and disturbances," TMC. Acad. J., vol. 9, pp. A19–A40, 2015.

[6] B. Fredriksson Möller, J. Arriagada, M. Assadi, I. Potts, "Optimisation of an SOFC/GT system with CO2-capture," J. Power Sources, vol. 131, pp. A320–A326, 2004.

[7] J. Shi, X. Xue, "Optimization design of electrodes for anode-supported solid Oxide Fuel Cells via genetic algorithm," J. Electrochem. Soc., vol. 158, pp. B143, 2010.

[8] Jarosław Milewski, Konrad Swirski, Massimo Santarelli, Pierluigi Leone. Advanced Methods of Solid Oxide Fuel Cell Modeling. [Online]. Available: http://www.springer.com.

[9] Y. Sahli, B. Zitouni, H. Ben Moussa, H. Abdenebi, "Three-Dimensional Numerical Study of the Heat Transfer on the Planar Solid Oxide Fuel Cell: Joule's Effect, " In *Progress in clean energy volume I: Analysis and Modeling,* ed., I. Dincer, C. Ozgur Colpan, O. Kizilkan and M. Akif Ezan, Ed. Switzerland: Springer, 2015, pp. 449–461.

[10] D. Saebea, Y. Patcharavorachot, S. Assabumrungrat, A. Arpornwichanop, "Analysis of a pressurized solid oxide fuel cell-gas turbine hybrid power system with cathode gas recirculation," Int. J. Hydrog. Energy, vol. 38, pp. A4748–A4759, 2013.

[11] X. Zhang, Y. Wang, J. Guo, T. Shih, J. Chen, "A unified model of high-temperature fuel-cell heat-engine hybrid systems and analyses of its optimum performances," Int. J. Hydrog. Energy, vol. 39, pp. A1811–A1825, 2014.

*Corresponding author email: sahli.sofc@gmail.com

Performance Analysis of Super and Transcritical Open-loop Cycles for LH_2 Regasification

Ahmed Laouir*

Department of Mechanical Engineering, University M.S. Benyahia, BP 98 Ouled Aissa 18000 Jijel, Algeria.

Abstract—**The paper addresses the subject of regasifying liquid hydrogen (LH_2) with a technology that takes advantage of the hydrogen coldness to produce mechanical energy. Liquid hydrogen undergoing regasification plays the role of a heat sink, associated with an external heat source, it becomes possible to run a thermodynamic cycle. A theoretical analysis is first given to discuss factors impacting or favouring the efficiency. From this, some original methods are proposed based on cycles using hydrogen at the same time as the working fluid. The cycles bring into play an internal heat transfer, the regeneration. Two types of cycles are studied, one with supercritical regeneration and a second with a transcritical one. The proposed systems features recompression operations to improve the efficiency. While the efficiencies can be significant, there is an important sensitivity to the quality of the mechanical components (pumps, compressors, turbines). Moderate or low isentropic efficiencies can strongly deteriorate the performances. The transcritical type necessitating an important re-compression work is the most sensitive to this factor.**

Keywords—Liquid hydrogen, Regasification, Cryogenics, Thermodynamics.

I. INTRODUCTION

Regasification is the cryogenic process intended to produce again a gas previously condensed in a liquefaction process. Nowadays regasification technology is mostly encountered in the liquefied natural gas (LNG) industry. While important research efforts have been consecrated to the improvement of different hydrogen liquefiers, liquid hydrogen (LH_2) regasifiaction using thermodynamic cycles is rarely encountered as a research subject.

Hydrogen is expected to be a major energy vector in the future and liquefaction will play an important role in hydrogen economy. As like as the LNG case, there will be probably a need for efficient solutions for regasifying LH_2. This will contribute to make the whole chain, from production to consumption, more profitable as a part of the energy consumed during liquefaction is recovered. In a similar way to the LNG case, the coldness of LH_2 offers an opportunity to run a thermal machine and to produce power. Some heat is absorbed from the environment or from other waste heat sources; a fraction of it is converted as a useful work and the other is discarded from the process in accordance with the second law of thermodynamics.

Focusing on alternatives using hydrogen at the same time as the working fluid in the thermodynamic cycle, some original regasification methods are proposed. The internal heat transfer, that is regeneration, is a critical operation regarding the efficiency. An effective regeneration can be performed if some rules are observed like avoiding phase transition and pressure values at which the heat capacity variation with temperature is important. In addition, flow rates of the heated and the heating steams should be properly chosen. The derived processes comport the specific feature to put into play recompression operations at convenient positions to improve the efficiency.

II. SOME FEATURES REGARDING THE IDEAL PROCESS

A reversible regasification process (ideal) will produce the maximum output W_{id} given by,

$$W_{id} = (h_g - h_l) - T_0(s_g - s_l) \quad (1)$$

where h and s are the enthalpies and entropies, subscripts g and l refers to the gas and the liquid respectively. T_0 is the surroundings temperature. From (1), the ideal work of regasification W_{id} can be represented as a surface in the temperature(T)-entropy(s) diagram as shown in figure 1a. Fig. 2 gives the variation in function of the delivery pressure P_g of the produced gas and T_0, liquid hydrogen is taken saturated at 1.2 bar. Long-distance pipeline transmission of hydrogen involves gas pressures ranging between 70 and 100 bar. Distribution for nearer consumers requires lower pressure levels allowing producing more work per kg of regasified LH_2.

As represented in Fig. 1.a, the ideal regasification can be performed using a once-through process composed of an isentropic pressure elevation until the liquid reaches T_0 followed by an isothermal expansion at T_0 during which the fluid absorbs a quantity of heat $Q_0 = T_0(s_g - s_l)$ from the surroundings.

*ahmed.laouir@gmail.com

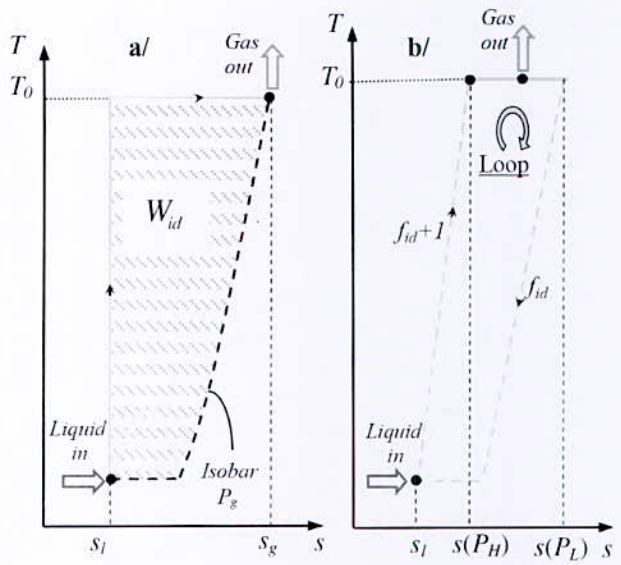

Fig. 1. a/ Ideal work of regazification b/ Principle of an open-loop regazification cycle

Actually this process is not feasible because of the extremely high pressure needed for increasing the fluid temperature from saturation to T_0 during the first stage.

In place of the previous method, the ideal process can be imagined as a loop fed with the liquid to be regasified and delivering the gas at an outlet. This constitutes an open-loop cycle in which a part f_{id} of the fluid is recirculated to close the loop as shown in Fig. 1.b. The only characteristics indicated for the cycle are: it comports an isothermal expansion absorbing heat between a high pressure P_H and a lower pressure P_L, the cycle is adiabatic elsewhere, the stream f_{id} is recirculated at P_L. As an ideal process, the cycle must absorb a quantity of heat equal to Q_0 and produce an output equal to W_{id}. The first condition leads to write,

$$T_0\left[s_g + f_{id}s(P_L) - (1+f_{id})s(P_H)\right] = T_0(s_g - s_l) \tag{2}$$

Equation (2) allows deriving the expression of the ideal recirculated flow f_{id},

$$f_{id} = \frac{s(P_H) - s_l}{s(P_L) - s(P_H)} \tag{3}$$

The second condition leads to write,

$$W_E + W_C = W_{id} \tag{4}$$

W_E is the expansion work between P_H and P_L and W_C is another work involved elsewhere in the loop. The energy balance for the expansion is, $W_E = f_{id}h(P_L) + h_g - (f_{id}+1)h(P_H) - Q_0$ and having $W_{id} = h_g - h_l - Q_0$, from (4) W_C expression is then,

$$W_C = h(P_H) - h_l + f_{id}(h(P_H) - h(P_L)) \tag{5}$$

Equation (5) shows that the compression or recompression is necessary and important to perform an ideal regasification.

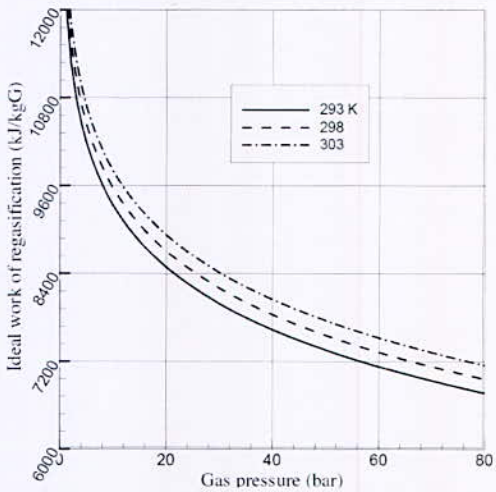

Fig. 2. Ideal work of regasification W_{id} for para-hydrogen

Fig. 3 represents the variation of the quantity f_{id} in function of the cycle's high pressure P_H and low pressure P_L. Increasing P_H strongly reduces f_{id}, which is beneficial for components size and capital cost reduction.

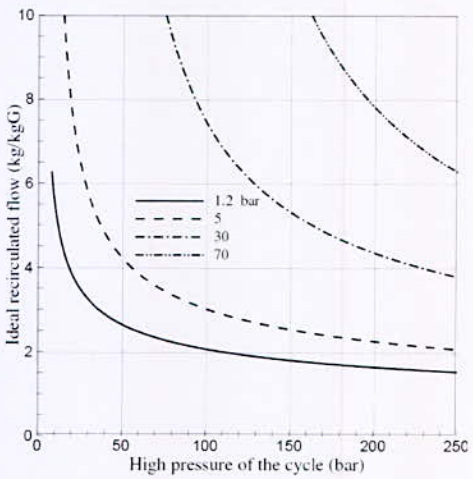

Fig. 3. Ideal recirculated flow f_{id}

III. IMPROVING REGENERATION WITH PARALLEL RECOMPRESSIONS

As stated before, the once-through process of Fig. 1a is unpractical. A simple way to produce some work [1] would be to increase LH_2 pressure to an acceptable value P_H then heating the stream to the temperature T_0 and then

expanding the gas to the desired pressure. This three-stages process is called direct expansion in the LNG regasifiaction practice. Compared to the ideal process of Fig 1.a, direct expansion causes important losses due to the direct and irreversible heat transfer from the heat source to the hydrogen stream at much lower temperature. How to heat the H_2 stream with minimum entropy production is the central problem to be addressed in order to improve significantly the efficiency of the process.

The pressurized LH_2 can be heated by regeneration that is by using a part of the expanded fluid at T_0 to heat the pressurized steam in a countercurrent heat exchanger. This option does not insure a significant improvement unless the internal heat transfer is effective enough namely performed with the least entropy production.

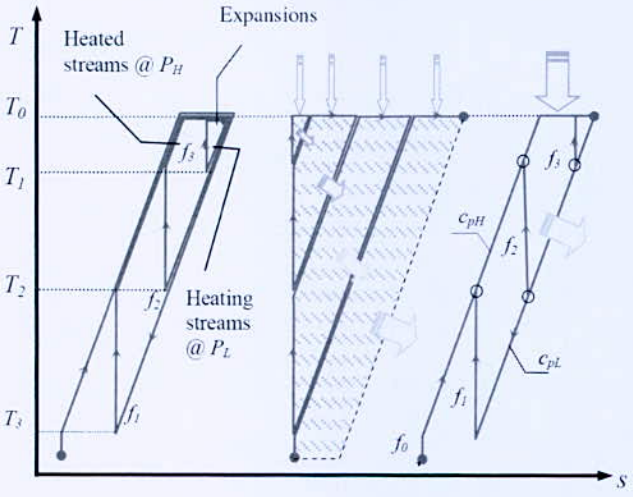

Fig. 4. Ideal regenerative path with recompression operations arranged in parallel.

Fig. 4 represents and explains the method that will be followed in order to perform and favor an effective regeneration. In the diagram *T-s*, isobars are drawn as straight lines to make presentation simple. LH_2 at P_H and T_3 is heated to T_0 by a stream f_1 at P_L. Assuming an ideal heat transfer, f_1 cools down to T_3. The same problem as before arises: how to heat f_1 again to T_0 without using directly the external heat source. The compression will be used as another mean permitting to elevate the fluid temperature without the need to a heating medium. The stream f_1 at P_L and T_3 once compressed to P_L heats up to T_2. To complete the heating to T_0 another stream f_2 at P_L is used then recompressed to rich T_1. The process is repeated until the last recompression suffices alone to heat up the fluid to T_0. This gives the spiral construction represented in Fig. 4. As shown the superposed loops so arranged are equivalent to an association of a number of cycles producing together a total work represented by the triangular surface. This corresponds to the ideal work of regasification shown in Fig. 1a.

IV. ADAPTING THE METHOD TO THE HYDROGEN

The analysis given in the previous section demonstrates the central role that the regeneration plays in improving efficiency. The question is how to adapt in the best possible way the approach explained to the actual fluid for which the isobars are of irregular shape. It can be easily shown that the criterion to be followed to perform an effective regeneration with the actual fluid is to work with two isobars having a heat capacity ration as stable as possible i.e. $c_{pH}/c_{pL} \cong cste$, this condition can be fulfilled by avoiding for both streams the occurrence of phase transition and the zone near the critical point where the heat capacity shows a sharp variation as shown in Fig.5.

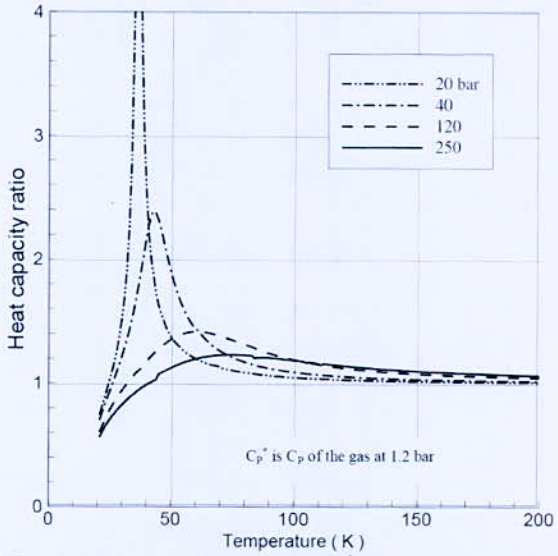

Fig. 5. Heat capacity ratio C_p/C_P^* of para-hydrogen.

Taking into account the constraints related to the properties of the fluid, there are two possible options to transpose the method:

1. Cycle With Supercritical Regeneration

The admitted liquid is pumped to a supercritical pressure P_H and heated countercurrently by another supercritical stream at lower pressure P_L, the regenerative loop is then entirely situated in the supercritical region. Fig. 6 represents a supercritical regasification cycle in the *T-s* diagram with P_H=250 bar and P_L=70 bar, the gas is delivered at 70 bar, a pressure suitable for long-distance pipeline transmission. The cycle comports four adiabatic expansions and three intermediate reheats. The stepped construction in dashed line shows that five ideal isentropic recompressions are needed in theory. With actual and optimized systems, the number of recompressions involved would fall to three or only two.

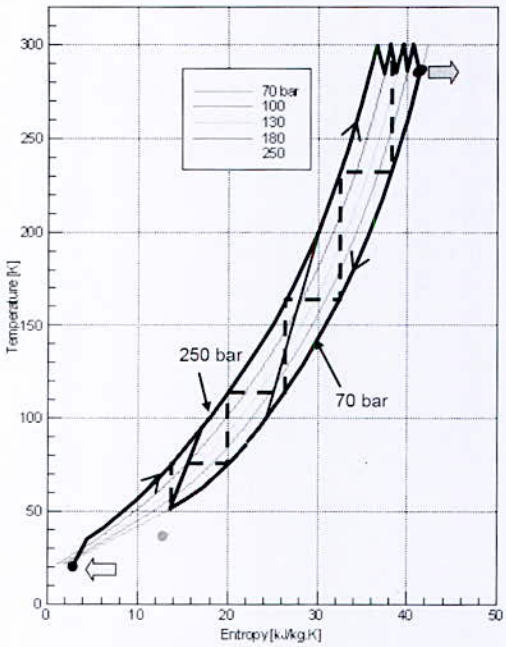

Fig. 6. Supercritical 250/70 bar cycle

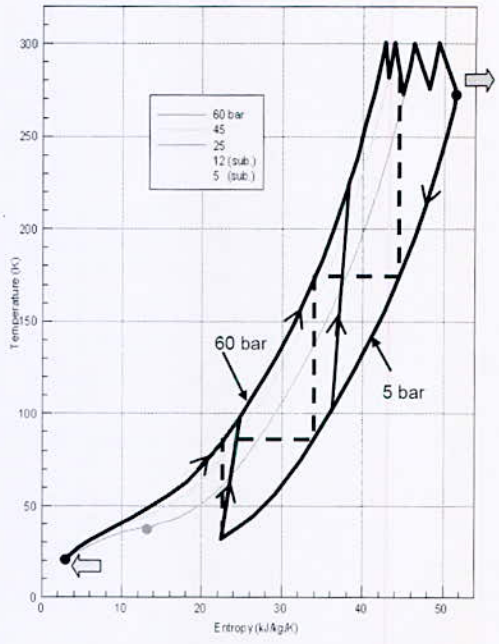

Fig. 7. Transcritical 60/5 bar cycle

2 *Cycle With Transcritical Regeneration*

The admitted liquid is pumped to a supercritical pressure P_H (not necessarily as high as in the previous case) the heating stream is a gas at relatively low pressure P_L. The loop is then transcritical i.e. distributed between the supercritical and subcritical zone.

Thanks to the greater compressibility of the gas, the recompression participates more strongly to the increase of the fluid temperature as shown in the example of Fig. 7. As a consequence less recompressions are needed compared to the supercritical case.

V. CONCLUSION AND PROSPECTS

From a theoretical and systematic analysis, original regasification methods are derived consisting of open-loop cycles using the regasified fluid as the working medium. Applicable to any cryogenic fluid subject to regasification the patented method [2] has been considered with LNG and the expected advantages discussed [3]. In a previous work, it has been suggested to use the method for regasifying LH_2 [4].

The present work is in the continuation of the precedent. A simulation program is written to evaluate quantitatively the performances that can be expected in the case of hydrogen considering the two configurations, super and transcritical. Accurate thermodynamic properties of para-hydrogen, calculated from an equation of state [5] are used for this purpose. The obtained results will be presented and analyzed.

REFERENCES

[1] R.O. Voth, W.R. Parrish, "Studies of hydrogen liquefier efficiency and the recovery of the liquefaction energy", Cryogenic division, National Bureau of Standars, Vol. NBSIR 77-862, 1977.

[2] A. Laouir, "Procedé de re-gazeification des fluides cryogeniques,", Algerian Patent DZ/P/2014/000696, Nov. 27, 2014.

[3] A. Laouir, "LNG regasification cycles with supercritical / transcritical regenerative loop," in *Proc. ECOS*, 2-6 July 2017, San Diego, California, USA.

[4] A. Laouir, "Open-loop cycles for LH_2 regasification," in *Proc. ISHH2*, 5-6 October 2016, Algiers, Algeria.

[5] W.C. Reynolds, Thermodynamic properties in SI, Department of mechanical engineering, Stanford University, 1979

Conducting Polymers as Electrolyte Membrane for Fuel Cells

F. Chouli[1*] A. Benyoucef[1] and J. R. Mirasol[2], I. Moulferaa[1] and I. Rajaa[1]

[1*]Department de Science et techniques, laboratoire de génie des procédés et chimie des solutions, Universite de Mascara., Bp 763, Mascara 29000, Algeria.

[2] Universidad de Málaga, Departamento de Ingeniería Química, Andalucía Tech., Facultad de Ciencias, Campus de Teatinos s/n, 29010 Málaga, Spain.

Abstract—**Use In this work nanocomposites were successfully synthesized by the oxidative polymerization of aniline with titanium(IV) oxide nanoparticles The morphological, structural, conductivity and electrochemical properties were studied, nitrogen adsorption-desorption studies demonstrated the high specific surface area of the synthesized nanocomposites were studied.**

These composite microspheres can potentially be used in commercial applications as fillers for antistatic, anticorrosion coatings and in photovoltaic devices [1]. The results showed that by modifying electrode with polyaniline polymer, power density in the microbial fuel cell increased up to 1.2 times of the graphite electrode [2]. In addition positive effect of TiO2 on the charge transfer rate was observed in microbial fuel cells [3].

The TiO2 morphology have an effect on the final behavior of the nanocomposites where the high polymer order and crystallinity is clear from X-ray diffraction patterns. FTIR spectral analysis shows the strong interaction between polymer and TiO2 that gives additional stability to the polymer.

Key words—Conducting polymers, nanocomposites, polyaniline, fuel cells.

I. INTRODUCTION

Titania is of tremendous interest for applications in photovoltaic devices such as solar cells, photo-catalysis, and photo-electrochemistry, titania is a key component of the dye-sensitized solar cell (DSSC). TiO_2 is used to transport electrons from the light absorbing layer to the current collector. Recently, there are many researches on nanostructured PANI/metal oxide composites used as anode of microbial fuel cells or cathode of dye-sensitized solar cells, PANI could be used to decorate a photoanode for its applications in photoelectrochemical fuel cells.

Composite materials formed by Nafion alternative polymers such as PES, SPEEK and CS and inorganic fillers such as Fe_3O_4, TiO_2, MMT, CNF, ACNF and CNT have been investigated as MFC membranes with promising results. The addition of inorganic fillers to the polymer electrolyte membrane in MFCs reduces the substrate oxygen cross over and improves the performance of the membrane during the microbial fuel cell operation.

In this work nanocomposites were successfully synthesized by the oxidative polymerization of p-anisidine and/or aniline monomers (at initial "p-anisidine: aniline" mole ratios of "100: 0", 50: 50", and "0: 100") with titanium (IV) oxide nanoparticles. The structural, conductivity and electrochemical properties of the synthesized nanocomposites were studied. These composite microspheres can potentially be used in commercial applications as fillers for antistatic, anticorrosion coatings and in photovoltaic devices. In addition Positive effect of TiO_2 on the charge transfer rate was observed in microbial fuel cells [1].

II. EXPERIMENTAL/THEORETICAL STUDY

1. X-ray diffraction

The X-ray diffraction of the powder nanocomposites were obtained using a Bruker CCD-Apex equipment with an X-ray generator (Cu Ka and Ni filter) operated at 40kV and 40mA.

2. Fourier transform infrared (FT-IR) spectroscopy

Fourier transform infrared (FT-IR) spectroscopy was recorded using a Bruker Alpha in KBr transmission mode.

3. Electrical conductivity measurements

Electrical conductivity measurements were carried out using a Lucas Lab resistivity equipment with four probes in-line. The samples were dried in vacuum during 24 h and pellets of 0.013 m diameter were prepared using a FTIR mold by applying a pressure of 7.4 108 Pa.

4. The electrochemical study

The electrochemical behavior of the polymers was studied by cyclic voltammetry. The electrochemical measurements were carried out using a conventional cell of three electrodes.

5. The thermogravimetric analysis (TGA)

The thermogravimetric analysis (TGA) was performed with a Du Pont thermogravimetric analyzer at a heating rate of 208 °C/min under nitrogen or air atmosphere. About 10 mg of sample was heated to 900 °C.

*Corresponding author email: faizachouli@yahoo.fr

III. RESULTS AND DISCUSSION

1. Fourier transform infrared (FT-IR) spectroscopy

The FTIR spectrum of the PANI/TiO_2 nanocomposites contains contributions from both TiO_2 nanoparticle and polymers. The main characteristic bands of doped polyaniline are assigned as follows: the band at 3,386cm-^{1} is attributable to N-H stretching mode, C-N and C-C stretching mode for the quinoid and benzenoid rings occur at 1,587 and 1,541 cm^{-1}, the bands at about 1,394 and 1,220 cm^{-1} have been attributed to C-N stretching mode for benzenoid ring, while the peak at 1000 cm^{-1} is assigned to a plane bending vibration of C-H (mode of ,N-Q-N, Q –N+H-B, and B-N+H-B), which is formed during protonation [2].

In spectrum of PPA/TiO_2, a band at 3,207 cm^{-1} appears showing the presence of chelate compounds. The band at 1,450 cm^{-1} may be due to -CH3 group or due to aromaticity. Additional bands at 1248; 1173 and 1026 cm^{-1} could be assigned to vibrations of the C-O-C bonds of the ether group [3] and aromatic C-O; respectively. The band at 872 cm^{-1} shows the presence of TiO_2.

2. X-ray diffraction

Fig. 2, shows the XRD pattern of TiO_2 nanoparticles and nanocomposites. In all samples, it can be observed all the diffraction peaks of TiO_2 that corresponds to anatase crystalline phase. Hence, the polymers do not change the structure of TiO_2. These results confirmed the presence of TiO_2 in composites.

Polymer is commonly added to metal oxides to increase the specific surface area of the electrode and the charge transfer capability (composite anode) or to increase proton conductivity.

The addition of inorganic fillers to the polymer electrolyte membrane in microbial fuel cells reduces the substrate oxygen crossover and improves the performance of the membrane during the microbial fuel cell operation [4].

In the XRD pattern of polymer/TiO_2 nanocomposites (Fig. 2) the peak of TiO_2 at around 25° is so intense that the characteristic peaks of polyaniline and poly(PA-co-ANI) cannot be observed. Also, it should be considered that the layer of polymer chains adsorbed on the surface of TiO_2 is, most probably, less than 1nm thick. In the composites a peak around 32° is observed that can be associated to the polymers.

These observations were also observed by other authors with TiO_2/polyaniline composites [5, 6].

The average crystallite sizes of TiO_2 nanoparticles, and the three samples of nanocomposites were estimated from the X-ray diffraction patterns using Scherrer formula [7]:

$$d = \kappa\lambda / B\cos\theta \qquad (1)$$

Where d is the average crystallite size, k is the X-ray wavelength, b is the full-width at half-maximum and h is the diffraction angle. The value of k depends on several factors, including the Miller index of reflection plane and the shape of the crystal. If shape is unknown, k is often assigned a value of 0.9. So the crystallite size of TiO_2 nanoparticle, and the nanocomposites was computed from XRD patterns see Table I.

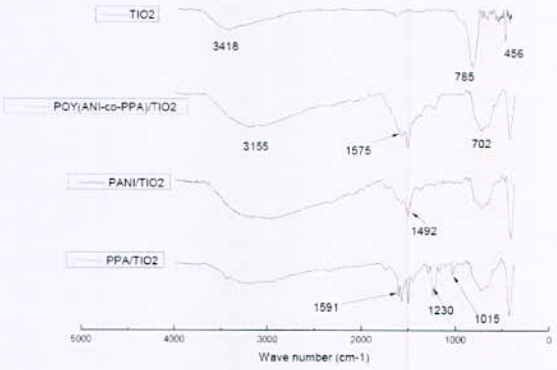

Fig. 1. FT-IR adsorption spectra of nanocomposites

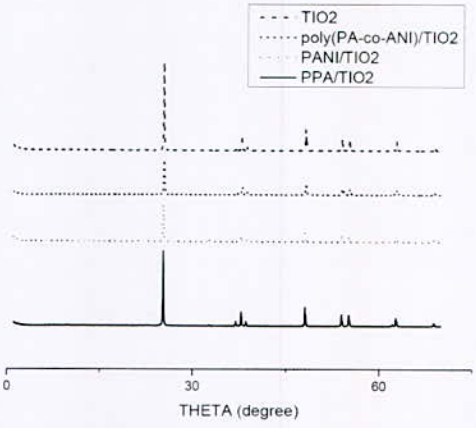

Fig. 2. XRD diffraction patterns of nanocomposites, and TiO_2 nanoparticle

TABLE I
THE AVERAGE CRYSTALLITE SIZE OF THE TIO_2 NANOPARTICLE AND THE THREE NANOCOMPOSITES WAS COMPUTED FROM SCHERRER FORMULA

Samples	PPA/TiO_2	Poly(PA-co-ANI)/TiO_2	PANI/TiO_2
d(nm)	46.64	31.73	42.45

3. Electrical conductivity measurements

Table II, shows the electrical conductivities, the composite with polyaniline has the higher conductivity and the lower conductivity is obtained with the PPA composite. In all the cases, the composites are not only electron conducting, but also proton conducting materials, so they can be used in the catalyst layer of fuel cell electrode and provide enhanced performance.

*Corresponding author email: faizachouli@yahoo.fr

4. The electrochemical study

Cyclic voltammetry experiments were performed to test the electroactivity of the polymer extracted from the nanocomposites. In the case of PANI/TiO_2 nanocomposite, two overlapped redox processes are observed. The first one appears at 0.36/0.25V; the second process is observed at 0.62/0.53V.

TABLE II
THE ELECTRICAL CONDUCTIVITY VALUES OF NANOCOMPOSITES

samples	PPA/TiO_2	Poly(PA-co-ANI)/TiO_2	PANI/TiO_2
Conductivity ($S.cm^{-1}$)	0.08	0.12	0.91

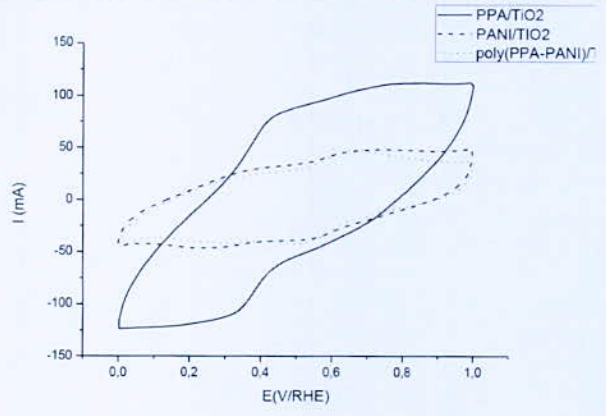

Fig. 3. Cyclic voltammograms recorded for a graphite carbon electrode covered by nanocomposites in 1 M $HClO_4$ solution. Scan rate 50 mV S^{-1}

The first redox process is due to the oxidation of the benzenoid form of polyaniline and the second one to the oxidation of the quinoid form of polyaniline.

5. The thermogravimetric analysis (TGA)

TGA is one of the thermal analysis techniques used to quantify weight change and thermal decomposition of the sample. The TGA curves of pure TiO_2 nanopowder only show a small 5.5% weight loss observed at 3408C, and can be ascribed to the elimination of water and the partial dehydroxylation of the TiO_2 nanopowder as shown in Fig. 4.

The thermal behavior of PPA pure is similar to that of PANI pure and exhibits a four-stage decomposition pattern. In the first stage, the weight loss starting practically from room temperature to 70°C is due to the loss of water molecules and moisture present in the polymer matrix. The second- and third-stage losses that occur from 70°C to 340°C are attributed to the loss of the dopant from the polymer chains. While the fourth stage loss from 350°C to 600°C is the result of the complete degradation and decomposition of the polymer backbone [8].

Stability of nanocomposites depends on the polymer type used (structure of the polymers and the interaction between the two components) [9].

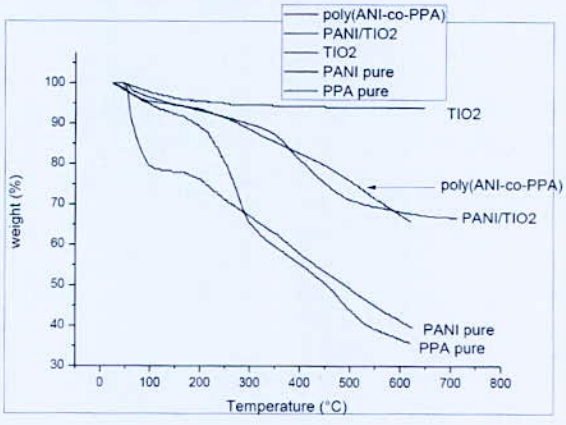

Fig. 4. Thermogravimetric analysis of PPA/TiO_2, poly(PA-co-ANI)/ TiO_2, PANI/TiO_2 nanocomposites, pure PANI, pure PPA, and TiO_2 nanoparticles

IV. CONCLUSION

The TiO_2 morphology have an effect on the final behavior of the nanocomposites where the high polymer order and crystallinity is clear from X-ray diffraction patterns. FTIR spectral analysis shows the strong interaction between polymer and TiO_2 that gives additional stability to the polymer. Future works would focus on improving the performance of the microbial fuel cells using this material as their anode material.

REFERENCES

[1] Zhao,C.E.,Wang,W.J.,Sun,D.,Wang,X.,Zhang,J.R.,Zhu,J.J. Chem. – Eur...20(2014), 7091–7097.
[2] X. Li, G. Wang, X. Li, and D. Lu, Surface properties of polyaniline/ nano TiO_2 composites, Applied Surface Science , 229(2004), 395-401.
[3] R.L. Pecsok, L.D. Shields, T. Cairns, and I.G. McWilliam, Modern Methods of Chemcal Analysis, 2nd ed., Wiley, New York (1976).
[4] M. Radoičić, Z. Šaponjić, I. A. Janković, G. Ćirić-Marjanović, S. P. Ahrenkiel, M. I. Čomor, "Improvements to the photocatalytic efficiency of polyaniline modified TiO2 nanoparticles Original Research Article Applied Catalysis B: Environmental," 136(2013), 133-139.
[5] M. Radoičić, Z. Šaponjić, I. A. Janković, G. Ćirić-Marjanović, S. P. Ahrenkiel and M. I. Čomor, Appl. Catalysis B: Environ., 136, 133 (2013).
[6] S. Sathiyanarayanan, S. Syed Azim, and G. Venkatachari, Synth. Metals, 157, 205 (2007).
[7] H.P. Klug and L.E. Alexander. Wiley, New York (1954).
[8] M.C. Gupta and S.S. Umare, Macromolecules, 25, 138 (1992).
[9] S. Bitao, M. Shixiong, S. Shixiong, T. Yongchun, and B. Jie, Front Chem. China, 2, 123 (2007).

*Corresponding author email: faizachouli@yahoo.fr

Characterization and Adsorption Behavior of Hydrogen on Calcium Exchanged LTA Zeolites

R. Melouki[1*], F. Benaliouche[1], P. L. Llewellyn[2] and Y. Boucheffa[3]

[1*]Ecole Militaire Polytechnique, 16111 Bordj El-Bahri, Algiers, Algeria.
[2]Aix-Marseille University, CNRS, MADIREL, UMR 7246, 13397 Marseille, France.
[3]Laboratoire d'Etude Physico-Chimique des Matériaux et Application à l'Environnement, Université des Sciences et de la Technologie Houari Boumediene, B.P. 32, El-Alia, Bab-Ezzouar, Algiers, Algeria.

Abstract— **Hydrogen adsorption at low temperature and high pressure is investigated over various Ca-exchanged A zeolites. The Ca-exchange degrees of the prepared samples range from 33% to 74% and the Si/Al ratio are nearly equal (≈1.1). Ca^{2+} ions are well dispersed in the zeolite framework while the structure is globally maintained. N_2 adsorption–desorption measurements show that Ca-exchanged zeolites exhibit a type Ib isotherm particularly at high degree of exchange, while a type III isotherm is shown at low Ca-exchange. The N_2 adsorption capacity increases noticeably with an increase of Ca-exchange degree. The hydrogen adsorption isotherms are determined using a manometric approach up to 4.5 bar at a temperature of -196°C. The obtained isotherms show maximum uptake exceeding 1.57% of hydrogen particularly for sample exchanged at high Ca-exchange degree. The estimated heat of hydrogen adsorption is found to be 4.08-4.11 kJ/mol. These results confirm the physical nature of adsorption. The fitting of isotherms using various macroscopic models such as Langmuir, dual Langmuir, Sips and Toth, demonstrate that Sips model is more representative of the H_2 adsorption evolution and clearly highlight differences in uptake depending on Ca-exchange degree, and pore size of A zeolite.**

Key words—Hydrogen, Adsorption, Ca-A zeolites.

I. INTRODUCTION

The use of hydrogen as an energy vector remains dependent on the development of the sure and efficacy means for storage. At present, hydrogen is stored either in gas form with high pressure or liquid at low temperature [1]. However, these forms of storage are not completely satisfactory in the field of the gravimetric and volumetric density. Currently several research works are interested in storage by adsorption in porous solids such [2], activated carbon [3], metal-organic frameworks (MOFs) and zeolites. For hydrogen storage, various types of zeolite are extensively investigated such as MFI, FAU, MOR and T-type. Among these zeolites, Linde Type A has attracted a great deal of attention for their superior adsorptive properties, strong hydrophilicity and their negative surface charge [2-4]. The pore size of Na-exchanged A zeolite is usually smaller than the kinetic diameter of the short-chain alkanes, thus achieving high adsorption efficacy for selective separation of hydrogen. In spite of numerous investigations in recent years, which were devoted to the status of exchanged metal ions in LTA zeolite and their interactions with guest molecules such as CO, O_2, N_2 H_2 at mild conditions [1-4], information related to the variation of hydrogen adsorption on A zeolite with calcium exchange degree at high pressure is limited and the associated phenomena are not well understood. The aim of this work is to understand of the relation between the textural properties, exchange degree and the hydrogen adsorption over Ca-exchanged zeolites. Hydrogen adsorption isotherms are carried out at -196°C and up to pressures of 4.5 bar. These experiments are combined with microcalorimetry to obtain a direct measurement of the hydrogen-cation interaction in the zeolite framework.

II. EXPERIMENTAL

The parent material used for this study is the sodium form of the LTA zeolite, which is designated as A0 supplied by Zeolyst International. Ca-exchanged zeolites are prepared by liquid ion exchange technique following procedure well described in our previous studies [5, 6]. The ion exchange procedure is repeated several times to ensure that the desired level of ion exchange is obtained. Framework of the exchanged materials is examined by a PANalytical-X'Pert PRO diffractometer. Powder X-ray diffraction (XRD) patterns are collected over a 2θ range of 3–50° using Cu-Ka radiation (k = 1.54060 Å). The surface area and pore volumes are characterized by nitrogen adsorption/desorption at -196°C in the 9×10^{-6}–0.99 relative pressure range. These characterizations are carried out with an automated manometric apparatus (Autosorb, Quantachrome). Prior to the measurements, all samples are outgassed at 300°C for 8 h. The hydrogen adsorption isotherms are determined using a manometric approach (PCT Pro-2000, SETARAM Instrumentation). Prior to measurement, the samples are activated under vacuum (10^{-2} mbar) at 150°C for 8 h. After, we have used Dewar vessel with liquid nitrogen to maintain temperature at -196°C during experience. The volume of hydrogen chamber with sample holder is measured using helium at the adsorption temperature. A stepwise hydrogen gas (purity = 99.999 %, Air Liquide) introduction method is used. The equilibrium for each dose is followed via the recording of the change of pressure versus time. The equilibrium is considered to be reached when no change

*Corresponding author email: melouki.redouane@gmail.com

in the pressure readings occurs over a 30 min period (reading error = 1 %).

III. RESULTS AND DISCUSSION

The elemental analysis shows Na^+ cations are partially exchanged by Ca^{2+}. The Ca-exchange degrees range from 33% to 74% and the Si/Al ratio are nearly equal (≈1.1) for all samples. The obtained zeolites are designated as follows: A0, A33, A44, A57 and A74 corresponding to exchange degree of 0%, 33%, 44%, 47% and 74%. XRD analysis indicates that Ca^{2+} ions are well dispersed in the zeolite framework while the structure is globally maintained. N_2 adsorption–desorption isotherms show that Ca-exchanged zeolites exhibit *Ib* type isotherm which is typical for microporous materials with a significant micropore size distribution (Fig. 1). The *Ib* type isotherm is particularly observed at high degree of exchange, while a type III isotherm is shown at low Ca-exchange. The N_2 adsorption capacity increases noticeably with an increase of Ca-exchange degree.

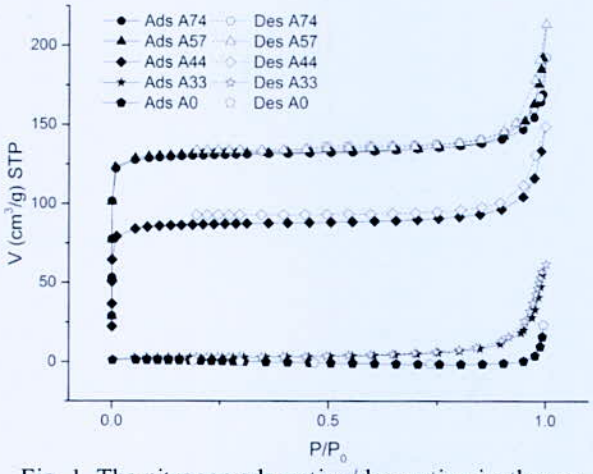

Fig. 1. The nitrogen adsorption/desorption isotherms, at –196 °C of Ca-A zeolites

Fig 2, show adsorption isotherms of hydrogen on different Ca-exchanged zeolites at -196 °C and up to 4.5 bar expressed as weight percent (wt%).

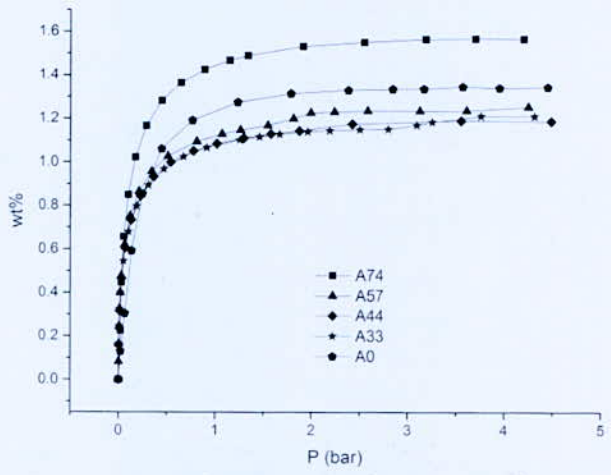

Fig. 2. Hydrogen isotherms obtained at –196 °C for various Ca-A zeolites

We observe that all of the isotherms show similar shape and clearly highlight differences in uptake depending on porous volume and Ca-exchange degree. The hydrogen adsorbed amount reported in wt% in table 1, is defined as mass of hydrogen (m_{ads}) per mass of the system, which consists of the sample mass (m_s) and the adsorbed hydrogen: $wt\% = [m_{ads} /(m_{ads} + m_s)] \times 100$. The maximum uptake of 1.57 % of hydrogen is obtained on a sample with upper surface area at higher Ca-exchange degree (A74). In A33, A44 and A57 samples, it would seem that the Ca-exchange degree decreases hydrogen uptake with a changing in isotherm shape. Indeed, the hydrogen uptake decreases from 1.35% to 1.19% when Ca-exchange degree increases from 0 to 44%. This result is surprising if we consider the increase of porous volume with the Ca-exchange rate. These results could be related to the major modification occurring during the mobility of Ca ions in the zeolite framework. It is not exclude the probable repulsion of hydrogen and/or its difficulty to be adsorbed when the Ca ions at low rates are located in inner access of α cage of A zeolite.

TABLE I
HYDROGEN UPTAKE AT 4.5 BAR AND –196 °C FOR VARIOUS CA-A SAMPLES

sample	A0	A33	A44	A57	A74
wt%	1.35	1.21	1.19	1.25	1.57

*Corresponding author email: melouki.redouane@gmail.com

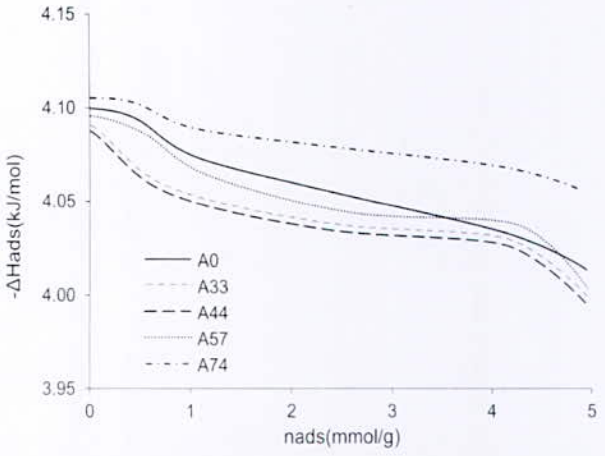

Fig. 3. Initial enthalpy of hydrogen adsorption at –196 °C on different Ca-A zeolites

The experimental isotherms are fitted using various macroscopic models including Langmuir, dual Langmuir, Sips, Jensen-Seaton and Toth. Sips model is more suited to describe the behavior of the H_2 adsorption and clearly highlight differences in uptake depending on Ca-exchange degree, and pore size of A zeolite. The order of the model correlation with hydrogen isotherms and experimental data is sequenced as follows: Sips > Jensen-Seaton > Toth > dual Langmuir > Langmuir. Indeed, the obtained results would further suggest the existence of various adsorption sites in the exchanged zeolites. The heat of adsorption as a function of hydrogen adsorption at –196 °C is measured by applying an apparatus developed by P. Llewellyn et al. [7, 2]. Results are shown in Fig. 3. The enthalpy values for hydrogen adsorption on different samples are close to 4.08-4.11 kJ/mol. These values are in agreement with those reported in literature [8-11] and confirm the physical adsorption mechanism of hydrogen uptake on Ca-A zeolite.

IV. CONCLUSION

This study highlights that hydrogen uptake on Ca-exchanged zeolites presents interesting values (up to 1.57 % at 4.5 bar and -196 °C). The hydrogen uptake is related to the Ca-exchange degree and zeolite surface area. Indeed, Ca-exchange up to 57% lead to increases in BET area and consequently to hydrogen uptake. The samples exchanged at high level showed the highest hydrogen uptake while a decrease of hydrogen uptake with a changing in isotherm shape is observed at low exchange. These behaviors could be related to the major modification occuring during the mobility of Ca ions in the zeolite framework. It is not exclude the probable repulsion of hydrogen and/or its difficulty to be adsorbed when the Ca ions at low rates are located in inner access of α cage of A zeolite. The hydrogen adsorption isotherms show that Sips model describe well the adsorption behavior and clearly highlights difference in uptake depending on Ca-exchange degree, and pore size of A zeolite. The initial enthalpy data for hydrogen adsorption confirm the physical mechanism of hydrogen adsorption on Ca-A zeolite.

REFERENCES

[1] M.F. Fellah, "A DFT study of hydrogen adsorption on Be, Mg and Ca frameworks in erionite zeolite," *Appl. Surf. Sci.*, vol. 394, pp. 9–15, 2017.

[2] R. Melouki, P.L. Llewellyn, S. Tazibet, Y. Boucheffa, "Hydrogen adsorption on activated carbons prepared from olive waste: effect of activation conditions on uptakes and adsorption energies," *J. Porous Mater.*, vol. 24, pp. 1–11, 2017.

[3] F. Rouquerol, J. Rouquerol, K.S.W. Sing, P. Llewellyn, G. Maurin, "Adsorption by Powders and Porous Solids", Academic Press, Oxford, 2014.

[4] J. Kärger, D.M. Ruthven, D.N. Theodorou, "Diffusion in nanoporous materials", Wiley –VCH Verlag GmbH, 2012, Vol 1.

[5] F. Benaliouche, N. Hidous, M. Guerza, Y. Zouad, Y. Boucheffa, "Characterization and water adsorption properties of Ag-and Zn-exchanged A zeolites, *Micropor. Mesopor. Mat.* vol. 209, 2015, pp 184.

[6] F. Benaliouche, Y. Boucheffa, F. Thibault-Starzyk, "In situ FTIR studies of propene adsorption over Ag- and Cu-exchanged Y zeolites", *Micropor. Mesopor. Mat.* vol. 147, 2012, pp. 10–16.

[7] P.L. Llewellyn, G. Maurin, "Gas adsorption microcalorimetry and modelling to characterise zeolites and related materials," *C. R. Chim.*, vol. 8, 2005, pp. 283–302.

[8] J. Li, E. Wu, J. Song, F. Xiao, C. Gen, "Cryoadsorption of hydrogen on divalent cation-exchanged X-zeolites," *Int. J. Hydrogen Energy*, vol. 34, 2009, pp. 5458–5465.

[9] H.W. Langmi, D. Book, A. Walton, S.R. Johnson, M.M. Al-Mamouri, J.D. Speight, P.P. Edwards, I.R. Harris, P.A. Anderson, "Hydrogen storage in ion-exchanged zeolites," *J. Alloys Compd.*, vol. 404–406, 2005, pp. 637–642.

[10] X.-m. Du, E.-d. Wu, "Physisorption of Hydrogen in A, X and ZSM-5 Types of Zeolites at Moderately High Pressures," *Chin. J. Chem. Phys.*, vol.19, 2006, pp. 457–462.

[11] H.W. Langmi, A. Walton, M.M. Al-Mamouri, S.R. Johnson, D. Book, J.D. Speight, P.P. Edwards, I. Gameson, P.A. Anderson, I.R. Harris, "Hydrogen adsorption in zeolites A, X, Y and RHO," *J. Alloys Compd.*, vol. 356–357, 2003, pp. 710–715.

*Corresponding author email: melouki.redouane@gmail.com

A Two-Dimensional Model of Water and Heat Management Under Flood Conditions Along the Flow Channel of a PEMFC

H. Abdi[1,3,*], N. Ait Messaoudene[2,3] and M. W. Naceur[3]

[1]Département de Mécanique, University of Blida 1, PO Box 270. Blida, Algeria.
[2]Moallem Binladin Research Chair on Quality and Productivity Improvement in the Construction Industry, University of Hail, Saudi Arabia.
[3]Laboratoire des Applications Energétiques de l'Hydrogène (LApEH), University of Blida 1, Algeria.

Abstract— **The current-voltage curve (I-V) is generally used to characterize proton exchange membrane fuel cells (PEMFC). The behavior of a PEM fuel cell is nonlinear and it is important to incorporate nonlinearity in the design process, optimization and control of PEMFC. Among the factors causing non-linearity is the non-uniform distribution of current density which results in local overheating, accelerated aging, reduced power and performance. This is very critical when the fuel cell experiences flooding due to excess water. The phenomenon of PEM flooding is not fully understood and few modeling works include its effect. In the present study, performance of a PEMFC is studied under cathode flooding conditions. A two-dimensional model based on the laws of conservation and electrochemical equations is proposed for simulating water and heat management. Computational results show that operating parameters have important influences on water transport characteristics and PEMFC performance.**

Key words—current-voltage curve (I-V), PEMFC, cathode flooding.

I. INTRODUCTION

Fuel cells are electrochemical devices that directly convert chemical energy of reactants into electrical energy. Several research studies have been devoted to the development of proton exchange membrane fuel cells (PEMFC) technology in recent years. However, there remain significant challenges that must be overcome, particularly in extending the lifetime of the fuel cell. This subject is a research issue because of the non-uniform distribution of current in the cell which results in local overheating, accelerated aging, lower performance and power output [1]. Among the most important factors that cause non-uniform distribution of current density in a PEM fuel cell is operating under flooding conditions.

Among the studies that focus on the study of the effect of water flooding on the non-uniform distribution of current in PEM cells, a noteworthy contribution has recently been performed by Karimi *et al.* [2]. In the same context, Jamekhorshid *et al.*, [3] have proposed a two-dimensional model of partial flooding of the gas diffusion layer (GDL) in order to study the distribution of local current density along the flow channel over a wide range of operating conditions of the cell. Models presented in [2, 3] assume isothermal operating conditions. In fact, the variation of the gas mixture temperature in the flow channel of the fuel cell is one of the important factors that must be taken into account during operation.

The present work focuses on studying the performance of a PEMFC under cathode flooding conditions. A two-dimensional model of water and heat management is proposed. The model is used for evaluating the cell performance in terms of local and average current density. The effects of varying operating parameters are studied.

II. MATHEMATICAL MODEL

Fig. 1 shows the schematic of a PEM fuel cell. The model used in this work is a quasi-stationary two-dimensional model with partial flooding of the gas diffusion layer. It reflects the heat and mass transfer occurring in a PEMFC. The model is based on the following assumptions: (a) oxygen reduction of occurs in the catalytic layer of negligible thickness, (b) uniform and constant temperature was assumed for solid parts (membrane, electrodes and bipolar plates), (c) the flow is fully developed, (d) the gas mixture is assumed to be an ideal gas, (e) no voltage drop along the of flow channels, (f) the flow channels of the anode and cathode are considered parallel to each other.

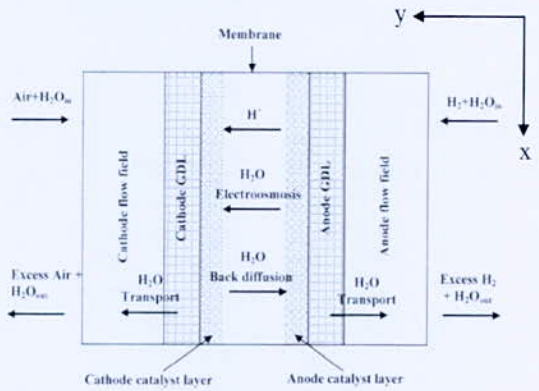

Fig. 1. Schematic of a PEM fuel cell.

1. Mass balance

At a local position (x) along the flow channel, the equations of molar flow rates for various species and for water vapor are given as follows [2, 3]:

*Corresponding author email: abdih1@yahoo.fr

$$\frac{dN_i(x)}{dx} = \xi_i \frac{w\, I(x)}{4F} \quad (1)$$

Anode channel: $\xi_{H_2} = -2, \xi_{w,a} = -4\alpha$

Cathode channel: $\xi_{O_2} = -1,\ \xi_{w,c} = 2 + 4\alpha,\ \xi_{N_2} = 0$

The parameter α represents the net water molecule per proton flux ratio. It is given by [4]:

$$\alpha = n_d - \frac{F}{I(x)} D_w \frac{dC_w}{dy} - C_w \frac{k_p}{\mu} \frac{F}{I(x)} \frac{dp_w}{dy} \quad (2)$$

where n_d, D_w, k_p, μ and t_m are respectively, the electro-osmotic coefficient, diffusion coefficient of water, permeability of water in the membrane, viscosity of water and membrane thickness. (dC_w/dy) and (dp_w/dy) are the water concentration and pressure gradient across the membrane respectively.

The amount of liquid water in the cell, and thus flooding state, depends on the difference between the partial pressure of water vapor and saturation pressure. The change in water vapor pressure along the flow channels depends on both the change in the liquid water and the flux of water vapor in and out of the membrane.

Anode:

$$\frac{dN^l_{w,a}(x)}{dx} = \frac{k_c\, h\, w}{R\,(T_a(x)+273)} \left(\frac{N^v_{w,a}(x)}{N^v_{w,a}(x) + N_{H_2}(x)} P_a(x) - P^{sat}_{w,a}(x) \right) \quad (3)$$

$$\frac{dN^v_{w,a}(x)}{dx} = -\frac{dN^l_{w,a}(x)}{dx} - \frac{w\,\alpha\, I(x)}{F} \quad (4)$$

Cathode:

$$\frac{dN^l_{w,c}(x)}{dx} = \frac{k_c\, h\, w}{R\,(T_c(x)+273)} \left(\frac{N^v_{w,c}(x)}{N^v_{w,c}(x) + N_{O_2}(x) + N_{N_2}(x)} P_c(x) - P^{sat}_{w,c}(x) \right) \quad (5)$$

$$\frac{dN^v_{w,c}(x)}{dx} = -\frac{dN^l_{w,c}(x)}{dx} + \frac{w\, I(x)\,(1+2\alpha)}{2F} \quad (6)$$

where k_c is the homogeneous rate constant for the condensation and evaporation of water reaction; h and w are respectively the height and width of the channel.

2. *Energy balance*

Local temperature in the anode and cathode flow channels is affected by latent heat and heat transfer between the solid surface and the gas. The energy balance equation for the gas mixture at the anode and cathode is given by [4]:

$$\sum_i (N_i(x) C_{p,i}) \frac{dT_k(x)}{dx} = (H^v_{w,k} - H^l_{w,k}) \frac{dN^l_{w,k}(x)}{dx} + U\, a\, (T_s - T_k(x)) \quad (7)$$

where index k represents either the anode or the cathode. U is the overall heat transfer coefficient and parameter a is the heat exchange area per unit length of the channel.

3. *Electrochemistry*

The cell potential can be calculated from the open circuit voltage, membrane ohmic resistance and activation polarization as follows [4]:

$$E_{cell} = E_{oc} - \eta_{act}(x) - \eta_{ohm}(x) \quad (8)$$

The overpotential at the anode is negligible compared to that at the cathode. $\eta_{act}(x)$ can be calculated from [3]:

$$\eta_{act}(x) = \frac{R(273+T_s)}{0.5F} \ln\left(\frac{I(x)}{(I^* P^{cat}_{O_2}(x)} \right) \quad (9)$$

$P^{cat}_{O_2}(x)$ is the oxygen partial pressure at the catalyst interface of the GDL.

$$P^{cat}_{O_2}(x) = \left(C^{bulk}_{O_2}(x) - \frac{I(x)}{4F} \left(\frac{1}{h_{O_2}} + \frac{t_{GDL}}{D_{O_{2-g}} [(1-s)\varphi]^{3/2}} \right) \right) R\,(T_c(x)+273) \quad (10)$$

where $C^{bulk}_{O_2}(x)$, h_{O_2}, $D_{O_{2-g}}$, s, t_{GDL} and φ are respectively, the oxygen concentration in the flow channel, mass transfer coefficient of oxygen, diffusion coefficient of oxygen, liquid water saturation, thickness of gas diffusion layer and GDL porosity.

Ohmic polarization is given by [4]:

$$\eta_{ohm}(x) = \frac{I(x)\, t_m}{\sigma_m(x)} \quad (11)$$

where $\sigma_m(x)$ is the membrane conductivity.

The average current density is given by:

$$I_{avg} = \frac{1}{L} \int_0^L I(x)\, dx \quad (12)$$

For solving the equations governing the transfer of heat and mass in the PEMFC, two options are available; namely, maintaining a constant average current density or constant voltage. In this work, the second option is adopted.

III. RESULTS AND DISCUSSION

Fig. 2 shows a comparison of simulation results for the current density profile from the present model with simulation results obtained by Jamekhorshid *et al.* [3] obtained for similar operating condition; i.e.: hydrogen and air inlet temperature: 80°C; cell temperature: 80°C; anode stoichiometry: S_a =1.2; cathode stoichiometry: S_c =1.75; anode inlet relative humidity: 100%; cathode inlet relative humidity: 85%. It can be seen that results of the present model is in reasonable agreement with results from [3]. The slight difference can be attributed to the fact that the model presented by Jamekhorshid *et al.* assumes isothermal operating conditions.

*Corresponding author email: abdih1@yahoo.fr

TABLE I
PARAMETERS USED FOR MODEL (BASE CASE)

Parameter	value	Parameter	value
E_{cell} (V)	0.6	S_a	1.2
U (W/cm² °C)	0.0025	S_c	1.8
k_c (1/s)	1.0	w	1
K_p (cm²)	1.58×10^{-14}	h (mm)	1
I^0 (A/cm²)	0.01	L (cm)	20
T_s (°C)	80	t_{GDL} (cm)	300×10^{-4}
T_a^{in}, T_c^{in} (°C)	80	φ (%)	60
P_a^{in}, P_c^{in} (atm)	1.5	t_m (cm)	50.8×10^{-4}
RH_a^{in},RH_c^{in} (%)	100	F (C/mol)	96485

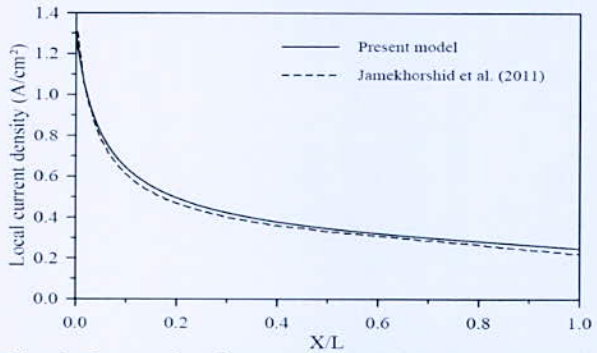

Fig. 2. Comparison between the model predictions and simulation results from (Jamekhorshid *et al.*, 2011).

1. Base case

The base case corresponds to a PEMFC operating with hydrogen and air at 1.5 atm, a temperature of 80 °C and a voltage of 0.6 V. The gaseous mixture at the anode inlet and cathode inlet are saturated with water vapor. The entrance humidification temperature is chosen to be the same as the cell temperature. Table (I) shows values for the input parameters for the base case. Other case studies are variations of the base case.

Fig. 3(a) shows the contribution of each water transport mechanism. The contribution of convective flux is very small (close to zero as shown in the Fig. 3(a)). With fully humidified anode and cathode inlet streams, the net water drag coefficient α is maximum at the inlet. As reactions proceed along the channel, water migrates from anode to cathode side and as a result, (α) decreases. It should be noted that diffusion water transport through the membrane depends solely on water concentration gradient across the membrane. As seen in Fig. 3(b), condensation of water occurs in the cathode when water vapor partial pressure exceeds saturation pressure. The amount of liquid water increases, because water generated from oxygen reaction is added to that transported from the anode. An increase in gas mixture temperature, due to latent heat of water condensation, is also noted in the cathode. The temperature of the gas mixture in the anode is kept constant because gases enter at the same temperature as that of the cell and no phase change occurs. The variation of liquid water saturation and local current density is shown in Fig. 4.

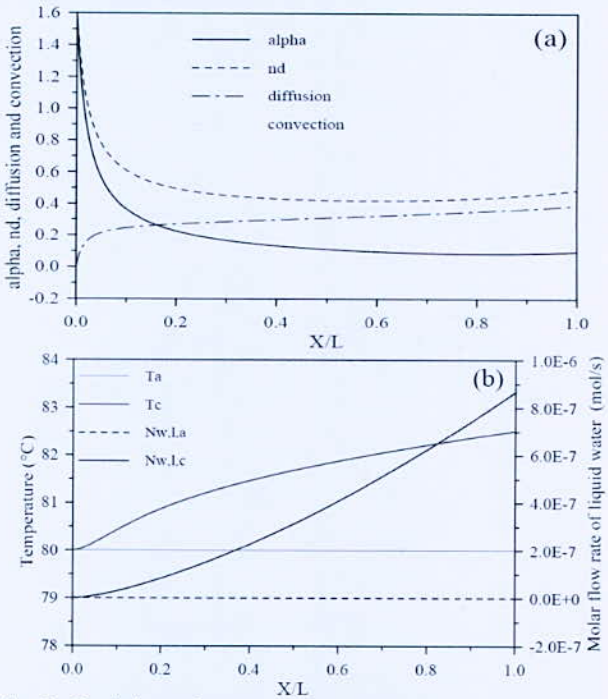

Fig. 3. Variation of: (a) water transport mechanisms; (b) molar flow rate of liquid water and gaseous mixture temperature

2. Parametric study for the base case

2.1. Effect of anode and cathode inlet humidity

Figs. 4 and 5 show the effect of anode and cathode inlet humidity on cell characteristics and flooding. As it can be seen from Fig. 4(a), an increase in RHa^{in} leads to flooding of a larger GDL portion, which leaves a smaller catalyst surface area accessible for O_2 reduction. As shown in Fig. 4(b), local current density decreases along the flow direction. Numerical results indicate that the more the anode is humidified; higher is the current density. Fig. 5 shows the effect of cathode inlet humidity on average current density. Simulations predict that there exists an optimal inlet humidity for which maximum cell power is be obtained.

2.2. Effect of inlet flow rate

Increasing molar flow rates of hydrogen and water vapor at the anode involves increasing anode stoichiometry. The effect of anode stoichiometry (S_a) on local current density is shown in Fig. 6. It can be seen that that increasing S_a leads to slightly higher local current density in the first part of the channel (up to X/L=0.6).

2.3. Effect of inlet temperature

The humidification temperature at the anode and cathode inlet is taken to be the same as the cell's temperature. Fig. 7(a) and (b) shows how an increase in

*Corresponding author email: abdihl@yahoo.fr

temperature may prevent cell flooding. A higher temperature enables better activation of reactions on the catalyst surface and also enhances transport of the reactants. Moreover, this also yields to an increase in local current density.

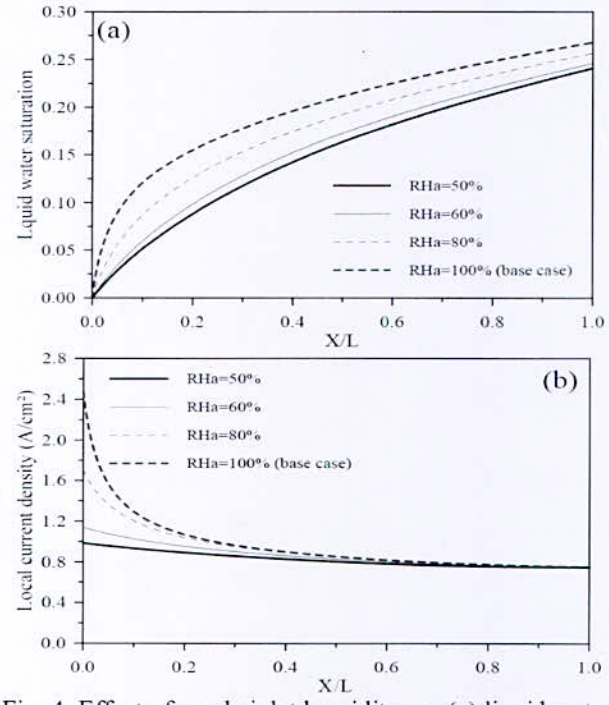

Fig. 4. Effect of anode inlet humidity on: (a) liquid water saturation; (b) local current density.

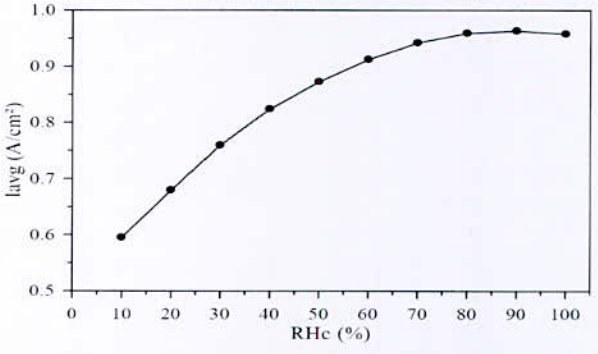

Fig. 5. Effect of cathode inlet humidity on average current density.

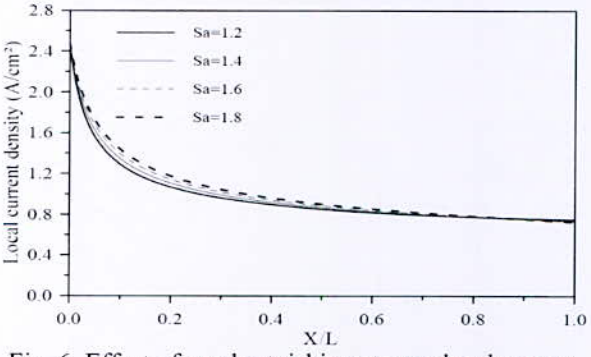

Fig. 6. Effect of anode stoichiometry on local current density.

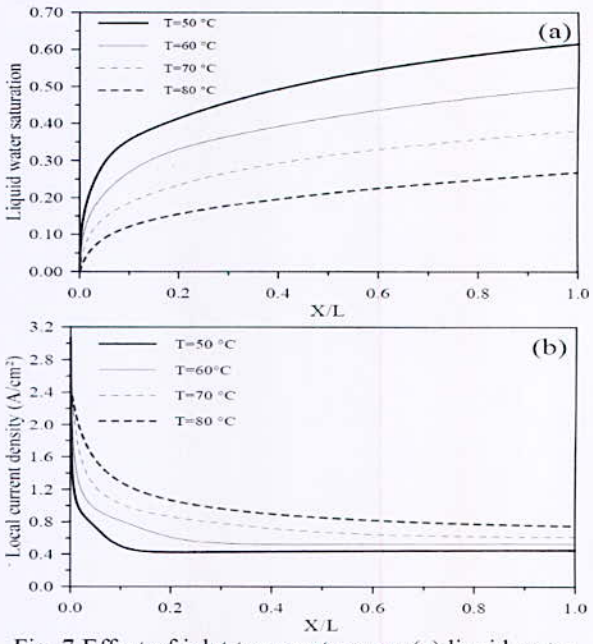

Fig. 7 Effect of inlet temperature on: (a) liquid water saturation; (b) local current density.

IV. CONCLUSION

In this study, the performance of a PEMFC is studied under conditions of flooded cathode. The effect of various operating parameters on local levels of saturation in liquid water and current density are studied. Based on computational results, the following conclusions can be formulated: (a) a greater amount of water is condensed in the cathode GDL when humidity at anode inlet increases. Moreover, this leads to an increase in current density. (b) Simulations predict that there exists an optimal inlet cathode humidity for which maximum cell power can be obtained. (c) Increasing anode stoichiometry involves increasing hydrogen and water vapor molar flows and leads to higher local current density. (d) Increasing anode and cathode inlet temperatures may prevent cell flooding.

REFERENCES

[1] J. J. Hwnag, W. R. Chang, R. G. Penng, P. Y. Chen, and A. Su, "Experimental and numerical studies of local current mapping on a PEM fuel cell," *Int. J. Hydrogen Energ.*, vol. 33, pp. 5718–5727, 2008.

[2] G. Karimi, A. Jamekhorshid, Z. Azimifar and X. Li, "Along-channel flooding prediction of polymer electrolyte membrane fuel cells," *Int. J. Energ. Res.*, vol. 35, pp. 883-896, 2011.

[3] A. Jamekhorshid, G. Karimi, and I. Noshadi, "Current distribution and cathode flooding prediction in a PEM fuel cell," *J. Taiwan Inst. Chem. E.*, vol. 42, pp. 622–631, 2011.

[4] J. Yi, and T. Nguyen, "An Along-the-channel model for proton exchange membrane fuel cells, *J. Electrochem. Soc.*, vol. 145, pp. 1149-1159, 1998.

*Corresponding author email: abdih1@yahoo.fr

Production d'Hydrogène par Vaporeformage d'Isooctane dans un Microréacteur: Effets Géométrique et Effets Inertiels

S. Chikhi

Faculté de physique, Université des Sciences et de la Technologie Houari Boumediene, BP 32 El Alia, Alger, 16111, Algérie.

***Résumé*—La procédure de production d'hydrogène propre par vaporeformage d'isooctane dans un *microréacteur* a été traitée. La simulation est modélisée par les équations de la conservation de la quantité de mouvement, de la conservation de la masse et de l'équation de la convection-diffusion, représentée par les équations de Navier-Stocks, l'équation de la continuité, et l'équation de Steffan-Maxwell respectivement. La résolution a été effectué par le logiciel COMSOL Multiphysics 3.5a, il discrétise les équations différentiels sous leurs forme conservative par la méthode des éléments finis à l'aide d'un schéma inconditionnellement stable. Une analyse d'effet de la géométrie et de l'hydrodynamique de l'écoulement montre que la masse d'hydrogène produite est proportionnelle au nombre d'obstacles sur les parois intérieures du micro canal, et au nombre de Reynolds de l'écoulement du mélange.**

Mots clés—Production d'hydrogène, Vaporéformage, isooctane.

I. INTRODUCTION

L'hydrogène est une source d'énergie propre et inépuisable, il n'existe pas à l'état moléculaire dans la nature, ce qui nécessite une étape de production avant de l'utiliser ou éventuellement le stocker. Plusieurs procédures de production sont développées et classés en fonction de nombreux paramètres comme le type d'énergie primaire et la pureté. Parmi ces techniques nous citons : l'oxydation partielle, l'électrolyse de l'eau, ou la dissociation thermochimique de l'eau, ou bien de la biomasse, et le vaporéformage des hydrocarbures, de fait la quasi-totalité de l'hydrogène disponible provient du reformage de gaz naturel.

Dans le présent travail nous allons modéliser et simuler la production d'hydrogène par le vaporéformage. Elle consiste essentiellement en une transformation des hydrocarbures en H_2, par une réaction avec de la vapeur d'eau, à l'aide d'un catalyseur à base de nickel. L'objet de ce travail est l'étude de la production d'hydrogène par reformage d'isooctane à la vapeur d'eau, réalisée par une réaction endothermique dans un microréacteur utilisant un catalyseur Ni/AL_2O_2.

II. METHODE

Dans un microréacteur de diamètre d=0,001 m et d'une longueur L=0,02 m. se déroule la réaction de vaporeformage d'isooctane qui nécessite une énergie ΔH = 1275 kJ/mol.

*Corresponding author email: scusthb@gmail.com

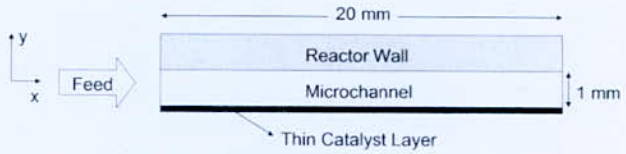

Fig. 1. Microréacteur

Selon la réaction suivante :

$$C_8H_{18} + 16H_2O \rightarrow 8CO_2 + 25H_2 \qquad (1)$$

L'étude numérique repose sur la modélisation donnant d'une part: l'évolution de la quantité de mouvement et de la conservation de la masse, représentées par les équations de Navier-Stocks faiblement compressibles et par l'équation de continuité.

$$\frac{\partial(\rho V)}{\partial t} + \nabla(\rho V.V) = \nabla P + \rho g \qquad (2)$$

$$\frac{\partial \rho}{\partial t} + div(\rho\, \vec{u}\,) = 0 \qquad (3)$$

Et d'autre part l'évolution des espèces chimiques mises en jeu dans la réaction simulée décrites par les équations de diffusion-convection de Stefan-Maxwell.

$$\sum_{j \neq i} \frac{x_i x_j}{\rho D_{ij}} \left(\frac{J_j}{C_j} - \frac{J_i}{C_i} \right) = \frac{\nabla \mu_i}{RT} = \nabla x_i \qquad (4)$$

Avec $i, j = 1.N$

La simulation a été réalisée à l'aide du logiciel COMSOL Multiphysics 3.5a, il résout les équations différentielles sous leur forme variationnelle par la méthode des éléments finis à l'aide d'un schéma inconditionnellement stable (numériquement).

III. RESULTATS ET DISCUSSION

1. Effets géométriques

Afin d'étudier l'impact des effets tourbillonnaires sur la masse d'hydrogène produite, nous avons introduit des obstacles sur les parois intérieures du micro-canal. Ces obstacles créent des zones vortex, qui permettent

d'augmenter le contacte parois/fluide, par conséquent le catalyseur/mélange, et de capter plus de molécules d'isooctane. L'influence de la géométrie a été traitée par deux paramètres : effet de la forme d'obstacle, nous avons utilisé trois formes d'obstacles: carré, arrondis, et triangulaire.

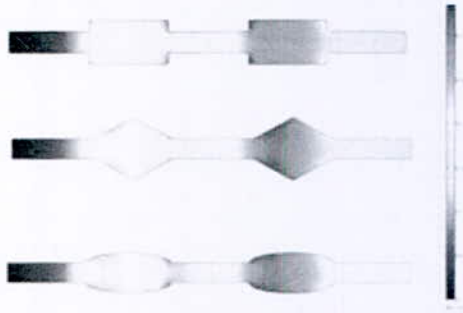

Fig. 2. Les trois différentes formes d'obstacle dans le micro-canal

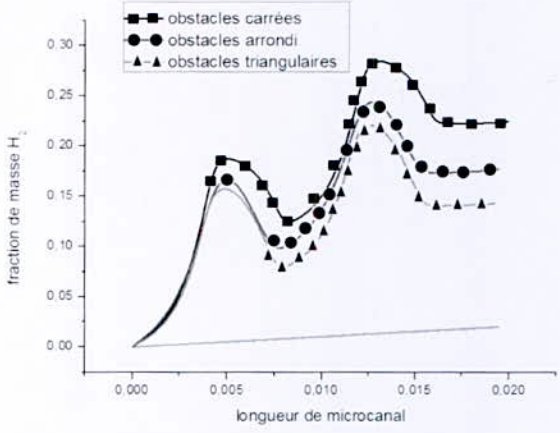

Fig. 3. L'hydrogène produit pour les trois formes d'obstacles

La fraction de masse d'H_2 trouvée pour ces différentes formes était respectivement de 11.5, 09 et 07 fois plus grande que le cas de référence (sans obstacles). L'effet de nombre d'obstacles utilisés: allant de 2 jusqu'à 16 obstacles par un pas de 2.

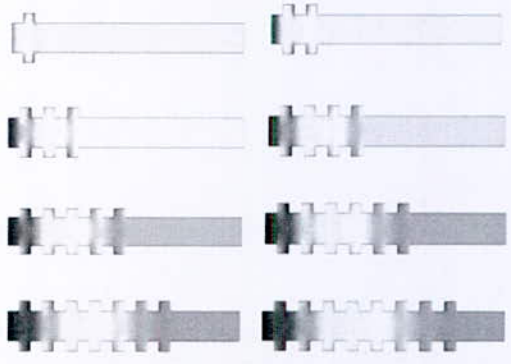

Fig. 4. La variation de nombre d'obstacles au micro réacteur

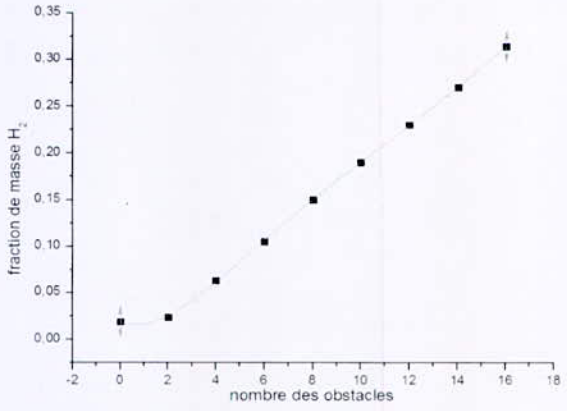

Fig. 5. La fraction d'hydrogène en fonction du nombre d'obstacle

On remarque que la masse d'hydrogène produite augmente linéairement avec le nombre d'obstacles.

2. *Effets inertiels*

Une étude inertielle a été effectuée dans le but de mettre en évidence l'influence de l'hydrodynamique sur la procédure de vaporéformage d'isooctane. Variant le nombre de Reynolds de Re=2000 jusqu'à Re=10000 pour les deux modèles de la turbulence K-eps et K-W.

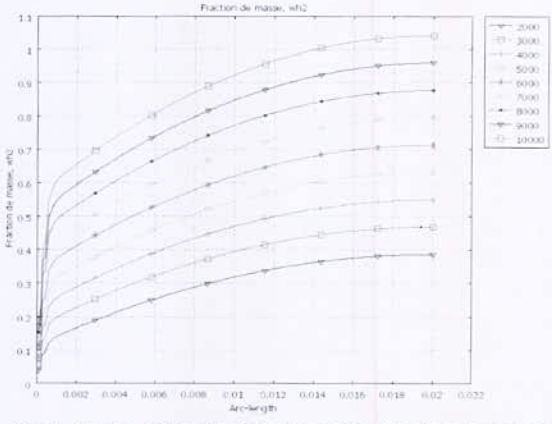

Fig. 6. La masse d'hydrogène pour les différents nombres de Reynolds: modèle K-eps

Pour ce régime, la hausse du nombre de Reynolds est proportionnelle à la fraction de la masse d'hydrogène, avec les maximas suivants : wh_{2Max}= 1,2 et Re_{Max}=10 000, c'est-à-dire (63,15) fois plus élevé que le cas de référence (laminaire).

De façon similaire au modèle de turbulence « k-eps », la fraction de masse d'hydrogène produite augmente jusqu'à wh2=1.4. Comparant les deux modèles ; il existe une différence de 20 % (Fig. 8).

*Corresponding author email: scusthb@gmail.com

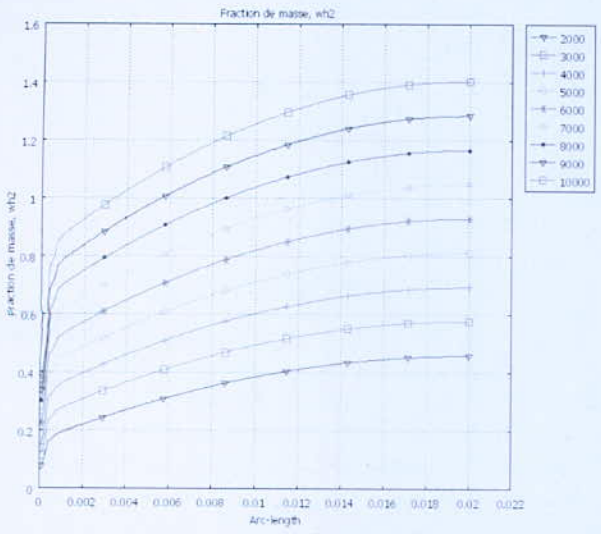

Fig. 7. La masse d'hydrogène pour les différents nombres de Reynolds : modèle K-W

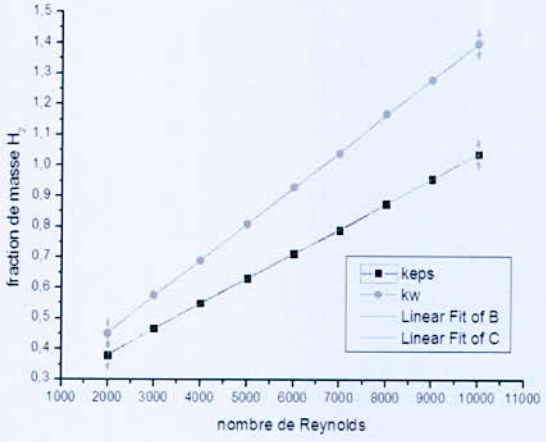

Fig. 8. La fraction des masses pour les deux modèles turbulents «kw» et «kε»

IV. CONCLUSION

Le vaporéformage d'isooctane dans un microréacteur est une des procédures de production d'hydrogène propre. La masse d'H_2 produite croit linéairement avec le nombre d'obstacles. La turbulence de l'écoulement dans le micro-canal améliore aussi cette technique, la fraction d'hydrogène à la sortie du micro canal est proportionnelle au nombre de Reynolds, nous constatons que le modèle turbulent K-W est plus compatible avec cette technique que le K-eps. Le tableau suivant représente les corrélations obtenues à partir des résultats précédents.

TABLE I
CORRELATIONS

Modèle	Correlation
En fonction de nombre d'obstacles	Wh_2=0.01878-0.00975*N+0.00814*N^2-9.408.10^{-4}*N^3+4.9.10^{-5}**N^4-9.43517.10^{-7}*N^5
Régime Turbulent kw	Wh_2=0.20733+1.2.10^{-4}*Re
Régime turbulent k-eps	Wh_2=0.21665+8.25.10^{-5}*Re

REFERENCES

[1] Andreassen K., Hydrogen production by electrolysis, Hydrogen Power: Theoretical and Engineering solutions, Kluwer Academic Publishers, the Netherlands (1998).

[2] Damien A., Hydrogène par électrolyse de l'eau, Techniques de l'Ingénieur (1992), J6366.

[3] Derek C., Auto-thermal Reforming of a Hydrocarbon Fuel in a Monolithic Reactor, the Nordic COMSOL Conference (2006).

[4] Johanna I., Summary of Electrolytic Hydrogen Production, Rapport NREL/MP-560-35948, (2004), (28 pages).

[5] Kathy A., Proton Energy Systems, Progress and New Directions in PEM Electrolysis, Colloque FCHEA Fuel Cell & Hydrogen Energy (2011).

[6] Padro C.E.G., Putsche V., Survey of the Economics of Hydrogen Technologies, National Renewable Energy Laboratory Technical Report, (1999) TP-570-27079.

[7] Richards J. W., Engelhardt V., The Electrolysis of Water, Processes and Applications, The Chemical Publishing Company, (2010),154 pages

[8] Sabonnadière J.C., Thierry A., Pierre B., et al. Nouvelles Technologies de l'énergie, Editions Hermès - Lavoisier, (2007), 290 pages.

[9] Vock A., Maloney T., Mitlisky F., Shiepe J., PEM Electrolysis-based refueling stations for Hydrogen fueled vehicles, Proceedings of EVS 18 Berlin, (2001).

*Corresponding author email: scusthb@gmail.com

The Role of Hydrogen Production in 100% Renewable Energy Systems in the Power and Industrial Gas Sectors

A. Aghahosseini*, D. Bogdanov, M. Fasihi and C. Breyer

Lappeenranta University of Technology, Skinnarilankatu 34, 53850 Lappeenranta, Finland.

Abstract—**In this paper, the "LUT Energy System model" based on linear algorithm with an hourly resolved configuration is used to assess the role of hydrogen in 100% renewable energy (RE) based power and industrial gas sectors. The study is done for 2030 assumptions. A mix of RE technologies and energy storage options is applied to provide energy security and system flexibility. The three chosen case study countries are Germany, Finland and Egypt. In countries with sustainable biomass resources, depending on the optimised cost, the model assumes that 60 mol.% of feedstock is converted into biomethane (CH_4) and the remaining 40 mol.% is CO_2 produced together as biogas. Therefore, the costs of H_2 to SNG conversion drops due to no extra cost for capturing the required CO_2 from air. The LUT model with additional biogas-to-SNG options and new functionality is called the Enhanced model and the regular model is called the Standard model. The results reveal that in the Enhanced model, where readily available CO_2 is captured from biogas, hydrogen production plays a vital role in securing a 100% RE powered system. This results in a lower cost of the energy system, in particular for Egypt (9% lower at 35 €/MWh) and Germany (3% lower at 62 €/MWh) in the Integrated scenario, where the gas demand for industrial sector is high. However, for Finland the decrease is only 1% to 54 €/MWh. Moreover, lower full load hour of electrolysers, additional installed capacity of hydrogen and higher system flexibility emphasise the benefits of hydrogen in the total energy system.**

Keywords— Hydrogen, power-to-gas, biomethane, CO_2 storage, 100% renewable energy.

NOMENCLATURE

AC	Alternating current
A-CAES	Adiabatic compressed air energy storage
Capex	Capital expenditure
CCGT	Combined cycle gas turbine
CSP	Concentrating solar thermal power
DAC	Direct air capture
FLH	Full load hours
GT	Gas turbine
HHB	Hot heat burner
HVDC	High voltage direct current
ICE	Internal combustion engine
LCOE	Levelised cost of electricity
LCOG	Levelised cost of gas
OCGT	Open cycle gas turbine
Opex	Operating and maintenance expenditures
PHS	Pumped hydro storage
PtG	Power-to-gas
PtH	Power-to-heat done by heating rod
PtX	Power-to-X
PV	Solar photovoltaic
RE	Renewable energy
SNG	Synthetic natural gas
ST	Steam turbine
$_{el}$	Electric units
$_{th}$	Thermal units
€	Euro

I. INTRODUCTION

Scarcity of fossil fuel resources, increasing energy demand, climate change and sharp reduction of renewable energy (RE) costs pave the way for 100% RE systems that offer vital improvements in the quantity and quality of energy services provided. In this regard, hydrogen technology is regarded with high interest for wide range of applications, including electricity generation [1]. Hydrogen technology can also be used as long-term storage in Power-to-Gas (PtG) systems [2] and for Power-to-X (PtX) applications, in particular for fuels and chemicals [3]. The objective of this study is to analyse the role of hydrogen production and the beneficial impact of the lower cost PtG process using biogas as a CO_2 source in a fully RE based system for 2030 technical and financial assumptions.

II. METHODOLOGY

A linear optimization model, called the *LUT Energy System* model, is used and further developed based on Matlab software (R2016b) [4] and the Mosek ApS optimizer [5]. It should be noted that, the regular LUT Energy System model is labelled the Standard model and the developed model, with regards to additional functionality for biogas upgrading and PtG technology, is labelled Enhanced model. The objective of the model is to minimise the total annual cost of the energy system, taking into account the applied RE and storage technologies. The model description, technical and financial assumptions for the Standard LUT Energy System model are discussed in detail in Bogdanov and Breyer [6] and Aghahosseini et al. [7]. Three countries are chosen as a case study: Germany, Finland and Egypt. Existing installed capacity, electricity demand growth and cost of each technology are collected from various sources in the literature. Simulations are performed in an hourly resolved configuration for the year 2030.

A block diagram of the proposed RE system is presented in Fig. 1, depicting the technologies used in the LUT Energy System model. The municipal bio-waste is used as feedstock to generate biogas for electricity production. Alternatively, biogas can be upgraded to biomethane. The generated biomethane is then stored to be used as fuel for CCGT and OCGT. In the Enhanced model, it is assumed that in countries with sustainable biomass resources, depending on the optimised cost, 60 mol.% of feedstock is converted into biomethane (CH_4) and the remaining 40 mol.% is CO_2 together forming biogas [8], [9]. Further, from volumetric point of view, raw biogas components

*Corresponding author email: arman.aghahosseini@lut.fi

contain of 50-70 vol.% CH_4 and 30-50 vol.% CO_2 [10]–[12]. Biogas also contains some other minor components that are negligible and not considered for this paper. The separated CO_2 in the biogas upgrading process can be utilised for SNG production. A block diagram of the new functionality added in the model is presented in Fig. 2 and the new assumptions are given in Table I.

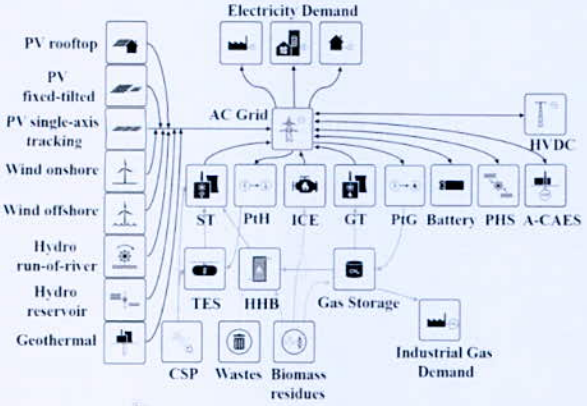

Fig. 1. Block diagram of the standard *LUT Energy System* model [13]

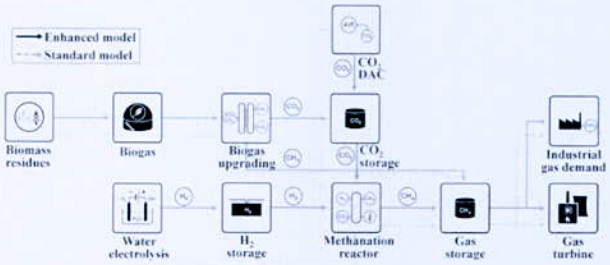

Fig. 2. Block diagram of the Standard and Enhanced energy system configuration with regards to the biogas upgrading process and PtG system

TABLE I
TECHNICAL AND FINANCIAL ASSUMPTIONS NEWLY ADDED TO THE LUT ENERGY SYSTEM MODEL TO UPDATE THE BIOGAS AND PTG TECHNOLOGY PRODUCTION PROCESSES.

	Hydrogen storage [14]	CO_2 storage [15]
Capacity	155,951 [MWh_{H2}]	3,300 [ton_{CO2}]
Capex	0.298 [€/kWh_{H2}]	891 [€/ton_{CO2}]
Opex	3 [% of capex p.a.*]	1 [% of capex p.a.]
Efficiency [%]	100	100
Life-time [a]	30	30
Energy/power ratio (h)	369	-
Self-Discharge (%/h)	0	-

* p.a. = per annum

III. RESULTS AND DISCUSSION

Two scenarios named Country-wide and Integrated have been investigated. The Country-wide scenario covers the electricity demand of the considered countries and the Integrated scenario supplies the electricity need for power and non-energetic industrial gas demand sectors. Similar scenarios have been studied for the whole world [13]. In this study, the scenarios are analysed with an Enhanced model with improved biogas upgrading method and PtG system. As described earlier, a system with similar components and configuration to the Audi e-gas plant [16], provided by ETOGAS GmbH (previously Solarfuel) in cooperation with MT-BioMethan GmbH, is designed to demonstrate the economic impact compared to a system with separated biogas upgrading and SNG production. In addition, the role of hydrogen production has been analysed in both systems.

Three countries have been exclusively studied to assess the new assumptions in the energy system model: Germany, Finland and Egypt. Selecting three countries with different geographical conditions, resource availability, and electricity demand help to understand the impact of the new function in the energy system model better and in more detail. Table II provides a detailed comparison of the financial parameters and the key findings of the energy system modelling in the Standard and Enhanced energy system models by 2030.

As can be seen in Table II, the Enhanced model shows less LCOE in both Country-wide and Integrated scenarios than the Standard model by 1-9%. It can be explained by the fact that additional functionality in the energy system makes the system more flexible and cost-competitive in comparison with the Standard model. Capturing a part of CO_2 requirement for methanation from the biogas upgrading plant without extra cost for the scrubbing process results in higher hydrogen generation and cost reduction.

Additional flexibility in the Enhanced model can be attributed to the hydrogen production. The hydrogen capacity increased substantially in the Enhanced model for both scenarios (Table II). In the Country-wide scenario, hydrogen contributes to a seasonal energy system balance via PtG, whereas for the Integrated scenario, hydrogen provides the seasonal balance and supplies the gas demand in the industrial sector. The share of hydrogen capacity increases in the Country-wide for Germany and Egypt by 600% and 200%, respectively. Whilst the capacity of hydrogen goes up, the full load hour (FLH) of electrolyser decreases providing additional flexibility to the power system.

The table data clearly shows that additional hydrogen capacity has a positive impact on the overall system in the Integrated scenario. This can be explained by lower FLH of electrolysers (3607 h for Egypt, 2897 h for Finland, and 2890 h for Germany) and higher hydrogen capacity in the Enhanced model. The highest impact can be observed for Egypt, where the gas demand is quite large and additional hydrogen capacity makes the entire system lower in cost. It is worth noticing that the levelised cost of gas (LCOG) slightly decreased by 0.4% in the Enhanced model for Egypt. With this in mind, the LCOG increased in Finland and Germany by 41 and 14 €/MWh_{th}, respectively. However, the LCOG for Finland is extremely high, which can be the result of a not fully optimised model and has to be studied further.

In Egypt, RE installed capacity increased by 53% from the Country-wide scenario to the Integrated scenario in the Enhanced model. RE capacity for Germany in the Integrated scenario surpassed that of the Country-wide

scenario by only 3%. In Finland, however, RE installed capacities remained constant for both scenarios. The same situation can be seen for all the three countries in the Standard model.

In the Enhanced model, the need for gas storage decreased by 64% (7 TWh_{th}) for Egypt in the Integrated scenario compared to the Country-wide scenario. In terms of storage capacities, battery storage capacity increased from 141 GWh_{el} to 189 GWh_{el}. In addition, hydrogen storage capacity sees a tremendous surge by 12 TWh (+1245%) in terms of capacity and 116 TWh (+1657%) in terms of storage throughput. This is due to additional demand for the gas sector in the Integrated scenario, which is mainly supplied through PtG technology. PtG output increased from 6 TWh_{th} to 94 TWh_{th} (99% of the total gas demand), whereas in terms of electrical units it decreased from 3 TWh_{el} to 2 TWh_{el}. As a result, the installed capacity of RE increased drastically to fulfil the electricity demand for the PtG process. Solar PV soared by 58 GW (+87%) in 2030, accounting for the highest capacity growth in Egypt. However, wind capacity remained unchanged in the Integrated scenario. Hydro reservoirs, run-of-river and sustainable biomass help to complement solar PV and wind energy and provide energy security in the system.

However, the situation is slightly different for the case of Germany. Almost all energy storage technologies levelled off in the Integrated scenarios, except A-CAES and gas storage. Similar to Egypt, gas storage dropped to supply the supplementary gas demand for the industrial sectors. Having said that, A-CAES increased moderately with 60% (3 TWh) higher throughput compared to the Country-wide scenario. For Finland, the numbers mostly plateaued in both scenarios due to very low demand for non-energetic industrial gas sector.

The Standard model indicates similar achievements for energy storage as reported above for the Enhanced model. However, in the Enhanced model, there is a larger observed hydrogen production in both scenarios (3-30 TWh_{th}), due to the freely available CO_2, resulting in a more flexible model compared to the Standard model. Consequently, there is a greater synthetic methane production in the Enhanced model. The gas output of PtG is also higher in the Integrated scenario because of additional demand for the non-energetic industrial gas sector.

IV. CONCLUSION

To detect the importance of hydrogen production in a 100% RE system by 2030, two scenarios named Country-wide and Integrated are modelled and optimised by two model setups with different PtG process configurations. Three countries, Germany, Finland and Egypt, were selected with different geographical conditions, resource availability, and electricity demand to assess the impact of the new function in the energy system model.

The Standard LUT Energy System model uses CO_2 DAC for PtG technology. On the other hand, the Enhanced model not only uses CO_2 DAC for PtG production, but also captures the extra CO_2 released from the biogas upgrading process and utilises it for PtG production. This results in higher hydrogen production due to cost reduction in production cost of synthetic methane. Germany and Egypt experienced the most hydrogen production due to higher non-energetic industrial gas demand. In terms of hydrogen capacity, Germany is the leader with 35 GW_{th} in the Country-wide scenario (+600% growth compared to the Standard model), whereas Egypt has the highest capacity in the Integrated scenario with 34 GW_{th}. Furthermore, higher system flexibility, lower FLH of electrolysers and additional installed capacity of hydrogen highlight the role of hydrogen in a 100% RE based system by 2030.

Consequently, the total energy system cost declined, especially for the Integrated scenario, where additional gas demand is needed for the industrial sector. Egypt leads in terms of cost reduction, from 39 €/MWh in the Standard model to 35 €/MWh in the Enhanced model, followed by Germany. Finland experienced the least cost reduction mainly because of less gas requirement (306 GWh_{th}) compared to the two other countries.

ACKNOWLEDGMENTS

The authors gratefully acknowledge the public financing of Tekes (Finnish Funding Agency for Innovation) for the 'Neo-Carbon Energy' project under the number 40101/14.

REFERENCES

[1] R. Sarrias-Mena, L. M. Fernández-Ramírez, C. A. García-Vázquez, and F. Jurado, "Electrolyzer models for hydrogen production from wind energy systems," *Int. J. Hydrogen Energy*, vol. 40, no. 7, pp. 2927–2938, 2015.

[2] G. Gahleitner, "Hydrogen from renewable electricity: An international review of power-to-gas pilot plants for stationary applications," *Int. J. Hydrogen Energy*, vol. 38, no. 5, pp. 2039–2061, 2013, Elsevier Ltd.

[3] A. Tremel, P. Wasserscheid, M. Baldauf, and T. Hammer, "Techno-economic analysis for the synthesis of liquid and gaseous fuels based on hydrogen production via electrolysis," *Int. J. Hydrogen Energy*, vol. 40, no. 35, pp. 11457–11464, 2015, Elsevier Ltd.

[4] The MathWorks, "MATLAB and Statistics Toolbox Release 2016b," *Inc.: Natick, MA, USA*, 2016.

[5] Mosek ApS, "The MOSEK Optimization Toolbox for MATLAB Manual." version 7.1, revision 28, Copenhagen, Denmark, 2015.

[6] D. Bogdanov, and C. Breyer, "North-East Asian Super Grid for 100% renewable energy supply: Optimal mix of energy technologies for electricity, gas and heat supply options," *Energy Convers. Manag.*, vol. 112, pp. 176–190, 2016, Elsevier Ltd.

[7] A. Aghahosseini, D. Bogdanov, and C. Breyer, "A Techno-Economic Study of an Entirely Renewable Energy-Based Power Supply for North America for 2030 Conditions," *energies*, vol. 10(8), 2017.

[8] A. M. I. Yousef, Y. A. Eldrainy, W. M. El-Maghlany, and A. Attia, "Upgrading biogas by a low-temperature CO2 removal technique," *Alexandria Eng. J.*, vol. 55, no. 2, pp. 1143–1150, 2016, Elsevier.

[9] A. M. Yousef, Y. A. Eldrainy, W. M. El-Maghlany, and A. Attia, "Biogas upgrading process via low-temperature CO2 liquefaction and separation," *J. Nat. Gas Sci. Eng.*, vol. 45, pp. 812–824, 2017, Elsevier B.V.

[10] M. Specht, "Impulsvortrag : Aktueller Stand der Power-to-Gas – Technologie Aktueller," in *Auditorium Friedrichstraße*, Berlin: Nov. 22, Centre for Solar Energy and Hydrogen Research (ZSW) in cooperation with Fraunhofer Institute for Wind Energy and Energy System Technology (IWES), and SolarFuel GmbH, 2011, [Online]. Available: https://goo.gl/BjVpD8. [Accessed: 02-Sep-2017].

[11] M. Specht, F. Baumgart, B. Feigl, V. Frick, B. Stürmer, U. Zuberbühler, M. Sterner, and G. Waldstein, "Storing bioenergy and renewable electricity in the natural gas grid," in *FVEE AEE Topics 2009*, Berlin: FVEE AEE - Topics 2009, 2009, pp. 69–78, [Online]. Available: http://www.fvee.de/fileadmin/publikationen/Themenhefte/th2009-1/th2009-1_05_06.pdf. [Accessed: 02-Sep-2017].

[12] M. Götz, J. Lefebvre, F. Mörs, A. McDaniel Koch, F. Graf, S. Bajohr, R. Reimert, and T. Kolb, "Renewable Power-to-Gas: A technological and economic review," *Renew. Energy*, vol. 85, pp. 1371–1390, 2016.

[13] C. Breyer, D. Bogdanov, A. Gulagi, A. Aghahosseini, L. S. N. S. Barbosa, O. Koskinen, M. Barasa, U. Caldera, S. Afanasyeva, M. Child, *et al.*, "On the

role of solar photovoltaics in global energy transition scenarios," *Prog. Photovoltaics Res. Appl.*, vol. 25, no. 8, pp. 727–745, Aug. 2017.

[14] E. R. Morgan, "Techno-Economic Feasibility Study of Ammonia Plants Powered by Offshore Wind," University of Massachusetts - Amherst, Ph.D. Dissertations, Department of Mechanical and Industrial Engineering, 2013[Online]. Available: http://scholarworks.umass.edu/open_access_dissertations/697.

[15] H. Karjunen, T. Tynjälä, and T. Hyppänen, "A method for assessing infrastructure for CO2 utilization: A case study of Finland," *Appl. Energy*, vol. 205, pp. 33–43, 2017, Elsevier.

[16] R. Otten, "Power-to-Gas - key technology for the energy turn around joining biomethane," *EBA Workshop: Future of Biomethane Production, Sustainable Product Development, AUDI AG, Brussels*, 2015. [Online]. Available: http://european-biogas.eu/wp-content/uploads/2015/09/4-EBA_Brussels_Audi_PtG_e-gas1.pdf. [Accessed: 13-Jun-2017].

TABLE II

THE KEY FINDINGS FOR THE CONSIDERED SCENARIOS IN THE STANDARD AND ENHANCED LUT ENERGY SYSTEM MODEL FOR GERMANY, FINLAND AND EGYPT FOR 2030 ASSUMPTIONS. RATIO OF KEY RE INSTALLED CAPACITIES TO TOTAL CAPACITY ARE IN BRACKETS.

		Standard model		Enhanced model		Relative difference	
Results parameters	Countries	Country-wide	Integrated	Country-wide	Integrated	Country-wide	Integrated
Total LCOE [€/MWh]	Germany	63.6	63.7	62.5	61.8	-2%	-3%
	Finland	54.9	54.9	54.3	54.3	-1%	-1%
	Egypt	46.3	38.8	45.3	35.5	-2%	-9%
LCOG [€/MWh$_{th}$]	Germany	-	63.4	-	77.3	-	+22%
	Finland	-	319.6	-	360.8	-	+13%
	Egypt	-	84.3	-	84.0	-	0%
Total ann. cost [b€]	Germany	35.8	37.0	35.2	36.4	-2%	-2%
	Finland	5.3	5.3	5.3	5.3	0%	0%
	Egypt	11.0	17.3	10.8	16.5	-2%	-5%
Total Capex [b€]	Germany	332	346	322	336	-3%	-3%
	Finland	51	51	53	53	+4%	+4%
	Egypt	96	155	95	147	-1%	-5%
Total RE capacities [GW]	Germany	328	338	329	338	0%	0%
	Finland	41	40	46	46	+12%	+15%
	Egypt	104	160	104	159	0%	-1%
Solar PV total [GW]	Germany	179 (55%)	182 (54%)	173 (53%)	179 (53%)	-3%	-2%
	Finland	11 (27%)	11 (28%)	14 (30%)	14 (30%)	+27%	+27%
	Egypt	67 (64%)	97 (61%)	67 (64%)	125 (79%)	0%	+29%
Wind total [GW]	Germany	89 (27%)	95 (28%)	91 (28%)	95 (28%)	+2%	0%
	Finland	13 (32%)	13 (33%)	16 (35%)	16 (35%)	+23%	+23%
	Egypt	22 (21%)	51 (32%)	22 (21%)	22 (14%)	0%	-57%
PtG electrolysers [GW$_{el}$]	Germany	3	14	12	18	+300%	+29%
	Finland	0	0	2	2	-	-
	Egypt	2	46	3	51	+50%	+11%
Hydrogen capacity [GW$_{th}$]	Germany	5	7	35	16	+600%	+129%
	Finland	0	0	2	2	-	-
	Egypt	1	21	3	34	+200%	+62%
Hydrogen output (from electrolysers) [TWh$_{th}$]	Germany	5	25	35	47	+600%	+88%
	Finland	0	0	7	7	-	-
	Egypt	4	119	7	123	+75%	+3%
Methane output (CO_2 from biogas + H2) [TWh$_{th}$]	Germany	0	0	27	27	-	-
	Finland	0	0	5	5	-	-
	Egypt	0	0	3	3	-	-
Methane output (CO_2 from DAC + hydrogen) [TWh$_{th}$]	Germany	4	19	0	10	-100%	-47%
	Finland	0	0	0	0	-	-
	Egypt	3	92	2	91	-33%	-1%
Gas storage throughput [TWh$_{th}$]	Germany	43	34	68	53	+58%	+56%
	Finland	9	8	14	14	+56%	+75%
	Egypt	8	1	11	4	+38%	+300%
Total electricity gen [TWh]	Germany	618	633	615	629	0%	-1%
	Finland	100	100	104	104	+4%	+4%
	Egypt	260	412	256	396	-2%	-4%

Design of Cuckoo Search Optimization Technique for Improving Renewable-Hydrogen Standalone System

I. Abadlia*[1], M. Adjabi[1], H. Bouzeria[2] and I. Benouareth[1]

[1,*]Department of Electrical Engineering, University of Badji Mokhtar Annaba, BP 12 Annaba 23000, Annaba, Algeria.
[2]Bouzeria Hamza, Department of transport engineering, University of Mentouri – Constantine -1-, 25000, Algeria.

Abstract—**In this work an employment of a cuckoo search optimization technique (CSOT) to improve renewable-hydrogen standalone systems is presented. In the first section, a solar-hydrogen power system is investigated and optimized using CSOT. The system composed of solar production is a photovoltaic generator (PVG) and a hydrogen system collected of an alkaline water electrolyser, hydrogen tank and proton exchange membrane fuel cell (PEMFC). Also, control feed bucks system as MPPT for PV system and a cascade control loop with PIDs controllers for fuel system are designed. An optimization process contains MPPT algorithm and PIDs gains is exploited. In the second set of the work, a wind turbine system (WTS) replaces the solar system and we kept the same topology of the power system with the same process of the optimization. Obtain results with comparative study between CSOT technique design and conventional method proves that the proposed optimization uses improved and add more performances.**

Key words—renewable-hydrogen standalone systems, PV system, wind turbine system, cuckoo search optimization.

I. INTRODUCTION

Hybrid production power systems are achieved out of industrial development in order to increase the efficiency of power sources. According to the intermittence and variability problems of such renewable energy source (RES), it is expected that hybrid systems were using or not the storage schemes be offered as an alternative replacement for traditional power sources. The main concern is the design of control among power generation system (PGS) that is the responsible how is examine and control the optimal system functioning [1].

In this work we propose an optimization using cuckoo search optimization technique of a hybrid PGS composed of photovoltaic generator/ wind turbine system and hydrogen fuel system used for standalone application. After presentation the power system and their proposed control, the process of the optimization is presented as flows by the results dissect the role of the design of the CSOT and the benefits of the proposal. At the last conclusions of the presented work are offered.

II. SYSTEM DESCRIPTION AND CONTROL

In this section, description of power system is presented and the principal of different control of PV, WTG and fuel sources are offered.

1. Description

Fig. 1, shows a standalone system incorporates a PV generator or wind conversion system and hydrogen system composed of alkaline water electrolyzer, H_2 tank and proton exchange membrane fuel cell. The goal of the work is to optimize the system to ensure the maximum conversion power under climatic conditions. Functioning power system is explained as: at first, PV power is used primary source and the surplus power used for water electrolysis to produce H_2 via the electrolyzer. The generated FC power works as a support to supplement the load demands when the PV energy is deficient during a period of low solar radiation or in the case of high load demands. Hydrogen system is used as source or storage system form gaz. At second step, we replace PV system by wind conversion system for the same goal.

2. Control

In this part, principal of different control of PV, WTG and fuel sources are presented as gives by Fig. 2.

- **PV control system**

Fig. 2(a), shows configuration of DC-DC boost converter with PV as input. Maximum power is reached when perturb and observe (P&O) [2] type MPPT algorithm changes regulate with PI controller and adjusts the duty cycle of the boost converter.

- **WT control system**

Fig. 2(b), shows configuration of control of PMSG Wind Turbine [3]. For maximum power extraction from the wind, the speed of the rotor can be adjusted by controlling the difference between the electrical output power and the aerodynamic power captured. Lower to medium wind speed, with a power converter, the electrical output power can be controlled by varying the electrical torque applied to the turbine and, therefore, the rotor speed. As the wind speed increases toward the higher wind speed region, the power generated by the turbine also increases. Once the maximum rating of the turbine is reached, mechanical power shedding is usually to protect the system.

- **FC control system**

Fuel generation control system is shown in Fig. 2(c). It is based on DC-DC boost converter operating with cascade control loop to ensure maximum power [4].

*Corresponding author email: i_abadlia@yahoo.fr

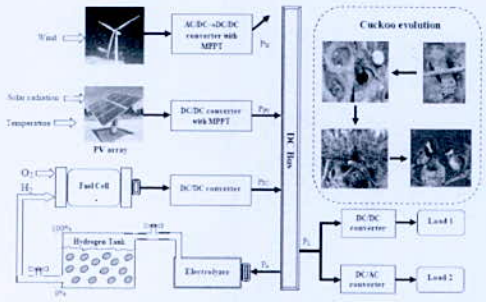

Fig. 1. System configuration

(a)

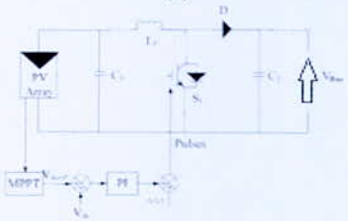

(b)

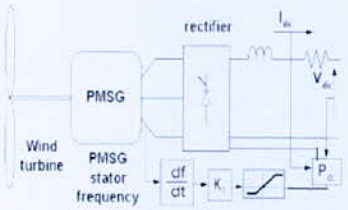

(c)

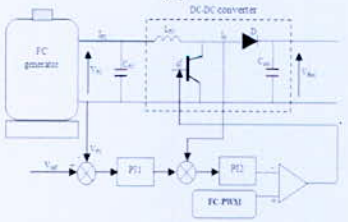

Fig. 2. System control: a) PV side control; b) WTG side control; c) FC side control

III. CUCKOO SEARCH OPTIMIZATION TECHNIQUE DESIGN

1. Cuckoo search method

Cuckoos are birds with an interesting and aggressive reproduction strategy. Some species lay their eggs in communal nests for the host birds to hatch them. For increasing the hatching probability cuckoos may have to remove the host eggs and replace them with their own eggs [5]. If the host birds discover an alien egg it will be either thrown away or the nest is abandoned. Inspired by cuckoo's reproduction behavior, in [6] a new meta-heuristic algorithm called Cuckoo Search (CS) is proposed. This method is based on three basic rules [7]:

1. Each cuckoo lay one egg (solution) at time in a randomly chosen nest;
2. The best nest (set of solutions), which has the best quality eggs will be carried over to the next generations. This is the intensification part of the method;
3. The number of nests n and the probability pa [0, 1] of an alien egg to be discovered and the nest to be abandoned are fixed.

2. Problem formulation

A. Case system with PVG

In first application a hybrid power system, composed of PV and FC generators, is optimized using CSO algorithm. The structure of the optimization process composed of:

1. PID controller's system gains:
- KP and KI of PI regulator of PV system (Fig. 2 a).
- KP1, KI1, KP2, KI2 of PIDs of FC system (Fig. 2 c).

So, the form of the optimization process as:

K_P	K_I	K_{P1}	K_{I1}	K_{P2}	K_{I2}

And fitness function of the CSO algorithm is:

$$\begin{cases} F1: V_{DCref} - V_{DC} \\ F2: V_{FCref} - V_{FC} \\ F3: V_{Busref} - V_{Bus} \end{cases} \quad (1)$$

2. MPP Tracking algorithm for PV system:
- To implement the CSO-based MPPT, duty cycle D is defined as a CS. D can be modified as follows:

$$D_i(k+1) = D_i(k) - A.D \quad (2)$$

Thus, the fitness function of the CSO algorithm is formulated as:

$$P\left(d_i^k\right) > P\left(d_i^{k-1}\right) \quad (3)$$

where A denote coefficient vector CS, P represents power, d is duty cycle, i is the number of current cuckoo, and k is the number of iterations.

To do this, at first an off-line optimization is effected to tune PID gains with using P&O algorithm and at second time an on-line CS optimization to adapt the MPPT.

B. Case system with WTG

At second time MPPT of WTS (Pdc) is optimized using CSO algorithm were PID gains of FC system is optimized and fixed in the first part. The basic idea of the proposed MPPT technique is to retrieve the optimal generator reference speed ωmr_{ref} (meaning the speed corresponding to the maximum generable power) for any instantaneous value of the wind speed. The adopted model of the wind turbine is the following. The power generated by a wind turbine can be written as [8]:

*Corresponding author email: i_abadlia@yahoo.fr

$$P_m = C_p(\lambda,\beta)\frac{\rho A}{2}v^3 \tag{4}$$

where Pm is the mechanical power of the turbine in watts, Cp is the performance coefficient of the turbine, ρ is the air density in kilograms per cubic meter, A is the turbine swept area in square meters, v is the free wind speed in meters per second, λ is the tip speed ratio, β is the blade pitch angle in degrees [9], and:

$$C_p(\lambda,\beta) = c1\left(\frac{c2}{\lambda_i} - c3\beta - c4\right)e^{\frac{-c5}{\lambda_i}} + c6\lambda \tag{5}$$

With:

$$\frac{1}{\lambda_i} = \frac{1}{\lambda + 0.08\beta} - \frac{0.035}{\beta^3 + 1} \tag{6}$$

and $c1 = 0.5176$, $c2 = 116$, $c3 = 0.4$, $c4 = 5$, $c5 = 21$, and $c6 = 0.0068$. The tip speed ratio λ is defined on the basis of $\lambda = \omega TR/v$, where ωT is the turbine angular speed. Torque produced by the turbine can be computed as

$$T_T = P_m / \omega_T = C_T(\lambda,\beta)\frac{\rho\pi R^3}{2}v^2 \tag{7}$$

where the torque coefficient of the turbine is defined as $CT(\lambda, \beta) = CP(\lambda, \beta)/\lambda$. It should be noted that both the turbine speed and torque must be converted to the machine level on the basis of the gear ratio n as follows: $\omega'_T = \omega_T$, $n = \omega_{rm}$ and $T'_T = T_T/n$.

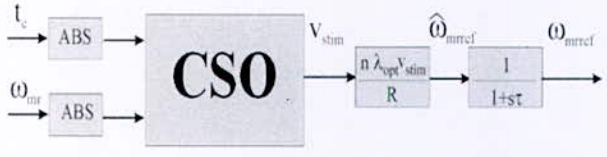

Fig. 3. Block diagram of the CSO-based MPPT algorithm

IV. RESULTS AND DISCUSSIONS

Two simulation tests are affected for the model system with parameters indicates by table 1. The first simulation is with PV system and the second with WTS were the optimization is considered in all cases.

A. Case optimization and simulation system with PVG

The first simulation test includes the optimisation of PID system control with using P&O type MPPT. After 10 running a global fitness function defined as F=F1×F2×F3. The optimum system functioning depending the small value of F as presented in Table 2.

TABLE I
MODEL PARAMETERS

Photovoltaic system	
Type	Fuji Electric Co. ELR-615-160Z, 50W
Rating	1500W
Series modules	5
Parallel modules	5
Short circuit current	3.28A
Open circuit voltage	21.6V
Maximum power/cell	50W
Fuel generator	
Type	Nexa Ballard 310-0027
Rating	1000W
Number of cells	40
Rated current	45
Rated voltage	28
Electrolyzer	
Electrolyte	Alkaline
Electrolyte section	300cm²
Distance between electrodes	3.0×10^{-4}
Temperature of the electrolyzer	52 °C
Cathode transfer coefficient	0.5
Anode transfer coefficient	0.3
PMSG Wind Turbine	
Rated power	2.2Kw
Rated voltage	220V
Rated frequency	50Hz
Pole-pairs	2
Stator resistance	2.9Ω
Rotor resistance	1.52Ω
Stator inductance	223mH
Rotor inductance	229mH
Moment of inertia	0.0048Kg.m²

TABLE II
TABLE 2: PIDS GAINS OPTIMIZATION RESULTS OF 10 RUNNING

run	K_P	K_I	K_{P1}	K_{I1}	K_{P2}	K_{I2}	F
1	0.647	8.943	1.693	17.11	0.373	4.148	6.654
2	0.638	8.745	1.639	18.24	0.303	4.748	3.751
3	0.634	8.839	1.429	17.85	0.352	4.436	2.984
4	0.672	9.073	1.729	17.64	0.483	4.027	7.493
5	0.643	8.872	1.386	16.93	0.306	4.830	4.674
6	0.626	8.963	1.952	18.04	0.394	5.017	1.734
7	0.684	8.841	2.054	17.93	0.428	4.714	5.874
8	0.632	9.104	1.846	17.86	0.315	4.824	5.679
9	0.641	8.952	1.734	17.05	0.303	4.693	3.463
10	0.652	8.893	1.845	18.17	0.379	4.753	4.186

To evaluate the performance of the proposed CSO based meta-heuristic MPPT algorithm (Fig. 3), it is performances were compared with P&O type MPPT algorithm. Fig. 4 (a) and (b) show an application of solar radiation profile as mastery all climatic conditions with presence of shading effects and a variable load via RL charge. In Fig. 5 (a) we observe a benefits of power using the adaptive CSO-MPPT technique compared with the P&O one as defined PB = PCSO-PP&O. Fig. 5(b), show a good follows of the power load for the reference that prove a good tuning of PID controllers by the off-line optimization of the system PIDs gains using CSOT. The generated Photovoltaic and hydrogen fuel powers as

*Corresponding author email: i_abadlia@yahoo.fr

given by Fig. 6 (a). Fig. 6 (b) shows H_2 tank level that proves that the system capable to produce and store the H_2 gaz were a surplus power exist.

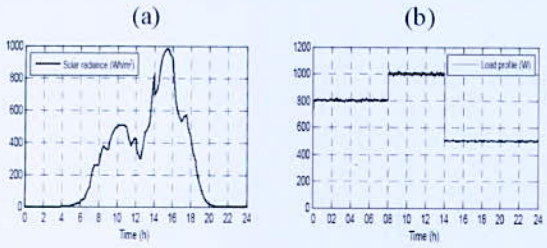

Fig. 4. Solar radiance profile; (b) load profile reference

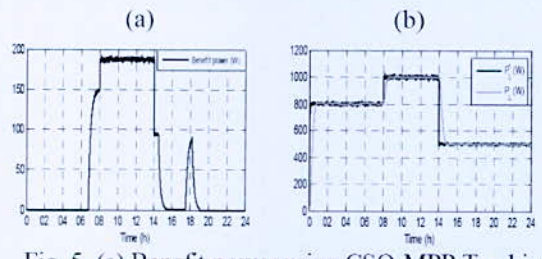

Fig. 5. (a) Benefit power using CSO-MPP Tracking; (b) Power demand with their reference

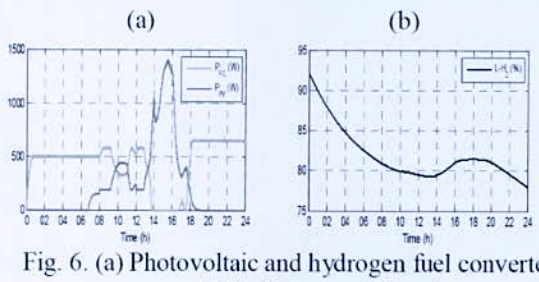

Fig. 6. (a) Photovoltaic and hydrogen fuel converted powers; (b) Hydrogen tank level

B. Case optimization and simulation system with WTS

In the second case of optimization and simulation we remove the PVG and we replaced by WTS. We kept also the PIDs gains of fuel system that optimized in the first case and only MPPT wind system is the object of optimization based on CSOT. Fig. 7 (a) show the speed of wind, in Fig. 7 (b) it observed that the electromagnetic torque follows the reference as the speed with good rejection (Fig. 7 (c)). WTG stator current is shown by Fig. 8 (a), different power system (Fig. 8 (b)) indicates a complimentarily of delivering power to the load. Fig. 8 (c) shows a good follows of the power reference.

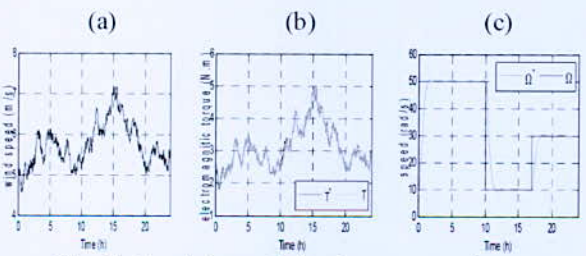

Fig. 7. (a) wind speed; (b) electromagnetic torque; (c) speed of WTG

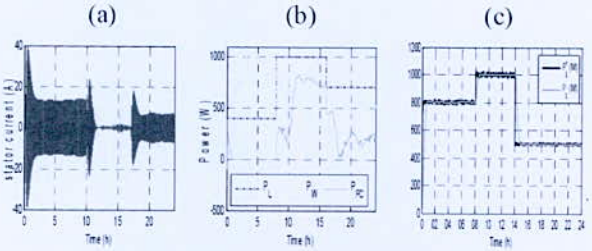

Fig. 8. (a) WTG Stator current; (b) Powers system; (c) Power demand with their reference

V. CONCLUSION

A hybrid renewable hydrogen production system is optimized using CSOT. At first, PVG with H_2 system is used. A simulation results indicates that the optimization process offered good performances to the power system. In the second step wind system is required with a success of the optimization propose.

REFERENCES

[1] Abadlia, I & Bouzeria, H. (2016). Energy management strategy based on fuzzy logic for compound RES/ESS used in stand-alone application. International Journal of Hydrogen Energy, 41(38), 16705-16717.

[2] Abadlia, I & Bouzeria, H. (2016). Active and reactive power neurocontroller for grid-connected photovoltaic generation system. JESystems, 12(1).

[3] Liu, H., Locment, F., & Sechilariu, M. (2016). Experimental analysis of impact of maximum power point tracking methods on energy efficiency for small-scale wind energy conversion system. IET Renewable Power Generation, 11(2), 389-397.

[4] Ruparathna, R., Hewage, K., & Sadiq, R. (2016). Improving the energy efficiency of the existing building stock: A critical review of commercial and institutional buildings. Renewable and Sustainable Energy Reviews, 53, 1032-1045.

[5] R. B. Payne, M. D. Sorenson, K. Klitz, "The Cuckoos", Oxford University Press, 2005.

[6] X.S. Yang, S. Deb, "Cuccko search via lévy fligths", Processings of World Congress on Nature & Biologically Inspired Computing", IEEE Publications, USA, pp.210-214, Dec. 2009.

[7] X.S. Yang, S. Deb, "Engineering Optimization by Cuckoo Search", Int. J. Math. Modelling & Numerical Optimization, pp. 1-17, Dec. 2010.

[8] L. L. Freris, Wind Energy Conversion System. London, U.K.: Prentice-Hall, 1990

[9] T. Senjyu, Y. Ochi, E. Muhando, N. Urasaki, and H. Sekine, "Speed and position sensor-less maximum power point tracking control for wind generation system with squirrel cage induction generator," in Proc. PSCE, Oct. 29–Nov., 1, 2006, pp. 2038–2043.

*Corresponding author email: i_abadlia@yahoo.fr

Optimal Sizing Based on LPSP Concept of a Stand-Alone Hybrid PV/FC/EZ/BAT System

N. Zidane and S. Lalouni

Laboratoire de Technologie Industrielle et de l'Information (LTII), Faculté de Technologie
Université de Bejaia, Algérie.

Abstract— **This paper presents an optimal sizing of a stand-alone hybrid system based on photovoltaic panels (PV) and fuel cells (FC) power generation, electrolyzer (EZ) and battery (BAT) bank as energy storage systems. The methodology aims are to find the optimal size of the set system's components, based on two optimization criteria: reliability, which is based on the concept of the loss of power supply probability (LPSP) and the system cost. For a load and a probability of loss of energy given under the criterion of a minimum price of the system, an optimum number of hydrogen storage tanks and photovoltaic modules have been calculated. Thus, from hourly data of solar irradiation, ambient temperature and consumption, we calculated the hourly power produced by the photovoltaic generator, the amount of hydrogen stored and the capacity of the battery required for this application, over a one-year analysis period. A typical consumption profile has been adopted. It corresponds to the profile generally at isolated sites. Computer simulation has carried out under MATALB environment to exhibit the performance of the optimization method.**

Key words— sizing, photovoltaic, fuel cell, electrolyzer, LPSP Method, hybrid system.

I. INTRODUCTION

Renewable power generation systems have been studied extensively [1,2]. Energy storage is needed in these systems due to the stochastic nature of solar energy. Traditionally, deep cycle lead acid batteries have been used as the means of energy storage. However, there are many environmental concerns associated with batteries; thus, other alternatives are sought for this application.

In this paper, a program is developed to size the components of a hybrid system to supply the load of a typical home in north Algeria that is not located far to the electric grid. The main contribution of this work is the calculation of the optimum number of hydrogen storage tanks and photovoltaic modules required for load consumption and a probability of loss of energy given under the criterion of a minimum price of the overall system and the instantaneous maximum power constraints of the system components [1,2,3].

II. SYSTEM DESCRIPTION AND MODELLING

The proposed hybrid system is depicted in Fig. 1. It contains a PV generator, an alkaline water electrolyzer, a storage gas tank, a proton exchange membrane fuel cell and the power electronic converters, interconnected to a DC bus to supply the AC load [4,7].

Photovoltaic cells are the source of the PV generator. In this paper, one diode model is adopted [4]. The output photovoltaic current I_{pv} is described by the following equation:

$$i_{pv} = i_L - i_0 \left(\exp\left[\frac{q(V_{pv} + r_s i_{pv})}{AKT} \right] - 1 \right) - \frac{V_{pv} + r_s i_{pv}}{r_{sh}} \quad (1)$$

Where V_{pv} and i_{pv} are respectively the solar cell voltage and current, r_{sh} and r_s are respectively internal shunt and series resistances, i_0 is the diode reverse saturation current, q is the electron charge, A is the ideality factor of the p-n junction, K is the Boltzmann constant, and T is the cell temperature.

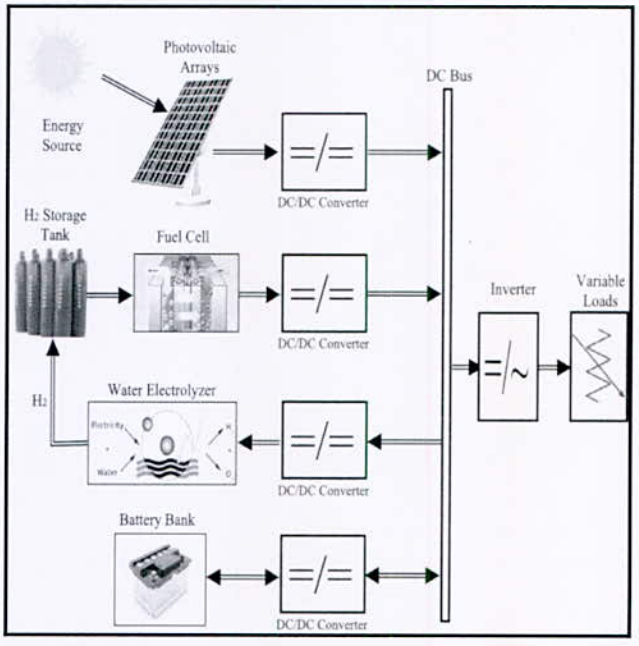

Fig. 1. Block diagram of the proposed system.

The Fuel cell model presents the most well-known type of fuel cells fueled by hydrogen and air [4]. The output voltage V_{fc} of a single cell can be defined in (2).

$$V_{fc} = E_{Nernst} - V_{act} - V_{ohm} - V_{con} \quad (2)$$

Where E_{Nernst} is the thermodynamic potential of the cell and it represents its reversible voltage; V_{act} is the voltage drop due to the activation of the anode and of the cathode;

*Corresponding author email: nourredine.zidane@univ-bejaia.dz

$$E_{Nernst} = 1.229 - 0.85.10^{-3}(T - 298.15) + 4.31.10^{-5}.T\left[\ln(pH_2) + \frac{1}{2}\ln(pO_2)\right] \quad (4)$$

$$V_{act} = -\left[\varepsilon_1 + \varepsilon_2 T + \varepsilon_3 T \ln(Co_2) + \varepsilon_4 T \ln(i_{fc})\right] \quad (5)$$

The Ohmic voltage drop V_{ohm} and V_{con} representing the voltage drop resulting from the concentration or mass transportation of the reacting gases [4] are given by (6) and (7).

$$V_{Ohm} = i_{fc}(R_M + R_c) \quad (6)$$

$$V_{con} = -B\ln(1 - J/J_{\max}) \quad (7)$$

Where pO_2, pH_2 is the partial pressure (atm) of oxygen and hydrogen respectively, C_{O2} concentration of oxygen in the catalytic interface of the cathode (mol/cm³), i_{fc} FC actual current (A), R_M the equivalent membrane resistance (Ω), J FC current density (A/cm²), $\mathcal{E}_1$, $\mathcal{E}_2$, $\mathcal{E}_3$ and $\mathcal{E}_4$ are parametric coefficients based on electrochemical kinetics and thermodynamic laws. B parametric coefficient used in the calculation of the concentration losses (V) and Rc membrane equivalent contact resistance (Ω).

III. SIZING METHOD BASED ON LOSS OF POWER SUPPLY PROBABILITY

1. Loss of Power Supply Probability Method

This method defines or determines the optimal number of the battery and module status based on two optimization criteria, namely: reliability, which is based on the concept of the loss of power supply probability and the cost of the system is shown in Fig. 2.

In two cases or Two scenarios are provided to describe the energy stored in batteries energy [8,9].

-First Scenario

If the energy produced by the two sources exceeds the energy required by the load, the hydrogen tank is loaded by considering the efficiency of load η_{Ez}.

$$E_{stor}(t) = E_{stor}(t-1) + \left(E_G(t) - \frac{E_L(t)}{\eta_{ond}}\right).\eta_{EZ} \quad (8)$$

Where η_{Ond} and η_{EZ} are respectively inverter and electrolyzer efficiency, $E_{stor}(t)$ the energy stored in the Hydrogen tank at one-hour t, $E_{stor}(t-1)$ the energy stored in the Hydrogen tank at the previous hour, $E_L(t)$ the energy requested by the load from one-hour T.

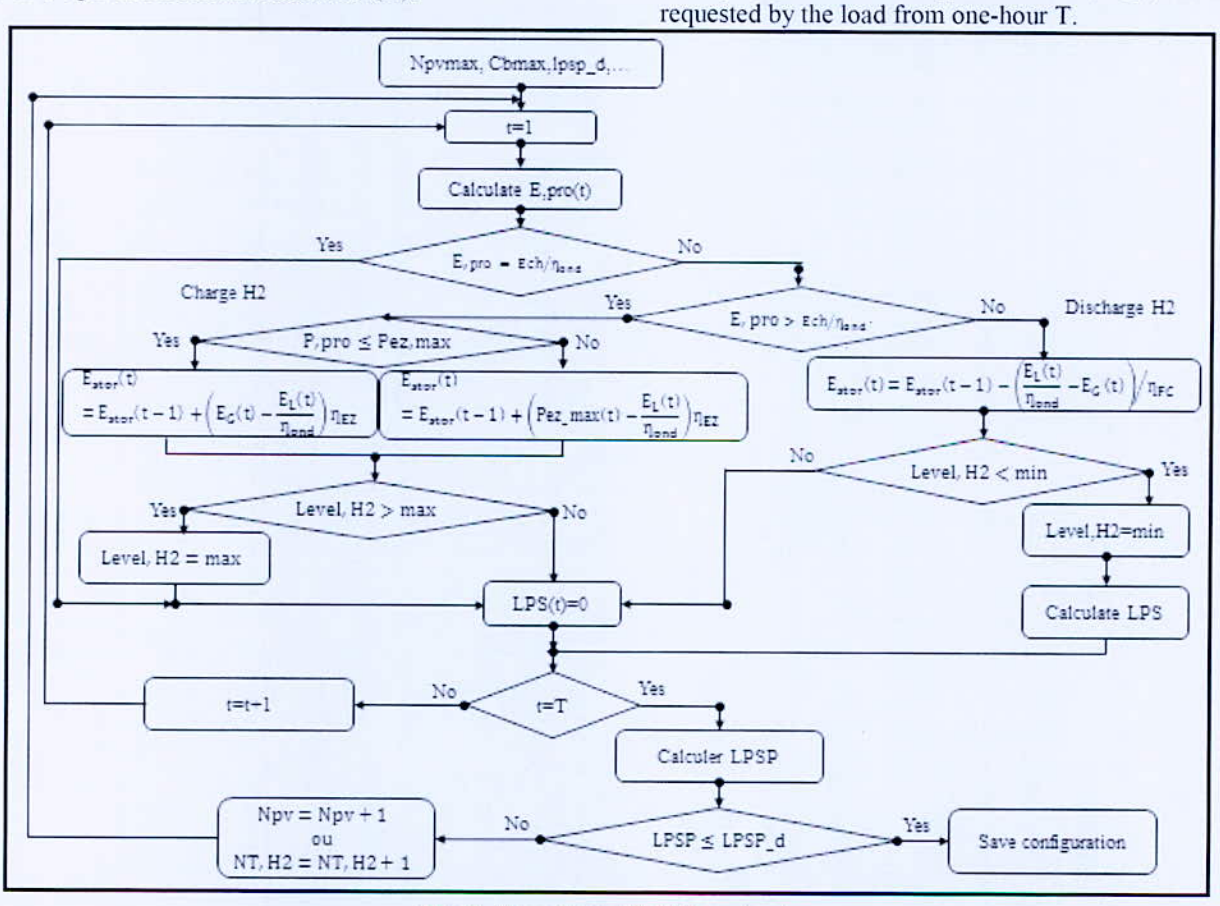

Fig. 2. Flowchart of LPSP method.

*Corresponding author email: nourredine.zidane@univ-bejaia.dz

- *Second Scenario*

When the energy required by the load is higher than the energy produced, the Hydrogen tank discharges to offset the deficit, in this case, the energy stored in the Hydrogen tank can be expressed by the following equation:

$$E_{stor}(t) = E_{stor}(t-1) - \left(\frac{E_L(t)}{\eta_{ond}} - E_G(t) \right) / \eta_{fc} \quad (9)$$

When stored energy in the Hydrogen tank and produced energy jointly by the two sources is insufficient to meet the demand for an hour T, the deficit is called loss of Power Supply (LPS), is expressed by:

$$LPS(t) = E_L(t) - (E_G(t) + E_{stor}(t-1).\eta_{FC}).\eta_{ond} \quad (10)$$

The hypothesis or LPSP for an analysis period T, is the report / ratio of the sum of all values of energy loss (LPS (T)) for the same period the total energy required. The LPSP is defined in (11).

$$LPSP = \sum_{t=1}^{T} LPS(t) / \sum_{t=1}^{T} E_L(t) \quad (11)$$

2. *Resource, consumption profile and components*

Solar irradiation data over a one-year period, which was collected at the Renewable Energy Development Center (CDER) Algeria are shown in Fig. 3 [10]. The average hourly consumption data for a typical house in northern Algeria are illustrated in Fig. 4. These data are used for the design of the plant and it is assumed that the energy generation and the load remain constant in each time interval.

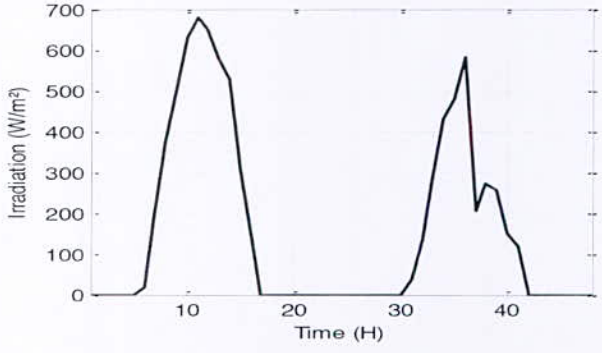

Fig. 3. Hourly irradiation profile.

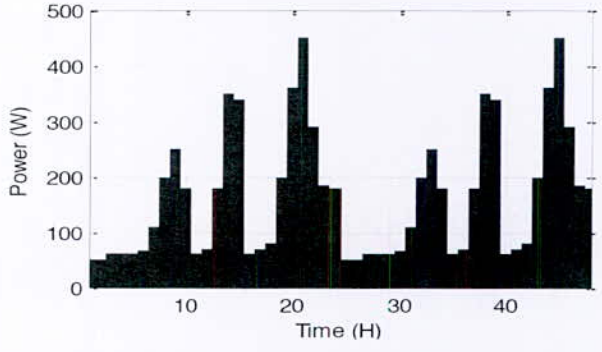

Fig. 4. Profile of one-day standard consumption.

IV. SIMULATION RESULTS AND DISCUSSION

LPSP is normally a very small number corresponding to the number of days the supply loses over a given time period. For example, in this study, the desired LPSP is ≤0.1, which corresponds to having a loss of power supply of approximately two days in a year [8]. The user will specify a range of PV panels and a range of hydrogen storage tank units to use and the program will calculate a LPSP for each possible configuration. In this study, the hydrogen storage tank unit size is set to 300 equivalent Watt-hours (8.1 liters under standard conditions, 9.09 grams of H_2). The program calculates the number of PV panels and the number of the hydrogen storage tanks that will satisfy this particular LPSP. The result for the case studied is shown in Fig. 5. It is clear from the figure that many different combinations of storage tanks and PV panels could be used to obtain the desired LPSP. The optimum couple (NT.H_2, Npv), satisfying desired LPSP, corresponds to a slope of the tangent (-b/a: b is the cost of a H_2 tank and a is the cost of a PV panel) to the curve at point contact. Result in using 19 PV panels of 110W each and 16 hydrogen storage tanks (corresponding to 4.8 kWh). The component parameters used in this study are reported in [4, 8, 10].

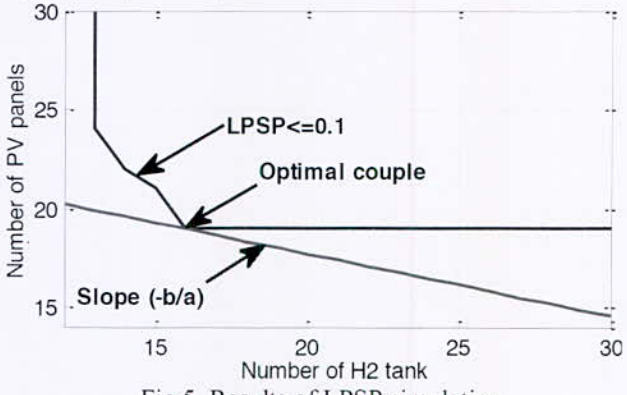

Fig.5. Results of LPSP simulation.

The size of the tank in liters is found using the ideal gas law given below [8].

$$V_{\tan k} = (T.R.n)/(P) \quad (12)$$

Where V_{tank} is the volume of the tank (liter), T is the temperature (298 K), R is the gas constant, n is the number of moles, and P is the tank pressure (13.6 atm).

The battery number is defined in (13) [11].

$$N_{bat} = Roundup\left[(C_{req})/(\eta.C_{bat}) \right] \quad (13)$$

Where *Roundup* returns the rounded-up value, C_{bat} is the rated capacity of each battery. C_{req} is the required storage capacity defined in (14) [11].

$$C_{req} = \max\left(\int \Delta P.dt\right) - \min\left(\int \Delta P.dt\right) \quad (14)$$

*Corresponding author email: nourredine.zidane@univ-bejaia.dz

ΔP is the power difference shown in Fig. 6. Fig. 7 shows the power generated by battery bank, power sent to electrolyzer and power generated by fuel cells. Fig. 8 shows the storage level (kWh equivalent) of the hydrogen storage system and the battery system.

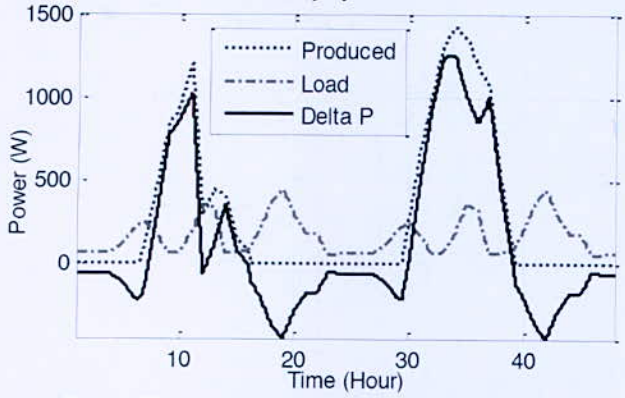

Fig. 6. PV power, Load power and the difference between generated and demanded powers.

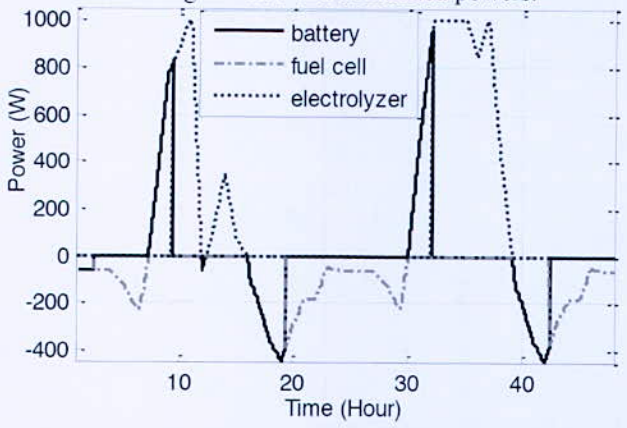

Fig. 7. Power split between the power sources to meet the load.

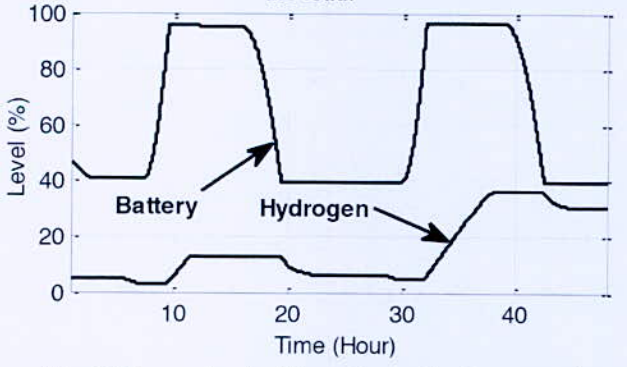

Fig. 8. Storage level of batteries and hydrogen tanks

IV. CONCLUSION

In this paper, we presented an optimal sizing based on LPSP concept of a stand-alone hybrid PV/FC/EZ/BAT System. This method, called LPSP (Loss of Power Supply probability), allows to calculate the optimum number of hydrogen storage tanks PV modules and return a given energy loss within the criterion of a minimum price. For sizing, we used the hourly values for an analysis period of two typical days of the year (ambient temperature and solar irradiation) with an identical load profile of a house in a secluded site.

The optimum determination of hydrogen tanks and photovoltaic panels depends on the site data, the profile of the load required and also on the efficiency of the components of the hybrid system. With an improvement in the efficiency of both fuel cell and electrolyzer, it is possible that a FC/EZ storage system may be economically competitive in the future. In prospect works, the implementation of an experimental prototype would be interesting to verify the proposed method.

REFERENCES

[1] N. Zidane, M. Hachemi, A. Aitouche, "Optimal sizing of wind-photovoltaic hybrid system by the LPSP method", *Systems and Control (ICSC)*, 2016 5th International Conference in Marrakesh, Morocco.

[2] A. Tofighi, M. Kalantar, "Power management of PV/battery hybrid power source via passivity-based control," *Renewable Energy* 2011 36: 2440-2450.

[3] J. Lagorse, D. Paire, A. Miraoui, "Sizing optimization of a stand-alone street lighting system powered by a hybrid system using fuel cell, PV and battery," *Renewable Energy* 2009, 34: 683–691

[4] J. M. Corrêa, F. A. Farret, J. R Gomes and M. G Simoes, "Simulation of Fuel-Cell Stacks Using a Computer-Controlled Power Rectifier with the Purposes of Actual High-Power Injection Applications," *IEEE transactions on industry applications*, vol. 39, no. 4, August 2003.

[5] T. Esram, PL. Chapman, "Comparison of photovoltaic array maximum power point tracking techniques," *IEEE Trans Energy Convers* 2007; 22:439-49.

[6] M. Uzunoglua, O.C. Onar, M.S. Alam, "Modeling, control and simulation of a PV/FC/UC based hybrid power generation system for stand-alone applications," *Renewable Energy* 2009 34: 509–520.

[7] Chun-Hua Li, Xin-Jian Zhu, Guang-Yi Cao, Sheng Sui, Ming-Ruo Hu, "Dynamic modeling and sizing optimization of stand-alone photovoltaic power systems using hybrid energy storage technology," *Renewable Energy 2009* 34: 815–826.

[8] D. B. Nelson, M.H. Nehrir, and C. Wang, "Unit Sizing of Stand-Alone Hybrid Wind/PV/Fuel Cell Power Generation Systems," *Renewable Energy* Volume 31, Issue 10, August 2006, P 1641-1656.

[9] S. Diaf, D. Diaf, M. Belhamel, M. Haddadi, and A. Louche, "A methodology for optimal sizing of autonomous hybrid PV/wind system", *Energy Policy*, Vol. 35, n° 11, pp 5708-5718, September 2007.

[10] A. T. SINGO, "Système d'alimentation photovoltaïque avec stockage hybride pour l'habitat énergétiquement autonome, " Doctoral theses in electrical engineering, University Henri Poincaré, Nancy-I, 2011.

[11] A. Askarzadeh, "Developing a discrete harmony search algorithm for size optimization of wind–photovoltaic hybrid energy system," *Solar Energy* 2013, 98: 190–195.

*Corresponding author email: nourredine.zidane@univ-bejaia.dz

First-Principles Study of the Structural and Thermodynamic Properties of the Complex K_2PtCl_6-Structure Hydrides Ba_2OsH_6

O. Boudrifa*

Laboratory for Developing New Materials and their Characterization, University of Setif 1, 19000 Setif, Algeria.

Abstract—**We report a systematic first-principles density functional theory study on the pressure dependence of the structural parameters, elastic constants and related properties and thermodynamic properties of the complex transition metal hydrides Ba_2OsH_6. The calculated structural parameters are in excellent agreement with the existing data in the scientific literature. The single-crystal elastic constants and related properties were predicted using the stress–strain method.**

The dependences of the lattice parameter, bulk modulus, volume thermal expansion coefficient, isobaric and isochoric heat capacity and Debye temperature on the pressure and temperature, ranging from 0 to 15 GPa and from 0 to 1000 K, respectively, were investigated using the quasi-harmonic Debye model in combination with first principles calculations.

Key words—Complex transition metal hydrides; first-principles calculation; pressure effect; elastic constants; thermodynamic properties.

I. INTRODUCTION

Hydrides have attracted a great deal of interest from experimentalists as well as theoreticians because of their wide range of applications, such as hydrogen solid-state storage [1–3], rechargeable batteries [3], smart windows [4,5] and switchable mirrors [6,7]. For hydrogen storage, the hydrides should adhere to a set of guidelines that include (i) rapid kinetics of the hydrogenation and dehydrogenation operation without deterioration of materials, (ii) low temperature at which the hydrogenation and dehydrogenation take place, and (iii) high hydrogen concentration and low total weight of hydrides [8, 9].

As members of the complex transition metals hydrides family, the A_2OsH_6 (A = Mg, Ca, Sr, Ba) compounds have been the subject of numerous theoretical and experimental investigations. Experimentally, the A2OsH6 (A = Mg, Ca, Sr, Ba) compounds have been synthetized and their structural and spectroscopic (infrared and Raman spectra) properties have been characterized [10–11]. Theoretically, numerous literature references are available for these hydrides investigating their structural [9, 12, 13, 14], electronic [13, 14] and optical [9] properties using first-principles calculations based on the density functional theory (DFT) within the generalized gradient approximation (GGA) and local density approximation (LDA). are generally grown on substrates and consequently the lattice mismatch and difference in the thermal expansion coefficients between the epitaxial layers and substrates can cause large stresses in the epitaxial layers, which in turn can affect their physical properties.

II. STRUCTURAL PROPERTIES

The CTMHs Ba_2OsH_6 crystalize in a cubic structure, space group Fm_3m (no. 225) [15] with four formula units in the conventional-cell (Z = 4). The Ba atoms are located at 8c (1/4, 1/4, 1/4), Os at 4a (0, 0, 0) and H at 24e (xH, 0, 0) Wyckoff sites; xH is the internal x-coordinate of the H atom. The calculated equilibrium structural parameters are tabulated in Table 1 along with the available experimental and theoretical data for comparison. There is an excellent agreement between our calculated lattice parameters and the experimental and earlier theoretical ones. The relative deviations (d(%)) between our calculated lattice parameters and the measured ones are approximately 0.08% in Ba_2OsH_6.

TABLE I

UNITS FOR MAGNETIC PROPERTIES OPTIMIZED LATTICE PARAMETERS (A, IN Å), INTERNAL COORDINATES (XH), CALCULATED BOND-LENGTHS (H- OS, A- OS AND H-A, IN Å), BULK MODULUS (B, IN GPA) AND BULK MODULUS PRESSURE DERIVATIVE (B') AT ZERO PRESSURE FOR THE MG2OSH6, CA2OSH6, SR2OSH6 AND BA2OSH6 MATERIALS. EXISTING EXPERIMENTAL AND THEORETICAL DATA ARE SHOWN FOR COMPARISON. B AND B' WERE OBTAINED FROM THE BIRCH, MURNAGHAN, BIRCH-MURNAGHAN AND VINET EOS.

	Present	Expt.	Others
a	6.6790	6.6828[19] 6.6828 [25]	6.69153[19] 6.6828[16] 6.6822[16]
B	78.50[1], 78.95[2] 78.48[3], 78.16[4]		
B'	3.98[1], 3.74[2] 4.14[3], 3.92[4]		
X_H	0.2530		0.25417 [15] 0.2560 [16]
$d_{H\text{-}Os}$	1.6897		
$d_{A\text{-}Os}$	2.8921		
$d_{H\text{-}A}$	2.3615		
ΔH	-5.05		
E_{coh}	-18.44		

*Corresponding author email: was.boud@gmail.com

III. THERMODYNAMIC PROPERTIES

Fig. 1, presents the lattice constant-temperature diagram at some fixed pressures for the Ba_2OsH_6 compounds. The lattice constant increases with increasing temperature at a given pressure and decreases with increasing pressure at a given temperature, i.e. the effects of temperature and pressure on the lattice parameter are opposite. Figure 1 shows that the lattice parameter expands evidently at high temperature with low pressure. The expanding of the lattice parameter with temperature is restrained at high pressure. The calculated lattice constants for Ba_2OsH_6 at room temperature and zero pressure is 9.72 Å. The temperature and pressure dependences of the bulk modulus for Ba2OsH6 compounds are plotted in Figure 1. One can observe that the bulk modulus B is nearly constant for temperature lower than 100 K and decreases linearly with increasing temperature when the temperature is higher than 100 K.

The bulk modulus B decreases with increasing temperature T at a given pressure, while it increases with increasing pressure P at a given temperature. The effect of increasing pressure on the bulk modulus of the Ba_2OsH_6 compounds is the same as that of decreasing temperature. However, the effect of pressure on the bulk modulus is more important than that of temperature. At zero pressure and ambient temperature, B is approximately equal to 36.68 GPa.

Temperature dependence of the volume thermal expansion coefficient α at some fixed pressures for the title compounds are plotted in Figure 1. Below 200 K, α increases quickly with temperature at a given pressure, especially at zero pressure.

Above 200 K, the ascending tendency becomes weaker and it gradually tends to a linear increase. The volume thermal expansion coefficient decreases strongly with rising pressure. From Figure 1, one can observe that for P = 12 GPa and T > 200K, the expansion coefficient α changes weakly, which means that under high pressure significant than that of pressure. The value of CV at 300 K and zero pressure is 216.76 J mol−1 K−1 for Ba2OsH6.

The Debye temperature is another essential fundamental thermodynamic parameter, which is directly related to many physical properties of solids, such as elastic constants, melting temperature and specific heat. Variation of the Debye temperature θ_D as a function of temperature at some fixed pressures is displayed in Figure 1. The θ_D is nearly constant in the 0–100 K range and then decreases linearly with increasing temperature.

Debye temperature increases almost linearly with capacity, the constant volume heat capacity, the volume thermal expansion coefficient, Debye temperature at some fixed pressures.

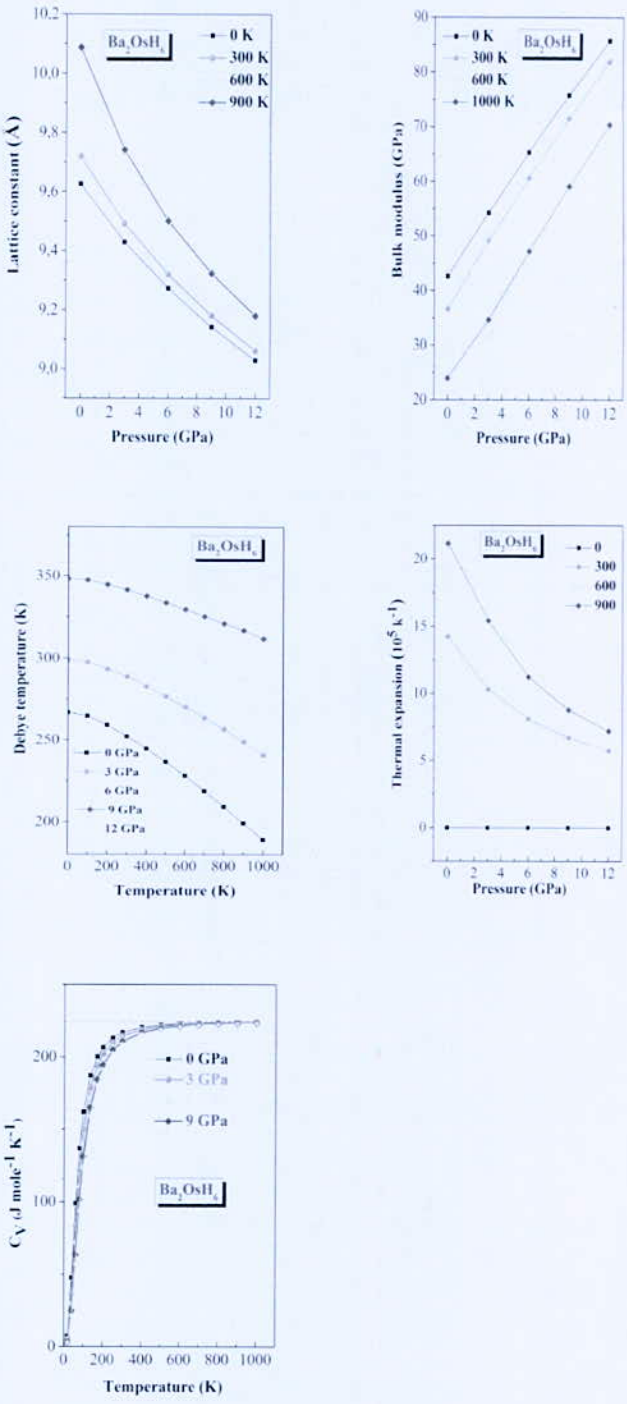

Fig. 1. Temperature dependence of the Lattice constant, bulk modulus, the constant pressure heat

Applied pressure at fixed temperatures. The calculated θD at zero pressure and temperature is

*Corresponding author email: was.boud@gmail.com

equal to 477 K for 252 K for Ba_2OsH_6. The values of θD obtained via the quasi-harmonic model for the title compounds are in acceptable agreement with those obtained from the elastic constants (271 K for Ba2OsH6). This might be an indication that the quasi-harmonic Debye model is a very reasonable alternative to account for the thermal effects with no expensive task in terms of computational time.

III. CONCLUSIONS

In this paper, we have investigated the structural, elastic and thermodynamic properties of the Ba2OsH6 hydrides using the PP-PW DFT method and the quasi-harmonic Debye model. The optimized structural parameters, including lattice parameter, atomic positions and interatomic bond-lengths, reproduce well the available experimental and theoretical data. The calculated cohesive energy and formation enthalpy demonstrate the chemical and thermodynamical stability of the examined compounds. We have evaluated the single-crystal and polycrystalline elastic moduli and their related properties. This serves to give an indication of the reliability of our predicted elastic constants. According to Pugh's criterion, may be classified as ductile material.

Temperature dependences of the lattice parameter, bulk modulus, isobaric and isochoric heat capacities, volume thermal expansion coefficient and Debye temperature are predicted in a temperature range from 0 to 1000 K at 0, 3, 6, 9 and 12 GPa using the quasi-harmonic Debye model.

REFERENCES

[1] B. Huang, F. Bonhomme, P. Selvam, et al. ''New ternary and quaternary metal hydrides with K2PtCl6-type structuresè''. J Less-Common Met. vol. 171, pp. 301–311, 1991

[2] P. Chen, ZT. Xiong, JZ. Luo, et al. ''Interaction of hydrogen with metal nitrides and imides''. Nature. Vol. 420, pp.302–304., 2002

[3] Schlapbach L, Züttel A. ''Hydrogen-storage materials for mobile applications''. Nature. Vol. 414, pp. 353–358, 2001

[7] Kresse G, Furthmüller J. ''Efficient iterative schemes for ab initio total-energy calculations using a plane-wave basis set''. Phys Rev B. vol. 54, pp. 11169–11186, 1996

[8] Karazhanov SZ, Sheripov U, Ulyashin AG. ''Classification of hydrides according to features of band structure''. Phil Mag. vol. , pp. 89, 1111–1120, 2009

[9] Karazhanov SZ, Ulyashin AG. ''Similarity of optical properties of hydrides and semiconductors for antireflection coatings''. Phil Mag. vol. 90, pp. 2925–2937, 2010

[10] K.M. Nicholson, D.S. Sholl, Inorg. Chem. 53 (2014) 11833

[11] M. Kritikos, D. Norbus, B. Bogdanovic, and U. Wilczok, J. Less-Common Met. 161, 337 (1990).

[12] R.O. Moyer Jr., C. Stanitski, J. Tanaka, J. solid State Chem. 3 (1971) 541.

[13] J. J. Reilly, and R. H. Wiswall, Inorg. Chem. 7, 2254 (1968).

[14] D. Noreus, K. W. Tarnroos, A, Borje, T. Szabo, W. Bronger, H. Spittank, G. Auffermann,and P.Muller, J. Less-Common Met. 139, 233 (1988).

[15] Kadir K, Moser D, Münzel M, et al. ''Investigation of counterion influence on an octahedral IrH6- complex in the solid state hydrides AAeIrH6 (A = Na, K and Ae = Ca, Sr, Ba, and Eu) with a new structure type''. Inorg Chem. vol. 50, pp. 11890–11895, 2011

[16] JJ. Reilly, RH. Wiswall. ''Reaction of hydrogen with alloys of magnesium and nickel and the formation of Mg2NiH4''. Inorg Chem. vol. 7, pp. 2254–22561, 1968

[4] Huiberts JN, Griessen R, Rector JH, et al. ''Yttrium and lanthanum hydride films with switchable optical properties''. Nature. Vol. 380, pp. 231–234, 1996

[5] van Mechelen JLM, Noheda B, Lohstroh W, et al. ''Mg–Ni–H films as selective coatings: tunable reflectance by layered hydrogenation''. Appl Phys Lett. vol. 84, pp. 3651–3653, 2004

[6] Richardson TJ, Slack JL, Armitage RD, et al. ''Switchable mirrors based on nickel–magnesium films''. Appl Phys Lett. vol. 78, 3047–3049, pp., 2001

*Corresponding author email: was.boud@gmail.com

Hydrogen Production via Steam Methane Autothermal Reforming using Metal Foam

A. Cherif[1*] and R. Nebbali[2]

[1*]Thermal-energy, Mechanical engineering, USTHB, Algiers, Algeria.
[2]Thermal-energy, Mechanical engineering, USTHB, Algiers, Algeria.

Abstract—**This work presents a numerical study of hydrogen production via steam methane reforming (SMR) process in an autothermal reactor. The methane combustion supplies the SMR with the required heat. The reactor, belonging to the wall coated reactors family, consists in a rectangular channel fitted with a metal foam. Two coated catalyst layers of order of micrometres are used to achieve more heat and mass transport and high level of compactness. SMR reaction is a high endothermic process requiring a great energy to achieve the activation conditions. Although the nickel catalysts reduces this energy, it is recommended to increase the thermal efficiency improvement, thus the methane conversion and the hydrogen yield, and as a result pollution effects are minimized. The direct insertion of heat source and heat sink in a single monolithic reactor avoid the resistances caused by the separation wall, which is used in Catalyst Plate Reactor. Moreover, using copper metal foam promotes the heat conduction, which is very small in gas phases. The depletion of methane in combustor and reformer catalyst simultaneously causes a smooth temperature profile avoiding the hot spots. The use of the metal foam improves the hydrogen yield from 4.97 % to 5.25%, and the catalyst length can be reduced by 15.61 % with the same results.**

Key words—Methane combustion, Steam methane reforming, Hydrogen energy, Catalysts Reaction Kinetics metal foam

I. INTRODUCTION

Hydrogen is expected to have extensive applications as an energetic vector in future energy strategies. It can be used to supply fuel cells or for producing ammonia for agriculture domain, and so on. On the other hand, the increase of energy demand and the different environmental issues caused by fossil sources accentuate the demand in clean and alternative energies.

Catalyst Plate Reactor 'CPR' operate simultaneously steam methane reforming and methane combustion reactions. Zanfir and *al.* [1] studied the behavior of a CPR for the case where the two operated catalyst beds are separated by a high thermal conductive wall. They analyzed the difference of the co-current and counter-current reactors, and they also studied the parameters sensitivity [2]. Mundhwa and al. [3] compared a segmented and continuous catalysts arrangement to show the performance properties. Another configuration analyze the (CPR) and autothermal is compared by Murmura and al. [4] shows the effect of oxygen feeding by the reactor wall. In the autothermal reactor the sink and source heat energy are provided and consumed in the same channel, whereas the feed of the two reactions are introduced simultaneously.

In this study, we analyzed the heat exchange and the species evolution in a monolithic channel supported by two opposite catalyst. The autothermal reactor include the sink 'reaction (I)' and the source 'reaction (II)' heat reactions. They provided and consumed in a same monolith channel, whereas the feed of the two reactions is introduced simultaneously. To find the reaction rate, we used the Xu and al. [5] correlation. The used metal foam enhance the heat conduction between the two opposite catalysts and as a result it helps in the hydrogen production and increase the heat efficiency, however it causes an additional pressure drop[6]. The copper foam used in this study is Cu-40-6.6 [7].

$$CH_4+H_2O \rightarrow CO+3H_2 \ (\Delta H_0= -206kJ/mol) \quad (I)$$

$$CH_4+2O_2 \rightarrow CO_2+2H_2O \ (\Delta H_0= 802kJ/mol) \quad (II)$$

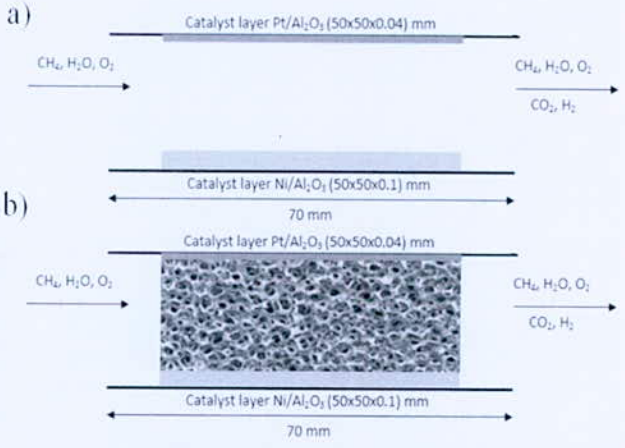

Fig. 1. Steam Methane Autothermal Reformer (70mm×50mm×2mm), a) without copper foam, b) within copper foam

II. THEORETICAL STUDY

An integrated monolithic plat microchannel reactor for Steam Methane Reforming (SMR) was modeled with a two-dimensional configuration to find the flow parameters of the gaseous fluids inside the reformer. The flow is assumed to be laminar, steady and occurring in the same direction. For the porous media the governing equations derived by the volume-averaging method [8]. the values of the adopted physical method are locally averaged for a

*Corresponding author email: ali.cherif@usthb.dz

representative elementary volume [9], Fig. 1, shows the geometry of the internal reformer schematically.

III. MATH

1. Governing equations

The heat transfer process and the flow field inside the porous reformer is described by continuity, momentum, energy and spices transfer equations. Consequently the following transport equations of the averaged physical properties for laminar flows, and taking into account the Darcy and Forchheimer effects [10].

Continuity:

$$\frac{\partial \rho_e u}{\partial x} + \frac{\partial \rho_e v}{\partial y} = 0 \tag{1}$$

Momentum:

$$\frac{\rho_e}{\varphi^2}\left(\frac{\partial uu}{\partial x} + \frac{\partial uv}{\partial y}\right) = -\frac{\partial p}{\partial x} + \frac{\mu}{\varphi}\left(\frac{\partial^2 u}{\partial x^2} + \frac{\partial^2 u}{\partial y^2}\right) - \frac{\mu}{K}u - \frac{\rho f}{\sqrt{K}}u\sqrt{u^2+v^2} \tag{2}$$

$$\frac{\rho_e}{\varphi^2}\left(\frac{\partial vu}{\partial x} + \frac{\partial vv}{\partial y}\right) = -\frac{\partial p}{\partial y} + \frac{\mu}{\varphi}\left(\frac{\partial^2 v}{\partial x^2} + \frac{\partial^2 v}{\partial y^2}\right) - \frac{\mu}{K}v - \frac{\rho_e f}{\sqrt{K}}v\sqrt{u^2+v^2} \tag{3}$$

Energy:

$$\frac{\partial \rho_e uT}{\partial x} + \frac{\partial \rho_e uT}{\partial y} = \frac{\lambda_e}{cp_e}\left(\frac{\partial^2 T}{\partial x^2} + \frac{\partial^2 T}{\partial y^2}\right) \tag{4}$$

Species:

$$\frac{\partial \rho_e uw_i}{\partial x} + \frac{\partial \rho_e uw_i}{\partial y} = D_{i,e}\left(\frac{\partial^2 \rho_e w_i}{\partial x^2} + \frac{\partial^2 \rho_e w_i}{\partial y^2}\right) \tag{5}$$

In the above equations u and v represent the component of the local gas velocity (ms^{-1}).while the x and y are the axial and vertical position (m), ρ_e is the effective density (kg/m^3) and μ is the dynamic viscosity ($kg\ m^{-1}\ s^{-1}$). T is local temperature (°C), φ=0.934, and K=0.473×10^{-7} [m^2] are the porosity and permeability of the copper foam, respectively. f= 0.06 [-] is the inertia coefficient, which depends on the microstructure of the copper foam and the Reynolds number, λ_e [$W\ m^{-1}\ k^{-1}$] and $D_{i,e}$ [$m^2\ s^{-1}$] are the effective thermal conductivity and the mass diffusivity of species i , w_i is the mass fraction of chemical species.

2. Reaction rate equations

$$r_{smr} = \frac{k_{smr}\left(p_{CH_4}p_{H_2O} - \frac{p^3 H_2 p_{co}}{k_{eq,smr}}\right)}{p_{H_2O}^{1.596}} \tag{6}$$

$$r_{MC} = \frac{k_{MCa}p_{CH_4}p_{O_2}}{\left(1+K_{CH_4}^{OX}p_{CH_4}+K_{O_2}^{OX}p_{O_2}\right)^2} \tag{7}$$

Where the r is the reaction rate in $mol/kg_{cat}/s$, and p_i is the partial pressure of each species in Pa, The reaction rate constants k_{SR} and k_{MC} as well as the methane and oxygen adsorption coefficients $k_{CH_4}^{OX}$ and $k_{O_2}^{OX}$, follow the Arrhenius-type law.

3. Boundary conditions

Inlet:

$u = 0.1\ ms^{-1}$; $T = 534°C$; $v = 0$

$v = w_{co} = w_{h2} = 0$

S/C= 1.4 (Steam to Carbon ratio)

O/C=0.598 (Oxygen to Carbon ratio)

Outlet:

$$\frac{\partial u}{\partial x} = \frac{\partial T}{\partial x} = \frac{\partial w}{\partial x}$$

Top and Bottom adiabatic wall:

$$u = v = 0\ ,\ \frac{\partial w_i}{\partial y} = 0$$

Top and Bottom wash coated wall:

$$u = 0\ ,\ v = 0$$

$$\frac{\partial T}{\partial y} = -\frac{\sum r_i \Delta H_{R,i}}{\lambda}$$

$$\frac{\partial w_i}{\partial y} = -\frac{s_i M_i}{\rho D_i}$$

$$s_i = R_I(v_i'' - v_i')$$

4. Results validation

The consistency between the numerical study of Lin et *al.* [11] and the results obtained by simulating the same conditions is shown in Fig. 4. Fig. 3, describes the geometry used by Lin et al.

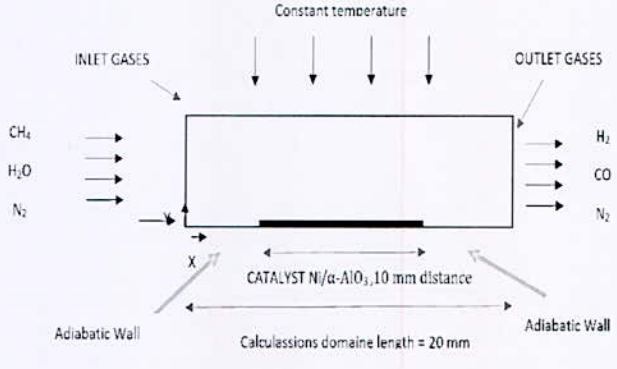

Fig. 3. Steam Methane Reformer schema of Lin et al work

*Corresponding author email: ali.cherif@usthb.dz

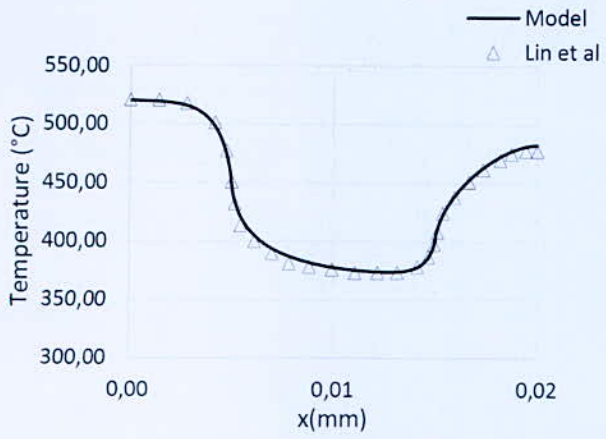

Fig. 4. Wall temperature

IV. RESULTS AND DISCUSSION

Fig. 5, shows the variation of the temperature in the channel without using copper foam (CF). The temperature increases until it reaches its highest value, due to the amount of the heat generated by methane oxidation, which is higher than methane reforming heat consumption. Beyond the temperature peak, the methane depletion causes the decrease of the reaction rate for both reactions, as a result the temperature decreases until it reaches the catalyst limit.

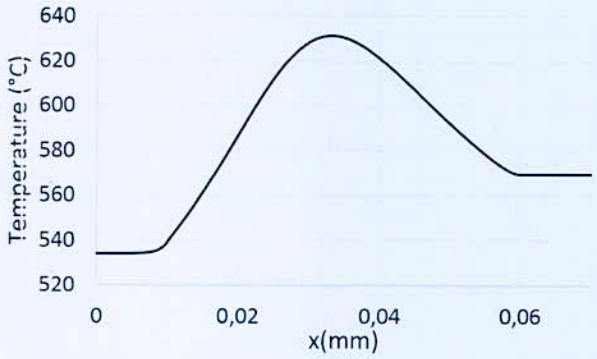

Fig. 5. Average temperature without Copper Foam

Fig. 6, describes the evolution of the mass concentration for each species. The H_2O presented in the produced and consumed cases is reduced because of the rate of the methane oxidation, which is lower than that of the steam methane reforming,

The difference in average temperature profile between the two cases (with CF and without CF) is shown in Fig. 7. The temperature with the presence of the metal foam is lower than that in the case when there is no metal foam. This is due to the energy involved by the upper catalyst that can conducted to the other catalyst faster as well as the consumption of this energy increase, thus the depletion of methane used in combustion reaction decreases.

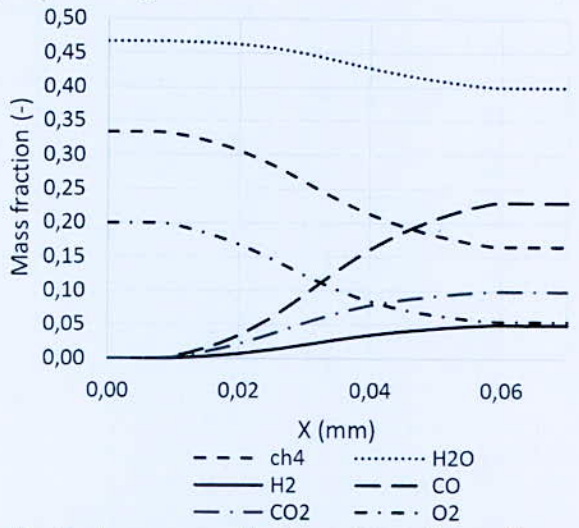

Fig. 6. Average mass fraction without Copper Foam

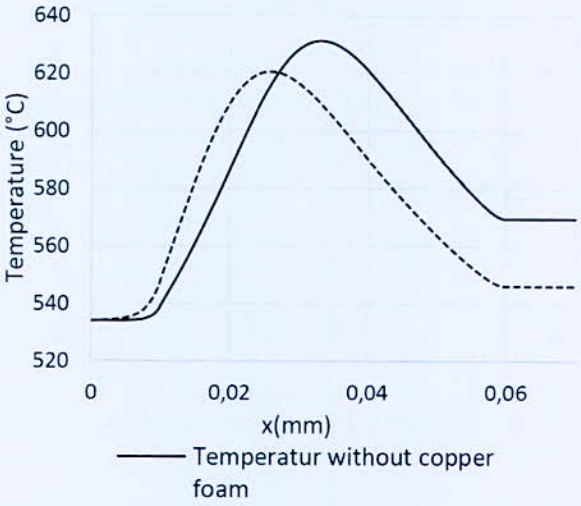

Fig. 7. Average Temperature (with Copper Foam and without Copper Foam)

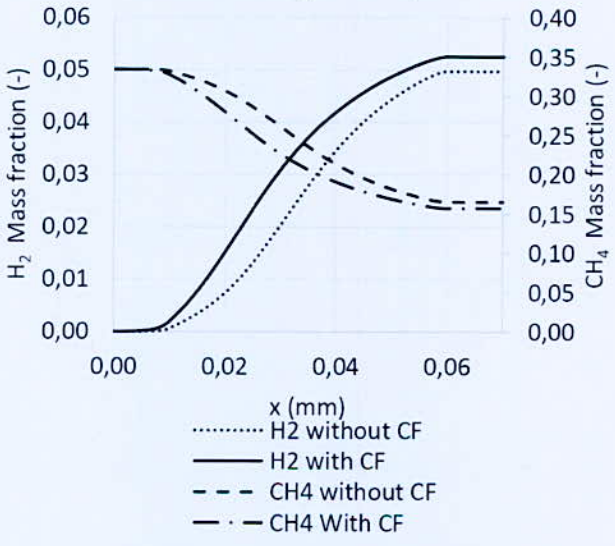

Fig. 8. H_2 and CH_4 Average mass fraction (with Copper Foam and without Copper Foam)

*Corresponding author email: ali.cherif@usthb.dz

The improvement of the hydrogen yield and methane conversion by using metallic foam is illustrated in Fig. 8. The species distribution is highly influenced by the temperature profile. In fact, the insertion of the metallic foam can reduce the reactor length about 15.61 %, which reduces the required amount of catalyst and the costs too. The high improvement noticed in the beginning of the reactor, after the maximum of temperature the improvement is reduced, because the reaction rate decreases proportionally with temperature.

V. CONCLUSION

In this study, a directly coupled autothermal reformer to produce hydrogen from methane was investigated by using a two-dimensional numerical model under steady state conditions. Two catalyst beds take place in opposite position, based on Pt/Al2O3 for the oxidation reaction and Ni/Al2O3 for the steam reforming reaction in a rectangular channel. The results shown that the performance of the coupled bed autothermal reactor in terms of the methane conversion can be improved when inserting metal foam, making the reactor more efficient economically, and give it a high level of intensification.

REFERENCES

[1] Zanfir, M. and A. Gavriilidis, *Influence of Flow Arrangement in Catalytic Plate Reactors for Methane Steam Reforming.* Chemical Engineering Research and Design, 2004. 82(2): p. 252-258.

[2] Zanfir, M. and A. Gavriilidis, *An investigation of catalytic plate reactors by means of parametric sensitivity analysis.* Chemical Engineering Science, 2002. 57(9): p. 1653 1659.

[3] Mundhwa, M. and C.P. Thurgood, *Numerical study of methane steam reforming and methane combustion over the segmented and continuously coated layers of catalysts in a plate reactor.* Fuel Processing Technology, 2017. 158: p. 57-72.

[4] Murmura, M.A., et al., *Modeling of autothermal methane steam reforming: Comparison of reactor configurations.* Chemical Engineering and Processing: Process Intensification, 2016. 109: p. 125-135.

[5] Xu, J. and G.F. Froment, *Methane steam reforming, methanation and water-gas shift: I. Intrinsic kinetics.* AIChE Journal, 1989. 35(1): p. 88-96.

[6] Ji, X. and J. Xu, *Experimental study on the two-phase pressure drop in copper foams.* Heat and Mass Transfer, 2011. 48(1): p. 153-164.

[7] Topin, F., et al., *Experimental Analysis of Multiphase Flow in Metallic foam: Flow Laws, Heat Transfer and Convective Boiling.* Advanced Engineering Materials, 2006. 8(9): p. 890-899.

[8] A, B., *Convection heat transfer.* 2013: p. 696.

[9] Carbonell, R.G. and S. Whitaker, *Heat and mass transfer in porous media.* Fundamentals of transport phenomena in porous media, 1984. 82: p. 121-198.

[10] Vafai, K. and C.L. Tien, *Boundary and inertia effects on convective mass transfer in porous media.* International Journal of Heat and Mass Transfer, 1982. 25(8): p. 1183-1190.

[11] Lin, K.K., et al., *Deduction of Proper Reaction Rate of Steam Methane Reforming over Catalyst Surface Validated with a Combination of One- and Two-Dimensional Simulations.* Journal of Thermal Science and Technology, 2012. 7(4): p. 633-648.

*Corresponding author email: ali.cherif@usthb.dz

Trends of Atomic Hydrogen Absorption in Fe_2Zr Laves Phases: Ab Initio and Wagner-Schottky Studies

L. Rouaiguia[1*], L. Rabahi[2, 3], D. Bradai[2], and A. Kellou[1]

[1]Theoretical Physics Laboratory, Faculty of Physics, USTHB Algiers, Algeria.
[2]Material Physics Laboratory, Faculty of Physics, USTHB Algiers, Algeria.
[3]Research Center in Industrial Technologies CRTI, P. O. Box 64, Cherraga 16014, Algiers, Algeria.

Abstract—**The Wagner-Schottky model was used to study the hydrogen content evolution with temperature in cubic C15-Fe_2Zr Laves phase. The used defect energies in the model were obtained using Pseudo-potential Density Functional Theory (DFT). The Wagner-Schottky model is based on the substitutional and interstitial sublattices configurations within the canonical ensemble. The relative stability of atomic hydrogen at various interstitial sites has been determined, and the effects of finite temperature on the evolution of defect concentrations, as well as the hydrogen site preference were discussed. It was found that deviation from the ideal stoichiometry in the C15-Fe_2Zr compound is caused by antisite defects in both sides of the stoichiometry, moreover, hydrogen atom prefers the 96g site at finite temperatures.**

Key words—DFT, Hydrogen absorption, Wagner-Schottky model, punctual defects.

I. INTRODUCTION

Laves phases form the largest group of intermetallic compounds, with more than 1400 binary and ternary compounds reported in the literature [1-3]. These materials are particularly attractive because of their unusual physical and chemical properties as well as their potential and effective applications [1-3]. Recently, they are considered as promising materials for hydrogen storage applications, owing to their high storage capacities, rapid kinetics and good cycling stability [4, 5].

Among these Laves phase materials, the $ZrFe_2$ compound is a promising candidate for hydrogen storage and presents a great potential for industrial applications. Under ambient conditions, $ZrFe_2$ compound can absorb only a small amount of hydrogen to form a solid solution with a composition of $ZrFe_2H_{0.16}$ [6]. However, formation of $ZrFe_2H_{3.5}$ hydride is possible with applying pressure of 0.35 GPa. Despite this, $ZrFe_2$ fails to fulfill the practical use and gravimetric density criterions laid down by the US Department of Energy (USDOE) [7], according to which, only materials with 4.5 wt % reversible hydrogen capacity under affordable conditions should be considered for commercial applications. One way to overcome these difficulties is through micro-alloying with substituting metals and /or creation of punctual defects. Especially since Laves phases present a large homogeneity ranges on both sides of the stoichiometric composition [2]. Therefore, fundamental understanding of the role of punctual defects in modifying the physical properties of Laves phases is indispensable.

The punctual defects, namely vacancies and anti-sites, as well as hydrogen absorption trends in the cubic C15-$ZrFe_2$ Laves phase are investigated in the framework of DFT calculations. To this purpose, different Wyckoff positions are considered for the hydrogen absorption analyzes. Effects of finite temperature on the defect concentrations and hydrogen site preference are considered using The Wagner-Schottky model.

II. COMPUTATIONAL DETAILS AND WAGNER-SCHOTTKY

The present study calculations were performed basing on the density functional theory (DFT) using pseudopotential method as implemented in the Quantum-Espresso [8]. The many-body problem of interacting electrons and nuclei was treated using a series of one-electron equations, the so-called Kohn-Sham (KS) equations [9, 10]. The generalized gradient approximation (GGA) of Perdew et al. (PBE) to the local density approximation was taken to include the exchange-correlation energy [11] and ultra soft pseudopotentials of Vanderbilt were used [12]. A kinetic energy cut-off of 40 Ry and a well converged value of the k-point mesh over the Brillouin zone were considered, Namely, 6 6 6 for the C15 supercell. All structures were allowed to fully relax using Broyden- Fletcher-Goldforb-Shanno (BFGS) scheme [13] until the total energy has converged to less than 10^5 eV/atom. The maximum force has converged to lower than 0.004 eV/Å.

The equilibrium point defect concentrations are obtained by minimizing the following Gibbs free energy of the system at temperature T:

$$\Delta G = \Delta H - T\Delta S . \qquad (1)$$

The formation enthalpy of the system which is a linear function of the defects concentrations is given by:

$$\Delta H = \Delta H_0^f + \sum_d H_d x_d \qquad (2)$$

Where x_d is the atomic concentration of defects of type d, with d being vacancies or antisites, H_d the formation enthalpy of isolated point defects of type d in

*Corresponding author email: leila.rouaiguia@usthb.dz

stoichiometric structure and ΔH_0^f is the formation enthalpy of the fully ordered stoichiometric alloy.

The effects of vibrational entropy are neglected and the configurational entropy is determined using the mean field approximation.

$$\Delta S_{conf} = k_B \ln\left(\prod_m \frac{N_s^m!}{\prod_i N_i^m!}\right) \quad (3)$$

Where k_B is Boltzmann's constant, N_s^m is the total number of sites on the m sub-lattice and N_i^m is the number of i species on the m sublattice. The minimization of the total Gibbs free energy, with respect to each variable, allows us to obtain the equilibrium concentrations of all point defects at any given total alloy composition and temperature.

III. RESULTS AND DISCUSSION

As a first step, the lattice parameter, bulk moduli, total magnetization and heat of formation of the C15-$ZrFe_2$ compound are predicted. The results are given in the TABLE I, together with some theoretical and experimental values collected from the literature.

TABLE I
STRUCTURAL PROPERTIES OF THE C15-$ZrFe_2$ COMPOUND AT 0K

	a (au)	B (GPa)	M (μ_B/Fe at)	ΔH_f (eV/At)
This Work	7.061	139.5	1.64	-0.288
Exp [14,15]	7.040	-	1.60	-
Theor [16]	7.046	149.24	1.58	-0.280

As it shown in TABLE I, the predicted values are in good agreement with X-ray diffraction measurements, as well as with theoretical values. The rest of this work is devoted to the punctual defects analysis, it is well known that ordered C15 Structure consists of two inter-penetrating face centered cubic sub-lattices, namely 16(d) and 8(a). In perfectly ordered stoichiometric $ZrFe_2$, 16(d) sub-lattice is entirely occupied by Fe atoms while the 8(b) one is occupied by Zr atoms. The deviation from the ideal stoichiometry is caused by the occurrence of constitutional point defects in the two sublattices. Those defects are vacancies and antisites, denoted as Va_{Fe}, Va_{Zr}, Fe_{Zr} and Zr_{Fe} respectively. The formation enthalpies of each point defect are obtained using the following equation [17]:

$$H_d = \frac{\Delta H_d - \Delta H_0}{x_d} \quad (4)$$

Where ΔH_d is the formation enthalpy of the C15-$ZrFe_2$ compound, containing one point defect of type d, whereas ΔH_0 is the formation enthalpy of the perfectly ordered C15-$ZrFe_2$. X_d refers to the defect concentration in the C15 structure. It can take a value of 1/24 for antisites and 1/23 for vacancies. The final results calculated at 0K are given in TABLE II below. At this temperature, the point defects structure are governed by their formation enthalpies and the point defects stable are considered as constitutional defects.

TABLE II
FORMATION ENTHALPIES (eV/atom) OF ISOLATED POINT DEFECTS IN C15-$ZrFe_2$ COMPOUND

HVa_{Fe}	HVa_{Zr}	HFe_{Zr}	HZr_{Fe}
2.64	2.816	0.777	1.251

As it can be seen, all the formation enthalpy values are positives, meaning that, punctual defects occurrence in the C15-$ZrFe_2$, requires external energy supply. Moreover, the deviation toward Zr-rich $ZrFe_2$ side can be caused either by Zr anti-sites and/or Fe vacancies. Similarly, the deviation toward Fe-rich $ZrFe_2$ can be accommodated either by Fe antisites or Zr vacancies. From Table 2, it can be seen that $HVa_{Zr} > HFe_{Zr}$ and $HVa_{Fe} > HZr_{Fe}$. Therefore, it could be concluded that antisites are the dominant constitutional defects in both side of stoichiometry in C15-$ZrFe_2$ compound.

Applying the Wagner-Schottky model, the point defect concentrations in the $ZrFe_2$ alloys at finite temperatures are calculated as a function of Zr concentration. It should be noticed that this model is only valid at intermediate and high temperatures. Consequently, several temperatures are considered and convergence is reached around 1373 K. below this temperature, insignificant curves are obtained, as shown in Fig.1. (a). However, the evolution with Zr concentration of punctual defect concentrations is successfully calculated at T= 1373K and T= 2073 K, the results are presented in Fig.1-(b)-(c) respectively.

As it can be seen, the major defects in $ZrFe_2$ at high temperatures are Zr and Fe anti-sites on the Zr-rich and Fe-rich sides respectively. Comparing the two figures, (b) and (c), all the punctual defects concentrations are found to be increased with temperature. This fact is attributed to the thermal defects which are activated in balanced combinations in order to maintain the overall composition of the alloy [17]. More interestingly, Fe vacancy concentration is less sensitive to the Zr concentration, meaning that deviation from stoichiometry in the C15-$ZrFe_2$ is only governed by Fe vacancies, Fe and Zr anti-sites. This fact is in good agreement with the highest formation enthalpy of Zr vacancies given in the TABLE II.

*Corresponding author email: leila.rouaiguia@usthb.dz

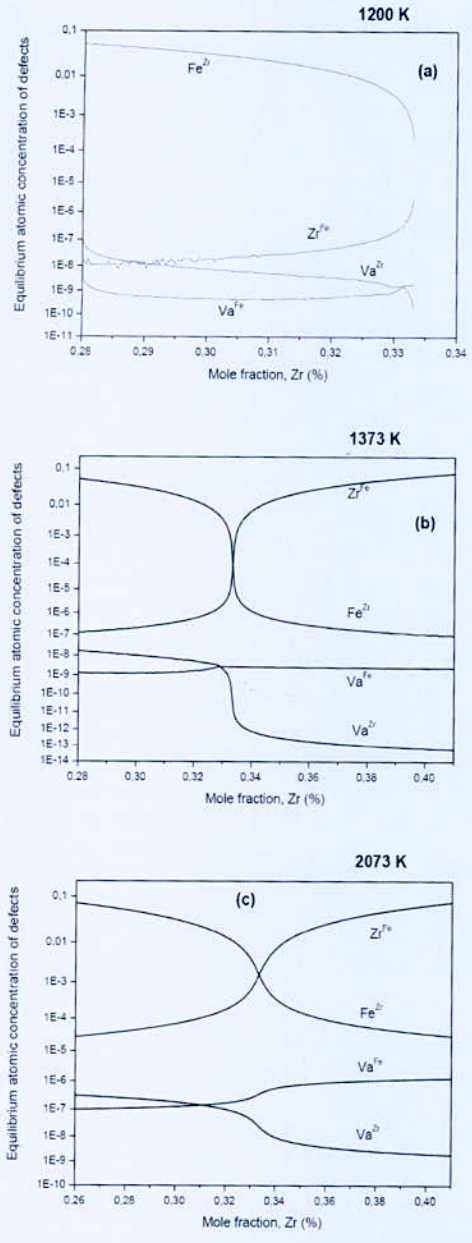

Fig. 1. Evolution with Zr concentration, of the equilibrium defects concentration calculated at: (a) 1200 K, (b) 1373 K and (c) 2073 K

Finally, the effects of finite temperature on hydrogen site preference in the C15-$ZrFe_2$ are also investigated in the present work. The hydrogen atomic trend at 0 K are already investigated in reference [18]. applying DFT calculations, rabahi et al found that 32*e* and 96*g* are the favorable sites for atomic hydrogen in the case of low H content (0.5H/f.u), whereas the 8*b* site is the less favorable one. With increasing H concentrations, the hydride stability is found to be decreased and maximal capacities of 4H/f.u and 6H/f.u are found in the cases of 32*e* and 48*f* sites respectively. Accordingly, only the above cited wyckoff sites are considered for the Wagner-Schottky analyses, namely 96*g*, 32*e*, 48*f* and 8*b*. In Fig.2, the evolution with temperature of the hydrogen concentration at the different wyckoff sites is reported.

At 0 K, the highest hydrogen concentration is found in the case of 48*f* site, followed by the 96*g*, whereas the lowest one is found in the case of 8*b*. This tendency is in good agreement with reference [18]. With increasing temperature, the hydrogen concentration decreases drastically in the 48*f* site. Unlikely, the concentrations increase with similar rates in the 96*g* and 32*e* sites, while it is less sensitive to the temperature variation in the 8*b* site. Comparatively, the occupancy of 48*f* site is more important site up to 200 K, beyond this temperature; 96*g* is the more important one.

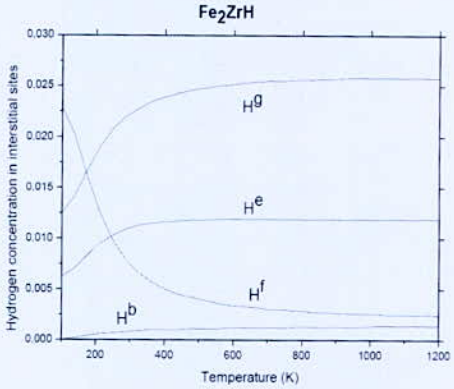

Fig. 2. Evolution with temperature, of the hydrogen concentration in 96*g*, 48*f*, 32*e* and 8*b* wyckoff sites

IV. CONCLUSION

The aim of this work is to use the DFT calculations, together with Wagner-Schottky model to investigate hydrogen trend and punctual defects in the C15-$ZrFe_2$ compound. The results show that anti-sites are responsible of the deviation from the stoichiometry in C15-$ZrFe_2$ at 0 K and finite temperatures, whereas this deviation is insensitive to the Zr vacancy concentration. Moreover, the thermal defects are activated at finite temperature in order to maintain the overall composition of the alloy. Finally, the 48*f* site is the more important at low temperatures, up to 200K and 96*g* is the more important one at intermediate and higher temperatures.

REFERENCES

[1] Stein F, Palm M, Sauthoff G, Structure and stability of Laves phases. Part I. Critical assessment of factors controlling Laves phase stability. Intermetallics 2004; 12 (7-9): 713–20.

[2] Liu C, Zhu J, Brady M, McKamey C, Pike L. Physical metallurgy and mechanical properties of transition-metal Laves phase alloys. Intermetallics 2000; 8:1119-29.

*Corresponding author email: leila.rouaiguia@usthb.dz

[3] Thoma D, Perepezko J. A geometric analysis of solubility ranges in Laves phases. Journal of Alloys Compd 1995; 224: 330-41.

[4] Koultoukis E D, Makridis S S, Pavlidou E, De Rango P, Stubos A K. Investigation of ZrFe2-type materials for metal hydride hydrogen compressor systems by substituting Fe with Cr or V. International Journal of Hydrogen energy 2014;39:21380-85.

[5] Hydrogen in Laves phase ZrX2 (X=V, Cr Mn, Fe, Co, Ni) compounds: Binding energies and electronic and magnetic structure.

[6] Banerjee S, Kumar A, Pillai C G S. Improvement on the hydrogen storage properties of ZrFe2 Laves phase alloy by vanadium substitution. Intermetallics 2014; 51:30-6.

[7] Pukazhselvan D, Kumar V, Singh S K. High capacity hydrogen storage: basic aspects, new developments and milestones. Nano Energy 2012; 1:566-89.

[8] Baroni S, Dal Corso A, De Gironcoli S, Giannozzi P, Cavazzoni C, Ballabio G, Scandolo S, Chiarotti G, Focher P, Pasquarello A, Laasonen K, Trave A, Car R, Marzari N, Kokalj A. http://www.quntum-espresso.org/.

[9] Hohenberg P, Kohn W. Inhomogeneous Electron Gas. Physical Review 1964; 136: B864-71.

[10] Kohn W, Sham L J. Self-Consistent Equation Including Exchange and Correlation Effects. Physical Review 1965; 140: A1133-8.

[11] Perdew J, Burke K, Ernzerhof M. Generalized Gradient Approximation Made Simple. Physical Review Letters 1996; 77: 3865-68. 0031-9007.

[12] Vanderbilt D. Soft self-consistent Pseudopotentials in a generalized eigenvalue formalism. Physical Review B 1990; 41: 7892-95.

[13] Fischer T, Almlof J. General Methods for Geometry and Wave Function Optimization. Journal of physical Chemistry 1992; 96:9768-74. 0022-3654.

[14] Brandes E A, Brook G B. Smithells Metals Reference Book. 7th ed. Butterw orth-Heinemann; 1992. Chapter 6.

[15] Pearson W B. A Handbook of LATTICE SPACINGS AND STRUCTURES OF METALS AND ALLOYS. In: Raynor G V, editor. 1st ed. International Series of Monographs on Metal Physics and Physical Metallurgy, New York: Pergamon Press; 1958, P.178; 182.

[16] K. Ali, A. Arya, P.S. Ghosh, G. K. Dey, A first principles study of cohesive, elastic and elastic properties of binary Fe-Zr intermetallics, Computational Materials Science 112 (2016) 52-66.

[17] Jiang C. Site preference of early transition metal elements in C15 NbCr2. Acta Materialia 2007; 55: 1599–05.

[18]] Rabahi L, Gallouze M, Grosdidier T, Bradai D, Kellou A. Energetics of atomic hydrogen absorption in C15-Fe2Zr Laves phases with ternary additions: a DFT study. International journal of Hydrogen energy. http://dx.doi.org/10.1016/j.ijhydene.2016.11.131.

*Corresponding author email: leila.rouaiguia@usthb.dz

Effect of Cycle Numbers on Physicals and Photoelectrochemical Properties of Fe_2O_3 Obtained by Electrodeposition Technique

Z. Landolsi[1, 2*], I. B. Assaker[1], S. Ammar[1], R. Chtourou[1]

[1*]Laboratoire de Nanomatériaux et Systèmes pour les Energies Renouvelables, Centre de Recherches et des Technologies de l'Energie Technopole borj cedria, Bp 95, hammamm lif 2050, Tunisie.
[2*]Faculty of Science of Bizerte, Jarzouna - Bizerte - 7021, Tunisia.

Abstract—**In this current study the electrodeposition method was proposed to fabricate reproducible and homogeneous hematite (α-Fe_2O_3) on fluorine doped tin oxide (FTO) films using cyclovoltametrie technique , This material is stable, non-toxic and widely present in nature, it seems interesting to us to work with this type of semiconductor. The effects of the cycle number on the structural, morphological properties of the obtained films were studied. In addition, the electrochemical behavior occurring in α-Fe_2O_3 electrode/NaOH electrolyte solution interface is primarily investigated by electrochemical impedance spectroscopy (EIS) method. The XRD analysis and Raman confirmed that the films are mainly successfully crystallized in α-Fe_2O_3 Rhombohedral phase and free from other iron oxide phases. A scanning electron microscope (SEM) was used to measure the size and shape of the nanoparticles. By increasing the cycle's number the experiment results show a remarkable change of nanoparticles. From impedance spectroscopy (EIS) and Mott-Schottky measurements, the charge transfer resistance of the α-Fe_2O_3 films obtained at 200 and 300 cycles are much better than the other cycles and all the films showed n-type semiconductors character.**

Key words— effect of cycles numbers, electrochemical impedance spectroscopy, electrodeposition technique.

I. INTRODUCTION

Hematite (α-Fe_2O_3) is a kind of typical n-type traditional semi-conductor, it possess attractive and unique properties such as high quantum yield, good thermodynamic stability at high temperatures, non-toxicity, and low cost. Moreover, it has emerged as a promising material for photoelectrochemical (PEC) water splitting thanks to its abundance, stability in aqueous environment, favorable position of the electronic valence band and optical band gap that lies in the 2.0-2.2 eV range, to absorb 45% of the incident solar radiation [1]. All these characteristics mean that hematite is used in many applications such as photocatalysis [2], pigment [3], and gas sensors [4].

So far, several kinds of techniques have been investigated to synthesis α-Fe_2O_3 films such as spray pyrolysis [5], chemical coprecipitation [6], sol-gel method [7], hydrothermal synthesis [8] and electrochemical technique [9-18]. Among these, electrochemical deposition is a simple technique, versatile and very convenient for producing large area devices. On the other hand, the possibility to control the morphology, the formed layers and the film thickness by adjusting the electrical parameters as well as the electrolytic solution composition makes it even more attractive. Indeed, electrochemical preparation of α-Fe_2O_3 films has been carried out by several studies. For instance, Q. Meng et al. [12] have electrochemically synthesized Fe_2O_3 films on conducting glass (ITO) from an acidic aqueous mixture solution containing $FeCl_2$ and $FeCl_3$. They focused on the effect of deposition time, current density, reaction temperature and electrolyte concentration in the morphological of α- Fe_2O_3 nanoparticles. Also, Y. Liu et al. [15] have studied the influence of Ni dopant concentration on Ni- Fe_2O_3 properties especially on the PEC performance.

However, to the best of our knowledge, there are few reports in the literature that have studies the electrical behavior of α- Fe_2O_3 [8,17].among these authors P.Shinde et al [17] have presented a detailed description about how to synthesize α- Fe_2O_3 photoanodes onto FTO substrates with their potential application in photoelectrochemical water oxidation for hydrogen by one-and two-step annealing methods .

In the present work, thin film of α- Fe_2O_3 was synthesized onto FTO substrate using a cyclic voltammetry process. The effects of number of cycles as well as the influence of thickness films on structural and electrical properties of the obtained films were studied.

II. EXPERIMENTAL STUDY

All chemicals of analytical reagent grade were purchased from Sigma_Aldrich and are used without further purification. Aqueous solution was prepared using iron (III) chloride ($FeCl_3$, 5.10^{-3}M), sodium fluoride (NaF, 5.10^{-3}M), potassium chloride (KCl, 0.1M) and hydrogen peroxide (H_2O_2, 1M, 35% purity). The deposition solution is acidic with a pH = 2 was carried out at ambient temperature with magnetic stirring (V = $5ms^{-1}$) which the FTO-coated glass substrate was used as working electrode (ET), the FTO glass must be cleaned thoroughly to avoid grease, dust, and scratches and they must immersed in an ultrasonic bath for 15 minutes, firstly in acetone, secondly in iso-propanol and finally in deionized water.

*Corresponding author email: *landolsizoubaida@gmail.com*

The wire of Pt was used as a counter electrode (CE) and Ag/AgCl as a reference (ER) electrode.

III. RESULTATS AND DISCUSSION

1. Structural analysis

X-ray diffraction (XRD) is a reliable technique to determine the crystal structures and phases of the as-prepared films.

Fig. 1, shows X-ray diffraction patterns recorded for α-Fe_2O_3 thin films grown on FTO-coated glass substrates (JCPDS 00-003-1114) under different deposition number of cycles. All samples are crystallized in α-Fe_2O_3 Rhombohedral phase after the heat treatment of 600°C.

It can be noticed that the intensity of the hematite peaks (104) and (110) increase with the number of cycles, at the same time the intensity of FTO (211) diffraction line decreased.

Making a comparison between the XRD patterns of the samples, with 25, 50 and 100 cycles it can be seen that the characteristic peak is (110) at 2θ= 35.70 and for 200 and 300 cycles the characteristic peak is (104) at 2θ=33.23.we can notice that the (110) and (104) orientation become more intense and narrow with the increase of cycle's numbers. Another characteristic peaks of (012) plane centered at 24.20° and (116) at 54.20°.

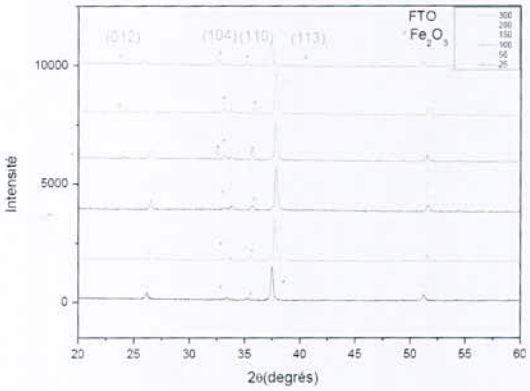

Fig. 1. XRD diffraction pattern of electrodeposited α-Fe2O3 onto (FTO)-coated glass substrates at various deposition numbers of cycles varying from 25 to 300 cycles

2. Morphological analysis

The morphologies of the different films of α-Fe_2O_3 electrodeposited on FTO substrates were examined on field emission scanning electron microscope (FESEM).

At 25 and 50 cycles (Fig. 2(b) and Fig. 2(c)) the obtained films are constituted of small grain with a small number of particles. With the increase of the number of cycle the particles gradually grows up, the shape of nanoparticles keeps the spherical structure and the films obtained become more compact and covered all the surface. This is related to the change of preferred orientation noticed by XRD analysis.

We can see that the grain size of α-Fe_2O_3 prepared with 200 and 300 cycles is relatively higher than the other films, which could be correlated to the enhancement of the characteristic (104) peak. We also note on the same images the presence of white spots called clusters this can be due to the regrouping process or to the operating mode used. In the film with 300 cycles (Fig. 2d) there are cracks and holes resulting from stress can be found. Moreover, the films deposited with 200 cycles (Fig. 2e) are compact and present an excellent uniform surface morphology with a more dense homogeneity of agglomerated crystallites and have better adherence to the FTO as compared to the other films [17].

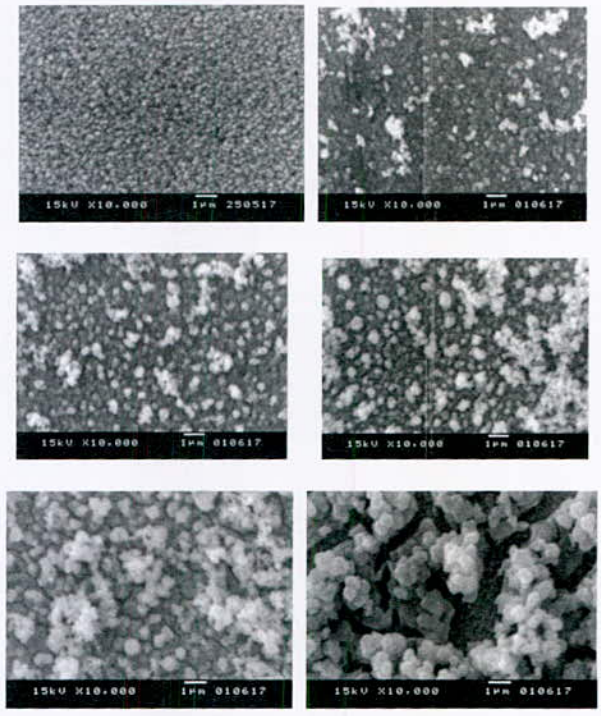

Fig. 2. SEM images of the samples: (a) FTO, (b) α- Fe_2O_3 25 cycles, (c) α- Fe_2O_3 50 cycles, (d) α- Fe_2O_3 100 cycles, (e) α- Fe_2O_3 200 cycles, (f) α- Fe_2O_3 300 cycles

3. Electrical properties

The charge transfer characteristics of hematite were studied by electrochemical impedance spectroscopy (EIS) [18].

We present in Fig. 6, the impedance diagram of α-Fe_2O_3 on FTO glass obtained by the Electrodeposition technique (imaginary impedance (-z") vs. real impedance (z')) in 1M NaOH solution .The measurements were recorded in the potentiostatic mode after stabilization of the open circuit potential at an AC frequency varying

*Corresponding author email: *landolsizoubaida@gmail.com*

from 100 kHz to 0.01 Hz, the series of samples were excited with XE Lampe of 200W.

As can be seen in this figure, the charge transfer resistance (expressed from the diameter of Nyquist plot arc) of the photoanodes fabricated with 25 and 50 cycles are high, being low for 100, 200 and 300 cycles, this can be attributed to a high carrier mobility . This semicircle in the Nyquist plots related to the charge transfer resistance at the electrode/electrolyte interface in the high frequency region while the linear curve related to the low frequency region. The smallest diameter α-Fe_2O_3's arc with 200 cycles indicated that the resistance of the charge transportation is significantly decreased [19].

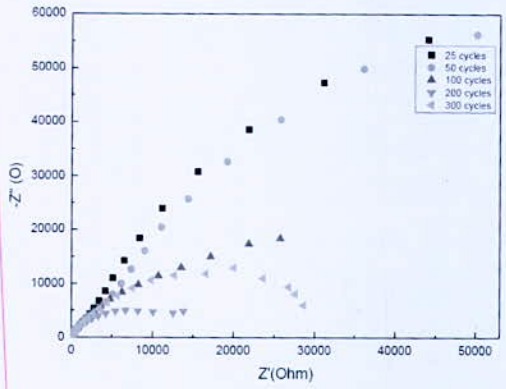

Fig. 6. Nyquist diagram of α-Fe_2O_3 for different cycles numbers (25, 50, 100, 200, 300cycles)

Mott Shottky (M-S) was used to determine the flat band potential (EFb) and the donor densities (Nd) by this formula:

$$\frac{1}{c^2} = B\left[\frac{2}{\varepsilon\varepsilon_0 S^2 N_d}(E - E_{Fb}) - \frac{KT}{e}\right]$$

The C represents the capacitance of the space charge region, ε0 is the vacuum permittivity (8.8542 10-14 F cm-1), ε is the dielectric constant (ε =80 for α-Fe_2O_3)[20], e is the positive elementary charge (e=1.602 10-19 C), S is the surface area of the electrode (1cm^2), Nd is the donor carrier density deduced from the slop of the graph (cm-3), E is the applied potential, EFb is the flat-band potential obtained from the intercept on the potential axis (1/Csc2=0), K is the Boltzmann's constant (1.38 10-23 J K^{-1}) and T is the absolute temperature.

All the samples of α-Fe_2O_3 with different cycle number were carried out in 1M NaOH at a frequency of 1 kHz are presented in Fig. 7. As can be seen, the linear region presents a positive slope indicating n-type semiconductors with electrons conduction.

We observed that the flat band potential (VFb) shifts to low values by increasing the number of cycle this may be due to the new morphology and the crystal structure the values are recapitulated in the table I.

The increase in cycle number favors the capture of charge which results an increase in the charge donors (ND) as indicated in Table I the ND increase from 0.59 10^{16} cm^{-3} at 25 cycles to 1.03 10^{16} cm^{-3} at 200 cycles. However, the ND decreases again at 300 cycles so 200 cycles is the best cycle's number prepare by cyclic voltammetry.

TABLE I
MOTT SHOTTKY RESULTS FOR THE ELECTRODEPOSITED A-Fe_2O_3 AT DIFFERENT NUMBER OF CYCLES

number of cycles	VFb (V)	slope (1010)	ND (10^{16}) (cm^{-3})
25	-0.75	2.95	0.59
50	-0.74	2.93	0.60
100	-0.76	2	0.88
200	-0.81	1.7	1.03
300	-0.98	2	0.88

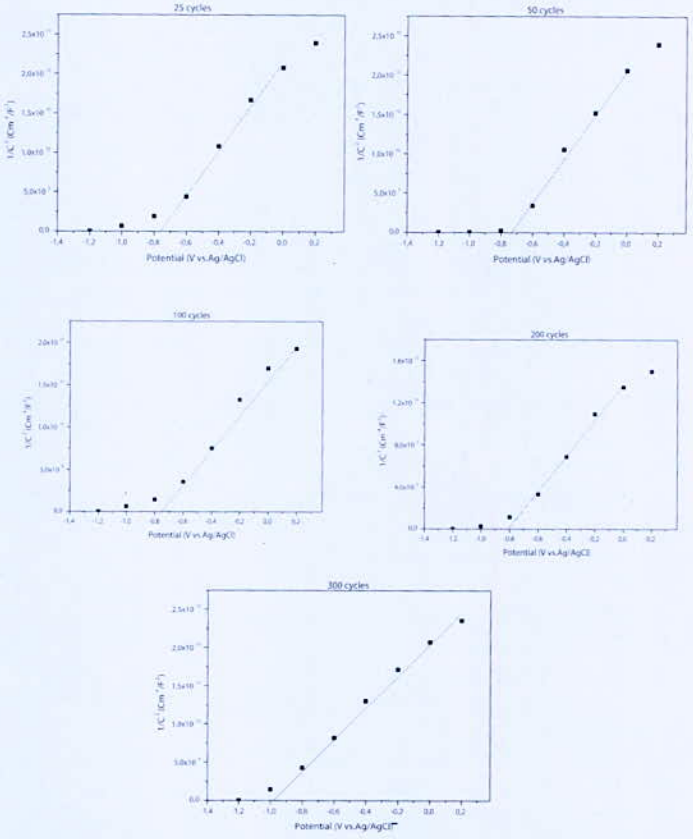

Fig. 7. Mott Shottky plots of α Fe_2O_3 film on FTO substrate with different number of cycles

IV. CONCLUSION

This study showed that the number of cycles (or thickness) is a very important parameter for obtaining good quality of films ,the Hematite (α-Fe_2O_3) deposited

*Corresponding author email: *landolsizoubaida@gmail.com*

on transparent FTO were prepared by the electrode position method .

The experimental results showed that the:

- XRD proved that after annealing all films crystallize in the Rhombohedral phase. The sizes, shapes and the number of grains of the α-Fe_2O_3 were varied with changing the number of cycle, the film deposited at 200 cycles is uniform and the size of grains is perfect.

From electrical measurements The Mott-Schottky plot shows that all the films are n-type semi conductors. The flat band potential (VFb) shifts to low values and the increase of charge donors (ND) depend by increasing the number of cycle up to 200 cycles so this thin layer (200) has the lowest value of the charge transfer resistance (RCT).

REFERENCES

[1] B.Landolo, B.Wickman, I.Zoric, A.Hellman,The rise of hematite:Origin and Strategies to Reduce the High Onset Potential for the Oxygen Evolution Reaction,journal of Materials Chemistry A,(2015).

[2] S.Shuang, Z. Xie, Z. Zhang , Enhanced photocatalytic properties of cds nanoparticles decorated Fe2O3 nanopillar arrays under visible light,journal of colloid and interface science 494 (2017)pp. 107-113.

[3] S.A. Jadhav, R. Bongiovanni, D.L. Marchisio, D. Fontana, C. Egger, Surface modification of iron oxide (Fe2O3) pigment particles with amino-functional polysiloxane for improved dispersion stability and hydrophobicity, Pigm Resin Technol 43 (2014) pp.219-227.

[4] P. Sun, Y.W. Liu, X.W. Li, Y.F. Sun, X.S. Liang, F.M. Liu, G.Y. Lu, Facile synthesis and gas-sensing properties of monodisperse alpha-Fe2O3 discoid crystals, Rsc Adv 2 (2012)pp. 9824-9829.

[5] S. S. Shinde, R. A. Bansode, C. H. Bhosale, K. Y. Rajpure,Physical properties of hematite α-Fe2 O3 thin films: application to photoelectrochemical solar cells, Journal of Semiconductors 32 (2011).

[6] S.Sankadiya, N.Oswal, P.Jain, N.Gupta, Synthesis and characterization of α-Fe2O3 nanoparticles by simple co-precipitation method, Physical Chemistry Research, 3 (2015) pp.193-198.

[7] S.Akbar, S.K.Hasanain, N.Azmat, M.Nadeem, Synthesis of Fe2O3 nanoparticles by new Sol-Gel method and their structural and magnetic characterizations,

[8] L. Li, C time, o. Liu , Y. Qiu , N. Mitsuzak , Z.Chen,The influence of the hydrothermal temperature and n morphology and photoelectrochemical response of α-Fe2O3photoanode ,journal of Alloys and Compounds 696 (2017) pp.980-987.

[9] S. S. Shendage, U. B. Patil, J. M. Nagarkar, Electrochemical deposition of highly dispersed palladium nanoparticles on nafion-graphene film in presence of ferrous ions for ethanol electrooxidation, Fuel Cells 13 (2013) pp.364-370.

[10] L. Li, C. Chang, H. Wu, J. Shiu, P. Wu, E. Diau, Morphological control of platinum nanostructures for highly efficient dye-sensitized solar cells, J. Mater. Chem. 22 (2012) pp. 6267-6273.

[11] M.Vanags, A.Šutka, J.Kleperis, P.Shipkovs, Comparison of the electrochemical properties of hematite thin films prepared by spray pyrolysis and electrodeposition , journal Ceramics International,41 (2015) pp.9024-9029.

[12] Q. Meng, Z. Wang, X. Chai, Z. Weng, R. Ding, L. Dong,Fabrication of Hematite (α-Fe2O3) Nanoparticles Using Electrochemical Deposition,journal of applied surface science 368 (2016) pp.303-308.

[13] G.Iervolino, I.antis, L.Sygellou, V.Vaiano, D.Sannino, P.Lianos, Photocurrent increase by metal modification of Fe2O3photoanodes and its effect on photoelectrocatalytic hydrogen production by degradation of organic substances, journal of Applied Surface Science, 400(2017) 176-183.

[14] S. L. Kadam, P. M. Padwal, S. M. Mane, S. B. Kulkarni, Electrodeposition of Fe2O3 nanoparticles and its supercapacitive properties,conference, (2016).

[15] Y.Liu,Y.Xiang Yu,W.De Zhang , Photoelectrochemical properties of Ni-doped Fe2O3 thin films prepared by electrodeposition,journal Electrochimica Acta 59(2012) pp.121-127.

[16] Z. Braiek, M. Gannouni, I.Ben Assaker, A.Bardaoui, A.Lamouchi, A. Brayek, R.Chtourou, Correlation between physical properties and growth mechanism of In2S3 thin films fabricated by electrodeposition technique with different deposition times, The European Physical Journal Applied Physics, 72 (2015).

[17] J. Cai, S.li, Z.Li, J.Wang,Y.Ren,G.Qin, Electrodeposition of Sn-doped hollow α-Fe2O3 nanostructuresfor photoelectrochemical water splitting, Journal of Alloys and Compounds 574(2013) pp.421-426.

[18] P.S.Shinde, A.Annamalai, J.H.Kim,S.H.Choi, J.S.lee, J.S.Jang, Photoelectrochemical, impedance and optical data for self Sn-diffusion doped Fe2O3 photoanodes fabricated at high temperature by one and two-step annealing methods, journal of Data in Brief 5(2015)pp.796-804.

[19] Y. Liu, Z. Xu, M. Yim, H. Fan, W. Cheng, L. Lu, Y. Song, J. Ma, X. Zhu, Enhanced photoelectrocatalytic performance of α-Fe2O3 thin films by surface plasmon resonance of Au nanoparticles coupled with surface passivation by atom layer deposition of Al2O3, Nanoscale Research Letters(2015).

[20] Mishra SK, Kumar D, Biradar AM, Rajesh (2012) Electrochemical impedance spectroscopy characterization of mercaptopropionic acid capped ZnS nanocrystal based bioelectrode for the detection of the cardiac biomarker— myoglobin. Journal of Bioelectrochem 88(2012) pp.118–126.

*Corresponding author email: *landolsizoubaida@gmail.com*

Analyses of Heat and Mass Transfers in a Metal Hydrogen Reactor Using the Lattice Boltzmann Method

F. Bouzgarrou[1*], A. Miled[1], F.Askri[1, 2]

[1*]Laboratory of Thermal and Energetic Systems Studies (LESTE), Engineering school of Monastir, University of Monastir, 5000 Monastir, Tunisia.

[2]Mechanical Department, Faculty of Engineering, King Khalid University, Abha, Saudi Arabia

Abstract—**In this paper, the hydrogen absorption process in a metal hydrogen reactor connected to a hydrogen reservoir is simulated by using the Lattice Boltzmann Method (LBM). A comparison of the numerical and experimental results has been done in order to validate the theoretical model describing the dynamic behavior of the reactor. In addition, the effects of the reservoir volume on the temperature and the hydrogen mass absorbed evolutions are investigated.**

Key words—Lattice Boltzmann Method, metal hydrogen reactor, heat transfer.

I. INTRODUCTION

Metal hydrides have received much attention due to their importance in many applications. Several studies based on various mathematical and numerical models have been carried out to study heat and mass transfers within metal-hydrogen reactors during the sorption phenomena. All these works were based on the conventional Computational Fluid Dynamics based methods which directly solve the continuum governing equations: the FVM [1-4], the FDM [5-6] and the CVFEM [7-10].

Recently, the Lattice Boltzmann Method has met with considerable success for the numerical simulation of different heat transfer problems including the hydrogen storage in metal hydrogen reactors (MHR) [11-12]. Hence, the purpose of this study is to apply the LBM for modeling and simulating heat and mass transfers during the absorption process in MHRs.

The physical configuration of the considered reactor is presented at first. Then, the macroscopic and mesoscopic (LBM) formulations describing the dynamic behavior of the MHR are detailed. Finally, the obtained results are discussed.

II. FORMULATION

1. Theoretical background

A cylindrical reactor with a radius R = 5 cm and a height H = 6 cm, filled with the $LaNi_5$ alloy and connected to a hydrogen tank is considered (Fig. 1). The reactor exchanges heat through the lateral and base areas with a cooling fluid at a constant temperature.

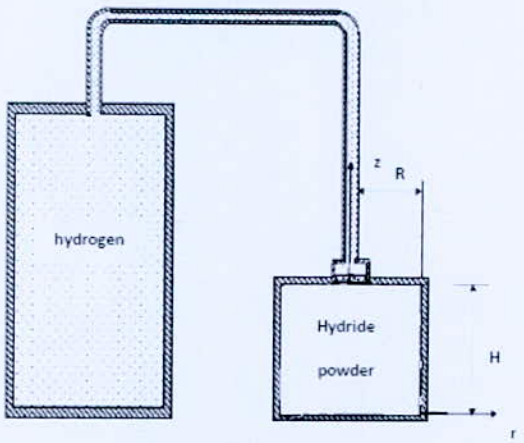

Fig. 1. Metal hydrogen reactor

Several assumptions are considered in order to simplify the study:

- ✓ The porous medium is homogeneous and isotropic,
- ✓ The two phases are in local thermal equilibrium,
- ✓ The transfers are two-dimensional,
- ✓ The gas is considered ideal from the thermodynamic view point,
- ✓ The radiative and convective heat transfers are negligible.

Taking into account the above assumptions, the governing equations governing in the reactor are as follow:

- Mass balance:

✓ For hydrogen : $$\varepsilon \frac{\partial \rho_g}{\partial t} = -\dot{m} \quad (1)$$

✓ For hydride : $$(1-\varepsilon)\frac{\partial \rho_s}{\partial t} = \dot{m} \quad (2)$$

Where ρ_g and ρ_s are, respectively, the gas and solid densities and ε is the porosity.

The hydrogen mass absorbed, $\dot{m}$, per unit time and unit volume is given by [8]:

$$m_a = C_a \exp\left(-\frac{E_a}{R_g T}\right) \ln\left(\frac{P}{P_{eq}}\right)(\rho_{ss} - \rho_s) \quad (3)$$

Where C_a is the absorption rate constant, E_a is the

*Corresponding author email: bouzgarroufatma@yahoo.fr

activation energy and ρ_{ss} is the density of the hydride at saturation.

The equilibrium pressure can be written as follows:

$$P_{eq} = f\left(\frac{H}{M}\right)\exp\left(\frac{\Delta H}{R_g}\left(\frac{1}{T}-\frac{1}{T_{ref}}\right)\right) \quad (4)$$

Where $f\left(\frac{H}{M}\right)$ is the equilibrium pressure at the reference temperature T_{ref}.

- Energy balance equation:

$$\left(\rho C_p\right)_{eff}\frac{\partial T}{\partial t} = \lambda_{eff}\left(\frac{\partial^2 T}{\partial z^2}+\frac{1}{r}\left(r\frac{\partial T}{\partial r}\right)\right)+\dot{m}\,\Delta H + \dot{m}\left(C_{pg}-C_{ps}\right)T \quad (5)$$

Where $\left(\rho C_p\right)_{eff} = \varepsilon\rho_g C_{pg} + (1-\varepsilon)\rho_s C_{ps}$ (6)

And $\lambda_{eff} = \varepsilon\,\lambda_g + (1-\varepsilon)\,\lambda_s$ (7)

- Initial condition

Initially, the temperature and the hydride density are assumed to be constant.

$$T(r,z,0) = T_0 \text{ and } \rho_s(r,z,0) = \rho_0 \quad (8)$$

- Boundary conditions:

- The symmetry about the z axis permits us to write

$$\left(\frac{\partial T}{\partial z}\right)_{r=0} = 0 \quad (9)$$

- The other walls of the reactor exchange heat with a cooling fluid at constant temperature T_f. So, we can write

$$-\lambda_{eff}\nabla T\,\vec{n} = h\left(T-T_f\right) \quad (10)$$

Where $\vec{n}$ is the normal vector of the corresponding wall and h is the convective heat transfer coefficient.

2. LBM formulation

The discrete Boltzmann equation in different directions is given by

$$\frac{\partial f_i}{\partial t}(\vec{r},t)+\vec{c}_i\nabla f_i(\vec{r},t) = \frac{1}{\tau}\left(f_i^{eq}(\vec{r},t)-f_i(\vec{r},t)\right) + \frac{\omega_i S}{\left(\rho C_p\right)_{eff}} \quad (11)$$

Where f_i is the particle distribution function denoting the number of particles surrounding the lattice node $\vec{r}$ and at time t moving in the i direction with the velocity $\vec{c}_i$. ω_i is the corresponding weight and τ is the relaxation time which is expressed for the D_2Q_9 lattice (Fig.2) by [11]:

$$\tau = \frac{3\,\alpha}{c^2}+\frac{\Delta t}{2} \quad (12)$$

f_i^{eq} is the equilibrium distribution function and S is the source term given by [11]

$$S = \dot{m}\,\Delta H + \dot{m}\left(C_{pg}-C_{ps}\right)T + \frac{\lambda}{r}\frac{\partial T}{\partial r} \quad (13)$$

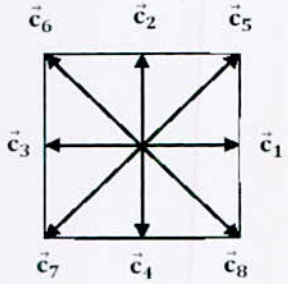

Fig. 2. The D_2Q_9 lattice [11]

After discretization, Eq.11 can be written as

$$f_i(\vec{r}+\vec{c}_i\Delta t, t+\Delta t) = f_i(\vec{r},t)+\omega(\vec{r},t)\left(f^{eq}{}_i(\vec{r},t)-f_i(\vec{r},t)\right)+\frac{\omega_i S\,\Delta t}{\left(\rho C_p\right)_{eff}} \quad (14)$$

Where $\omega = \frac{\Delta t}{\tau}$ (15)

The temperature is obtained after summing f_i over all directions

$$T(\vec{r},t) = \sum_{i=0}^{8} f_i(\vec{r},t) \quad (16)$$

And the equilibrium distribution function is expressed as follows

$$f^{eq}{}_i(\vec{r},t) = \omega_i T(\vec{r},t) \quad (17)$$

- Initial and boundary conditions

Initially, the distribution function is equal to the equilibrium distribution function

$$f(ip,i,j) = f^{eq}(ip,i,j) \quad (18)$$

At the adiabatic wall, the boundary condition can be written as:

$$f(ip,i,j) = f(jp,i,j) \quad (19)$$

III. RESULTS AND DISCUSSION

In order to validate the numerical code based on the LBM, we have realized a comparison between the theoretical predictions, experimental data [13] and numerical results given by the CVFEM [8] of the pressure during the absorption process. As shown in figure 3, the present method yields reasonably good solutions compared with CVFEM and experimental results.

The values of geometrical dimensions and operating

*Corresponding author email: bouzgarroufatma@yahoo.fr

conditions used in different simulations are mentioned in table I.

TABLE I
VALUES OF DATA USED IN SIMULATIONS

Symbol	Quantity	Value
T_0	Initial bed temperature	293 K
T_f	Heating fluid temperature	293 K
P_0	Initial temperature	8 bar
R	Reactor radius	0.025 m
H	Reactor height	0.06 m
V_t	Tank volume	0.001755 m^3

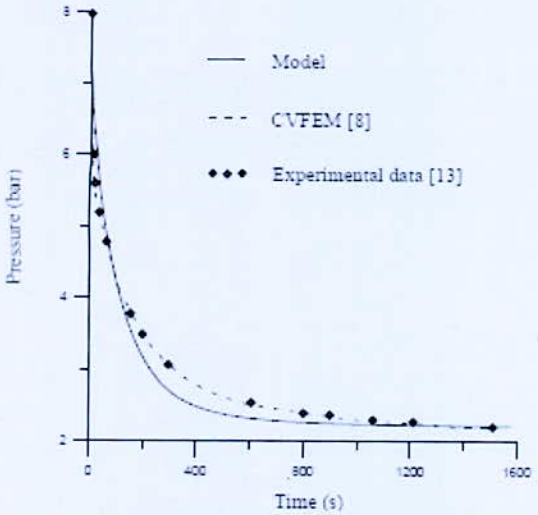

Fig. 3. Temporal evolution of the pressure during the absorption process

The effect of the reservoir volume on the dynamic behavior of the metal hydrogen reactor is tested. Two cases are simulated.

In the first case, the tank volume is varied from 10150 cm^3 to 16000 cm^3 while the initial pressure is kept constant ($P_0 = 12$ bar) .

Fig. 4 shows that the variation of the tank volume has no considerable effect on the maximum of the hydride temperature. Also, we note that the increase of the tank volume reduces the time of the charging process (Fig.5).

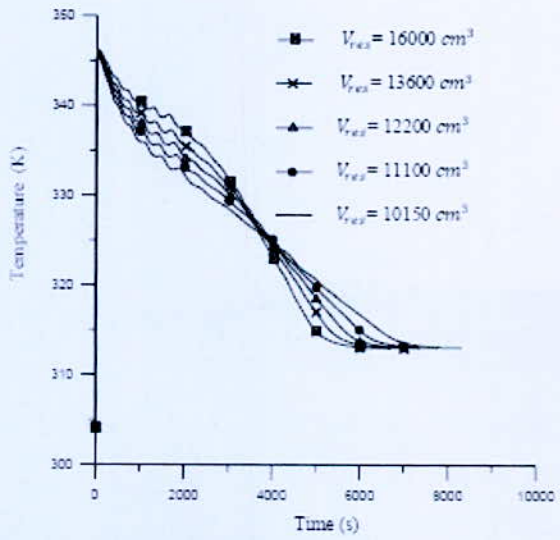

Fig. 4. Effect of the tank volume on the temperature evolution

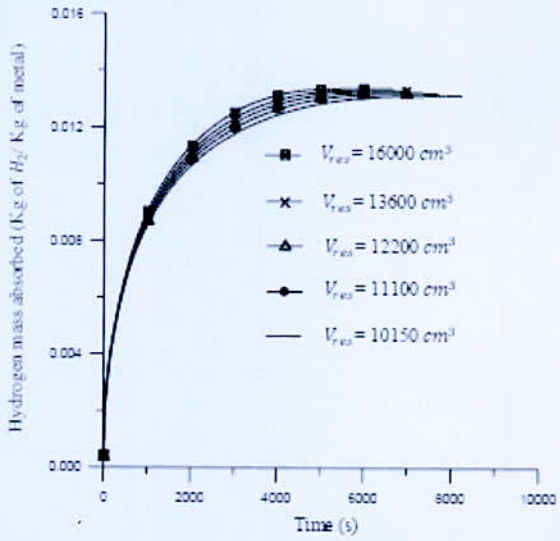

Fig. 5. Effect of the tank volume on the hydrogen mass absorbed

For the second case, Furthermore, the hydrogen mass initially introduced into the reservoir is kept constant ($m_{H_2} = 5$ g) and the tank volume is varied from 10150 cm^3 to 16000 cm^3. It can be noticed that the temperature in the hydride bed decreases and the time of the absorption process increases by increasing the reservoir volume. In addition, it was noted that the decrease of the volume under 11000 cm^3 has no significant effect on the time of the charging process (Fig. 6 and Fig. 7).

*Corresponding author email: bouzgarroufatma@yahoo.fr

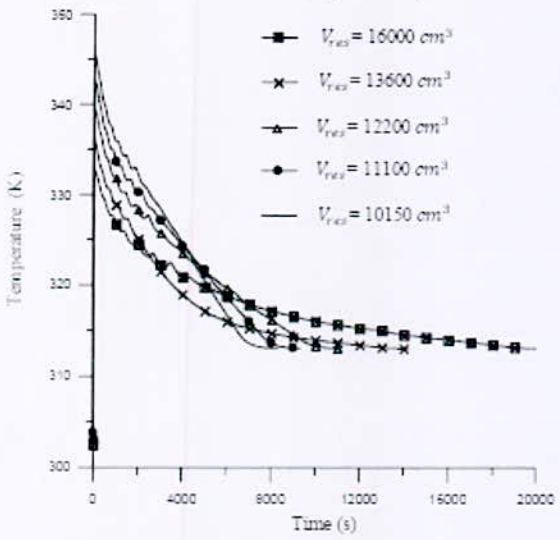

Fig. 6. Effect of the tank volume on the temperature evolution

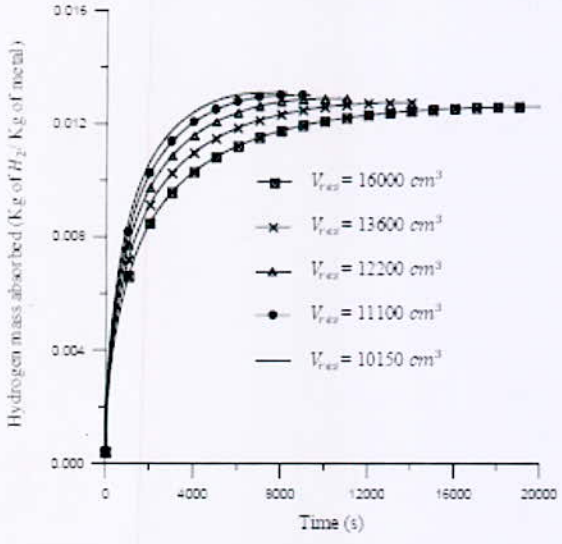

Fig. 7. Effect of the tank volume on the hydrogen mass absorbed evolution

IV. CONCLUSION

A numerical code based on the Lattice Boltzmann Method has been developed to study the heat and mass transfers in a metal hydrogen reactor connected to a hydrogen tank. The numerical approach is validated by comparison with experimental results and a good agreement is obtained. The volume effect of the reservoir was studied and numerical results shown that the hydride temperature and the charging process depend on this operating parameter.

As a perspective, the aim of the next work is to investigate the effect of integration of a heat exchanger on reactor behavior.

REFERENCES

[1] F. Askri, A. Jemni, S. Ben Nasrallah. Study of two-dimensional and dynamic heat and mass transfer in a metal-hydrogen reactor. Int. J. Hydrogen Energy 28 (2003) 537-557.

[2] A. Dogan, Y. Kaplan, T. Nejat Veziroglu. Numerical investigation of heat and mass transfer in a metal hydride bed. Applied Mathematics and computation (2004) 169-180.

[3] P. Muthukumar, S. Venkata Ramana. Numerical simulation of coupled heat and mass transfer in metal-hydride based hydrogen storage reactor. Journal of alloys and compounds 472 (2009) 466-472.

[4] Ali Boukhari. Numerical Investigation of Heat and Mass Transfer Processes while the Desorption of Hydrogen Gas Stored in MmNi4.6Fe0.4-H6. International Journal of Energetica 1 (2016) 1-11.

[5] F. Laurencelle, J. Goyette. Simulation of heat transfer in a metal hydride reactor with aluminium foam. Int. J. Hydrogen Energy 32 (2007) 2957- 2964.

[6] Fei Han, Weizhong Dai. Numerical simulation of hydrogen desorption in metal-hydride reactor. International Mechanical Engineering Congress & Exposition IMECE. Houston, Texas, USA, 2012.

[7] F. Askri, A. Jemni, S. Ben Nasrallah. Prediction of transient heat and mass transfer in a closed metal-hydrogen reactor. Int. J. Hydrogen Energy 29 (2004) 195-208.

[8] F. Askri, A. Jemni, S. Ben Nasrallah. Dynamic behavior of metal–hydrogen reactor during hydriding process. Int. J. Hydrogen Energy 29 (2004) 635-647.

[9] F. Askri, M. Ben Salah, A. Jemni, S. Ben Nasrallah. Optimization of hydrogen storage in metal-hydride tanks. Int. J. Hydrogen Energy 34 (2009) 897-905.

[10]H. Ben Maad, F. Askri, S. Ben Nasrallah. Numerical investigation of heat and mass transfer during the desorption process of an Mg2NiH2 reactor. Int. J. Hydrogen Energy 38 (2013) 4597- 4610.

[11] F. Askri, M. Ben Salah, A. Jemni, S. Ben Nasrallah,. A new algorithm for solving transient heat and mass transfer in metal hydrogen reactor. Int. J. Hydrogen Energy 34 (2009) 8315-8321.

[12] Mehran Valizadeh, Mojtaba Aghajani Delavar, Mousa Farhadi. Numerical simulation of heat and mass transfer during hydrogen desorption in metal hydride storage tank by Lattice Boltzmann method. Int. J. Hydrogen Energy 41 (2016) 413-424.

[13] A. Jemni, S. Ben Nasrallah, J. Lamloumi. Experimental and theoretical study of metal-hydrogen reactor. Int. J. Hydrogen Energy 7 (1999) 631-644.

*Corresponding author email: bouzgarroufatma@yahoo.fr

Thermal Modeling of a Thermochemical Reactor for Solar Hydrogen Production

D. Darfilal[1, 2*] C. Seladji[1]

[1]Département de Génie mécanique / Laboratoire Energétique et Thermique Appliquée ETAP, Abou-Bekr BELKAÏD University, B.P 119, 13000 Tlemcen, Algeria.
[2]Centre de Développement des Satellites CDS / Algerian Space Agency ASAL / BP 4065, Ibn Rochd USTO 31130 Oran, Algeria.

Abstract—**Solar water splitting is a promising process for the storage and conversion of sunlight power into clean-burning hydrogen gas, this paper present a CFD thermal analysis of hydrogen production via a proposed packed bed thermo-chemical receiver/reactor system. The idea of this study is the use of packed bed of spherical ceramic particles coated with active redox ferrite materials, The first step is an endothermic reaction, nickel ferrite (NiFe2O4) dissociate thermally into nickel oxide (NiO), ferrous oxide (FeO) and oxygen at 1473 K, this reaction take place under 2 KW concentrated solar energy. The second is the hydrolysis step at 1073 K to form hydrogen and NiFe2O4, the latter is recycled to the first step for a new production cycle. The CFD code solves the momentum equation, energy equations and species transport equation. The temperature fields of the reactor solid & the fluid phases were attained using the local thermal non-equilibrium model (LTNE). The LTNE model sources terms were computed through the user-defined functions to couple the energy equations of the fluid phase and solid phase. The complete model was used to analyse numerically the reaction through the packed bed in order to predict the thermal behavior under different conditions.**

Key words—Hydrogen, solar, reactor, thermochemical.

I. INTRODUCTION

Hydrogen is actually considered as the most promising green fuel vector for the future as it has prodigious capability of reducing greenhouse gas and other environmental pollutants emitted by fossil energy systems. It is considered that engines operating with hydrogen [1-3] can tremendously reduce dependence on nonrenewable fuel sources [4].

The use of hydrogen as an alternative fuel vector unlocks potential means of converting energy from solar radiation to storable chemical energy. It is envisaged that the hydrogen will replace smoothly fossil energy resources in automotive industry through fuel cell technology. It would be more efficient as fuel for internal combustion engines with comparable performance, emitting just water vapour [4, 5] The exploitation of the massive amount of solar radiation and its conversion to chemical storable energy such as hydrogen is a subject of primary technological interest [6]. There are basically three methods and their combinations for producing hydrogen using solar radiations namely photochemical, electrochemical and thermochemical [7, 8]. The latter is based on the use of concentrated solar radiation as the driving force that produce hydrogen from transformation of its feedstock [4].

Recently, enormous efforts has been made in developing concentration systems that exceed 5000 suns solar concentration ratios, capable of achieving temperatures above 1400°C, needed to release two-step thermochemical reactions using metal oxide. Ferrite-based thermochemical cycle has been the most explored cycle [9]. Ferrite-based cycle has been extensively studied in solar furnace of DLR, Tokyo Institute of Technology [11] and Sandia national laboratories [12, 13].

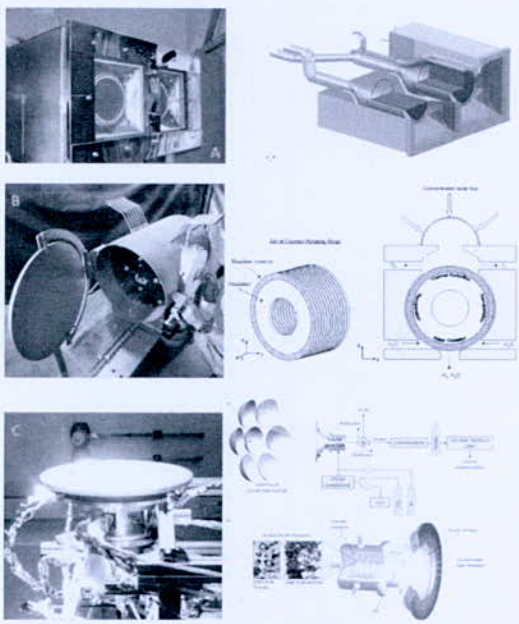

Fig. 1. Solar reactors: (A) HYDROSOL 2, (B) CR5, (C) SOLARJET

II. MODELLING

The study presents an approach to the computational modelling of a volumetric solar receiver/reactor consisting of an absorption cavity that is filled by a packed bed of ceramic spheres and irradiated from the flow inlet face. The variation of cavity thermal response is examined for different sphere packing arrangements while a comparison with experimental and theoretical results is shown. The model of the bed of packed spheres is based

*Corresponding author email: ddarfilal@cds.asal.dz

on two-dimensional scalar transport in a homogeneous porous medium for which distinct solid and fluid temperature fields are retained.

1. Assumptions

The model approach used in this model is macroscopic, which is based on the averaging of fundamental flow equations such as continuity, momentum and energy as well as turbulence over a representative volume of the porous media [14]. The most research efforts in computation of turbulent flow in porous media [15-17] have been focused on developing macroscopic equations through the averaging volume techniques of the $k-\varepsilon$ turbulence model.

The governing equation assumptions are the following:

- Uniform porosity through the porous structure.
- The flow field is steady and turbulent
- Effect of Buoyancy, Hydrodynamic dispersion, viscous dissipation is negligible.
- Thermal expansion is negligible.

2. Continuity and momentum equation

According to the cited assumptions, the averaged continuity and momentum equation for the proposed model are:

$$\nabla(\rho\bar{v}) = 0 \tag{1}$$

$$-\frac{\mu}{\alpha}<v>-\frac{\rho_f C_2 \varepsilon_p}{\sqrt{\alpha}}[<v>.<v>]+\frac{\mu}{\varepsilon_p}\nabla^2<v>-\nabla<P>=0 \tag{2}$$

Where α is the permeability of the porous media, C_2 is the inertial coefficient. The first and the second term on the right hand side are the momentum source terms. The equation neglects the convective term as the flow is fully developed. The turbulence model are obtained by averaging the standard turbulence kinetic energy and the dissipation rate equation.

$$\nabla.(\rho_f v <k_t>) = \nabla.\left[\left(\mu+\frac{\mu_{t\varepsilon}}{\sigma_k}\right)\nabla(\varepsilon_p <k_t>)\right] \tag{3}$$

$$+P_i+G_i-\rho_f\varepsilon_p<\varepsilon>$$

$$\nabla.(\rho_f v <\varepsilon>) = \nabla.\left[\left(\mu+\frac{\mu_{t\varepsilon}}{\sigma_\varepsilon}\right)\nabla(\varepsilon_p <\varepsilon>)\right]+ \tag{4}$$

$$C_1 P_i\frac{<\varepsilon>}{<k_t>}+C_2\frac{<\varepsilon>}{<k_t>}(G_i-\rho_f\varepsilon_p<\varepsilon>)$$

Where $C_1, C_2, \sigma_k, \sigma_\varepsilon$ are $k-\varepsilon$ model constants, P_i is the production rate of $<k_t>$ due to gradients of v and G_i is the generation rate of the intrinsic average of k_t due to the action of the porous solid phase .

3. Energy equations

In LTNE energy model approach, the solid and fluid phases are spatially coincident and interact between them with regard to heat transfer (source term), two equation are solved separately for the fluid and solid phases in this proposed model. The Fluid phase equation under steady state conditions is:

$$(\rho C_p)_f <v>.\nabla<T_f> = \nabla.\{k_{feff}.\nabla<T_f>\}+S_{conv} \tag{5}$$

Solid phase energy equation under steady state condition is the following:

$$\nabla.\{k_{seff}.\nabla<T_s>\}-S_{conv}=0 \tag{6}$$

S_{conv} Present the source term of the convective heat exchange between the solid and the fluid phases.

$$S_{conv} = h_{fs}A_{fs}(<T_s>-<T_f>) \tag{7}$$

Where h_{fs} present the coefficient of the convective volumetric heat transfer and A_{fs} is the exchange area between the solid matrix and the fluid.

4. Convective volumetric heat transfer coefficient

According to the following references [18] and [19] the volumetric heat transfer coefficient is constant over the length of the reactor. The model used to calculate the heat transfer coefficient and the interfacial area density is a general correlation, which can be used for all Particle Reynolds Number [20]:

$$h_{fs} = \frac{k_f(2+1,1.Pr^{\frac{1}{3}}.Re^{0.6})}{d_p} \tag{8}$$

The area correlation for this model is given by:

$$A_{fs} = \frac{6.(1-\varepsilon_p)}{d_p} \tag{9}$$

5. Permeability and inertial loss coefficients

Ergun Equation is a semi empirical correlation applicable over a vast range of Reynold numbers and it is applicable for many type of packing:

$$\frac{|\Delta p|}{L} = 150\frac{\mu}{D_p^2}((1-\varepsilon)^2/\varepsilon^3)v_\infty+(1.75\rho/D_p)((1-\varepsilon)/\varepsilon^3)v_\infty^2 \tag{13}$$

From Ergun correlation, the permeability and inertial loss coefficients are identified as:

$$\propto = \frac{D_p^2}{150}\frac{\varepsilon^3}{(1-\varepsilon)^2} \tag{14}$$

$$C_2 = \frac{3.5}{D_p}\frac{(1-\varepsilon)}{\varepsilon^3} \tag{15}$$

*Corresponding author email: ddarfilal@cds.asal.dz

6. Species transport equation

In this work the two steps reactions were modeled separately (reduction and hydrolysis). The main objectives of these simulations are to study the kinetics of the reactions and the evaluation of the impact of these reactions on the temperature distribution.

The species transport equation is expressed as:

$$\nabla(\rho\vec{u}Y_i) = \rho D_{i,m}\Delta Y_i + M_i R_{chem\,i} \quad (16)$$

Reduction reaction:

The thermal reduction is an endothermic reaction, it needs a temperatures >1400 K [6]. In this case the source term related to the chemical reaction (using Arrhenius-type temperature dependence model) is given by:

$$S_R = k_{0,R}\, exp\left(\frac{-E_{a,R}}{R_g T_s}\right) \Delta H_{red} \quad (17)$$

Hydrolysis reaction:

The second step of the cycle is an exothermic reaction. This reaction is carried out at temperatures around 1200 K. The volumetric heat source term in this case is given by:

$$S_H = k_{0,H}\, exp\left(\frac{-E_{a,H}}{R_g T_s}\right) [H_2O]\, \Delta H_{hyd} \quad (18)$$

III. RESULTS AND DISCUSSION

The model was validated with experimental and numerical results obtained by [22] using the same thermo-physical properties of the cited model . Figures 2 & 3 presents the variation of temperature through the position. The results showed good agreement with [22] experimental and numerical studies.

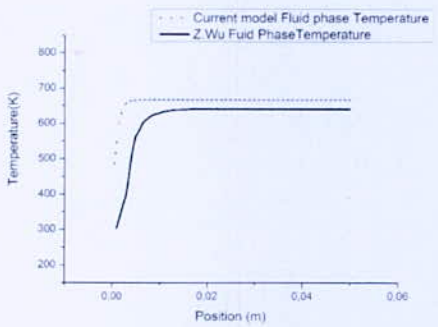

Fig. 2. Fluid phase model validation

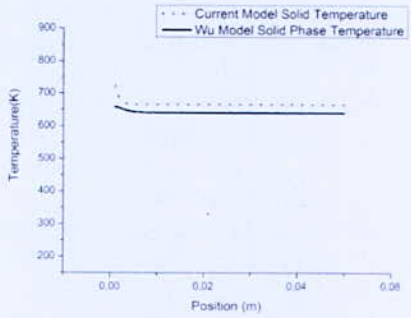

Fig. 3. Solid phase model validation

In order to optimise the performances of the packed bed solar receiver, a series of sensitivity studies was conducted

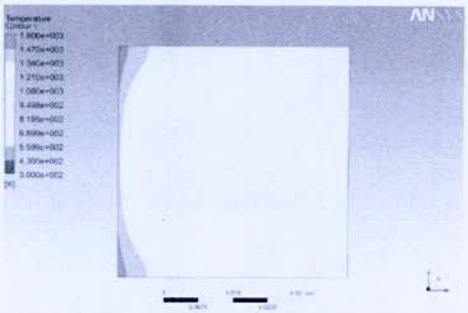

Fig. 4. Solid phase Temperature distribution

The effect of the reaction is shown in the following figures:

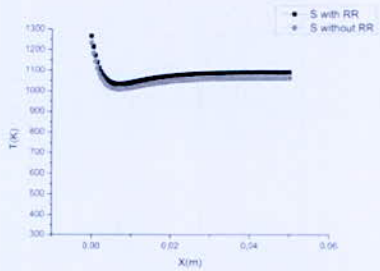

Fig. 5. Solid temperature distribution with and without reduction reaction RR

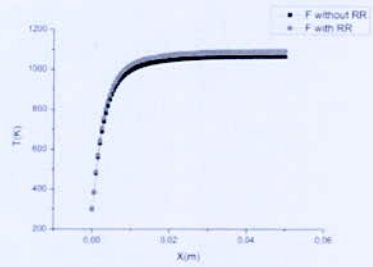

Fig. 6. Fluid temperature distribution with and without reduction reaction RR

*Corresponding author email: ddarfilal@cds.asal.dz

IV. CONCLUSION

A 2D CFD model was developed to predict the packed bed reactor performances at different boundary conditions. Simulations were first carried out for inert gas flow and then chemical reactions were implemented to see the effect on the temperature distribution. The simulations were also compared with experimental data. The results are summarized as: Generalized macroscopic model has been developed for the modeling of the packed bed reactor, the ideal temperature distribution with the maximum solid temperature located inside the absorber is realizable, this temperature distribution is dependent on the working conditions and the porous media properties.

REFERENCES

[1] C. White, R. Steeper, and A. Lutz, "The hydrogen-fueled internal combustion engine: a technical review," International journal of hydrogen energy, vol. 31, pp. 1292-1305, 2006.

[2] J. M. G. Antunes, "The use of hydrogen as a fuel for compression ignition engines," 2011.

[3] J. G. Antunes, R. Mikalsen, and A. Roskilly, "An investigation of hydrogen-fuelled HCCI engine performance and operation," International journal of hydrogen energy, vol. 33, pp. 5823-5828, 2008.

[4] R. Chaubey, S. Sahu, O. O. James, and S. Maity, "A review on development of industrial processes and emerging techniques for production of hydrogen from renewable and sustainable sources," Renewable and Sustainable Energy Reviews, vol. 23, pp. 443-462, 2013.

[5] K. Blok, R. Williams, R. Katofsky, and C. A. Hendriks, "Hydrogen production from natural gas, sequestration of recovered CO2 in depleted gas wells and enhanced natural gas recovery," Energy, vol. 22, pp. 161-168, 1997.

[6] C. Agrafiotis, M. Roeb, A. G. Konstandopoulos, L. Nalbandian, V. Zaspalis, C. Sattler, P. Stobbe, and A. Steele, "Solar water splitting for hydrogen production with monolithic reactors," Solar Energy, vol. 79, pp. 409-421, 2005.

[7] L. Xiao, S.-Y. Wu, and Y.-R. Li, "Advances in solar hydrogen production via two-step water-splitting thermochemical cycles based on metal redox reactions," Renewable Energy, vol. 41, pp. 1-12, 2012.

[8] O. BIČÁKOVÁ and P. Straka, "The resources and methods of hydrogen production," Acta Geodyn. Geomater, vol. 7, p. 175, 2010.

[9] D. Yadav and R. Banerjee, "A review of solar thermochemical processes," Renewable and Sustainable Energy Reviews, vol. 54, pp. 497-532, 2016.

[10] A. G. Konstandopoulos and S. Lorentzou, "Novel Monolithic Reactors for Solar Thermochemical Water Splitting," On Solar Hydrogen & Nanotechnology, pp. 621-639, 2009.

[11] H. Kaneko, Y. Ishikawa, C.-i. Lee, G. Hart, W. Stein, and Y. Tamaura, "Simulation study of Tokyo Tech rotary-type solar reactor on solar field test at CSIRO in Australia," in Proceedings of the ASME 2011 5th International Conference on Energy Sustainability (ES2011), ESFuelCell2011-54568, Washington, DC, 2011.

[12] ADMIN. (2014, 22 august). High-Efficiency Solar Thermochemical Reactor for Hydrogen Production. Available: http://energy.sandia.gov/high-efficiency-solar-thermochemical-reactor-for-hydrogen-production/

[13] R. Perret, "Solar Thermochemical hydrogen production research (STCH)," Sandia National Lab.(SNL-CA), Livermore, CA (United States)2011.

[14] H. D. Lopez-Hernandez, "Experimental analysis and macroscopic and pore-level flow simulations to compare non-Darcy flow models in porous media," 2007.

[15] D. Getachew, W. Minkowycz, and J. Lage, "A modified form of the κ–ε model for turbulent flows of an incompressible fluid in porous media," International Journal of Heat and Mass Transfer, vol. 43, pp. 2909-2915, 2000.

[16] M. H. Pedras and M. J. de Lemos, "Computation of Turbulent Flow in Porous Media Using a Low-Reynolds K-ε Modeland AN Infinite Array of Transversally Displaced Elliptic Rods," Numerical Heat Transfer: Part A: Applications, vol. 43, pp. 585-602, 2003.

[17] F. E, MACROSCOPIC MODELING OF TURBULENCE IN POROUS MEDIA

[18] C. Xu, Z. Song, and Y. Zhen, "Numerical investigation on porous media heat transfer in a solar tower receiver," Renewable Energy, vol. 36, pp. 1138-1144, 2011.

[19] B. Alazmi and K. Vafai, "Analysis of variants within the porous media transport models," Journal of Heat Transfer, vol. 122, pp. 303-326, 2000.

[20] K. Vafai and A. Amiri, "Non-Darcian effects in confined forced convective flows," Transport phenomena in porous media, vol. 1, pp. 313-329, 1998.

[21] K. K, Modeling of composite heat transfer in open-cellular porous materials at hight temperatures

[22] Z. Wu, C. Caliot, G. Flamant, and Z. Wang, "Coupled radiation and flow modeling in ceramic foam volumetric solar air receivers," Solar Energy, vol. 85, pp. 2374-2385, 2011.

*Corresponding author email: ddarfilal@cds.asal.dz

Effect of Bluff-Body Shape on Stability of Syngas Combustion Case of Methane-Hydrogen-Air Flame

M. Alliche*[1], F. Z. Khaladi[2], S. Chikh[2]

[1]Laboratoire LMP2M, Université de Médéa, Quartier Ain Dheb, Medea, 26000, Medea, Algeria.
[2]Laboratoire LTPMP, Université de Technologie Houari Boumediene, Alger, Algeria.

Abstract—**The aim of this study is to perform a numerical simulation of a non-premixed turbulent of syngas combustion. A methane-air flame enriched by hydrogen is considered. The selected axisymmetric configuration is composed by a central injector of methane-hydrogen mixture surrounded by a bluff-body, which is surrounded by a co-axial air jet. The Ansys CFX software is used to solve the equations governing turbulent reactive flow (Navier Stokes averaged). The Turbulence is modeled using the k-ε model. The EDM (Eddy Dissipation model), then the FRC model (Finite Rate Combustion) combined with EDM are used to modeling the combustion phenomena. We analyze the influence of flow strain, heat losses and shape of bluff-body on the flame. The results show some concordance with the temperature profile given by experience to a hydrogen rate of 50%. The flame structure near the bluff body and further downstream shows dependence on the thermal properties and shape of the bluff body.**

Key words—*Non-premixed combustion, Hydrogen enrichment, EDM and FRC models, Syngas, bluff-body.*

I. INTRODUCTION

Turbulent combustion in engineering applications continues to pose a very important challenge to modellers due to the multitude and complexity of processes which interact within such systems. Turbulence, chemical kinetics, thermal radiation and pollutants formation coupled with complex geometry and boundary conditions are typical of such complications. Standard approaches, based on Reynolds or Favre averaging, using first- or second-order closure models have been used extensively to compute flows in many such applications, including reactive systems [1]. These methods have manageable computational requirements, and can handle thermal radiation and complex geometry. One main disadvantage is that high temperature chemistry is very difficult to account for, as the representative source terms are highly nonlinear and hence impossible to close. Various approaches have been developed to account for turbulent combustion and the associated heat release and density fluctuations. Recent gas turbine combustors use a combination of the two for a more efficient combustion process. They incorporate flame holders in the form of bluff bodies or swirlers for a primary or secondary combustion in high speed reacting flows. These two methods are very prominent among combustion systems over a long time. Researchers have been studying the effects of fluid flow inside a combustion chamber which is characterized by high turbulence caused by the wake formation. The bluff-body burner geometry is a suitable compromise as a model problem, where both methods can be tested and validated [2, 3].

In bluff body combustion, a no-streamlined body is placed in high-speed conditions, which produce a recirculating zone. This wake region allows the combustion products to settle in this region and ignit continuously the incoming flow of fuel and air from which the flame propagates into the free stream. Although a premixed combustion regime is becoming increasingly popular for industrial gas turbines because of their potential for very low NOx emissions, combustion in conventional aircraft gas turbines occurs predominantly in the non-premixed diffusion flame regime. In such devices, turbulent mixing exerts a dominant influence and better understanding necessarily requires an accurate prediction of the turbulent velocity field. Mare et al [4] observed that accurate description of the inlet section of the combustor plays a significant role in the prediction of temperature distribution over the flow region in a can-type model gas turbine combustor using numerical simulation technique. Decreasing the equivalence ratio changes the flame shape [5] due to reduced flame speed such that the flame fronts overlap the convecting Kelvin–Helmholtz vortices along the shear layer. Ziani et al [6] compared three turbulence models for no-premixed combustion. These authors compare the numerical results of the literature and experimental data. The evaluation resulted in the conclusion that the modified k-ε model is the most appropriate for simulating the non-premixed turbulence combustion.

The bluff body stabilized flames have found wide range of applications because of their relatively low-pressure drop and simple geometry [7]. The combustion with a bluff body stabilized fame of gases fuel for both the premixed and non-premixed flame conditions have also been numerically and experimentally investigated by many researchers. Giacomazzi et al [8] studied the combustion in a bluff-body flame anchored in a straight channel. Their study presents results for both cold and reactive flows using eddy dissipation concept for a turbulence intensity of 3 to 4 % and an equivalence ratio equal to 0.65. The impact of increased reactant temperature on the dynamics of bluff-body stabilized premixed flows was investigated by Erickson et al [9]. Schefer et al [10] measured the velocity in a turbulent bluff-body stabilized methane flame. The flow

*Corresponding author email: alliche.mounir@univ-medea.dz

configuration consisted of a 5.4mm diameter fuel jet separated from an outer, annular-air flow by a 50mm diameter bluff-body.

While a bluff-body has a desirable effect of flame stabilization by creating a recirculation zone, it may also pose adverse effects on flame stability by the unsteady vortex shedding into the flow field [11–14], causing fluctuations in the region of flame stabilization. Therefore, it is of fundamental and practical interest to understand the detailed physical mechanism of bluff-body flame stabilization within a narrow channel premixed combustor.

The main objective of the present work is to identify a correct model for a given geometry and then analyse the effects of the various parameters on the overall efficiency of the system. We study the interaction between the flame structure, the flow field and the coupled heat transfer with the flame holder of a (CH4-H2)/Air flame stabilized on a heat conducting bluff body in a channel. The impact of the bluff body shape on the flame properties is particularly investigated.

II. NUMERICAL METHOD

1. Geometry and flow configuration

The geometry of the combustion chamber is shown in Fig 1. The configuration used here is the bluff-body stabilized CH4 flame investigated experimentally at the Sandia National Laboratories and the University of Sydney documented in [1, 15]. It has an outer diameter of 50 mm with a concentric fuel jet of diameter of 3.6 mm.

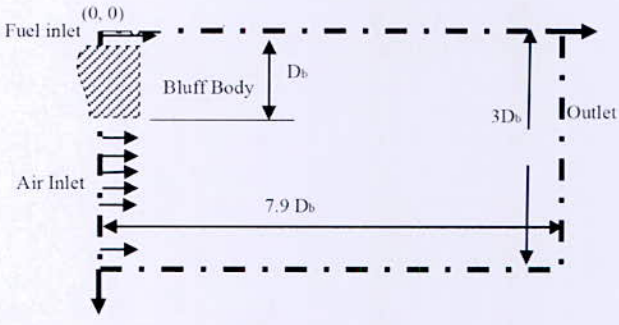

Fig. 1. Schematic of the combustion chamber (D_b=50mm and $Ø_{fuel\ inj}$=3.6 mm)

2. Computational modelling

The modelling of the geometry was done using Ansys ICEM CFD. Since the geometry is cylindrical without any swirler or tangential velocity inlet, the model can be assumed to be an axi-symmetric problem. The computational domain of the axi-symmetric model of the combustor with boundary conditions is shown in Figure 1. A fine mesh is imposed around the hollow cylindrical bluff body for precise measurements of the flow conditions. Zero velocity impermeability boundary conditions are specified at the bluff body walls. The boundary conditions are also presented in Fig 1. The top edge has been taken as wall, the left edge as velocity inlet, the right edge as pressure outlet and the bottom edge as axis. The velocity inlet 1 is for the fuel inlet and the velocity inlet 2 is for the air inlet. A total of 20236 nodes and 104876 elements were used for meshing the geometry. Map-type rectangular meshes with an interval size of 0.2 mm were used.

3. Numerical model validation

The wall material was steel and the surface reaction effects were eliminated. In computational domain, the atmosphere inside the combustor is considered as a fluid and the bluff body shapes are subtracted from the mentioned domain. It means in the solution process the bluff body is assumed as a shape which fluid cannot flow through it. Based on this assumption, the material of bluff body and heat conduction model in this section is not considered and the main discussion is about the whole of micro-combustor. Besides, comparatively to the results of ref [10, 15] which thermal conjugate was applied for bluff body, our results are acceptable. Ansys Ansys CFX12 was use to solve the momentum equations, energy, species, mass and heat transfer in different states. The first-order upwind scheme was applied for discretization and for the pressure-velocity coupling, the SIMPLE Algorithm was used. The K-Epsilon model has been used in this work.

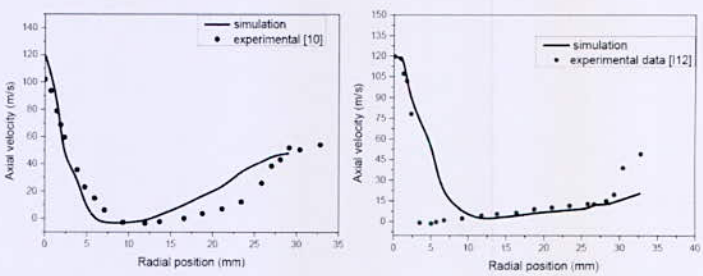

Fig. 2. Comparison between numerical and experimental results at 30mm (left) and 3 mm (right) from Bluff Body

Indeed, gradient is set least squares cell based, pressure is standard, momentum and energy are second order upwind and turbulent kinetic energy and turbulent dissipation rate are set first order upwind. The structured square grid system with around 100,000 cells for all cases was set in the final simulation. Three step refinements were applied to increase the quality of the meshes. In all cases the initial guess for fuel-air mixture was set at 1600K to ignite the mixture in numerical iteration. The simulations were done by a core i5 computer with 4 GB of RAM. The effect of swirl on turbulence is included in the RNG model, enhancing accuracy for swirling flows. The corresponding plots obtained using this model has been shown in Fig 2.

*Corresponding author email: alliche.mounir@univ-medea.dz

III. RESULTS AND DISCUSSIONS

The numerical simulations have been done using ANSYS CFX 12.0 for all the cases involved in this study. The results comprises of 4 sections. In the first section, the model has been analysed for various values of the velocity ratio (from 0.5 to 2.6). In the subsequent sections, the analysis was done for various values of the velocity (from 60 to 110 m) and equivalence ratio equal to 0.5. In the final section, a comparative study had been done for two shapes of a bluff body with the same frontal area.

1. Variation in the velocity ratio

This section presents the exhaust temperature and CO_2 results for the combustion process of methane and air at an equivalence ratio of 0.5. The case details with different velocity values for the fuel and air has been shown in Table 1 below. The average exhaust gas temperature and the mass fraction results for the cases have been summarized in the graph shown in Fig 3.

TABLE I
CASE DETAILS WITH VARYING INLET VELOCITY RATIOS

Case	Inlet Air velocity (m/s)	Inlet Fuel velocity (m/s)
1	40	120
2	50	100
3	90	60
4	100	50

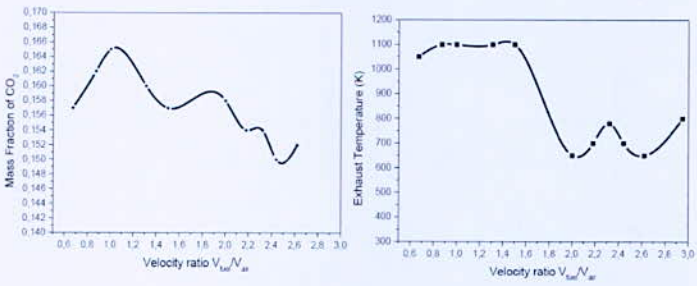

Fig. 3. Evolution of CO_2 mass fraction and exhaust temperature in function of velocity ratios at an equivalence ratio of 0.5

The above result shows that the exhaust gas temperature decreases first and then increases with the decrease of velocity ratio. The lowest temperature is reached at a velocity ratio of 2 and the value was found out to be 678K. Below this point, a uniform temperature of about 1000K is obtained. Thus the optimal combustible velocity ratio is found out to be within 0.6 and 1.8.

The mass fraction of CO_2 is also seen to be comparatively higher at lower velocity ratios; the maximum being 0.165 at a velocity ratio of 1. This clearly shows that the difference in velocity between the fuel and the air inlets should be low for higher exhaust temperatures and for a better efficient combustion process.

2. Variation in the velocity magnitude

This section presents the average exhaust gas temperature results at an equivalence ratio of 0.5 and with varying values of the velocity magnitude at a velocity ratio of 1. The velocity values were varied over a range from 60m/s to 110m/s. Fig 4 summarizes the cases and results. The results show that the average exhaust temperature increases first and then decreases as the velocity increases. The temperature was higher over the range of 70m/s to 95m/s and reaches a maximum of 1153K at 80m/s.

3. Variation in the equivalence ratio

This section presents the average exhaust gas temperature results for different velocities and equivalence ratios at a velocity ratio of 1. The velocity values were similar to the previous analysis with equivalence ratio of 0.4, 0.5 and 0.6 simulated for all the cases. The graph shown in Fig 4 depicts the results. The above graph shows the exhaust gas temperature values for equivalence ratio of 0.5. The result shows that comparatively high combustion efficiency can be maintained over the whole equivalence ratio range at a moderate velocity magnitude. The maximum temperature reached for an ER of 0.5 is 1153K at 80m/s.

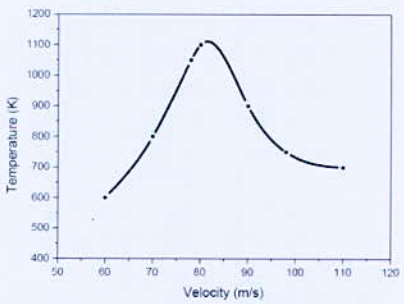

Fig. 4. Values of temperature results obtained with different velocities at an equivalence ratio ϕ= 0.5

4. Variation in the bluff body shape

This section presents the average exhaust gas temperature and pressure drop results for the two bluff body shapes namely (a) circular plate and (b) cylindrical solid and the results are shown in Fig 5. The results show that combustion with cylindrical solid bluff body produces temperatures that are almost double to that produced by the circular plate. This is seen by the enormous pressure drop across the solid bluff body which is of the order of 25 kPa compared to the 10 kPa drop seen around the circular plate. Fig 6 shows the streamlines and temperature contour for two bluff body shapes: cylindrical and triangular.

*Corresponding author email: alliche.mounir@univ-medea.dz

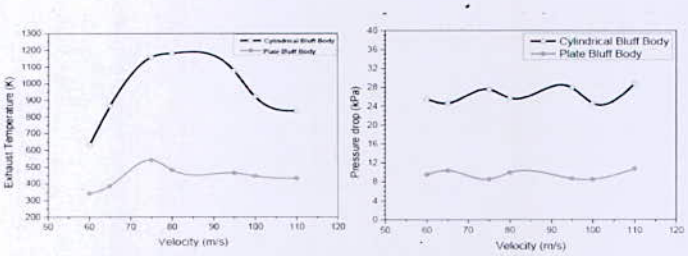

Fig. 5. Evolution of Exhaust Temperature (right) and pressure drop (left) with varying inlet velocity values for circular plate and solid cylinder as bluff body

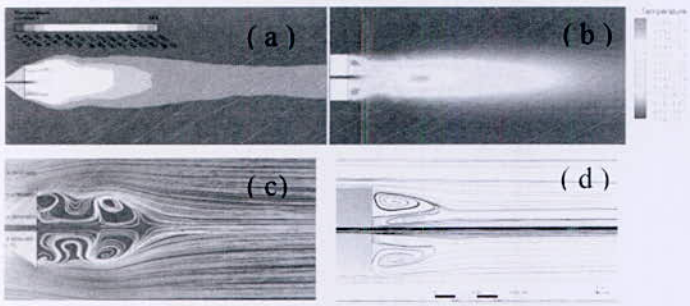

Fig. 6. Effect of the shape of the bluff body on the temperature contour and streamlines (Triangular BB (a and c), Cylindrical BB (b and d))

IV. CONCLUSION

Combustion characteristics of lean methane-hydrogen–air mixture in a combustor with bluff body stabilized no-premixed flow regime were investigated. The simulations were validated with the experimental results from literature. We examine the Effects of the inlet velocity ratio, velocity value; equivalence ratio and the bluff body shape on the combustion efficiency and exhaust gas temperature. The following conclusions have been drawn from this study.

1) This study reveals that, combustion with cylindrical solid bluff body produces temperatures that are almost double to that produced by the circular plate but with significantly higher-pressure drop, which is the key driver for drag force.

2) Then, it was seen that the inlet velocity ratio and the velocity magnitude also exerts a significant effect on the combustion characteristics. Decreasing the velocity ratio initially shows moderate variation in the temperature.

3) After a particular stage, there seems to be higher temperature values when the ratio is near unity i.e. when the air and fuel are at nearly the same velocity magnitude. Furthermore, with the increase of inlet velocity, the high temperature zone is pushed toward the downstream of the combustor chamber. However, the exhaust gas temperature reaches a peak value at a moderate inlet velocity under a fixed equivalence ratio.

4) These variation tendencies indicate that the combustion characteristics are in fact determined by many factors like disorderliness, heat losses, recirculation zones, momentary pressure drops, turbulence and their complicated interactions.

REFERENCES

[1] B. B. Dally, D. F. Fletcher & A. R., "Masri Flow and mixing fields of turbulent bluff-body jets and flames", Combustion Theory and Modelling, 2:2, 193-219, 1998.

[2] M. Senda, N. Sawada and M. Tsuchiya, "A numerical prediction of turbulent non premixed flame stabilised by a bluff body with laminar flamelet model", *9th Symp. on Turbulent Shear Flows (Kyoto)* , 1993, p 103.

[3] A. R. Masri, B. B. Dally, R. S. Barlow and C. D. Carter, "The structure of the recirculation zone of a bluff-body combustor", *25th Int. Symp. on Combustion* (Pittsburgh, PA: Combustion Institute) , 1994, pp 1301-8.

[4] F. Mare, W. P. Jones and K. R. Menzies, "Large eddy simulation of a model gas turbine combustor", Combustion and Flame 137, 278–294, 2004.

[5] S. G. Tuttle, S. Chaudhuri, K. M. Kopp-Vaughan, T. R. Jensen, B. M. Cetegen, M. W. Renfro, J. M. Cohen, "Lean blow off behaviour of asymmetrically bluff body stabilized flames", Combustion and Flame, Volume 160, Issue 9, Pages 1677-1692, 2013.

[6] L. Ziani, A. Chaker, K. Chetehouna, A. Malek, B. Mahmah, "Numerical Simulations of non-premixed turbulent combustion of CH_4–H_2 mixtures using the PDF approach", International Journal of Hydrogen Energy 38(20):8597–8603, July 2013

[7] G. Boudier, L. Y. M. Gicquel, T. Poinsot, D. Bissieres, C. Bérat, "Comparison of LES, RANS and experiments in an aeronautical gas turbine combustion chamber", Proceedings of the Combustion Institute, 31, 3075–3082, 2007.

[8] E. Giacomazzi, V. Battaglia, C. Bruno, "The coupling of turbulence and chemistry in a premixed flame", Combustion and Flame, 138, 320–335, 2004.

[9] R. R. Erickson, M. C. Soteriou, "The influence of reactant temperature on the dynamics of bluff body stabilized premixed flames", Combustion and Flame, 158, 2441–2457, 2011.

[10] R. W. Schefer, M. Namazian and J. Kelly, "Velocity Measurements in a Turbulent non-premixed Bluff-Body Stabilized Flame", Combustion Science and Technology, Volume 56, Issue 4-6, pp. 101-138, 1987.

[11] A. Fan, J. Wan, Y. Liu, B. Pi, H. Yao, K. Maruta, W. Liu, Int. J. Hydrogen Energy 38, 11438–11445, 2013.

[12] J. Wana, A. Fan, K. Maruta, H. Yao, W. Liu, "Experimental and numerical investigation on combustion characteristics of premixed hydrogen/air flame in a micro-combustor with a bluff body", international journal of hydrogen energy 37, 19190-19197, 2012.

[13] H. Suzuki, Y. Inoue, T. Nishimura, K. Fukutani, K. Suzuki, Int. J. Heat Fluid Flow 14, 2–9, 1993.

[14] J. Hertzberg, I. Shepherd, L. Talbot, "Vortex shedding behind rod stabilized flames", Combustion and Flame 86, 1–11, 1991.

[15] B. B. Dally, A. R. Masri, R. S. Barlow, G. J. Fiechtner, "Instantaneous and mean compositional structure of bluff-body stabilized non-premixed flames", Combustion and Flame,114:119-48, 1998.

*Corresponding author email: alliche.mounir@univ-medea.dz

Hybrid Sulfur Cycle for Hydrogen Production Using SDE and Off-Grid Solar System: Algerian Potential

I. Nouicer*, A. Khellaf, S. Menia, M.R. Yaiche, N. Kabouche, F. Meziane, R. Medjebour

Centre de Développement des Energies Renouvelables, (CDER), B.P. 62, Route de l'Observatoire, 16340, Bouzaréah, Algiers, Algeria.

Abstract—**An efficient production of clean hydrogen on a large scale using renewable sources such as solar, wind or biomass is a promising future. Using nuclear energy, the hybrid sulfur cycle (HyS) is one of the most promising thermo-chemical processes for hydrogen production. Only two sub-reactions have been used in simplest thermo-chemical processes, the first process is an electrochemical reaction such as SO_2 depolarized electrolysis (SDE) and the second process is a thermo-chemical reaction. Overall, SDE process (first reaction) converts sulfur dioxide (SO_2) and water (H_2O) to produces hydrogen (H_2) at the cathode and sulfuric acid (H_2SO_4) at the anode. In this study, two parts of a detailed modeling approach have been used to estimate hydrogen production in a desired location. In the first part, a method of modeling and simulation of photovoltaic (PV) module using a mathematical model to estimate the maximum power delivered as a function of ambient temperature and solar irradiation. A validation model with experimental data of commercial PV module has been determined. Simulation and modeling method with extraction of proposed circuit parameters model are practice, simple and fast way for power electronics designers to modeling PV systems. The second part, estimation equation for hydrogen production of SO_2 depolarized electrolysis as a function of current consumed was presented. The coupling of these two parts allows estimating hydrogen production rate as a function of power consumption of PV systems in a desired location (for different location in Algeria).**

Key words—Solution Processes (SP), Energy Efficiency (EE), Solar Hydrogen Production (SHP), Photovoltaic System (PS), SO_2 Depolarized Electrolysis (SDE).

I. INTRODUCTION

A great interest in both research and commercial community for hydrogen production as an energy carrier in the energy sector. However, many current methods of hydrogen production can bring pollutants production (greenhouse gas like: CO_2, N_2O …), so it is indispensable to search an alternative methods. Actually, thermo-chemical cycles (Hybrid Sulphur (HyS) cycle) is one of the most alternative methods that can produce hydrogen using renewable sources [1-5].

This paper will focus on the influence solar irradiation on hydrogen production with coupling of two parts: photovoltaic (PV) module and SO_2 depolarized electrolysis (SDE) allows us to estimate hydrogen production rate as a function of power consumption of PV systems in a desired location (Bouzareah's station). A validation with experimental data for these two systems will be determined.

II. PART OF SYSTEM BASED ON RENEWABLE ENERGY

The configuration of our **model system** is depicted in **figure 1**. The aim of this system is to determine the hydrogen quantity dispatch by SO_2 depolarized electrolysis. Photovoltaic panel produce an optimal power energy using the renewable energy sources.

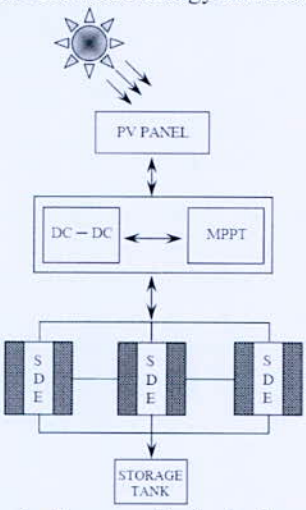

Fig. 1. Schematic diagram of solar hydrogen production system

1. SDE model development

The operating principle of SDE is show in figure 2. Sulfur dioxide (SO_2) gas is injected into the electrolyser through the anode reacting with water (H_2O) which is introduced through the cathode via reaction 2, the result of this reaction gives: Sulfuric acid (H_2SO_4) and protons (H^+) that migrate to the cathode. At each current density value, the production rate of H_2SO_4 is constant and determined by the Faraday law. At each point of the electrode where the current passes, the production quantity and the concentration of H_2SO_4 is the same at given current, as well as the water flow [6-8]. Thus, the water flow through the membrane is given by the following expression:

$$N_w = \frac{\rho_M}{M_M \delta_M}\int_{\lambda_a}^{\lambda_c} D_{w,F}\,d\lambda - \frac{\xi\lambda_a i_{H_2SO_2}}{\lambda_c F} + \frac{P_M \Delta P}{\delta_M} \quad (1)$$

ρ_M : Membrane density [2.0 g /cm^3].

M_M : Molecular weight of membrane [1100 g/mol].

*Corresponding author email: ilyes.nouicer@gmail.com

δ_M : Thickness of membrane.
$D_{w,F}$: Fickian diffusion coefficient of water[cm^2/s].
λ : Water content.
λ_c : Water content at the cathode, constant which was measured to be 22 at 30°C and 18 at 80°C.
λ_a : Water content at the anode.
$i_{H_2SO_4}$: Current density [A/cm^2].
ξ : Electro-osmotic drag coefficient H_2O/H^+.
P_M : Membrane permeability [mol/cm s/kPa].
$\Delta P = (P_c - P_a)$: Membrane pressure differential [600 kPa].
P_c : Pressure at cathode [kPa].
P_a : Pressure at anode [kPa].
F : Faraday's constant [96485.3329 C/mol].

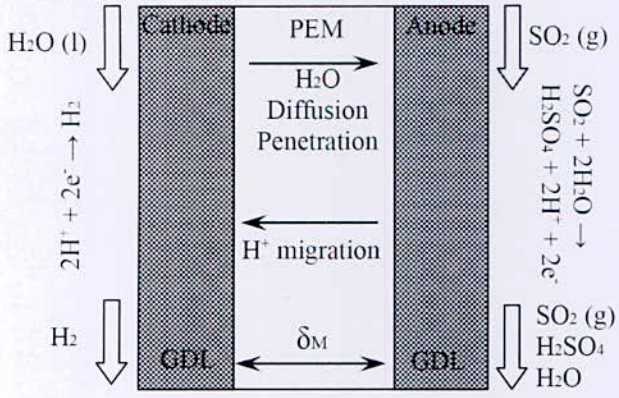

Fig. 2. Schematic of SDE model system

$SO_2 + 2H_2O \rightarrow H_2SO_4 + 2H^+ + 2\,e^-$ $\quad V^0_{SO_2} = 0.17$ V vs SHE (Standard Hydrogen Electrode) (2)

The expression for Fickian diffusion coefficient of water $D_{w,F}$ given by Fuller [5] can be represented as a function of temperature and water content λ and given below by :

$$D_{w,F} = 2.1\ 10^{-3}\ \lambda \exp\left(\frac{-2436}{T}\right) \quad (3)$$

T: Cell temperature [°K].

The water content at the anode λ_a is determined by the water activity in the following equation:

$$\lambda_a = 0.043 + 17.81\ a_w - 39.85\ a_w^2 + 36\ a_w^3 \quad (4)$$

Where a_w is the water activity given by the following water and H_2SO_4 balance:

$$a_w = \frac{N_w - \frac{i_{H_2SO_2}}{F}}{N_w} \quad (5)$$

Several parameters can manage the operation and SDE process, the voltage across the two electrodes (equation (3)) is a function of four essential parameters: reversible cell voltage (V_r), anode overvoltage (V_a), cathode overvoltage (V_c) and the ohmic loss (iR_o).

$$V = V_r + V_a + V_c + iR_o \quad (6)$$

The first term V_r in equation (6) is a function of temperature and sulfuric acid concentration in anolyte, when the sulfuric acid concentration increases the reversible cell voltage increases. The second term V_a is a function of the sulfide dioxide concentration, the current density as well as the catalyst surface area. At the moment, when the current density increases the anode overvoltage also increases and SO_2 concentration decreases. But, SO_2 concentration depends on the sulfuric acid concentration, pressure and temperature in MEA, which is limited by saturation of their concentration. The third term V_c is a function of the current density and catalyst surface area. Overall, the last term ohmic loss (iR_o) is caused by the resistance created between electrolyte and membrane electrode assembly (MEA). This resistance is a function of current density. The study of all these parameters allows us to reduce the cell voltage and to improve the performance of the SDE process [6]. A validation model (**figure 3**) of obtained results with experimental data has been showed. A programming language was used to simulate the model developed to show the results and compared with the original features.

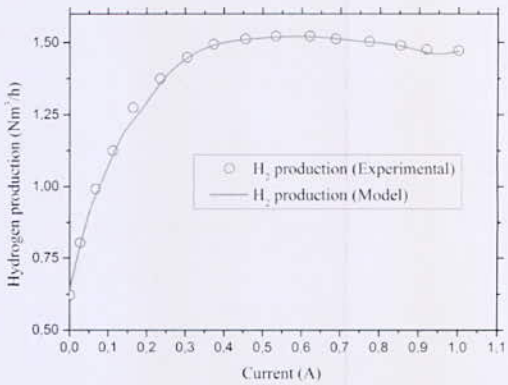

Fig. 3. Polarization characteristics of SDE compared between model values and experimental data

2. *Modeling of photovoltaic modules*

Energy required for creation of an electron-hole pairs in p–n junction from an external disturbance (incident light) can be provided by ionizing radiation. A potential energy voltage created between p-n junction and charge carriers start to flow through an external load [9].

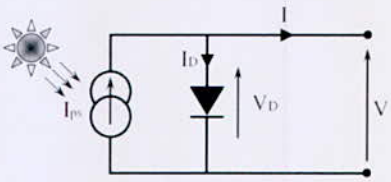

Fig. 4. The ideal model of photovoltaic cell

The four important components for photovoltaic cells are: resistors, current source and diodes. **Figure 3** represent the equivalent circuit of an ideal photovoltaic cell. Applying the Gustav Robert Kirchhoff's voltage and courant law, we get the basic mathematical formula of I(V) characteristic for an ideal photovoltaic cell :

$$I = I_{pv} - I_D = I - I_0\left(\exp\left(\frac{qV}{akT}\right) - 1\right) \quad (7)$$

1. I_{pv} [A]: Photo-generated current by the incident light (directly proportional to sun irradiation).

*Corresponding author email: ilyes.nouicer@gmail.com

2. I_D [A] : Shockley diode equation,
3. I_0 [A] : Dark current.
4. q : Electron charge, 1.60217646 10^{-19} C.
5. k [J/K] : Boltzmann constant, 1.3806503 .10^{-23}.
6. T [K] : Temperature of p-n junction.
7. a : Diode ideality constant.

3. *The single diode R_p model*

The ideal single diode model does not represent the I-V characteristic of a practical photovoltaic module. Other additional parameters are needed to complete the theoretical concept of cell modeling [9].

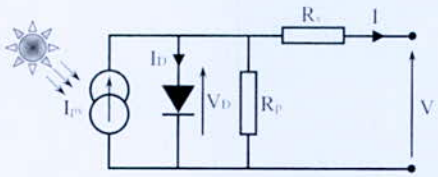

Fig. 5. The photovoltaic circuits of single diode model (R_p model)

In reality, losses caused by different impedance due to : resistance caused by the contact Schottky barrier (contact between semiconductor and electrodes surfaces), resistance caused by semiconductor material and finally resistance caused by cathodes and anodes material. These losses can add to the basic equation supplementary parameters. **Figure 4** represent the equivalent circuit of photovoltaic circuits of single diode model. Applying Gustav Robert Kirchhoff's law, the output current is re-written as follows [9] :

$$I = I - I_0\left(\exp\left(\frac{qN_S(V+IR_S)}{akT}\right) - 1\right) - \frac{V+IR_S}{R_p} \quad (8)$$

- R_s [ohm]: Series resistor.
- R_p [ohm]: Parallel resistor.
- N_s : Cells connected in series.

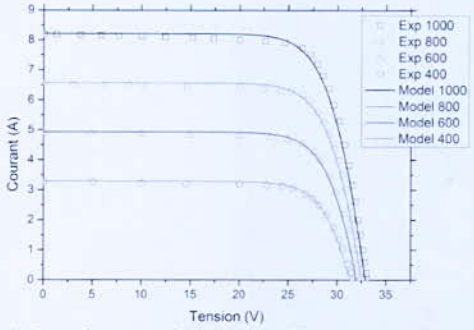

Fig. 6. I-V characteristics for a PV module compared between experimental data and model values at different radiation

A validation model (**figure 6**) of results obtained with experimental data of commercial KC200GT photovoltaic module at different radiation has been determined [10]. A programming language was used to simulate the model developed to show the results and compared with original features.

III. RESULTS AND DISCUSSION

Figure 7 shows the minutely solar radiation over the year 2014 for Bouzareah's station. The power performance of a semi-conductor PV module is a function of various physical variables of the PV module material (diode ideality, band gap...) and geographical position (temperature of PV module and the solar radiance on the PV module surface).

For this location, **table 1** resumes the monthly maximal power point and temperature value.

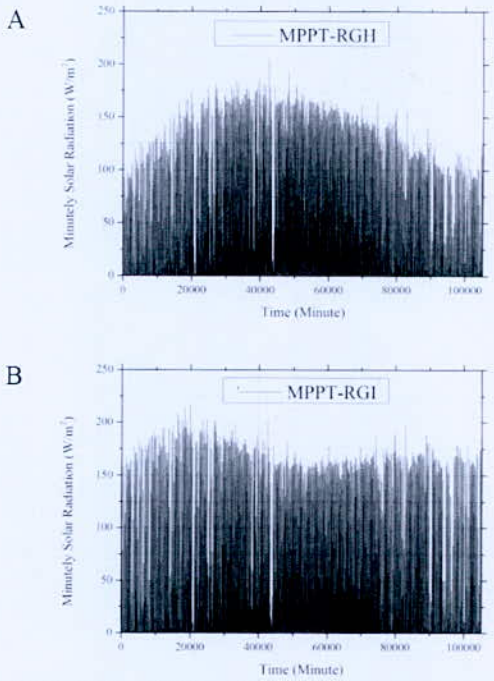

Fig. 7. Typical variation of minutely global solar radiation (A - horizontal and B - inclined) in Bouzareah's station

TABLE I
MONTHLY AVERAGE OF MAXIMAL POWER POINT AND TEMPERATURE VALUE

Month	Pmax-RGH (W)	Pmax-RGI (W)	T (°C)
January	18,37	29,24	12,69
February	27,49	38,32	12,83
March	32,28	38,58	12,01
April	48,42	50,88	17,10
May	50,31	47,24	16,70
June	52,20	46,19	21,11
July	53,54	49,10	23,54
August	47,16	47,72	24,80
September	37,68	43,15	24,20
October	29,65	41,21	21,20
November	19,37	29,36	17,04
December	16,00	26,83	11,51

1. *Evaluation of hydrogen production in Bouzareah's station*

In this part, we present the evaluation of hydrogen production over Bouzareah's station using SDE

*Corresponding author email: ilyes.nouicer@gmail.com

electrolysis (9 cells in series) and renewable solar energy. **Figure 8** shows the minutely hydrogen production over the year 2014 for Bouzareah's station. However, hydrogen production volume varies according to the season and the geographical position. For this location, table 2 resumes the monthly hydrogen production over this year. The best hydrogen production flow rate is in months: from May to August.

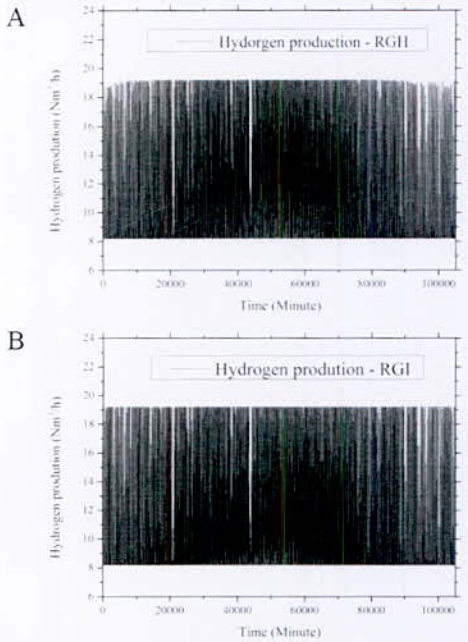

Fig. 8. Typical variation of minutely hydrogen production (A - horizontal and B - inclined) in Bouzareah's station

TABLE II
MONTHLY AVERAGE OF HYDROGEN PRODUCTION

Month	H_2-RGH (Nm^3/h)	H_2-RGI (Nm^3/h)
January	10,75	11,13
February	11,44	44,66
March	11,69	11,72
April	12,72	12,58
May	12,87	12,59
June	13,08	12,69
July	13,25	12,92
August	12,87	12,71
September	12,28	12,31
October	11,71	11,98
November	10,82	11,11
December	10,46	10,84

IV. CONCLUSION

Two parts of a detailed modeling approach have been used to estimate hydrogen production in Bouzareah's station. In the first part, a method of modeling and simulation of photovoltaic (PV) module using a mathematical model to estimate the maximum power delivered as a function of ambient temperature and solar radiation. A validation model with experimental data of commercial PV module has been determined. We found that the maximal power point is from April to August. The second part, estimation equation for hydrogen production of SO_2 depolarized electrolysis as a function of current consumed was presented. The coupling of these two parts allows us to estimate hydrogen production rate as a function of power consumption of PV systems. We found that the hydrogen production is important compared to other systems of hydrogen production.

REFERENCE

[1] Xue, L., Zhang, P., Chen, S., Wang, L., & Wang, J. (2013). Sensitivity study of process parameters in membrane electrode assembly preparation and SO_2 depolarized electrolysis. International Journal of Hydrogen Energy, 38(25), 11017-11022.

[2] Krüger, A. J., Krieg, H. M., Van der Merwe, J., & Bessarabov, D. (2014). Evaluation of MEA manufacturing parameters using EIS for SO_2 electrolysis. international journal of hydrogen energy, 39(32), 18173-18181.

[3] Krüger, A. J., Krieg, H. M., Grigoriev, S. A., & Bessarabov, D. (2015). Various operating methods and parameters for SO_2 electrolysis. Energy Science & Engineering, 3(5), 468-480.

[4] Liberatore, R., Ferrara, M., Lanchi, M., & Turchetti, L. (2017). Integration of photovoltaic and concentrated solar thermal technologies for H_2 production by the hybrid sulfur cycle. In AIP Conference Proceedings, Vol. 1850 (1), 100013-1–100013-7.

[5] Weidner, J. W., & Holland, C. E. (2015). U.S. Patent No. 9,057,136. Washington, DC: U.S. Patent and Trademark Office.

[6] Weidner, J. W., & Holland, C. E. (2017). U.S. Patent No. 9,574,276. Washington, DC: U.S. Patent and Trademark Office.

[7] Staser, J. A., Gorensek, M. B., & Weidner, J. W. (2010). Quantifying individual potential contributions of the hybrid sulfur electrolyzer. Journal of the electrochemical society, 157(6), B952-B958.

[8] Motupally, S., Becker, A. J., & Weidner, J. W. (2000). Diffusion of water in Nafion 115 membranes. Journal of The Electrochemical Society, 147(9), 3171-3177.

[9] Chin, V. J., Salam, Z., & Ishaque, K. (2015). Cell modelling and model parameters estimation techniques for photovoltaic simulator application: A review. Applied Energy, 154, 500-519.

[10] www.kyocera.com.sg/products/solar/pdf/kc200gt.pdf. Date of site consultation: 30/08/2017.

*Corresponding author email: ilyes.nouicer@gmail.com

Technologies Solaires à Concentration et Production d'Hydrogène

H. Farsi* et I. Hebili

Laboratoire de Mécanique Energétique et Systèmes de Conversion, Université des Sciences et de la Technologie Houari Boumediene (USTHB), BP 32, EL Alia, 16111 Bab Ezzouar, Alger, Algérie

Résumé—**Le présent article porte sur l'utilisation de l'énergie solaire thermique à concentration (CSP) pour la production d'un hydrogène propre. La sélection d'un site adéquat pour un tel système nécessite une valeur élevée de la composante normale directe du rayonnement solaire (DNI), mais aussi une très bonne estimation de cette valeur. Aussi, dans cet article, nous nous attelons à analyser les ressources solaires d'un site particulier (Hassi R'Mel) à travers cinq jeux de données de différentes natures : des mesures au sol ainsi que des valeurs provenant de bases de données satellitaires. Cette analyse comparative a montré que l'estimation du DNI reste une opération très délicate car les cinq jeux de données présentent des profils et des valeurs qui sont parfois assez différents. Cependant, l'examen au plus près de ces données a permis de cadrer au mieux la valeur du DNI du site faisant l'objet de l'étude.**

Mots clés— hydrogène, solaire thermique à concentration (CSP), évaluation des ressources solaires, DNI.

I. INTRODUCTION

Le présent travail s'inscrit dans la perspective de l'utilisation des technologies solaires thermiques à concentration (Concentrating Solar Power - CSP) pour la production d'un hydrogène propre à grande échelle. Nous présentons dans un premier temps et de manière très brève les procédés de fabrication de l'hydrogène ainsi que les technologies CSP. Nous nous focalisons par la suite sur la partie solaire. La mise en œuvre d'un système de production d'hydrogène à partir du CSP nécessite de l'installer sur un site qui présente des valeurs élevées de la composante directe du rayonnement solaire (Direct Normal Irradiation - DNI). Si le système est alimenté exclusivement par l'énergie solaire, ceci permettra de s'assurer de la disponibilité de cette ressource énergétique. Dans le cas, où le système est alimenté de manière hybride (CSP / énergie fossile, par exemple), ceci permettra de maximiser la part de l'énergie solaire dans la consommation globale d'énergie du système. Le choix d'un site présentant des valeurs élevées et bien estimées de DNI est donc une opération cruciale, à considérer en amont d'un projet de production d'hydrogène via le CSP. A cet effet, nous présentons dans cette étude une estimation des valeurs de DNI pour un cas d'étude qui est celui du site de Hassi R'Mel. Ce dernier abrite la centrale de production d'électricité hybride CSP / gaz, dénommée Solar Power Plant One (SPP1) qui présente une capacité installée de 150 MW électrique, dont 25 MW provenant d'un champ solaire CSP (technologie cylindro-parabolique). Il s'agit d'un site emblématique qui a vu l'installation en Algérie du premier système énergétique basé sur le CSP. Il était prévu d'installer au niveau de ce site un technopôle solaire favorisant le développement des technologies solaires à concentration pour différentes applications (production d'électricité, de chaleur et de carburants).

II. PROCEDES DE FABRICATION DE L'HYDROGENE ET TECHNOLOGIES CSP

L'hydrogène industriel est actuellement produit principalement par reformage du gaz naturel ou d'hydrocarbures liquides, ou bien par électrolyse de l'eau (voir **Fig.1**). Les procédés de production d'hydrogène faisant appel au CSP se partagent principalement en deux familles : les électrolyses et les cycles thermochimiques. Ces derniers sont d'ailleurs les procédés les plus utilisés. L'objectif de ces cycles est de réaliser la décomposition de l'eau à une température inférieure à celle de la décomposition directe. Des substances chimiques sont introduites, à travers une série de réactions de combinaisons avec l'eau et entre elles, puis de dissociations, pour arriver à la production d'hydrogène et d'oxygène, tout en restituant les substances chimiques initiales [1].

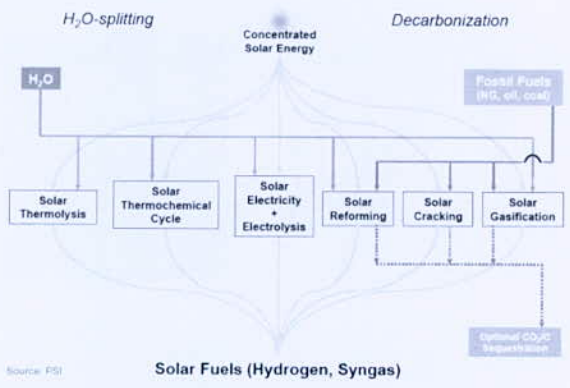

Fig.1. Procédés de production de carburants solaires [2]

*Corresponding author email: hichem.farsi@yahoo.fr

Concernant le CSP, les technologies existant à l'heure actuelle sont multiples (cylindro-parabolique, Fresnel, tour solaire, parabolique). Celle qui permet d'atteindre des températures très élevées, nécessaires pour les procédés de fabrication d'hydrogène, est la "tour solaire" [2]. Il s'agit d'un champ d'héliostats qui suivent la course du soleil pour concentrer le rayonnement solaire au niveau d'un récepteur situé au sommet d'une tour. Le système utilise un fluide caloporteur (air, eau, huile synthétique, sels fondus, ...) qui est chauffé par les rayons concentrés du soleil. La chaleur ainsi produite pourra être utilisée à différents usages : production de carburants, de chaleur ou d'électricité. Il est à souligner que cette technologie est actuellement utilisée pour la production d'électricité, et que des procédés (thermochimiques) de production d'hydrogène nécessitent une concentration plus élevée du rayonnement solaire. Ainsi, des dispositifs expérimentaux particuliers sont dédiés pour la production de l'hydrogène solaire : fours solaires, simulateurs solaires (voir **Fig.2**). A titre d'exemple, nous pouvons citer le grand four solaire d'Odeillo dans les Pyrénées orientales en France (1 MW).

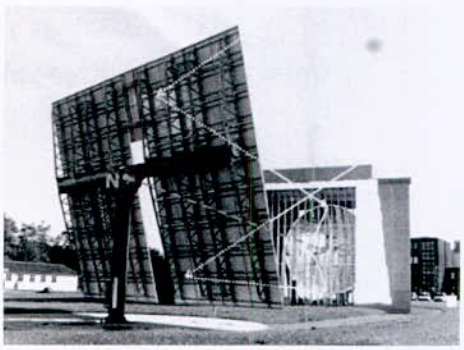

a)

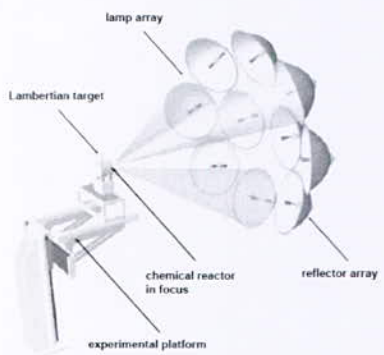

b)

Fig. 2. Dispositifs solaires
a) Four solaire, b) Simulateur solaire [2]

III. PRESENTATION DES JEUX DE DONNEES DU DNI

Les ressources solaires (DNI) du site de Hassi R'Mel sont analysés sur la base de cinq jeux de données [3]. Ceci nous permet de mener une analyse comparative en se basant sur des données qui proviennent de différentes sources (mesures au sol, satellite). Ces jeux de données sont classés suivant qu'ils soient récupérés en amont du projet de la centrale SPP1, en aval de ce projet, ou enfin en ayant recours aux bases de données satellitaires. Les cinq jeux de données sont les suivants :

1. Les données METEONORM du constructeur de la centrale SPP1 (la société espagnole ABENER) récupérés en amont du projet (en 2005). L'outil METEONORM se base sur des données satellitaires et des mesures au sol.
2. Les données de mesures au sol de l'Unité de Recherche Appliquée en Energies Renouvelables (URAER) de Ghardaïa récupérés en amont du projet (en 2005). Avant le lancement du projet, les promoteurs du projet ne disposaient pas de données de mesures au sol au niveau du site de Hassi R'Mel ou à sa proximité immédiate. Ils ont eu recours donc aux données de mesure au sol du site de l'URAER de Ghardaïa. Malgré l'éloignement de ce site par rapport au site de Hassi R'Mel (70 km), il a été convenu d'examiner quand même ces données.
3. Les données de mesures au sol d'ABENER récupérées en aval du projet (en 2012). Il s'agit des données obtenues avec la station de mesure au sol installée sur le site de la centrale SPP1 en 2011, date à laquelle la centrale a été mise en exploitation. Il s'agit aussi d'une mesure du DNI au cœur du site qui nous intéresse. Ces données devraient donc être d'une excellente précision.
4. Les données issues de la base de données satellitaire NASA SSE. Les bases de données solaires sont précieuses dans l'optique d'analyser le gisement solaire d'un site, complétant les données issues des mesures au sol, lorsque ces dernières sont disponibles.
5. Les données issues de la base de données satellitaire SWERA. Nous avons choisi de ne pas utiliser uniquement une seule base de données solaire dans notre analyse. Ceci nous permet d'enrichir notre étude et accroître notre champ de comparaisons.

IV. RESULTATS ET DISCUSSIONS

L'analyse menée dans le cadre de cette contribution, montre que l'estimation du DNI reste une opération délicate car les cinq jeux de données présentent des profils et des valeurs qui sont parfois assez différents et donc tirer une conclusion de cette analyse n'est pas une mince affaire. L'analyse est conduite en étudiant successivement les évolutions mensuelles du DNI, ainsi que la somme annuelle de chaque jeu de données.

*Corresponding author email: hichem.farsi@yahoo.fr

1. Analyse des valeurs mensuelles du DNI

Les courbes d'évolution au cours d'une année des valeurs mensuelles du DNI sont présentées dans **Fig.3**. Concernant les données METEONORM, la courbe d'évolution des valeurs mensuelles du DNI suit la logique saisonnière, puisque les valeurs basses sont enregistrées en saison froide et les valeurs hautes en saison chaude. Les valeurs sont comprises entre un minimum de 132 $kWh.m^{-2}$ et un maximum de 261 $kWh.m^{-2}$. Par ailleurs, nous constatons que la courbe comprend deux *pics* : Le premier au mois de Mars tandis que le deuxième est observé au mois de Juin. Il y a lieu aussi de noter la faible valeur observée pour le mois d'avril en comparaison avec les autres mois (hors hiver).

Le DNI du site de Ghardaïa se situe entre une valeur minimale de 133 $kWh.m^{-2}$ et une valeur maximale de 205 $kWh.m^{-2}$. Une stagnation irrégulière est observée tout au long de l'année avec quelques hausses. Deux pics sont relevés et présentent des valeurs comparables : Le premier au mois d'avril et le second au mois d'Octobre. Cette courbe présente un comportement différent de celui observé pour les données précédentes (METEONORM) qui respectaient la logique saisonnière.

L'examen des données de mesures au sol de la centrale SPP1 indique des valeurs qui se situent entre un minimum de 101 $kWh.m^{-2}$ et un maximum de 218 $kWh.m^{-2}$. Il ressort aussi du graphique que les valeurs du DNI passent par deux étapes : D'abord, une croissance régulière de janvier à mai. Ensuite, une décroissance à partir des mois de juin-juillet jusqu'à la fin de l'année. La courbe suit ici la logique saisonnière.

Concernant les deux dernières courbes, nous notons que pour la base de données NASA SSE, les valeurs mensuelles du DNI se situent entre un minimum de 124 $kWh.m^{-2}$ et un maximum de 282 $kWh.m^{-2}$, tandis que pour la base de données SWERA, les valeurs se situent dans la fourchette [117 $kWh.m^{-2}$, 179 $kWh.m^{-2}$]. La logique saisonnière des valeurs de DNI est mieux respectée pour NASA SSE que pour SWERA.

Malgré la difficulté de conclure avec la variabilité du DNI selon le jeu de données considéré, nous observons que les données fournies par METEONORM et NASA SSE surestiment les données correspondant aux mesures au sol. A contrario, les valeurs fournies par SWERA sont la plupart du temps bien en dessous des valeurs des autres bases de données. Nous pouvons dire ainsi que les données prises en amont du projet par le constructeur du projet (ABENER) pour évaluer les ressources solaires du site abritant la centrale SPP1 seraient surestimées. Une surestimation de la valeur vraie du DNI peut poser problème dans le sens où cela peut présenter un risque dans le sous-dimensionnement du champ solaire (superficie des miroirs) et donc une production de chaleur solaire plus faible pendant la phase d'exploitation du système énergétique. La surestimation du DNI par ABENER devrait cependant être relativisée par le fait qu'il y a lieu de tenir compte dans cette analyse de la variabilité de la ressource solaire d'une année à l'autre. Nous pensons aussi que la mesure du DNI sur une période plus longue (à partir de 2 ans de mesures au sol sur le site) reste le moyen le plus solide pour juger de la pertinence de valeurs du DNI.

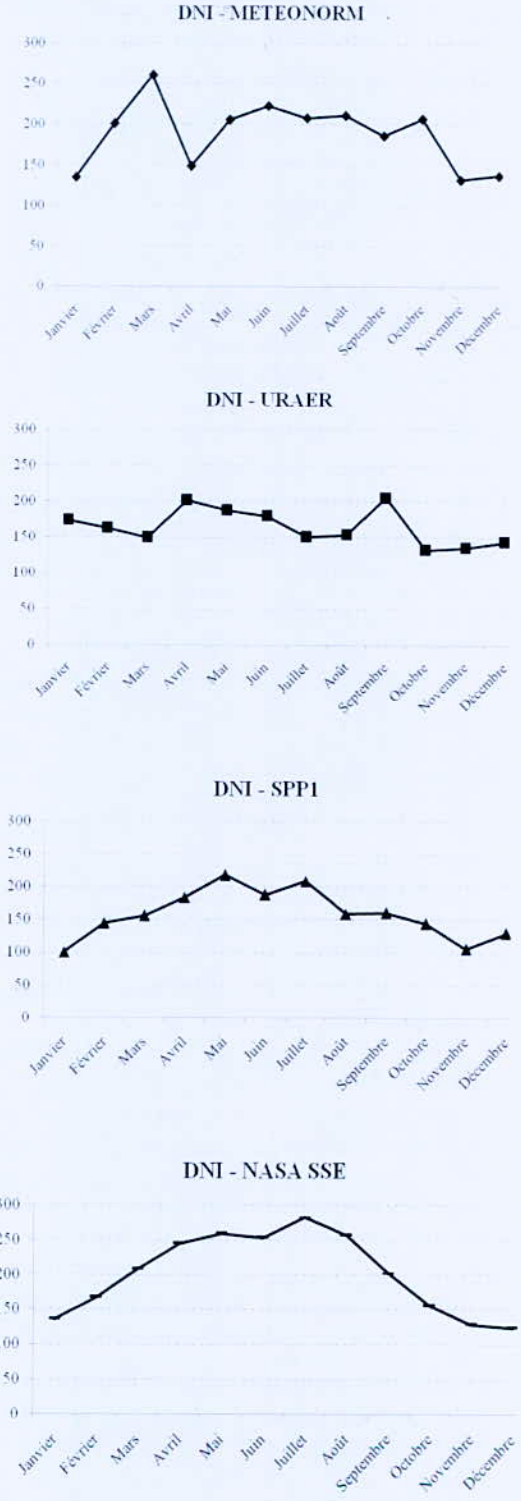

*Corresponding author email: hichem.farsi@yahoo.fr

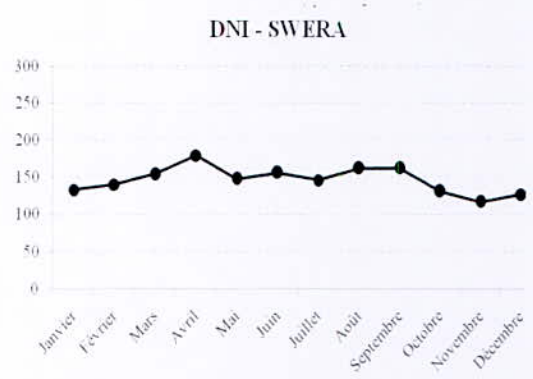

Fig. 3. Evolutions des valeurs mensuelles du DNI pour le site de Hassi R'Mel [3]

2. Analyse des sommes annuelles du DNI

Les cinq jeux de données présentent des valeurs assez différentes (allant de 1756 kWh.m^{-2} à 2420 kWh.m^{-2}).
La somme annuelle du DNI fournie par NASA SSE est de 2420 kWh.m^{-2}. Cette valeur qui est bien supérieure aux autres jeux de données, peut trouver son explication dans le fait que la résolution spatiale est importante (111 km), mais aussi dans le fait que ces données sont issues uniquement de mesures satellitaires. Ces dernières ne détectent pas certaines conditions locales du site qui peuvent causer une diminution des valeurs du DNI. Sur le site de Hassi R'Mel, ces conditions peuvent être : l'humidité élevée (rejets gazeux des unités de traitement voisines), la présence de poussières (trafic routier) ou bien la pollution de l'air du fait de la présence des torches à proximité du site. La somme annuelle du DNI fournie par METEONORM est de 2257 kWh.m^{-2}, ce qui situe cette valeur entre celle de NASA SSE et SWERA. L'outil METEONORM se caractérise par la combinaison entre des données satellitaires et des données de mesures au sol. Enfin, la base de données SWERA indique une somme annuelle du DNI de 1756 kWh.m^{-2}, une valeur bien inférieure aux valeurs des autres jeux de données. Pour les données obtenues avec les mesures au sol sur le site même de SPP1, il ressort que la somme annuelle du DNI n'est pas très élevée et avoisine les 1900 kWh.m^{-2}. Il y a lieu de souligner que les valeurs communiquées par la station de mesures au sol présentaient à certains moments des informations incorrectes, dont des valeurs d'irradiation incohérentes pendant la nuit. Par ailleurs, il faut savoir que la somme annuelle du DNI peut varier d'une année sur l'autre (jusqu'à 30 %). Il faudrait donc au moins 5 ans (respectivement 10 ans) de mesures pour être sûr d'avoir moins de 10 % (respectivement 5 %) d'erreur sur la valeur moyenne à long terme. Donc le jeu de données analysé et qui couvre seulement une année (2012) peut présenter un écart par rapport à une année type ou moyenne. Enfin, pour les données obtenues avec les mesures au sol de l'URAER (Ghardaïa), la somme annuelle du DNI, à l'image des données de SPP1, n'est pas suffisamment élevée (1980 kWh.m^{-2}). La station de mesures au sol était installé sur le site il y avait à peine quelques mois (2004). L'éloignement de l'URAER du site de Hassi R'Mel (70 km) pourrait expliquer lui aussi cette valeur relativement faible en rapport avec ce site.

V. CONCLUSIONS

Le travail mené dans le cadre de cette contribution, nous a éclairés quant aux valeurs à considérer pour le dimensionnement d'une installation CSP destinée à la production de l'hydrogène sur un site donnée. Le travail en question a porté sur la comparaison de cinq jeux de données pour le site de la centrale hybride CSP / gaz de Hassi R'Mel (SPP1). Le présent travail a le mérite de baser la détermination du DNI à partir d'une étude comparative faisant appel à des sources diversifiées (mesures au sol, données satellitaires, une combinaison des deux). Les cinq jeux de données présentent des sommes annuelles de DNI assez différentes (allant de 1756 kWh.m^{-2} à 2420 kWh.m^{-2}). Les données de NASA SSE et de METEONORM présentent une valeur située vers la limite haute. Les mesures au sol de SPP1 et de l'URAER (Ghardaïa) présentent des valeurs situées vers la limite basse. Les données METEONORM qui ont été utilisées par le constructeur (ABENER) de SPP1, semblent surestimer les données de mesures au sol. Une surestimation de la valeur vraie du DNI peut poser problème car il y a un risque dans le sous-dimensionnement du champ solaire et donc une production de chaleur solaire plus faible.
L'estimation du rayonnement solaire direct (DNI) reste une opération très délicate car les différents jeux de données présentent des profils et des valeurs qui peuvent être assez différents et donc tirer une conclusion devient très difficile. Néanmoins, cette étape de détermination du DNI reste une étape cruciale pour le bon dimensionnement d'un système de production d'hydrogène à partir des technologies CSP.

REFERENCES

[1] H. Derbal, M. Belhamel et A. M'Raoui "L'hydrogène, vecteur énergétique solaire" *Revue des énergies renouvelables ICRESD-07* Tlemcen, pp. 237–247, 2007.

[2] "Solar fuels from concentrated sunlight" IEA SolarPACES, 2009.

[3] I. Hebili, "Contribution à l'étude de la centrale électrique hybride gaz / solaire thermodynamique (à concentration) de Hassi R'Mel, dénommée *SPP1* (Solar Power Plant One)." Mémoire de fin d'études de Master, Faculté de Génie Mécanique et du Génie des Procédés, Université des Sciences et de la Technologie Houari Boumediene (USTHB), Alger, Algérie, 2017.

*Corresponding author email: hichem.farsi@yahoo.fr

Dynamics and Thermodynamics Properties of $L1_0$ FePdH

Ahmed Boufelfel*

Laboratoire de physique, Université 08 mai 1945, BP401 Guelma 24000 Algérie.

Abstract—**Dynamics and thermodynamics properties of mono equi-atomic multilayer of Fe/Pd $L1_0$ tetragonal structure where H is placed in Fe or Pd or both layers with formula 2(FePd)nH (n=0,1,2,3) are reported. These findings are computed using a combination of density-functional theory total-energy calculations and density-functional perturbation theory lattice dynamics in the generalized gradient approximation. The lattice dynamics is fully described in the first Brillouin zone. The contribution to the lattice vibrations energy of each atom is determined for each case of study. Hydrogen optical phonons are well separated from the rest but acoustical phonons overlap with those of Fe and Pd. Hydrogenation of FePd increases considerably the heat capacity and the Debye temperature at high temperatures.**

Key words—Hydride, FePd, DFT, Heat Capacity, Debye Temperature.

I. INTRODUCTION

At the present time high demands in the mobile market applications for efficient, cost effective, safe and clean energy carrier that can deliver electricity for a long time and recharged fast. Currently, hydrogen can be produced in a large quantity in a fair amount of time but practical means to store it are still a big hurdle in its use as a fuel or energy carrier. Solid hydrogen storage system is believed to be reliable, simple to fabricate and much safer than the use of other phases of hydrogen. Up till now mainly metal hydrides are investigated [1]. Metal hydrides are metals which have been bonded to hydrogen to form a new compound. Solid metal hydrides have been studied for many years, particularly for understanding the process of metal embrittlement upon absorption of hydrogen at interstitial sites [2].

Earlier, I reported on the electronic, magnetic and elastic properties of mono equi-atomic multilayer of $L1_0$ tetragonal structure of 2(FePd)nH (n=1,2,3) hydride [3]. Now, I will present the dynamics and thermodynamics properties of these hydrides. These findings are computed using a combination of density-functional theory total-energy calculations and density-functional perturbation theory lattice dynamics in the generalized gradient approximation. The vibrational free energy, the temperature dependence of the entropy, Debye temperature and the specific heat are calculated using the quasi harmonic approximation. These results are the foundation for the evaluation of these materials for a practical use as storage of hydrogen.

*Corresponding author email: ahboufelfel@gmail.com

First I will give the methods of calculations with the details of the input parameters. Second the results of the energies of the crystals displacements at 0K in the harmonic approximation are given. Finally the quasi-harmonic approximation is used to extrapolate the values of the energies at finite temperature. All the results will be discussed in the framework of their potential preparations in a bottom up process and eventually tested for applications in energy storage.

II. METHODS

$L1_0$ FePd system is a tetragonal equiatomic layered structure. Layers are occupied by Fe and Pd alternatively in the c direction. For hydrogen locations inside the conventional cell taken in this study, hydrogen atoms occupy Fe layers only (2(FePd)1H) or in Pd layers only (2(FePd)2H) or in all layers (2(FePd)3H). The positions are dictated by the crystallographic group number of this phase ($L1_0$, Group number 123 in the international classification P4/mmm).

All calculations reported in this work have been performed with the public domain PWSCF code included in the Quantum-Espresso (QE) distribution, based on density-functional theory, periodic-boundary conditions, plane-wave basis sets, and pseudopotentials to represent the ion-electron interactions [4]. All pseudopotentials calculations results were obtained for gradient-corrected (GGA) density functional, PBE. In all calculations ultra soft pseudopotentials were used. The electronic Kohn-Sham wave functions were expanded using a plane-wave basis set, up to a kinetic energy cut-off of 1200Ryd. Monkhorst-Pack grids were used to sample the Brillouin zone, a 12x12x12 grid was used, giving convergence of better than 10^{-10} meV in the total energy per unit cell. The plane wave energy cutoff was chosen as 55 Ry. BFGS quasi-newton algorithm, based on the trust radius procedure, is used for cell and ion dynamics as implemented in QE. In DFPT method the dynamical matrix is calculated from the linear response of electronic density and diagonalized to get the normal phonons modes frequencies at any wave vector **q**. It simply uses the same cells used in the ground state electronic structure calculations. The code determines the lattice dynamical properties via the dynamical matrices at any **q** point; this is called 'Single-q calculations'. To compute the full phonon dispersions, a bridge from reciprocal to real space is mandatory in order to compute the interatomic force constants (IFC) in real space through a Fourier transformation of the dynamical matrices.

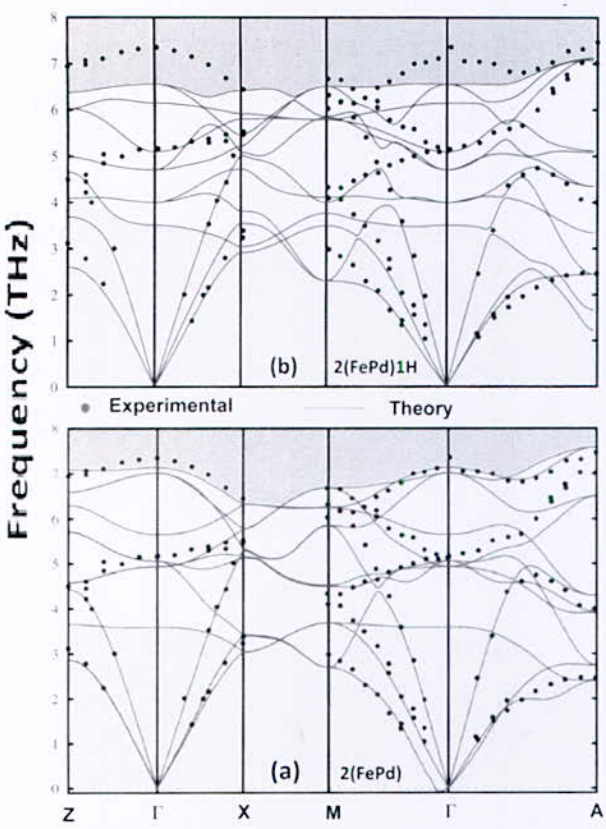

Fig. 1. Phonons Energy Dispersions (a)$L1_0$ 2(FePd) (b)$L1_0$ 2(FePd)1H

The calculations were done on a 4x4x4 **q**-mesh with a 12x12x12 **k**-mesh.

III. RESULTS AND DISCUSSION

1. Vibrational modes of 2(FePd)nH (n=0,1,2,3)

In Fig. 1, I show the only experimental data available [5] in the literature for $L1_0$ FePd phonons dispersion which I draw in dots in both panels and the solid lines are my calculated results. In panel (a) is direct comparison between the measured and the calculated phonons dispersion for FePd which is very satisfactory especially for the acoustic branches. Here the separation between the acoustical and optical phonons is not clear. For the eye guidance only I shaded the ambiguous parts of the acoustical and optical parts in light and dark gray respectively. In panel (b) for the sake of comparison, the same experimental results for FePd are drawn on the same scale for the calculated 2(FePd)1H where I did not show the higher frequencies for figure clarity. The frequencies of the FePd optical modes clearly are shifted towards To further understand this behavior in depth I calculated an atom-projected partial phonon density of states, $g_i(\omega)$, and atom-resolved phonon contributions to the free energy $F_{vibi}(V,T)$ obtained from $g_i(\omega)$

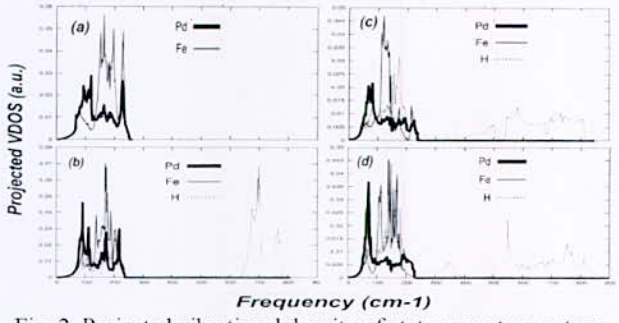

Fig. 2. Projected vibrational density of states per atom nature (a)$L1_0$ 2(FePd) (b)$L1_0$ 2(FePd)1H (c)$L1_0$ 2(FePd)2H (d)$L1_0$ 2(FePd)3H

$$F_{vib}(V,T) = k_B T \int d\omega\, g_i(\omega) \ln\left[2\sinh\left(\frac{h\omega_{nq}}{2k_B T}\right)\right] \quad (1)$$

$$g_i(\omega) = \sum \left|e^i_{nk}\right|^2 \delta(\omega - \omega_{nk}) \quad (2)$$

where k_B is the Boltzmann constant, and ω_{nq} is the frequency of the phonon mode for wave vector q and volume V, i is an atomic label and e^i_{nk} is polarization vectors of atom i for a given mode n and wave vector k. In Fig. 2, I present the atom projected vibrational density of states for Fe, Pd and H atoms in the four considered structures. The lower frequencies correspond mainly to Fe and Pd contributions where a clear separation between their acoustical and optical phonons is not obvious. In Fig. 2(a), the case is clearly demonstrated where Fe and Pd bands overlap. In Fig. 2(b), where H is added to the Fe layers the H contribution to the VDOS is separated into two parts acoustical (lower frequencies) and optical (higher frequencies) bands. The separation between H optical phonons and the rest of the phonons is really important but in Fig. 2(c) where H is only in Pd layers the gap disappeared and the vibrations modes of H are widely spread on a larger region. Finally, in Fig. 2(d) where H is in every layer, phonons wise it is a hybrid state between the last two cases where the gap in H frequencies exists but with a smaller value. For an in depth comparison of vibrations modes of an atomic type in every case of material studied I show in Fig. 3 the H content on the projected VDOS of the other two atoms Fe and Pd and on itself. In Fig. 3a & b, I zoomed out on small frequency region up to 300cm^{-1} to show the transformations which occur to the the samples with their correspondent line color. The general trend is H content tends to shift DOS of Fe and Pd further towards lower frequencies. The components of atom-specific phonon VDOS in the different directions are not shown here for space reasons. For Fe and Pd components in the low frequencies region point that the component in the perpendicular direction of the multilayer structure for Pd has a larger contribution in the lowest frequency of that region and for Fe its major contribution is in the top frequencies of the same region.

*Corresponding author email: ahboufelfel@gmail.com

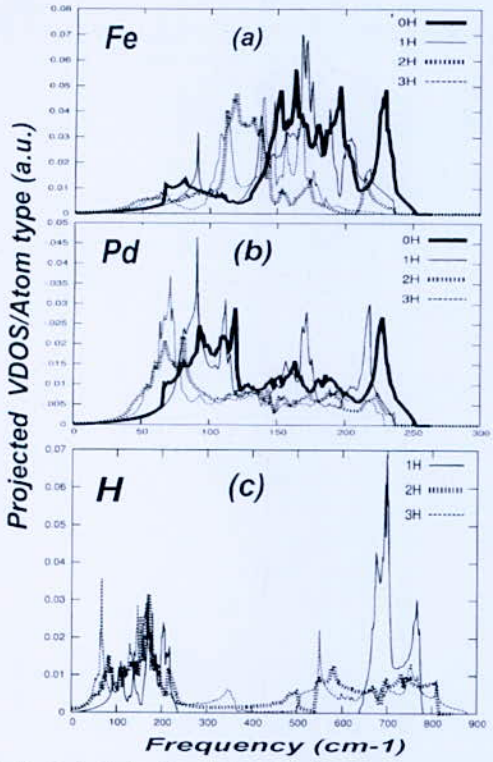

Fig. 3. Projected vibrational density of states per atom nature (a) Fe (b) Pd (c) H in 2(FePd)XH (X=0,1,2,3)

The rest of the spectra are the combination of in plane directions of the layers.

Another interesting result is the case of materials with phonons band gap where decomposition of optical and acoustical into spatial components (g_x, g_y, g_z) is possible. In Fig. 4(a), is shown the decomposition of the projection of VDOS of H atom in 2(FePd)1H. The most important component for the optical modes is in z direction which is the direction perpendicular to the layers and the contribution to the acoustical modes is small. For 2(FePd)2H and 2(FePd)3H in Fig. 4(b) and 4(b) the dominant component in the acoustical frequencies is in the z direction and the optical mode is formed by only the in plane modes.

2. *Thermodynamics properties of 2(FePd)nH (n=0,1,2,3)*

$F(V,T)$ was calculated as a sum of the total energy, $E(V)$, and phonon contribution, $F_{vib}(V,T)$:

$$F(V,T)= E(V)+ F_{vib}(V,T). \qquad (3)$$

At zero pressure, the Gibbs free energy is equal to the Helmholtz free energy. The vibrational entropy S at a given temperature T and constant volume can be found by minimizing the Helmholtz free energy with respect to the temperature. The heat capacity per unit cell at constant volume, C_V, is the temperature derivative of the entropy. In Fig. 5, I show the influence of H on the heat capacity, measurable quantity, versus the temperature.

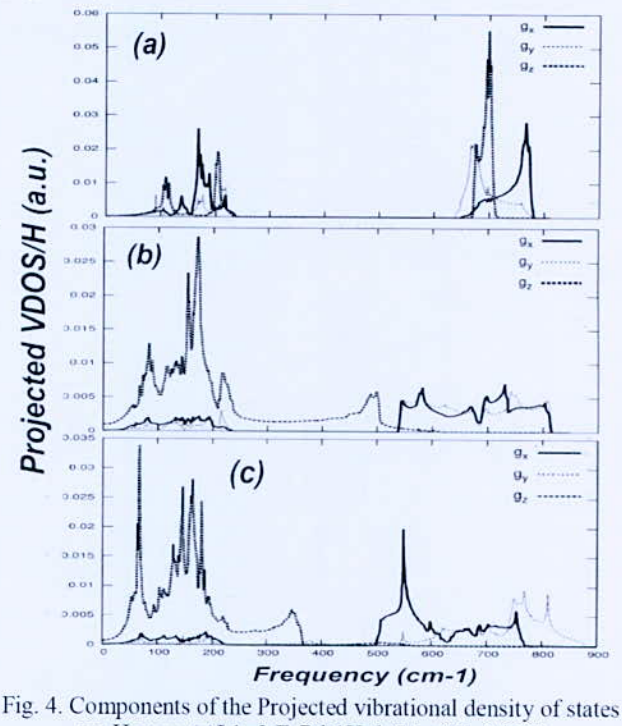

Fig. 4. Components of the Projected vibrational density of states per H atom (a)$L1_0$ 2(FePd)1H (b)$L1_0$ 2(FePd)2H (c)$L1_0$ 2(FePd)3H

The curves diverge gradually as the temperature rises. The trend is the consequence of the entropy variation as shown in lower inset. The vibrational free energy per formula unit is represented in the upper inset of Fig. 5.

The Debye temperature (Θ_D) for each temperature is deduced from the comparison of the previously calculated heat capacity with the known Debye model relation:

$$C_V = 9N_{at}\frac{1}{x^3}\int_0^x y^4 \frac{e^y}{\left(e^y-1\right)^2}dy \qquad (4)$$

where $x = \frac{\theta_D}{T}$ and N_{at} is the total number of atoms.

TABLE I
THERMODYNAMIC QUANTITIES DEDUCED FROM LATTICE DYNAMICS AT 300 K

Fomula/1cell	S_V/k_B	Θ_D(300K)	C_V(300K)/k_B
2(FePd)	5.43	309.87	3.80
	(4.30)	(318.7)	(5.64)
2(FePd)1H	5.67	560.55	4.22
2(FePd)2H	6.61	590.61	4.66
2(FePd)3H	7.33	634.41	5.44

In table I, the first column is the chemical formula per unit cell, the second column is vibrational entropy, the third column Θ_D the Debye temperature, and the last column specific heat per atom where everything is at 300 K. The values in parentheses are those reported by Mahdenne et al. [5] calculated in the harmonic approximation using Schober's model fed with their experimental data. For the values of the specific heat they extrapolated it using Debye's law.

*Corresponding author email: ahboufelfel@gmail.com

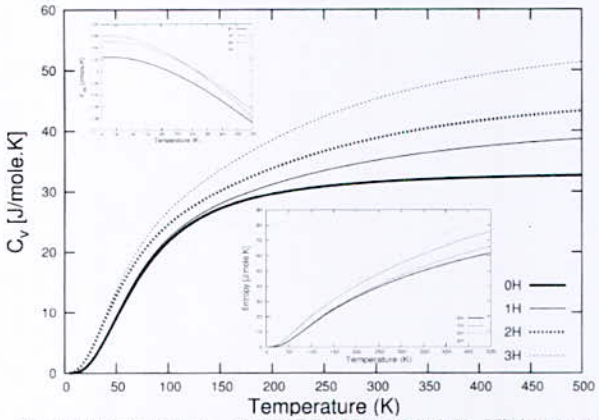

Fig. 5. Calculated Cv of 2(FePd)nH (n=0,1,2,3). Higher inset is Helmholtz energy and lower inset is the entropy.

In comparison their values are fairly close to my values. On the other hand the Debye temperature depends on the hydrogen content. The last column is table 1 is the heat capacity at room temperature. Compared to ref 5 my value is underestimated for FePd; may be due to the missing part of the magnons interactions contribution to the heat capacity.

In the future as a follow up of this work classical molecular dynamics will be performed since the quasi harmonic approximation is only valid for temperatures below the Debye temperature. Also, the influence of pressure is very important in metal hydrides for many reasons. For instance, great interests have been reported in FeHx [6-7] and PdHx [8] in order to examine the hydrogenation of these hydrides at high pressures. However, experimentally, up to date, it is known that a hydride is formed only at high pressures, and hydrogen is released rapidly and completely after the hydride is recovered to ambient conditions. Therefore, the behavior of hydrogen has been much more difficult to study than the other light elements. Most of the techniques used for the preparation of these hydrides are classical top down chemistries. I think that nanoscale bottom up techniques should be revisited in order to create stable structures at room temperature and above like the ones I am reporting.

IV. CONCLUSION

2(FePd)nH (n=0,1,2,3) lattice dynamics are fully described in the first Brillouin zone and my results agree very well with the experimental data where available. The contribution to the lattice vibrations energy of each atom is determined for each case of study. Hydrogen optical phonons are well separated from the rest but acoustical phonons overlap with those of Fe and Pd. Hydrogenation of FePd increases considerably the heat capacity and the Debye temperature at high temperatures. I sincerely hope that these findings will find experimentalists who are attracted and willing to test them for comparison.

ACKNOWLEDGMENTS

This work was supported by the Algerian ministry of higher education and scientific research, CNEPRU program, under contract number B00L02UN2401 2015 0004.

REFERENCES

[1] Broom D. P., 2011 Hydrogen Storage Materials, Green Energy and Technology, Springer-Verlag,.

[2] Humphries, T. D., Sheppard, D. A., & Buckley, C. E. 2017 Recent advances in the 18-electron complex transition metal hydrides of Ni, Fe, Co and Ru. *Coordination Chemistry Reviews, 342, 19-33*

[3] Ahmed Boufelfel, 2016 Ab initio calculations of L_{10} FePdH multilayered structure, *international journal of hydrogen energy, 41, 4719-4728.*

[4] Giannozzi, P., Baroni, S., Bonini, N., Calandra, M., Car, R., Cavazzoni, C., ... & Wentzcovitch, R. M. (2009). QUANTUM ESPRESSO: a modular and open-source software project for quantum simulations of materials. *Journal of Physics: Condensed Matter*, *21*(39), 395502.

[5] Mehaddene, T., Kentzinger, E., Hennion, B., Tanaka, K., Numakura, H., Marty, A., ... & Pierron-Bohnes, V. 2004. Lattice dynamics and migration enthalpies in $CoPt_3$ and FePd. *Physical Review B*, *69*(2), 024304.

[6] Iizuka-Oku, R., Yagi, T., Gotou, H., Okuchi, T., Hattori, T. and Sano-Furukawa, A., 2017. Hydrogenation of iron in the early stage of Earth's evolution. *Nature communications*, *8*, *14096.*

[7] Matsuoka, T., Hirao, N., Ohishi, Y., Shimizu, K., Machida, A. and Aoki, K., 2011. Structural and electrical transport properties of FeHx under high pressures and low temperatures. *High Pressure Research*, *31*(1), pp.64-67.

[8] Eduardo A. Crespo, Margarita Ruda , Susana Ramos de Debiaggi, Eduardo M. Bringa, Fabia´n U. Braschi, Graciela Bertolino 2012 Hydrogen absorption in Pd nanoparticles of different shapes, *international journal of hydrogen energy,* 37, 14831-148.

*Corresponding author email: ahboufelfel@gmail.com

Hydrogen Production by Carbon Monoxide Conversion during Water-Gas-Shift Reaction in a Membrane Reactor at Low Temperature

D. Alihellal[1*] and L. Chibane[2]

[1*, 2]Laboratoire de Génie des Procédés Chimiques (LGPC), Département de Génie des Procédés, Faculté de Technologie, Université Ferhat Abbas Sétif 1, Algérie.

Abstract—**The performances of water gas shift reaction at low temperature (LT-WGS) on a palladium-based membrane reactor were investigated using a $CuO/ZnO/Al_2O_3$ catalyst. The effects of the some important operating parameters (temperature, pressure in the reaction zone, H_2O/CO molar ratio, gas hourly space velocity (GHSV) and sweep gas ratio) on the performance of the membrane reactor were studied in terms of carbon monoxide conversion and hydrogen recovery. The modeling results showed that a substantial carbon monoxide conversion can be obtained at low temperature (210°C). The amount of recovered hydrogen can be strongly affected by the pressure difference in the reaction zone and in the permeation zone. The increase in temperature, the pressure, the H_2O/CO molar ratio and the sweep gas ratio makes it possible to achieve good performances. Moreover, the increase in the GHSV space velocity generally implies an incredible reduction in conversion or in hydrogen recovery.**

Key words—Membrane reactor, LT-WGS reaction, Hydrogen production, $CuO/ZnO/Al_2O_3$ catalyst.

Acronyms

A	Reactor section (m^2)
A_m	Section of the membrane (m^2)
$F_{H_2}^P$	Hydrogen flux in the permeation zone ($mol.s^{-1}$)
J_{H_2}	The hydrogen permeation flux ($mol.m^{-2}.s^{-1}$)
k_P	The thermodynamic equilibrium constant
L	Reactor Length (m)
$P_{H_{2perm}}$	Partial pressure of H_2 in the permeation zone (kPa)
$P_{H_{2ret}}$	Partial pressure of H_2 in the reaction zone (kPa)
P_e	The permeability of hydrogen ($mol.m^{-1}.s^{-1}.kPa\text{-}^{0.5}$)
r_{WGS}	The WGS reaction rate ($mol.g^{-1}.h^{-1}$)
X_{CO}	Conversion of carbon monoxide in the WGS reaction (%)
Y_{H_2}	Removed hydrogen fraction (%)
z	Axial reactor coordinate
δ	The membrane thickness (m)
ρ	The density (kg/m^3)

I. INTRODUCTION

Water gas shift is well known at industrial as reaction that has been used for the generation of hydrogen [1], this is a further conversion of CO and H_2O to H_2 and CO_2 according to the reaction (1) [2, 3]:

$$CO_{(g)} + H_2O_{(g)} \leftrightarrow CO_{2(g)} + H_{2(g)} \quad \Delta H^0 = -41.1 Kj/mol \qquad (1)$$

The WGS is an exothermic, reversible and thermodynamic equilibrium limited reaction [4]. It can operate in two modes at high temperature and low temperature [5] depending on the catalyst used. It is generally catalyzed by several metals such as iron [6], copper [7, 8], cobalt [9, 10], nickel [11] and even Platinum [12, 13], which gives birth to several kinetics and mechanism for the WGS reaction [13, 14-16]. To separate hydrogen from the reaction zone and improve the conversion of CO several types of perm-selective membranes to hydrogen are used in the WGS reactors [1, 12, 17] such as zeolite membranes [18, 19], silica membranes [20, 21] and palladium membranes [22-24]. However, the palladium membranes are considered as a promising alternative solution for producing high hydrogen purity in industrial processes and showed good performances compared to other types of membranes [25, 26].

The aim of this work is focused on investigating the WGS reaction in a palladium-based membrane reactor over a $CuO/ZnO/Al_2O_3$ catalyst based on Langmuir Hinshelwood kinetics at low temperatures (LT-WGS). A set of simulation results is, then, provided illustrating the effect of some operating parameters and the performance during WGS reaction in terms of carbon monoxide conversion and hydrogen recovery.

II. MATHEMATICAL MODEL

1. Reactor and operating conditions

1. 1. Membrane Reactor

A schematic of the membrane reactor considered here is shown in Fig. 1. The membrane was placed inside the reactor shell and the catalyst outside the membrane tube. The WGS reaction took place on the catalyst and the hydrogen selectively penetrates through the membrane to the permeation side. The removal of hydrogen from the reaction zone forces the chemical equilibrium of the reaction on the side of the desired product. The sweeping gas dilutes the product and increases the partial pressure difference on the side of the membrane resulting in a

*Corresponding author email: alihellald@yahoo.com

higher driving force. After reaction, the feed stream leaves the reactor as a retaining stream, which is enriched in CO_2 [27].

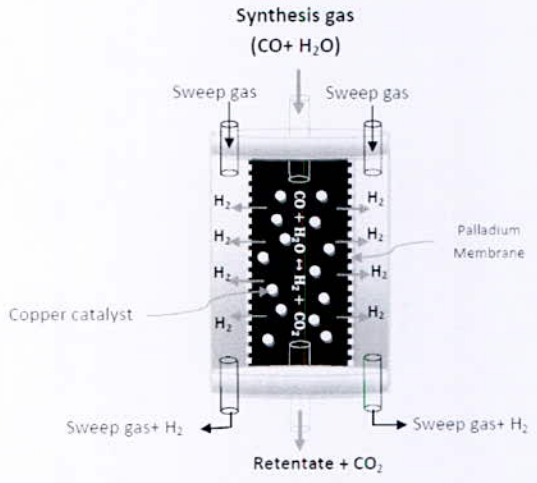

Fig. 1. Schematic representation of the membrane reactor

1. 2. Reactor parameters and operating conditions

The various operating conditions, the reactor dimensions studied and the properties of the Pd-Ag membrane are given in the table I:

TABLE I
REACTOR PARAMETERS AND OPERATING CONDITIONS

Parameter	Numerical value	Reference
Temperature (°C)	190-210	[22]
Initial total pressure (kPa)	150-300	[22]
Initial pressure in the permeation side (kPa)	101.3	[22]
The weight of the catalyst (kg)	$3*10^{-3}$	[22]
Thickness of Pd membrane (m)	$50*10^{-6}$	[22]
Longueur du réacteur (m)	$5*10^{-2}$	[28]
Rayon du réacteur (m)	$7.75*10^{-3}$	[28]
H_2O/CO ratio	1-4	[22]
Permeation of the membrane $Pe°$ (mol/(m s $kPa^{0.5}$))	$9.88*10^{-6}$	[22]
Activation energy Ea (kj/mol)	26.63	[22]

2. Kinetics and Molar balance

The kinetic velocity expression and the kinetic parameters of the WGS reaction on a copper-based catalyst ($CuO/ZnO/Al_2O_3$) are given according to the following model [22]:

$$r_{WGS} = \frac{k(P_{CO}P_{H_2O} - \frac{P_{CO_2}P_{H_2}}{k_P})}{(1 + K_{CO}P_{CO} + K_{H_2O}P_{H_2O} + K_{H_2}P_{H_2} + K_{CO_2}P_{CO_2})} \quad (2)$$

2. 1. Molar balance in the reaction zone

The partial mass balances for CO, H_2O and CO_2 are, respectively:

$$\frac{dF_{CO}}{dz} = -\rho A r_{WGS} \quad (3)$$

$$\frac{dF_{H_2O}}{dz} = -\rho A r_{WGS} \quad (4)$$

$$\frac{dF_{CO_2}}{dz} = \rho A r_{WGS} \quad (5)$$

To express the molar balance of hydrogen in the reaction zone of the membrane reactor, the amount of hydrogen that has passed through the membrane ($F_{H_2}^P$) must be subtracted. Then, for the membrane reactor, the molar balance of the hydrogen can be written as follows:

$$\frac{dF_{H_2}}{dz} = \rho A r_{WGS} - \frac{dF_{H_2}^P}{dz} \quad (6)$$

Using the following definition of conversion, we can write for the conversion rate of carbon monoxide:

$$\frac{dX_{CO}}{dz} = \frac{\rho AL}{F_{CO}^0} r_{WGS} \quad (7)$$

2. 2. Molar balance in the permeation zone

The mass balance in the permeation side relates only to hydrogen. Thus, the hydrogen removed by the membrane Pd is given by equation:

$$\frac{dF_{H_2}^P}{dz} = A_m J_{H_2} \quad (8)$$

With J_{H2} is the permeation flow of hydrogen, given by the following expression:

$$J_{H_2} = \frac{P_e}{\delta}(P_{H_2ret}^{0.5} - {}^{0.5}_{H_2rperm}) \quad (9)$$

Therefore the quantity of hydrogen permitted is expressed by:

$$\frac{dY_{H_2}}{dz} = \frac{A_m P_e}{F_{CO}^0 \delta}(P_{H_2ret}^{0.5} - {}^{0.5}_{H_2rperm}) \quad (10)$$

where

$$Y_{H_2} = \frac{F_{H_2}^P}{F_{Co}^0} \quad (11)$$

The set of differential equations obtained is solved by the Runge-Kutta method of order 4 in order to determine the performance of the WGS reaction; either the conversion rate X_{CO} or the amount of hydrogen permitted through the membrane (Y_{H2}).

II. RESULTS AND DISCUSSION

1. Effect of the pressure in the reaction zone

Fig. 2(a), shows the effect of total pressure on the conversion of carbon monoxide to the reactor outlet. From the results obtained it is found that an increase in the conversion of carbon monoxide is observed when the pressure increases. This explains why the reaction of WGS is promoted by high pressures.

The effect of pressure on the amount of hydrogen recovered in the permeation zone is shown in Fig. 2(b). It is observed that the increase in pressure leads to an important increase in the amount of hydrogen recovered, from 60% to 150 kPa to 78% to 300 kPa.

It can thus be concluded that the best conversion and permeability are obtained for a pressure of P_T = 300 kPa.

*Corresponding author email: alihellald@yahoo.com

2. Effect of the H_2O/CO ratio

Fig. 3(a), shows the H_2O/CO ratio effect on the conversion of carbon monoxide, an increase in conversion is observed with increasing this molar ratio. The best conversion is obtained at a ratio H_2O/CO equal to 4.

Fig. 3(b), represents the effect of H_2O/CO ratio on the recovered hydrogen, it can also be seen that the increase in this parameter makes the amount of hydrogen recovered improving. In this case, however, the large amount of permeability is obtained with a ratio of 2, while for ratios of the order of 3 and 4.

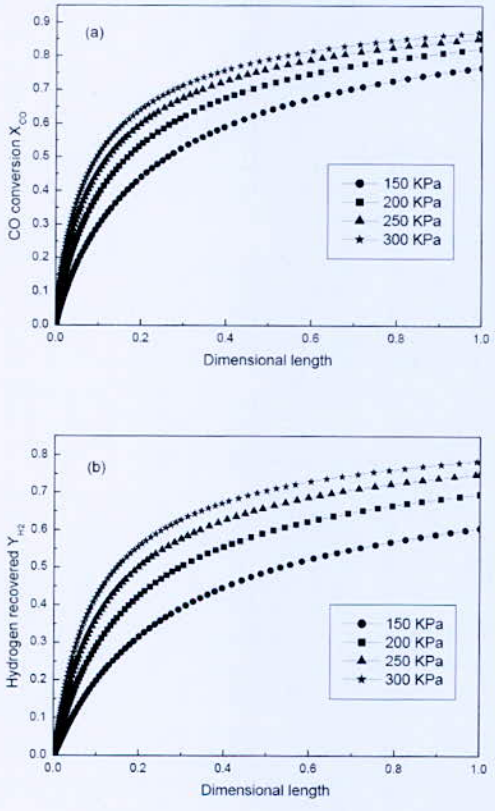

Fig. 2. Effect of pressure on the conversion of carbon monoxide (a) and hydrogen recovered (b) (T = 210 °C, H_2O/CO = 1, GHSV = 2000h^{-1}, I = 3)

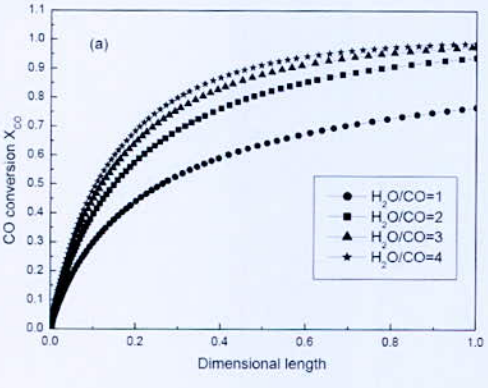

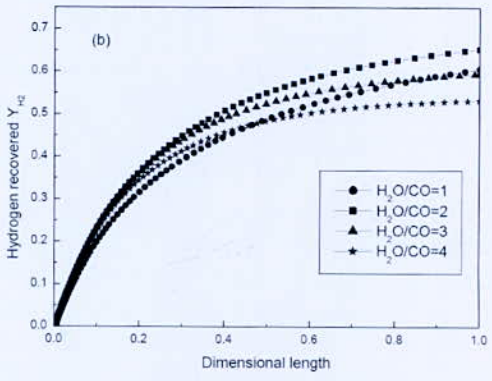

Fig. 3. Effect of H_2O/CO ratio on the conversion of carbon monoxide (a) and hydrogen recovered (b) (T = 210 °C, P_T = 150 kPa, GHSV = 2000 h^{-1}, I = 3)

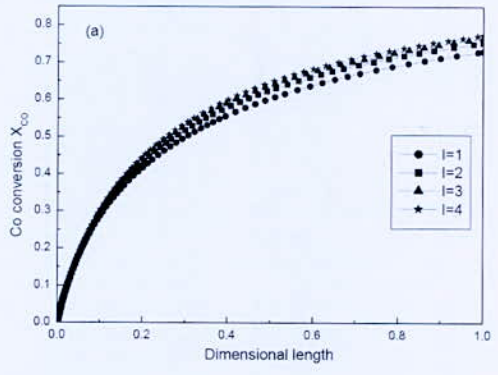

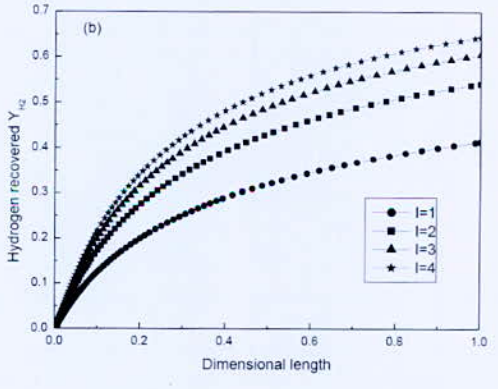

Fig. 4. Effect of the inert ratio I on the conversion of carbon monoxide (a) and hydrogen recovered (b) (T = 210 °C, P_T = 150 kPa, GHSV = 2000 h^{-1}, m = 1)

3. Effect of the inert gas ratio I

Fig. 4(a), shows the change in the degree of conversion of the reaction with the ratio I. According to the results obtained, the conversion of carbon monoxide increases with the increase of the inert ratio, where the completed conversion is equal to 78% for a ratio I of the order of 4. Fig. 4(b), shows the effect of inert ratio on the amount of hydrogen recovered. It is observed that the permeability

*Corresponding author email: alihellald@yahoo.com

increases significantly with the increase of the inert ratio. This implies that as the flow of carrier gas (inert) increases, the amount of H_2 passing through the membrane will be high. In this case we found that the high permeability was obtained at a ratio of 4.

III. CONCLUSION

The main simulation results show that, under the investigated operating conditions, the amount of recovered hydrogen can be strongly affected by the pressure difference in the reaction zone and in the permeation zone. The increase the H_2O/CO molar ratio and the sweep gas ratio makes it possible to achieve good performances. Finally, it can be concluded that the carbon monoxide conversion over $CuO/ZnO/Al_2O_3$ catalyst during LT-WGS reaction is one of an encouraging routes for hydrogen production and its purification. Under the obtained favorable conditions, the reverse water gas shift reaction is mainly blocked on favor of the direct reaction of hydrogen production and consequently, on favor of the pure hydrogen recovery.

REFERENCES

[1] M. E. Adrover, E. López, D. O. Borio, M. N. Pedernera, "Simulation of a membrane reactor for the WGS reaction: Pressure and thermal effects," *Chem. Eng. J.*, vol. 154, pp.196-202, 2009.

[2] A. Arab, D. Sharafie, M. Fazli, "Theoretical study of water-gas shift reaction on the silver nanocluster," *J. Phys. Chem. Solids.*, Vol. 109, pp. 100-108, Oct. 2017.

[3] X. Dong, H. Wang, Z. Rui, Y.S. Lin,"Tubular dual-layer MFI zeolite membrane reactor for hydrogen production via the WGS reaction: Experimental and modeling studies," *Chem. Eng. J.*, Vol. 268, pp. 219-229, May. 2015.

[4] J. A. Francesconi, M. C. Mussati, P. A. Aguirre,"Analysis of design variables for water-gas-shift reactors by model-based optimization," *J. Power Sources.*, vol. 173, pp. 467-477, 2007.

[5] S. Saeidi, F. Fazlollahi, S. Najari, D. Iranshahi, J. J. Klemeš, L. L. Baxter,"Hydrogen production: Perspectives, separation with special emphasis on kinetics of WGS reaction: A state-of-the-art review,"*J. Ind. Eng. Chem.*, vol. 49, pp. 1-25, 2017.

[6] M. Ocwieja, A. Węgrzynowicz, J. Maciejewska-Prończuk, P. Michorczyk, Z. Adamczyk, M. Roman, E. Bielańska,"Preparation of iron oxide nanoparticles doped by chromium for application in water-gas shift reaction," *Colloids. Surf. A.*, Vol. 523, pp. 71-80, June. 2017.

[7] C. Price, L. Pastor-pérez, E. le Saché, A. Sepúlveda-Escribano , T. R. Reina,"Highly active Cu-ZnO catalysts for the WGS reaction at mediumehigh space velocities: Effect of the support composition," *Int. J. Hydrog. Energy.*, Vol. 42, Issue. 16, pp. 10747-10751, April. 2017.

[8] J. L. Santos, T. R. Reinaa, S. Ivanova, M. A. Centeno, J. A. Odriozola,"Gold promoted $Cu/ZnO/Al_2O_3$ catalysts prepared from hydrotalcite precursors: Advanced materials for the WGS reaction," *Appl. Catal., B.*, vol. 201, pp. 310-317, 2017.

[9] A. Jha, Y.Lee, W.Jang, J. Shim, K. Jeon, H. Na, H. Kim, H. Roh, D. Jeong , S. Jeon, J. Na, W. Yoon,"Effect of the redox properties of support oxide over cobalt-based catalysts in high temperature water-gas shift reaction," *J.* Mol. Catal., vol. 433, pp. 145-152, 2017.

[10] L. Wang, H. Liu, Y. Chen, S. Yang, "Reverse water gas shift reaction over co-precipitated $CoeCeO_2$ catalysts: Effect of Co content on selectivity and carbon formation," *Int. J. Hydrog. Energy*, Vol. 42, Issue. 6, pp. 3682-3689, February. 2017.

[11] L. Pastor-Pérez, R. Buitrago-Sierra, A. Sepúlveda-Escribano,"CeO_2-promoted Ni/activated carbon catalysts for the watere gas shift (WGS) reaction," *Int. J. Hydrog. Energy.*, Vol. 39, Issue. 31 , pp. 17589-17599, October. 2014.

[12] C. Cornaglia, S. Tosti, M. Sansovini, J. Múnera, E. A. Lombardo,"Novel catalyst for the WGS reaction in a Pd-membrane reactor," *Appl. Catal., A.*, vol. 462-463, pp. 278-286, 2013.

[13] D. Miao, G. Cavusoglu, H. Lichtenberg, J. Yu, H. Xu, J.D. Grunwaldt, A. Goldbach,"Water-gas shift reaction over platinum/strontium apatite catalysts," *Appl. Catal. B.*, vol. 202, pp. 587-596, 2017.

[14] N. Liu, L. Guo, Z.Cao, W. Li, X. Zheng, Y. Shi, J. Guo,Y. Xi,"Mechanisms of the Water Gas Shift Reaction Catalyzed by Ruthenium Carbonyl Complexes," *J. Phys. Chem. A.*, vol. 120 , Issue. 15, pp. 2408-2419, 2016.

[15] N. Liu, L. Guo, Z. Cao, A.Li, X. An,"Density Functional Theory Study of Water-Gas Shift Reaction on TM@Cu12 Core-Shell Nanoclusters[1]," *Prot. Met. Phys. Chem.*, Vol. 52, N°. 3, pp. 387-398, 2016.

[16] R. M. Van Natter, J. S. Coleman, C. R. F. Lund,"DFT models for active sites on high temperature water-gas shift catalysts," *J. Mol. Catal. A-Chem.*, vol. 292, pp. 76-82, 2008.

[17] W. Chen, Ch. Tsai, Y. Lin, R. Chein, C. Yu,"Reaction phenomena of high-temperature water gas shift reaction in a membrane reactor," Fuel., vol. 199, pp. 358-371, 2017.

[18] Y. Zhang, Z. Wu, Z. Hong, X. Gu, N. Xu, "Hydrogen-selective zeolite membrane reactor for low temperature water gas shift reaction," *Chem. Eng. J.*, vol. 197, pp. 314-321, 2012.

[19] Z. Tang, S. Kim, G. K. Reddy, J. Dong, P. Smirniotis, "Modified zeolite membrane reactor for high temperature water gas shift reaction," *J. Membr. Sci.*, vol. 354, pp. 114-122, 2010.

[20] S. Battersby, M. C. Duke, S. Liu, V. Rudolph, J. C. D. Costa,"Metal doped silica membrane reactor: Operational effects of reaction and permeation for the water gas shift reaction," *J. Membr. Sci.*, vol. 316, pp. 46-52, 2008.

[21] S. Giessler, L. Jordan, J. C. D. Costa, G. Q. (Max) Lu,"Performance of hydrophobic and hydrophilic silica membrane reactors for the water gas shift reaction," *Sep. Purif. Technol.*, vol. 32, pp. 255-264, 2003.

[22] A. Basile , S. Curcio, G. Bagnato, S. Liguori, S. M. Jokar, A. Iulianelli,"Water gas shift reaction in membrane reactors: Theoretical investigation by artificial neural networks model and experimental validation," *Int. J. Hydrog. Energy.*, Vol. 40, Issue. 17, pp. 5897-5906, 2015.

[23] L. N. Baloyi, B. C. North, H. W. Langmi, B. J. Bladergroen, T. V. Ojumu;"The production of Hydrogen through the use of a 77wt%Pd 23wt%Ag Membrane Water Gas Shift Reactor," *South African Journal of Chemical Engineering.*, Vol. 22, pp. 44-54, Dec. 2016.

[24] S. Bittanti, L. Bolzani, S. Canevese, A. De Marco, F. Drago, P. Pinacci,"Modeling for a Palladium Membrane Water-Gas Shift Reactor," *IFAC Proceedings Volumes*, Vol. 46, Issue. 6, pp. 48-53, 2013.

[25] K. Ghasemzadeh, R. Zeynali, A. Basile,"Theoretical study of hydrogen production using inorganic membrane reactors during WGS reaction," *Int. J. Hydrog. Energy.*, Vol. 41, Issue. 20, pp. 8696-87051, June. 2016.

[26] H. Li, J. W. Dijkstra, J. A. Z Pieterse, J. Boon, R. W. van den Brink, D. Jansen,"WGS-mixture Separation and WGS Reaction Test in a Bench scale Multi-tubular Membrane Reactor," *Energy . Procedia., vol.* 4,pp. 666-673, 2011.

[27] M. Brachit, P. T. Alderiesten, R. Kloster, R. Pruschek, G. Haupt, E.Xue, J. R. H. Ross, M. K. Koukou, N. Papayannakos, "Water gas shift membrane reactor for CO_2 control in GICC systems: Techno-economic feasibility study," *Third international conference on carbon dioxide removal, in Cambridge,* Massachusetts, USA 1996.

[28] Y. J. A. Manrique, "Modeling and simulation of water gas shift reactors: from conventional packed-bed to membrane reactors," Master Thesis. in Chemical Engineering, University of Porto, Italy, 2010.

*Corresponding author email: alihellald@yahoo.com

Modeling Approach for the Factors Affecting the Performance of Polymer Electrolyte Membrane Fuel Cells PEMFC

M. Blal[1*], A. Benatillah[2], S. Laribi [3] , Y. Sahli [4]

[1*, 3, 4] Unite de Recherche en Energies Renouvelables en Milieu Saharien (URERMS), Centre de Developpement des Energies Renouvelables (CDER), 01000, Adrar, Algeria.

[2] Laboratory of LEESI, Faculty of Engineering Sciences, University of Ahmed Draia, Adrar, Algeria.

Abstract*— *A fuel cell polymer electrolyte membrane (PEM) is presented on the basis of mathematical models. In addition to providing power fuel cell to the overall performance, based on parameters related to materials and for improvement, these models are performance tools for exploring control strategies and Understanding of the contributions to the cell of the various components to guide researchers for improve performance. Changing patterns by varying the parameters affected PEMFC, in this work, the mathematical models are described and the PEMFC are programmed by using Matlab ® to simulate our studies. The fuel cell models are validated in different operating conditions and verified with the literature data. In the end, we reached the model 02 is applicable.

Key Words—performance, Modeling, validation, simulation, fuel cells.

I. INTRODUCTION

In our days the climate change and air pollution are negatives points for production and consumption of energy. This work proposes two dynamic models of fuel cell (PEM) fed with hydrogen and oxygen, which are produced by an electrolyser. In this study, we show that certain very important condition of pressure and temperature, as well as physical parameters, we have introduced the main physico- chemical phenomena in a fuel cell; this domain has been studied by many researchers. Rahimi et al. [1] improved the performance of PEM fuel cells effective to remove water by using channels gas. In this work are analyzed seven flow field, which the results showed that used two serpentine channels at the beginning and one at the end it has the best performance. So, the geometry of the channels affects the performance. Xiong et al. [2] studied the Modeling and Experimental Validation System fuel cell/battery for management and control the power. This study shows the power DC/ DC converters, including unidirectional and bidirectional by Utilized (TDC) to application the power management for system. Duplex mode of operation of the DC / DC converter is automatically enabled by a managing of power with (SOC).

Massimo et al. [3] provided the model of PEMFC regeneration exploiting hydrogen and oxygen to energy store. This presented PEMFC model for designing and explore the optimal fuel cells in Operating conditions.

Christophe et al. [4] have developed the fuel cell 3D-model and experimental verification for study effects of along cell surface. In this work was to monitor the behavior of fuel cells through its interaction with the local conditions thanks to the model. As well as analysing and structuring GDL and its impact on local conditions. The comparison was made in three very distinct systems humidity (humid mid dry, quite humid) between the model and the measures for local conditions (temperature and density current distributions) to validate the model and approach. Hong Sun et al. [5] presented a numerical study the effects of temperature and mass transfer high temperature on the PEM fuel cell. In this topic has been the development of a two-dimensional model, single-phase for the study of high temperature fuel cell with poly (2, 5-benzimidazole) (ab-PBI) membrane. Research results show that the temperature distribution is uneven in the membrane (ab-PBI) and the resistance is greatly influenced by the operating temperature. Other findings indicate that the increase in the degree of porosity and the cell temperature in the layer diffusion, deployment and lower layer thickness. Everyone improve the performance of PEM fuel cells. Vesselin et all. [6] They have put modeling and experimental characterization of PEM fuel cells in various gas compositions anode at high temperature.in this article the experimental campaign has been conducted on a single primary cell models that were built ad hoc, with all of the pure H_2 gas and increased anodic nutrition. That show different performance both with pure H_2 and with increasing gas operation. In this paper, we studied two models of PEMFC to investigation with previous studies with various internal and external parameters and conditions, at the end we got a number of conclusions that described in our present work.

II. THEORETICAL STUDY

1. *Assumptions*

* The gases used for chemical reactions are Hydrogen and oxygen.
* The system studied is one-dimensional.
* The membrane used is cation exchange.

*Corresponding author email: blal.physique@gmail.com

* The thickness of the left and right diffusion layer is constant and equal value.
* Water transport in the membrane, are not considered.
* No parasitic reaction.
* The membrane well be electronic insulator.
* The electrodes non-dissociated.
* The concentration of the protons H^+ in a membrane can be considered as constant.
* Considering that the water activity is equal to
* The membrane to be impermeable to Gases of hydrogen and oxygen.
* We consider that the water pressure is equal to 1 bar.

2. *Model PEMFC development*

We considered the reactions are oxidation of H_2 and the reduction of O_2 , that take at the anode and the cathode, respectively of a PEM FC are:

Anode: $2H_2 \rightarrow 4e + 4H^+$ (1)

Cathode: $O_2 + 4e + 4H^+ \rightarrow 2\,H_2O$ + heat (2)

The hydrogen gas flows in the anode channel diffuses through the porous GDL, and finally reaches the reaction sites, where it is electrochemically oxidized as described by Eq. (1). The protons transfer through the membrane. Oxygen flows in the cathode channel and transports to the GDL, where oxygen reacts with the protons coming from the anode through the membrane and the electrons coming from the external circuit to given by Eq (2). The reactions are shown in Fig (1). Was designed according in paper, [7].

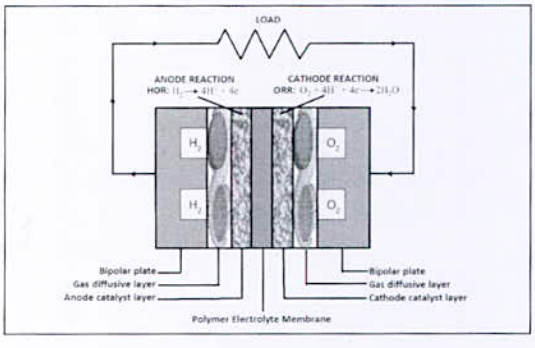

Fig. 1. Schematic diagram of PEMFC

III. MATH

1. *Output voltage*

Typical characteristics of fuel Cell are normally expressed in the form of a polarization curve, which is a plot of cell voltage versus cell current. To determine the voltage-current relationship of the cell, the cell voltage has to be defined as the difference between ideal voltages as it is described in the current section. The output voltage of the signal cell is given by [8].

$$U_{cell} = E - U_{activ} - U_{con} - U_m \quad (3)$$

The electric power produced by fuel Cell equals the product of voltage and current (I), thus power is given as follows:

$$P = I \times V_{cell} \quad (4)$$

The global PEMFC is composed of N cells, thus U is given as follows:

$$U = N \times (E - U_{activ} - U_{con} - U_{mem}) \quad (5)$$

With

$$E = E_0 + \left({}^{RT}/_{nF(a_{H_2O})} \right) \times \left[lin\left(P_{H_2} P_{O_2}^{\frac{1}{2}} \right) \right] \quad (6)$$

a_{H_2O} is the water activity ($a_{H_2O} = 1$) .Many authors use a value of 1.23 V for E_0 at standard temperature (T=298K) and pressure (P=1bar). The standard reversible cell voltage can be expressed as [9].

$$U_{activ} = (RT/\alpha nF) \times [\, lin(I/I_0)] \quad (7)$$

α is charge Transfer coefficient, I_0 exchange current.

$$U_{con} = -(RT/nF) \times \left[lin\left(1 - \left({}^{I}/_{I_{lim}}\right)\right)\right] \quad (8)$$

Where I_{lim} is the maximum current.

$$U_m = R_{mem} \times I \quad (9)$$

R_{mem} is the equivalent resistance of the membrane.

$$U_{mem\_con} = (RT/nF) \times [\, lin({}^{c_s}/_{c_{mem}})] \quad (10)$$

Where n is the number of electrons transferred in the reaction, c_{mem}, c_s are respectively the concentration in the membrane and into the solution.

$$U_{mem\ con} = U^{an}_{mem\ con} + U^{ca}_{mem\ con} \quad (14)$$

$$U^{an}_{mem\_con} = (RT/2F) \times \left[lin\left({}^{C_{H_2}}/_{c_{mem}}\right)\right] \quad (11)$$

$$U^{ca}_{mem\_con} = (RT/4F) \times \left[lin\left({}^{C_{O_2}}/_{c_{mem}}\right)\right] \quad (12)$$

$$U_{mem\_con} = (RT/nF) \times [\, lin({}^{c_s}/_{c_{mem}})] \quad (13)$$

Where C_{H_2} and C_{O_2} are the hydrogen and oxygen concentration at the layer diffusion interfaces membrane-solution, respectively. At the layer diffusion interfaces membrane-solution the molar concentration can be written by Fick's law since as [10].

$$\partial C/\partial x = -\left({}^{I}/_{nDFA}\right) \quad (14)$$

At anode $$\int_{C_{H_2}}^{C^{eq}_{H_2}} \partial C = -\int_0^{\delta} \left({}^{I}/_{2D_{H_2}FA}\right) \partial x \quad (15)$$

At cathode $$\int_{C_{O_2}}^{C^{eq}_{O_2}} \partial C = -\int_0^{\delta} \left({}^{I}/_{4D_{O_2}FA}\right) \partial x \quad (16)$$

$$C_{H_2} = \left({}^{I\delta}/_{2D_{H_2}FA}\right) + C^{eq}_{H_2} \quad (17)$$

$$C_{O_2} = \left({}^{I\delta}/_{4D_{O_2}FA}\right) + C^{eq}_{O_2} \quad (18)$$

Where $C^{eq}_{H_2}$ is the molar concentration of Hydrogen in Channel of fuel cell at equilibrium, $C^{eq}_{O_2}$ is the molar concentration of Oxygen in Channel of fuel cell at equilibrium, δ is the thickness of the diffusion layer, D_{H_2} is H_2 diffusion coefficient in diffusion layer, D_{O_2} is O_2 diffusion coefficient in diffusion layer. When the

*Corresponding author email: blal.physique@gmail.com

Hydrogen and Oxygen are ideal gases, the molar concentration in Channel of fuel cell can be expressed as :

At anode $C_{H_2}^{eq} = P_{an}/RT$ (19)

At cathode $C_{H_2}^{eq} = P_{ca}/RT$ (20)

Where P_{an} and P_{ca} are pressures of hydrogen and oxygen in Channel of fuel cell.When the hydrogen and oxygen are not ideal gases, the voltage increases, the current increases and gradients in the diffusion layers too. When the gradient is extreme, the concentration of the ion is constant in the membrane-solution interface. The resistance then increases sharply and the current is capped at a maximum value, called the limit current (I_{lim}). The molar concentration in Channels of fuel cell is denoted by [11].

$$C^{eq} = (\delta I_{lim})/2DFA \quad (21)$$

$$C_{H_2}^{eq} = \left(\delta I_{lim}/2D_{H_2}FA\right) \quad (22)$$

$$C_{O_2}^{eq} = \left(\delta I_{lim}/4D_{O_2}FA\right) \quad (23)$$

2. Numerical models results

We are performing simulations to characterize of different types of PEMFC by parameters of our validated numerical models. We have performed some Comparison From previously experimental on the fuel cell at three conditions of previous works, where the reference modele is consisted of 20 cell stack, which the Cells are related on series. We explored the effect of important Parameters on the PEMFC performance in curves following.

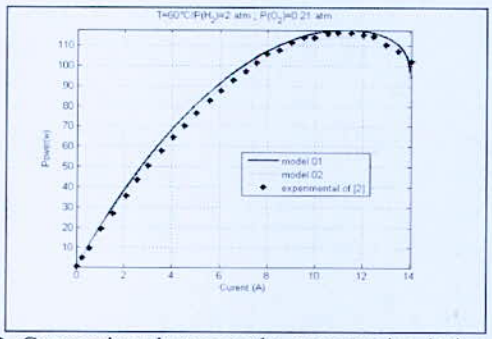

Fig. 2. Comparison between the present simulation and experimental results at low temperature

The models are verified with previous study of Ya-Xiong Wang, the validation of numerical models at 60°C is shown in **Fig.2**, which can say For Model 02 result a good agreement with experimental measurements [2]. **Fig. 3** explores the individual effects of the charge transfer coefficient on the power curve.

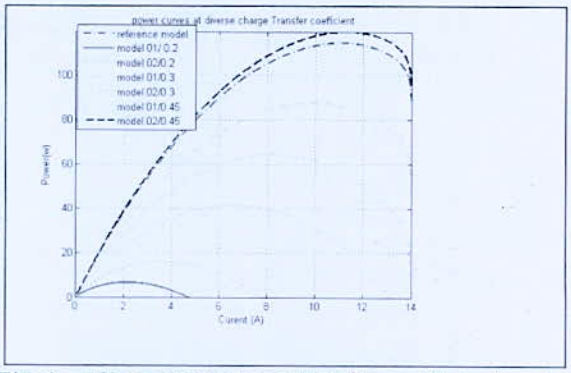

Fig. 3 . Effect of the charge transfer coefficient on the power curve

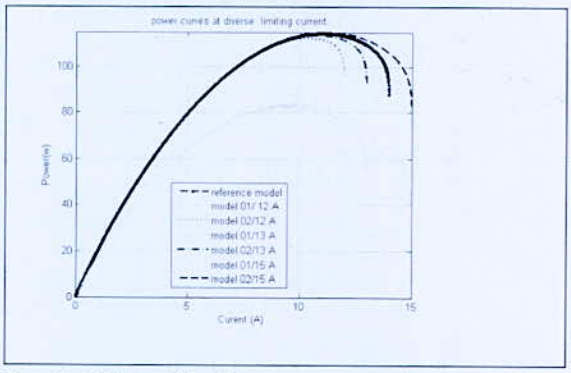

Fig. 4. Effect of limiting current on the power curve

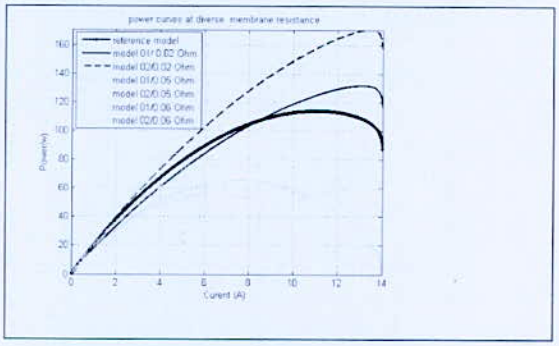

Fig. 5. effect of the membrane resistance on fuel cell power

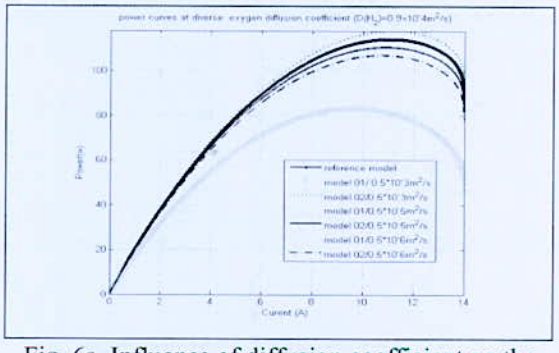

Fig. 6a. Influence of diffusion coefficient on the performance of the fuel cell(Hydrogen diffusion Coefficient)

*Corresponding author email: blal.physique@gmail.com

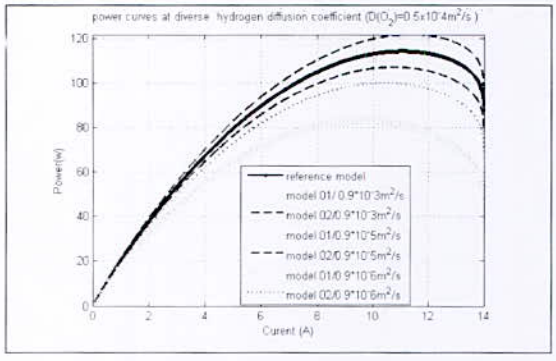

Fig. 6b. Influence of diffusion coefficient on the performance of the fuel cell(Oxygène diffusion coefficient)

In general, the power curve Increase with increasing transfer coefficient, the good performances obtained at value of transfer coefficient equal to α=0.45, Then **Fig. 4** show the effect of limiting current on the power curve in range 12 A-15A, the curves are stopped at the value of limiting current. We note that the effectiveness of the model 02 is better than the efficiency of the model 01, and that the model 02 is approached reference model at value of α=0.45. In **Fig.5** can be seen that the power decrease with the increase of membrane resistance, because the increase of the resistance results lead to an increase of lost power by membrane. The Influence of diffusion coefficient on the performance of the fuel cell are Illustrated in **Fig. 6** it is found that the hydrogen diffusion has an effect on the performance of the fuel cell is the Best by oxygen diffusion. In addition we observed that the model 01 has not changed by diverse diffusion Coefficient.

IV. CONCLUSION

The object of this document is to explain to the reader the various factors that influence the performance of the fuel cell for a clearer understanding of the electrochemical cell behavior. Experimental data of [2] which compared to our works is a Good agreement that thus validating the dynamic method utilized in this work. If you want to get the best must PEMFC, You should consider the following parameters: Increase the active area, decrease the membrane resistance and increase membrane exchange capacity. These three parameters can be manipulated through the preparation the membrane in industrially.

ACKNOWLEDGEMENTS

The work described in this paper was supported by the Research Unit in Renewable Energy (URERMS) Adrar, Algeria and University of Science and Technology Mohamed Boudiaf (USTOMB) Oran, Algeria. This research has been accomplished by all authors listed in the paper.

REFERENCES

[1] M. Rahimi, A.A. Ranjbar, A. Ramiar, E. Alizadeh, M. Aghaee. Improving PEM fuel cell Performance and effective water removal by using a novel gas flow field. Int J Hydrogen Energy (2015) 1-15.

[2] Ya-Xiong Wang, Kai Ou, Young-Bae Kim. Modeling and experimental validation of hybrid Proton Exchange membrane fuel cell/battery system for power management control. Int J Hydrogen Energy40 (2015) 11713-11723.

[3] Massimo Guarnieri,Piergiorgio Alotto, Federico Moro. Modeling the performance of Hydrogèn Oxygen unitized regenerative proton exchange membrane fuel cells for energy storage. J. Power Sources 297(2015)23-32.

[4] Christophe Robin, Mathias Gerard, Julien d'Arbigny. Development and experimental validation of a PEM fuel cell 2D-model to study heterogeneities effects along large-area cell surface. Int J Hydrogen Energy40 (2015) 10211-10230.

[5] Hong Sun, Chen Xie, Hao Chen, Saif Almheiri. A numerical study on the effects of temperature and mass transfer in high temperature PEM fuel cells with ab-PBI membrane. Applied Energy160 (2015)937-944.

[6] Vesselin Krassimirov Krastev, Giacomo Falcucci, Elio Jannelli. 3D CFD modeling and Experimental characterization of HT PEM fuel cells at different anode gas compositions. Int J Hydrogen Energy39 (2014) 21663-21672.

[7] Uktam R. Salomov, Eliodoro Chiavazzo, Pietro Asinari . Pore-scale modeling of fluid flow through gas diffusion and catalyst layers for high temperature proton exchange membrane (HT-PEM) fuel Cells. Computers and Mathematics with Applications 67 (2014) 393-411.

[8] Giaouris D, Stergiopoulos F, Ziogou C, Ipsakis D, Banerjee S, Zahawi B, et al. Nonlinear stability analysis and a new design methodology for a PEM fuel cell fed DC-DC boost converter. Int J Hydrogen Energy 23(2012) 18205e15.

[9] Harrison KW, Hern andez-Pacheco E, Mann M, Salehfar H. Semiempirical model for determining PEM electrolyzer stack characteristics. J Fuel Cell Sci Technol 3 (2006) 3-220.

[10] Marangio F, Santarelli M, Calı. M. Theoretical model and experimental analysis of a high Pressure PEM water electrolyser for hydrogen production. Int J Hydrogen Energy 34(2009) 58-1143.

[11] Weidong He,Bin Wang, James H. Dickerson. Overall concentration polarization and limiting Current density of fuel cells with nanostructured electrodes. Nano Energy 1(2012)828-832.

*Corresponding author email: blal.physique@gmail.com

Pure Hydrogen Generation from Methane Steam Reforming Reaction over Ru/SiO_2 Catalyst in a Packed Bed Membrane Reactor

A. Yahia-Cherif* and L. Chibane

Laboratoire de Génie des Procédés Chimiques (LGPC), Département de Génie des procédés, Faculté de Technologie, Université Ferhat Abbas Sétif 1, 19000, Sétif, Algérie.

Abstract—**In this work, the production of high-purity hydrogen from the methane steam reforming reaction carried out in a fixed-bed catalytic reactor integrating a hydrogen permselective membrane was numerically studied. For this objective, some assumptions have been used to develop an isothermal model in which the influence of various operating parameters on the performance of the membrane reactor has been studied. The reactor under study was packed with Ru/SiO_2 catalyst particles. Under the optimal conditions, it was found that the optimal H_2/CO ratios, which are desirable for the Fischer-Tropsch process, can be obtained between 550°C and 600°C. The conversion of methane was highly affected by the reaction pressure; in other hand the increased reaction pressure increases the driving force in which affect positively the amount of the hydrogen removal, and consequently the conversion was improved. The concept of palladium-membrane reactor could operate at the optimal conditions can produce high amount of pure hydrogen recovery (3.2) equivalent to the nearly complete conversion of methane (99.66%).**

Key words— Methane steam reforming, Hydrogen production, Membrane reactor.

I. INTRODUCTION

Hydrogen is available in sufficient quantities in fossil fuels and water. This could result in a widespread use of hydrogen as a source of energy and substitution for fossil fuel. This step will lead to a situation where the energy will be obtained exclusively from renewable sources and where natural gas and oil will be used only as raw material [1]. Currently, about 80-85% of the hydrogen demand in the world was produced by methane steam reforming process [2], this demand is ever increasing both in the petrochemical industries as a feedstock for a variety of processes, and in the petroleum processing industries for preliminary hydro processing of a wide range of feedstocks. Clean energy applications such as fuel cells are also other important aspects of hydrogen usage. Other applications of hydrogen include synthesis gas usage for a variety of processes such as Fisher–Tropsch synthesis [3-6].

The SRM is a reversible and highly endothermic process. Conventionally, it consists to reacts the methane gas with the steam of water carried out in a packed bed at high temperature (700-1000°C) and at a pressure range of (3-4 MPa) with S/C of (2.5). Under these conditions, the methane conversion is about 80%. It drives to the obtaining of a mixture gas rich in hydrogen, which H_2/CO ratio equal to 3 [7, 8].

II. THEORETICAL STUDY

1. Abbreviations and Acronyms

D_{int}	Reactor internal diameter, m
E_p , ΔE_p	Activation energy of Hydrogen permeation, J/mol
F	Molar flow rate, mole/s
$F_{H_{2,p}}$	Molar flow rate of hydrogen in membrane side, mole/s
ΔH	Reaction enthalpy, J/mol
I	Sweep gas to methane ratio
J, J_i	Permeation flux of hydrogen through the Pd membrane or the spices i, mole/s.m²
k	Kinetic constant
K	Equilibrium constant
K_i	Adsorption Constant
L, l	Reactor length, m
P	Partial Pressure, Pa
P_0	Standard pressure in the permeate side, Pa
P_i	Partial pressure of compound i, Pa
$P_{r,i}$	Partial pressure of the compound i in the reaction zone, Pa
$P_{p,i}$	Partial pressure of the compound i in the permeation zone, Pa
Q	Specific permeability, mole. m/m². s.Pa.
Q_0	Pre-exponential factor
R	Reaction rate, kmol/kg.h
R	Gas constant = 8.314 J/mole.K
T	Temperature, K
W	Mass of catalyst, g
X_{CO_2}	Carbon dioxide conversion
X_{CH_4}	Methane conversion
Y_{H_2}	Hydrogen recovery
Z	Axial coordinate, m
Greek symbols	
δ	Membrane thickness, m
η	Effectiveness factor
υ_{ij}	Stoichiometric coefficient of compound i for the reaction j,
ρ	Density, kg/m³
Ω	Right section of the reactor, m²
Acronyms	
F-T	Fischer-Tropsch
GHSV	Gas Hourly Space Velocity
H/C	Hydrogen to Carbon
MSR	Methane Steam Reforming
S/C	Steam to methane ratio
WGS	Water Gas Shift
Subscripts/superscripts	
0	Reactor Input

* A. YAHIA CHERIF: ycherif2014@hotmail.com

i Reaction species i
j Reaction j
p Permeation zone
r reaction zone
s Solid

2. Reactions kinetics

MSR process is limited by a thermodynamic equilibrium of the following three reactions:

$$CH_4 + H_2O \rightleftharpoons CO + 3H_2 \qquad \Delta H^{\circ}_{298K} = 206\,kj/mol \quad (1)$$

$$CO + H_2O \rightleftharpoons CO_2 + H_2 \qquad \Delta H^{\circ}_{298K} = -41\,kj/mol \quad (2)$$

$$CH_4 + 2H_2O \rightleftharpoons CO_2 + 4H_2 \qquad \Delta H^{\circ}_{298K} = 165\,kj/mol \quad (3)$$

The high temperature operation causes strong limitations, such as carbon formation and large energy consumption by the processes. One possible way to liberate this reaction from these limitations consists to carry out the MSR at low temperature. Under this condition, the thermodynamic equilibrium was shifting and is favored also by removing hydrogen from the products mixture. This has been done by using reactors that combine steam reforming and hydrogen-permeable membranes [6, 9]. The fixed-bed catalytic reactors equipped with hydrogen perm-selective membranes are an interesting alternative for producing high purity hydrogen in one single step. This reduces the size of the reactor and the required amount of catalyst.

The kinetics of the catalytic steam reforming of methane (MSR) over Ru/SiO$_2$ is as follows [7, 10]:

$$r_1 = \frac{k_1}{p_{H_2}^{2.5}} p_{CH_4} p_{H_2O}(1-\beta_1), \quad \beta_1 = \frac{p_{CO} p_{H_2}^3}{p_{CH_4} p_{H_2O} K_{eq1}} \quad (4)$$

$$r_2 = \frac{k_2}{p_{H_2}} p_{CO} p_{H_2O}(1-\beta_2), \quad \beta_2 = \frac{p_{CO_2} p_{H_2}}{p_{CO} p_{H_2O} K_{eq2}} \quad (5)$$

$$r_3 = \frac{k_3}{p_{H_2}^{3.5}} p_{CH_4} p_{H_2O}^2(1-\beta_3), \quad \beta_3 = \frac{p_{CO_2} p_{H_2}^4}{p_{CH_4} p_{H_2O}^2 K_{eq3}} \quad (6)$$

k_j are the kinetic constants of reactions given by the Arrhenius law:

$$k_j = k_{0,j} exp(-\Delta E_j / RT) \quad (7)$$

K_{eqj} (j= 1− 3) are the equilibrium constants defined by the Vant'Hoff law:

$$K_{eqj} = k_{eq0,j} exp(-\Delta H_j / RT) \quad (8)$$

The equilibrium and kinetic constants of used reactions are illustrated respectively in Table I.

3. Fixed bed membrane Reactor model

Fig. 1, shows the schematic of the studied membrane reactor in which filled with Ru/SiO2 catalyst (density: 700 kg/m3). The catalyst bed packed inside the cylindrical membrane was considered to be of 6.2 ×10-2m length and 9.5×10-3 m diameter.

The considered membrane consists of a composite material with cylindrical shape, formed by three layers (from inside to outside): porous stainless steel (SS) support, yttria-stabilized zirconia (YSZ) interphase, and palladium active layer [11-13].

Table II shows the most significant properties of the membrane used in this study. The membrane is selective to hydrogen, and the permeation being controlled by diffusion of hydrogen in the palladium layer (according to Sievert's law). The shell side of the membrane is the annular space located between the membrane and the external tube. It constitute the permeate side, and provides heat through the external tube.

TABLE I
KINETIC AND EQUILIBRIUM CONSTANTS AND FOR THE RU/SIO$_2$ CATALYST BASED [10]

N°	K_{eqj}	$k_j^{500°C}$	E_{aj}
1	$exp(53.14 - 26830/T)$	$4.6 mol\, kg_{cat}^{-1} s^{-1} Pa^{0.5}$	$140\ kj\ mol^{-1}$
2	$exp(-4.04 - 4400/T)$	$1.7\ 10^{-4} mol\, kg_{cat}^{-1} s^{-1}$,	$4.2\ kj\ mol^{-1}$
3	$exp(49.10 - 22430/T)$	$0.41 mol\, kg_{cat}^{-1} s^{-1} Pa^{0.}$	$144\ kj\ mol^{-1}$

The hydrogen partial pressure gradient required to obtain important permeation rates is achieved by maintaining the shell side at a constant total pressure (1 bar), and by means of a sweep gas. In this work, steam has been considered as sweep gas because can be easily separated from hydrogen by condensation after the reactor [10]. The sweep gas is fed co-currently and the membrane reactor is assumed to operate under steady state with negligible diffusion limitations due to the used fine catalyst particles.

The mole balance for all components and hydrogen in the reaction side are given by the following equations:

$$\frac{dF_i}{dl} = \rho\, \Omega \sum_{j=1}^{3} \eta_{ij} \upsilon_{ij} r_j \begin{cases} i = CH_4, H_2O, CO, CO_2 \\ j = 1, 2\ and\ 3 \end{cases} \quad (9)$$

In the permeation side, the hydrogen mole balance is given by [10]:

$$J_{H_2} = \frac{Q}{\delta_{Pd}} \left[\left(p_{H_{2r}}\right)^{0.5} - \left(p_{H_{2p}}\right)^{0.5} \right] \quad (10)$$

For CH_4 and CO_2 the mole balance as function of conversions is as follows:

$$\frac{dX_{CH_4}}{dz} = \frac{W}{F^0_{CH_4}} (r_1 + r_3) \quad (11)$$

$$\frac{dX_{CO_2}}{dz} = \frac{W}{F^0_{CH_4}} (r_2 + r_3) \quad (12)$$

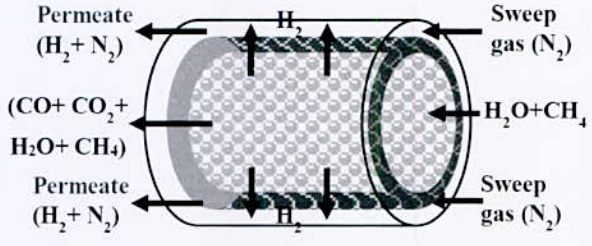

Fig. 1. Schematic of the fixed bed membrane reactor

* A. YAHIA CHERIF: ycherif2014@hotmail.com

The hydrogen recovery [14]:

$$\frac{dY_{H_2}}{dz} = \pi D_{int} \frac{Q}{F^0_{CH_4} \delta_{Pd}} \left[\left(p_{H_{2r}}\right)^{0.5} - \left(p_{H_{2p}}\right)^{0.5} \right] \quad (13)$$

TABLE II
MEMBRANE PROPERTIES

Shell internal diameter, D_{int}	1.27×10^{-2} m
Shell external diameter, D_{ext}	1.52×10^{-2} m
Pd thickness, δ_{Pd}	27×10^{-6} m
Hydrogen selectivity	100 %
Specific permeability	$Q = 1.1 \times 10^{-8} exp\left(-\frac{12600}{R}\left(\frac{1}{T} - \frac{1}{673}\right)\right) mol/m\,s\,Pa^{0.5}$
Shell total pressure P_t	0.101 MPa

III. RESULTS AND DISCUSSION

The aim of this work is to study the effect of different operating parameters on performance (methane conversion: X_{CH_4}, and hydrogen recovery: Y_{H_2}) of a palladium-based membrane reactor in which the steam reforming reactions take place under the following conditions: temperature (400°C-600°C), Pressure (1-5bar) and space velocity (3000 - 12000 h^{-1}).

The conversion of methane and of carbon dioxide were calculated by using the equations obtained from the mass balances in the gas phase (11 and 12) and the amount of hydrogen recovery through the palladium membrane was obtained by using eq. (13). This system of differential equations was solved numerically by *ode15s* which is an algorithm of the Runge-Kutta method, (using the software MATLAB R2012a).

A systematic analysis was carried out at temperature range (300-600°C) and under a pressure (P_r =3 bar) and with steam to carbon ratio (S /C) of 1.75. Fig.2 shows the influence of temperature on the methane convection, on the amount of hydrogen recovery, and on the CO and CO_2 selectivity. When the GHSV is equal to 8000 h^{-1}, the CH_4 conversion and the CO_2 selectivity increases with increasing temperature, this is due to the kinetics of the steam reforming reaction. it was obtained that the increasing temperature from 350°C to 550°C possess a positive effect on methane conversion and on hydrogen recovery (for example it passes a 0.67 to 1.26) by favoring the endothermic reactions. For the temperatures higher than 500°C, the CO_2 selectivity remains constant, which may be explained by the occurrence of the exothermic reverse WGS reaction. For the same temperatures, it was found that the optimal H_2/CO ratios, which are desirable for the F-T process, can be obtained between 550°C and 600°C.

The conversion of methane was highly affected by the reaction pressure; in other hand the increased reaction pressure increases the driving force in which affect positively on the amount of the hydrogen removal, and consequently the conversion was improved as indicated in Fig. 3.

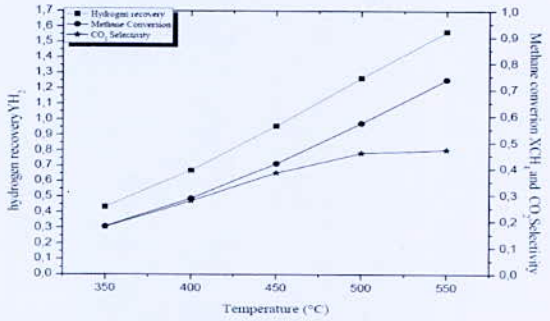

Fig. 2. Temperature effect on methane conversion, CO_2 selectivity and the amount of hydrogen recovery (S/C=1.75, Pp=1bar, Pr=3 bar, I=3)

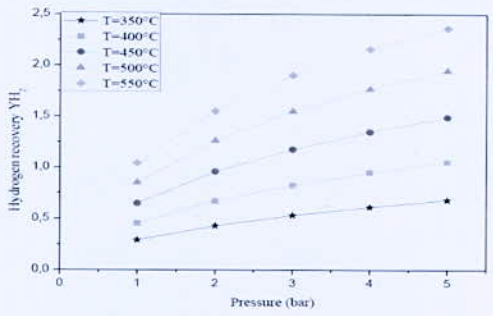

Fig. 3. Effect of pressure in the reaction zone on hydrogen recovery (S/C=1.75, Pp=1bar, I=3)

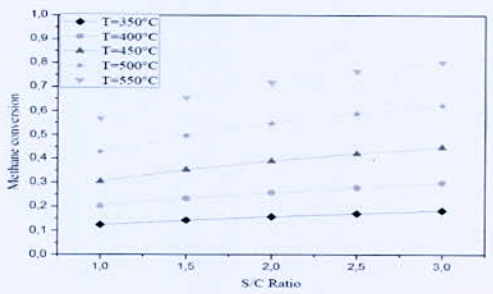

Fig. 4 (a). Effect of (S/C) ratio on Methane conversion (S/C=1.75, Pp=1bar, I=3)

The study of the effect of the steam to water molar ratio shows that increasing this ratio increases the conversion of methane, for (S/C=1.75) we obtained (71.6%) of methane conversion (Fig. 4(a)).

The hydrogen recovery for the used game of temperatures (350°C to 550°C). Except for hydrogen removal, it was found that there was an optimal value of this ratio (1.75) conducting for a maximum of hydrogen recovery as presented by Fig. 4 (b). An increase of S/C ratio above 1.75 improves hydrogen production by reforming reactions. However, it will risk having a dilution of hydrogen in the reaction zone caused by the excess of steam, which reduces the amount of hydrogen recovered.

* A. YAHIA CHERIF: ycherif2014@hotmail.com

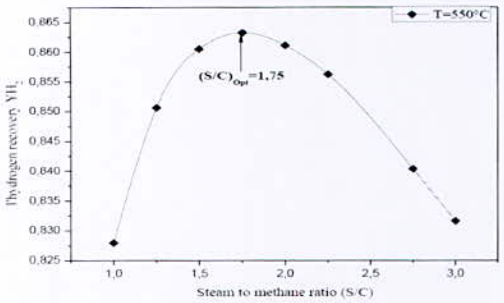

Fig. 4 (b). Effect of (S/C) ratio hydrogen recovery (S/C=1.75, Pp=1bar, I=3)

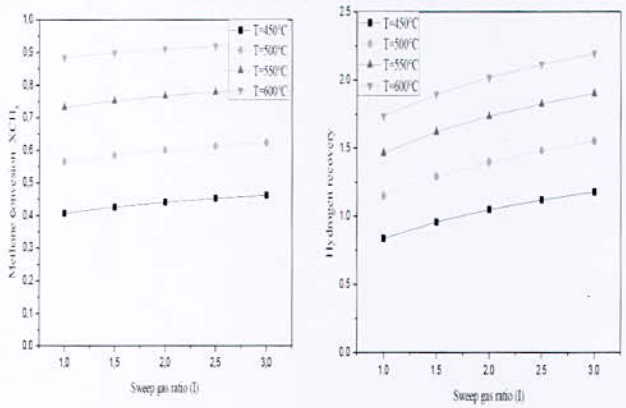

Fig. 5. Effect of sweep gas ratio on Methane conversion and Hydrogen recovery (S/C=1.75, Pp=1bar, I=3)

The effect of the parameters describing the permeate side show that the good performance could be obtained when a thin layer of Pd was deposited during membrane preparation. The effect of the sweeping gas show that the conversion and the removal hydrogen increase with sweep ratio increasing, we had (61% methane conversion and 1.5 hydrogen recovered). Therefore, the hydrogen removal from the permeate side across a Pd thin layer can shift the equilibrium significantly in the direction of hydrogen production (Fig. 5).

IV. CONCLUSION

Methane steam reforming over a Ru/SiO_2 catalyst has been studied at temperatures (350-600°C) by means of a mathematical 1D model. The influences of the main operating variables on the membrane reactor were studied systematically.

The obtained results show that the conversion of methane increases with increasing temperature and steam to methane ratio. Consequently, the optimum operating conditions were determined. It was found that, within the variables range considered, the membrane reactor performs exultant which methane conversion as a 99.66% and the amount of the hydrogen removed from the permeate side was about 3.2. It appears that higher H_2O/CH_4 ratios than stoichiometry are necessary to avoid carbon formation. Finally, a temperature of 500 to 600°C is necessary in order to obtain suitable conversion values.

REFERENCES

[1] W. Arpe, "Chimie Organique Industrielle", 3rd ed. Ed. *De Boeck Université s.a.*, 2000, pp.1-25.

[2] AP. Simpson, AE.Lutz, " Energy Analysis of Hydrogen Production via Steam Methane Reforming", *Int. J. Hydrogen Energy*, vol.32, pp. 4811-4820, 2007.

[3] B. Bao, M. M. El-Halwagi, N. O. Elbashir, "Simulation, Integration, and Economic Analysis of Gas-To-Liquid Processes", *Fuel Processing Technology, vol.*91, pp.703-713, 2010.

[4] M. A. Nieva, M. M. Villaverde, A. Monzón, T. F. Garetto, A. J. Marchi, " Steam-Methane Reforming at Low Temperature on Nickel-Based Catalysts ", *Chem. Eng. J.*, vol.235, pp. 158-166, 2014.

[5] A. M. Dehkordi, M. Memari, "Compartment model for steam reforming of methane in a membrane-assisted bubbling fluidized-bed reactor", *Int. J. hydrogen energy*, vol. 34, pp. 1275-1291, 2009.

[6] E. Juste., " Elaboration de Réacteurs Catalytiques Membranaires a Microstructures et Architectures Contrôlées", *Ph.D. dissertation, Dept. Tech., Limoges Univ.*, pp. 4-13, 2008.

[7] M.A. Soria, C. Mateos-Pedrero, P. Marín, S. Ordóñez, A. Guerrero-Ruiz, I. Rodríguez-Ramos, "Kinetic Analysis of the Ru/SiO_2-Catalyzed Low Temperature Methane Steam Reforming", *Applied Catalysis A: General,* vol. 413, pp. 414366-414374, 2012.

[8] Chen Z, Grace JR, Lim CJ, Li A, " Experimental Studies of Pure Hydrogen Production in a Commercialized Fluidized-Bed Membrane Reactor with SMR and ATR Catalysts ", *Int. J. Hydrogen Energy,* vol. 32,pp.2359-66, 2007.

[9] T. Tsuru, T. Morita, H. Shintani, T. Yoshioka, M. Asaeda, " Membrane Reactor Performance of Steam Reforming of Methane Using Hydrogen-Permselective Catalytic SiO_2 Membranes", J. *Memb. Science,* vol.316, pp.53-62, 2008.

[10] P. Marín, Y. Patiño, F. V. Díez, S. Ordóñez, "Modelling of Hydrogen Perm-Selective Membrane Reactors for Catalytic Methane Steam Reforming", *Int. J. Hydrogen Energy,* vol.37, pp. 18433-18445, 2012.

[11] R. Sanz, JA. Calles, D. Alique, L. Furones, S. Ordóñez, P. Marín et al.,"Preparation, Testing and Modelling of a Hydrogen Selective Pd/YSZ/SS Composite Membrane" *Int. J. Hydrogen Energy,* vol.36 pp. 15783-15793, 2011.

[12] G.Barbieri, A.Brunetti, G. Tricoli, E. Drioli,"An Innovative Configuration of a Pd-Based Membrane Reactor for the Production of Pure Hydrogen. Experimental Analysis of Water Gas Shift", *J. Power Sources,* vol. 182, pp. 160-167, 2008.

[13] W. Yu, T. Ohmori, S. Kataoka, T. Yamamoto, A. Endo, M. Nakaiwa et al., "A Comparative Simulation Study of Methane Steam Reforming in a Porous Ceramic Membrane Reactor Using Nitrogen and Steam as Sweep Gases", *Int. J. Hydrogen Energy,*vol.33,pp.685-692,2008.

[14] J. S. Oklany, K. Hou, R. Hughes, "A Simulative Comparison of Dense and Microporous Membrane Reactors for the Steam Reforming of Methane", *Applied Catalysis A: General*, vol. 170, pp.13-22, 1998.

* A. YAHIA CHERIF: ycherif2014@hotmail.com

CFD Study of Methane-Hydrogen Behavior in a Non-Premixed Combustion Chamber

M. E. H. Attia[1*], A. Boukhari[2], F. Bouras[1] and Z. Driss[3]

[1*] Department of Physics, Faculty of Science, University of El Oued, 39000 El Oued, Algeria.
[2] Department of Mechanical Engineering, Faculty of Technology, University of El-Oued, 39000 El-Oued, Algeria.
[3] Laboratory of Electro-Mechanic Systems (LASEM), ENIS, University of Sfax, Tunisia.

Abstract—**In this paper, the numerical results of the study of a turbulent flame of methane-hydrogen/air generated by a cylindrical burner are presented. The numerical simulations are carried out using the CFD code "FLUENT" and "Gambit" for the meshing process. The finite volume method was used to solve the Navier-Stokes equations governing the flow. The coupling of the LES/PDF models is used to model the turbulence/chemistry interaction in the system's transport equations. The results of the calculations are expressed and analyzed in terms of axial velocity, temperature and mass fraction of carbon monoxide CO. The results of the numerical calculations are compared and validated against experimental data. In addition, the same parameters considered above are used in the study of the combustion behavior of CH_4/H_2 fuels. The obtained results confirm the fact of considering hydrogen as a clean non-polluting fuel compared to methane, since it has no carbon monoxide emissions in combustion products. Besides this fact, the hydrogen gas velocity in the flame is significantly higher by comparing it to the methane gas velocity.**

Key words— Non-Premixed Combustion; Turbulence; Hydrogen; Methane; CFD Simulation.

I. INTRODUCTION

Today, with increasing concerns about the reduction of energy production and protection of the environment, research on alternative fuels has been widely studied in recent years by a large number of researchers. In addition, the increasingly rigorous regulation of CO_2 emissions on the one hand and the depletion of fossil fuel reserves on the other have prompted the scientific community to find alternatives to these fuels. Indeed, the increase in the car fleet has led to an increase in the consumption of conventional fuels, which are responsible for the continuous increase in emissions of pollutants. Research in the fields of fuel quality and combustion will lead to a gradual reduction of pollutant emissions, increased environmental protection and improved living conditions. The addition of hydrogen to methane has an effect on reducing the ignition time of the mixture and increasing the ignition advance and reducing pollution [1].

In this context, natural gas offers many economic and environmental benefits. It is mainly made up of methane, natural gas at lower levels of pollutant emissions compared to other fossil fuels. With regard to carbon dioxide, the combustion of natural gas generates respectively 30 to 40% less than oil and coal with the same amount of energy consumed. However, emissions of pollutants from natural gas combustion can be reduced. An interesting alternative is to substitute hydrogen for part of the natural gas, creating a less polluting hybrid fuel. This solution is a first step towards a hydrogen economy in order to gradually adapt infrastructures, standards and regulations as well as inform and prepare the public [2]. Evatt and al. [3] used the Direct Numerical Simulation to study the effects of H_2 enrichment on lean premixed methane–air flames. They found that lower CO emissions per unit fuel consumption are observed for the enriched flame, consistently with experimental data. In their experimental work, Akansu and al. [4] considered to control the effect of a spark ignition engine of mixtures of hydrogen and methane. Although, they obtained the test results for a four-cylinder engine with mixtures of hydrogen in methane of 0, 10, 20 and 30% by volume. Showing that NO emissions increase, HC, CO and CO_2 emission amounts decrease with increasing hydrogen percentage.

The main objective was the numerical simulation of non-premixed turbulent combustion in a cylindrical combustion chamber supplied by methane-hydrogen/air. We used the commercial CFD code FLUENT. Three parameters are considered: the average axial velocity, the temperature and the mass fraction of the carbon monoxide CO. In the first step, we validate the coupling of the large eddy simulation (LES) models and the probability density function (PDF) approach [5,6] with the experimental data in the same stations and the same conditions. The results show that the select models give a satisfactory agreement with all the regions considered. In the second step, the same parameters considered previously are used in the study of the combustion behavior of methane-hydrogen fuels. The two CH_4-H_2 fuels are compared to choose the least carried out on the environment.

II. BURNER CONFIGURATION

The configuration which confines the combustion chamber is given in figure 1. The cylindrical combustion chamber, presenting a radius R4=61.15 mm and a length L=1 m, is supplied by two coaxial jets CH_4 or H_2/air. The central jet presents an internal radius equal to R1=31.57 mm and an outer radius R2=031.75 mm, in order to inject methane or hydrogen with an inlet mass flow rate Q1=7.2 g/s at a temperature T1=300 K. The annular jet has an internal radius equal to R3=46.85 mm, which injects air with an inlet mass flow equal to Q2=137

*Corresponding author email: attiameh@gmail.com

g/s and a preheated temperature T2=750 K. The chamber of combustion is pressurized by a value equal to p=3.8 atm and to a constant temperature wall equal to T=500 K [5,6]. In the aim to present and compare our results we have carried out the simulations based on the normalization of lengths (x-position and radii) and velocity using characteristic values, i.e. injector radius (R≡R3) and inlet air velocity (U ≡V2).

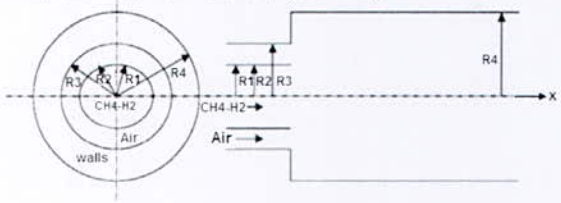

Fig. 1 Schematic presentation of the burner

III. GOVERNING EQUATIONS

In this paper, we studied the behavior of non-premixed turbulent combustion in three dimensions using numerical simulation. The governing equations for the compressible flow can be written in Cartesian coordinates as summarized in Table I.

TABLE I
GOVERNING EQUATIONS

Description	Equation
Continuity	$\frac{\partial \overline{\rho}}{\partial t} + \frac{\partial}{\partial x_i}(\overline{\rho u_i}) = 0$
Momentum	$\frac{\partial \overline{\rho u_i}}{\partial t} + \frac{\partial}{\partial x_j}(\overline{\rho u_i}\widetilde{u_j}) = -\frac{\partial}{\partial x_j}[\overline{\rho}(\overline{u_i u_j} - \widetilde{u_i}\widetilde{u_j})] - \frac{\partial \overline{p}}{\partial x_j} + \frac{\partial \overline{\tau_{ij}}}{\partial x_i}$
Energy	$\frac{\partial}{\partial t}\overline{\rho h} + \frac{\partial}{\partial x_i}(\overline{\rho u_i}\widetilde{h}) = -\frac{\partial}{\partial x_i}[\overline{\rho}(\overline{u_i h} - \widetilde{u_i}\widetilde{h})] + \frac{\partial \overline{p}}{\partial t} + \frac{\partial}{\partial x_j}\overline{u_j \tau_{ij}}$
Species	$\frac{\partial}{\partial t}\overline{\rho Y_f} + \frac{\partial}{\partial x_i}(\overline{\rho u_i}\widetilde{Y}_f) = -\frac{\partial}{\partial x_i}[\overline{\rho}(\overline{u_i Y_f} - \widetilde{u_i}\widetilde{Y}_f)] + \overline{\omega}_f$
Thermo-dynamic state	$\overline{p} = \overline{\rho} R_m \widetilde{T}$

In these equations, the unresolved Reynolds stresses $(\overline{u_i u_j} - \widetilde{u_i}\widetilde{u_j})$ require a subgrid scale turbulence model. The unresolved species fluxes $(\overline{u_i Y_f} - \widetilde{u_i}\widetilde{Y}_f)$ and the enthalpy fluxes $(\overline{u_i h} - \widetilde{u_i}\widetilde{h})$ require a probability density function (PDF) approach. The filtered chemical reaction rate is characterized by $\overline{\omega}_f$.

The LES models and the PDF approach explained and detailed in previous work [5,6].

IV. RESULTS AND DISCUSION

Firstly, we have validated our trend to couple the LES models and the PDF approaches against the experimental data [6] at same stations and for same conditions. Secondly, we have exploited the same parameters considered previously to study the combustion behaviour of methane-hydrogen fuels.

1. Numerical Validation

1.1 Axial Velocity

Comparison of the predicted radial profiles of the mean axial velocity with the experimental data in the stations x/R=0.14 and x/R=4.67 are presented in figure 2. In fact, the numerical and experimental profiles have almost the same tendency. Thus, the mean relative gap between the numerical calculations and the experimental reference data [6] is about 7%, which is almost acceptable in combustion applications. The high values of the axial velocity are located in the center of the burner presented by the peaks in the x/R=0.14 and x/R=4.67 stations. In the last station x/R=4.67, the difference between the numerical profile and the experimental profile may be due to the fact that the fully developed methane and air intake conditions were assumed in the simulations. However, in the experiment, the inlet flow devices were located only a short distance upstream of the burner. In the two recirculation regions shown in schematic presentation of the burner (figure 1), the negative axial velocity values are observed due to turbulence. The first region located at the fuel jet is due to the delay of the generated flow. However, for the second region it is caused by the sudden change between the conditions of entry of coaxial jets (CH_4/Air).

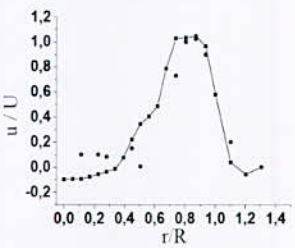

(a) x/R=0.14

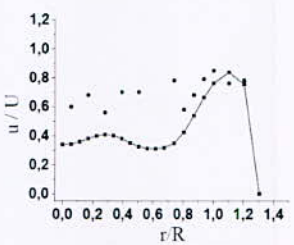

(b) x/R=4.67

Fig. 2 Radial profiles of average axial velocity, ___ Simulation, • Experiment [6]

1.2 Temperature

Figure 3 shows the comparison of the radial profiles of the mean temperature obtained by the numerical simulation of the coupled LES/PDF models and the experimental data considered in reference [6], for the same stations defined by x/R=1.57 and x/R=4.52. Numerical and experimental profiles have almost the same tendency. The mean relative gap between the numerical calculations and the experimental data is about 10%, which concedes satisfactory agreement between

*Corresponding author email: attiameh@gmail.com

simulations and experiments. The high temperature values are located around the flame zone and begin to decrease with the radial distance to reach the temperature of the cooling isothermal wall at T=500 K. The shear layers which are in the same zone where fuel and air meet. The shear zone is created to improve the mixing of the two coaxial jet streams (CH_4/Air) to supply the combustion chamber with a rich mixture. Furthermore, the apex based on the temperature profiles is attenuated downstream of the burner. As a result, this disagreement is due to regions with high temperature fluctuations and to the difficulty of perfectly ensuring the conditions of experience of the walls.

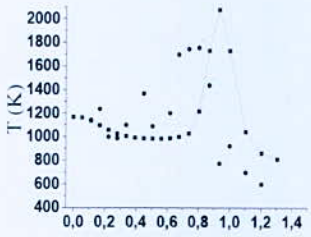

(a) x/R=1.57

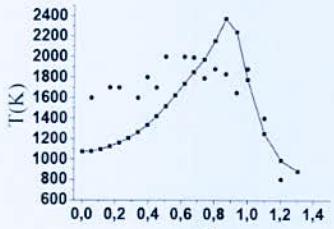

(b) x/R=4.52

Fig. 3 Radial profiles of average temperature, ___ Simulation, • Experiment [6]

1.3 Mass Fraction of Carbon Monoxide CO

Figure 4 illustrates the comparison of the numerical and experimental radial profiles of the mass fraction of carbon monoxide CO for different stations of the burner defined by x/R=0.21 and x/R=3.84. In fact, the numerical calculations of the CO mass fraction significantly present a good agreement with the experimental data [6]. The gap between the numerical results and the experimental data is about 5%. The high values of the CO mass fraction located in the center of the combustion chamber decrease as they move away from the burner center. The radial profiles of the mass fraction of CO have the same tendency with the radial temperature profiles which explain the high CO values in the reaction zone (the flame zone). This zone is rich and reactive and produces monoxide of carbon CO. In the first station x/R=0.21, the CO values are low compared to the second station x/R=3.84. Turbulence is caused by the mixing effect of fuel and air, which allows their mixing and combustion to produce CO with high values.

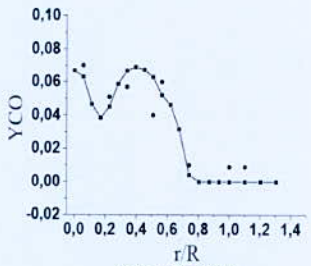

(a) x/R=0.21

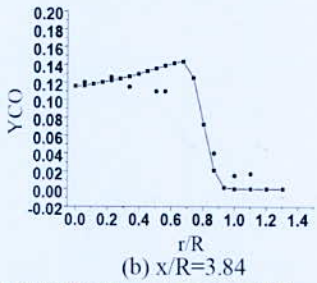

(b) x/R=3.84

Fig. 4 Radial profiles of average CO mass fraction, ___ Simulation, • Experiment [6]

2. Comparison of H_2 and CH_4 Fuels

2.1 Axial Velocity

Figure 5 illustrates the comparison between the mean axial velocity of H_2 and CH_4 in different stations, defined by x/R=0.14 and x/R=4.67, in a three-dimensional combustion chamber. These profiles are characterized by peaks in the stations. The numerical profiles of H_2 and CH_4 have almost the same tendency especially in the first station, and the values of axial velocity of hydrogen elevated with respect to the methane velocity especially in the last station. The values of rate of hydrogen velocity are greater than 1. In these conditions, the values of the velocity of the H_2 are high in the middle of the combustion chamber compared with the speed of CH_4. Thus, we can also see the H_2 speed profiles completely applicable on the profiles of the CH_4 near the burner walls in both stations. Indeed, it has been observed that the velocity of hydrogen is greater than the speed of methane almost the molar mass of hydrogen is less than the molar mass of methane.

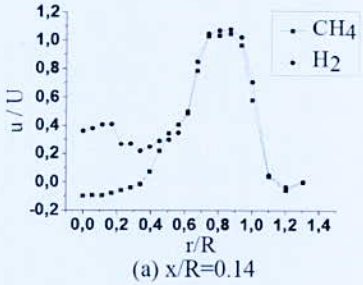

(a) x/R=0.14

*Corresponding author email: attiameh@gmail.com

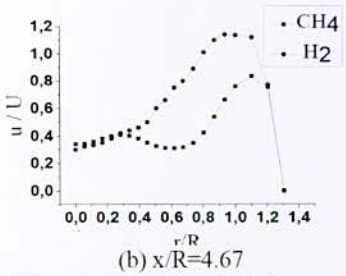

(b) x/R=4.67

Fig. 5 Profiles of the axial velocities considered for hydrogen and methane

2.2 Temperature

Figure 6 shows the distribution of the average temperature of hydrogen and methane. The radial temperature profiles for the two fuels have the same tendency, are presented by the peaks in the stations defined by x/R=1.57 and x/R=4.52. The temperature high values are in the flame zone for both H_2 and CH_4 fuels, as this area is the same area of chemical reactions. The positions of the peaks in all stations move at the jet of air for the case of hydrogen, with a slight increase compared to the values of the temperature of the methane. In the middle of the combustion chamber, the values of the temperature of the methane is equal to T=1200 K and decreases at the value of the hydrogen temperature until T=600 K, in both stations. The observed shift of CH_4 and H_2 temperatures obtained by calculations is owed to the molar masses difference between theses fuels, since the chemical composition is the key parameter in rising combustion temperatures.

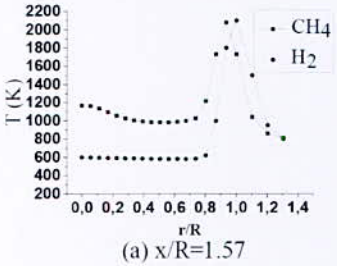

(a) x/R=1.57

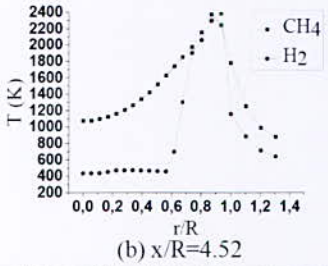

(b) x/R=4.52

Fig. 6 Profiles of the temperatures considered for hydrogen and methane

2.3 Mass Fraction of Carbon Monoxide CO

The curve of the numerical calculation of the CO mass fraction of methane is presented in figure 4. The curve of the hydrogen profiles is a straight line of the form $y_{co}=0$ applicable to the x-axis. The results clearly illustrate that the fuel CO values of hydrogen are zero and are quite important for methane fuel. Whereas in the center of the combustion chamber, the values of the mass fraction of CO are high for the fuel CH_4, equal to $y_{co}=0.06$ for the first station x/R=0.21. Indeed, it is observed that the quantity of carbon monoxide is double for the second station x/R=3.84 and is characterized by $y_{co}=0.12$. The CO mass fraction values decrease with the radial distance.

V. CONCLUSION

In this paper, we have presented the results obtained by numerical simulations using CFD code FLUENT tools in non-premixed turbulent combustion fueled by two methane-hydrogen/air fuels. The main results obtained in this study:

- The results give a satisfactory agreement between the numerical calculations of the coupled LES/PDF models and the experimental data.
- The emission of carbon monoxide is non-existent for combustion of hydrogen in the combustion chamber at all monitoring stations but exists for methane.
- Generally, a certain temperature discrepancy between the studied fuels was observed in different stations, which can be owed to the molar masse role played in combustion flame temperatures.
- The hydrogen velocity is faster than that of methane since the molar mass of hydrogen is smaller than methane.

With these results, we can confirm the fact that hydrogen is better than methane when used as fuel, because it is cleaner and less harmful to the environment.

REFERENCES

[1] A. Mameri. "Etude numérique De la combustion turbulente du prémélange pauvre méthane/air enrichi a l'hydrogène," Ph.D. dissertation, Univ., Orléans, France 2009.

[2] A. Rakib. "Valorisation du méthane en hydrogène par reformage catalytique," Ph.D. dissertation, Univ., Littoral Côte d'Opale, France 2012.

[3] Evatt R. Hawkes and Jacqueline H. Chen. "Direct numerical simulation of hydrogen-enriched lean premixed methane– air flames," *Combustion and Flame*, vol. 138, pp. 242–258, 2004.

[4] S. Orhan Akansu, N. Kahraman, and B. Çeper. "Experimental study on a spark ignition engine fuelled by methane–hydrogen mixtures," *Int Journal of Hydrogen Energy*, vol. 32, pp. 4279 – 4284, 2007.

[5] F. Bouras, M.E.H. Attia, F. Khaldi and M. SI-AMEUR. "Control of the Methane Flame Behavior by the Hydrogen Fuel Addition: Application to Power Plant Combustion Chamber," *Int Journal of Hydrogen energy*, vol. 42, pp. 8932- 8939, 2017.

[6] C.D. Pierce and P. Moin, "Progress-variable approach for large-eddy simulation of non-premixed turbulent combustion," *Journal of Fluid Mechanics*, vol. 504, pp. 73-97, 2004.

*Corresponding author email: attiameh@gmail.com

Heat and Mass Transfer Study of Hydrogen Desorption Process in an Annulus-Disc Reactor

A. Boukhari[1, 3*], M. E. H. Attia[2], A. Atia[1] and R. Bessaïh[3]

[1*]Department of Mechanical Engineering, Faculty of Technology, El-Oued University, El-Oued 39000, Algeria.
[2]Department of Physics, Faculty of Science, El-Oued University, El-Oued 39000, Algeria.
[3]LEAP Laboratory, Department of Mechanical Engineering, University of Constantine, Constantine 25000, Algeria.

Abstract— **In this work, we have carried out a numerical study of two-dimensional coupled heat and mass transfer processes in a unit disc of an annulus-disc reactor filled with the intermetallic (Mischmetal) compound $LaNi_5$, during the hydrogen gas desorption. Using the finite volume method bundled in the CFD code OpenFOAM®, temperature and amount of desorbed hydrogen and their time-averaged quantities inside the metal hydride bed are presented for different heat transfer fluid temperatures, and different metal thermal conductivities. Impacts of both effects on the metal hydride reactor performance in terms of discharging time are examined by means of a set of numerical simulations. The dehydriding time minimization relates to the adjustment of the amount of heat addition to the packed bed reactor. An excellent accord was recorded for the present simulations results compared against the literature-reported experimental data. We have attempted to examine and explain the effects of some parameters (HTF temperature and delivery pressure) on the dynamical performances of hydrogen desorption involved in MH packed bed reactors design and optimization.**

Key words— **Metal hydride, $LaNi_5$, Desorption, Numerical simulation, Coupled heat and mass transfer.**

I. INTRODUCTION

The fact of using hydrogen as a universal energy carrier among various clean alternative energy sources, makes it worthy of extensive consideration in the field of scientific researches, because its abundance in nature and diversity of its primary energy sources that can be used to produce it; including sustainable resources such as solar, wind and biomasses, in addition to the currently exploited alternatives such as fossil fuels and nuclear power. Furthermore, its use in fuel cells produces water as a side effect, the latter being a nature-friendly product, which makes this energy alternative (hydrogen energy) environmentally safe and economically beneficial in the chart of its industrial applications.

Nevertheless for many practical applications, the hydrogen use as a fuel is limited by various restrictions ranging between storage and transport problems. For this reasons, a variety of hydrogen storage techniques have been developed in the recent years. Among these technologies, one can mention the solid-state hydrogen reversible storage technique, where it is stored as metal hydrides in intermetallic compounds, carbon or nano-carbon materials. Above and beyond the security and its lower cost, the latter storage technique using metal hydrides have attracted considerable attention, due to their relatively higher volumetric density compared to that of issued from liquid hydrogen techniques, but a low hydrogen absorption capacity came into sight [1].

The obvious dependency of H_2 gas sorption rates on heat transfer and reaction kinetics of the MH packed beds were argued by the literature [2]. Some deign of the MH reactors configurations had been studied in the geometrical framework notoriously; the two-dimensional models of the works [3-5], and some other three-dimensional models.

The heat exchangers development and design processes require the use of Computational Fluid Dynamics (CFD) methods. Principally, while investigating coupled heat and mass transfer processes in porous media, e.g. packed bed reactors employed in energy storage systems [6], or in the design and modeling of fuel cells. Krokos et al.[7] presented an original approach for the design optimization of a sort of multi-tubular (metal hydride) MH storage tank, equipped with up to 9 tubular MH reactors, used in on-board applications involving hydrogen storage techniques. They numerically investigated the cooling tubes arrangement inside the packed bed, and found that a regular configuration of the cooling tubes yielded an optimal end result in accord to their meticulous 3D Cartesian mathematical model. Consequently, the main objective of this work is to investigate numerically the coupled processes of heat and mass transfer, during the sorption of H_2 gas in an Annulus-Disc Reactor (ADR) unit containing $LaNi_5$ intermetallic compound. A practical configuration of an ADR would consist of many annular discs to provide hydrogen gas, which is desorbed from the MH packed bed, and flowing into the inner tube. In this paper, the simulation was performed by application of the finite volume technique bundled in the general purpose, open source CFD code OpenFOAM to resolve the mathematical models describing such a device with $LaNi_5$ as the dehydriding metal.

Numerical calculations for the present investigation were carried out by means of the adoption of the famous two-dimensional mathematical model of Demircan et al. [4], to examine and explain the influence of the heating fluid temperature and the H_2 gas delivery pressure on the dynamical performances of the considered MH reactor system.

*Corresponding author email: fibonali2379@gmail.com

II. MATHEMATICAL MODEL

At present, the considered mathematical model for the annulus-disc reactor (represented in Fig. 1) is similar to that present in the works of Demircan et al.[4], with the $LaNi_5$-H_6 as the dehydriding solid, which is filling the annular space between the inner central H_2-delivery tube and the outer peripheral heating wall. The annulus disc is traversed by a number of heating tubes in this case of the hydrogen desorption process. For the reason of angular periodicity, we will restrict the computational domain to half of the sector area between two adjacent heating tubes. In the present work, the thermo–physical properties of H_2 gas and the working alloy adopted are the commonly used in literature [5, 9-10].

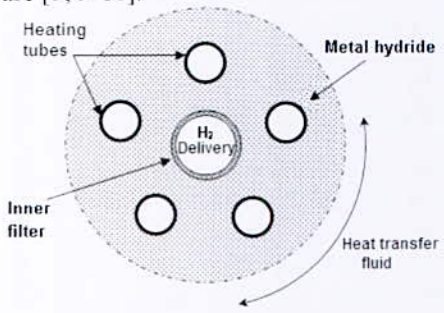

Fig. 1. Schematic section view of the studied ADR unit disc equipped with isothermal heating tubes

Generally, the simplifying assumptions considered while applying the present mathematical model are the following:

1. The gas phase is ideal from the thermodynamic viewpoint.
2. Porosity is uniform and its variation with desorption is negligible.
3. Mass transfer takes place through the porous filter (H_2 delivery), as well as the hydrogen outlet temperature and pressure are maintained constants.
4. The temperature field is the same for gas and solid phases (local thermal equilibrium hypothesis) in this porous medium, despite the fact that radiative heat transfer is negligible.
5. The radial temperature variation of the heating tubes is negligible; consequently they are considered isothermal tubes.

1. Volume-Averaged Governing Equations

The additional source term included in the RHS of the continuity equation denote the amount of hydrogen flowing from the bed with time;

$$\varepsilon\frac{\partial\rho_g}{\partial t}+\vec{\nabla}\cdot(\rho_g\vec{V})=\dot{m} \tag{1}$$

and here denote the amount of hydrogen that is out-flowing from the solid with time;

$$(1-\varepsilon)\frac{\partial\rho_s}{\partial t}=-\dot{m} \tag{2}$$

The perfect gas state equation states that;

$$\rho_g=\left(PM_{H2}\right)/\left(R_gT\right) \tag{3}$$

where M_{H2} and R_g denote the hydrogen molecular weight, and the universal gas constant respectively.

By including the Forchheimer modification term in momentum equations, we have;

$$\frac{\rho_g}{\varepsilon}\left[\frac{\partial\vec{V}}{\partial t}+\vec{V}\cdot\vec{\nabla}\left(\frac{\vec{V}}{\varepsilon}\right)\right]=-\vec{\nabla}\cdot P+\frac{\mu}{\varepsilon\rho_g}\left(\Delta\vec{V}\right)+S_D \tag{4}$$

where $S_D=-\left[\frac{\mu}{K}+\frac{1.75\rho_g}{\sqrt{150K\varepsilon^3}}\left|\vec{V}\right|\right]\vec{V}$ is the source term instead of the additional pressure drop in the bed due to viscous effects. In these equations $\left|\vec{V}\right|$ is the magnitude of the hydrogen flow velocity, where K and ε are the permeability and the porosity of this porous medium. The energy equation in the metal bed can be expressed in terms of a single temperature variation;

$$\begin{aligned}&\left[\varepsilon\rho_gC_{pg}+(1-\varepsilon)\rho_sC_{ps}\right]\frac{\partial T}{\partial t}+(\rho_gC_{pg}\vec{V})\vec{\nabla}T=\ /\\&\vec{\nabla}\cdot\left[\left(\varepsilon\lambda_g+(1-\varepsilon)\lambda_s\right)\vec{\nabla}T\right]-\dot{m}\left[\Delta H-T(C_{pg}-C_{ps})\right]\end{aligned} \tag{5}$$

2. Reaction Kinetics

The amount of hydrogen that is desorbed from the metal with time is directly related to the reaction rate of the dehydriding process, the latter is expressed as [6]:

$$\dot{m}=C_d\exp\left(-\frac{E_d}{R_gT}\right)\left[\frac{P-P_{eq}}{P_{eq}}\right]\left[\rho_s-\rho_0\right] \tag{6}$$

Where C_d is a material-dependent absorption rate constant, E_d is the activation energy, ρ_0 is the H_2-free MH density, and P_{eq} is the equilibrium pressure obtained from the van't Hoff relationship;

$$P_{eq}=P_0\exp\left(A-\frac{B}{T}+\varphi_{slp}(\xi-\xi_0)+\varphi_{hys}\right) \tag{7}$$

where φ_{slp} is the slope factor of the plateau pressure in the sorption PCI of $LaNi_5$ alloy, and φ_{hys} is its hysteresis factor, P_0 is the reference pressure (1 atmos), A and B are van't Hoff constants [9].

3. Initial and Boundary Conditions

At $t=0$; $P(x,y,0)=P_0$, $T(x,y,0)=T_0$, $\rho_s(x,y,0)=\rho_{s0}$.

And later for $t>0$;

- At the hydrogen gas delivery (i.e. the central tube); $P=P_0$, $T=T_0$.
- At the lateral heating wall :

$$-\left(\varepsilon\lambda_g+(1-\varepsilon)\lambda_s\right)\frac{\partial T}{\partial\vec{n}}=h(T-T_f) \tag{8}$$

*Corresponding author email: fibonali2379@gmail.com

where h is the conductance between the MH bed and the heat transfer fluid (HTF) at temperature T_f, and $\vec{n}$ is the normal unit vector outward the boundary.

- The embedded heating tubes, which are assumed to be isothermal, having the value $T = T_f$.
- The symmetry condition type is supposed to prevail at all the other boundaries.

III. SOLUTION TECHNIQUE

The governing equations are solved after discretization with the finite volume method bundled in the open source package OpenFOAM®. The technique to obtain numerical solution consists of describing the governing differential equations into a general algebraic form, then to integrate those numerically over a finite volume-meshed computational domain. The aforesaid general algebraic form of transport equation is written as [10]:

$$\frac{\partial(\rho\phi)}{\partial t} + \vec{\nabla}\cdot(\rho\vec{V}\phi) = \vec{\nabla}\cdot(\Gamma\vec{\nabla}\phi) + S_c \qquad (9)$$

where ϕ denotes a generic transported physical quantity (the field variable), Γ denotes the diffusion coefficient and S_c is all source terms. Also, the pressure-velocity coupling is solved by means of the transient solver for incompressible, buoyant flows in porous media using the PIMPLE (merged PISO-SIMPLE version) algorithm [10].

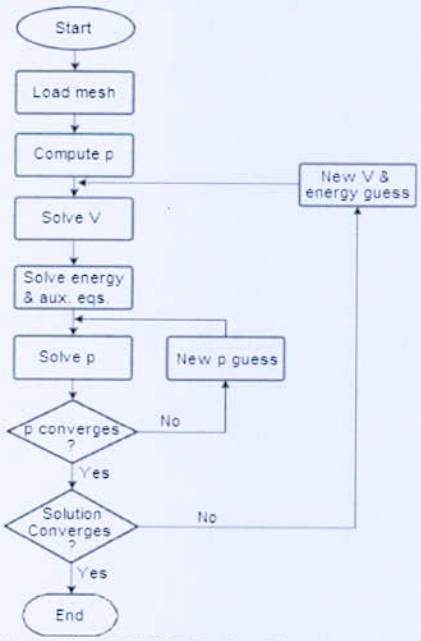

Fig. 2. The PIMPLE algorithm flowchart

IV. RESULTS AND DISCUSSION

1. Numerical Results Validation

We have carried out a number of simulations in aim to validate the considered mathematical model, by comparison of the results with some experimental data figuring in the literature, namely the data from the work of Jemni et al. [8], in which the authors have investigated a cylindrical shaped MH reactor containing the $LaNi_5$-H_2 hydride. In addition, we have assumed the axial symmetry to apply the adopted 2D approach. Fig. 3 shows the temperature history inside the MH bed reactor at three selected points within it. The HTF temperature and the delivery pressure were $T_f = 20°C$ and $P = 8\,bars$ for this case, respectively. These simulation results showed a good agreement (with a mean relative not exceeding 3% in almost) judged against the considered experiments, divulging that the adopted model can be used for further examination of the dynamical performances of MH reactors.

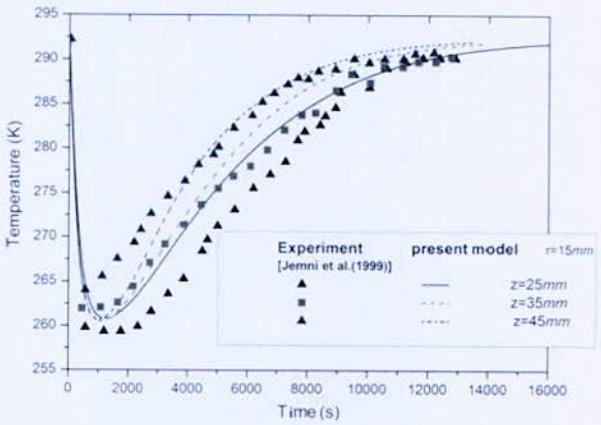

Fig. 3. Temperature evolution at selected points within a cylindrical-shaped MH tank experimented by Jemni et al. [8] in the hydriding case with HTF at 20°C

2. Hydrogen Desorption from the $LaNi_5$-H_6 Alloy

The heat and mass transfer dynamical behavior inside the annulus-disc reactor is inspected by means of a set of numerical simulations centering attention on the packed bed containing the intermetallic compound $LaNi_5$, considered as hydrogen-saturated ($LaNi_5H_6$) porous material. This AB_5-type alloy, which present equilibrium pressures near atmospheric conditions at the ambient temperature, and can stock up to 1.42 wt% reversibly. Desorption numerical simulations presented in this paper were carried at constant discharging pressure of P= 1 bar, and at temperature of 20 °C. Simulations are realized for the HTF temperature range ; T_f= 20°, 25°, 30° and 35°C, in the aim to inspect the heating temperature influence on the hydrogen desorption time. Delivery pressure effects on the MH reactor performance versus discharging times, and related H_2 desorbed fraction, are examined by carrying out a number of numerical simulations ranging in the interval; P = 0.1, 0.5, 1, 1.5, and 2 bars.

2.1. HTF Temperature Effect

Initially, the system is discharged at an outlet pressure of 1 bar and outlet temperature of 20°C. The corresponding hydrogen concentration is 1.44 wt%.

*Corresponding author email: fibonali2379@gmail.com

Fig. 4 showing the temporal evolution curves of the bed-averaged desorption fraction of hydrogen gas, confirms the conclusion that the heating temperature augmentation is a favorable parameter in the MH reactor desorption performance.

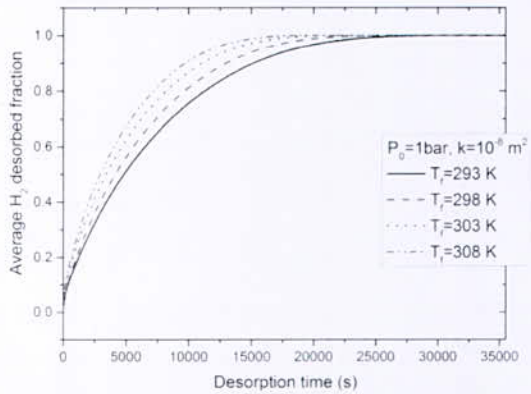

Fig. 4. HTF temperature effect on H_2 gas desorption at constant discharging pressure

The average desorbed fraction plots show that a complete desorption takes a delay of 5.55 hr in case of HTF temperature of 20 °C. Nevertheless, the same bed-averaged fraction requires only about 4 hr and 10 min to be completely desorbed from the hydride in the case of HTF temperature T_f=35°C, which represents about 25% of the reaction time reduction. Consequently, the heating temperatures affect positively (i.e. enhances) the examined MH reactor performance while desorption

2.2. Delivery Pressure Effect on Discharging Time

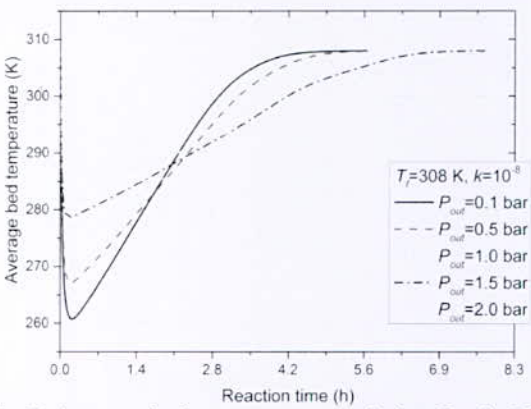

Fig. 5. Average bed temperature evolution for the MH reactor heated at T_f=35°C

Fig. 5 shows that an increase in delivery pressure corresponds to an increase in desorption time, and this is being after the two first hours. Thus, this obvious result led to the conclusion that the outlet pressure is not a key parameter to be optimized in the MH reactor design.

V. CONCLUSION

A 2D mathematical model describing the transient coupled heat and mass transfer processes in packed hydride bed during desorption of H_2 gas has been adopted. Where, the hydrogen desorption in this MH bed is numerically investigated in an annulus-disc reactor unit. Calculations were performed using the finite volume numerical technique packaged in the CFD code OpenFOAM. The simulations results showed a good agreement with the experimental data stated in the literature. As a result of investigating the effects of the heating fluid temperature effects on discharging time, simulations results shows that high HTF temperature led to significant improvement in reaction time, which makes it a key parameter in MH reactors design and optimization, which could be enhanced by employing a nanofluid as the HTF or embedding a metal foam inside the bed reactor in some future surveys. Also, we have investigated the influence of delivery pressure on desorption time, which is proved to adversely affect the discharging time.

REFERENCES

[1] L. K. Heung, "Using metal hydride to store hydrogen", DOE report, WSRC-MS-2003-00172, 2003.

[2] K. Aldas, M. D. Mat, and Y. Kaplan, "A three-dimensional mathematical model for hydrogen absorption in a metal hydride bed", *Int. J. Hydrogen Energy*, vol. 27, pp. 1049-1056, 2002.

[3] A. Chibani, and C. Bougriou, "Effect of the tank geometry on the storage and destocking of hydrogen on metal hydride ($LaNi_5$-H_2)", *Int. J. Hydrogen Energy*, vol. 42, pp. 23035-23044, 2017.

[4] A. Demircan, M. Demiralp, Y. Kaplan, M. D. Mat, and T. N. Veziroglu, "Experimental and theoretical analysis of H_2 absorption in $LaNi_5$-H_2 reactors", *Int. J. Hydrogen Energy*, vol. 30, pp. 1437-1446, 2005.

[5] A. Boukhari, and R. Bessaïh, "Numerical heat and mass transfer investigation of hydrogen absorption in an annulus-disc reactor", *Int. J. Hydrogen Energy*, vol. 40, pp. 13708-13717, 2015.

[6] A. Dogan, Y. Kaplan, and T. N. Veziroglu, "Numerical investigation of heat and mass transfer in a metal hydride bed", *App. Math. Computation*, vol. 150, pp. 169-180, 2004.

[7] C. A. Krokos, D. Nikolic, E. S. Kikkinides, M. C. Georgiadis, and A. K. Stubos, "Modelling and optimization of multi-tubular metal hydride beds for efficient hydrogen storage", *Int. J. Hydrogen Energy*, vol. 34, pp. 9128-9140, 2009.

[8] A. Jemni, S. Ben Nasrallah, and J. Lamloumi, "Experimental and theoretical study of a metal–hydrogen reactor", *Int. J. Hydrogen Energy*, vol. 24, pp. 631-644, 1999.

[9] G. Sandrock, and G. Thomas. (23/01/2012). *IEA/DOE/SNL Hydride Databases*. [Online]. Available: http://hydpark.ca.sandia.gov.

[10] "*OpenFOAM, The Open Source CFD Toolbox User Guide*", Version v1606+, OpenCFD Ltd., 2016.

*Corresponding author email: fibonali2379@gmail.com

Parametric Study of High Temperature Water Gas Shift Reaction for Hydrogen Production in a Palladium Membrane Reactor

I. Eddi[1] and L. Chibane[1]

[1] Laboratoire de Génie des Procédés Chimiques (LGPC), Département de Génie des procédés, Faculté de Technologie, Université Ferhat Abbas Sétif 1, 19000, Sétif, Algérie.

Abstract—**In this work, a numerical study of a reactor-hydrogen separator in which the catalytic high temperature water-gas-shift reaction (HT-WGS) was carried out over an industrial Fe_3O_4-Cr_2O_3-CuO catalyst. Indeed, a parametric sensitivity study was done by using the mathematical model developed for this purpose. The reactor performance was evaluated based on the CO conversion and on H_2 recovery at a large game of operating conditions such as reaction temperature (350-500°C), reaction pressure (1-6atm), gas hourly space velocity (GHSV:2000-6000h^{-1}), H_2O/CO feed molar ratio (1:1 to 4:1) and sweep gas flow rate (50-150mL/min of N_2). In order to determine the optimal conditions allow to the best performance, a non-isothermal model describing the reactor under study operating at steady state is proposed. The main results showed that higher CO conversion (99.9%) and H_2 yields can be achieved with the parameters range already indicated.**

Key words—Hydrogen production, HT-Water gas shift, Membrane reactor, Pd membrane

I. INTRODUCTION

The Water-Gas Shift (WGS) reaction (1) has been identified as one of the processes which both hydrogen yield and purity can be improved by using a membrane reactor [1].

$$CO+H_2O \leftrightarrow H_2+CO_2 \qquad \Delta_r H^{\circ}_{298K} = -41\ kJmol^{-1} \qquad (1)$$

The reaction is kinetically and thermodynamically limited because it is both a reversible and exothermic [2]. Therefore, Industrially WGS reaction is performed in a two-stage adiabatic reactor [3]: a high-temperature shift (HTS, typically 643-673 K, 10-60 bar) and a low-temperature shift (LTS, ~ 473 K, 10-40 bar), utilizing Fe-Cr and Cu-ZnO-Al2O3 catalysts, respectively [2,4]. HTS is characterized by fast kinetics, but the final CO conversion is limited by equilibrium constituting a rigid limit for a conventional reactor (CR) as a «closed system» [4]. One novel approach for improving the performance of WGS is the implementation of catalytic membrane reactors [5]. Among different technologies, the membrane one seems to be promising. In particular, due to the attractive possibility of realizing both reaction and gas separation/purification in the same device [6].The use of a Pd membrane reactor for WGS reaction suppresses the equilibrium limitations [1]. Because during the reaction a selective membrane continuously removes products from the reaction medium shifts the reaction toward the formation of products, making it possible to reach higher conversion (the so-called "shift effect") [4]. The main objective of the present study is to develop a simplified model to understand the effects of several WGS membrane reactor design and operational parameters on its performance. A novel configuration for hydrogen production from the water gas shift reaction is proposed, using high temperature to enhance the rate of reaction and employing a hydrogen separation membrane for the collection of the high purity hydrogen product by the immediate evacuation of hydrogen across the membrane at moderate temperatures and other investigated parameters.

II. MEMBRANE REACTOR DESCRIPTION

In the present work, WGS was carried out in a fixed-bed membrane reactor packed with an industrial Fe_3O_4-Cr_2O_3-CuO catalyst [7]. The membrane reactor configuration "Fig.1" is quite simple and consists of a stainless steel module where tubular dense self-supported Pd-Ag membrane. The inner tube is porous (membrane) and the outer tube is impermeable. The reactants were fed into the tube side of the reactor, while a sweep gas was fed into the shell side. Operating conditions and reactor dimensions are listed in TABLE I.

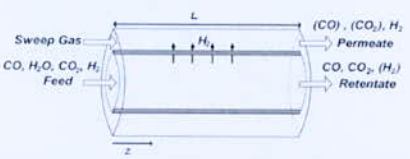

Fig. 1. Schematic representation of the membrane reactor

TABLE I
OPERATING CONDITIONS AND REACTOR DIMENSIONS

	Values	Reference
Initial total pressure (atm)	1-6	[4]
Permeation pressure zone (atm)	1	[8]
H_2O/CO feed molar ratio	1-4	[3,6]
GHSV (h^{-1})	2000-6000	[3]
Sweep gas flow rate (mL/min of N_2)	50-150	[6]
Catalyst		
Porosity	0.3	[9]
Density (Kg m^{-3})	7633.65	[9]
Membrane properties		
Membrane thickness (m)	50.10^{-6}	[3]
Pe^0 [mol/(m s $kPa^{0.5}$)]	$9.88.10^{-6}$	[3]
Ea [kJ/mol]	26.63	[3]
Reactor dimensions		
Reactor length (cm)	5	[10]
Membrane diameter (cm)	0.775	[10]

III. MATHEMATICAL MODEL

The mathematical model proposed for describing the reactor under study is based on the following main assumptions:

- Adiabatic operation at steady state.
- No radial concentration distributions in the tube or on the shell side of the reactor.
- Plug flow in both compartments of the reactor (no axial mixing) and ideal gas behavior.
- Negligible mass and heat-transfer resistances.
- Permeation through the membrane is proportional to the difference in the partial pressure of each component between the tube and shell side.

In the following paragraph, the governing equations are separately presented for each part of Pd-Ag membrane.

1. Retentate side (reaction side)

- ***Reaction rate correlations***

An empirical power law type rate expression (2) is used to describe the WGSR kinetics [7]:

$$R_{WGS} = k_0 . e^{\frac{-E_a}{RT}} . P_{CO}^{a} P_{H_2O}^{b} P_{CO_2}^{c} P_{H_2}^{d} \left(1 - \frac{1}{K_{eq}} . \frac{P_{CO_2} P_{H_2}}{P_{CO} P_{H_2O}}\right) \quad (2)$$

Where Pj is the partial pressure of gas component j (kPa); R_{WGS} the WGS reaction rate (mol gcat^{-1} s^{-1}) and a, b, c, d is the reaction order of CO, H_2O, CO_2, H_2, respectively. R: is the universal gas constant. The temperature dependence of the thermodynamic equilibrium constant is described by [7]:

$$K_{eq} = \exp\left(\frac{4577.8}{T} - 4.33\right) \quad (3)$$

The various parameters of the used kinetic model are summarized in TABLE II.

TABLE II
KINETICS MODEL PARAMETERS [7]

A*	E_a (kJ mol^{-1})	Apparent reaction orders			
		a [CO]	b[H_2O]	c[CO_2]	d[H_2]
-700	-111	1	0	-0.36	-0.09

*(molg(catalyst)$^{-1}$s^{-1}kPa$^{-(a+b+c+d)}$)

The catalytic performance and separation ability of the Pd-Ag membrane reactor for the WGS reaction have been evaluated in terms of the carbon monoxide conversion (X_{CO}) and hydrogen recovery (Y_{H2}). Both parameters were calculated according to equations (4) and (5), respectively:

$$X_{CO} = \frac{F_{CO}^0 - F_{CO}}{F_{CO}^0} \quad (4)$$

$$Y_{H_2} = \frac{F_H^P}{F_{CO}^0} \quad (5)$$

The partial pressures used for evaluate reaction rates are:

$$P_j = \frac{F_j}{F_{CO}^0 \left(1 + \theta_{H_2O} + Y_{H_2}\right)} P_T \quad \text{With} \quad \theta_{H_2O} = \frac{F_{H_2O}^0}{F_{CO}^0} \quad (6)$$

The total molar flow rate in reactor inlet is calculated by:

$$F_T^0 = \frac{(GHSV * V / 3600)}{22.4e-3} \quad \text{With} \quad F_T^0 = F_{CO}^0 + F_{H_2O}^0 \quad (7)$$

- ***Mass balance equation***

For each species the following mass balances equation:

$$\frac{dF_j}{dz} = \rho A \sum_{i=1} \upsilon_{ij} R_i \quad (8)$$

Where F_j is the molar flow rate, z the axial coordinate, υ_{ij} the stoichiometry coefficients (i refers to the reaction and j to the species), Ri: the rate of WGS reaction, A: is the surface area of reaction side, ρ: is the catalyst density. After some mathematical arrangements and by introduction of a dimensionless length (ζ) to (8), we get:

$$\frac{dX_{CO}}{d\zeta} = \frac{\rho A L}{F_{CO}^0} R_{WGS} \quad (9)$$

2. Mole balance in permeate side

The mass balance in permeate side is given by the following the Richardson's law equation [11]:

$$\frac{dY_{H_2}}{dz} = \frac{A_M}{F_{CO}^0} . \frac{Pe^0}{\delta} \exp\left(-E_a / RT\right)\left(P_{H_2ret}^{0.5} - P_{H_2perm}^{0.5}\right) \quad (10)$$

Where Pe^0, and Ea are the pre-exponential factor, apparent activation energy, respectively. δ is the membrane thickness. P_{H_2ret} and P_{H_2perm} are the H_2 partial pressures in reaction and permeate sides, respectively. By introducing the dimensionless form, we get:

$$\frac{dY_{H_2}}{d\zeta} = \frac{2\pi r_M L}{\delta F_{CO}^0} . Pe^0 \exp\left(-E_a / RT\right)\left(P_{H_2ret}^{0.5} - P_{H_2perm}^{0.5}\right) \quad (11)$$

The pressure of hydrogen in the permeation zone and a sweep gas ratio (I) are defined respectively as [11]:

$$P_{H_2perm} = \frac{Y_{H_2} P_{perm}}{Y_{H_2} + I} \quad \text{With} \quad I = \frac{F_I^0}{F_{CO}^0} \quad (12)$$

3. Heat balance

The heat balance in reaction zone for an adiabatic reactor is given by the following expression [12]:

$$\frac{dT}{d\zeta} = \frac{(-\Delta H_R) R_{WGS} \rho A L}{\Sigma Cp_j * F_j} \quad (13)$$

Cp_j is the specific heat of species j and is given by [13]:

$$Cp_j / R = A_j + B_j * T * 10^{-3} + C_j * T^2 * 10^{-6} + \frac{D_j}{T^2} * 10^5 \quad (14)$$

The Enthalpy is a function of the temperature T:

$$\Delta_r H_i(T) = \Delta_r H^{\circ}_{298K} + \sum_j \nu_{i,j} * \int_{298K}^{T} C^{i}_{P_i}(T)dT \quad (15)$$

TABLE III
SPECIFIC HEAT CAPACITIES OF SPECIES [13]

Compound	$C^{0}_{P,i}(T), J/(molK)$
H_2	$27.01+3.508\times10^{-3}T+0.69\times10^{5}T^{-2}$
CO_2	$45.369+8.688\times10^{-3}T+9.619\times10^{5}T^{-2}$
CO	$28.068+4.631\times10^{-3}T+0.258\times10^{5}T^{-2}$
H_2O	$28.849+12.055\times10^{-3}T+1.006\times10^{5}T^{-2}$

IV. NUMERICAL SOLUTION STRATEGY

The obtained ordinary differential equations (9), (11) and (13) describing the behavior of the reaction and permeate sides are solved numerically using the Runge–Kutta algorithm performed on MATLAB software with the following initial conditions: $X_{CO}=0$ and $Y_{H2}=0$.

V. RESULTS AND DISCUSSION

A parametric sensitivity analysis was carried out to explore the effect of the operating conditions on the level of CO conversion and H_2 recovery. According to "Fig. 2a", the obtained results show that in different case (all temperature range 350°C – 500 °C) the H_2O/CO molar ratio was positively affects the CO conversion because the kinetics is favored for higher steam content. In case of H_2 recovery as shown in "Fig.2b", a particular behavior was observed in which it was found that the pure H_2 yield stimulated by reducing the H_2O/CO molar ratio. This is may be explained by the fact that the water evaporation can influences the solution-diffusion mechanism of H_2 across the membrane. At the lower H_2O/CO molar ratio and for a given total pressure, the partial pressure of steam was reduced, and consequently the partial pressures of gaseous species including H_2 were increase. As a result, H_2 permeation rates are promoted by lowering H_2O/CO ratios and higher H_2 yields were achieved for smaller H_2O/CO ratios .On the other hand, as expected, "Fig.3" show that both CO conversion and H_2 recovery increase with the temperature increasing. As the WGS reaction is an exothermic reaction which increases exponentially with temperature. The optimum temperature for this process was observed at 450°C, the CO conversion close to 99.9%. In fact, higher temperatures enhance the hydrogen permeating flux from the reaction side to the permeate side and promoting a higher CO conversion [13]. From a general point of view, the presence of a sweep gas in the membrane permeate side acts as a promoter of the permeating flow of H_2 through the membrane, because it reduces the partial pressure of H_2 in this side, favoring an increase of the hydrogen permeation driving force [3]. As illustrated in "Fig.4a" and "Fig.4b" Both CO conversion and H_2 recovery increase with the flow rate of the sweep gas increasing from 50 to 150 mL/min. Besides, by analyze "Fig.5a", it was found that, increasing of GHSV causes a significant decrease in CO conversion from 60 to 10 %. Nevertheless, increasing GHSVs affect negatively the H_2 recovery as presented in "Fig. 5b". Consequently, it was be concluded that increasing GHSVs affect negatively both CO conversion and H_2 recovery due to the shorter contact times within the catalyst and the WGS reactants inside the reactor. Furthermore, as shown in "Fig.6", it is clearly seen that, a higher reaction pressure favors an increment of the hydrogen permeation driving force, enhancing the hydrogen removal for permeation and allowing a higher H_2 recovery in the permeate side.

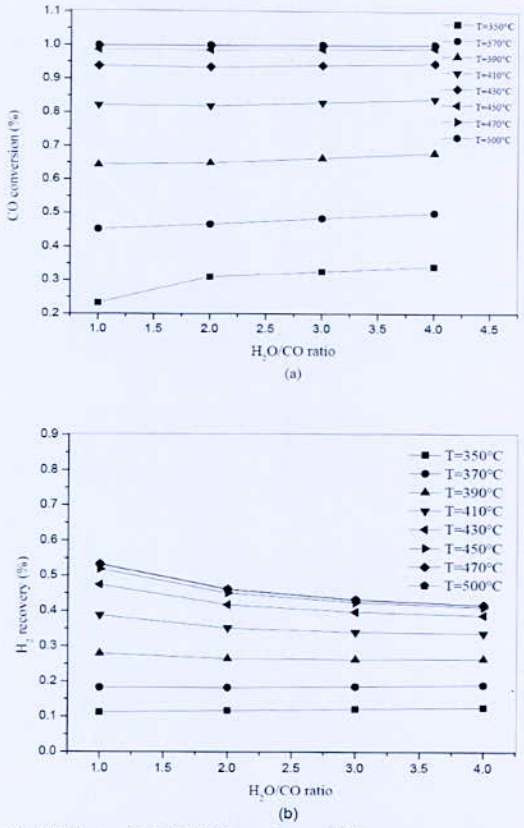

Fig. 2. Effect of H_2O/CO ratio at different temperatures. (a) CO conversion and (b) H_2 recovery (P_T = 1atm, flow rate =50 mL/min, GHSV=2000h^{-1})

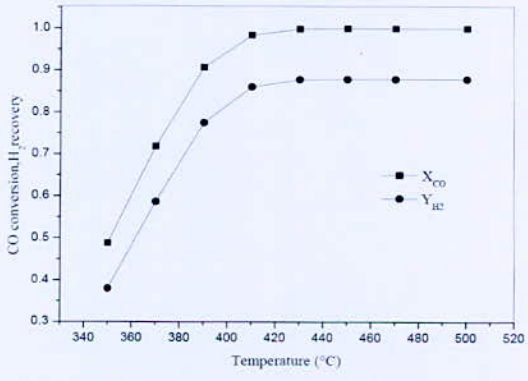

Fig. 3. Effect of temperature on CO conversion and H_2 recovery (P_T = 3 atm, sweep gas flow rate =80 mL/min, GHSV=2000 h^{-1}, H_2O/CO feed molar ratio=1/1)

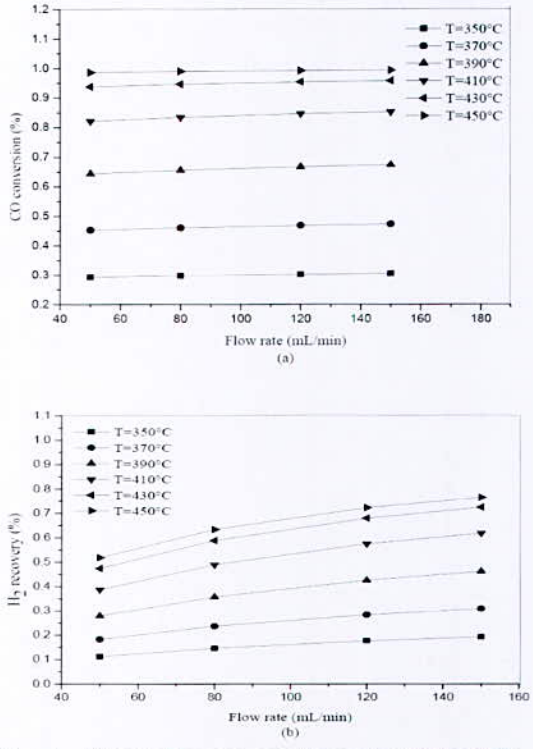

Fig. 4. Effect of sweep gas flow rate on reaction performance. (a) CO conversion and (b) H_2 recovery (P_T = 1 atm, H_2O/CO feed molar ratio=1/1, GHSV=2000 h^{-1})

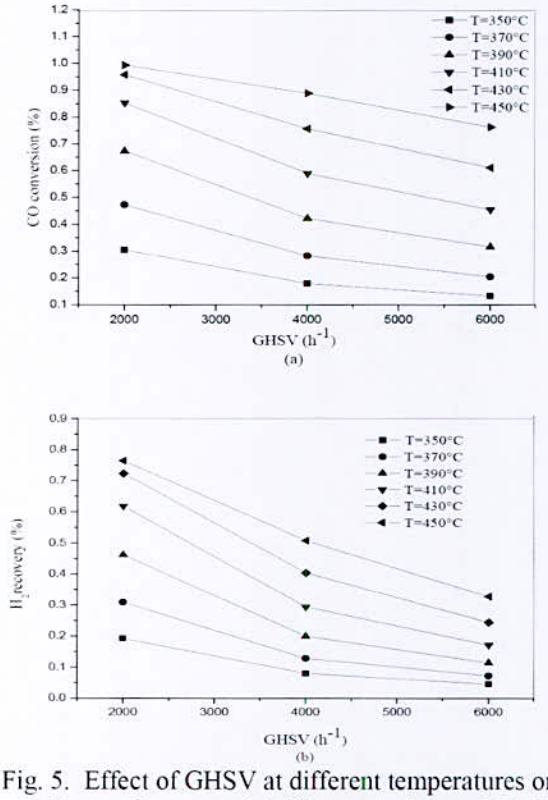

Fig. 5. Effect of GHSV at different temperatures on reaction performance. (a) CO conversion and (b) H_2 recovery (P_T = 1 atm, sweep gas flow rate =50 mL/min, H_2O/CO feed molar ratio=1/1)

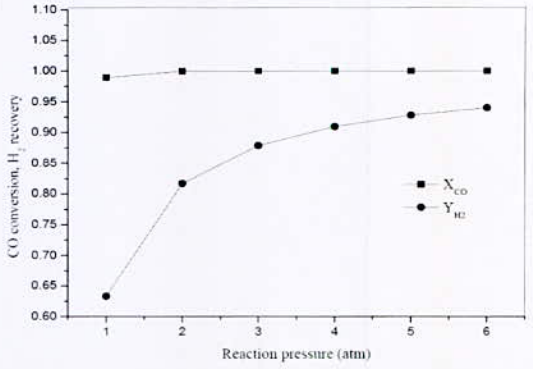

Fig. 6. Effect of reaction pressure on CO conversion and H_2 recovery (T = 450°C, H_2O/CO feed molar ratio=1/1, sweep gas flow rate =80 mL/min, GHSV=2000 h^{-1})

VI. CONCLUSIONS

The simulation results demonstrate that higher CO conversion levels and H_2 yields can be achieved by increasing the temperatures, sweep gas flow rate and increasing reaction pressure, reducing the GHSV and reducing the H_2O/CO feed molar ratio. Finally, this model provides a basis for evaluating reactors under varying operating conditions and H_2 separation rates, thereby reducing the experimental burden associated with catalytic membrane reactor development.

REFERENCES

[1] Baloyi, L.N., North, B.C., Langmi, H.W., Bladergroen, B.J., Ojumu, T.V., South African J. Chem. Eng., 2016.

[2] I.J.Oluku, Degree of Master, Regina univ, Saskatchewan, 2013.

[3] A. Basile, S. Curcio, G.Bagnato.,S.Liguorz S.M. Jokar , A. Iulianelli ,Int.J.Hydrogen.Eng.

[4] A.Basile, L.D. Paola. Faisal I. Hai and V. Piemonte. Number 76.2015.

[5] P. Boutikos J. Membr. Sci, 350 2010, 378–386.

[6] D. Mendes A,Mendes,L Asia-Pac. J. Chem. Eng.2010; 5: 111 – 137.

[7] B. Smith R J., Int. J.Chem Eng, 2010.

[8] S.S. Hla and Leigh D. Morpeth, Chem.Eng.J., 2015.

[9] Wei-Hsin Chena, Mu-Rong Lin, Int. J. hydrogen energy 33 (2008).

[10] Y. J. Alves Manrique, .Master. Thesis, Dep.Chem. Eng.,Porto univ.,2010.

[11] L. Chibane, B. Djellouli, Int. J. Chem. Eng. and Applications, 2011.

[12] M.K.Lenzi and P. M. Ndiaye, Dr Vivek Patel (Ed.),"2012.

[13] E. Demirel and N. Ayas Theoretical Foundations of Chem.Eng, 2017,pp.76-87.

Effect of Temperature and Pressure on Production Rate and Purity Level of Hydrogen and Oxygen Produced by an Electrolyzer Supplied by HES in the Adrar Region

S. K. Kirati *, M. Hammoudi, I. M. A. Mousli

Theorical and Applied Fluid Mechanics Laboratory, Department of Energetic and Fluid Mechanics, Physics Research Institute, University of Science and Technology Houari Boumediene (USTHB), 16111 Algiers, Algeria.

Abstract— **In this work, we are interested in the effect of the operating conditions of the electrolyzer such as temperature and pressure on the production rate and the purity level of hydrogen and oxygen produced by an electrolyzer powered by excess electricity from an HES hybrid energy system (PV, wind, genset) in the Adrar region.**

A model was used to predict the production rate of hydrogen and oxygen as a function of available power, operating temperature and pressure. The estimation of the purity level of the gases produced was made possible by the development of a prediction model based on experimental data. This latter concerns the influence of current density, temperature and operating pressure on the evolution of the gases contamination produced by an electrolyzer.

In order to reproduce the actual operating conditions, taking into account the electrical demand of the Adrar region, we developed a program HES-H_2 production with MATLAB®/SIMULINK® integrating different models developed and used to produce annual and daily simulations.

The use of these models will allow us to optimize the production conditions according to the desired quality of the gas intended for devices such as fuel cell, internal combustion engine or methanation.

Analysis of our results shows that the hydrogen production rates are proportional to the operating temperature, whereas an increase in the operating pressure leads to a reduction in hydrogen production, and the purity level of the gases produced is inversely proportional to temperature and pressure.

Key words—Hydrogen production rate, hydrogen purity level, alkaline electrolyzer, hybrid energy system, contamination, security.

I. INTRODUCTION

In this work, we are interested in the Adrar region in the south-west of Algeria, which covers an area of 425 000 km² and has considerable solar and wind renewable energy potential. It has been the subject of several studies, mostly on renewable energy and hydrogen production [1-5]. Currently, the region is connected to the PIAT network (Pole InSalah - Adrar - Timimoun) and has a diesel generator set with a total power of 120 MW to satisfy local electrical demand.

The following study deals with the impact of the operating conditions of the electrolyzer, such as temperature and pressure on the production rate and the purity level of hydrogen and oxygen. The alkaline electrolyzer is powered by excess energy from a hybrid energy system (PV, wind, genset) with a penetration rate of renewable energy RE_{rate} = 40% of the conventional power (Fig. 1). PV and wind turbine power are respectively 70% and 30% of the total renewable energy. This corresponds to 33.55 MW PV and 14.45 MW in seventeen wind turbines of 0.85 MW.

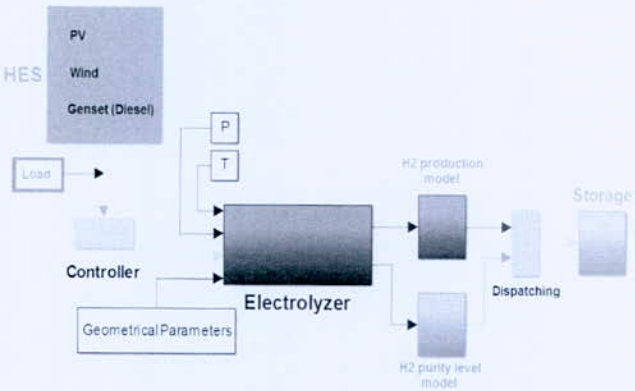

Fig. 1. HES-H_2 production

The multiple uses of hydrogen and oxygen require a different purity level depending on the requirements of transformation devices such as the conversion of hydrogen into mechanical (engine), electrical (fuel cell) [6] or chemical energy (methanation) [7]. The objective is to predict in real time the production rates and the purity levels of the gases produced (H_2, O_2) for given temperatures and pressures, thus configured power and set operating conditions to meet demand.

Thus, the model developed in this study makes it possible to predict the evolution in real time of the purity level of the gases produced, taking into account the fluctuating nature of the available power (renewable), the operating conditions (temperature, pressure) of the electrolyzer. For this purpose, we carried out a program HES-H_2 production under MATLAB®/SIMULINK® integrating the different models developed and used to perform the annual and daily hourly simulations. This program makes it possible to calculate the quantities and the qualities of the gases produced for different operating conditions.

*Corresponding author email: sid.i27@hotmail.com

II. THEORETICAL STUDY

Analysis of literature shows that most studies have focused on the effects of operating conditions such as temperature on the amounts of produced hydrogen [8-11].

Our work deals with the effect of operating conditions on the production rate and purity level of the gases produced, which influences the choice of the type of transformation device during the conversion phase.

The multiple uses of hydrogen and oxygen requires a different degree of purity level depending on the requirements of hydrogen and oxygen transforming devices into mechanical energy (engine), electric (fuel cell) or chemical energy (methanation).

1. Production rate

The hydrogen production rate is related to the current absorbed (i_{ele}) by the electrolyzer, whereas the current is related to the cell voltage of the electrolyzer (U_c) by an implicit relation given by the model used in this study, whose evolutions are reported in the literature [12-14].

$$i_{ele}(A) = P_{ele} / U_c \quad (1)$$

The mass flow rate of hydrogen produced is given by the relation:

$$\dot{m}_{H_2}(kg/h) = \eta_F \frac{3600 M_{H_2}}{nF}(P_{ele}/U_c) \quad (2)$$

Where η_F is the faradic efficiency, n is the number of electrons, F is the Faraday constant, M_{H2} is the molar mass of hydrogen and P_{ele} is the power absorbed by the electrolyzer.

The cell voltage (U_c) used in the model is proposed by M. Hammoudi et al. 2012 [12] is given as a function of the operating conditions (temperature, pressure) and characteristics of the electrolyzer.

$$U_c(V) = E_{rev(T,P_0)} + \frac{RT}{nF}\left((P - p_{H2O})^{1.5}/(\frac{p_{H2O}}{p^*_{H2O}})\right) + \frac{2.3026RT}{nF\alpha^{a/c}}\left(\log\frac{i}{i_0^{a/c}} - \log(1-\theta)\right) + \sum\left(\frac{e_i}{\sigma_i S_i}\right)i + \frac{e_i}{\sigma_i S_i}\left((1-\varepsilon)^{1.5} - 1\right)i \quad (3)$$

The first term describes the reversible voltage cell, whereas the rest of the equation describes the overvoltage of the materials.

2. Purity level

The purity level of the gases produced (H_2, O_2) is influenced by the available power to the electrolyzer and the operating parameters [8-11].

In the case where the electrolyzer is supplied by an intermittent source, the absorbed currents during the electrolysis are between its safe limit of 20% and 30% of its nominal current density 100%. The lower safety limit is imposed by the manufacturers and corresponds to 4% by volume of hydrogen in oxygen [12-14] which can cause an explosion.

In this work, we propose an empirical model of the purity level of hydrogen and oxygen as a function of the operating parameters [15]. The model is based on experimental data from the literature and allows to predict the evolution of the purity level as a function of the variation of the current density and the operating parameters (T, P).

In this part, we focused on the quality of hydrogen produced. The first source of contamination originates from the parasitic reaction in each compartment, while the second comes from the diffusivity of the gases through the membrane. This latter effect is strongly influenced by the operating conditions and the physical state of the electrolyzer.

Different parameters can influence the contamination of the gases produced, such as the temperature which favors transfer by diffusion, the difference in pressure favors the migration of the gases produced between the two compartments. To take into account the effects of temperature and pressure as well as the current density (j), we propose the correlation developed in this work:

$$Q(\%) = 100 - \left[\left(C_1 + C_2T + C_3T^2\right)\left(C_4 + C_5\left(\frac{P - P_0}{P_0}\right)\right)\right]/j \quad (4)$$

Equation (4) gives the evolution of the quality of the gases produced depending on the temperature, the pressure and the current density. The three terms are independent, a nonlinear function for temperature and current density, while it is linear for the evolution of pressures. The coefficients of equation (4) are given in Table I [16].

TABLE I
COEFFICIENTS OF THE GAS QUALITY EQUATION [16]

	C1	C2	C3	C4	C5
Q_{H2} (%)	275	1.77	0.0107	0.126	0.0009
Q_{O2} (%)	70	-2	0.025	1	0.00202

III. RESULTS AND DISCUSSION

The following simulations show the evolution of hydrogen production rates and purity levels for a typical day of the year for different operating parameters such as temperature and operating pressure.

The statistical analysis of the hourly evolution of the power available to the storage (power produced less the power load) makes it possible to extract the maximum power, mean power and its standard deviation during a year in the region of Adrar.

In this work, we have adopted a strategy of dimensioning the electrolyzer corresponding to 25% of the maximum power, in order to benefit as much as possible from the available potential. The total power of

*Corresponding author email: sid.i27@hotmail.com

all the electrolyzers is 4.8 MW distributed in three electrolyzer of 1.5 MW and a single one of 300 kW.

To show the effect of temperature on the hydrogen production rate and purity level, a pressure of 30 (bar) is used. Then, the operating temperature is fixed to realize simulations for different pressures.

1. *Temperature and pressure effect on the hydrogen production rate*

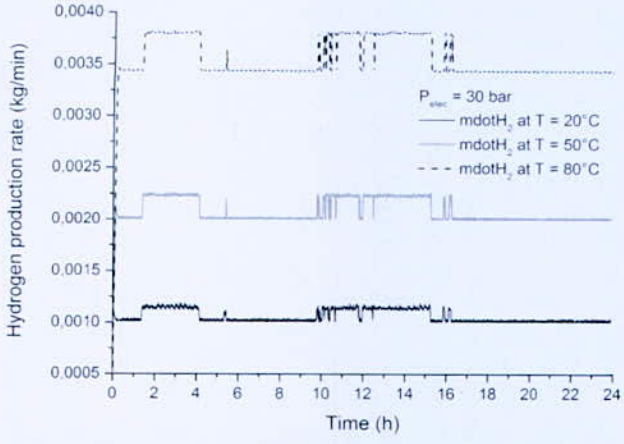

Fig. 2. Temperature effect on the hydrogen production rate at P = 30 bar

Analysis of the results of Fig. 2 shows that for higher operating temperatures (80°C.) more hydrogen is obtained, up to 2.14 (kg/h). The increase in temperature induces a decrease of the cellular tension in an electrolyzer and implies a better absorption of the currents as has been shown in the work of M. Hammoudi [12] Ulleberg [13] W. Hug [14], under these conditions, the electrolyzer absorbs more current and thus produces larger hydrogen quantities.

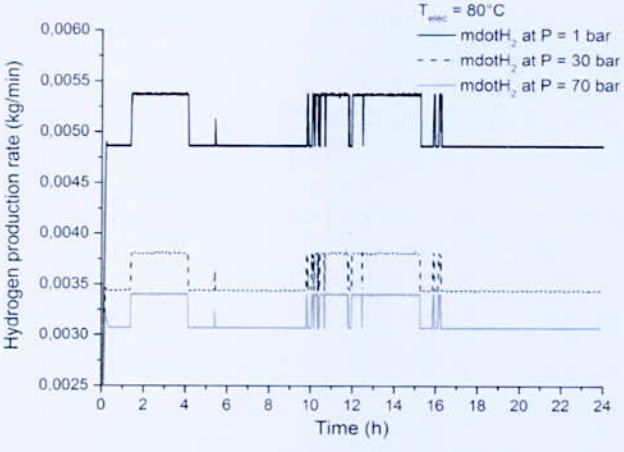

Fig. 3. Pressure effect on the hydrogen production rate at T = 80 °C

La Fig. 3 describes the daily evolution of the quantities of hydrogen produced at a fixed temperature for different pressures. While higher operating pressures negatively affect hydrogen production rates. We move from 0,0054 (kg/min) for 1 (atm) at 0.0034 (kg/min) for 70 (bar).

Pressurized electrolyzers are used to reduce energy consumption to storage at high pressure. the results found are in perfect agreement with the bibliography [12,17,18].

2. *Temperature and pressure effect on the hydrogen purity level*

In this study we present the effect of pressure on the hydrogen purity level.

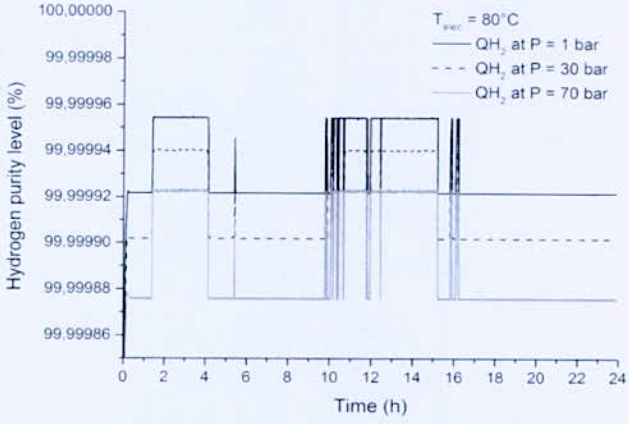

Fig. 4. Pressure effect on the hydrogen purity level at T = 80 °C

The pressure favors the migration of molecules from one compartment to another (poison gas), which implies a reduction in the gas purity level. Fig. 4 clearly shows that the hydrogen purity level is inversely proportional to the operating pressure, so the quality decreases with increasing pressure.

3. *Annual production rate*

The analysis of the results shows that the largest quantity of hydrogen produced annually is obtained for the conditions P = 1 atm, T = 80°C (Table. II). Using operating conditions at high pressures, it is possible to reduce the quantities of energies allocated to the compressor during the storage phase, even if the quantities of hydrogen produced are lower.

TABLE II

HYDROGEN QUANTITY FOR DIFFERENT TEMPERATURE AND PRESSURE

	T = 20°C	T = 50°C	T = 80°C
P = 1 atm	$m_{H2,\,year}$ = 2578 kg	$m_{H2,\,year}$ = 4423 kg	$m_{H2,\,year}$ = 6862 kg
P = 30 bar	$m_{H2,\,year}$ = 1443 kg	$m_{H2,\,year}$ = 2840 kg	$m_{H2,\,year}$ = 4854 kg
P = 70 bar	$m_{H2,\,year}$ = 1244 kg	$m_{H2,\,year}$ = 2509 kg	$m_{H2,\,year}$ = 2522 kg

*Corresponding author email: sid.i27@hotmail.com

IV. CONCLUSION

We studied in this work the influence of the operating parameters such as temperature and pressure on the production rates and purity level of the gases produced by an alkaline electrolyzer, powered by a hybrid energy system HES in the Adrar region in southern Algeria.

We have developed an empirical model of the quality of hydrogen produced, based on experimental data from the literature. The model takes into account the effect of current density, temperature and pressure. We developed a program HES-H_2 production under MATLAB®/SIMULINK® in order to carry out our simulations.

The increase in temperature favors the production of hydrogen, and reduces nonmonotonically its quality, having a minimum in the vicinity of 50°C. Increasing the pressure decreases the amount of hydrogen produced and its quality. On the other hand, it increases the efficiency of the production system by reducing the energies allocated to the compressor during the storage phase.

ACKNOWLEDGMENTS

This work has been supported by Sotraco Group and based on a research for a preparation of physics Ph.D. carried out at the institute of physics at the Algerian University of the Sciences and technologies of Houari Boumediene (USTHB).

REFERENCES

[1] R. Boudries, "Analysis of solar hydrogen production in Algeria: Case of an electrolyzer–concentrating photovoltaic system". International Journal of Hydrogen Energy, vol 38, 2013, pp. 11507–11518.

[2] M. Douaka, N. Settoub, "Estimation of hydrogen production using wind energy in Algeria". Energy Procedia, vol 74, 2015, pp. 981–990.

[3] R. Boudries, A. Khellaf, A. Aliane, L. Ihaddaden, F. Khida, "PV system design for powering an industrial unit for hydrogen production", International Journal of Hydrogen, vol 39, 2014, pp. 15188–15195.

[4] D. Ghribi, A. Khelifa, S. Diaf, M. Belhamel, "Study of hydrogen production system by using PV solar energy and PEM electrolyser in Algeria". International Journal of Hydrogen Energy, vol 38, 2013, pp. 8480–8490.

[5] R. Boudries, R. Dizène, "Potential of hydrogen production in Algeria". International Journal of Hydrogen Energy, vol 33, 2008, pp. 4476–4487.

[6] J. M. Ohi, N. Vanderborgh, G. Voecks. "Hydrogen Fuel Quality Specifications for Polymer Electrolyte Fuel Cells in Road Vehicles". Report to the Safety, Codes and Standards Program Fuel Cell Technologies Office. U.S. Department of Energy. November 2, 2016.

[7] G. Gahleitner. "Hydrogen from renewable electricity: An international review of power–to–gas pilot plants for stationary applications". International journal of hydrogen energy, vol 38, 2013, pp. 2039–2061.

[8] H. Janβena, J.C. Bringmanna, B. Emontsa, V. Schroederb. "Safety–related studies on hydrogen production in high–pressure electrolysers". International Journal of Hydrogen Energy, vol 29, 2004, pp. 759–770.

[9] H. Janβen, B. Emonts, H.G. Groehn, H. Mai, R. Reichel, D. Stolten. "High–pressure electrolysis–the key technology for efficient H2 production". HYPOTHESIS IV, Proceedings vol.1, Stralsund, September 9–14, 2001, pp. 172–7.

[10] S.A. Grigoriev. "High–pressure PEM water electrolysis and corresponding safety issues". International Journal of Hydrogen Energy, vol 36, 2011, pp. 2721–2728.

[11] S.A. Grigoriev, P. Millet, S.V. Korobtsev, V.I. Porembskiy, M. Pepic, C. Etievant. "Hydrogen safety aspects related to high–pressure polymer electrolyte membrane water electrolysis". International Journal of Hydrogen Energy, vol 34, July 2009, pp. 5986–91.

[12] M. Hammoudi, C. Henao, K. Agbossou, Y. Dubé, M. Doumbia, "New multi–physics approach for modelling and design of alkaline electrolyzers". International Journal of Hydrogen Energy, vol 37, 2012, pp. 13895–13913.

[13] Ulleberg, "Modeling of advanced alkaline electrolyzers: a system simulation approach". International Journal of Hydrogen Energy, vol 28, 2003, pp. 21–33.

[14] W. Hug, "Intermittent operation and modeling of an alkaline electrolyzer". International journal of hydrogen energy, vol 18 No. 12, 1993, pp. 973–977.

[15] S. K. Kirati, M. Hammoudi, I. A. M. Mousli, "Hybrid Energy System for hydrogen production in the Adrar region (Algeria): production rate and purity level". International Symposium on Sustainable Hydrogen, Algiers (October 2016).

[16] S. K. Kirati, M. Hammoudi, I. A. M. Mousli, "Hybrid Energy System for hydrogen production in the Adrar region (Algeria): production rate and purity level". International Journal of Hydrogen Energy xxx, 2017, pp. 1-16.

[17] K. Onda, K. Takahiro, K. Kikuo, K. Hattori. "Prediction of production power for high-pressure hydrogen by high–pressure water electrolysis". Journal of Power Sources, vol 132, 2004, pp. 64–70.

[18] A. Roy, S. Watson, D. Infield. "Comparison of electrical energy efficiency of atmospheric and high–pressure electrolyzers". International Journal of Hydrogen Energy, vol 31, 2006, pp. 1964–79.

*Corresponding author email: sid.i27@hotmail.com

Evaluation of A Hybrid Solar Photovoltaic-Bioenergy System for Powering Remote Dwelling in Rwanda

G. Ituze[1*] and A. Khellaf[2]

[1*] Energy Engineering, Pan African University Institute of Water and Energy Sciences, B.P. 119, Pole Chetouane, Tlemcen 1300, Algeria.

[2] Centre de Développement des Energies Renouvelables en Algerie(CDER), Route de L'Observatoire, Bouzareah, 16340 Algiers Algeria.

Abstract— The use of energy has always been important to improve the living standard of human beings. The electricity access in Rwanda is still low. In remotes area, the situation is even worst and access to modern energy services is practically inexistent. Renewable energy, by its availability and its adaptability to the remote areas, is the best way to get these regions out of the energy poverty and to improve the quality of life of their population.

The present work deals with this issue for the case of Kabasega Village in Gicumbi district Northern Province of Rwanda. An off-grid hybrid system based on solar PV and biomass with a Fuel cell as a backup has been proposed. The target of this research has been first to evaluate the renewable energy resources in the chosen area in order to determine its potential in meeting the local energy needs. After that, a survey has been conducted to determine the village energy load demand. HOMER software has then been used to optimize a suitable system that meets the energy needs of the village.

Key words—Renewable Energy, off-grid power System, HOMER, hydrogen, fuel cell.

I. INTRODUCTION

For the development of any country, energy always plays a very important role. For energy to be produced in an environment-friendly way, there must be an urgent need and understanding of shifting from existing fossil fuel energy based systems to the one based on renewable resources. That change will result in a reduction of carbon dioxide (CO_2) emissions that cause harm to the atmosphere and human health as well [1], changing from fossil fuel to renewables will also help countries to achieve their sustainable goals by providing access to clean, secure, reliable and affordable energy through renewable energies [1]. Renewable energy resources are not only available worldwide but their technologies are commercially well established; all could attract the world to focus on those replenished resources [2-3]. It is difficult and rare for one single source of energy to supply clean, reliable and cost-effective power. The combination of multiple power resources can then be a good way to provide a solution [4], that combination is also known as hybrid systems and those systems are important in achieving a cost effective and reliable power generation.

The access to electricity in Sub-Saharan African (SSA) is very low, and even the little accessible electricity is erratic and unaffordable. Fossil fuels and biomass used in a conventional way are the main sources of energy; they present though harmful effect [5]. However, Africa, especially sub-Saharan Africa, has low access to electricity, the continent itself has a good potential of renewable energy resources such as wind potential, solar irradiation, hydro potential, geothermal and biomass potentials [3]. Rwanda is endowed with various energy resources, which include renewable energy like hydropower, geothermal, biomass in form of firewood and charcoal, and solar. It has also conventional energy like methane gas, peat and diesel generators. However, there are still untapped resources which results in low electrification rate of 23% in 2015 [6]. The rural areas are more affected with having low access to the electricity.

Approximately 85% of Rwanda primary energy is from biomass in the form of wood that used directly as fuel at 57% or converted into charcoal by 23%; with smaller amounts of crop and peat by 5%. Non-biomass counts15% of that primary energy which includes 11% of imported petroleum products mainly used in the transport sector and the other 4% used for electricity [7]. This paper is structured as follows: an introductory part, energy potential in kabasega, results and discussion and then conclusion.

II. ENERGY POTENTIEL IN KABASEGA

To meet the energy needs of Kabasega, a hybrid solar PV-biomass stand-alone system with Fuel Cell as a back up is proposed. First the energy situation in the region is presented. The energy needs are then estimated through a survey carried out among the local population. After that, the solar irradiance and the bioenergy have been estimated from aquired solar and biomass data. To this end, MATLAB has been used. Finally HOMER has been used to size this system.

1. Solar Resources Assessment

The global solar radiation data have been acquired from Rwanda Meteorological Agency. These data have collected daily every 10 minutes daily. The monthly average global radiation H_M is given by:

*Corresponding author email: igemma06@yahoo.fr

$$H_M = \frac{\sum H_d}{N_i} [kWh/m^2/day] \quad (1)$$

Where H_d is the daily global radiation and N_i is number of days of the month.

2. *Biomass Resources Assessment*

Agriculture and livestock farming are the main activities in the selected area. The major crops in the area are wheat, sorghum, and maize [8]. Cattle, goat and poultry are the major livestock. For the present work, biomass considered is daily manure from cattle, goat and poultry. The village has around 150 cattle, 70 goats and 1000 poultry. This leads to a daily manure production of 10, 2.6 and 0.3 kg respectively [9]. The total available manure is 1982 kg per day.

3. *Electrical Load Assessment*

The off-grid study was conducted for the Kabasega village, a remote area in Gicumbi district northern province of Rwanda. It is an isolated region with 892 people and 198 households. It is estimated that 130 households will have access to electricity from the proposed hybrid system. Per household, six fluorescent lamps and two cell phones are considered. Eighty 19-inch TV sets, one hundred clock radio, ten refrigerators, five irons and five laptops are considered for the whole village. The village has two hair salons with one lamp and three electric shavers for each saloon. It also has five small shops with three lamps for each shop; and a nursery school with two lamps.

4. *HOMER analysis*

The Hybrid Optimization Model for Electric Renewable, HOMER software is used to design and optimize the off-grid power system.

4.1 Load Input

According to the carried-out survey, the electric load in Kabasega village includes mainly bulbs for lighting purpose and appliances for homes. The daily average load demand of 243kWh/day and peak load demand of 49.3kW have been determined. The HOMER evaluation results are presented in Figure 1. This figure shows also the primary daily load profile and the seasonal load profile of the village-based on their electrical energy use.

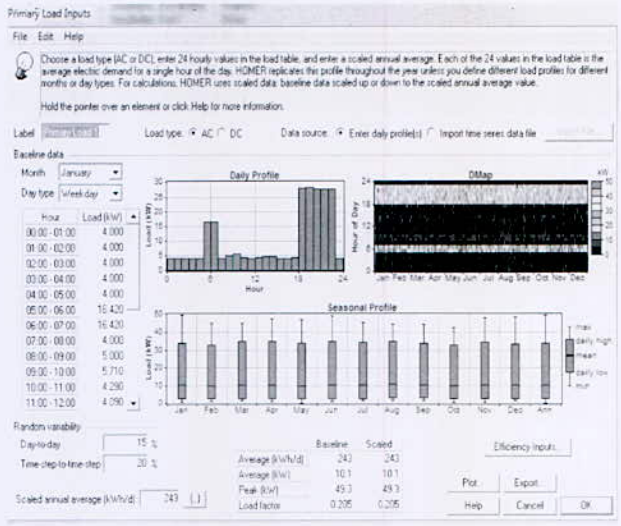

Fig.1 Load Input data

From the figure above, it is clear that the demand is high 6PM up to 11PM with 49.3 Kw of peak power and very low from 11PM up to 5AM.

4.2 Solar PV Input

Figure 2 presents the solar input which is the calculated monthly average.

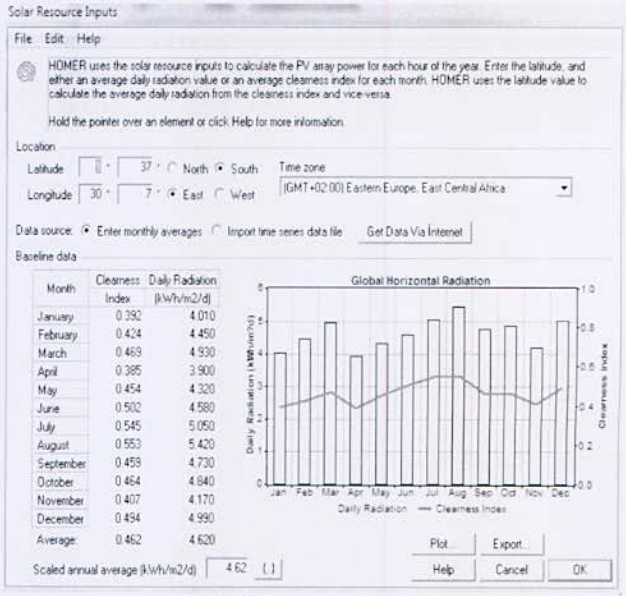

Month	Clearness Index	Daily Radiation (kWh/m2/d)
January	0.392	4.010
February	0.424	4.450
March	0.469	4.930
April	0.385	3.900
May	0.454	4.320
June	0.502	4.580
July	0.545	5.050
August	0.553	5.420
September	0.459	4.730
October	0.464	4.840
November	0.407	4.170
December	0.494	4.990
Average	0.462	4.620

Scaled annual average (kWh/m2/d) 4.62

Fig.2. Solar PV Input data

From the above figure, it is obvious that in the months of March, July, August and December have high irradiance while in January and april have low irradiance.

4.3 Biomass Input

The biomass potential in the village has been calculated; two tonnes per day are available. Considering some losses in biomass collection and a small portion of biomass to be

*Corresponding author email: igemma06@yahoo.fr

used for fertilization purposes, only 75% of the total biomass is retained for electricity production in the present study as shown in figure 3.

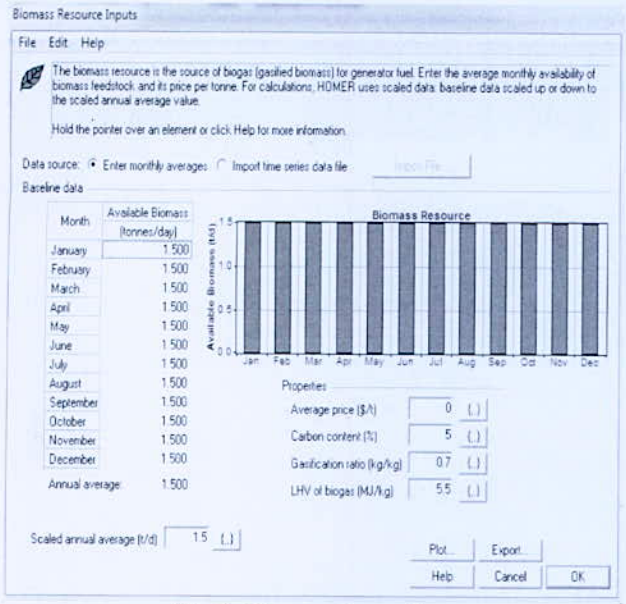

Fig.3. Biomass Input data

3.4 Additional Input

Table I below shows the additionally inputs data and other parameters.

Table I: Additional inputs to HOMER

Options	Considered sizes	lifetime	Other parameters
PV	0, 25, 80 (kW)	20 years	Derating factor 80%
Biomass (biogas-generator)	0, 25, 90 (kW)	40000 hours	Minimum load ratio 30 %
Fuel cell	0.25, 5 (kW)	35000 hours	Minimum load ratio 1%
Electrolyzer	0, 10, 20, 30 (kW)	15 years	Efficiency 80%
converter	0, 7, 28, 45 (kW)	15 years	Inverter efficiency 90%
Hydrogen tank	0, 3, 18, 20 (kg)	20 years	Initial tank level 20%

III RESULTS AND DISCUSSION

The system is designed in such a way that Biomass and Solar are the main sources of energy. The electrolyzer and the fuel cell act as back up.

Biomass electricity generator produces an alternating current that supplies directly the load. The energy produced by solar PV is a Direct Current that is first converted into AC by the converter and then supplied to the load. Electrolyzer generates hydrogen from the produced excess energy. The produced hydrogen is stored in hydrogen tank which is used by the fuel cell to generate DC electricity in case of low production. The system configuration is shown in figure 4.

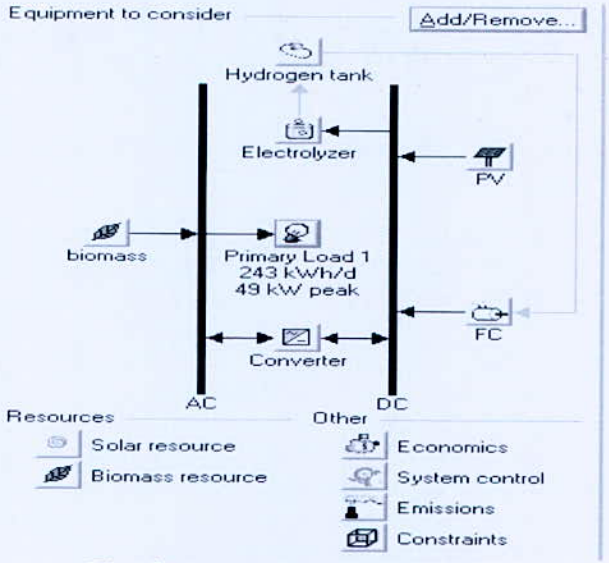

Fig.4 System configuration in HOMER

For the off-grid electrification of Kabasega village, HOMER provides various combinations of the hybrid systems with Solar PV, Biomass, Electrolyzer, hydrogen tank, fuel cell and converter as shown in figure 5.

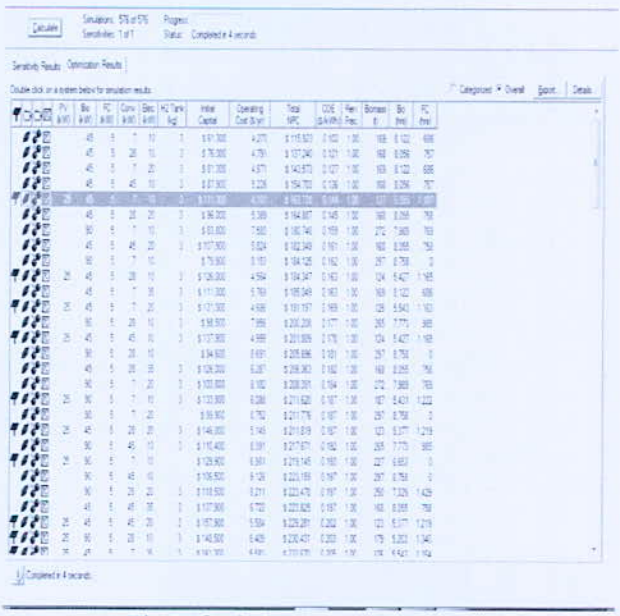

Fig.5. Optimization results details

*Corresponding author email: igemma06@yahoo.fr

From the optimum system configuration, the electricity production is summarized in figure 6.

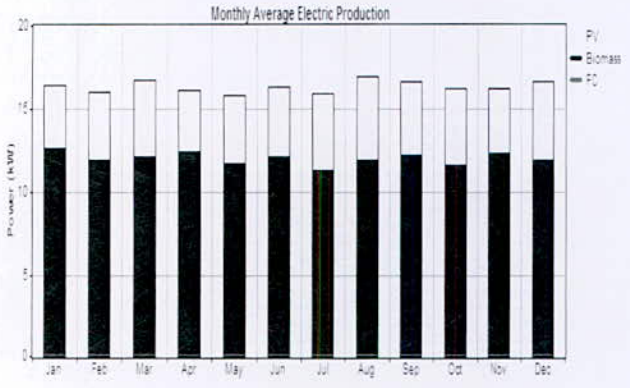

Fig 6. Electricity production from the optimum system configuration

This figure shows the evolution of the monthly electricity production over the year. It is clearly shown that the highest PV electricity production occurs in the month of August. This could be explained by the fact that it is the month of the highest solar radiation. Concerning biomass, the highest produced electricity from this resource, is over the month April. This is due to the fact that solar radiation is at its lowest; therefore, there is a resort to the biomass resource. The power produced from the fuel cell is small compared to the other sources but still, it is necessary as it is the best way of ensuring the electricity availability.

IV CONCLUSION

Using the outcome of a survey, the work describes the load demand profile of the village-based on population's need for electricity. In this study, it has been found that, besides hydropower, the village has sizable energy potential in both solar and biomass resources. About 4.62 kWh/m^2 of average daily solar radiation and 2 tonnes per day of manure from cattle, goat, and poultry have been identified as the potential of chosen renewable energy resources.

Without storage system, renewable energy based power system could not satisfy the load demand adequately. Therefore, a system made up of an electrolyzer and a fuel cell has been added first as a mean of storing the excess electricity in the form of hydrogen then as a backup in case the production cannot meet the load. Using HOMER software, the hybrid system has been modeled and simulated to determine the optimum system meeting the village's load demand at low-cost. This load demand is 243kWh per day with peak power of 49.3 kW. A solar PV-biomass-fuel cell system with 25 kW PV, 45 kW biomass, 5 kW Fuel cell, 7 kW converter, 10 kW electrolyzer and 3 kg hydrogen tank satisfy this load demand. The origin of the produced electricity is 72%,27% and 1% from biomass, solar PV, and Fuel cell respectively. The Levelized cost is estimated at 0.144$/kWh.

REFERENCES

[1] Ali Heydari, Alireza Askarzadeh, "Optimization of a biomass-based photovoltaic power plant for an off-grid application subject to loss of power supply probability concept" Applied Energy, 165 601–611, 2016.

[2] International Energy Agency (IEA), "Africa energy outlook: A Focus on Energy Prospects in Sub-Saharan Africa",2014.

[3] Uwisengeyimana, J. de Dieu, A. Teke, T. Ibrikci, "Current Overview of Renewable Energy Resources in Rwanda" Journal of Energy and Natural Resources. Vol. 5, No. 6, 20, pp. 92-97, 2016.

[4] Kiranpreet Kaur, Gursewak Singh Brar "Solar-Biogas-Biomass Hybrid Electrical Power Generation for a Village (a case study)", International Journal of Engineering Development and Research(IJEDR), ISSN: 2321-9939, Vol. 4, Issue 1, 2016.

[5] Agence Française de Développement, "Access to Electricity in Sub-Saharan Africa: Lessons Learned and Innovative Approaches" October, 2013.

[6] Ituze Gemma, Mwongereza Jean d'Amour, Abimana Colette, Rwema Michel, Chisale Paul, "Energy Landscape of Rwanda and Institutional Framework. Science Research" Vol. 5, No. 3, 2017, pp. 16-22, doi: 10.11648/j.sr.20170503.11, 2017.

[7] Ministry of Infrastructure, "Energy Sector Strategic Plan 2013/14 - 2017/18" 2015.

[8] Northern province Gicumbi district, "District Development Plan (2013-2018)" Rwanda.

[9] Sharmin Sobhan, Tanvir Ahmad, Md. Jakaria Rahimi, Md. Habib Ullah, Shaila Arif, "HOMER Based Feasibility Study of Off-Grid Biogas Power Generation Model Using Poultry Litter for Rural Bangladesh" American Journal of Engineering Research (AJER), e-ISSN: 2320-0847 p-ISSN: 2320-0936, Volume-5, Issue-1, pp-21-33,2016.

*Corresponding author email: igemma06@yahoo.fr

Effect of Lightweight Element Boron and Lithium on the Elastic and Thermodynamic Properties of ZrH_2 Hydrides: First Principles Calculation

A. Djellouli[1*], K. Benyelloul[2], Y. Bouhadda[2] and A. Adjadj[3]

[1*]Department of science and technology University of Ghardaia
[2]Unité de Recherche Appliquée en Energies Renouvelables, URAER, Centre de Développement des Energies Renouvelables, CDER, 47133, Ghardaïa, Algeria.
[3]Department of physics University Ibn-Khaldoun Tiaret.

Abstract—**The effect with lightweight elements (Boron and Lithium) on the elastic and thermodynamic properties of a ZrH_2 are investigated by means of first-principles calculations based on the density functional theory (DFT) with generalized gradient approximation (GGA) and projected augmented wave (PAW) [1]. Our obtained results show that the ground state properties such as lattice parameter and bulk modulus are in good agreement with the experimental and theoretical values [2, 3]. Also, the lattice parameter and bulk modulus slightly decreased with the B and Li content. In addition that obtained enthalpy of formation and gravimetric capacity for Zr_6BLiH_{16} are -73.37 kJ/molH_2 and 2.77 wt%, respectively. Our calculated elastic constant indicated that the Zr_7BH_{16} and Zr_6BLiH_{16} are mechanically stable, it may be considered that the Zr_6BLiH_{16} hydrides as a probable candidate for hydrogen storage application. In the other hand, elastic constants (C_{ij}), bulk modulus (B), shear modulus (G), Young's modulus (E_H) and Poisson ration (v) are calculated. The obtained ratio (B/G) shows that all the considered hydrides are ductile materials.**

Key words—Zirconium hydrides, first-principles calculation, enthalpy of formation.

I. INTRODUCTION

The zirconium transition alloys is interesting apply in hydrogen storage, with their low thermal neutron capture cross section and good corrosion resistance, zirconium-based alloys are commonly used as fuel cladding material in the core of nuclear power reactors. While in service, the fuel cladding is in contact with water, which promotes the oxidation of Zr. This process releases free hydrogen, a portion of which enters the alloy and gives rise to the formation of hydrides once the solid solubility limit has been exceeded. This can have a detrimental effect on the integrity and longevity of the material, as it can lead to phenomena such as embitterment and delayed hydride cracking [1, 2].

Zirconium alloy have been widely used as the cladding materials of light water reactors, and hydrogen behavior in the cladding has been watched with keen interest because of high burn up of nuclear fuel in recent years. Problems such as embitterment of the cladding have stirred interest in the characteristics of zirconium hydride. Zirconium hydride is also of interest as a moderator in nuclear applications [3].

In this article we studied the effect with lightweight elements (boron and lithium) on the elastic and thermodynamic properties of a ZrH_2 using a functional density theory calculation method (DFT).

II. THEORETICAL STUDY

The present calculation was investigated based on the density functional theory (DFT) and performed by means of Vienna Ab-initio Simulation Package (VASP) [4]. The projector augmented wave (PAW) method [4,5] as implemented in the Vienne Ab-initio Simulation Package (VASP) code [6,7]. The functional to describe the exchange-correlation interaction was treated by the generalized gradient approximation (GGA) [6] has been adopted of the Perdew-Wang 91 (PW91) [7] for all hydrides. The cut-off energy is set to be 550 eV. For the Brillouin zone integrations we use the Monkhorst-Pack [8] and the k-point were sampled by $11\times11\times11$ for ZrH_2, Zr_7BH_{16} and Zr_6BLiH_{16} hydrides.

ZrH_2 has a fcc (face cantered center) lattice parameters are a=4.817 Å [9]. A supercell of $1\times1\times2$ of ZrH_2 unit cell has been used for this study. For Zr_7BH_{16} a single atom Zr was substituted by B, whereas, for Zr_6BLiH_{16} two atoms were substituted by B and Li, respectively. The unit cells are presented in Fig. 1.

III. RESULTS AND DISCUSSION

At zero pressure, the calculated equilibrium lattice parameters, bulk modulus (B) and its pressure derivative (B') for the tetragonal structure ZrH_2 and Zr_7BH_{16} and Zr_6BLiH_{16} are displayed in Table 1. From this Table, the optimized lattices parameters for ZrH_2 hydrides are consistent with the experimental data [9]. Unfortunately, in case of Zr_7BH_{16} and Zr_6BLiH_{16}, no other available experimental or theoretical data that could be used for further comparison. The bulk modulus (B) and its pressure derivative (B') for ZrH2, Zr7BH16 and Zr6BLiH16 hydrides are estimated by fitting the total energy as a function of volumes [23]. The obtained bulk modulus (B) for ZrH2 (138.06 GPa), is in good agreement with the theoretical value [9]. From our obtained values of

*Corresponding author email: aekdjellouli@gmail.com

bulk modulus (see Table 1), it is found that the values progressively decrease with decrease in order B (ZrH2) > B (Zr7BH16)> B (Zr6BLiH16).

TABLE I
STRUCTURAL PROPERTIES OF HYDRIDES

System	Properties	a_0 (Å)	B (GPa)
ZrH_2	Experimental	4.817[a]	
	Present calculation	4.822	138.06
	Previous work	4.823[a]	133[a]
Zr_7BH_{16}	Present calculation	4.8088	123.53
Zr_6BLiH_{16}	Present calculation	4.7816	110.16

[a]: Ref [9]

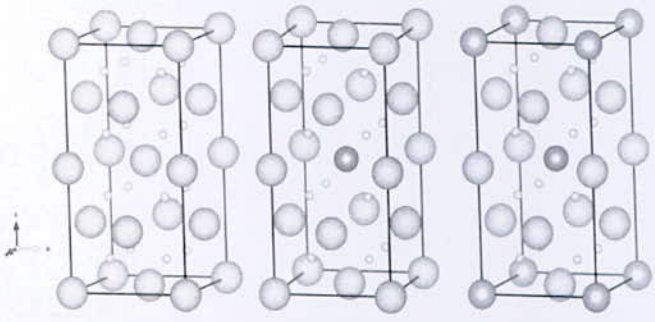

Fig. 1. Unit cell for ZrH_2, Zr_7BH_{16} and Zr_6BLiH_{16} hydrides (Zr: green spheres, Li: blue spheres, B: brown spheres, H: small yellow spheres)

TABLE II
ELASTICS PROPERTIES OF HYDRIDES

	Zr_7BH_{16}	Zr_6BLiH_{16}
C_{11}	117.41	136.93
C_{12}	133.96	102.12
C_{13}	127.15	107.69
C_{33}	126.87	125.66
C_{44}	80.02	92.38
C_{66}	52.37	102.01
B_V	126.47	114.94
B_R	126.91	114.82
B_H	126.69	114.87
G_V	40.71	62.82
G_R	-2.79	26.36
G_H	18.96	44.59
B_H/G_H	6.68	2.57
E_H	54.17	118.45
Mu	0.4287	0.3682

In other hand, the lattice parameters decreases in the same order when we replace one or two Zr by B and B-Li. Along the decrease of the lattice parameters, we can remark that the gravimetric capacity increase from 2.14 (ZrH_2) to 2.77 (Zr_6BLiH_{16}). The value of the total energy of the H_2 molecule is calculated, the obtained value is -6.67581 eV. Also, the total energies for pur elements have been estimated and reported in Table 3. using the total energies, the calculated value of formation enthalpy (ΔH) for ZrH_2, Zr_7BH_{16} and Zr_6BLiH_{16} are -84.87 kJ/mol H_2, -84.87 kJ/mol H_2 and -73.37 kJ/mol H_2, respectively.

The elastic constants are very important, provide a link between mechanical, physical and dynamical behaviours and also measure the resistance of crystal to an externally applied stress of crystals [10, 11].

TABLE III
THERMODYNAMICS PROPERTIES OF HYDRIDES

System	E_{tot} (eV)	ΔH(kJ/mol H_2)
Zr	-8.4515	
Li	-1.894	
B	-6.6758	
H_2	-6.7442	
ZrH_2	-16.95182	-169.44
Zr_7BH_{16}	-126.827	-84.87
Zr_6BLiH_{16}	-119.316	-73.37

At normal pressure, the elastic constants C_{ij}'s of hydrides Zr_7BH_{16} and Zr_6LiH_{16} are computed by applying the strain energy-strain curve method [12]. The six obtained independent elastic constants (C_{11}, C_{12}, C_{13}, C_{33}, C_{44}, C_{66}) are summarized in Table 2. Unfortunately, there are no theoretical results and experimental data for comparing with the present work. Additionally, the obtained elastic constants are positive and satisfy Born criteria [13]. Suggesting that hydrides object of study are mechanically stable.

IV. CONCLUSION

The structural and elastic properties of the hydrides Zr_7BH_{16} and Zr_6BLiH_{16} are investigated by the Ab-initio calculations based on density functional theory (DFT) implemented in VASP code with GGA exchange correlation. From our obtained values of bulk modulus it is found that the values progressively decrease with decrease in order B (ZrH_2) > B (Zr_7BH_{16})> B (Zr_6BLiH_{16}). The lattice parameter and bulk modulus slightly decreased with the B and Li content. In addition that obtained enthalpy of formation and gravimetric capacity for Zr7BH16 are -84.87 kJ/mol H2 and 2.42 wt% for Zr_7BH_{16} and -73.37 kJ/molH_2 and 2.77 wt% for Zr_6BLiH_{16} respectively. Our calculated elastic constant indicated that the Zr_7BH_{16} and Zr_6BLiH_{16} are mechanically stable, it may be considered that the Zr_6BLiH_{16} and Zr_7BH_{16} hydrides as a probable candidate for hydrogen storage application. In the other hand, elastic constants (C_{ij}), bulk modulus (B), shear modulus (G), Young's modulus (E_H) and Poisson ration (v) are calculated. The obtained ratio (B/G) shows that all the considered hydrides are ductile materials. Some of our theoretical results for the different hydrides are obtained for the first time such as elastic properties (elastic constants, bulk modulus, shear modulus, Young's modulus). For our knowledge, the elastic constants have not yet been calculated hence our results can serve as a prediction for future investigation.

REFERENCES

[1] M.P. Puls, The Effect of Hydrogen and Hydrides on the Integrity of Zirconium Alloy Components, Springer, London, 2012.

*Corresponding author email: aekdjellouli@gmail.com

[2] D.O. Northwood, U. Kosasih U, Int. Metals Rev. 28 (1983) 92.
[3] S.Y. Thermal and mechanical properties of zirconium hydride, Journal of Alloys and Compounds 293–295 (1999) 23–29
[4] G. Kresse, J. Furthmuller. Efficient iterative schemes for ab-initio total energy calculation using a plane-wave basis set. Phys. Rev. B 54(1996) 11169-86.
[5] G.Kresse, J.Hafner. Ab-initio molecular dynamics for liquid metals. Phys.Rev.B 47(1993) 558-61.
[6] JP.Perdew, Y.wang. Accurate and simple analytic representation of the electron-gas correlation energy. Phy.Rev.B 45(23)(1992) 13244-9.
[7] JP.Perdew, JA.Chevary, KA.Jackson, MR.Pederson, DJ.Singh, C.Fiolhais. Atoms, molecules, solids, and surfaces: Applications of the generalized gradient approximation for exchange and correlation. Phy.Rev.B 46(11) (1992) 6671-6687.
[8] HJ.Monkhost, JD.Pack. Special points for Brillouin-zone integrations. Phys.Rev.B 13 (1976) 5188-92.
[9] P.Zhang, B-T.Wang, C-H He, P.Zhang. First-principles study of ground state properties of ZrH2. Compt.Mat.Sce. 20(2011) 3297-3302.
[10] G. Sudha Priyanga, A.T.Asvini Meenaatci, R.Rajeswara Palanichamy, K.Iyakutti. Structural, electronic and elastic properties of alkali hydrides (MH: M=Li, Na, K, Rb, Cs): Ab initio study. Comp. Mater. Scie. 84 (2014) 206
[11] T. Chihi, M. Fatmi, A. Bouhemadou. Structural, mechanical and electronic properties of transition metal hydrides MH2 (M=Ti, Zr, Hf, Sc, Y, La, V and Cr). Solid State Sciences 14 (2012) 583-586.
[12] P. Ravidran, L. Fast, PA. Korzhavyi, B. Johanson, Density functional theory for calculation of elastic properties of orthorhombic crystals: application to TiSi2. J.Appl.Phys.84 (1998)4891-4904.
[13] M. Born, On the stability of crystal lattices I math.Proc.Camb.Philos.Soc. 36(1940) 160.

*Corresponding author email: aekdjellouli@gmail.com

Comparative Study of LCOE and Hydrogen Production Costs by PV-Electrolyser System in Different Representative Regions of Algeria

M. I. Mousli[1*], M. Hammoudi[1], S. K. Kirati[1]

[1] Theatrical and Applied Fluid Mechanics Laboratory, Department of Energetic and Fluid Mechanics, University of Science and Technology Houari Boumediene (USTHB), 16111 Algiers, Algeria.

Abstract—The purpose of this work is to identify the sites where the production of hydrogen would be the best, in term of quantity and cost. Three geographical areas representative of the existing climates in Algeria: coastal region (Oran, Algiers and Annaba), high plateaus (Nâama Ghardaïa, Tébessa) and the Sahara (Adrar, Tamanrasset and Illizi) were studied. To reflect the real conditions, the weather data of each production site were collected. The system of production and of storage of hydrogen is composed of a photovoltaic installation with a peak power of 1 MW, an alkaline electrolyser and hydrogen storage system. The analysis of the results showed a dependence of the production costs of electricity compared to the type of modeling considered for the energy productivity of the site (hourly, monthly and annual). The results showed that the annual approach gave an undervaluation of the production costs of electricity compared to the monthly approach. The study also showed that the production costs of electricity and hydrogen are inversely proportional to the latitude and the longitude of the site: the costs are lower while going from north towards the south and the west towards the east. The variation enters the production costs of Hydrogen between the town of Algiers (Northern) and the town of Tamanrasset (Southern) is of 7.71%., whereas the variation of the production cost of Hydrogen between the town of Oran (Western) and the town of Annaba is of 4.66%. Finally, a new comparison criterion between the quantity and the production costs of Hydrogen made it possible to identify the best strategy for the dimensioning of the electrolyser.

Key words—PV - Electrolyzer system, Levelized cost of electricity, Levelized cost of Hydrogen production.

I. INTRODUCTION

Hydrogen may be used as fuel in almost every application where fossil fuels are being used today but without harmful emissions [1]. However, Hydrogen is not primary source of energy but rather an energy carrier. Hydrogen can be obtained by different ways, but the "renewable energy-hydrogen" combination (RE-H2) by electrolysis is probably one of the most environmental friendly strategies [2]. Numerous researches are related to the Hydrogen production from RE sources as wind and solar power [3-6]. According to its geographic position in the world, Algeria has one of the largest solar potentials in the world with more than 16,900 TWh / yr [7]. The renewable energy program adopted for the 2015-2030 period would install electrical power of renewable origin with a value of 22,000 MW by 2030. Hydrogen, green energy carrier is a reliable and effective means of seasonal storage of electricity. The aim of this research is to identify the potential hydrogen production sites that would provide the optimal quantity and cost effectiveness. In order to do so, the study has been conducted on three regions, each standing for a type of the existing Algerian climates: Costal region (Oran, Algiers, Annaba), Highlands (Nâama, Ghardaïa, Tébessa) and Sahara (Adrar, Tamanrasset, Illizi).In order to imitate the actual field conditions, the meteorological data of each production site has been taken into account. The hydrogen production and storage system is made of a photovoltaic unit with a peak power of 1 MWp, an alkali electrolyser and a storage system for hydrogen and oxygen. In order to measure with acuity the energy quantity produced by the PV field and the available quantities of hydrogen on each site, the Matlab / Simulink was used. This program, developed by par Kirati et al [8] includes the various models of the existing literature that measure the evolution of the production according to the variation of the working conditions. In addition, there will be a comparison of the productivity yields of each site, with three modelizations based on hourly, monthly and annual rates.

II. THEORETICAL STUDY

1. Estimation of electricity production cost

The estimation of the production cost of one kWh of electricity (LCOE) using the solar power from the PV field is detailed in (1)

$$LCOE(\$/kWh) = \frac{I_o + \sum_{i=1}^{N} \frac{COM\,(1+c)^i}{(1+a)^i}}{\sum_{i=1}^{N} \frac{E_o\,(1-b_{PV})^i}{(1+a)^i}} \quad (1)$$

The mathematical development of (1) leads to

$$LCOE(\$/kWh) = \frac{P_{PV} \times CAPEX \times \left(1 + OPEX \times \left(\frac{1+c_{PV}}{a-c}\right) \times \left(1 - \left(\frac{1+c_{PV}}{1+a}\right)^N\right)\right)}{\left(\frac{Etapvx}{Etapv0}\right) \times E_{PV} \times \left(\frac{1-b_{PV}}{a+b}\right) \times \left(1 - \left(\frac{1-b_{PV}}{1+a}\right)^N\right)} \quad (2)$$

I_0: Initial Investment of the PV system, COM: Cost of operation and maintenance, a: discount rate, b_{PV}: degradation rate of PV, C_{PV}: Operating and Maintenance growth rate of the PV system, N: Project lifetime, E_0: Available electric energy.

*Corresponding author email: h2mousli@outlook.com

2. Estimation of hydrogen production cost

The average production cost of a kg of hydrogen ($LCOH_2$) is determined by the following equation

$$LCOH_2(\$/kg) = \frac{CAPEX_{elec} + \sum_{i=1}^{N} \frac{COM_{elec} \cdot (1+c_{elec})^i}{(1+a)^i} + LCOE \cdot E_e}{\sum_{i=1}^{N} \frac{m_{H_2} \cdot (1-b_{H_2})^i}{(1+a)^i}} \quad (3)$$

Where $CAPEX_{elec}$ is the Capital expenditure of the electrolyzer plant, COM_{elec}: Operational expenditure of the electrolyzer plant, b_{H2}: loss rate of Hydrogen system, C_{elec}: Operating and Maintenance growth rate of the electrolyzer system, m_{H2}: quantity of Hydrogen produced. Hammoudi et al [9] model was used in order to estimate hydrogen quantities produced by the PV –Alkaline Electrolyser system in optimal production conditions (Electrolyzer pressure = 30 bar, electrolyzer temperature = 80 °C).

3. Electrolyzer sizing

In the scope of this study, we compared five sizing possibilities of the nominal power of the electrolyser, based on a statistic study of available solar capacities ($P_{PV\ site}$) for each site.

$$P_{elec} = P^{max}_{PV\ site} \quad (S1)$$

$$P_{elec} = P^{moy}_{PV\ site} \quad (S2)$$

$$P_{elec} = 25\% \cdot P^{max}_{PV\ site} \quad (S3)$$

$$P_{elec} = P^{moy}_{PV\ site} + 1.96\ P^{SD}_{PV\ site} \quad (S4)$$

$$P_{elec} = P^{moy}_{PV\ site} + 2.6\ P^{SD}_{PV\ site} \quad (S5)$$

Where is the P_{elec} electrolyzer power, $P^{moy}_{PV\ site}$ is the average Photovoltaic power in the site, $P^{SD}_{PV\ site}$ is the standard deviation Photovoltaic power.

III. RESULTS AND DISCUSSION

The results of the electricity production costs from the PV array have been simulated using (2) and adopting the parameters given in the following table.

TABLE I
PHYSICAL AND ECONOMIC PARAMETERS OF ELECTROLYSER AND PV SYSTEM

Parameter	PV system	Electrolyzer
CAPEX	[1 -1.4] (M.$/MWp)	[0.6-1] (M.$/MWp)
OPEX/CAPEX	1%	6%
Discount rate	7.5 %	7.5%
Degradation/Loss	0.5 %	1%
OM growth rate	1%	1%
Life time	25 yr	25 yr

* The annual operating life of the electrolyser would not exceed 2015 (hr /yr) and therefore an electrolyser with a lifetime of 50 000 hr. should (lifetime reference) hold the 25 years of the project without replacement.

1. Levelized cost of PV electricity production

The calculation of the LCOE depends on the estimation of the energy produced by the PV field as shown in Eq (1). A modelization taking into account the effects of variation in the weather (temperature and radiation) of the site in question allowed to estimate more precisely the energy produced during the year. A second approach to the LCOE, taking into account that the PV field capacity and the monthly and annual productivity are compared and presented in Fig. 1.

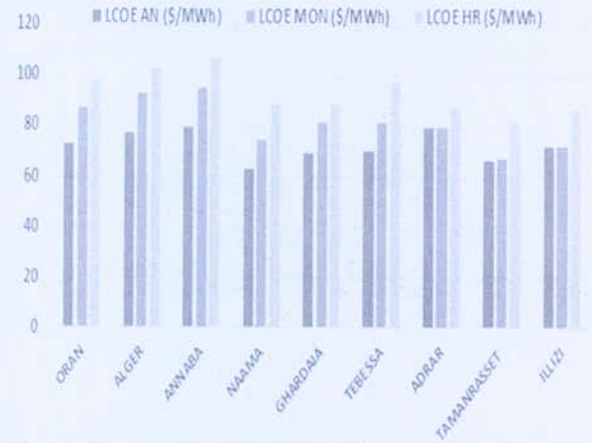

Fig. 1. Comparative LCOE in different sites of Algeria

Analysis of the results shows that LCOE decreases from east to west in both costal and highland regions, whereas Tamanrasset seems to be an exception in the southern regions of Algeria, benefiting from a clemency climate. In addition, there is also a significant difference with LCOE depending on hourly, monthly or annual basis. Estimation of LCOE on an hourly basis is more important, followed by monthly LCOE and annual LCOE whatever the studied site. Comparison between hourly and annual modelization models allows us to estimate the relative gap between LCOE for each site. It points out that Nâama had the lowest annual LCOE 63.34 ($/MWh), which can be explained by the climatic conditions favorable to the production of electricity starting from a field statement: (temperature and speed of favorable wind), but also by an important solar radiation having a productivity around 1838 kWh/kW. The gap between the two models is the widest being close to 40%, thus justifying the use of hourly simulations in order to determine a more accurate LCOE. This gap is lower in the other sites and reaches 9% in the Adrar region. Considering the annual calculation approach as a reference: it is noted that for the region of Algiers (North), the difference with the monthly approach is + 20.36% while the difference with the hourly approach is 32.84%. For the region of Ghardaïa (Hauts plateaux) the difference is +17.42% with the monthly approach whereas it increases to 27.57% for the hourly approach. For the region of Adrar (South) the annual LCOE and almost identical to the LCOE monthly (+0.37% deviation) while it is +19.49% for the hourly LCOE.

2. Levelized cost of Hydrogen production: $LCOH_2$

The amounts of hydrogen production at the various sites were calculated. Fig. 2, shows the simulated

*Corresponding author email: h2mousli@outlook.com

Hydrogen production over one year for the Naâma site taking into account the region climatic variations. The Levelized cost of Hydrogen production (LCOH2) for all the studied sites was calculated on the basis of Eq .3 and using the economic parameters relative to the electrolyser presented in TABLE I.

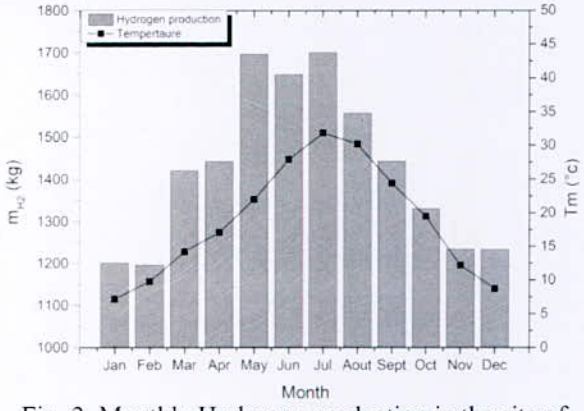

Fig. 2. Monthly Hydrogen production in the site of Naâma

The obtained results, which are shown in Fig. 3, show that the hourly, monthly and annual variation approaches give exactly the same values. This is due to the fact that the production of Hydrogen is proportional to the energy available on the site.

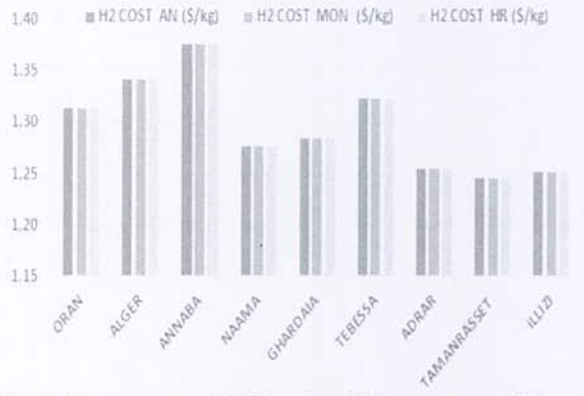

Fig. 3. Comparative $LCOH_2$ for different sites of Algeria

It is noted that the production costs of hydrogen increase while going from the south of Algeria towards north. Between the town of Tamanrasset (Southern) and the town of Ghardaïa (high plateaus) the variation of the $LCOH_2$ is estimated at 3.17%. This variation of $LCOH_2$ increases between the town of Ghardaïa and the town of Algiers (Northern) to reach 4.45%. The weakest cost is observed in the area of Tamanrasset with a LCOH2 equalizes with 1.25 S/kg, while the highest cost is noted in the town of Annaba with a cost $LCOH_2$ of 1.38 S/kg Nâama presents average costs of 1.28S/kg. Except in the cities of the south, the costs increase while going from the west towards the east. For the coastal regions the LCOH2 increases de1.32 S/kg for the site of Oran (western) has 1.38 S/kg for the site of Annaba is a variation of 4.54%. For the areas of the high plateaus, the variation of $LCOEH_2$ between the town of Nâama (western) and the town of Tébessa is of 3.12%. For the cities of the South, the variation of the $LCOH_2$ between the town of Adrar and the town of Illizi are of 0.20% whereas it is of 0.75% between Adrar and Tamanrasset

3. Electrolyzer sizing

In order to choose an electrolyser in adequation with the capacity of a 1 MWp PV Field, the five strategies listed previously were used. The results for each site and strategy are gathered in the following table

TABLE II
RELATIVE ELECTROLYSER POWER VS STRATEGY

	$P_{elec}/P_{PV,DC}$ (%)							
	Ora	**Alg**	**Ann**	**Naa**	**Gha**	**Adr**	**Tam**	**Ili**
S1	100	100	100	100	100	100	100	100
S2	47,9	48,2	39,6	38,0	47,0	41,9	41,8	48,0
S3	25	25	25	25	25	25	25	25
S4	93,5	94,1	85,0	84,2	93,1	89,1	87,8	93,8
S5	108,4	109,0	99,8	99,2	108,2	104,5	102,8	108,7

The obtained results for the various strategies show important differences between the relative powers of the electrolyser. Except for (S1) and (S3), the relative powers obtained are also different from a site to another.

TABLE III
HYDROGEN PRODUCTION VS LCOEH2 FOR FIVE DIFFERENT SIZING ELECTROLYZER STRATEGIES

Strategy	Parameter	ORA	ALG	NAA	GHA	TAM	ILL
S1	H2 PROD (kg)	23493	22269	25993	26423	27012	27098
	LCOH2 ($/kg)	1,03	1,09	0,93	0,92	0,90	0,89
	COP_{H2}^{-1}	22799	20485	27910	28841	30142	30332
S2	H2 PROD (kg)	17971	16822	20565	20865	21492	21562
	LCOH2 ($/kg)	1,04	1,12	0,91	0,90	0,87	0,87
	COP_{H2}^{-1}	17215	15083	22542	23204	24621	24780
S3	H2 PROD (kg)	12195	11944	12559	12470	12872	12801
	LCOH2 ($/kg)	1,32	1,34	1,28	1,29	1,25	1,25
	COP_{H2}^{-1}	9273	8895	9828	9705	10331	10218
S4	H2 PROD (kg)	23494	22270	25994	26425	27021	27099
	LCOH2 ($/kg)	1,03	1,09	0,93	0,92	0,90	0,89
	COP_{H2}^{-1}	22801	20487	27913	28845	30161	30336
S5	H2 PROD (kg)	23493	22269	25992	26421	27017	27095
	LCOH2 ($/kg)	1,03	1,09	0,93	0,92	0,90	0,89
	COP_{H2}^{-1}	22799	20485	27906	28836	30151	30327

The analysis of the results of simulations carried out and whose results are partially presented in table 3 shows that for the Coastal regions: the most powerful strategies of production in term of production costs and produced quantity are (S1), (S4) and (S5) followed by (S2) then (S3). The relative differences between the strategies can reach 27% for the production costs and 48% for the produced quantities of Hydrogen. For the Areas of the high plateaus and south: the strategy of the most powerful production in term of cost is it (S2) followed by (S4), (S5) and (S1) then it (S3). The relative variations in term of cost can reach 40% for the two regions and 52% in term of quantity of Hydrogen produced. It appears clearly that the optimal strategies of production at better cost vary according to the areas considered. In order to hold account as well production costs and produced quantities

*Corresponding author email: h2mousli@outlook.com

a comparison criterion was defined making it possible to rule on the best strategy to adopt for each site: the ratio between the production costs and the produced quantity (COP_{H2}). The lowest value will correspond to the best strategy. As showed in Fig. 4, the analysis of the results reveals that (S4) presents the best performances of production independently of the studied sites.

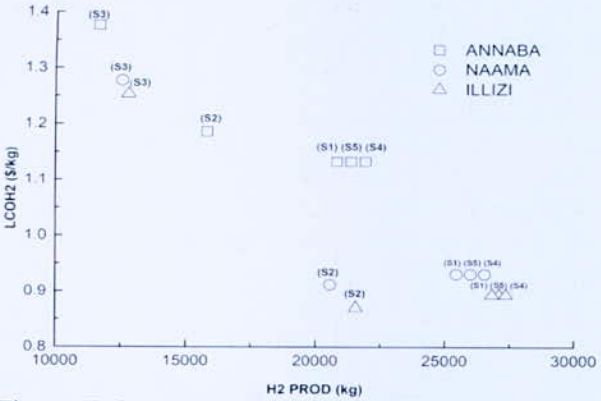

Fig. 4. Hydrogen production cost Vs Hydrogen quantity for different electrolyzer sizing strategies

For the coastal regions; the best coefficient of performance of production of Hydrogen is observed in the town of Oran ($LCOH_2$= 1.03 $/kg; m_{H2} =23493 kg), for the high plateaus regions; the best coefficient of performance of production of Hydrogen is observed in the town of Nâama ($LCOH_2$= 0.91 $/kg; m_{H2} =26424 kg). For the areas of the south; the best coefficient of performance of production of Hydrogen is observed in Illizi ($LCOH_2$= 0.89 $/kg; m_{H2} =27099 kg).

IV. CONCLUSION

A preliminary comparative study on the production costs of electricity and the manufacturing costs of Hydrogen was carried out on new sites representative of Algeria. Three types of modeling of the energy productivity in each site was taken into account. The value of the LCOE differs from an approach has another in same site. The annual average LCOE of the cities of north (Oran - Algiers - Annaba) is estimated at 76.84 $/MWh whereas the average and time monthly LCOE is estimated at 92.11 $/MWh and 102.84 $/kg, respectively. Time modeling always presents the largest LCOE followed by monthly modeling then annual modeling and that whatever the area. It is as observed as the LCOE is inversely proportional to the latitude of the site but also to its longitude. The average time LCOE increases cities of North towards the South while passing by the high plateaus. It drops by 102.84 $/MWh for the coastal regions with 79.36 $/MWh for the areas of the high plateaus and finished with 73.13 $/MWh for the areas of the south. This same rise is noticed while going from the west towards the east. The LCOE increases by 3.94% between the town of Oran (North Western) and the town of Algiers (center), and 2.79% between the town of Algiers (North center) and the town of Annaba (North East). According to the study carried out on the dimensioning of the electrolyser, it is concluded that the best strategy to be adopted is it (S4) because it presents the best quantity report/ratio of hydrogen produced versus production costs. According to this strategy this report/ratio of performance is inversely proportional to the latitude of the site, it decreases while going from north towards the south. Illizi is the area which presents the best report/ratio of performance of production of Hydrogen ($LCOH_2$= 0.89 $/kg; m_{H2} =27099 kg). This work will be extended to the study of operating and climatic conditions impact on the costs and the quantities of hydrogen production.

REFERENCES

[1] F Barbir. "PEM electrolysis for production of hydrogen from renewable energy sources," Solar Energy 78 (2005) 661-669.

[2] E Amores, J Rodriguez, C Carreras. "Influence of operation parameters in the modeling of alkaline water electrolyzers for hydrogen production," International Journal of Hydrogen Energy 39 (2014) 13036-13078.

[3] P Hunag, Kuo J, WU Z. "Applying small wind turbines and a photovoltaic system to facilitate electrolysis hydrogen production," International Journal of Hydrogen Energy 41 (2016) 8514-8524

[4] A Ursùa, EL Barrios, J Pascual, A San Martin, P Sanchis. "Integration of commercial alkaline water electrolysers with renewable energies: limitations and improvements," International Journal of Hydrogen Energy xxx (2016) I-I0

[5] A Khalilnejad, GH Riahi. "A hybrid wind-PV system performance investigation for the purpose maximum hydrogen production and storage using advance alkaline electrolyzer," Energy Conversion and Management 80 (2014) 398-406.

[6] K Sopian , MZ Ibrahim, W Wan Dauda, M Othman , B Yatima , N Amina . "Performance of a PV- wind hybrid system for hydrogen production," Renewable Energy 34(2009) 1973-1978.

[7] B Mahmah, Belhamel M, S Chader , A M'raoui, F. Haroudi, Etievant C, et al. "Project Maghreb Europe: production d'Hydrogène Solaire. Phase I: Etude d'Opportunité et de faisabilité du Projet," 20th World Energy Congress – Rome; Nowember 11th-15th, 2007.

[8] S. K. Kirati, M. Hammoudi, I. A. M. Mousli, "Hybrid Energy System for hydrogen production in the Adrar region (Algeria): production rate and purity level," International Journal of Hydrogen Energy xxx (2017) 1-16.

[9] M. Hammoudi, C. Henao, K. Agbossou, Y Dubé, Ml Doumbia. "New multi-physics approach for modelling and design of alkaline electrolyzers," International Journal of Hydrogen Energy 37 (2012) 138.

*Corresponding author email: h2mousli@outlook.com

Power Management of Fuel Cells and Ultracapacitors for Technobus

H. Bouzeria[1*], I. Abadlia[2] and I. Benouareth[3]

[1*]Department of transport engineering, University of Brothers Mentouri – Constantine -1-, Algeria.
[2, 3]Departement of Electrical engineering, University Badji Mokhtar – Annaba, Algeria.

Abstract— **This paper present the hybridization of fuel cell/ultracapacitor applied to electric buses. They present an optimal design methodology for identifying pathways for progress and guiding the definition of future energy-efficient propulsion chains. They are based on a systemic engineering approach that builds on three main levers: the architecture of the propulsion chain, the energy management strategy and the definition of power electrical organs.**

In this study, an energy management method is proposed for a hybrid electric bus and an energy planning system. The energy sharing law between ultracapacitors and fuel cells brings another advantage, peeling in the current in the battery-with beneficial consequences on the losses and the life of the battery.

The results of simulations, with Matlab/Simulink, highlight the interest of parallel hybridization design an efficient propulsion chain. Every moment of the cycles followed, the stresses of electric power components are determined and analyzed to specify optimal sizing and an energy management system are capable of extending the technobus autonomy while ensuring a good battery life.

Key words—Technobus, ultracapacitor, propulsion, electric machine, power electronics, simulation.

I. INTRODUCTION

High prices for gasoline and oil are here to stay. As China, India and other nations rapidly increase their demand for fossil fuels, future fighting over energy looms large. In the meantime, power plants that burn coal, oil and natural gas, as well as vehicles everywhere, continue to pour millions of tons of pollutants and greenhouse gases into the atmosphere annually, threatening the planet. Well-meaning scientists, engineers, economists and politicians have proposed various steps that could slightly reduce fossil-fuel use and emissions. These steps are not enough. Therefore, this convinces us to dramatically change to hydrogen power, which would be the reasonable answer to this energy crisis problem. New advanced technologies, such as hydrogen fuelled vehicles with fuel cells, can only be accepted by the public if they are perceived as safe, and at the same time, are able to provide full customer satisfaction including normal fuelling convenience. The attitude toward a technology and the risk and satisfaction perceived are strongly dependent on the individual and his or her experience, interest and social background. Furthermore, beyond finding new alternative fuels for internal combustion engines, researchers are working on hydrogen fuel cells that offer another path toward environmentally acceptable power [1–4]. To produce electricity, most PEM fuel cells must be supplied either with hydrogen or with hydrocarbon compounds that can be catalytically decomposed into hydrogen.

There are many types of FCs characterized by their electrolytes. One of the most promising ones to be utilized in electric vehicle applications is the polymer electrolyte membrane FC (PEMFC) because of its relatively small size, lightweight nature, and ease of construction [5,6]. In addition, PEMFC may also be used in residential and commercial power systems [7].

Consequently, the ultracapacitor converter is driven to realize a classical dc bus voltage regulation. The battery converter is driven to maintain the ultracapacitors at a given state-of-charge, here the ultracapacitor voltage regulation. Then, the FC converter is also driven to maintain the batteries at a given state-of-charge, here the battery voltage regulation. As a result, the hybrid system composes of three-controlled variables:

- the dc bus voltage v_{Bus},
- the ultracapacitor voltage V_{UC}, and the battery voltage V_{Bat}.

And three-control variables:

- the ultracapacitor current reference i_{Uref},
- the battery current reference i_{bus}, and the FC current reference i_{FCREF}.

II. SYSTEM STUDY

The study system is shown in Fig. 1. This system consists of Fuel cell, ultracapacitor, power converters, induction machine and control.

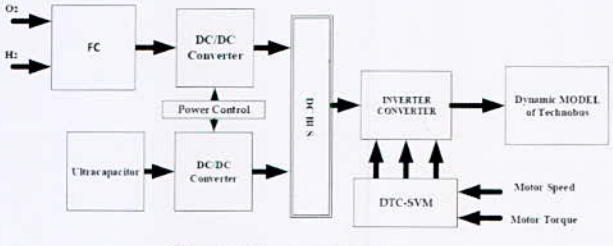

Fig. 1. Proposed system

As depicted in Fig. 1, one may write the classical power conservation law (without losses) of the FC/ Ultracapacitor hybrid power source as follow:

$$P_{load} = P_{UC} + P_{FC} \quad (1)$$

*Corresponding author email: bouzeria.hamza@umc.edu.dz

III. SPACE VECTOR PULSE WIDTH MODULATION

The SVPWM deems the motor and the inverter as one object, trying to provide motor with circular magnetic field with constant amplitude. According to ideal flux circle generated by three-phase symmetric sinusoidal voltage, using the effective voltage vector generated by different switch patterns of inverter to approximate the standard flux circle. So we defined the following variables [8]:

$$\begin{cases} U_{ref\,a} = U_\beta \\ U_{ref\,b} = U_\alpha(1.73) - U_\beta \\ U_{ref\,c} = -U_\alpha(1.73) - U_\beta \end{cases} \quad (2)$$

The conducting time of each inverter switch is shown in Table II.

TABLE II
T1 AND T2 IN DIFFERENT SECTORS

N	1	2	3	4	5	6
T_1	-Z	Y	X	Z	-Y	-X
T_2	X	Z	-Y	-X	-Z	Y

With,

$$\begin{cases} X = U_\beta . T(1.73)/U_{dc} \\ Y = \left(3U_\alpha + U_\beta(1.73)\right)T/2U_{dc} \\ Z = \left(-3U_\alpha + U_\beta(1.73)\right)T/2U_{dc} \end{cases} \quad (3)$$

So, the action time are defined as following:

$$\begin{cases} T_a = (T - T_1 - T_2)/4 \\ T_b = 0{,}5T_1 + T_a \\ T_c = 0{,}5T_2 + T_b \end{cases} \quad (4)$$

Assign T1, T2 and T3 according to Table III, where are defined as the conducting time of phase a, b and c, respectively. Through domain of action times are illustrate by "Fig. 2"

TABLE III
CALCULATION OF SWITCH POINT

N	1	2	3	4	5	6
T_1	T_c	T_a	T_b	T_c	T_a	T_b
T_2	T_a	T_c	T_b	T_a	T_a	T_c
T_3	T_b	T_b	T_a	T_b	T_c	T_a

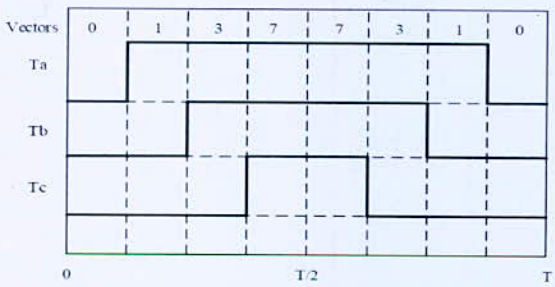

Fig. 2. SVM voltage vector timing

IV. DTC-SVM CONTROL OF IM

The technic of direct torque control with space vector pulse width modulation (DTC-SVM) is based on closed loop flux and torque control, the calculation of reference voltage vector is based on demand.

This differentiation algorithm is very sensitive to disturbances. In case of errors in the feedback signals, the differentiation algorithm may not be stable and this is very serious drawback of these methods that causes torque and flux ripple with deteriorate the performance of system. The proposed method DTC-SVM based on amplitude stator voltage and stator flux angle is used to modify the control system. In this method, the amplitude of stator voltage is controlled by PI torque and PI flux controller. The stator flux angle is controlled by rotor angular frequency and slip angular frequency. Fig. 3, shows the block diagram of sensor DTC –SVM based on amplitude voltage and stator flux angle. This control system consists of PI controller for slip angular frequency, PI torque controller, PI flux controller and Cartesian to polar transformation block to calculate amplitude of stator voltage, while polar to Cartesian block is used to calculate stator voltages in direct and quadrature reference frame at next sampling time. In this method, the PI speed controller is used to optimize the reference torque (T_{ref}) of the motor from the error between reference speed and the rotor speed (ω_{ref}, ω_r) respectively as:

$$T_{ref} = K_p(\Delta\omega + \frac{1}{T_i}\int \Delta\omega dt) \quad (5)$$

Where,

$$\Delta\omega = \omega_{ref} - \omega_r \quad (6)$$

Then, the optimized torque is compared with the estimated torque to generate an error signal. This signal is the input of PI torque controller that computes the value of d-q axis voltage. The output of PI torque controller can be expressed as:

$$V_{sq} = K_p(\Delta T_e + \frac{1}{T_i}\int \Delta T_e dt) \quad (7)$$

Where

$$\Delta T_e = T_{ref} - T_e \quad (8)$$

The reference flux is compared with real flux to generate error signal. The error signal is applied to the PI flux controller to compute the value of d-axis voltage. The d-axis voltage can be derived as:

$$V_{sd} = K_p(\Delta\varphi + \frac{1}{T_i}\int \Delta\varphi dt) \quad (9)$$

Where,

$$\Delta\varphi = \varphi_{ref} - \varphi_e \quad (10)$$

Based on Cartesian to polar block, these q and d axis voltages are converted into amplitude voltage.

*Corresponding author email: bouzeria.hamza@umc.edu.dz

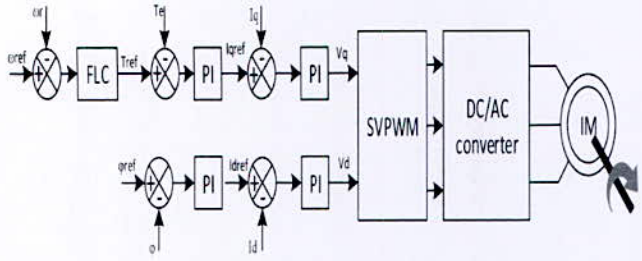

Fig. 3. Scheme of DTC-SVM

V. Simulation and Interpretation

The results of simulation are reported in Fig. 4, Fig. 5, Fig. 6, Fig. 7 and Fig. 8. There are four main periods:

1st case [0→4s]: Accelerate 70%, the bus power increases and we observe peak on the power of the SOC of SC, then the bus maintain to use the ultracapacitor at startup. After some time and up to the production of hydrogen. The bus consumes the power of the fuel cell.

2nd case [4→8s]: in this period we are going to accelerate the bus to 50% maintain the hydrogen production is decreased after a period, and the battery charge by energy recovery of the fuel cell.

3rd case [8→12s]: Accelerate the bus to 80%, we observe an increase in the power of pill and increase in use the plow power. The bus uses the maximum power of UC (25 kW) while awaiting the fusing power production of the fuel cell

4th case [12→20s]: Now we are going to accelerate the bus to -70%, we observe that the hydrogen production is decreased and it stops after a period, the energy recovery loads UC to the limited value.

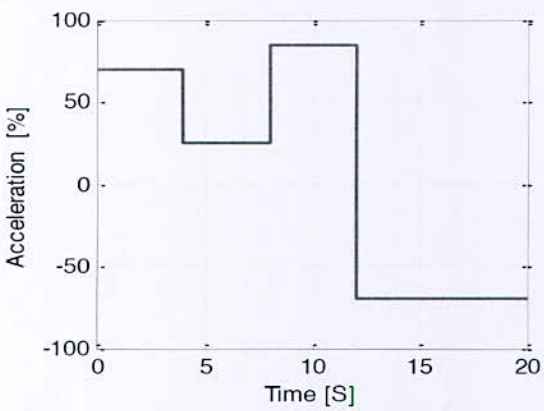

Fig. 4. Acceleration response

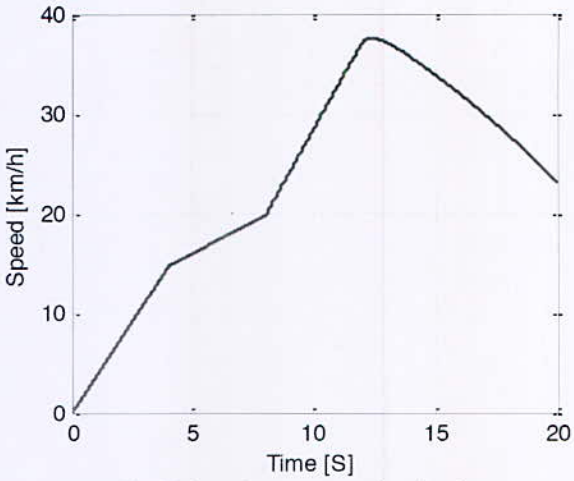

Fig. 5. Speed response of technobus

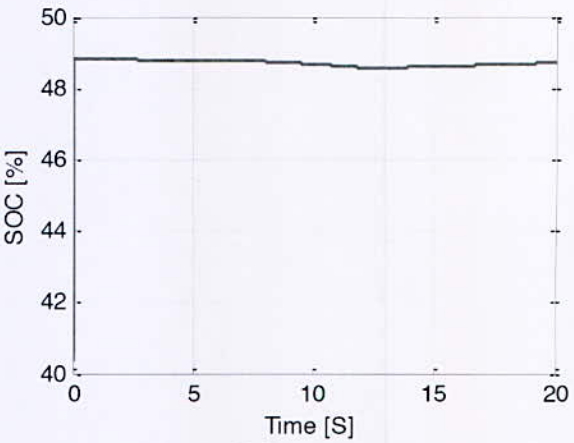

Fig. 6. SOC of ultracapacitor

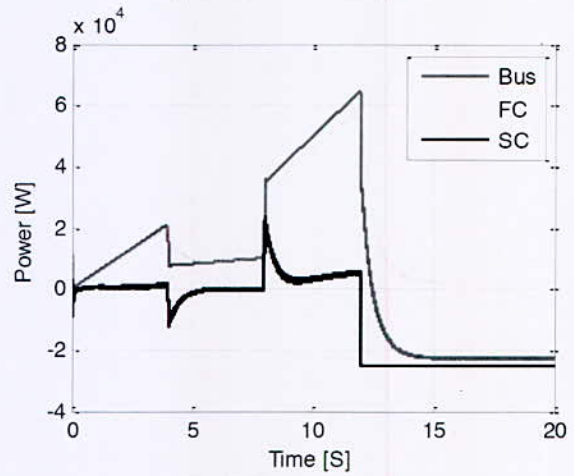

Fig. 7. Power responce

*Corresponding author email: bouzeria.hamza@umc.edu.dz

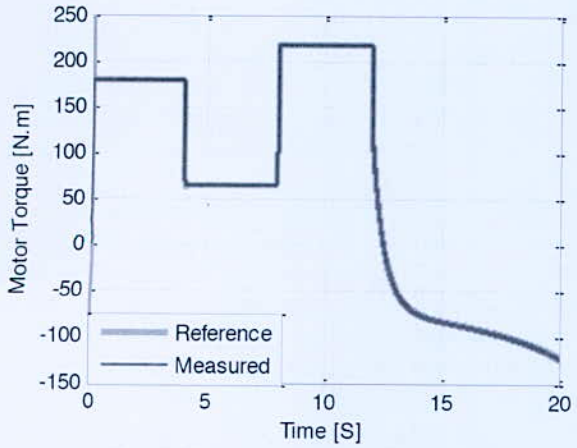

Fig. 8. Torque response of technobus

From the simulation results, when we obtained from Matlab / Simulink we can see that the DTC-SVM control follows the set point and ensures a high dynamic effeciency during the different periods.

Concerning the power management, it is noted that the ultracapacitor ensures the continuity of the system during the transitional regime of hydrogen production and it is able to extend the autonomy of ultracapacitor while including a good autonomy.

VI. CONCLUSION

The growing environmental concerns related to greenhouse gas emissions and the depletion of fossil fuels bring public transport manufacturers to propose electric buses that are increasingly efficient.

The results of simulations, with Matlab/Simulink, highlight the interest of parallel hybridization design an efficient propulsion chain. Every moment of the cycles followed, the stresses of electric power components are determined and analyzed to specify optimal sizing and an energy management system are capable of extending the technobus autonomy while ensuring a good battery life.

REFERENCE

[1] Schulte I. et al. Issues affecting the acceptance of hydrogen fuel. Int J Hydrogen Energy; vol 29 pp 677–85. 2004

[2] W. Schmittinger, A. Vahidi, J. Power Sources 180. pp 1–14, 2008.

[3] Phatiphat Thounthong, Stephane Raël, Bernard Davat. "Energy management of fuel cell/battery/supercapacitor hybrid power source for vehicle applications "Journal of Power Sources N°193, pp 376–385.2009.

[4] M. Romer, G.H. Miley, N. Luo, R.J. Gimlin, IEEE Trans. Energy Convers. 23 (2008) 171–178.

[5] De Miranda, P. E. V., Carreira, E. S., Icardi, U. A., et al. Brazilian hybrid electric-hydrogen fuel cell bus: Improved on-board energy management system. International Journal of Hydrogen Energy, 2017, vol. 42, no 19, p. 13949-13959.

[6] Li, Jianwei, Zhang, Min, Yang, Qingqing, et al. SMES/battery hybrid energy storage system for electric buses. IEEE Transactions on Applied Superconductivity, 2016, vol. 26, no 4, p. 1-5. M.C. Péra, D. Candusso, D. Hissel, J.M. Kauffmann, IEEE Ind. Electron. Mag. Vol.1 pp 28–37, 2008.

[7] X. Wang, Y. Xing, Z. He and Y. Liu, "Research and simulation of DTC Based on SVPWM pf PMSM", Procedia Engineering, International Workshop on Information and Electronics Engineering, Vol. 29, pp. 1685-1689, 2012.

Nomenclature

i_{FCREF}	Reference current of fuel cell
H_2	Hydrogen
K_p, K_I	Coefficient of proportionnel and integral
O_2	Oxygen
P_{FC}	Power of Fuel Cell
P_{load}	Power load
P_{uc}	Power ultracapaciter
T_e, T_l	Electromagnetic and load torque
φ_{ref}, φ_r	flux reference and measured, respectively
ω_{ref}, ω_r	Speed reference and measured, respectively

Abbreviations

DTC	Direct torque control
FC	Fuel cell
FLC	Fuzzy logic controller
IM	Induction machine
PEM	proton exchange membrane
PI	Propotionnel integral controller
PWM	Pulse width modulation
SVM	Space Vector Modulation
SOC	State of charge

*Corresponding author email: bouzeria.hamza@umc.edu.dz

Hydrogen Production by Biological Process

S. Menia*, I. Nouicer, H. Tebibel, A. Khellaf

*Centre de Développement des Energies Renouvelables, B.P. 62, Route de l'Observatoire, Bouzaréah 16340 Algiers, Algeria.

Abstract—**Hydrogen is a viable alternative source to replace conventional fossil fuels due to its clean, renewable and energy efficient nature (122 kJ/g). This energy efficiency is 2.75 times higher than that of hydrocarbon fuels. When hydrogen is used as a fuel, its main combustion product is water, which can be recycled to produce more hydrogen, but unlike fossil fuels, hydrogen gas is not readily available in nature and the production methods commonly used are quite expensive. During the last years, a significant use of hydrogen has been demonstrated for buses, ships and submarines, including chemical and petrochemical applications. Currently, about 98% of the hydrogen comes from fossil fuels. Globally, 40% of the hydrogen is produced from natural gas or steam reforming of hydrocarbons, 30% from petroleum, 18% from coal and the remaining 4% from electrolysis of water. However, these processes and those involving power generations are expensive and not always environmentally friendly. Biological processes for the production of hydrogen provide an alternative method of hydrogen production can operate at ambient temperatures and pressures are less energy consuming and more environmentally friendly compared to conventional chemical methods. This approach is not only ecological, but also opens up new ways for the exploitation of unlimited renewable energy resources. In addition, they can also use various wastes, which facilitate the recycling of waste.**

Biological hydrogen generation employing carbohydrate rich biomass as a renewable resource is one of the different methods in which processes can occur via an anaerobic process (dark fermentation) and a photosynthesis process (photo-fermentation).

Key words—hydrogen, photo fermentation, dark fermentation.

I. INTRODUCTION

The growing demand for energy requires scientists, engineers and a host of research teams to develop different schemes to produce energy with reduced environmental impact and carbon footprint [1-6].

In the past years, the interests of research and development have been oriented towards renewable energy technologies such as anaerobic digestion (AD) of organic biomass and waste. For alternative energy carriers, hydrogen could be the fuel of the future because of its high energy content, respect for the environment and also because it can give important social, economic and environmental qualifications. Hydrogen is a carbon-free clean fuel, because the only final by-product of its combustion is water. Hydrogen can also be useful for addressing global warming and increasing pollution problems. In addition, it is preferable to methane because of its wider industrial applications, i.e. H_2 is used in the synthesis of ammonia and the hydrogenation of edible oil, petroleum, coal and of the schist oil. Hydrogen can be used directly in combustion engines because of its higher energy per unit of weight among known gaseous biofuels (143 GJ/t) or to generate electricity via fuel cell technologies. Thus, the creation of a hydrogen economy that incorporates the production and use of hydrogen as an energy carrier could lead to sustainable energy systems in the future [7].

Hydrogen can be produced from less energy-consuming and more environmentally friendly biological processes in terms of overall CO_2 reduction. These technologies for the production of renewable bio hydrogen have the potential to become cost-competitive because they can use low-value biomass as a raw material, for example municipal, agricultural and industrial waste, and wastewater. Bio hydrogen can be produced by both autotrophic and heterotrophic microorganisms. In autotrophic conversions (also known as direct or indirect bio photolysis), solar energy is directly converted to hydrogen by photosynthetic reactions via photosynthetic microorganisms, namely microalgae and photosynthetic bacteria. Under heterotrophic conditions, organic substrates are transformed into simpler organic compounds with simultaneous production of molecular hydrogen. There are two types of heterotrophic conversions, photo-fermentation carried out by photosynthetic bacteria and dark fermentation carried out by anaerobic bacteria which transform carbohydrates into bio hydrogen [7].

The objective of this study is to compare the various bio-hydrogen production techniques.

II. THEORETICAL STUDY

1. Bio hydrogen

Hydrogen has been recognized as one of the cleanest potential fuels for the future, where it is a promising alternative to conventional fossil fuels, which are rapidly depleted because they are used indiscriminately and harm the environment because the harmful gases are released during their combustion. Bio-hydrogen is also environmentally friendly because it only releases water vapour and energy during combustion. Hydrogen also has

*Corresponding author email: s.menia@cder.dz

the highest energy content, 142 kJ/g or 61,000 Btu /lb of all known fuels. Today, 40% of the hydrogen is produced from natural gas, 30% from heavy oil and naphtha, 18% from coal, 4% from electrolysis and 1% from biomass. Hydrogen is used as fuel for an internal combustion engine or fuel for fuel cells. However, the largest users of hydrogen are fertilizers and petroleum industries with respectively 50% and 37% of consumption. Due to the use of renewable energy resources, sustainability is achieved and in view of the energy crisis and environmental distress, the biological production of hydrogen at contiguous temperature and atmospheric pressure is receiving increasing attention in the present era. Unlike chemical and electrochemical fuels, the biological processes of hydrogen production are catalysed by microorganisms in an aqueous environment at optimum temperature and atmospheric pressure. The characteristics of these microorganisms differ widely from one another in terms of substrate and process conditions. In addition, these techniques are ideally suited to the decentralized generation of energy in pilot plants and their location where biomass and waste are readily available, avoiding energy costs and transport costs [8].

2. *Bio-hydrogen production methods*

The biological production of hydrogen involves the use of specialized microbes in a bioreactor. Common methods for the production of biological hydrogen include dark fermentation, photo fermentation, direct photolysis, indirect photolysis and sequential fermentation [9].

Enzymes play an important role in catalysing the production of bio-hydrogen. Recent studies of the enzymatic potential of hydrogen production show that they possess complex metal groups as active sites. In this case, the three predominant enzymes involved in this reaction are as follows: Nitrogenase, Fe-hydrogenase and Ni-hydrogenase in which Fe-hydrogenase is widely used in bio photolysis and nitrogenase in the photo-fermentation process [8].

Photo fermentation

In photo-fermentation, gaseous hydrogen is produced by anaerobic bacteria that metabolize volatile organic acids including lactic acid, acetic acid and butyric acid in the presence of light. These volatile acids are used by microbes as a source of carbon for their metabolism thus releasing hydrogen as a by-product [9].

$\Delta G_0 = +\ 104$ kJ

$$2CH_3COOH + 2H_2O + \text{light energy} \longrightarrow 4H_2 + 2CO_2 \quad (1)$$

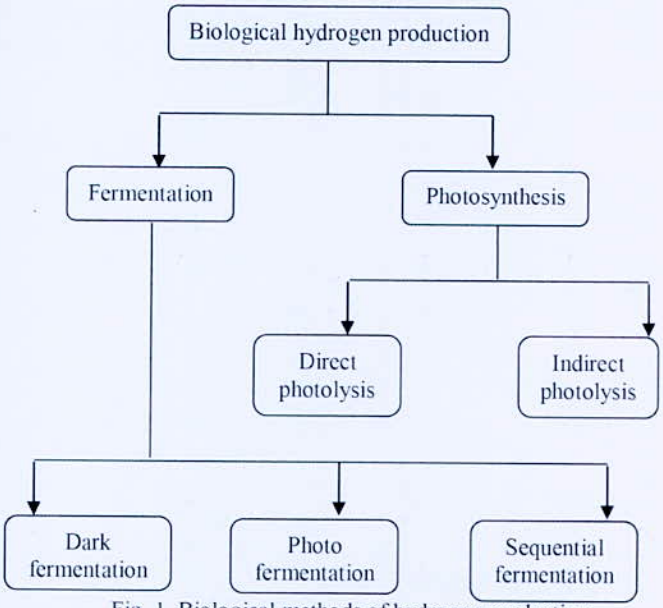

Fig. 1. Biological methods of hydrogen production

Gibbs' positive energy implies that an external energy source is needed for the continuation of the process. Light energy in this regard provides energy to microbes. The productivity of the photo-fermentation process of hydrogen is very dependent on the available light energy. A study using Rhodobacter sphaeroides with various volatile acids as a carbon source reported a maximum hydrogen yield of 794 mmol H_2/mole-substrate for 2 g/l lactate and 2 g/l succinate. The design of a reactor for photo-fermentation and the selection of a specialist in bio-hydrogen are the most important factors for improving production yields. The use of transparent columns or tubes is favourable because it maximizes the penetration of light into the reactor contents. A study of Rhodobacter sphaeroides in a column bioreactor observed an optimal operation at pH 7.5 for the production of hydrogen. The study reported a maximum hydrogen production rate of 40 ml/h [9].

Dark fermentation

In dark fermentation, hydrogen is produced by carbohydrate substrates. Fermentation reactions can operate at mesophilic temperatures, thermophilic, extreme thermophilic or hyper-thermophilic. Depending on the fermentation route and the finished products, the production of hydrogen varies considerably with regard to bacterial species such as Enterobacteria, Bacillus and Clostridium and the various forms of preferred carbohydrates as substrates [8]. The process involves the production of intermediates or volatile chemicals including acetate, ethanol, propionate or butyrate depending on the mechanism used. The route that

*Corresponding author email: s.menia@cder.dz

produces the acetate is the most favourable because it can give up to four molecules of hydrogen per hexose [9].

$\Delta G_0 = -184.2$ kJ

$$C_6H_{12}O_6 + 2H_2O \longrightarrow 2CH_3COOH + 4H_2 + 2CO_2 \quad (2)$$

When the butyrate is the final product, a theoretical maximum of 2 mole of H_2/mole of glucose is obtained [8].

$$C_6H_{12}O_6 + 2H_2O \longrightarrow CH_2CH_2CH_2COOH + 2H_2 + 2CO_2 \quad (3)$$

Negative energy implies that energy is released and that the process can proceed without an additional source of energy [9].

The production of hydrogen by these bacteria strongly depends on process parameters such as pH, the hydraulic retention time (HRT) and the partial pressure of the gas which affects the metabolic equilibrium. Thus, the finished fermentation products produced by a bacterium depend on the environmental conditions in which it grows. The finished products of fermentation such as ethanol, butanol and lactate contain hydrogen which has not been released as a gas and to maximize the yield of H_2, the metabolism of the bacterium should be directed away from alcohols and reduced acids to volatile fatty acids (VFA). C pasteurianum is a classic producer of H_2 and VFA, but its metabolism can be directed away from the production of hydrogen and towards the production of solvents by high concentrations of glucose, by the CO and by limiting the concentrations of Fe [8].

Sequential fermentation

The dark fermentation and the photo fermentation were considered as important technologies of production of hydrogen. However, the disadvantage of the dark fermentation / photo fermentation process is a lower hydrogen yield due to the accumulation of short chain organic acids and the costs of pure organic acids. These problems can be overcome by adopting the sequential technique of photo fermentation and dark fermentation. Waste from dark fermentation is used as a substrate for photosynthetic bacteria in the photo-fermentation process. The sequential process of dark fermentation and photo-fermentation has a theoretical maximum hydrogen yield of 12 moles of H_2/mole of sugar. A sequential fermentation is a promising technique for increasing hydrogen production from carbohydrate-rich waste and wastewater. The technique seems to be the most attractive approach for providing clean and sustainable energy in the future by providing a higher hydrogen yield compared to single-stage approaches of dark fermentation and photo-fermentation [10].

$\Delta G_0 = +3.2$ kJ

$$C_6H_{12}O_6 + 6H_2O \longrightarrow 12H_2 + 6CO_2 \quad (4)$$

Various researchers have reported the technique of dark sequential fermentation and photo-fermentation to increase the production of hydrogen. The improved yield of hydrogen produced from cassava starch by mixed bacteria by a combination of dark fermentation and photo fermentation was reported by Cheng et al [11]. In the dark fermentation phase, the maximum yield of hydrogen was 2.53 mole H_2/mole hexose, using mixed anaerobic bacteria. In photo-fermentation, immobilized mixed bacteria were used to produce hydrogen from soluble metabolite products of dark fermentation. The maximum yield of the hydrogen in photo-fermentation was 3.54 mole H_2/mole hexose. The total hydrogen yield increased considerably from 2.53 to 6.07 mole H_2/mole hexose by mixed bacteria and cellular immobilization combined with dark fermentation and photo fermentation. Similarly, Su et al reported that the hydrogen yield of cassava starch increased considerably from 240.4 ml of H_2/g starch in the dark fermentation to 402.3 ml of H_2/g of starch in combined mode [12].

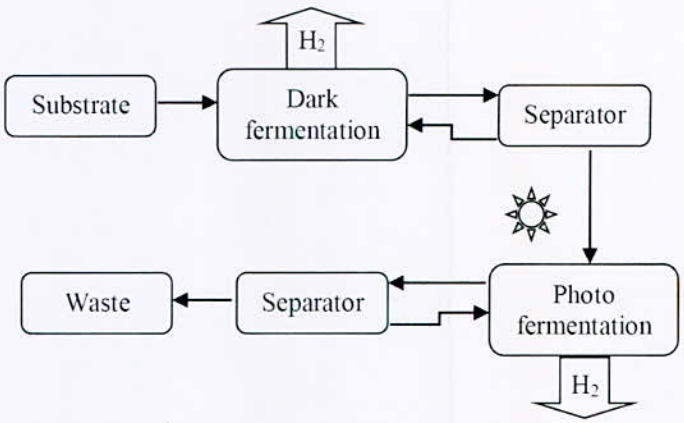

Fig. 2. Scheme for sequential dark and photo fermentation process for hydrogen production from biomass

III. CONCLUSION

In conclusion, organic production of hydrogen is the most difficult commitment of the past decade, as global energy demand increases, fossil fuel resources are reduced and the need to minimize greenhouse is becoming more and more worrying.

Since steam re-sealing or partial oxidation of fossil hydrocarbon fuels operates at high temperatures, chemical methods require very high operating costs. It is necessary to develop a new process in order to obtain hydrogen with a low cost of production. The biological method has potential as an alternative to current renewable technologies, as it offers promising benefits such as operating under mild conditions and an acceptable conversion rate.

*Corresponding author email: s.menia@cder.dz

There are various technologies used for the biological production of hydrogen including bio photolysis of water by cyanobacteria and green microalgae, photo fermentation, dark fermentation and bio-electrochemical processes. The production of hydrogen using bio photolysis systems by cyanobacteria and green microalgae becomes an alternative method of recovering gaseous energy and can be applied in the production of renewable energy.

In dark fermentation, the conversion of organic compounds to hydrogen by a complex process involves a diverse group of bacteria with series of biochemical reactions. While in photo-fermentation, the conversion of organic compounds to gaseous hydrogen can take place only in the presence of light. By combining the two processes, it is currently the most interesting approach that can be used to increase the production of hydrogen. In this process, in addition to having higher levels of hydrogen production, fast and simple operation, it can be used with a variety of organic waste as substrates. Thus, compared to hydrogen production through photosynthesis, the production of hydrogen via fermentation is more suited to produce cleaner energy and to treat organic waste more efficiently.

REFERENCES

[1] D. E. Algapani, W. Qiao, M. Su, F. di Pumpo, S. M. Wandera, F. Adani, R. Dong, Bio-hydrolysis and bio-hydrogen production from food waste by thermophilic and hyper thermophilic anaerobic process, *Bio resource Technology 216*, 2016, pp. 768–777.

[2] K. Chandolias, S. Pardaev, M. J. Taherzadeh, Bio hydrogen and carboxylic acids production from wheat straw hydrolysate, *Bio resource Technology 216*, 2016, pp. 1093–1097.

[3] R. Jariyaboon, S. O-Thong, P. Kongjan, Bio-hydrogen and bio-methane potentials of skim latex serum in batch thermophilic two-stage anaerobic digestion, *Bio resource Technology 198*, 2015, pp. 198–206.

[4] G. Kumar, P. Bakonyi, S. Periyasamy, S. H. Kim, N. Nemestóthy, K. Bélafi-Bakó, Lignocellulose bio hydrogen: practical challenges and recent progress, *Renewable Sustainable Energy Review 44*, 2015a, pp. 728–737.

[5] V. L. Pachapur, S. J. Sarma, S. K. Brar, Y. Le Bihan, G. Buelna, M. Verma, Bio hydrogen production by co-fermentation of crude glycerol and apple pomace hydrolysate using co-culture of Enterobacter aerogenes and Clostridium butyricum, *Bio resource Technology 193*, 2015, pp. 297–306.

[6] G. Kumar, A. Mudhoo, P. Sivagurunathan, D. Nagarajan, A. Ghimire, Chyi-How Lay, C. Y. Lin, D. J. Lee, J. S. Chang, Recent insights into the cell immobilization technology applied for dark fermentative hydrogen production, *Bio resource Technology 219*, 2016, pp. 725–737.

[7] A. Ghimire, L. Frunzo, F. Pirozzi, E. Trably, R. Escudie, P. N. L. Lens, G. Esposito, A review on dark fermentative bio hydrogen production from organic biomass: Process parameters and use of by-products, *Applied Energy 144*, 2015, pp. 73–95.

[8] B. Bharathiraja, T. Sudharsanaa, A. Bharghavi, J. Jayamuthunagai, R. Praveenkumar, Bio hydrogen and Biogas-An overview on feedstocks and enhancement process, *Fuel 185*, 2016, pp. 810–828.

[9] M. M. Arimi, J. Knodel, A. Kiprop, S. S. Namango, Y. Zhang, S. U. Geißen, Strategies for improvement of bio hydrogen production from organic-rich wastewater: A review, *Biomass and Bioenergy 75*, 2015, pp. 101-118.

[10] L. Singh, Z. A. Wahid, Methods for enhancing bio-hydrogen production from biological process: A review, *Journal of Industrial and Engineering Chemistry 21*, 2015, pp. 70–80.

[11] J. Cheng, H.B. Su, J.H. Zhou, W.L. Song, K.F. Cen, *International Journal of Hydrogen Energy 36*, 2011, 450.

[12] H.B. Su, J. Cheng, J.H. Zhou, W.L. Song, K.F. Cen, *International Journal of Hydrogen Energy 34*, 2009, 1780.

*Corresponding author email: s.menia@cder.dz

Exploring the Efficiency of NiAl-CO_3 and NiFe-CO_3 in the Process of CO_2 Reforming of Methane: Prioritizing the Role of Carbon Resistance While Maintaining Elevated Catalyst Activity

M. Sehailia[1*], F. Touahra[1, 2], F. Bali[2], N. Aider[2, 3], B. Djebarri[2, 4], A. Saadi[2], K. Bachari[1] and D. Halliche[2]

[1*]Centre de Recherche Scientifique et Technique en Analyses Physico-chimiques (CRAPC), BP 384-Bou-Ismail-RP 42004, Tipaza, Algeria.

[2]Laboratory of Natural Gas Chemistry, Faculty of Chemistry (USTHB), BP 32 16111 Algiers, Algeria.

[3]Département de Chimie, Faculté des Sciences (UMMTO), Tizi-ouzou, Algeria.

[4]Department de Chimie, Faculty of sciences, University of M'hamed Bougara, Independence Avenue, 35000 Boumerdès, Algeria.

Abstract—**CO_2 reforming of methane, also named dry reforming of methane, is a method of producing hydrogen from the reaction of carbon dioxide with methane ($CH_4+CO_2 \leftrightarrow 2H_2+2CO$). The major problem associated with this reaction is the sintering of the active phase and carbon formation. The carbon generated during this reaction can be the result of direct decomposition of methane ($CH_4 \leftrightarrow C+2H_2$) or the Boudouard reaction ($2CO \leftrightarrow CO_2+C$). Many ideas were put forward by scientists to develop catalysts bearing both high activity and high resistance to coke. The activity of a catalyst is related to the metal surface area, i.e., the number of active sites. This implies that the catalytic activity is proportional to the high dispersion of metal particles. The aim of the present work is to investigate the use of NiAl-CO_3 and NiFe-CO_3 derived hydrotalcite-like compounds, previously prepared by co-precipitation method with Ni^{2+}/Al^{3+}=2 at pH =12 in the reaction of dry reforming of methane. The products obtained after heat treatment under air at 800 °C were characterized by XRD, ICP, SEM-EDX and TEM. After reduction, the catalysts were evaluated in the reforming of methane reaction under continuous flow with CH_4/CO_2 ratio equal to 1, at atmospheric pressure and a temperature range [400-700°C]. The catalytic activity was tested in a fixed bed reactor. At 700 °C, the catalysts showed significant CH4 conversions, i.e, 87.0% and 79.0% for NiAl-CO_3 and NiFe-CO3 respectively; this was compared to 91.0%, and 84.0% for CO_2 conversions. Despite NiAl-CO_3 derived catalyst exhibiting rather high catalytic activity compared to NiFe-CO_3, the latter showed a good resistance to metal sintering and carbon deposition.**

Key words—hydrotalcite, microwave, Ni, methane dry reforming.

I. INTRODUCTION

The reaction of dry reforming of methane has long been established by the scientific community as one of the many solutions that can be utilised to tackle the great challenge of global warming [1, 2, 3, 4]; the process uses two major greenhouse gases, i.e., CO_2 and CH_4, to produce syngas, a mixture containing CO and H_2 [5]. The generated gas is then converted to other value added hydrocarbons *via* the Fischer-Tropsch synthesis. To effect the process of dry reforming of methane, many catalysts have been exploited to enhance the efficiency of the overall reaction; catalysts such as Rh, Ru, Pt and Ni have all shown distinct activities for this type of reaction, however, to minimise costs, scientists elected to focus most of their efforts in investigating the efficiency of Ni derived catalysts as one of the main promoters for such reaction [4]. Most supports utilised in this case comprises of metal oxides such SiO_2, Al_2O_3 and La_2O_3 [6, 7]. It has been well acknowledged in literature that the nature of the support plays an important role in determining the mechanism of the reaction. Inactivated supports such as SiO_2 tend to have reactions driven via activating both CH_4 and CO_2 on the metal catalyst, e.g., Ni [8]. However, the presence of metal oxide supports such as Al_2O_3 tend to play a role in activating CO_2 from the one hand while CH_4 is activated over the metal catalyst [9]. One of the main drawbacks associated with the reaction of dry reforming of methane are: (i) the sintering of metal sites which tend to increase the size of metal particles, thus, reducing the catalyst's conversion efficiency and (ii) the formation of coke, mainly generated from the concurrent process of methane decomposition, on the catalyst's surface, thus preventing direct contact between the active catalyst and reactants [10]. To address these challenges, many ideas were put forward by scientists among which the incorporation of certain additives such as MgO in Ni/Al_2O_3 type catalysts was found to reduce the acidity of the material and prevent sintering of the active metal sites *via* the formation of $MgAl_2O_4$ spinel phase, the latter can act by minimising interactions between Ni and Al_2O_3, thus, extending the life time of the catalyst at elevated temperatures [11]. The addition of other additives such as CeO_2, which can act as an oxygen storing specie, have also shown superior resistance to coking in dry reforming of methane reactions. CeO_2 can act as a promoter to oxidise the dehydrogenated CHx intermediates during the process of methane decomposition, thus eliminating the formation of coke as byproduct [12]. Moreover, the small particle size of the metal catalyst was also found to influence the activity of the catalyst as well as increasing its ability to coke resistance. In this paper, we were successfully able to make NiAl-CO_3 and NiFe-CO_3 derived catalysts, namely $NiAl_{cal}$-R and $NiFe_{cal}$-R, both

*Corresponding author email: moussa.sehailia@crapc.dz

synthesised from structurally unique hydrotalcite-type materials, and studied their catalytic activity in the reaction of dry reforming of methane.

II. RESULTS AND DISCUSSION

In this study, NiAl-CO_3 and NiFe-CO_3 were synthesised using co-precipitation method. $Ni(NO_3)_2$ was added slowly to a solution containing either $Al(NO_3)_3$ or $Fe(NO_3)_3$ in the presence of NaOH (2M) and sodium carbonate (0.5M). The addition was performed at room temperature over the course of 5 hours while stirring. The resulting mixture was refluxed at 70 °C for 15 hours. The obtained gel was washed with distilled water to remove $NaNO_3$. The resulting product was then dried at 100 °C in an oven overnight until a homogenous powder is obtained. The solids were then subjected to calcination at 800 °C for 6 hours with temperature increments of 5 °C/min.

Analysis of the carbonated materials using ICP demonstrated the presence of a ratio Ni/Al = 2.03 and Ni/Fe = 2.44. Table I summarises the quantitative elemental compositions found within NiAl-CO_3 and NiFe-CO_3.

TABLE I
CHEMICAL COMPOSITION OF THE SYNTHESISED INTERMEDIATES NIAL-CO3 AND NIFE-CO3

Material	Chemical composition (mass %)					Proposed chemical formulae	Calculated molar ratio (M^{2+}/M^{3+})	Theoretical molar ratio (M^{2+}/M^{3+})
	Ni	Al	Fe	N	C			
NiAl-CO_3	39.32	8.90	-	0.015	2.41	$[Ni_{0.67}Al_{0.33}(OH)_2][(NO_3)_{0.015}(CO_3)_{0.2}, 0.22\ H_2O]$	2.03	2
NiFe-CO_3	41.70	-	16.20	0.15	2.04	$[Ni_{0.71}Fe_{0.29}(OH)_2][(NO_3)_{0.011}(CO_3)_{0.17}, 0.51\ H_2O]$	2.44	2

The specific surface areas of our materials prior to and after calcination (NiAlcal and NiFecal) were also studied using N2 physisorption technique at -196 oC (Micromeritics ASAP 2020). The results are summarised in Table II.

TABLE II
SPECIFIC SURFACE AREA AND PORE SIZE VOLUME FOR THE SYNTHESISED MATERIALS PRIOR TO AND AFTER CALCINATION

Samples	Prior to calcination			After calcination (at 800°C)		
	S_{BET} (m^2/g)	Pore volume (cm^3/g)	Mean diameter of pores (nm)	S_{BET} (m^2/g)	Pore volume (cm^3/g)	Mean diameter of pores (nm)
NiAl-CO_3	90	0.345	12.91	120.5	0.251	10.90
NiFe-CO_3	57.5	0.116	10.26	105.2	0.081	9.74

Prior to calcination, S_{BET} for NiAl-CO_3 was slightly higher than that for NiFe-CO_3, however, such effect was reversed after calcination whereby we notice a slightly larger S_{BET} in case of NiAl-CO_3. This phenomenon was perhaps attributed to the degasing effect of H_2O and CO_3^{2-} which are present on the surfaces' pores; this process prompts a reduction in the size of the pores, which is clearly reflected on Table II, thus leading to an increase in the specific surface area of the material.

Following reduction at 750 °C, S_{BET} of Ni^0 within $NiAl_{cal}$-R and $NiFe_{cal}$-R were reduced to 105.50 m^2/g and 87.11 m^2/g respectively (Table III).

TABLE III
SURFACE AREA AND PARTICLE SIZE OF SYNTHESISED MATERIALS AFTER REDUCTION

Sample	S_{BET} (m^2/g)		Particle size of the reduced solid (nm)				
	Calcined	Reduced	[a](Ni^0)	Alloy: [a](γ-NiFe)	[b](Ni^0)	Alloy [b](γ-NiFe)	Alloy: [c](γ-NiFe)
NiAl-CO_3	120.51	105.50	17	-	16.5	-	-
NiFe-CO_3	116.20	87.11	17.5	29	17.20	27	28

Equally, small Ni^0 particle sizes were also obtained after reduction. The particle sizes of Ni^0 in NiFe alloys were 65% greater than those in $NiAl_{cal}$-R.

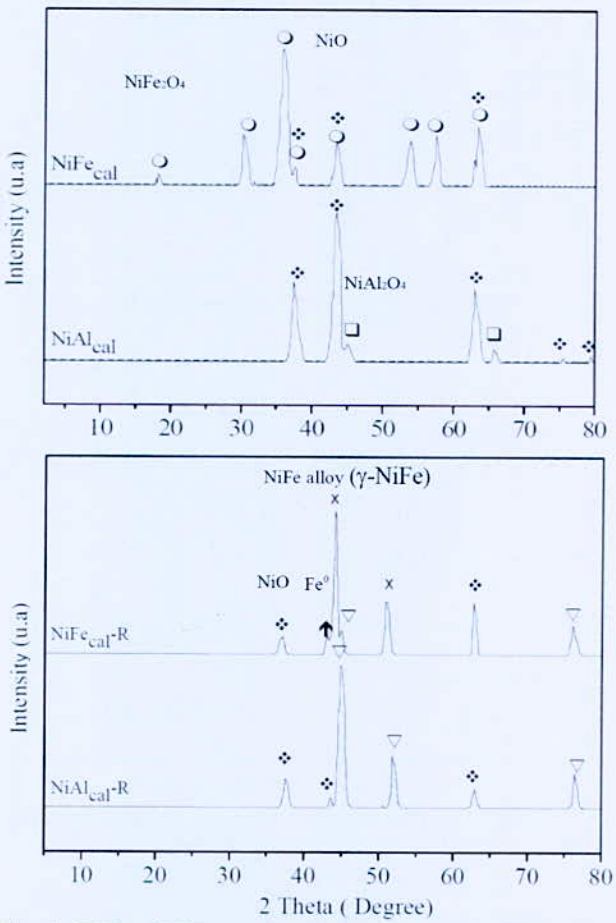

Fig. 1. XRD of $NiFe_{cal}$, $NiAl_{cal}$, $NiAl_{cal}$-R and $NiFe_{cal}$-R

*Corresponding author email: moussa.sehailia@crapc.dz

XRD analysis of both materials following calcination at 800 °C clearly demonstrated the presence of metal oxides (Fig. 1). In the case of $NiFe_{cal}$, XRD analysis depicted the presence of $NiFe_2O_4$ spinel phases [JCPDS n° 10-0325] as well as NiO [JCPDS n° 47-1049].

Similar observations are reported in the case of $NiAl_{cal}$; the latter shows the presence of $NiAl_2O_4$ spinel phase [JCPDS n° 10-0339] as well as that of NiO phase [JCPDS n° 47-1049]. The obtained results are in agreement with those observed by other researchers in the field.

Reduction of the calcined materials ($NiFe_{cal}$-R and $NiAl_{cal}$-R) at 750 °C showed reduction of NiO species to Ni^0 with small amounts of NiO still remaining on the surface; Ni^0 was observed at 2θ =44.5, 51.8 and 76° [JCPDS n° 04-0805] for $NiAl_{cal}$-R. Meanwhile, alloys of NiFe were observed at 2θ = 43.5° and 50.7° [JCPDS n° 47-1417] for $NiFe_{cal}$-R.

Analysis of the reduced species using SEM and TEM techniques showed the presence of uniform and homogeneous dispersion of Ni^0 particles on the surface of $NiAl_{cal}$-R material. However, in the case of $NiFe_{cal}$-R we observe a less uniform dispersion of Ni^0 on the surface of the material (Fig. 2).

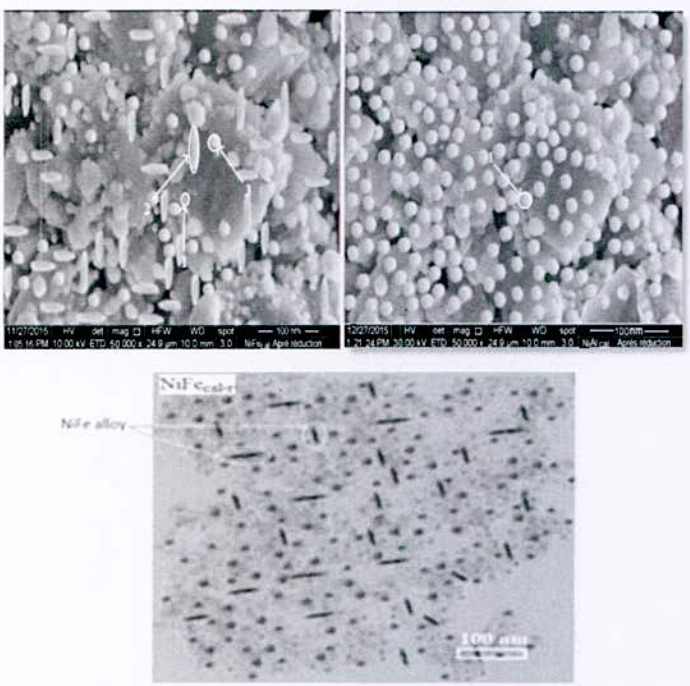

Fig. 2. (From top left to bottom) SEM for $NiFe_{cal}$-R, $NiAl_{cal}$-R and TEM for $NiFe_{cal}$-R

Indeed, we can observe the presence of a small number of spherical Ni^0 particles dispersed over the surface of $NiFe_{cal}$-R as well as other slightly larger agglomerates of NiFe alloys in the form of elongated shapes.

1. Application of $NiAl_{cal}$-R and $NiFe_{cal}$-R in the Reaction of Dry Reforming of Methane

Initially, we elected to investigate the effect of temperature on the activity of our catalyst in the reaction

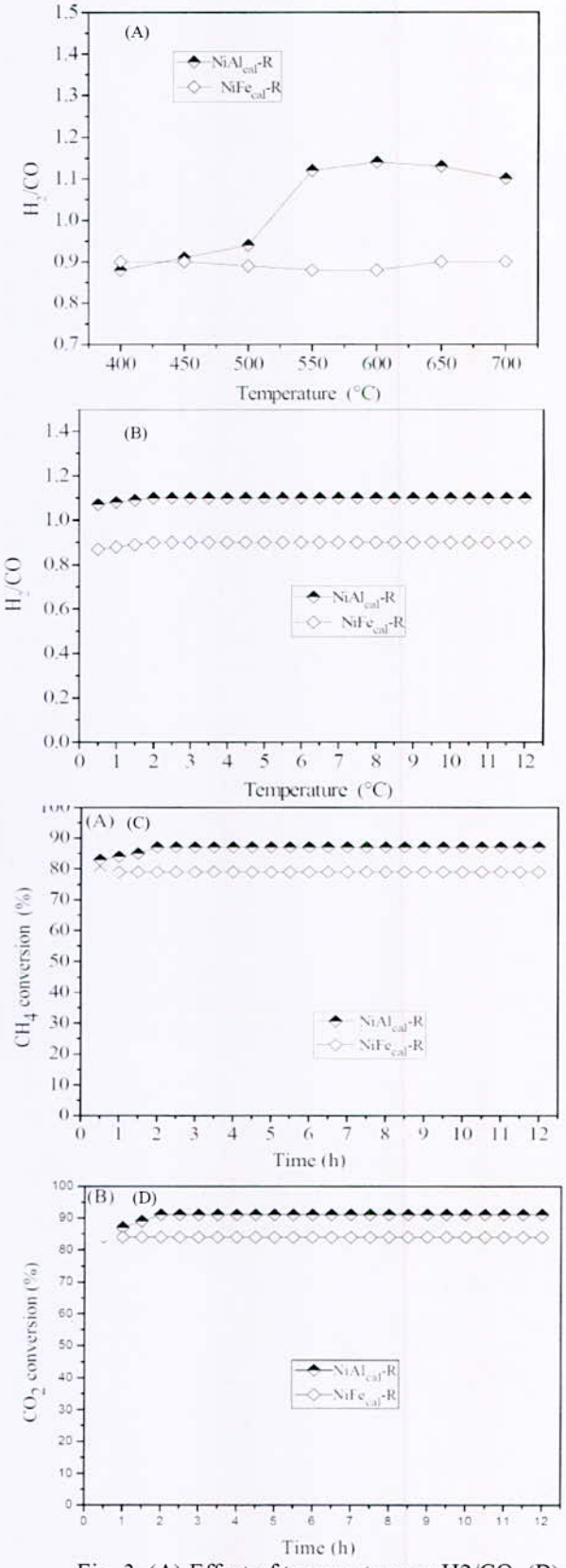

Fig. 3. (A) Effect of temperature on H2/CO, (B) stability of catalyst over time, (C) CH_4 conversion and (D) CO_2 conversion for $NiAl_{cal}$-R and $NiFe_{cal}$-R

*Corresponding author email: moussa.sehailia@crapc.dz

of dry reforming of methane, i.e., in the range [400-700 °C]. The feed gas ratio CH4/CO2 has always been maintained at 1. Fig. 3(A), depicts the variation in H2/CO ratio obtained at various temperatures. Although the ratio H2/CO was higher in the case of $NiAl_{cal}$-R at temperatures above 450 °C, we tend to observe more or less similar H2/CO ratios in the case of $NiFe_{cal}$-R; such phenomenon could well be associated with the reverse water gas shift reaction ($CO_2 + H_2 \leftrightarrow H_2O + CO$) being more pronounced upon using $NiFe_{cal}$-R as a catalyst.

The stability of our catalysts was also studied over a prolonged period of time, i.e., 12 hours reaction time at 700 °C. The obtained results are illustrated in in Fig. 3(B). In spite of the higher H2/CO ratio obtained in the case of $NiAl_{cal}$-R, both catalysts were able to show a stable and steady conversion over the course of time.

We also noticed approximately a 10% difference in CH_4 conversion between both catalysts with $NiAl_{cal}$-R being superior in activity than $NiFe_{cal}$-R; a similar trend with regards to CO_2 conversion was also observed. Such phenomenon is associated with higher S_{BET} value obtained for $NiAl_{cal}$-R compared to that of $NiFe_{cal}$-R (Fig. 3). To our expectations, and in spite of the higher activity of $NiAl_{cal}$-R compared to that of $NiFe_{cal}$-R, we notice a lower amount of carbon deposition on the latter catalyst compard to the former; EDX analysis after reaction showed a significantly lower carbon deposition on $NiFe_{cal}$-R (2.21%) compared to $NiAl_{cal}$-R (15.2%) (Table IV).

TABLE IV
SURFACE AREA, PARTICLE SIZE AND CARBON DEPOSITION AFTER REACTION OF DRY REFORMING OF METHANE

Samples	S_{BET} (m^2/g)		Size of particle (nm)		Estimation of carbon deposited	
	After reduction	After reaction	After reduction [a](Ni^0)	After reaction [b](Ni^0)	Carbon balance (%)	(%) of carbone by EDX
$NiAl_{cal}$-R	105.50	86.22	16.5	22	85.50	15.20
$NiFe_{cal}$-R	70.22	55.21	17.20	18	98.25	2.21

III. CONCLUSION

Our results demonstrate that although $NiAl_{cal}$-R with smaller S_{BET} tend to have greater CH_4 and CO_2 conversions, the tendency toward carbon formation remain a greater challenge to address, however, we believe that the incorporation of Fe in our case played a positive role in reducing the amount of carbon, most possibly *via* Mars-Van Krevelen mechanism:

$CH_4 \rightarrow C_{Ni} + 2H_2$
$Fe + xCO_2 \rightarrow FeOx + xCO$
$FeOx + C_{Ni} \rightarrow xCO + Ni + Fe$
$FeOx + H_2 \rightarrow Fe + H_2O$

As a result, we believe that it is necessary to strike the right balance between both CO_2 and CH_4 conversion and carbon deposition whereby sacrificing a small reduction in the conversion of reacting gas to compensate for a reduction in carbon may prompt the overall process more efficient.

ACKNOWLEDGMENTS

The authors of this manuscript would like to thank the General Directorate for Scientific Research and Technological Development (DGRSDT) under the umbrella of the Ministry of Higher Education and Scientific Research, Algeria, for generously funding this project.

REFERENCES

[1] M. Usman, et al. "Dry reforming of methane: Influence of process parameters—A review", Renewable and Sustainable Energy Reviews, 45 (2015) 710-744.
[2] J. Zhang, et al. "Coke-resistant Ni@ SiO_2 catalyst for dry reforming of methane", Applied Catalysis B: Environmental, 176 (2015) 513-521.
[3] O. Muraza, et al. "A review on coke management during dry reforming of methane", International Journal of Energy Research, 39 (2015) 1196-1216.
[4] Lavoie, Jean-Michel. "Review on Dry Reforming of Methane, a Potentially More Environmentally-Friendly Approach to the Increasing Natural Gas Exploitation." *Frontiers in Chemistry* 2 (2014): 81.
[5] Jahangiri, Hessam, et al. "A review of advanced catalyst development for Fischer–Tropsch synthesis of hydrocarbons from biomass derived syn-gas." *Catalysis Science & Technology* 4.8 (2014): 2210-2229.
[6] Touahra, F., et al. "Effect of the Ni/Al ratio of hydrotalcite-type catalysts on their performance in the methane dry reforming process." *Applied Petrochemical Research* 6.1 (2016): 1-13.
[7] Touahra, F., et al. "Enhanced catalytic behaviour of surface dispersed nickel on LaCuO 3 perovskite in the production of syngas: an expedient approach to carbon resistance during CO 2 reforming of methane." *international journal of hydrogen energy* 41.4 (2016): 2477-2486.
[8] Kroll, V. C. H., et al. "Methane reforming reaction with carbon dioxide over Ni/SiO 2 catalyst: II. A mechanistic study." *Journal of Catalysis* 164.2 (1996): 387-398.
[9] Pakhare, Devendra, and James Spivey. "A review of dry (CO2) reforming of methane over noble metal catalysts." *Chemical Society Reviews* 43.22 (2014): 7813-7837.
[10] Ashok, J., and S. Kawi. "Steam reforming of toluene as a biomass tar model compound over CeO 2 promoted Ni/CaO–Al 2 O 3 catalytic systems." *international journal of hydrogen energy* 38.32 (2013): 13938-13949.
[11] Kambolis, A., et al. "Ni/CeO 2-ZrO 2 catalysts for the dry reforming of methane." *Applied Catalysis A: General* 377.1 (2010): 16-26.
[12] Theofanidis, Stavros Alexandros, et al. "Enhanced carbon-resistant dry reforming Fe-Ni catalyst: Role of Fe." *Acs Catalysis* 5.5 (2015): 3028-3039.

*Corresponding author email: moussa.sehailia@crapc.dz

Effect of NG Enrichment with H_2 on Combustion Characteristics of a Dual-Fuel Diesel Engine

S. Ouchikh [1], M. S. Lounici [1]*, L. Tarabet [2], A. Boussadi [1], K. Loubar [3] and M. Tazerout [3]

[1]* Laboratoire d'Energétique, Mécanique et Ingénieries, UMBB, Boumerdes 35000, Algeria.
[2] Laboratoire des systèmes thermiques, EMP, M1 BP17 Bordj El Bahri, Algeria.
[3] GEPEA, UMR 6144, DSEE, Ecole des Mines de Nantes, 44307 Nantes, France.

Abstract—**Depleting crude reserves and stringent pollution norms have forced researchers' attention on the use of alternative fuels in engines. Therefore, improving utilization of prominent low carbon or carbon free alternative fuels such as natural gas and hydrogen is necessary. Natural gas, with the advantages of abundant reserves and reduced exhaust emissions, is one of the most attractive alternative fuels for internal combustion engines. A promising technique for its use in internal combustion engines is the dual fuel concept. However, natural gas dual-fuel engine suffers from certain drawbacks mainly at low loads. Those problems are due to the physicochemical and combustive properties of natural gas, such as poor lean-burn capability, high ignition energy and slow burning velocity. These properties can be improved by addition of hydrogen that possesses wide flammability limit and fast burning velocity. In the present study, the effect of NG enrichment with various H2 blends on combustion characteristics of a dual fuel engine is investigated. Results showed that in-cylinder pressure, rate of pressure rise raised compared to NG dual-fuel operation. Heat releases rate increased with hydrogen addition. Maximum cumulated heat release was obtained with 10%H2.**

Key words—IC engine, Dual fuel, Natural gas, Hydrogen, Combustion characteristics.

I. INTRODUCTION

The possible depletion of fossil fuels and the stringent emission norms have created the need for alternate fuels and engine developers are prompted to investigate the viability of such fuels [1]. Among the various alternative fuels, natural gas (NG) is very promising and highly attractive in the transportation sector [2]. Few alternative fuels offer the distinct and unquestionable advantages of natural gas [3]. A promising technique for the use of NG in internal combustion engines is the dual fuel (DF) concept [4].

In dual fuel technology, natural gas is mixed with air before introduced into the combustion chamber. The gas-air mixture is then ignited by a liquid diesel pilot injection using the original diesel fuel injection system [5]. The most of the engine power output is provided by the gaseous fuel, while a pilot amount of the liquid fuel, is injected near the end of the compression stroke to act as an ignition source [6]. The use of natural gas in diesel engines has been proved to be one of the most practical ways to improve the economy and reduce the harmful emissions of the conventional diesel engines [2]. However, there are still some critical problems in the dual-fuel operation mode and many investigations have confirmed that at low load, the engine efficiency decreases compared to conventional diesel. The unburned hydrocarbons (HC) and carbon monoxide (CO) emissions are higher in dual fuel mode [5, 7-9]. This reveals a poor utilization of the gaseous fuel, due mainly to combination of low temperature and very poor air-natural gas mixture inside the combustion chamber of the engine, resulting in a bad and slow combustion of the gaseous fuel [3, 8].

Various solutions have been proposed by previous researchers to overcome obstacles concerning dual-fuel operation mode [6, 7]. An effective method to improve gaseous fuel combustion characteristics, especially lean burn limits and burning velocity is to mix the natural gas with the fuel that possesses wide flammability limit and fast burning velocity. Hydrogen (H2) is thought to be the best gaseous candidate for natural gas [8]. The wide flammability limit property of hydrogen makes it an ideal fuel to combine with natural gas [9].

Several studies have been reported on utilization of NG enriched with hydrogen (HCNG) as a fuel for compression ignition (CI) engines and the outcomes are very promising. Lounici et al. [3] investigated experimentally the use of natural gas enrichment with various H2 blends as a technique for improving dual fuel combustion especially at low engine loads. They found an important reduction in brake specific fuel consumption (BSFC) with 10%H2 blend compared to pure NG. Zhou et al. [10] tested a diesel-H2-CH4 fuel mixture in a 4-stroke CI engine. An improvement was seen especially at low loads concerning engine performance and CO and HC emissions. This improvement increased with H2 rate increase. Talibi et al. [11] conducted an experimental investigation of combusting methane-hydrogen mixtures, pilot-ignited by diesel fuel, it was found that increasing the proportion of H2 reduced the ignition delay period and peak heat release rates, but only at high engine loads. The reduction of combustion duration promoted by hydrogen addition results in increased engine efficiency respect to natural gas.

In the present study, the influence of NG enrichment with various H2 blends on combustion characteristics of a CI engine is investigated. The combustion characteristics were evaluated at different engine loads.

*Corresponding author email: mslounici@hotmail.com

II. EXPERIMENTAL SETUP AND EXPERIMENTAL PROCEDURE

A single cylinder air-cooled Lister Petter (TS1) diesel engine with output power of 4.5 kW at 1500 rpm is used to carry out engine tests. The experimental setup scheme is shown in Fig. 1.

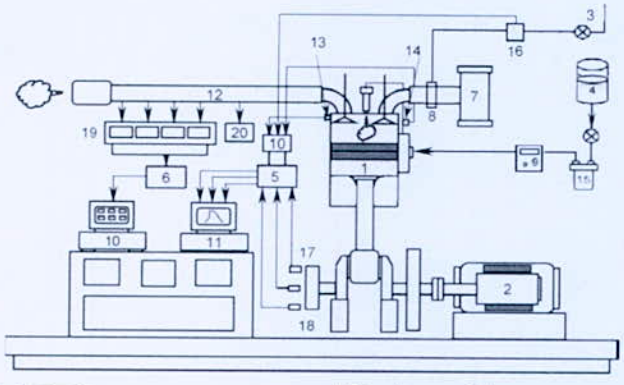

1. Test engine
2. Dynamometer
3. Gaseous fuel supply
4. Gasoil tank
5. A/D card for pressure
6. A/D card for Analyzer
7. Air tank
8. Air-gas Mixer
9. Diesel flow meter
10. Charge Amplifier
11. Fast data acquisition system
12. Slow data acquisition system
13. Cylinder pressure sensor
14. Injection pressure sensor
15. Liquid fuel filter
16. Gaseous fuel flow meter
17. TDC encoder
18. Speed sensor
19. Exhaust gas analyzer
20. Smoke meter

Fig. 1. Experimental setup scheme

To carry out dual fuel engine experiments, the engine was conveniently modified. It is supplied with natural gas from the local distribution network and hydrogen from a bottle. Natural gas and hydrogen flow rates are adjusted with mass flow controllers (Brooks 5851S for NG and Bronkhorst F-112AC for H2

III. MODEL FOR HEAT RELEASE EVALUATION

Heat release calculations are an attempt to get information about the combustion process in an engine. A single-zone and zero-dimensional heat release rate model was used in this study. In this model, the heat release rate is calculated by performing the first law of thermodynamics analysis of the average pressure versus crank angle variations considering the cylinder contents as the mixture of ideal gases with the specific heat being dependent on temperature inside the cylinder;

The HRR at each CA is determined by the following formula:

$$\frac{dQ}{d\theta}=\left[\frac{\gamma}{\gamma-1}\right]P\frac{dV}{d\theta}+\left[\frac{1}{\gamma-1}\right]V\frac{dP}{d\theta} \qquad (1)$$

Where θ is the crank angle in terms of degree (CA), P is the in-cylinder pressure in terms of (Pa) at a given crank angle, V is the cylinder volume in terms, and γ is the specific heat ratio (C_p/C_v). A constant value (1.35) of γ is retained [7] in this study.

IV. RESULTS AND DISCUSSION

In-cylinder pressure, peak pressure and heat release are important parameters which can signify the combustion process. In the following sections, these parameters are analyzed and discussed.

1. Effect on in-cylinder Pressure

Fig. 2 shows P-θ diagram for conventional diesel, NG DF and HCNG DF with various blends. Compared with diesel operation it is obvious that increasing hydrogen fraction in the fuel blend results in the increase of in-cylinder pressure. Enhancement of cylinder pressure in the presence of hydrogen is due to higher flame speed.

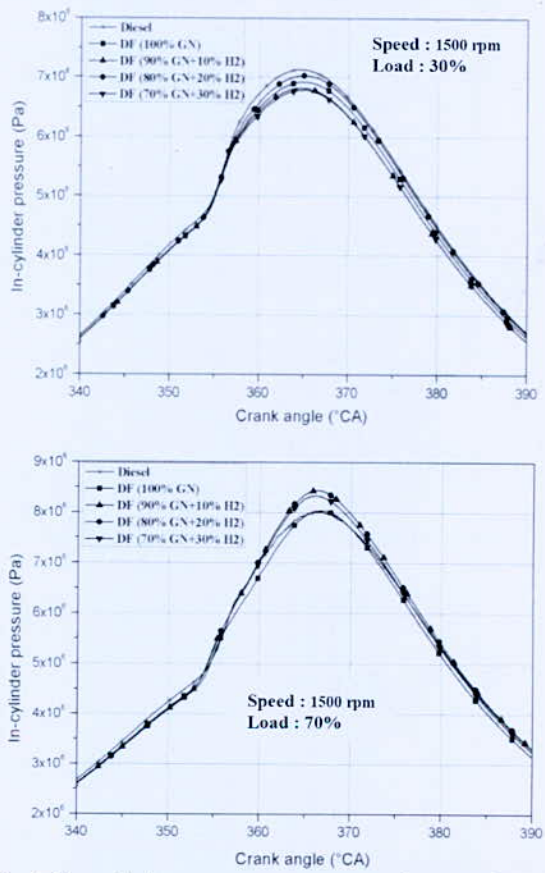

Fig. 2. In-cylinder pressure versus crank angle for NG DF, HCNG DF and conventional diesel modes

2. Effect on Rate of pressure rise (ROPR)

Fig. 4 shows RoPR variations at different engine load for different mixture blends. It is observed that The ROPR increased with the rise in engine load for all tested blends due to increase in the quantity of fuel injected in the cylinder. At a given load, all HCNG blends showed relatively higher RoPR compared to DF operation. This was due to higher hydrogen content in the test fuel.

*Corresponding author email: mslounici@hotmail.com

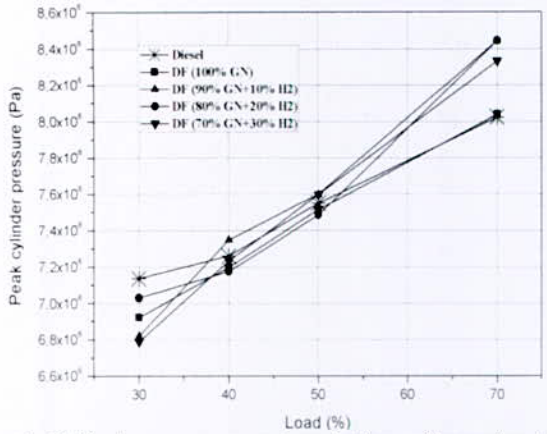

Fig. 3. Cylinder pressure peak variation with engine load

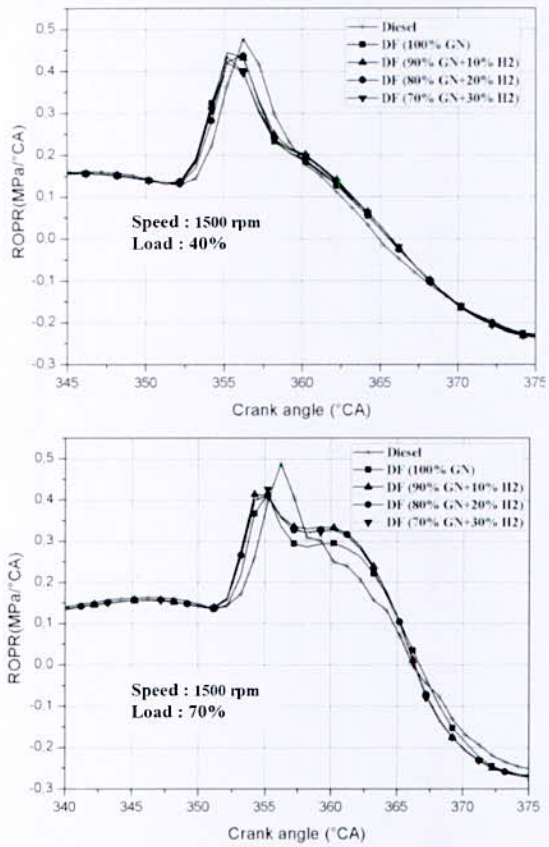

Fig. 4. Rate of pressure rise for different engine loads

3. *Effect on Heat release rate (HRR)*

Hydrogen as fuel has higher diffusivity (0.63 cm²/s) in air resulting in formation of more homogeneous gaseous fuel charge (air+HCNG) inside the engine cylinder. Therefore, the increase in charge homogeneity with HCNG leads to better-premixed charge combustion characteristics with corresponding higher peak HRR. The total heat release rate trace (Fig. 5) shows an enhancement in the premixed gaseous fuel combustion phase (second peak) for HCNG DF case as compared to NG DF mode.

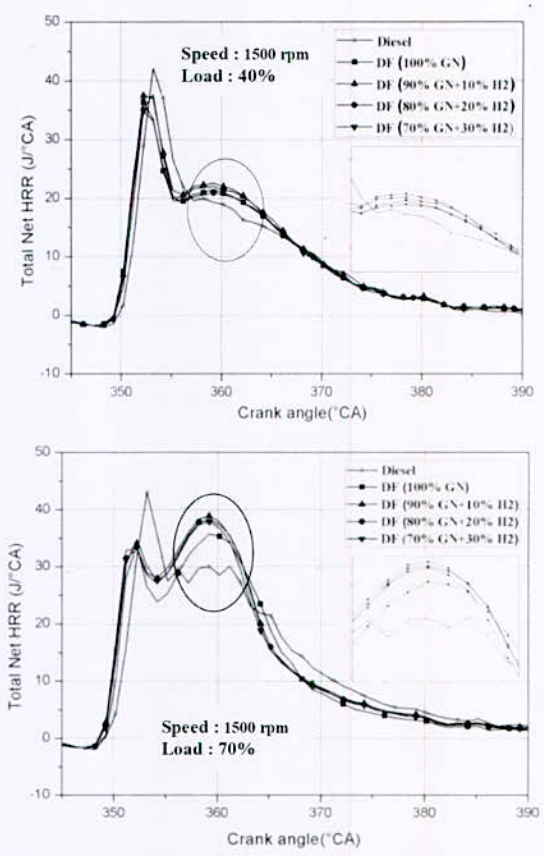

Fig. 5. Total net heat release rate versus crank angle for NG DF, HCNG DF and conventional diesel modes

4. *Effect on Cumulative heat release (CHR)*

As seen in the Fig.6, CHR increased with the rise in the engine load due to the increase in the quantity of fuel injected into the cylinder. However, there was not any tendency in the change of CHR with increasing of addition hydrogen. Maximum CHR was obtained at 10%H2 condition for 40, 50, and 70% engine load.

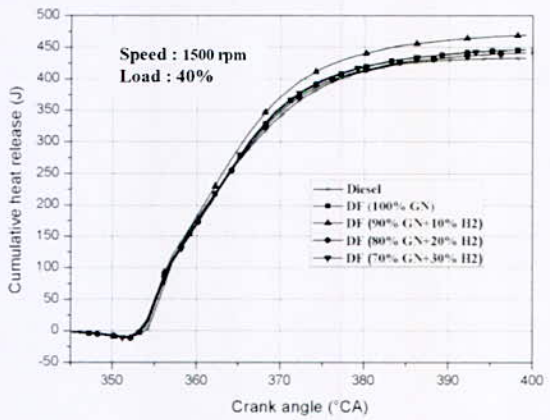

*Corresponding author email: mslounici@hotmail.com

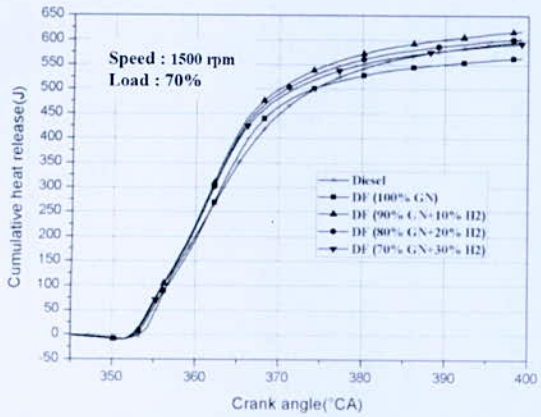

Fig. 6. Cumulative heat release for different engine load

V. CONCLUSION

In this study, combustion characteristics of a single cylinder CI engine running with various HCNG mixtures were investigated. The main results are summarized in the following points:

- RoPR raised for all HCNG blends compared to NG DF operation. The increase is between 5.56% and 48.59% on hydrogen diesel dual fuel mode.
- HRR increased depending on the increase of hydrogen addition. Higher heat release rate was obtained with 10HCNG and 20 HCNG.
- Maximum CHR was obtained with 10%H2 operation for 40, 50, and 70% engine load.
- In terms of BTE, an important benefit of hydrogen addition, reaching to increase an 11.8% with the 10%H2 blend compared to the pure NG.

REFERENCES

[1] S. Srihari, S. Thirumalini, K. Prashanth, "An Experimental Study on the Performance and Emission Characteristics of PCCI DI Engine Fuelled with Diethyl ether-Biodiesel-Diesel Blends," *Renewable Energy*, vol. 107,pp. 440-447, 2017.

[2] L. Wei, P. Geng, "A review on natural gas/diesel dual fuel combustion emissions and performance," *Fuel Processing Technology*, vol. 142, pp. 264–278, 2016.

[3] M. S. Lounici, A. Boussadi, K. Loubar, M. Tazerout, "Experimental investigation on NG dual fuel engine improvement by hydrogen enrichment," *International Journal of Hydrogen Energy*, vol. 39, pp. 21297-21306, 2014.

[4] T. Korakianitis, A. Nmasivayam, R. Crookes, "Natural-gas fueled spark-ignition (SI) and compression-ignition (CI) engine performance and emissions," *Progress in Energy and Combustion Science*, vol. 37, pp. 89-112, 2011.

[5] B. Sahoo, N. Sahoo, U. Saha, "Effect of engine parameters and type of gaseous fuel on the performance of dual-fuel gas diesel engines—A critical review," *Renewable and Sustainable Energy Reviews*, vol. 13, pp. 1151–1184, 2009.

[6] M. M. Abdelaal, A. H. Hegab, "Combustion and emission characteristics of a natural gas-fueled diesel engine with EGR," *Energy Conversion and Management*, vol. 64, pp. 301–312, 2012.

[7] M. S. Lounici, K. Loubar, L. Tarabet, M. Balistrou, D.C. Niculescu, M. Tazerout, "Towards improvement of natural gas-diesel dual fuel mode: An experimental investigation on performance and exhaust emissions," *Energy*, vol. 64, pp. 200-211, 2014.

[8] S. S. Sandhu, "Improvement in Performance and Emission Characteristics of a single cylinder SI engine operated on blends of CNG and Hydrogen," In *Proc. Of World Academy of Science, Engineering and Technology. World Academy of Science, Engineering and Technology (WASET)*, 2013, pp. 698.

[9] P. Rahnama, A. Paykani, R. D. Reitz, "A numerical study of the effects of using hydrogen, reformer gas and nitrogen on combustion, emissions and load limits of a heavy duty natural gas/diesel RCCI engine," *Applied Energy*, vol. 139, pp. 182–198, 2017.

[10] J. Zhou, C. Cheung, C. Leung, "Combustion, performance and emissions of a diesel engine with H2, CH4 and H2-CH4 addition," *International Journal of Hydrogen Energy*, vol. 39, pp. 4611-4621, 2014.

[11] M. Talibi, R. Balachandran, N. Ladommatos, "Influence of combusting methane-hydrogen mixtures on compression ignition engine exhaust emissions and in-cylinder gas composition," *International Journal of Hydrogen Energy*, vol. 4, no. 42, pp. 2381-2396, 2017.

*Corresponding author email: mslounici@hotmail.com

Experimental Characterization and Design of a Power Unit Equipped with a PEM Fuel Cell Supplied by Solar Hydrogen

A. Djafour[1*], Abd. Gougui[1], Y. Babasidi[1], k. Hebieb[1], H. Boutelli[1], and B. Azoui[2]

[1*]Faculté des Sciences Appliquées, Laboratoire LAGE, Univ Ouargla, Ouargla 30 000 Algérie.
[2] Faculté de Technologie, Laboratoire LEB, Univ Hadj Lakhdar Batna, Batna 05000 Algérie.

Abstract— **This paper intends a small-scale stand-alone power unit, based on both experimental work and computer simulations. The power unit in this study uses photovoltaic energy as energy input, with storage in a set of batteries for cloudy days, and hydrogen as long-term energy storage. The laboratory power unit comprises a hydrogen subsystem (metal hydride, a Proton Exchange Membrane fuel cell, PEMFC), DC/DC converter, controlled characterization of the individual system components, and a programmable electronic load). In this study, an experimental characterization of the elements of the fuel cell is realized, and then the final statement of the electric charge. Other experiments were conducted to determine the relationship between the fuel cell current and the hydrogen consumption. Also, the characterization of the power flows through the DC/DC converter. From a proper consumption curve of the fuel cell and the loss in the DC/DC converter, we determined the relationship between the flow of hydrogen and the available power at the load. To meet the daily energy needs throughout the year, the minimum power of the photovoltaic field will install has been calculated after the calculation by simulation using a computer program under Matlab the values of global radiations, with the choice of the optimal monthly angle levels of solar modules surfaces on the Ouargla site, and the introduction of technical features required of other system components, for the operation of our fuel cell systems in a stand-alone solar photovoltaic system to power a lighting system of a locality for ten hours each night.**

Key words— Solar energy; photovoltaic system; electrolyser; hydrogen; PEM fuel cell; characterization; Sizing.

I. INTRODUCTION

Algeria is one of the countries that is characterized by sunny days due to its climate diversities. The sunshine duration can reach annually 3900 hours in the arid and semi-arid areas and the energy received daily on a horizontal surface of $1m^2$ is approximately 5 kWh over most of the country. These specifications make Algeria favorite to solar applications, [1,2]. However, control problems arise due to large variances of PV output power under different insulation levels. To overcome this problem, PV power plants are integrated with other power sources or storage systems such as hydrogen generator, storage and fuel cells. Their feasibility in coordination with PV systems has been successfully demonstrated for both grid-connected and stand alone applications [3].

In this paper a PV-fuel cell hybrid generation system is designed. An electrolyser coupled to the PV array is employed for hydrogen production, with the use of batteries to ensure the continuity of operations during the days of penury. The hydrogen produced is stored in metal hydride cylinders to meet the needs of hydrogen for a Proton Exchange Membrane Fuel Cell, PEMFC.

II. EXPERIMENTAL STUDY

In this study an experimental characterization of the elements of the fuel cell has been realized in the laboratory by using a test bench (Heliocentris FC50), which contains a PEM fuel cell of current 8A at 40W rated output. This system is fed by hydrogen stored in Metal hydride canisters of capacity 225 liters under pressure of 10 bars. Our test bench is equipped with a cooling fan of the fuel cell and a system for displaying currents, voltages, hydrogen flow and operating temperature of the fuel cell. During the experiments, we use data acquisition software, provided by the Heliocentris Company. This software offers the option of operation and data acquisition via a PC - as an alternative to the manual operation. The PC assumes the control, resulting in the rotary switches on the fuel cell module and on the electronic load having no effect [4].

1. *Characterization of the Fuel Cell*

The experiments for the characterization of the fuel cell system (Heliocentris FC50) have been conducted in the laboratory by using of the elements shown in fig 1.

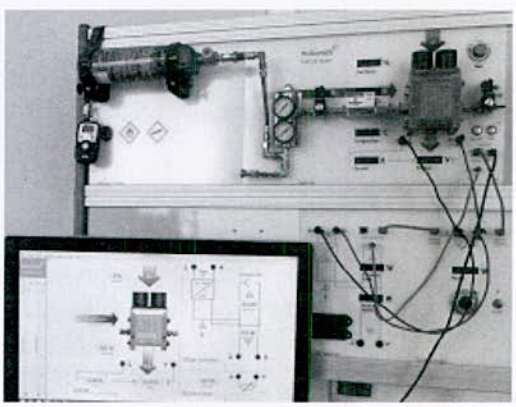

Fig. 1. Test bench

The fuel cell is directly connected to the variable electronic load, and then we feed the fuel cell by the

*Corresponding author email: djafour.ah@univ-ouargla.dz

hydrogen from metal hydride bottles. In giving the start command, the fuel cell starts to work, with the change of the value of the load the system stores the data in the acquisition unit. Among the characteristics that we found, voltage-current, power-current and the stack efficiency of the PEM fuel cell. Other experiments were conducted to determine the relationship between the fuel cell current and the hydrogen consumption. Also, the characterization of the power flows through the DC/DC converter. From a proper consumption curve of the fuel cell and the losses in the DC/DC converter, we determined the relationship between hydrogen flow and available power at the load.

III. THEORETICAL CALCULATION

For the operation of our fuel cells system in a stand-alone solar photovoltaic system, to power a lighting system of a locality in Ouargla, we need to produce the hydrogen required to operate the fuel cells, with his fuel consumption (Nl/min) at rated output. To meet the daily energy needs throughout the year, the minimum power of the photovoltaic field will install has been calculated. An illustrative scheme of the unit is presented in Fig.2.

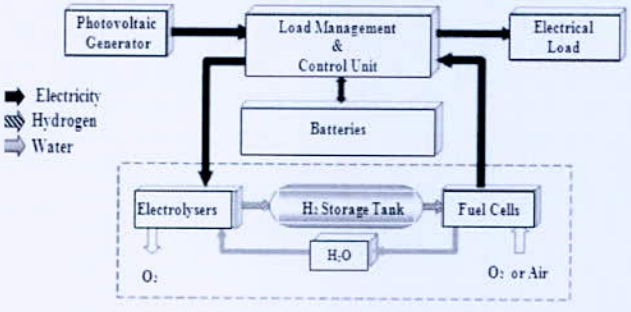

Fig. 2. Photovoltaic-fuel cells hybrid generation system

1. Generator Sizing

For the design of a photovoltaic system, we start from the needs of the energy, charge in this case is the electrolyser load, Ecj (kWh / day), on the site where the average daily global radiation incident on the collector or modules surface, is Es (kWh / m². day), to have in the end the necessary size of the PV generator. To complete the design we based on the following assumptions, [5]:

- Molar flux produced by the electrolyser is the same as the molar flow consumed by the fuel cell.
- Demand is constant during the study period.
- Performance of the system components is constant.

2. Final Statement of the Electric Charge

We want to illuminate for ten hours each night, a parking station of the total surface of 400 m^2 with fluorescent lamps powered by a system of fuel cells supplied by solar hydrogen. With six lamps of fluorescent types of power 40W each we can illuminate a surface of 200 m^2, [6], with these lamps the number of total lamps to be used is 12 lamps that can illuminate an area of 400m^2.

3. Other System Components

The Battery Park is made taking into account the daily consumption E_{cj} (kWh/day) and a number of days of autonomy (D_{Aut}), this number varied depending on the application and geographical situation; in our case we take autonomy of one day. For the choice of the regulator, the first parameter to consider is the power of the regulator, or the maximum current that can be controlled for a given voltage. For the voltage, the regulator will be able to supporters about the double of its rated voltage,[5,7].

IV. EXPERIMENTAL RESULTS

1. Characteristics of the Fuel Cell

With the use of the data stored in the acquisition unite, the characteristics of voltage-current (V-I), power-current (P-I) of the fuel cell (Heliocentris FC50), are plotted as shown in Fig.3.

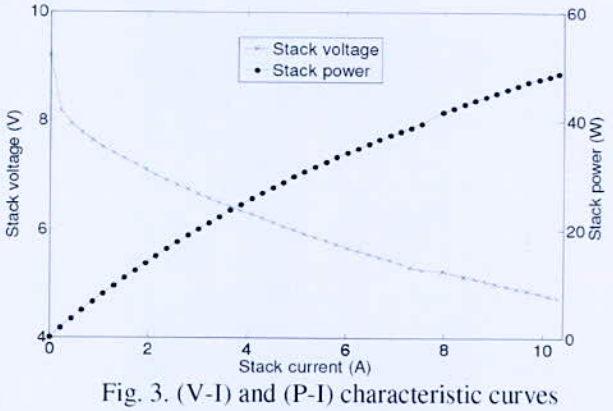

Fig. 3. (V-I) and (P-I) characteristic curves

Voltage-current and power-current characteristic curves are the most important characterizing curves of a fuel cell. It can be used to determine the suitability of the fuel cell for various areas of application. In addition, these characteristic curves can be used to determine which loss mechanisms have an effect on the fuel cell.

2. Fuel Cell Hydrogen Consumption

The stored data are used to determine the relationship between the fuel cell current and the hydrogen consumption, as shown in Fig.4.

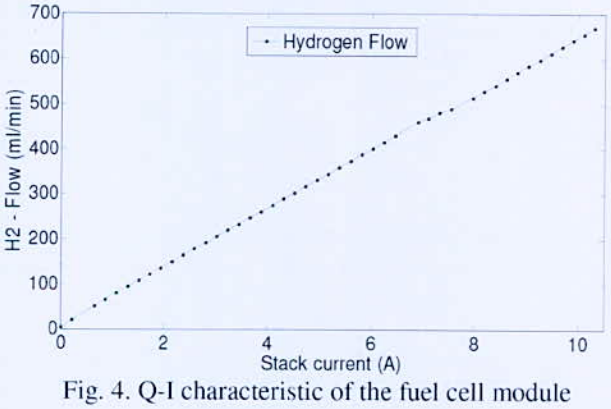

Fig. 4. Q-I characteristic of the fuel cell module

*Corresponding author email: djafour.ah@univ-ouargla.dz

The measured curve of the flow rate of hydrogen – current (Q-I), is almost linear according to the Faraday's law, also the curve shows that a small hydrogen flow occurs when no current is produced in the fuel cell, this flow is considered such as flight rate because no hydrogen is converted in the chemical reaction.

3. *DC/DC Converter Losses*

In the first experiment, we have connected the electronic load directly to the fuel cell without the DC/DC converter, the converter is used to feed own consumption of the fuel cell. In the second experiment we have connected the electronic load to the fuel cell through the DC/DC converter. For the two cases, in giving the start command, the fuel cell starts to work, with the change of the value of the electronic load the system stores the data in the acquisition unit. The measurement results for the two experiments are presented in Fig.5.

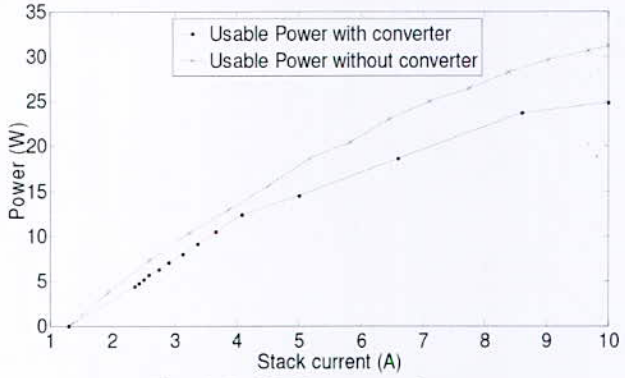

Fig. 5. DC/DC converter losses

Measured curves in fig.5, shown that the available power with converter curve lies below without a converter. The difference between curves corresponds to the converter losses which occur during the voltage conversion. Increasing conversion losses can be seen in the divergence of the curves with increasing currents.

4. Discussion

After measurements of the performance of PEM fuel cell system components in the laboratory. It has been noticed that the measured overall efficiency of our fuel cell system at nominal power level is 23.16%, this value is low compared to the usual efficiency of the fuel cell which is about (45–65%), [8]. The low efficiency of our fuel cell system is due to the internal requirement of the fuel cell in addition to the losses in the converter. Therefore for industrial use of these systems, it is necessary to minimize losses due to system components.

V. CALCULATION RESULTS

We assume that the fuel cells functioning with his current of 8A at rated output and according to fig.4 and fig.5 the rated hydrogen flow for each fuel cell are 528Nml/min to feed a power of 22W to the load. To ensure the power of 12 lamps for ten hours each night we need twenty-two fuel cells, the necessary amount of hydrogen to operating this number of fuel cells for ten hours each night is 6969.6Nl. For that we use two electrolysers of 1750W and 0.39Nm^3/h of hydrogen each [9], to operate for nine hours each day with the consumption of 31.5kWh/day which must be provided by the photovoltaic generator.

1. Solar Radiation on a Tilted Surface

To determine the solar radiation on panels surface, we have used the coordinates of Ouargla site (latitude 31° 52' N, longitude 5° 24' E). Measurement data of insulation are provided from the National Office of Meteorology for a period of 11 years of observation (2005-2015). Using Liu and Jordan model, [10,11,12] and by using a chart executed under Matlab we have calculated the monthly average daily radiation incident on a south-facing surface in Ouargla with the optimal inclinations. The simulation results are presented in Table I.

TABLE I
MONTHLY AVERAGE DAILY GLOBAL RADIATION AT MONTHLY OPTIMUM TILT ANGLE

Month	β_{opt}	H_{cp}[Wh/m^2.j]
Jan	61	6074.9
Feb	52	6296.4
Mar	36	6098.5
Apr	17	6422.9
May	0	6766.1
Jun	-7	6393.1
Jul	-4	7044.5
Aug	11	6876.8
Sep	29	6070
Oct	47	6140.5
Nov	59	6131.7
Dec	63	5739.6

2. Generator Required Power (P_G)

Using the electric power needs calculated in the previous section and the average annual value of the insulation duration, with taking into consideration the energetic losses due to the batteries charge [13]. The equation of the generator required power (P_G) in kW can be written as.

$$P_G = \frac{E_{cj}}{H_d * K} \quad (1)$$

With, *Ecj*: Energy consumed per day (kWh / day).
Hd: Annual average value of insulation duration (h/day).
K: Correction coefficient for systems with batteries. The value used in our calculations is equal to 0.68, [13].
Required number of modules N_T is calculated as follow:

$$N_T = \frac{P_G}{Pu_{module}} \quad (2)$$

With, *Pu*: Unit power of the module, it can be written as:

$$P_U = \frac{Es * S * \eta}{Dd_{Av}} \quad (3)$$

*Corresponding author email: djafour.ah@univ-ouargla.dz

With, *Es*: annual average value of solar energy in Wh/m^2.day, from Table I, Es = 6337,92 Wh/m^2.day.
D_{dAV}: Average day duration (hours). In our case, D_{dAV} = 9h/day.[11].
S: Module area (m^2) and η: module efficiency.
We choose photovoltaic modules SPR-X21-345(Si-mono) from Sun power.[14]
-The storage capacity in C_{20} that is necessary is calculated by [7]:

$$C_{20}=\frac{E_{cj}*D_{Aut}}{R_T*P_d*V} \quad (4)$$

With, R_T: Temperature reduction coefficient (%)
P_d: Maximum authorized depth of discharge (%)
V: Working voltage (V)
We choose the Deka 8G8D AGM solar Battery of 12V, 225Ah in C_{20} with R_T = 0,9 and P_d = 0,8 [15].

3. System Sizing Results

Table II summarizes the results of the calculation with the developed mathematical model to design the main elements of the system for producing hydrogen, needed to operate the fuel cells system.

TABLE II
SYSTEM SIZING RESULTS

Parameters	Resultants
The consumption Ecj [Wh/j]	31500
Generator power P_G[W]	5147
Number of modules	20
Module area (m^2)	2,162
Module in parallel	20
Storage capacity in C_{20} [Ah]	911,46
Number of batteries branches	4
Number of batteries in series	4

VI. CONCLUSION

In this study experimental tests which are developed provide the possibility to evaluate the performance and the characterization of PEM fuel cell system components in the laboratory. It has been noticed that the losses caused by the system component are great due to the internal requirement of the fuel cell in addition to the losses in the converter, to optimize the usable power the internal losses most be minimized for example displays would it few in industrial fields. For the purpose of good management of the electrical energy produced by the PV system a simulation has been made to know how to produce the hydrogen requirements from free solar energy and store it in bottles to the operation a group of PEM fuel cells, used to power a group of lighting lamps of the locality that can make a stand-alone hybrid power generation system. As perspective, we hope in the future, experienced all the system and also with variable loads.

REFERENCES

[1] B.Azoui and M. Chabane, "A Comparative Study of PV Systems in Semi Arid and Arid Zones in Algeria", IEEE, Power Engineering Conference (UPEC), 2015.

[2] R. Boudries, R. Dizene." Potentialities of hydrogen production in Algeria". Int J Hydrogen Energy 2008; 33 (17): 4476 – 4487.

[3] Ro K, Rahman S. ''Two loop controller for maximizing performance of a grid-connected photovoltaic-Fuel cell hybrid power plant''. IEEE Trans Energy Conver 1998;13(3):276–81.

[4] Heliocentris, GmbH. Germany:"Experiment cuide" http://www.heliocentris.com site visited in April 2016.

[5] A. Djafour, M.S. Aida and B.Azoui, ''Photovoltaic assisted fuel cell power systems'', Energy Procedia 50 (2014) 306–313.

[6] A.Benatiallah, A. Moulay ali, D.Benatiallah, S.bentouba, S.Makhloufi '' Etude et dimensionnement d'un système d'éclairage solaire public à Adrar '' Quatrième ICERE. Mars, 2012, Hammamet Tunisie.

[7] A. Labouret, M. Villoz. "Solar Photovoltaic Energy", Fourth edition 2009 Dunod, Paris.

[8] Keliang Zhoua, J.A.Ferreirab,S.W.H. de Haan "Optimal energy management strategy and system sizing method for stand-alone photovoltaic-hydrogen systems", Int J Hydrogen Energy 2008; 33: 477– 489.

[9] H. Miland. "Operational experience and control strategies for a stand-alone power system based on renewable energy and hydrogen». doctor engineer thesis, Norwegian University, 2005.

[10] A. Djafour. " Etude d'un système de production d'hydrogène solaire". Thèse de Doctorat, Université de Ouargla. 2013, Algérie.

[11] Beckman W.A, Duffie J.A. "Solar engineering of thermal processes" A wiley- interscience, publication, New York. 1980.

[12] K. Messaitfa. "Evaluation de l'apport quantitatif des inclinaisons optimales d'un système de pompage photovoltaïque". Enersole 01, Adrar, 2001. Algérie.

[13] H. Abdi, N. Ait Messaoudene, M. Omari, Y. Bekhta. " Etude et dimensionnement d'une installation solaire de production d'H_2 ". WIH2 Ghardaïa, 2007. Algérie.

[14] SPR-X21-345 Datasheets, available at the site https://us.sunpower.com/, visited in Mai 2016.

[15] https://www.solarelectricsupply.com/, site visited in Mai 2015, Solar Electric Supply, Inc, Solar Batteries.

*Corresponding author email: djafour.ah@univ-ouargla.dz

A Numerical Investigation on the Effect of the Intake Valve Closing on Hydrogen Dual Fuel Engine Performances

A. Menaa[1, 3], F. Amrouche[1], M. S. Lounici[2] and M. Kessal[3]

[1]Centre de Développement des Energies Renouvelables, Bouzaréah 16340 Algiers, Algeria.
[2]Laboratoire d'énergétique, mécanique et ingénieries, UMBB, Boumerdès, 35000, Algérie.
[3]Département Transport et Distribution des Hydrocarbures, UMBB, Boumerdès (Ex-INH), 3500 Algérie.

Abstract—**The aim of this work is, first, to study the effect of advancing the intake valve closing on the performances of a hydrogen dual fuel engine. Then, to compare between the characteristics of the hydrogen dual fuel mode and the diesel mode. This is achieved through a dynamic simulation using CFD code ANSYS Fluent, performed on a single cylinder diesel engine, at constant engine speed of 1500 [rpm]. The results were then validated with experimental data. According to the results, advancing IVC (IVC 30) can increase the induced airflow in the intake and prevent the engine from backfire phenomena. The indicated work, peak in-cylinder pressure, in-cylinder temperature and NOx emission are higher for the hydrogen dual fuel mode compared to diesel mode. However, the CO2 emissions were found to be lower for the hydrogen dual fuel mode.**

Key words—CFD ANSYS Fluent, hydrogen dual fuel engine, intake valve close timming.

I. INTRODUCTION

Renewable hydrogen is proposed to be an alternative to conventional nonrenewable fossil fuels [1]. Indeed, compared to other fuels, hydrogen has very attractive combustion properties such as high diffusivity, high flame speed, wide flammability range and much more. These properties can help to improve the internal combustion engine performances and prevent the exhausted emissions. However, abnormal combustion such as pre-ignition, backfire and knock phenomenon can occur while using hydrogen in internal combustion engine [2, 3, 4, 5]. The backfire or pre-ignition decreases the output power of an engine [1, 6]. Moreover, the rise of the intake manifold pressure resulting from backfire and pre-ignition is susceptible to harm the intake system [7]. Various solutions are proposed by researchers to overcome those problems: (i) decreasing the overlap period, (ii) retarding the timing of the intake valve opening (iii) use of leaner mixtures, (iv) exhaust gas recirculation and (v) intake air cooling [8, 9, 10].

The aim of this work is to study the effect of intake valve close (IVC) timing in order to improve volumetric efficiency and prevent the backfire phenomena of a hydrogen dual fuel engine. For this, an intake valve close timing of 30 CAD [°] and the standard IVC timing are used. To achieve this goal, a numerical simulation using CFD code ANSYS Fluent is used and the results are validated with experimental data.

II. NUMERICAL MODELING

1. Geometric Configuration

The engine simulated is driven from Lister Petter TS1 mono cylinder, four stroke and direct injection diesel engine with a displacement of 0.63 liters. The details about the engine are summarized in Table I. Fig. 1, shows the engine computational mesh.

TABLE I
ENGINE AND INJECTOR CHARACTERISTICS

Description	Parameter value
Make and model	Lister petter TS1
No. of cylinders	1
Displacement volume [cm^3]	630
Rated output [kw]	5.4
Rated speed [rpm]	1500
Bore × Stroke (mm]	95.3 × 88.9
Compression ratio	18.0 :1
Connecting rood length [mm]	165.3
Intake valve opening and closing	36 °BTDC and 69 °ABDC
Exhaust valve opening and closing	76 °BTDC and 32 °ABDC

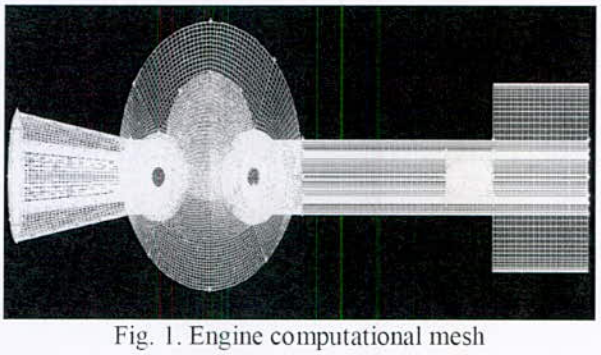

Fig. 1. Engine computational mesh

2. Numerical modeling procedure and validation

The CFD code software used in this study is ANSYS Fluent v16.0. Various numerical, physical and chemical models exist to model the biphasic, reactive and turbulent flow in internal combustion engine with ANSYS Fluent. The turbulent flow were modeled using the k-ε RNG model [14], this choice has already done by refs [12, 15]. The "discrete phase" model available in ANSYS

*Corresponding author email: a.menaa@cder.dz

FLUENT makes it possible to model the two-phase jet in the combustion chamber. This model uses several sub-models that can define; droplet size, velocity distribution, sprays angle, particle trajectory, spray breakup, collision, coalescence and particle evaporation. For the breakup of the jet, ANSYS FLUENT offers four models: the Taylor Analogy Breakup model (TAB), the WAVE model of Reitz, the KHRT model and the Stochastic Secondary Droplet (SSD). The Wave model considers that the breakup of the liquid jet is due to the relative velocity difference between the liquid phase and the gaseous phase, this model is the most popular used for high injection pressure [16]. The combustion model used in this study is Rate/Eddy Dissipation scheme [17] with one reaction for gasoil and one reaction for hydrogen. The reaction rate is equal to the minimum of the laminar finite rate or Eddy Dissipation scheme. For the initiation of combustion, or the ignition delay, the Hardenberg & Hase (H&H) correlation is used. The ignition is ensured by the gasoil fuel in the dual fuel engine mode, also, the knock is assumed to do not occur, and the ignition delay correlation are applied to the gasoil fuel.

The boundaries conditions chosen in this study are the atmospheric pressure for the inlet and outlet, the temperature is 310 [K] for inlet and 340 [K] for wall. The thermal conditions and the heat transfer losses at the wall are introduced as the convection heat transfer using a User Defined Function. Some of the most commonly used heat transfer models are those developed by Anand, Woschni, Prandt, Assanis and Hohenberg. The Hohenberg model performs best in comparison with the Woschni and Assanis models: it predictes the in-cylinder pressure closest to the experiment [18]. In this study, Hohenberg numerical model are used. The initiation parameters, the mass fraction species and temperature, are taken from the first full cycle simulation.

3. Numerical validation

Fig. 2, shows the experimental results [13] and the 3D numerical simulations profiles of the in-cylinder pressures of the cold flow (without injection and combustion). The numerical and experimental results are in good agreement. However, a slight difference was noticed, the error in the maximum pressure is 0.88 [bar] (1.68%). This difference can be justified by the numerical and physical models chosen. Moreover, the choice of the initial conditions i.e. mixture composition and thermodynamic conditions can induce an inaccuracy in the numerical result [19]. The use of an adequate model to define the heat exchange, the real gas model to calculate the proprieties of mixture also can improve the quality of result. This difference, points out the necessity of having the exact geometric dimension, the clearance distance squish and bowl dimension. Indeed, as seen by V. Chintala et al and B. RIBEIRO et al [11, 20], a difference of 1 [mm] in clearance distance engender a difference greater than 1.00 in volumetric compression ratio.

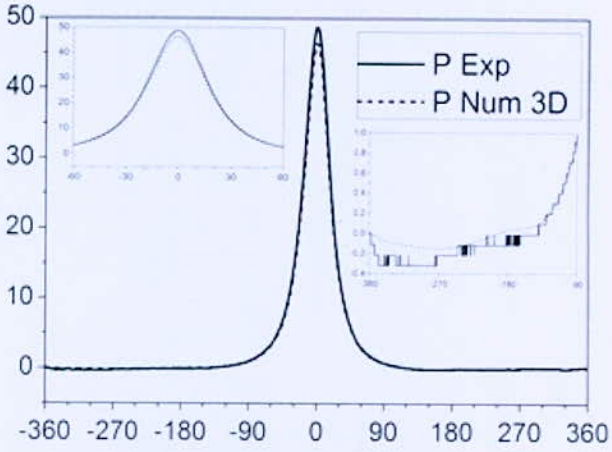

Fig. 2. In-cylinder pressure

III. RESULTS AND DISCUSION

Fig. 3, presents a comparison between the in-cylinder air mass for two IVC timings and two operated engine modes (diesel and dual fuel). The in-cylinder mass are higher for IVC 30 compared to IVC 70, and the mass backflow are greater in IVC30. It can also be seen that, retarding the IVC (IVC70) leads to an air mixture back flow and reduced induced intake mass. Moreover, according to Fig. 4, the hydrogen mass concentration increases in the intake manifold after intake valve closing. In this case, the backfire phenomena can occurs. The mass induced are lower in dual fuel mode compared to the diesel-operating mode. This is due to the different densities.

Advanced ICV timing to 30 CAD [°] can eliminate the backflow and prevent the concentration of the hydrogen in the intake manifold after intake valve closing are near zero. Thus prevent the backfire risk in the engine.

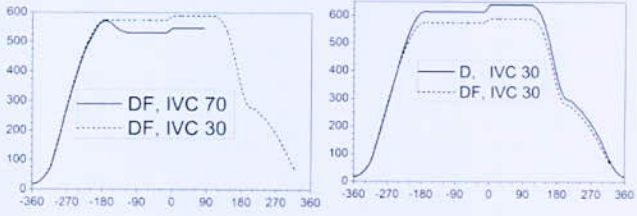

Fig. 3. Mass in-cylinder [mg]

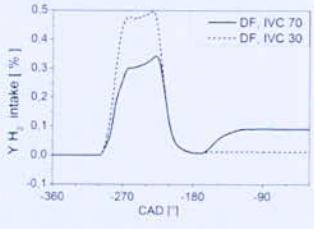

Fig. 4. Hydrogen mass fraction in the intake manifold

Fig. 5, shows the evolution of the indicated work for two IVC and two engine modes operating (diesel and dual fuel). It can be noted, that the work consumed at intake

*Corresponding author email: a.menaa@cder.dz

and compression stroke is higher in case of IVC30 compared to IVC 70. The higher work consumption in IVC30 can be justified by the high mass of air induced in the intake manifold. However, the work produced (at the end of expansion stroke) is similar for both engine-operating modes.

The work developed (expansion stroke) is higher in dual fuel mode compared to diesel engine mode, the increased indicated work is justified by the high laminar flame speed and high diffusivity of hydrogen fuel.

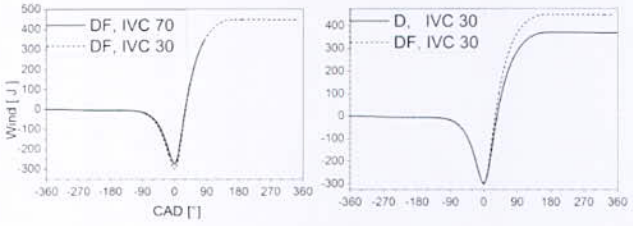

Fig. 5. Indicated work [J]

Fig. 6, shows the in-cylinder pressure at two IVC and engine operating modes. The pressure are higher at IVC 30 compared to IVC 70. Advancing IVC leads to decreasing the effective compression ratio. The same results were obtained by X. Zhang [21] and M. Jia [22]. The in-cylinder pressure are higher in dual fuel mode compared to the diesel one. The increased in-cylinder pressure is justified by the increase of the in-cylinder temperature as demonstrated in Fig. 7, and to the improved combustion efficiency that is due to the high laminar flame speed and diffusivity or to the better mixing quality of hydrogen-air mixture [1, 2].

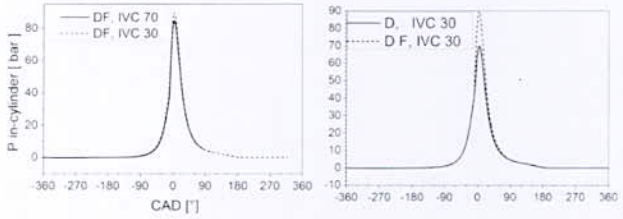

Fig. 6. In-cylinder pressure [bar]

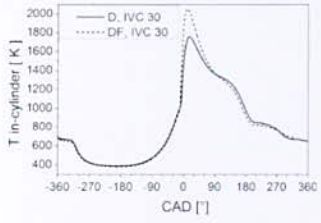

Fig. 7. In-cylinder temperature

Fig. 8, shows the CO_2 and NOx emissions. The CO_2 emissions are lower for dual fuel mode, this can justified by the increased H/C ratio in the air-fuel mixture [2, 3]. However, the NOx emissions are higher for the dual fuel mode compared to diesel mode. Increased NOx emissions can be explained by the increase of the in-cylinder temperature [1, 2, 3, 4].

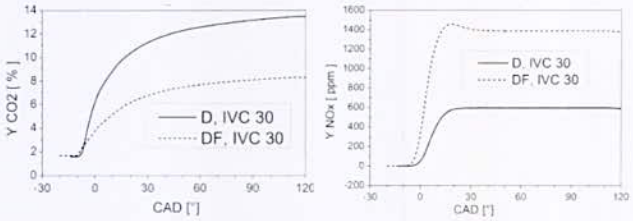

Fig. **8**. NOx and CO_2 concentration

IV. CONCLUSION

Numerical 3D dynamic simulations using CFD code ANSYS Fluent was performed for a single cylinder dual fuel (hydrogen- gasoil) engine. The purpose of this work was to optimize the hydrogen TMI system. This was done by investigating the effect of the IVC timing on preventing the backfire phenomena and improving the volumetric efficiency of a dual-fuel diesel engine. The following results were obtained:

The emergence IVC30 [°] ABDC is the best choice because it prevents the backfire and pre-ignition while ensuring a high volumetric efficiency.

The comparison between the combustion characteristics of dual fuel (hydrogen- gasoil) mode and the baseline (diesel mode) shows an increase of the peak in-cylinder pressure, in-cylinder temperature and the NOx specific emissions.

To improve the combustion characteristics of the dual fuel mode compared to the diesel one, it is suggested to adopt the strategy of retarding the diesel start of injection (DSOI).

REFERENCES

[1] H. Köse and M. Ciniviz, "An experimental investigation of effect on diesel engine performance and exhaust emissions of addition at dual fuel mode of hydrogen," Fuel Processing Technology, pp. 26 - 34, 2013.

[2] M. Deb, G.R.K. Sastry, P.K. Bose and R. Banerjee, "An experimental study on combustion, performance and emission analysis of a single cylinder, 4-stroke DI-diesel engine using hydrogen in dual fuel mode of operation," International Journal of Hydrogen Energy, vol. 40, no. 27, pp. 8586-8598, 2015.

[3] N. Saravanan, G. Nagarajan, G. Sanjay, C. Dhanasekaran and K.M. Kalaiselvan, "Combustion analysis on a DI diesel engine with hydrogen in dual fuel mode," Fuel, vol. 87, no. 17–18, pp. 3591-3599, 2008.

[4] N. Saravanan and G. Nagarajan, "An insight on hydrogen fuel injection techniques with SCR system for NOx reduction in a hydrogen–diesel dual fuel engine," International Journal of Hydrogen Energy, vol. 34, p. 9 0 1 9 – 9 0 3 2, 2009.

[5] M. Deb, A. Paul, D. Debroy, G.R.K. Sastry, R. S. Panuaand P.K. Bose "An experimental investigation

*Corresponding author email: a.menaa@cder.dz

of performance-emission trade off characteristics of a CI engine using hydrogen as dual fuel," Energy, vol. 85, pp. 569 - 585, 2015.

[6] L.Xing-hua, L. Fu-shui, Z. Lei,S. Bai-gang and H. J. Schock "Backfire prediction in a manifold injection hydrogen internal combustion engine," International Journal of Hydrogen Energy, vol. 33, p. 3847 – 3855, 2008.

[7] S. Verhelst and T. Wallner "Hydrogen-fueled internal combustion engines," Progress in Energy and Combustion Science. Vol. 35, PP. 490–527, 2009.

[8] L. Kwang-Ju, H. Thanh Cong, L. Jong-Tai, "A study on realization of high performance without backfire in a hydrogen-fueled engine with external mixture," international journal of hydrogen energy, vol. 35, pp. 1 3 0 7 8 - 1 3 0 8 7, 2010.

[9] L. Jongtai, L. Kwangju, L. Jonggoo and A. Byunghoh "High power performance with zero NOx emission in a hydrogen-fueled spark ignition engine by valve timing and lean boosting," Fuel, vol. 128, p. 381–389, 2014.

[10] L. Das, "Fuel induction techniques for a hydrogen operated engine," International Journal of Hydrogen Energy, vol. 15, no. 11, pp. 833 - 842, 1990.

[11] V. Chintala and K.A. Subramanian, "Experimental investigation of hydrogen energy share improvement in a compression ignition engine using water injection and compression ratio," Energy Conversion and Management, vol. 108, p. 106–119, 2016.

[12] A. C. Clenci, V. Iorga-Siman, M. Deligant, P. Podevin, G. Descombes, R. Niculescu "A CFD (computational fluid dynamics) study on the effects of operating an engine with low intake valve lift at idle corresponding speed," Energy, vol. 71, p. 202e217, 2014.

[13] S. Awad, Contribution à l'étude de la valorisation énergétique des résidus graisseux et de leur combustion dans les moteurs à combustion interne, Université de Nantes: Thèse de Doctorat, 2011.

[14] R. D. REITZ, "Turbulence Modelingof Internal Combustion Engines Using RNG k-ε Models," Combustion Science and Technology, vol. 106, no. 4-6, pp. 267-295, 1995.

[15] A. Lakshminarayanan, "Modelling Diesel Combustion," Dordrecht Heidelberg London New York: Springer, 2009.

[16] Tettnang, Germany, Günter P. Merker, Graz, Austria and Rudiger Teichmann "Combustion Engines Development (Mixture Formation, Combustion, Emissions and Simulation)", Wiesbaden: Springer-Verlag, 2009.

[17] M.C. Cameretti, R. Tuccillo, L. De Simio, S. Iannaccone and U. Ciaravola , "A numerical and experimental study of dual fuel diesel engine for different injection timings," Applied Thermal Engineering , vol. 101, p. 630 – 638, 2016.

[18] A. A. Hairuddin, T. Yusaf and A. P. Wandel, "A review of hydrogen and natural gas addition in diesel HCCI engines," Renewable and Sustainable Energy Reviews, vol. 32, p. 739–761, 2014.

[19] V. Fraioli, E. Mancaruso, M. Migliaccio and B. M. Vaglieco "Ethanol effect as premixed fuel in dual-fuel CI engines: Experimental and numerical investigations," Applied Energy, vol. 119, pp. 394 - 404, 2014.

[20] B. RIBEIRO, J. MARTINS, "Direct Comparison of an Engine Working under Otto, Miller and Diesel cycles: Thermodynamic Analysis and Real Engine Performance," SAE International, vol. 01, pp. 0261-0271, 2007.

[21] X. Zhang, HuWang, Z. Zheng, R. D. Reitz and Mingfa Yao,"Effects of late intake valve closing (LIVC) and rebreathing valve strategies on diesel engine performance and emissions at low loads"; Applied Thermal Engineering, Vol. 98; PP. 310–319, 2016.

[22] M. Jia, M. Xie, T. Wang and Z. Peng, "The effect of injection timing and intake valve close timing on performance and emissions of diesel PCCI engine with a full engine cycle CFD simulation", Applied Energy, Vol. 88, PP. 2967–2975, 2011.

*Corresponding author email: a.menaa@cder.dz

Contribution to the Study of the Production of Wind Energy and Hydrogen in Different Sites of Algeria

M. Baik*, M. Hammoudi, S. K. Kirati, Y. Salhi

Theoretical and Applied Fluid Mechanics Laboratory, Department of Energetic and Fluid Mechanics, University of Science and Technology Houari Boumediene (USTHB), 16111 Algiers, Algeria.

Abstract **This work deals with wind potential and energy storage producing Hydrogen in different regions in Algeria; Jijel in the North and Adrar and Tamanrasset in the South. The aim of this work is studying the impact of the Cut in speed on the wind energy production using different wind generator with different cut in velocities. The second aim is studying the effect of the electrolyzer pressure on hydrogen production and on compressor consumption during hydrogen storage. For that, we consider the real climatic conditions of those regions such temperature, wind velocity and the altitude of chosen sites.**

Key words **wind energy in Algeria, hydrogen, electrolysis.**

I. INTRODUCTION

Algeria has a huge and diversified potential for renewable energy. Numerous studies on the potential of renewable energy and its exploitation [1-2]. Recently a growing interest is focused on its wind potential, although less known, but it remains very important. It is mainly located in the region of Adrar and Tamanrasset, but also in some coastal regions like Jijel and Bejaia [3] , whereupon the Algerian government engaged itself to develop renewable sources to cover 20% of the national electricity needs by 2030 with renewable energy and 35% in 2040 [4]. For the national market, the updated renewable energy program consists of installing a 22 000 MW of RE sources by 2030 with 5000 MW of wind power [5].

The intermittence of renewable energies and their dependence on climatic conditions hamper the use of renewable energies in energy mixes. In order to overcome this major disadvantage, the use of energy storage becomes necessary. Hydrogen is the best alternative for seasonal storage to adapt to annual changes in consumption in these regions [6-8]. The production of hydrogen by electrolysis supplied by a renewable source presents an excellent potential for integrating renewable energies into the energy mix and promotes the use of a clean and sustainable source produced locally [9-10].

In this work, we first propose to highlight the potential of wind energy in different regions of representative Algeria (Jidjel, Adrar and Tamanrasset).

In this section, we deal with the production of electricity by a wind farm of 10 MW of total power, in each region. The study is made for two types of wind turbines, with 0.85 MW and 2.5 MW rated power and having different characteristics. This first part aims to identify the optimal machine for each region studied. In order to take into account the climatic effects of each region (coastal, highlands and south of the country), we introduced the altitude and temperature effects in the model describing the evolution of the power delivered by each type of machine. As such, we have developed a program under Matlab/Simulink, allowing to perform hourly simulations over a period of one year. Afterwards, the hydrogen production is simulated using different electrolyzer pressure; 70 bar, 30 bar and 1 bar. That is mainly done to show the impact on hydrogen production and compressor energy consumption.

II. THEORETICAL STUDY

1. *Wind potential*

. The available wind power, expressed in Watt per square meter, is generally considered a better indicator of the wind potential than wind speed [11]. In fact, it takes into account the frequency distribution of the wind speed and the dependence of wind power on air density and the cube of wind speed. Thereby the available wind potential can be calculated us follows [12].

$$P_{avail} = \frac{1}{2}\rho V^3 \qquad (1)$$

Where ρ is the air density which is about 1.23 kg/m^3.
V is the average cubic wind speed (m/s) details on its determination are given in [12].

The wind energy production is simulated using two types of wind turbines; 12 x 0.85 MW and 4 x 2.5MW with 3.5m/s and 2m/s cut-in wind velocity respectively. The wind energy production depends mainly on wind speed. Other parameters like air density and hub height are taken into account. The wind power delivered by the wind turbine given by the following fitted equation of the power characteristic curve [10].

$$P_{wind} = \left[\frac{0.0182 + 0.8 \cdot V_2^7}{8.75^7 + V_2^7}\right] \cdot \rho \cdot P_{wmax} \qquad (2)$$

P_{wmax} is the rated power of each wind turbine and V_2 represents the wind velocity at the hub height and it is calculated as follow.

*Corresponding author email: mouloud.baik@hotmail.fr

$$V_2 = V_1 \cdot \left(\frac{Z_2}{Z_1}\right)^{\alpha} \quad (3)$$

Z_1 : The altitude of the site (m).

Z_2 : Z_1 + hub height (m)

α : Coefficient relating to the nature of the ground.

2. *Hydrogen production*

In this work, we assume the use of an alkaline electrolyzer of 2.5 MW which represents 25% of the wind farm power with a maximum current density of 0.5 A / cm². The hydrogen production rate of an electrolyser is mainly given by Faraday's Law. The normalized hydrogen flow rate calculated by using the following expression [13]:

$$Q = \xi_F \cdot \frac{3600 \cdot RT}{nFP_0} \cdot N_c \cdot i \quad (4)$$

With

ξ_F : Represents the current efficiency.

P_0 : Atmospheric pressure (bar).

N_c : Number of cells.

i : Current density (A/m²).

n: Number of electrons.

R, T and F are gas constant, temperature of electrolyzer

3. *Hydrogen compression*

To simplify the calculations, we consider compression of hydrogen as an isentropic process and assume no heat exchange between the compressor and environment and the process is reversible. By assuming hydrogen behaves as an ideal gas, the isentropic work to compress hydrogen gas from pressure P_1 to pressure P_2 is given by the equation (4) given in [14]. In our case we assume a storage at the pressure P_2= 150 bar.

$$W_{isentrop} = \frac{RT_1\gamma}{\gamma - 1} \cdot \left[\left(\frac{p_2}{p_1}\right)^{\frac{\gamma-1}{\gamma}} - 1\right] \quad (5)$$

Where T_1 is the temperature of hydrogen in Kelvin at pressure P_1 ic heat ratio of the gas and is equal to 1.4.

However, since adiabatic hydrogen compression is not reversible process, the deviation from ideal behavior should be taken into account. Therefore, the real compressor work can be given by

$$W_{real} = \frac{W_{isentrop}}{\eta_{adiab}} \quad (6)$$

Where η_{adiab} is the adiabatic efficiency of the compression process. Its value varies between 75% and 80% [15].

III. RESULTS AND DISCUSSION

1. *Available wind potential and Energy*

According to the equation (1) the available potential obtained is nearly the same in Jijel and Tamanrasset with 77.80 W/m² and 81.10 W/m² respectively. The highest wind potential is recorded in Adrar with 215.49 W/m².

To view the effect of the cut-in wind speed we simulated the wind energy production in each region by using a wind farms of 10 MW. For each farm we simulated the production using two types of wind turbine generator; 0.85 MW and 2.5 MW characterized with the 3.5 m/s and 2 m/s cut in speed. Thus the nominal power of the whole wind farm is obtained by adding the production of 4 turbines of 2.5 MW or 12 turbines of 0.85 MW. For each region, the operating conditions are the same. In Fig. 1, we portrayed the energy produced over the year.

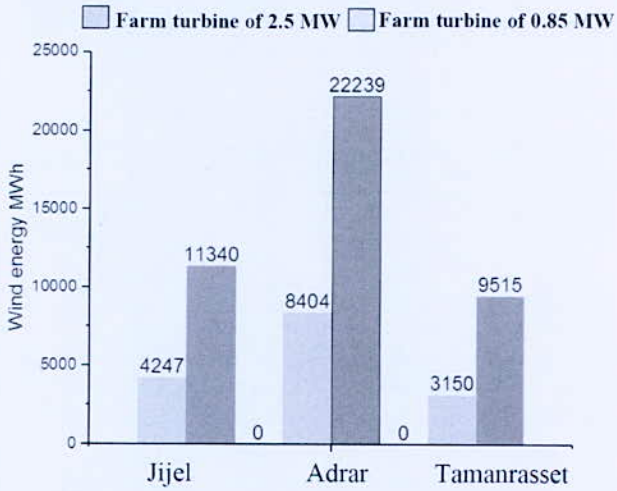

Fig. 1. Wind energy production in each regions using two types turbine generator

As we can see it, there is a significant difference between the energy produced by using the farms of 0.85 MW turbine generator and the energy which is produced using the farm of 2.5 MW turbine generator. Indeed the energy produced by the farm of 2.5 MW turbines is 2.6 times greater than the energy produced by the farm of 0.85 MW wind turbine in Jijel and Adrar, and 3 times greater in the region of Tamanrasset. This difference is mainly due to the weak cut-in speed (2 m/s) of the wind turbine of 2.5 MW which leads to an effective time run over the year for the wind farm.

2. *Hydrogen production and Compressor consumption*

To highlight the impact of electrolyzer pressure on compressor consumption and hydrogen production we simulated different electrolyzer pressure from 1bar to 70 bar. The electrolyzer is assumed to be fed by the wind

*Corresponding author email: mouloud.baik@hotmail.fr

farm of 2.5 MW wind turbines. Since the behavior is the same in each region, we simulated the production in the region of Adrar only. The Fig. 2, shows hydrogen production for different electrolyzer pressure. The wind energy produced in Adrar over the year is about 22239 MWh. As we see, the highest amount of hydrogen (243664 Kg) is produced at lowest pressure (1 bar). In addition, we observe that the hydrogen production decreases by 24% to reach the amount of 181192 Kg when the electrolyzer pressure increases from 1 bar to 70 bar.

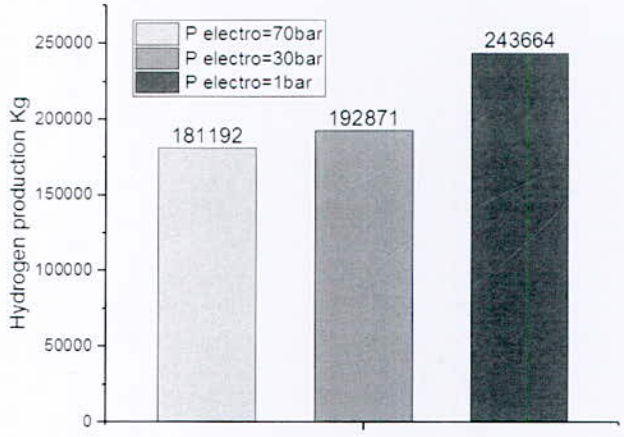

Fig. 2. Hydrogen production for different electrolyzer pressure over the year

TABLE I
COMPRESSOR ENERGY CONSUMPTION

Electrolyzer pressure (bar)	1	30	70
Compressor consumption (MWh)	996	156	66
Hydrogen production (Kg)	243664	192871	181192

However, as is shown in the Table I, the energy required by the compressor to store the hydrogen is more significant when the hydrogen initially is produced at low pressure. Indeed, when the hydrogen is produced under 1bar, the compressor requires 966 MWh to store 243664 Kg of hydrogen. This corresponds to an energy requirement of 3.96 kWh/kg. For an a production at 30 bar pressure, the storage cots 0.80 kWh/kg In the case where the hydrogen is produced at 70 bar electrolyzer pressure, the compressor requires 66 MWh to store 181192 kg of hydrogen, which represents an average of 0.36 kWh/Kg. Therefore, even if we lose 24% of the hydrogen when the production occurs at high electrolyzer pressure, from an energetic point of view, it remains more interesting.

IV. CONCLUSION

In the present work, a simulation of wind energy production is made for three different region in Algeria; Adrar, Jijel and Tamanrasset. It appears that wind potential is mainly high in each region. Thus, wind sources can make an alternative sources for energy production in Algeria specifically in coastal and remote areas.

For a better exploitation of the wind potential, the impact of the cut in speed of turbine generator is studied and a comparison between two types of wind generator with 3.5 m/s and 2 m/s cut in speed. As is demonstrated above, more the cut in speed is less, more the wind energy production is significant. The amount of energy produced is at least 2.6 times greater using the wind generator with 2 m/s cut in speed.

In the second part of our work we studied the impact of the electrolyzer pressure on compressor consumption and hydrogen production. Assuming power from the wind energy produced, we performed simulations for different hydrogen production pressures. The analysis shows that the increase in pressure induces a decrease for hydrogen produced and reduces which reduces the efficiency of the electrolyser. However, the production of hydrogen at high pressure reduces drastically the energy requirement to storage. Indeed, we found that when the hydrogen is produced at high pressure 70 bar, the overall hydrogen storage system, requires 0.36 kWh/ Kg, while it requires 3.96 kWh/kg at atmospheric pressure.

According to this study, we were able to evaluate the usefulness of using high-capacity wind turbines (2.5 MW) characterized by low cut in speed. As for hydrogen production, we have seen that production at high pressures is more advantageous even if the quantities of Hydrogen produced are reduced.

However, to ascertain economically the study, it is indispensable to optimize the size of the equipment for each region and several technologies should be compared based on their costs. This remains the next step of the present study.

ACKNOWLEDGMENT

The authors gratefully acknowledge the SOTRACO group for supporting us to accomplish this work and have brought at our disposal the necessary data.

REFERENCES

[1] R. Boudries Khellaf, R. Dizene and M. Belhamel Evaluation of the Hydrogen potential in Algeria. (2007)113 116.

[2] Douaka M., Settoub N., Estimation of hydrogen production using wind energy in Algeria. Energy Procedia 74 (2015) 981

[3] D. Rekioua, S. Bensmail, N. Bettar Development of hybrid photovoltaic-fuel cell system for stand-alone application. International Journal of Hydrogen Energy xxx (2013) 1 -8.

[4] http://www.sonelgaz.dz/?page=article&id=34

[5] M. Abbas, Z. Belgroun, H. Aburidah and N. Kasbadji olic trough power plant for electricity generation under

*Corresponding author email: mouloud.baik@hotmail.fr

Mediterranean Green Energy Forum, Energy Procedia 42 (2013) 93 102.

[6] R. Boudries -
Production System in Algeria 'Rev. Energ. Ren. Drylands, 2002. 17.

[7] M. Hammoudi, C. Henao, K. Agbossou, Y. Dube´, and M.L. Doumbia: New multi-physics approach for modelling and design of alkaline electrolyzers.

Energy System for hydrogen production in the Adrar

International Symposium on Sustainable Hydrogen, Algiers, (October 2016).

[9] Christian Henao, Kodjo Agbossou, Mhamed Hammoudi, Yves Dubé, Alben Cardenas: Simulation tool based on a physics model and an electrical analogy for an alkaline electrolyser.

[10] B. Mouloud, M. Hammoudi, Y. Salhi . S.K. Kirati. Simulation of hydrogen production from RE sources and its utilization applying fuel cell in Algeria.

International Symposium on Sustainable Hydrogen, Algiers, (October 2016).

[11] S. Diaf, M. Belhamel, M. Haddadi and A. Louche Assessment of wind energy resource in southern Algeria *Revue des Energies Renouvelables Vol. 10 N°3 (2007) 321 – 333*

[12] N. Kasbadji Merzouk et M. Merzouk Estimation du potentiel énergétique éolien utilisable Application au pompage dans les Hauts Plateaux. *Revue des Energies Renouvelables Vol. 9 N°3 (2006) 155 – 163*

[13] R. L. Leroy, C. T. Bowen. The Thermodynaémics of Aqueous Water Electrolysis. J. Electrochem. Soc: Electrochemical science and technology. Pages 1954-1962 September 1980.

[14] J.M Smith, H C Van Ness, M M Abbot: *Introduction to Chemical Engineering Thermodynamics*: McGraw Hill

[15] E Tzimas, C Filiou, S.D Peteves: *Hydrogen Storage:State of the Art and Future Perspective*, European Commission, 2003.

*Corresponding author email: mouloud.baik@hotmail.fr

A Novel Single Sensor Variable Step Size MPPT for PEM Fuel Cell Power System

A. Harrag[1, 2*] and H. Bahri[3]

[1]CCNS Laboratory, Electronics Department, Faculty of Technology, Ferhat Abbas University Setif 1, 19000 Setif, Algeria.
[2]Optics and Precision Mechanics Institute, Ferhat Abbas University Setif 1, Cite Maabouda, 19000 Setif, Algeria.
[3]Electrical Engineering Department, Faculty of Technology, Mohamed Boudiaf University, 28000 Msila Algeria.

Abstract—**This paper proposes a novel single sensor variable step size maximum power point tracking method for PEM fuel cell power system composed of 7kW PEM fuel cell powering 50Ω resistive laod via a DC-DC boost converter driven using the proposed MPPT controller. The proposed MPPT algorithm uses only one sensor in order to reduce the cost and the complexity of the MPPT controller. The performance of the proposed single sensor MPPT controller is evaluated using the implemented Matlab/Simulink PEM Fuel Cell power system model. Simulation results show that the proposed single sensor MPPT controller can provide similar results using only one sensor which reduces the cost as well as the complexity of the PEM fuel cell power system.**

Key words—Fuel cell, PEMFC, MPPT, boost DC-DC, fixed step, variable step, single sensor.

I. INTRODUCTION

Fuel cells have no moving parts. Nearly silent, they can be as much as 2.5 times as efficient as internal-combustion engines. In the last two decades, they became widely and publicly recognized as a vanguard technology that may launch hydrogen energy on its way to becoming a major, environmentally benign, sustainable, renewable component of the world's energy mix for both transportation and stationary applications [1].

The viability, efficiency, and robustness of the fuel cell technology depend on understanding, predicting, monitoring, and controlling the fuel cell system under a variety of environmental conditions and a wide operating range [2].

Fuel cells are an energy conversion device that uses the catalytic oxidation of hydrogen at an anode with the catalytic reduction of oxygen at a cathode to release energy as electricity and heat with the non-polluting by-product of water. So long as hydrogen and oxygen fuel is supplied a fuel cell will provide a continuous energy output [3].

Among various fuel cells, the low temperature proton exchange membrane fuel cell (PEMFC) and the high temperature solid oxide fuel cell (SOFC) have been identified as the likely fuel cell technologies that will capture the market in the future. In order to operate and control PEMFC systems, it is necessary to investigate dynamic characteristics of PEMFC through modelling and simulations. PEMFCs operate best at temperatures between 60 and 90◦C. The fuel cell stack itself can operate at an efficiency of 50 to 60% [4].

The power/current (P/I) characteristic of a PEM fuel cell is quite similar to the power/voltage (P/V) characteristic of a PV cell. The voltage depends very much on the current. To supply a load with a constant voltage, power electronics are necessary. The power electronics are also needed to adjust the point on the P/I curve corresponding to the actual power demand. Therefore, the operation of a fuel cell in applications with varying load demands without power electronics is impossible [5].

The last decade has seen a huge development of the maximum power point tracking (MPPT) controller for fuel cell power systems [6-8]. Among them: Perturb and observation [9], incremental conductance [10], sliding mode controller [11], fractional order filter controller [12], hysteresis controller [13], extremum seeking control [14], fuzzy logic controller [15], particle swarm optimization controller [16], water cycle algorithm controller [17], unified tracker algorithm controller [18], eagle strategy controller [19], neural network controller [20].

Inspired by the work done the last decade on PV systems that are similar in terms of characteristics by taking P/I characteristic for PEM fuel cell systems instead of P/V characteristic for PV systems [21-23], this paper presents a novel single sensor variable step size maximum power point tracking method for PEM fuel cell power system composed of 7kW PEM fuel cell powering 50Ω resistive laod via a DC-DC boost converter driven using the proposed MPPT controller. The proposed MPPT algorithm uses only one sensor in order to reduce the cost and the complexity of the MPPT controller. The performance of the proposed single sensor MPPT controller is evaluated using the implemented Matlab/Simulink PEM Fuel Cell power system model. Simulation results show that the proposed single sensor MPPT controller can provide similar results using only one sensor which reduces the cost as well as the complexity of the PEM fuel cell power system.

The remainder of this paper is organized as follows. In Section 2, the fuel cell modeling is described; while Section 3 presents the proposed single sensor MPPT. The simulation results and discussions are presented in Section 4. Section 5 stated the main conclusions of this work.

*Corresponding author email: a.b.harrag@gmail.com

II. PEMFC MODELING

PEM fuel cell is an energy conversion device that uses the catalytic oxidation of hydrogen at an anode with the catalytic reduction of oxygen at a cathode to release energy as electricity and heat with the non-polluting by-product of water [24] (Fig. 1).

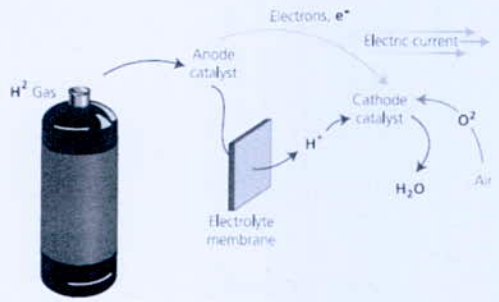

Fig. 1. PEM Fuel Cell

Oxidation of hydrogen reaction at anode:

$$H_2 \rightarrow 2H^+ + 2e^- \quad (1)$$

Reduction of oxygen reaction at a cathode:

$$O_2 + 4e^- \rightarrow 2O^{-2} \quad (2)$$

The overall hydrogen PEM Fuel Cell reaction is:

$$H_2 + \frac{1}{2}O_2 \rightarrow H_2O + \text{electricalenergy} + \text{heat} \quad (3)$$

The output voltage of each cell can be defined by following expression:

$$V_{FC} = E_{nernst} - V_{conc} - V_{ohmic} - V_{act} \quad (4)$$

E_{nernst} is the reversible open circuit voltage defined by [25]:

$$E_{nernst} = 1.229 - (8.5 \times 10^{-4})(T - 298.15) + (4.385 \times 10^{-5}T[\ln(P_{H2}) + 0.5\ln(P_{O2})] \quad (5)$$

where

T is the temperature (K);

P_{O2} the oxygen pressure (bar);

P_{H2} the hydrogen pressure (bar).

V_{con} is the concentration voltage loss from the transport of hydrogen and oxygen given by:

$$V_{con} = -b \cdot \ln(1 - \frac{i_{FC}/A}{I_{max}}) \quad (6)$$

where

b is the concentration loss constant;

i_{FC} is the cell current (A);

A is the is cell active area (cm^2);

I_{max} is the maximum current density (A/cm^2).

V_{ohmic} is the ohmic voltage loss given by:

$$V_{ohmic} = (R_M + R_C)i_{FC} \quad (7)$$

where

R_C is the contact resistance (Ω);

R_M is the membrane resistance (Ω);

i_{FC} the cell current (A).

V_{act} is the activation voltage lost defined by [25]:

$$V_{act} = \xi_1 + \xi_2 \cdot T + \xi_3 \cdot T \cdot \ln(C_{O2}) + \xi_4 \cdot T \cdot \ln(i_{FC}) \quad (8)$$

where

$\xi_{i\ (i=1\ to\ 4)}$ are parametric coefficients for each cell;

C_{O2} is the oxygen's concentration ($mol/_{cm3}$).

III. SINGLE SENSOR MPPT CONTROLLER

To decreases the cost and complexity of the PEM fuel cell power system, the MPPT algorithm can use only one sensor based on [23]:

$$P_0 = I_0^2 . R \quad (9)$$

where

P_0 is the output power;

I_0 is the output current;

R_L is the load resistance.

Tracking the maximum of P_0 reduced to track:

$$\frac{\partial P_0}{\partial D} = \frac{\partial I_0}{\partial D} = 0 \quad (10)$$

According to the equation of the boost converter, we have:

$$I_0 = I_{fc}(1 - D) \quad (11)$$

where I_{fc} is the fuel cell current.

According to (10), we have:

$$\frac{\partial I_0}{\partial D} = \frac{\partial(I_{fc}(1-D))}{\partial D} = (1 - D)\frac{\partial I_{fc}}{\partial D} + I_{fc}\frac{\partial(1-D)}{\partial D}$$

$$\rightarrow \frac{\partial I_{fc}}{\partial D} - \frac{I_{fc}}{1-D} = 0 \quad (12)$$

Equation (12) means that the maximum power point is achieved when this condition is met.

IV. RESULTS AND DISCUSSION

The model of the 7kW PEM Fuel Cell supplying a 50 Ω resistive load via a DC-DC boost converter drived using the single sensor MPPT controller implemented and analyzed using Matlab/Simulink environment. The parameters of the 7kW PEM Fuel Cell are given in Table 1; while the DC-DC boost converter parameters are given in Table II. The developed Matlab/Simulink PEM fuel cell power system model is shown in Fig. 2.

TABLE I
PEM FUEL CELL PARAMETERS

Parameter	Value
Maximum Power at MPP (W)	7000
Cell open circuit voltage (V)	1.29
Number of cells	50
Cell active surface (cm^2)	200
Hydrogen partial pressure H_2 (bar)	2.6
Oxygen partial pressure O_2 (bar)	0.3

TABLE II
DC-DC BOOST CONVERTER PARAMETERS

Parameter	Value
L (mH)	5
C (μF)	1000
Switching frequency Fs (KHz)	10
Resistive Load (Ω)	50
Vg (nominal voltage (V)	47

*Corresponding author email: a.b.harrag@gmail.com

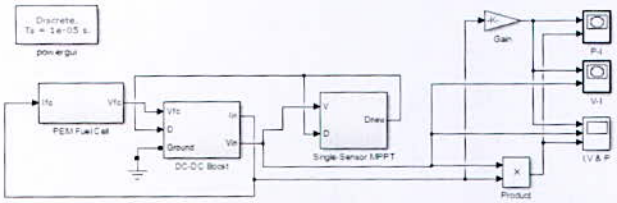

Fig. 2. Matlab/Simulink PEM Fuel Cell power system

Fig. 3 to Fig. 5, present the current, voltage and power curves using the proposed single sensor MPPT controller.

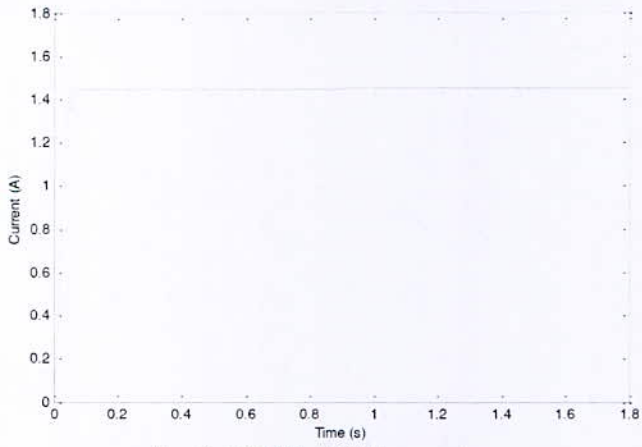

Fig. 3. PEM Fuel Cell current

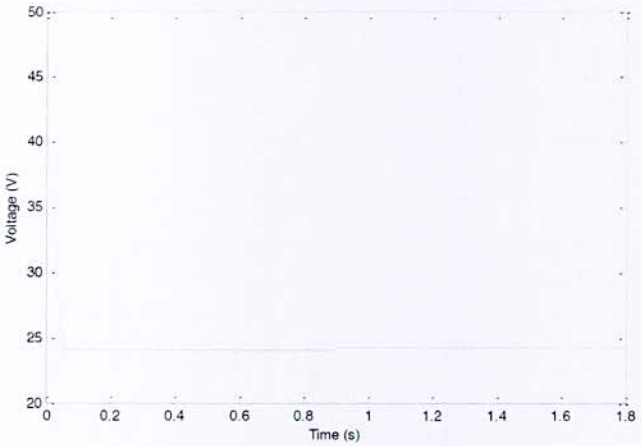

Fig. 4. PEM Fuel Cell voltage

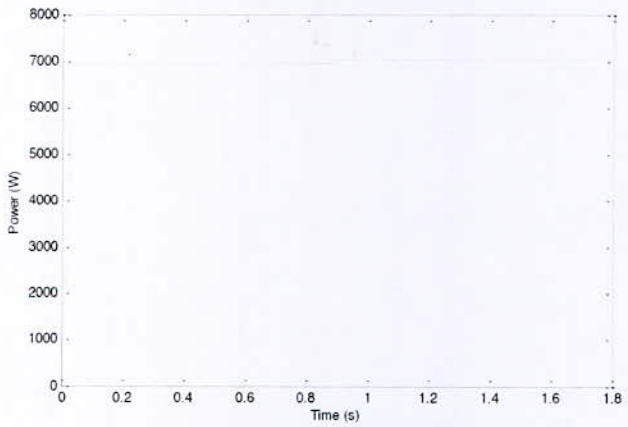

Fig. 5. PEM Fuel Cell power

While Fig. 6 and Fig. 7, provide the V-I and P-I characteristics, respectively.

From Fig. 3 to Fig. 7, we can see clearly that the proposed single sensor MPPT controller tracks correctly the maximum power provided by the PEM fuel power system by driving the PWM duty cycle using only one sensor for the PEM fuel cell voltage.

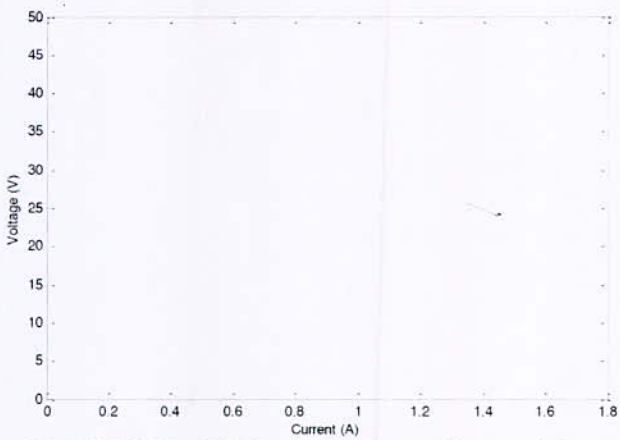

Fig. 6. PEM Fuel Cell voltage-current characteristics

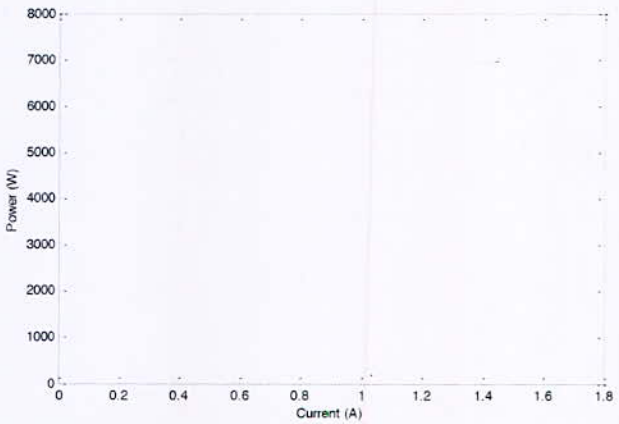

Fig. 7. PEM Fuel Cell power-current characteristics

V. CONCLUSION

This paper deals with the development of a single sensor MPPT controller used to track the maximum power of 7kW PEM fuel cell power system. The proposed single sensor MPPT controller has been studied successfully using a 7kW PEM fuel cell supplying a 50Ω resistive load via a DC-DC boost converter drived using Matlab/Simulink Environment. Simulation results show that the proposed single sensor MPPT controller can effectively track the maximum power using only one sensor for the PEM fuel cell voltage.

REFERENCES

[1] N. Sammes, Fuel Cell Technology, Reaching Towards Commercialization, Springer-Verlag London Limited 2006.

[2] J. Milewski, K. Swirski, M. Santarelli and P. Leone, Advanced Methods of Solid Oxide Fuel Cell

*Corresponding author email: a.b.harrag@gmail.com

Modeling, Springer London Dordrecht Heidelberg New York, 2011.
[3] C. Kunusch et al., Sliding-Mode Control of PEM Fuel Cells, Advances in Industrial Control, Springer-Verlag London Limited 2012
[4] A. Luque and S. Hegedus, Handbook of Photovoltaic Science and Engineering, John Wiley & Sons Ltd, The Atrium, Southern Gate, Chichester, West Sussex PO19 8SQ, England 2003
[5] Ramos-Paja CA, Spagnuolo G, Petrone G, Giral R and Romero A. Fuel cell MPPT for fuel consumption optimization. In Proceedings IEEE International Symposium on Circuits and Systems (ISCAS); 2010. p. 2199-202.
[6] Becherif M and Hissel D. MPPT of a PEMFC based on air supply control of the motocompressor group. Int J Hydrogen Energy 2010; 35(22):12521-30.
[7] Karami N, Outbib R and Moubayed N. Fuel Flow Control of a PEM Fuel Cell with MPPT. In Proceedings IEEE International Symposium on Intelligent Control (ISIC); 2012. p. 289-94.
[8] Sarvi M, Barati MM. Voltage and current based MPPT of fuel under variable temperature conditions. In: Proceedings Universities Power Engineering Conference (UPEC); 2010.p. 1e4.
[9] Romdlony MZ, Trilaksono BR, Ortega R. Experimental study of extremum seeking control for maximum power point tracking of PEM fuel cell. In: International Conference on System Engineering and Technology (ICSET); 2012. p. 1e6.
[10] Abdi SH, Afshar K, Bigdeli N, Ahmadi S. A novel approach for robust maximum power point tracking of PEM fuel cell generator using sliding mode control approach. Int J Electrochem Sci 2012; 7:4192e209.
[11] Liu J, Zhao T, Chen Y. Maximum power point tracking of proton exchange membrane fuel cell with fractional order filter and extremum seeking control. In: Proceedings ASME/IEEE International Conference on Mechatronic and Embedded Systems and Applications (ICMESA); 2015. p. 1e6.
[12] Park JD, Ren Z. Hysteresis controller based maximum power point tracking energy harvesting system for microbial fuel cells. J Power Sources 2012; 205:151e6.
[13] Ettihir K, Boulon L, Agbossou K, Kelouwani SMPPT. Control strategy on PEM fuel cell low speed vehicle. In: Proceedings IEEE Vehicle Power and Propulsion Conference (VPPC); 2012. p. 926e31.
[14] Jiao J, Cui XA. Real-time tracking control of fuel cell power systems for maximum power point. J Comput Inf Syst 2013; 9(5):1933e41.
[15] Venkateshkumar M, Sarathkumar G, Britto S. Intelligent control based MPPT method for fuel cell power system. Int. Conference on Renewable Energy and Sustainable Energy (ICRESE); 2013. p. 253e7.
[16] Soltani I, Sarvi M, Marefatjou H. An intelligent, fast and robust maximum power point tracking for proton exchange membrane fuel cell. World Appl Program 2013; 3(7):264e81.
[17] Avanaki I.N, Sarvi M. A new maximum power point tracking method for PEM fuel cells based on water cycle algorithm. J Renew Energy Environ 2016; 3(1):35e42.
[18] Fathabadi H. Novel highly accurate universal maximum power point tracker for maximum power extraction from hybrid fuel cell/PV/wind power generation systems. Energy; 2016(116):402e16.
[19] Sarvi M, Parpaei M, Soltani I, Taghikhani MA. Eagle strategy based maximum power point tracker for fuel cell system. IJE Trans A Basics 2015;28(4):529e36.
[20] Harrag A, Bahri H, Novel neural network IC-based variable step size fuel cell MPPT controller, Int. Journal of Hydrogen Energy, 42(5), 2017:3549-3563.
[21] M.A. Abdourraziq M. Ouassaid and M. Maaroufi, A Fuzzy Logic MPPT for Photovoltaic Systems using Single Sensor, Int. Renewable and Sustainable Energy Conf. (IRSEC), 17-19 Oct. 2014, Ouarzazate, Morocco.
[22] C. C. Hua, W.T. Chen and Y.H. Fang, A Hybrid MPPT with Adaptive Step-Size based on Single Sensor for Photovoltaic Systems, Int. Conf. on Inf. Science, Electronics and Electrical Engineering (ISEEE), 26-28 April 2014, Sapporo, Japan.
[23] A. Chikh and A. Chandra, An Optimal Maximum Power Point Tracking Algorithm for PV Systems With Climatic Parameters Estimation, IEEE Trans. on Sustainable Energy 6(2),2015:644-652.
[24] Spiegel C. PEM modeling and simulation using matlab. Burlington, MA: Academic Press; 2008.
[25] Y. T. Chen and J.H. Lai, A Novel Variable Step-Size MPPT Method for PV System with Single Sensor, 2014 IEEE 9th Conference on Industrial Electronics and Applications (ICIEA), pp. 719-722.

*Corresponding author email: a.b.harrag@gmail.com

PEM Fuel Cell Hydrogen Support Using PV-Electrolyzer Generation System

H. Bahri[1] and A. Harrag[2, 3*]

[1]Electrical Engineering Department, Faculty of Technology, Mohamed Boudiaf University, 28000 Msila Algeria.
[2]CCNS Laboratory, Electronics Department, Faculty of Technology, Ferhat Abbas University Setif 1, 19000 Setif, Algeria.
[3]Optics and Precision Mechanics Institute, Ferhat Abbas University Setif 1, Cite Maabouda, 19000 Setif, Algeria.

Abstract— **In consequence of increasing global energy consumption, the environmental problems such as pollution and the drain of conventional energy resources such as coal, gas and liquefied petrol. To tame this is by implementing seeming ''Technology of Renewable Energy''. Hydrogen is one of the promising alternative fuels for the future because it has the capability of storing energy of high quality. Therefore, the hydrogen has been visualized to become the cornerstone of future energy systems, hydrogen produced from water electrolysis under interaction Electrochemical. Water electrolyzer converts electricity into chemical energy which produces hydrogen and oxygen and this can be achieved by passing DC electric current between two electrodes separated by electrolyte, the direct current electric is delivered by source renewable energy Photovoltaic or Wind system. The main for this paper is to study the different parties of indirect coupling PV with alkaline electrolyzer for production hydrogen. By utilization Matlab Simulink the characteristics of current-voltage for both systems (PV and Electrolyzer) have been presented. The principal parameters affecting the performance of the alkaline electrolyzer.**

Key words—PV, Fuel cell, PEMFC, Electrolyzer.

I. INTRODUCTION

Energy refers to a kind of force or power that enables us to do work. Nature has provided us with a variety of natural sources of energy. Conventional energy directly means the energy source which is fixed in nature like oil, gas and coal, these sources of energy are being used since a long time and used extensively in such a way that their known reserves have been depleted to a great extent.

The global energy requirements of the future, depletion of fossil fuels and climate pollution, for these purpose renewable energy resources or Non-conventional energy any energy resource that is naturally regenerated over short time scale, attract more attention and have made necessitous its exploited [1]. Currently, there are much renewable energy, most notably wind, solar and hydrogen [2].

Most renewable energy comes either directly or indirectly from the sun. Sunlight, or solar energy, can be used directly for heating and lighting homes and other buildings, for generating electricity, and for hot water heating, solar cooling, and a variety of commercial and industrial uses. Solar cells convert sunlight directly into electricity. They are made of semiconducting materials. When sunlight is absorbed by these materials, the solar energy knocks electrons loose from their atoms, allowing the electrons to flow through the material to produce electricity. This process of converting light (photons) to electricity (voltage) is called the photovoltaic (PV) effect [3]. Photovoltaic system can't be produced during night and cloudy days but it can be used again and again during day time, so is necessary storing energy to overcome these drawbacks by integration photovoltaic system with other energy sources such as battery, hydrogen and Fuel Cell to ensure reliable supply of electricity to the load [4].

In this paper electrolyzer system has been introduced with photovoltaic system to produce hydrogen, this one is the simplest element on earth, it consist of only one proton and one electron and it is an energy carrier, not an energy source. Hydrogen can store and deliver usable energy, but it doesn't typically exist by itself in nature and must be produced from compounds that contain it. The most practical device used hydrogen to produce electricity is the fuel cell, this one is an electrochemical system which converts the chemical energy of hydrogen and oxygen to electrical energy and heat [5]. Several types of fuel cell exist in the literature, among them PEMFC (Proton exchange Membrane Fuel Cell), it has many advantages such as: fast and easy start-up, its high power density and low temperature operation, PEMFCs are perfect candidates for both stationary and transport applications [6].The aim is to simulate the indirectly coupling of the PV system with alkaline electrolyzer. The model for both systems are presented in the form of mathematical equations and by using MATLAB/Simulink can be helps to illustrate the different characteristic curves of the PV and electrolyzer as well as study the different effects of different parameters such as solar irradiance, current density and operating temperature are studied to determine their effect on hydrogen production rate.

II. PV SYSTEM MODELING

Photovoltaicisthedirectconversion of light intoelectricity at theatomiclevel. Somematerialsexhibit a propertyknown as thephotoelectriceffectthat causes them to absorbphotons of light and releaseelectrons. Whenthese free electrons are captured, anelectriccurrentresultsthat can be used as electricity. PV panel consists a number of photovoltaiccellsconnected in series and parallel. The PV cell can be presented as diode in parallelwith a photocurrentsource and parallel/series resistor [7]. The output currentofPVcell/isgivenbyequationbelow [8]:

$$I = I_{ph} - I_s\left(e^{\frac{q(V+IR_s)}{NKT}} - 1\right) - \frac{V+IR_s}{R_{sh}} \quad (1)$$

The photo-current is given by equation

$$I_{ph} = (I_{sc} + K_i(T - T_{ref}))\frac{\Im}{1000} \quad (2)$$

The saturation current is described as follow:

$$I_s = I_{sref}\left(\frac{T}{T_{ref}}\right)^3 e^{\left[\left(\frac{1}{T_{ref}} - \frac{1}{T}\right)\frac{qE_g}{NKT}\right]} \quad (3)$$

with

$$I_{sref} = \frac{I_{sref}}{\left(e^{\left[\frac{qV_{ref}}{KAT}\right]} - 1\right)} \quad (4)$$

where I is the output net current of PV cell, Iphis the light-generated photocurrent, Isc is the Short Circuit Current, Is is the reverse saturation current of the diode, V is the cell output

*Corresponding author email: a.b.harrag@gmail.com

voltage, Eg is the band gap energy of semiconductor, Rs is the series resistor of the PV cell, Rshis the shunt resistor of the PV cell, Q is the electron charge, is the sun irradiation, Ki is the cell short circuit current temp. coef, N is the diode ideality factor, T is the working temperature of the p-n junction, Tref is the nominal reference temperature and K is the Boltzman's constant.

The current-voltage curve of a PV cell describes its energy conversion capability at the existing conditions of irradiance and temperature. Due to the non linear nature of relations I-V and P-V, under these conditions environmental, the maximum power point changes continuously, consequently the energy produced change. An MPPT technique therefor used to maximize power extraction under all conditions [9].

III. MPPT CONTROL ALGORITHM

There are several MPPT methods available in the literature the most popular can be classified as Perturbation and observation (P&O) [10], Incremental conductance (I&C) algorithm [11], sliding mode algorithm[12], fuzzy logic control[13],and neural network[14]. Among these techniques Perturbation and Observation (P&O) is characterized by the most used technique because of the many factors of which: low cost, ease of implementation and to its relatively good tracking performance, when compared to the other techniques [15]. Nevertheless, the conventional P&O algorithm has two problems major the first represented in oscillation around the MPP and the second response speed [16].

IV. WATER ELECTROLYSIS PROCESS

Water electrolysis has a long history in the chemical industry, is the decomposition of water into oxygen and hydrogen gas due to an electrical current produced from direct current being passed through the water. This process is characterized by can be production hydrogen based on electricity from renewable energy sources. This operation is very fast, simple used and most importantly hydrogen produced is very high purity. Hydrogen is produced by the reaction chemical at the level anode (oxidation process) and cathode (reduction process) of the electrolyzer when connected in source electrical [17]. In the literature there are several types of electrolyzer, among these and the most popular is alkaline water electrolysis, Solid Oxide Electrolysis and Proton Exchange Membrane (PEM) electrolysis [21], in this part we limit ourselves to studying only two types.

1. Alkaline water electrolyzer

Alkaline electrolyzer is the most widely used technology for water electrolysis, consists of two electrodes anode and cathode separated by a membrane these entire placed in basin with it electrolyte. The most solution used in the electrolyte of alkaline water electrolyzer is potassium hydroxide (KOH) [18]. Fig. 1, bellow presented the operating of alkaline electrolyzer, due the traffic of hydroxide ion (OH^-) located in cathode through the polymeric membrane to reach the hand anode, at this time hydrogen being generated on the cathode side. The set of chemical reactions can be evaluated as follows [19]:

Cathode: $2H_2O + 2e^- \rightarrow H_2 + 2OH^-$ (5)

Anode: $2OH^- \rightarrow (1/2).O_2 + H_2O + 2e^-$ (6)

Finally the total reaction is: $H_2O \rightarrow H_2 + (1/2)\,O_2$ (7)

2. Polymer Electrolyte Membrane water electrolyzer

A PEM is abbreviation to Polymer Electrolyte Membrane, this technology of electrolyzer is composed of anode and cathode chamber when water supplied only one of the two but the most widely used is anode feed mode, two electrodes and a proton exchange membrane allows only hydrogen ions which are passed towards the other side a cathode.

The production of hydrogen in this process passes through the following stages [20]:

- In the anode the water is dissociated into oxygen, proton and electron it can be expressed this reaction chemical as follow:

$$2H_2O \rightarrow O_2 + 4H^+ + 4e^- \quad (8)$$

- In the cathode, is the seat of production hydrogen gas by the collection of protons resultants in the anode which are passed through the PEM to gather with electrons coming from renewable energy source:

$$4H^+ + 4e^- \rightarrow 2H_2 \quad (9)$$

3. Mathematical Modeling

In order to see hydrogen gas outside, the equation below must be realized, is necessary split the water molecule by used direct current streaming from photovoltaic system passed between two electrodes separated by an aqueous electrolyte.

$$H_2O + \text{Electrical Energy (DC)} \rightarrow H_2 + (1/2).O_2 \quad (10)$$

Therefore, the question that arises:

- The minimum amount of electric voltage must be supplied by electricity in order to obtain electrolysis reaction? So, the minimum voltage or rather reversible voltage to the reaction can be determined from Gibbs equation[25]:

$$\Delta G = z.F.\upsilon_{rev} \quad (11)$$

$$\upsilon_{rev}\ \Delta G/(z.F) = 237.2/(2*96485) = 1.229 \quad (12)$$

However, during the electrolysis process, the voltage requirement increases due to the activation over voltage and ohmic overvoltage. Thus, the voltage required is equal to [25]:

$$\upsilon_e = \upsilon_{rev} + \upsilon_{act} + \upsilon_{ohm} \quad (13)$$

while:

$$\upsilon_{act} = s \times \log\left(\frac{K_1 + \frac{K_2}{T_e} + \frac{K_3}{T_e}}{\delta} I_e + 1\right) \quad (14)$$

$$\upsilon_{ohm} = \frac{\varepsilon_1 + \varepsilon_1 T_e}{\delta} I_e \quad (15)$$

The actual amount of hydrogen production is less than the theoretical one due to Faraday efficiency which is the ratio of actual hydrogen production to theoretical amount. An empirical expression to depict the Faraday efficiency is given by [21]:

$$\eta = \frac{\left(\frac{I_e}{\delta}\right)^2}{\chi_1 + \left(\frac{I_e}{\delta}\right)^2} \chi_2 \quad (16)$$

To determine the total hydrogen production rate in the electrolyzer that consists of several cells connected in series, the equation for the operation is stated as below [22]:

$$\varphi_{H_2} = \eta_F \frac{N_c I_e}{zF} \quad (17)$$

The parameter used to draw the electrolyzer characteristics are listed in Table II and III from [23].

*Corresponding author email: a.b.harrag@gmail.com

TABLE II
CONSTANTS PARAMETERS FOR THE ELECTROLYZER

Constant Parameters	Sym.	Units	Value
Overall current across the cell	I_e	A	/
Reversible voltage	υ_{rev}	V	1.229
Temperature of the electrolyzer	T_e	°C	/
Area of Electrode	δ	m^2	0.25
Faraday's Constant	F	C/mol	96485
Number of Electrons	Z	/	2
Coeff. for overvoltage on electrodes	S	V	0.185
	K_1	$A^{-1}m^2$	1.002
Coeff. for overvoltage on electrodes	K_2	$A^{-1}m^2C$	8.424
	K_3	$A^{-1}m^2C^2$	247.3
Parameters related to ohmic resistance of electrolyte	ε_1	$\Omega\ m^2$	$8.05e^{-5}$
	ε_2	$\Omega\ m^2C$	$-2.5e^{-7}$

TABLE III
Faraday Efficiency Parameters

Constant Parameters	Units		Value	
Temperatures	°C	40	60	80
χ_1	mA^2cm^{-4}	150	200	250
χ_2	0....1	0.99	0.985	0.98

The output simulation results of the I_e-υ_e and I_e-η_F curves are presented in Fig. 1 and Fig. 2.

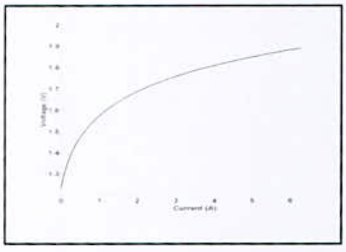

Fig. 1. Characteristic of the electrolyzer I_e-V_e

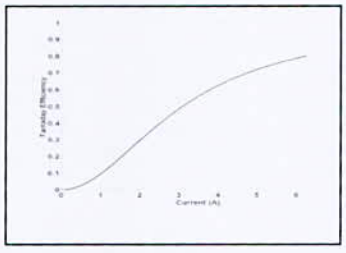

Fig. 2. Characteristic of the electrolyzer I_e-η_F

V. COUPLING I-V CURVE OF PV SYSTEM WITH Ie-Ve STACK ALKALINE WATER ELECTROLYZER

Fig. 3, shows the current-Voltage curves for the both systems PV at 1000 W/m² irradiance indirectly coupled with the different number of water alkaline electrolyzer cells between 16 to 22 cells operating at temperature 40°C. Intersection points of these two characteristics represent the operating point when the stack electrolyzer (number of cells connected in series and parallel) is indirectly coupled to the PV system.

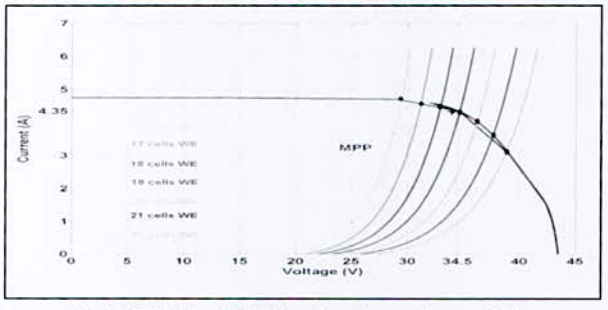

Fig. 3. PV I-V and alkaline electrolyzer characteristics

To search the optimum point for both systems, table IV shows the maximum power, MPPT efficiency and hydrogen production rate. Through the spreadsheet in the bottom we can observe the highest power of the coupling PV-electrolyzer is achieved for 19 cells with MPPT efficiency. The value of this one (99.76%) improve that the indirectly coupling PV with alkaline electrolyzer are working at the optimum operating point. On the contrary maximum hydrogen production not subject to the same operation conditions for maximum MPPT efficiency in this indirectly coupling PV-Alkaline Electrolyzer.

TABLE IV
INDIRECT COUPLING PV WITH ALKALINE ELECTROLYZER

Nb. r of cell of water electrolyzer	V(V)	I(A)	Maximum Power output (W)	MPPT efficiency (%)*	Hydrogen Production rate (Nm^3/h)
16	29.41	4.7	138,22	92.14	0.033
17	31.17	4.58	142,75	95.16	0.035
18	32.96	4.53	149,31	99.54	0.037
19	34.64	4.32	149. 64	99.76	0.040
20	36.24	4.06	147,13	98.06	0.041
21	37.65	3.64	137,05	91. 36	0.043
22	38.88	3.15	122,47	81.64	0.046

*MPPT efficiency = Actual PV output/Maximum PV output

VI. POLARIZATION CURVES OF ALKALINE ELECTROLYZER

Simulation studies in this party are carried out at different level of temperatures which are at 40°C, 60°C and 80°C.Fig. 4,shows that the stack voltage against current density the current input through buck converter is increased similar to stack voltage, this can be interpreted by during the reaction chemical more water molecules dissociated into hydrogen and oxygen molecules, and it the value of stack voltage will keep increasing according to the current. Besides, at different level of temperatures (40°C,60°C and 80°C) the stack voltage decrease due to the decrease in ohmic resistance. Fig. 4 and Fig. 5, show the curves represent the activation and ohmic over potentials as a function of current density respectively. In alkaline electrolysis, the activation over potentials occur due the cell needs energy at start-up the chemical reaction at the electrodes (Anode and cathode) [28], while the ohmic over potentials of the alkaline electrolyzer is present due to the transports of hydrogen and oxygen through the electrolyte to the electrodes [28]. From Fig. 5, current density increases Offset by a slight increase, the effect of temperature can be observed no significant effect on activation over potentials. On the contrary the effect of temperature an ohmic over potentials it is clear because the increase temperature allows to reduces the electrolyte resistance, the curve provide a linear relationship between ohmic and current density.

Fig. 7, shows the relationship between faraday efficiency and current density under different level temperature. Concerning current density, the faraday efficiency increases from 0.7 to 0.8 concurrently with increasing current density. The faraday efficiency decrease when the operating temperature increases; while Fig. 8, shows the production of hydrogen as a function of current density and at different level temperature. This one it does not have much effect in hydrogen flow rate from electrolyzer. As we know the water dissociated by using the electrical current, so at higher current density, higher hydrogen flow rates produce.

*Corresponding author email: a.b.harrag@gmail.com

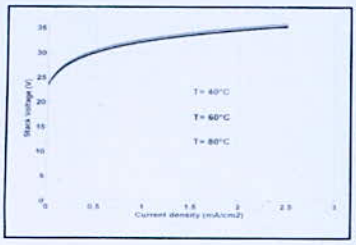

Fig. 4. Polarization curve $I_e - \upsilon_e$

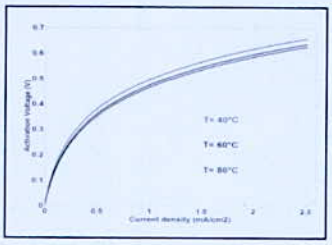

Fig. 5. Polarization curve activation overpotentials contribution

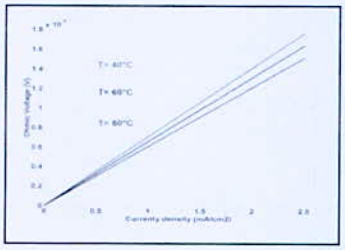

Fig. 6. Polarization curve ohmic losses overpotentials

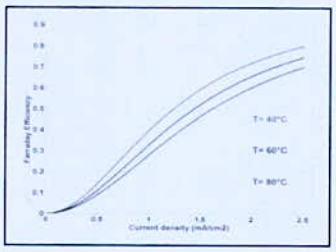

Fig. 7. Polarization curve faraday efficiency overpotentials

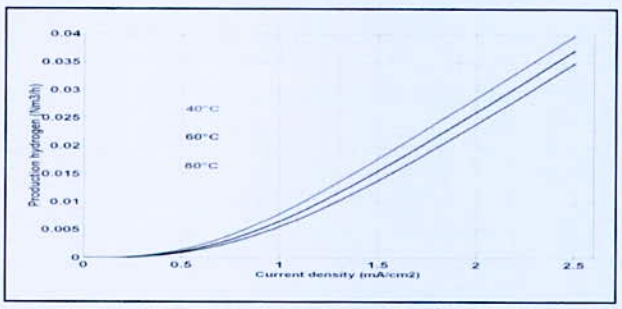

Fig. 8. Production hydrogen as function current density

VII. CONCLUSION

The both system had been studied each alone, and the two models of PV and alkaline electrolyzer implemented in MATLAB/Simulink to extract its curves. For alkaline electrolyzer quite simply it can be noticed that the operating temperature affects the voltage, but did not affect the hydrogen production despite lower power requirement. Results show that the PV system produced maximum power when coupled with 19 cells.

REFERENCES

[1] S. Sadeghi and M. Ameri, Comparison of different power generators in PV-battery-power generator hybrid system, Journal of Mechanical Science and Technology, 28(1), 2014: 387-398.

[2] N. Karami, Nazih Moubayed and Rachid Outbib, Energy management for a PEMFC–PV hybrid system, Energy Conversion and Management, 2014:154-168.

[3] A. Kumar, P. Chaudhary and M. Rizwan, Development of Fuzzy Logic based MPPT Controller for PV System at varying Meteorological parameters, IEEE, 2015..

[4] A.R. Ghahnavieh , S.A. Nowdeh, Optimal PV–FC hybrid system operation considering reliability, Electrical Power and Energy Systems, 2014:325-333.

[5] P. Kumar, A. Gupta, R. Kumar Pachauri, K. Yogesh Chauhan, Utilization of Energy Sources in Hybrid PV/FCPower Assisted Water Pumping System, Int. Conf. on Computational Intelligence & Communication Technology, 2015.

[6] C. Lebreton, M. Benne, C. Damour, N. Yousfi-Steiner, Brigitte Grondin-Perez, Daniel Hissel, Jean-Pierre Chabriat, Fault Tolerant Control Strategy applied to PEMFC water management, int. Journal of hydrogen energy, 2015:10636-10646.

[7] R. Garraoui, M. Ben Hamed and L. Sbita, MPPT controller for a photovoltaic power system based on fuzzy logic, 10th Int. Multi-Conf. on Systems on Signals & Devices (SSD), 18-21 March 2013.

[8] Z. Mokrani, D. Rekioua, T. Rekioua, Modeling, control and power management of hybrid photovoltaic fuel cells with battery bank supplying electric vehicle, Int. Journal of Hydrogen Energy, 2014:1-10.

[9] E. Elgharboui, A.Essadki and N. Tamou, MPPT Commands for a photovoltaic generator using the Incremental Conductance Method and the fuzzy logic command, IEEE, 2014.

[10] N. Tlili, B. Neily and F. Ben Salem, Modeling and simulation of hybrid system Coupling a Photovoltaic Generator, a PEM Fuel Cell and an Electrolyzer (Part I), 2014.

[11] M.H. Namin, S. Afsharnia, Grid-Connected PV with Maximum Power point Tracking technique implemented in Real Case study of variable radiation, 2008.

[12] M. I. Arteaga Orozco, J. R. Vázquez, P. Salmerón, S. P. Litrán, F. J. Alcántara '' Maximum power point tracker of a photovoltaic system using sliding mode control, Int. Conf. on Renewable Energies and Power Quality (ICREQ'09) Valencia (Spain), 15-17 April 2009.

[13] M. T. Makhloufi, M. S. Khireddine, Y. Abdessemed and A. Boutarfa, Maximum Power Point Tracking of a Photovoltaic System using a Fuzzy Logic Controller on DC/DC Boost Converter, IJCSI, 11, 2014.

[14] A. M. Zaki, S. I. Amer, M. Mostafa, Maximum Power Point Tracking for PV System Using Advanced Neural Networks Technique, IJETAE, 2, 2012.

[15] V. DegaRajaji, D. Akhila John, D. Amulya John, Power Compensation using Fuzzy Logic Based For Grid Interactive PV System, IJIREEICE 3(2), 2015.

[16] S. Abdourraziq, R. El Bachtiri, A Perturb and Observe Method using Dual Fuzzy Logic Control for Resistive Load, Recent Advances in Environmental Science and Biomedicine, 107.

[17] R. Boudries, A. Khellaf, A. Aliane, L. Ihaddadeand F. Khida, PV system design for powering an industrial unit for hydrogen production, international journal of hydrogen energy, 2014.

[18] A. Beainy, N. Karami and N. Moubayed, Simulink Model for a PEM Electrolyzer Based on an Equivalent Electrical Circuit, 2nd Renewable Energy for Developing Countries-REDEC, Nov 2014.

[19] A. Ursu and P. Sanchis, Staticdynamic modelling of the electrical behaviour of a commercial advanced alkaline water electrolyser'' International journal of hydrogen Energy, 37, 2012:18598-18614.

[20] N. F.Maged, N.M. Eskander, A. M Sharaf, A Stand Alone Robust PV-FC-Eletrolyzer Utilization Scheme, Int. Journal of Engineering Research, 4, 2015:145-150.

[21] F.Z. Aoualia, M. Becherifb, A.Tabanjatb, M. Emzianec, K. Mohammedia , S. Krehid, A. Khellaf, Modelling and experimental analysis of a PEM electrolyzer poweredby a solar photovoltaic panel, Energy Procedia, 62, 714-722.

[22] A.S Tijani, N.A BintiYusup and A. H. Abdol Rahim, Mathematical modelling and simulation analysis of advanced alkaline electrolyzer system for hydrogen production, 2nd Int Conf. on System-Integrated Intelligence: Challenges for Product and Production Engineering, 2014, 798-806.

[23] A. Khalilnejad, A. Sundararajan, A.I. Sarat, Optimal design of hybrid wind/photovoltaic electrolyzer for maximum hydrogen production using imperialist competitive algorithm, J. Mod. Power Syst. Clean Energy.

[24] A. Khalilnejad, A. Sundararajan, A. Abbaspour and A. Sarwat, Optimal Operation of Combined Photovoltaic Electrolyzer Systems, Energies 9, 2016..

A. Ursu'a, L. Marroyo, E. Gubia, L.M. Gandia, P. M. Dieguez, P. Sanchis, Influence of the power supply on the energy efficiencyof an alkaline water electrolysis, International Journal of Engineering Research, 2009, 3221-3233.

*Corresponding author email: a.b.harrag@gmail.com

Numerical Modeling of an Active Electrocaloric Refrigerator Based on Hydrogen Liquefier

B. Kehileche[1], Y. Chiba[2*], N. Henini[1] and A.Tlemçani[1]

[1]Faculty of technology, department of electrical engineering, University of Medea, Medea, Algeria.
[2]Faculty of technology, department of mechanical engineering, University of Medea, Medea, Algeria.

Abstract—**This work deals with the study of the hydrogen liquefier operating through an active electrocaloric refrigerator cycle. For this purpose, the two-dimensional numerical model has been developed for predicting the thermal efficiency of such a liquefier. The transient energy equation is considered to simulate the heat transfer between electrocaloric material and hydrogen throughout the regenerator bed. The electrocaloric material based on polymer has been used in the regenerator bed. The obtained results, including mainly the temperature cold reservoir and the coefficient of performance of the active electrocaloric refrigerator with the applied electrical field are presented and discussed.**

Key words—Hydrogen, electrocaloric effect, liquefaction.

I. INTRODUCTION

Elctrocaloric refrigerator based on Hydrogen liquefier is a new environmentally friendly cooling technology with a potential for high energy efficiency. The technology is based on the electrocaloric effect; the electrocaloric effect is a phenomenon in which a material shows a reversible temperature change under an applied electric field [1-6]

A Refrigerant is a gas/liquid that is employed in the Air Conditioning systems and Refrigerators. Without refrigerant, Air Conditioners, Refrigerators or any other freezing technology will not be possible. Liquid hydrogen (LH2) is the liquid state of the element hydrogen. Hydrogen is found naturally in the molecular H2 form. To exist as a liquid, H2 must be cooled below hydrogen's critical point of 33 K. However, for hydrogen to be in a fully liquid state without boiling at atmospheric pressure, it needs to be cooled to 20.28 K (252.87 C). At the present time [8-10], a number of hydrogen refrigerators and liquefiers are being used to maintain experimental apparatus at low temperatures. For example, several 21-27 K hydrogen refrigerators are used for continuous refrigeration of liquid hydrogen bubble chambers. Refrigeration at this temperature level is also being planned for experimental apparatus associated with nuclear reactors and electromagnets. Certain applications may require temperature below those obtainable with hydrogen [8-13].

In this work, we studied the effect of parameters (thermal performance) in elctrocaloric refrigerator based on hydrogen liquefier. The temperature distribution (solid -fluid) is determined by the standard heat transfer equation implemented in COMSOL multiphysics software.

II. DESCRIPTION OF AN ELECTROCALORIC REFRIGERATION DEVICE

Design and operation of the device of elctrocaloric is presented in Fig. 1. The main steps of the elctrocaloric cycle are:

1. The elctrocaloric material is polarized adiabatically by application of an electrical field.
2. By circulation of carrier fluid in the regenerator bed for exchanging the heat.
3. Adiabatic depolarization of the elctrocaloric material under zero electrical fields.
4. Cold recovery by moving of carrier fluid in the regenerator bed for exchanging the heat.

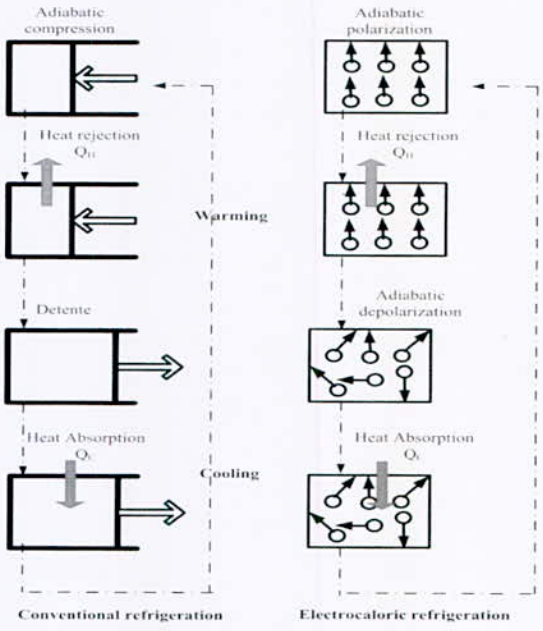

Fig. 1. Schematic diagram of an electrocaloric refrigerator device

III. MODELLING GEOMETRY

By neglecting boundary effects in the transversal direction (the z-direction in Fig. 2), the Active electrocaloric regenerator can be confined to two dimensions in COMSOL multiphysics. Fig. 2, shows a

*Corresponding author email: chiba.younes@univ-medea.dz

schematic of the full 3-D geometry considered in the development of the mathematical model.

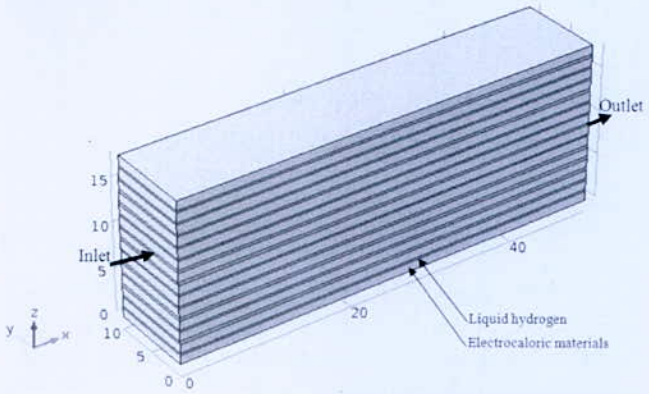

Fig. 2. Close up of the regenerator geometry

TABLE I
GEOMETRIC PARAMETER OF THE REGENERATOR

Geometry	L	L	e_s	e_f
(mm)	50	10	1	0.3

Polarization	t_{Pol}	t_{Depol}	Δt
(s)	0.1	0.1	0.1

Velocity	U
(m/s)	0.05

IV. GOVERNING EQUATIONS OF ELECTROCALORIC MODEL

The governing equations of the active an elctrocaloric refrigerator mathematical model consists of a set of coupled partial differential equations, which were solved with the commercial software COMSOL Multiphysics the mathematical model [9, 12-13].

The velocity distribution in the fluid is determined by solving the momentum (Eq. 1) and continuity equations (Eq. 2) as implemented in COMSOL for an incompressible fluid with constant (temperature independent) properties [11-13]

$$\rho_f\left(\frac{dU}{dt} + (U.\nabla)U\right) - \mu_f \nabla^2 U + \nabla p = 0 \qquad (1)$$

$$\nabla . U = 0 \qquad (2)$$

For the solid domains (Electrocaloric materials) the temperature distributions determined by the standard heat transfer equation.

$$\rho_{p,s}\frac{\partial T_s}{\partial t} - k_s \nabla^2 T_s = 0 \qquad (3)$$

The temperature distribution in the fluid is determined by the heat transfer equation implemented in COMSOL for an incompressible fluid with convective terms.

$$\rho_f c_{p,f}\left(\frac{\partial T_f}{\partial t} + (U.\nabla)T_f\right) - k_f \nabla^2 T_f = 0 \qquad (4)$$

The solids and the fluid are assumed in perfect thermal contact with the following boundary condition.

$$\left(k_f \frac{\partial T_f}{\partial y}\right)_{y=E_{f_1}} = \left(k_s \frac{\partial T_s}{\partial y}\right)_{y=E_{f_1}} \qquad (5)$$

Once steady cyclic state is obtained, the resulting cooling capacity and coefficient of performance can be calculated as follows [14]:

$$\dot{Q}_C = \dot{m}_{nf} c_{nf} \left(T_C - T_L\right). \qquad (6)$$

And coefficient of performance:

$$COP = \frac{\dot{Q}_C}{\dot{Q}_H - \dot{Q}_C + \dot{W}_P} \qquad (7)$$

V. RESULTS AND DISCUSSIONS

Fig.3 and Fig.4, show the temperature distribution in the active an electrocaloric refrigerator (the hot blow/ the cold blow) respectively, and the temperature profiles in the x-direction at various times during the steady state electrocaloric refrigerator cycle with the present operating parameters. The temperature profiles are determined at the middle of the regenerator plate and at the middle of the fluid channel (Liquid hydrogen) of the active an electrocaloric refrigerator geometry shown in Fig.3.

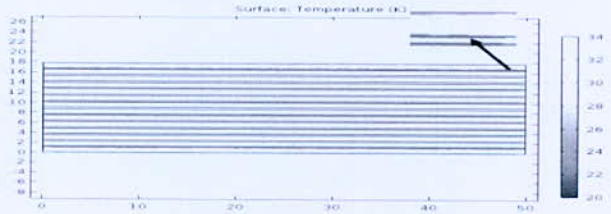

Fig. 3. Temperature distribution during the hot blow

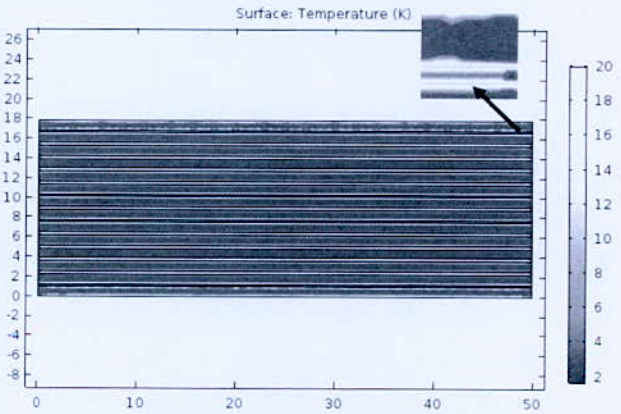

Fig. 4. Temperature distribution during the cold blow

*Corresponding author email: chiba.younes@univ-medea.dz

After polarization and depolarization, the temperature span (Fig. 5) was 32K (from 2K to 34K). Since electrocaloric refrigerator based on Hydrogen liquefier generated a growing interest of industrial, policy makers and researchers. Experimental researches as well as theoretical research are oriented today in several domains such as, research on new materials presenting a high level of electrocaloric effect,

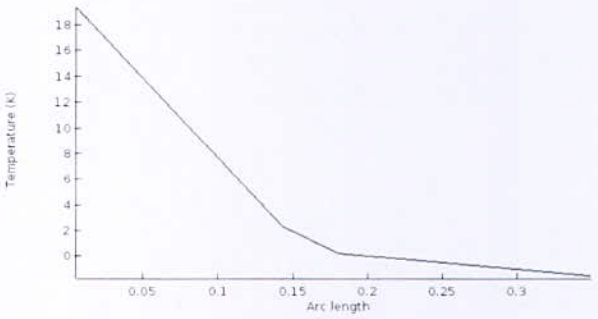

Fig. 5. Variation of average temperature cold reservoir

Fig. 6 and Fig. 7. show respectively evolution of coefficient of performance as function of temperature span and cold temperature.

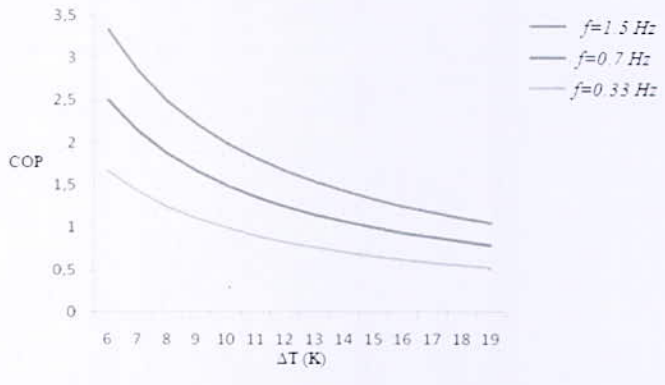

Fig. 6. Evolution of coefficient of performance as function of temperature span

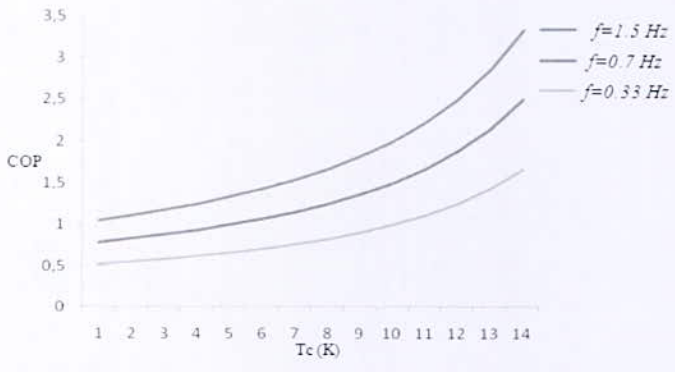

Fig. 7. Evolution of coefficient of performance as function of cold temperature

VI. CONCLUSION

This work described the development of a 2-D mathematical model of an active electrocaloric refrigerator with a regenerator made of parallel plates, which were arranged in a stack configuration. The electrocaloric refrigerator model was developed using the commercial COMSOL Multiphysics software.

Multilayer structure is the most rational solution for electrocaloric based on cooling structure. It provides specific heat raising and operational point temperature controlling.

Multilayer structures fabrication, investigation, thermal and physical characterisation should be considered as a perspective trend in electrocaloric-based cooling structure research.

Finally, the cost of producing liquid from gaseous hydrogen is an economic barrier to the early adoption of liquid hydrogen as an energy carrier. Decreasing the liquefaction costs is partially dependent on increasing the efficiency of the liquefaction process above the current 30 to 35 percent.

NOMENCLATURE

Symbols	Meaning	Unit
COP	coefficient of performance	
C_p	specific heat	J kg $^{-1}$°C^{-1}
E	electric field	V m^{-1}
P	polarization	C m^{-2}
T	temperature	°C
k	thermal conductivity	Wm^{-2}K^{-1}
L	length	Mm
l	width	Mm
e	thickness	Mm
p	pressure	Pa
$\dot{m}_f$	mass-flow rate	kg s^{-1}
$\dot{Q}$	heat rate	W
μ_f	viscosity	kgm^{-1}s^{-1}
ρ	density	kgm^{-3}

REFERENCES

[1] Y. Chiba, A. Smaili, C. Mahmed, M. Balli, O. Sari "Thermal investigations of an experimental active magnetic regenerative refrigerator operating near room temperature", *International journal of refrigeration* Vol 37. pp 36-42.january 2014.

[2] C. Aprea, A. Greco, "A comparison between electrocaloric and magnetocaloric materials for solid state refrigeration", *International journal of heat and technology* Vol 35. No 1. pp 225 – 234. March 2017.

[3] R.Pirc, B. Roi , Z Kutnjak. , R.Blinc , X.Li, Q. Zhang "Electrocaloric effect and dipolar entropy change in ferroelectric polymers" , *Ferroelectrics* Vol 426. pp 38-44. 2012.

[4] M. Ozbolt, A. Kitanovski, J. Tusek, A. Poredo "Electrocaloric refrigeration: Thermodynamics, state

*Corresponding author email: chiba.younes@univ-medea.dz

of the art and future perspectives". *International Journal of Refrigeration* .V40. pp174-188. 2014

[5] T. Correia, Q. Zhang "electrocaloric materials new generation of coolers" , pp 1-14 Springer 2014 .

[6] J.F. Scot "Electrocaloric Materials", Cavendish Laboratory, Cambridge University, 2011.

[7] C. Aprea, A. Greco, A. Maiorino, C. Massellil "Electrocaloric refrigeration: an innovative, emerging, ecofriendly refrigeration technique" , UIT Heat Transfer Conference Vol 796, N1 2016 .

[8] K. Kamiya , H. Takahashi, T. Numazawa, "Hydrogen Liquefaction by Magnetic Refrigeration ", International Cryocooler Conference, Inc., Boulder.CO.2007

[9] D. B. Chelton J. W. Dean T. R. Strobridge "Helium Refrigeration and Liquefaction Using a Liquid Hydrogen Refrigerator for. Precooling", Office of technical services, USA

[10] K. Kirstein, J. Henri, "Numerical modeling and analysis of the active magnetic regenerator", Technical University of Denmark 2010

[11] T. Frank, P. Nini, S. Anders, "Numerical modeling and analysis of a room temperature magnetic refrigeration system" Technical University of Denmark 2008.

[12] S. Lionte, C.Vasile, M. Siroux "Approche multiphysique et multi-échelle d'un régénérateur magnétothermique actif", Institut National des Sciences Appliques INSA 2015.

[13] Y. Chiba, A. Smaili, O. Sari "Enhancements of thermal performances of an active magnetic refrigeration device based on nanofluids", *Mechanika.* Vol 23, pp 31-38. 2017

*Corresponding author email: chiba.younes@univ-medea.dz

Complete Modelling of an Off Grid Hybrid Renewable Hydrogen Production System

H. Tebibel* and A. Khellaf

Centre de Développement des Energies Renouvelables, CDER, 16340 Algiers, Algeria.

Abstract—**This paper presents a modelling study of an off grid hybrid renewable hydrogen production system (HRHPS) which consists of photovoltaic (PV) array, wind turbine, lead acid battery banc, power converters, water electrolyser and hydrogen tank. Mathematical models of each system components briefly presented are used to build a simulation codes under Matlab software. Behaviour of the system components is simulated using theses codes based on real components specifications.**

Key words— Renewable hydrogen production, PV energy, Wind energy, Water electrolysis, Modelling.

I. INTRODUCTION

Due to the expensive cost of building and testing real prototypes, it is obvious that their design requires appropriate computing tools to simulate functioning before actual set-up [1]. Numerous computer program devised to simulate the performance of energy systems such as TRNSYS and HOMER have been built and are suitable for the investigation of renewable energy system (RES) with hydrogen production[2,3]. This paper presents a complete model based renewable hydrogen production system that we developed as a foundation for our next research activities. Next section gives a full description of the system under study.

II. SYSTEM DESCRIPTION

The configuration of the off grid hybrid renewable hydrogen production system (HRHPS) under study in this paper is depicted in Fig. 1. This system consists of a photovoltaic (PV) array, wind turbine (WT), a lead-acid battery bank used as an energy storage system (ESS), water electrolyser (WE) to produce hydrogen and a gas tank for hydrogen storage. PV array and wind turbine are connected to the DC bus via Maximum Power Point Tracking (MPPT) DC/DC converter and AC/DC rectifier, respectively, while the water electrolyser is linked to this bus through DC/AC inverter. Power converters used in this configuration are unidirectional.

PV array, which consists of several modules connected in series and parallel, converts solar energy directly intoelectricity. WT transforms the kinetic energy of wind into electrical energy. ESS stores the excess of power generated by the renewable energy source (RES) and supports the electrolyser when necessary. WE splits water molecular into hydrogen and oxygen by using power provided by RES. Hydrogen produced is supplied to the demand or stored in the gas tank during the periods of over production. Tank supplies the hydrogen deficit when necessary.

tebibelhammou@gmail.com or h.tebibel@cder.dz

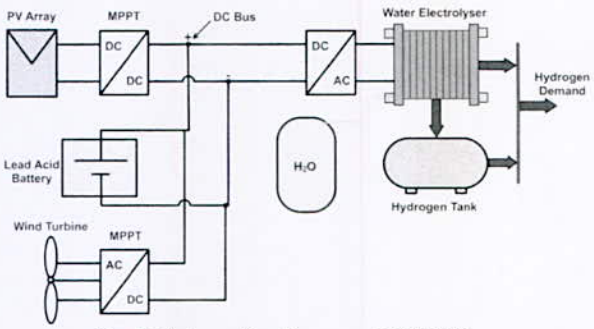

Fig. 1. Schematic diagram of HRHPS

III. SYSTEM MODELING

1. PV array

The current versus voltage (I-V) characteristic of PV cell based on the single diode four parameters model is expressed by the following equation [4]

$$I_{pv} = I_L - I_0 \left[\exp\left(\frac{q\left(V_{pv} + I_{pv} \cdot R_s\right)}{\gamma \cdot k \cdot T_c} \right) - 1 \right] \quad (1)$$

Photocurrent I_L, which depends on the solar irradiance G and cell temperature T_c, is as follow

$$I_L = \left(\frac{G}{G_{ref}} \right) \left(I_{L,ref} + \mu_{Isc} \left(T_c - T_{c,ref} \right) \right) \quad (2)$$

Where μ_{Isc} is the temperature coefficient of the short circuit current. Diode saturation current I_0 is described by

$$I_0 = I_{0,ref} \left(\frac{T_c}{T_{c,ref}} \right)^3 \exp\left(\frac{q \cdot \varepsilon_G}{\gamma \cdot k} \left(\frac{1}{T_{c,ref}} - \frac{1}{T_c} \right) \right) \quad (3)$$

Cell temperature, which depends on the ambient temperature T_a and solar irradiance G, can be estimated by the following equation

$$T_c = T_a + G\left(\frac{NOCT - 20}{800} \right) \quad (4)$$

PV cell power output can be estimated by this equation

$$P_{pv} = I_{pv} \cdot V_{pv} \quad (5)$$

The aforementioned equations are used to simulate the static behaviour of the Shell SP75 PV module in order to test the accuracy of the modelling procedure. Parameters of this module can be found in Ref [5].

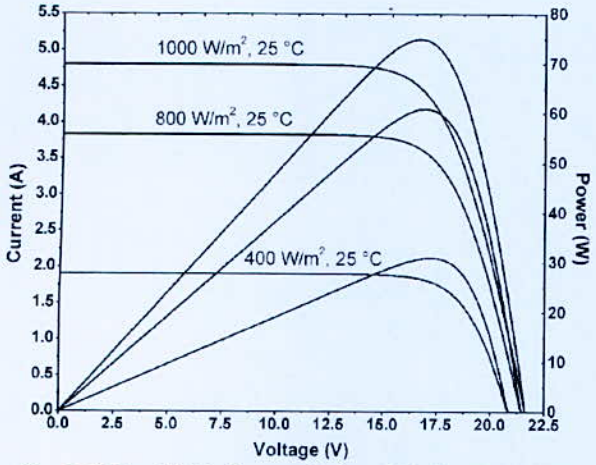

Fig. 2. I-V and P-V characteristics of Shell SP75 PV module under 25 °C and different solar irradiance levels

Fig. 2, shows the I-V and P-V characteristics under different conditions of solar irradiance.

2. Wind turbine

Mathematical model used to calculate the power generated by the wind turbine can be given as follow [6]

$$P_{wt}(v)=\begin{cases}0, & v\le v_{cin}\ \text{or}\ v\le v_{coff}\\ P_{rat}\left(v-v_{cin}\right)/\left(v_{rat}-v_{cin}\right) & v_{cin}\le v\le v_{rat}\\ P_{rat} & v_{rat}\le v\le v_{coff}\end{cases} \quad (6)$$

Wind speed at specific level can be estimated, based on data of wind speed at reference level, by using the following expression [7]

$$v(z)=v(z_a)\left(z/z_a\right)^{\alpha} \quad (7)$$

This model is used to simulate the static behaviour of raumenergy 3.5 kW WT [8]. Fig.3, illustrates the wind speed versus power generated by this WT.

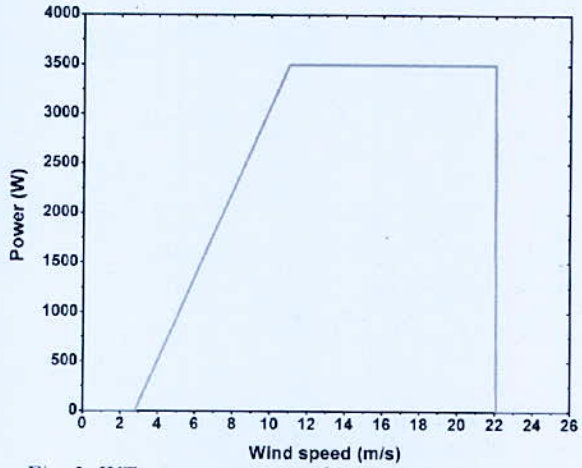

Fig. 3. WT power curve as a function of wind speed

3. Lead-acid battery

The relationship between voltage V_b, current I_b, and state of charge SoC_b of the battery undercharging and discharging mode can be described by the following formulas [9]

in charge ($I_b>0$)

$$V_b=\left(2+0.16\,SoC_b\right)+\frac{I_b}{C_{10}}\left(1-0.025\Delta T\right)\times\left(\frac{6}{1+I_b^{0.6}}+\frac{0.48}{\left(1-SoC_b\right)^{1.2}}+0.036\right) \quad (8)$$

in discharge ($I_b<0$)

$$V_b=\left(2.085-0.12\left(1-SoC_b\right)\right)-\frac{|I_b|}{C_{10}}\left(\frac{4}{1+|I_b|^{1.3}}+\frac{0.27}{SoC_b^{1.5}}+0.02\right)\left(1-0.007\Delta T\right) \quad (9)$$

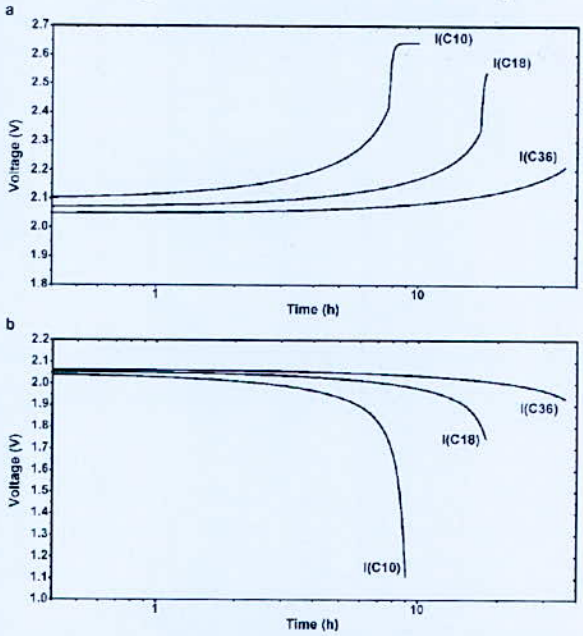

Fig. 4. Charging (a) and discharging (a) curves of Tudor STTH-180 lead acid tubular battery at various current and 25 °C

SoC_b can be defined as a function of the round-trip efficiency η_b and loss rate δ of the battery by the following equation [10]

$$SoC_b^{t+1}=SoC_b^{t}(1-\delta)+100\cdot\eta_b\frac{\int I_b\partial t}{Q} \quad (10)$$

Tudor STTH-180 lead acid tubular battery is chosen to test the simulation model [11]. Fig.4, depicts the charging and discharging curves of this battery at various current and 25 °C.

4. Water electrolyser

The voltage versus current of an electrolyser cell is given by following equation [12]

$$V_{cell}=V_{rev,T,P}+\frac{r_1+r_2\cdot T}{A_{el}}I_{el}+\left(s_1+s_2\cdot T+s_3\cdot T^2\right)\times\ln\left[\left(\frac{t_1+t_2/T+t_3/T^2}{A_{el}}\right)I_{el}+1\right] \quad (11)$$

tebibelhammou@gmail.com or h.tebibel@cder.dz

Reversible voltage can be determined in the temperature range 25-200 °C (298-473 K) by the equation

$$V_{\text{rev},T,P} = V_{\text{rev},T,1} + \frac{\mathrm{R}\cdot T}{2\mathrm{F}} \ln\left(\frac{\left(P - P_{\mathrm{H_2O}}\right)^{1.5}}{P_{\mathrm{H_2O}}/P^{0}_{\mathrm{H_2O}}}\right) \quad (12)$$

According to the Faraday's law, the hydrogen production rate of an electrolyser with n_{cell} cell stack can be estimated by the given formula [13]

$$m_{\mathrm{h_2}} = \eta_{\mathrm{F}} \frac{n_{\text{cell}} \cdot I_{\text{el}}}{2\mathrm{F}} \quad (13)$$

Alkaline electrolyser installed at the PHOEBUS plan is the object of simulation study [14]. Fig. 5, shows the variation of one cell of this electrolyser as a function of current density at various operating temperature.Power consumed and the amount of hydrogen produced by this electrolyser cell as a function of the current density is depicted in Fig. 6 under 80 °C and 1 atm.

5. Power converter

Power converter is characterized by the variation of the parameters in a second-order polynomial as follow [15]

$$P_{\text{out,n}} = b_0 + b_1 \cdot P_{\text{in,n}} + b_2 \cdot P^2_{\text{in,n}} \quad (14)$$

Normalised input $P_{\text{in,n}}$ and output $P_{\text{out,n}}$ power of the converter can be calculated by the following formulas

$$P_{\text{out,n}} = \frac{P_{\text{out}}}{P_{\text{con}}} \quad (15)$$

$$P_{\text{in,n}} = \frac{P_{\text{in}}}{P_{\text{con}}} \quad (16)$$

Thus, the power converter efficiency is considered as the ratio of the output power to the input power of the converter and can be expressed by

$$\eta_{\text{con}} = \frac{P_{\text{out}}}{P_{\text{in}}} \quad (17)$$

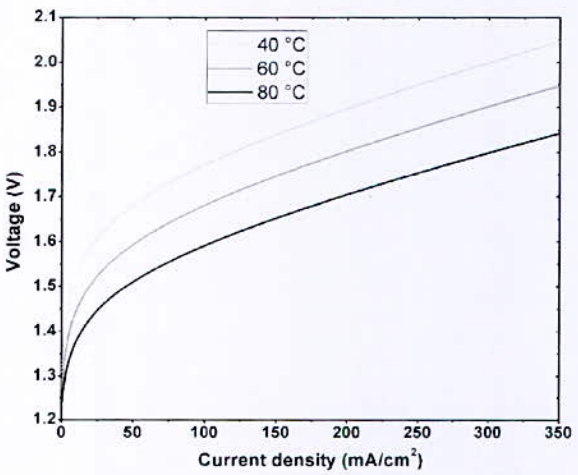

Fig. 5. Current density versus one cell voltage curves under different temperature levels

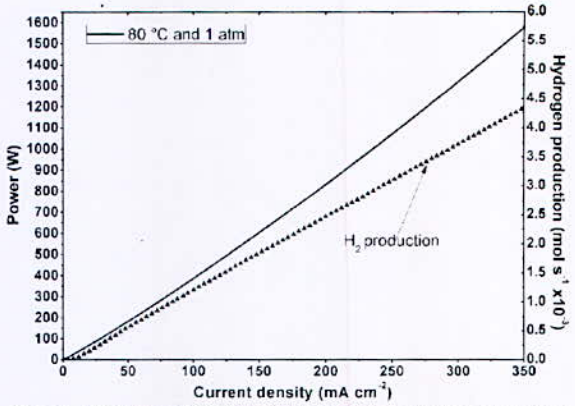

Fig. 6. Power consumed and hydrogen produced versus current density of one electrolyser cell at 80 °C and 1 atm

The variation of the converter efficiency as a function of the normalized input power is presented in Fig. 7 for high level power conversion performance. The values of the variables b_0, b_1 and b_2 are respectively -0.0035, 0.995 and -0.01.

6. Hydrogen tank

The level of hydrogen tank can be determined using mass balance using the given equation [16]

$$m^{t+1}_{\text{ht}} = m^{t}_{\text{ht}} + (m_{\mathrm{h_2}} - m_{\mathrm{h_2,d}}) \quad (18)$$

SoC value of hydrogen tank can be estimated by the following equation

$$SoC^{t+1}_{\text{ht}} = SoC^{t}_{\text{ht}} + 100 \cdot (m_{\mathrm{h_2}} - m_{\mathrm{h_2,d}}) / M_{\text{ht}} \quad (19)$$

IV. CONCLUSION

Complete modelling of an off grid hybrid renewable hydrogen production system has been illustrated in this paper. Mathematical models of PV cell, wind turbine, lead acid battery, alkaline water electrolyser and hydrogen tank have been presented. Behaviour of Shell SP75 PV module, raumenergy 3.5 kW WT, Tudor STTH-180 lead acid battery and electrolyser installed at the PHOEBUS plan have been simulated.

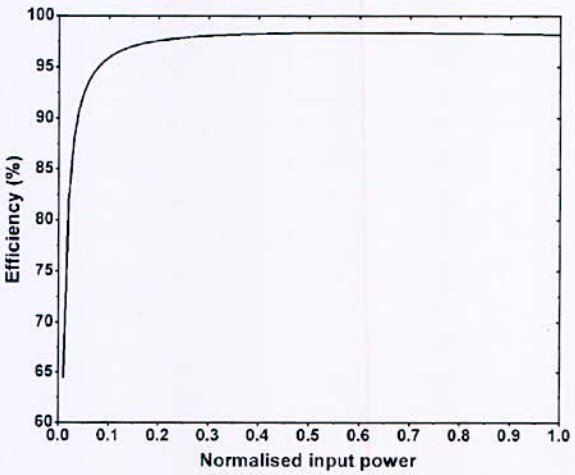

Fig. 7. Power converter efficiency as a function of normalised input power

ACKNOWLEDGMENT

General Direction of Scientific Research and Technological Development is gratefully acknowledged for supporting this work.

NOMENCLATURE

Variables	
A_{el}	electrode area of the electrolyser cell, cm^2
F	Faraday constant, s A/mol
I_{el}	electrolyser cell current, A
I_L	Photocurrent, A
I_{pv}	photovoltaic current, A
I_0	diode saturation current, A
k	Boltzmann's constant, m^2 kg/s^2 K
$m_{h_2,d}$	hydrogen demand, kg
m_{h_2}	hydrogen amount produced by electrolyser, kg
m_{ht}	hydrogen amount in the tank, kg
M_{ht}	hydrogen tank capacity, kg
$NOCT$	nominal operating cell temperature, °C
P_{pv}	photovoltaic power, W
q	electron charge, C
r	Empirical coefficient
R_s	series resistance, Ω
s	Empirical coefficient
SoC_{ht}	hydrogen tank state of charge, %
SoC_b	battery state of charge, %
T_a	ambient temperature, K
T_c	solar cell temperature, K
V_{pv}	photovoltaic voltage, V

Greek letters	
η_b	Round-trip efficiency of the battery, %
n_{cell}	Number of electrolyser cell
η_F	Faraday efficiency, %
γ	diode ideality factors
δ	battery rate of loss, %

REFERENCES

[1] S. Pedrazzi, G. Zini and P. Tartarini, "Complete modeling and software implementation of a virtual solar hydrogen hybrid system,"Energ. Convers. Manage., vol.51,pp. 122–129, 2010.

[2] R.L. Shrivastava, Vinod Kumar and S.P. Untawale, "Modeling and simulation of solar water heater: A TRNSYS perspective," Renew. Sust. Energ. Rev., vol. 67, pp. 126–143, 2017.

[3] K. Vikas, N. Savita and B. Prashant, "Optimization of hydrogen based hybrid renewable energy system using HOMER, BB-BC and GAMBIT," I. J. Hydrogen. Energ., vol. 41, pp.16743-16751, 2016.

[4] R. Chenni, M. Makhlouf, T. Kerbache and A. Bouzid, "A detailed modeling method for photovoltaic cells," Energy vol. 32, pp.1724-1730, 2007.

[5]https://www.altestore.com/static/datafiles/Others/Shell _SP75_Data_Sheet.pdf. Available 18 October 2017.

[6] S. Diaf, M. Belhamel, M. Haddadi and A. Louche, "Technical and economic assessment of hybrid photovoltaic/wind system with battery storage in Corsica island," Energ. Policy., vol. 36, pp. 743–754, 2008.

[7] S. Bhattacharjee and S. Acharya, "PV–wind hybrid power option for a low wind topography," Energ. Convers. Manage., vol. 89, pp.942-954, 2015.

[8]https://articles.extension.org/sites/default/files/3.5kW _Spec_Sheet.pdf. Available 19 October 2017.

[9] N. Achaibou, M. Haddadi and A. Malek, "Lead acid batteries simulation including experimental validation," J. Power. Sources., vol. 185, pp.1484-1491, 2008.

[10] M. Castañeda, A. Cano, F. Jurado, H. Sánchez and L. M. Fernández ,"Sizing optimization, dynamic modeling and energy management strategies of a stand-alone PV/hydrogen/battery-based hybrid system," I. J. Hydrogen. Energ., vol. 38, pp.3830-3845, 2013.

[11] J. B. Copetti and F. Chenlo, "Lead/acid batteries for photovoltaic applications. Test results and modelling. J. Power. Sources., vol. 47, pp.109-118, 1994.

[12] Ø. Ulleberge, "Stand-alone power systems for the future: Optimal design, operation and control of solar-hydrogen energy systems," Ph.D thesis, Norwegian University of Science and Technology Trondheim, 1998.

[13] Ø. Ulleberge, "Modeling of advanced alkaline electrolyzers: a system simulation approach," I. J. Hydrogen. Energ., vol. 23, pp.21 -33, 2003.

[14] C. Meurer, H. Barthels, W. A. Brocke, B. Emonts and H. G. Groehn, "PHOEBUS—An autonomous supply system with renewable energy: six years of operational experience and advanced concepts," Sol. energy., vol. 67, pp.131 -138, 1999.

[15] K. Peippo, andP. D. Lund, "Optimal sizing of grid-connected PV-systems for different climate and array orientations: a simulation study," Sol. Energ. Mat. Sol.C, vol. 53, pp. 1313–1332, 2016.

[16] L. Valverde-Isorna, D. Ali, D. Hogg, and M. Abdel-Wahab, "Modelling the performance of wind– hydrogen energy systems: Case study the Hydrogen Offi ce in Scotland/UK," Renew. Sust. Energ. Rev., vol. 53, pp. 1313–1332, 2016.

tebibelhammou@gmail.com or h.tebibel@cder.dz

Hydrogen Production via Reforming of Methane over NiAl-CO_3 Synthesised by Microwave

F. Touahra[1, 2*], D. Halliche[1], F. Bali[1], M. Sehailia[2], N. Aider[1], B. Djebarri[1], Z. Abdelsadek[1] and K. Bachari[2]

[1*] Laboratoire de Chimie du Gaz Naturel, Faculté de Chimie, USTHB, BP32, El Alia, Alger, Algérie.
[2]Centre de Recherches Scientifiques (CRAPC), BP 248, Alger, 16004, Algérie.

Abstract—**Improving the carbon resistance of Ni-based catalysts for the dry reforming of methane (DRM) through the metal-hydrotalcite interaction is an attractive strategy. The NiAl-CO_3 hydrotalcite-like compounds, prepared by microwave, over different microwave power between 100W and 900W (2.45 GHz frequency) this is performed in the hope of obtaining the smaller particle size and better dispersion of Ni. The products obtained, after heat treatment under air at 800 °C, were characterized by several techniques such as: Chemical analysis (AAS), X-ray diffraction (XRD), Brunauer-Emmette Teller method (BET) and temperature programmed reduction (TPR). After reduction, the catalysts were evaluated in the reforming of methane reaction under continuous flow with CH_4/CO_2 ratio equal to 1, at atmospheric pressure and a temperature 700°C. The catalytic activity was tested in a fixed bed reactor. At this temperature, the amount of CH_4 consumed was in its lowest in the presence of catalyst treated at 100 watts ($NiAl_{100W\text{-}cal}$-R) whereas the amount of CH_4 and CO_2 conversion increased to 45% in case of catalyst treated at 600 watts ($NiAl_{100W\text{-}cal}$-R).**

Key words—CO_2 reforming of methane, hydrotalcite, microwave, Ni oxide, hydrogen

I. INTRODUCTION

Hydrogen is conventionally produced via the process of steam reforming reaction. In recent years, increased concerns related to the contribution of greenhouse gases to global warming have augmented interest in replacing steam with carbon dioxide instead. CO_2 reforming of methane, also known dry reforming of methane (DRM) is a method of producing hydrogen from the reaction of carbon dioxide and methane ($CH_4 + CO_2 \leftrightarrow 2H_2 + 2CO$). The major problem associated with this reaction comes in the form of sintering of the active phase and carbon formation [1]. The carbon generated during this reaction can be the result of direct decomposition of methane ($CH_4 \leftrightarrow C + 2H_2$) or the Boudouard reaction ($2CO \leftrightarrow CO_2 + C$) [1, 2]. Many efforts by various researchers focused on the development of catalysts bearing both high activity and high resistance to coke. The activity of a catalyst is primarily related to the metal surface area, i.e., the number and size of active sites [2, 3]. This implies that, generally, the catalytic activity benefits from a high dispersion of the metal particles. The aim of the present work is to investigate the utilization of NiAl-CO_3 hydrotalcite-like compounds, prepared by microwave-assisted hydrothermal treatment; this is performed in the hope of obtaining a smaller particule size of Ni.

II. EXPERIMENTAL

1. *Catalyst synthesis*

Samples NiAl-CO_3 hydrotalcite-like compounds were synthesized prepared by microwave method at different power (between 100Watts and 900Watts for 30 minutes). Two aqueous solutions were pepared: solution 1 containing $Ni(NO_3)_2.6H_2O$ and $Al(NO_3)_3.9H_2O$, was added to solution 2 containing NaOH and Na_2CO_3. After traited in microwave, the precipitates were filtered and washed using distilled water to remove all residual salts. The resulting slurry was then dried overnight at 100 °C in dry oven. The four samples obtained after calcination at 800°C for 6 h were assigned the following references: $NiAl_{100W\text{-}cal}$, $NiAl_{300W\text{-}cal}$, $NiAl_{600W\text{-}cal}$ and $NiAl_{900W\text{-}cal}$.

2. *Characterization*

The chemical composition of each material was determined using atomic absorption spectroscopy (AAS) Varian spectra AA-110. X-ray diffraction (XRD) was performed with Siemens D500 diffractometer using monochromatized CuKa radiation (γ = 1.5418 Å) with 0.05° (2θ) steps and 5 s counting time in the range (20-80°). The paticule size for Ni was calculated from XRD using the Debye-Scherrer equation [4]:

$$D_{hkl} = \frac{0.9\,\lambda}{\beta_{hkl}\cos\theta}$$

Where D_{hkl} is the crystallites size, λ is the wavelength of Cu- K, β_{hkl} is the peak with half maximum and θ is the Bragg diffraction angle. The specific surface area was determined following BET measurements under nitrogen adsorption–desorption isotherms in a Micrometrics Tristar 3000. The calcined samples were analyzed by temperature programmed reduction (TPR) TriStar 3000 V6.01, equipped with a TCD detector. 50 mg of the catalyst was loaded into the reactor and flushed with helium for 1 h at 200°C. The temperature was lowered to room temperature and helium was replaced by 5 % hydrogen gas in argon. After 1 h of flushing, the temperature was raised to 900°C with increments of 10°C per minute. The morphology of uncalcined samples was investigated using scanning electron microscopy (SEM) Jeol 320. Transmission Electron Microscopy (TEM) images of the catalysts before and after reaction were taken by JEOL-JEM-1200EX at 100 kV.

*Corresponding author email: ftouahra@gmail.com

1. Catalytic testing

The catalytic tests were performed under atmospheric pressure, in a tubular fixed-bed quartz reactor (ID = 6 mm and L = 16 cm), and placed in a furnace. The catalyst grains (100 mg) were kept in place using quartz wool plugs. A thermocouple was placed on top of the catalyst's bed to measure the actual temperature. For comparison, all catalysts were reduced with pure hydrogen at 750°C over a period of 1 h. Following reduction, the temperature was lowered under argon to the initial reaction's temperature and a feed gas mixture containing CH_4:CO_2:Ar in a ratio of 20:20:60 was passed through. The total flow rate was 20 mL/min. The reaction products were analyzed using gas chromatograph (Delsi), equipped with a thermal conductivity detector (TCD) and carbosieve-B column, in the presence of carrier gas argon.

III. RESULTS AND DISCUSSION

1. Chemical analyses

To determine the metal content of all catalysts, calcined at 800 °C, atomic absorption spectroscopy (AAS) was used. The obtained results are depicted in Table 1. The results of the elemental analysis by AAS show that the molar ratios Ni^{2+}/Al^{3+} are in good agreement with those calculated, taking into account the initial salt concentration. This confirms the quantitative precipitation of the precursor salt.

TABLE I
CHEMICAL COMPOSITIONS OF THE ALL CATALYSTS.

Samples	Molar ratio $R = \frac{nNi^{2+}}{nAl^{3+}}$	Proposed formula
$NiAl_{100W}$	2.03	$Ni_{0.67}Al_{0.33}$
$NiAl_{300W}$	2.03	$Ni_{0.67}Al_{0.33}$
$NiAl_{600W}$	2.03	$Ni_{0.67}Al_{0.33}$
$NiAl_{900W}$	2.03	$Ni_{0.67}Al_{0.33}$

2. X-ray diffraction analysis

X-ray diffraction patterns for calcined and uncalcined are illustrated in Fig. 1.

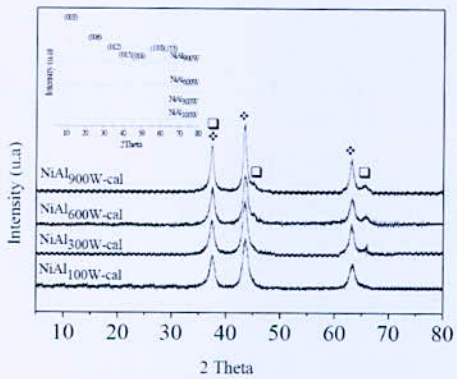

Fig. 1. XRD pattern of calcined products. Inset XRD of the sample not calcined, ❖NiO, ❑ $NiAl_2O_4$

Typical hydrotalcite-like type structure is present in all samples (Inset XRD in Fig. 1). The peaks observed correspond to the layered double hydroxides structure Takovite [JCPDS file 15-0087]. After calcination, the lamellar structure disappears and only NiO phase is observed [JCPDS file 47-1049] in the case of solid $NiAl_{100W\text{-}cal}$. The spectrum of samples $NiAl_{300W\text{-}cal}$, $NiAl_{600W\text{-}cal}$ and $NiAl_{900W\text{-}cal}$ depicts two series of broad peaks corresponding to reflections close to those of NiO and $NiAl_2O_4$ spinel phases [5], where $2\theta = 19.14°$, 31.17°, and 37.56° [JCPDS file 10-0339].

3. Temperature programmed reduction (TPR)

Fig. 2, depicts the TPR profile of our samples following calcination. In case of all samples, two reduction peaks were observed. The first peak observed is assigned to the reduction of NiO weakly interacting with the support. The second peak is assigned to the reduction Ni^{2+} to Ni^0 in $NiAl_2O_4$ or for the Ni^{2+} strong interaction of NiO with the alumina. The reduction temperature is shifted to higher values while there is an increase in microwave power. The results indicate that higher in microwave power have an effect on increasing the interaction between the oxides present in the catalysts; this is probably owing to the formation of periclase Al_2O_3 and/or $NiAl_2O_4$ phase [5, 6].

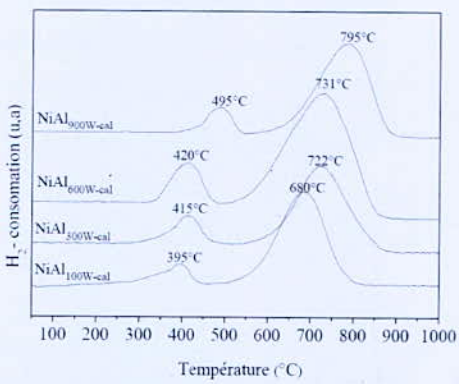

Fig. 2. TG analysis of $NiAl_{100W\text{-}cal}$, $NiAl_{300W\text{-}cal}$, $NiAl_{600W\text{-}cal}$ and $NiAl_{900W\text{-}cal}$

4. X-ray diffraction after reduction

After reduction at 750°C, the diffraction lines resulting from the formation of nickel metal phase located at 2h = 44.7°, 51.41° and 76.13° [JCPDS file 04-0850] were also observed with NiO, which decreased after reduction. The results indicate that a part of NiO was reduced to Ni metal.

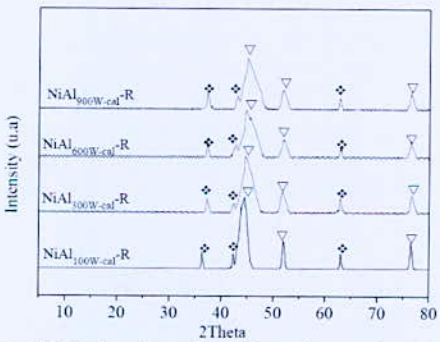

Fig. 3. XRD for the reduced catalysts, ❖NiO, ▽Ni^0

*Corresponding author email: flouahra@gmail.com

5. SEM & TEM analyses after reduction

Following reduction, the morphology of Ni^0 particles observed by SEM and MET is shown in Fig. 4 and Fig. 5 respectively. It is evident from the displayed images that, the metal particles were uniformly distributed over the surface of the material while the higher particle size was obtained in the case of $NiAl_{100W\text{-}cal}$-R compared to others catalysts.

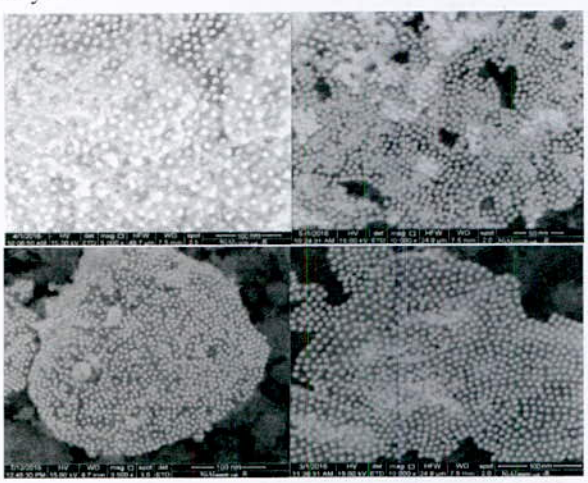

Fig. 4. SEM images of reduced catalysts at 750°C

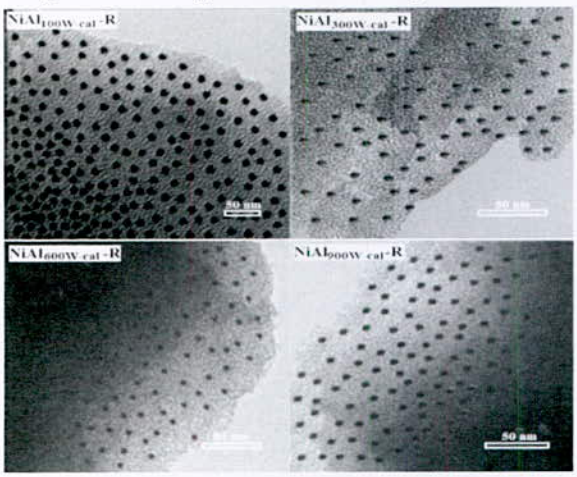

Fig. 5. TEM images for the reduced catalysts at 750°C

6. Catalytic activity tests

The catalytic activities of were tested under identical experimental conditions, in the presence of equi-molar amounts of methane and carbon dioxide under atmospheric pressure. The conversions of CH_4 and CO_2 and H_2/CO molar ratio vs. time are presented in Fig. 6. The catalytic performance of our synthesized materials reaches its maxima during the first 2 h of the reaction, after which the amounts of methane and carbon dioxide conversion remain remained constant after 10h reaction time, indicating that no perceptible deactivation took place over that period.

$NiAl_{600W\text{-}cal}$-R catalyst showed higher CO_2 and CH_4 conversions than $NiAl_{100W\text{-}cal}$-R, $NiAl_{300W\text{-}cal}$-R and $NiAl_{900W\text{-}cal}$-R. This phenomenon is primarily attributed the larger S_{BET} of the catalysts after reduction when compared to that of $NiAl_{100W\text{-}cal}$-R (50.3%), $NiAl_{300W\text{-}cal}$-R(22.9%) and $NiAl_{900W\text{-}cal}$-R (25.5%) and also can be explained by lower size of nickel particle of the $NiAl_{900W\text{-}cal}$-R catalyst compared with other catalysts (Table 2). In all cases expected $NiAl_{600W\text{-}cal}$-R, CO_2 conversion was higher than that of CH_4 in all tests and the obtained molar ratio of the resulting H_2/CO was always less than one, potentially owing to the reverse water-gas shift reaction ($CO_2 + H_2 \leftrightarrow H_2O + CO$). $NiAl_{600W\text{-}cal}$-R catalyst showed H_2/CO molar ratio closed to unity and the difference between CH_4 and CO_2 conversion was also minimal. This result could be explained by the favor a clean CO_2 reforming of methane rather than other.

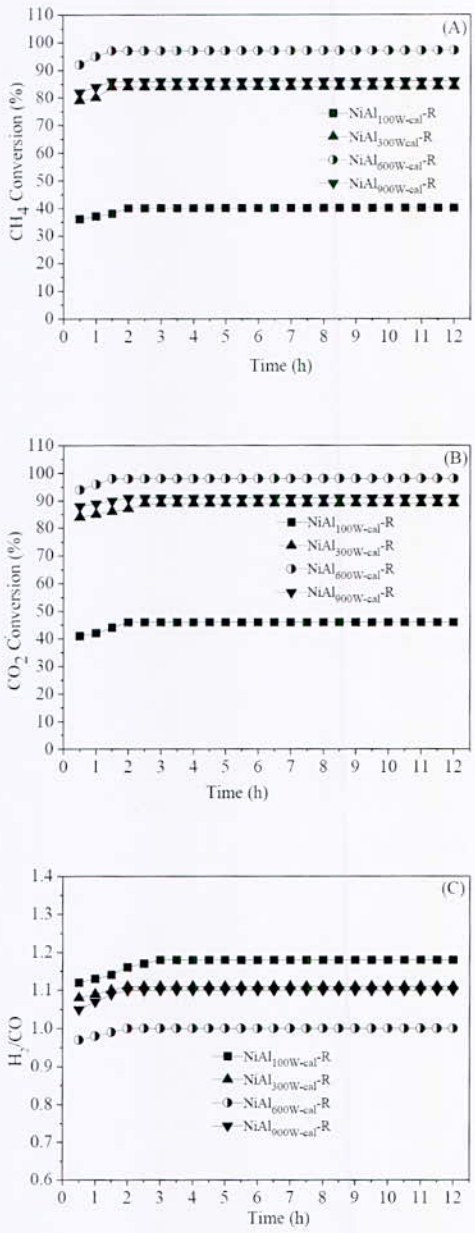

Fig. 6. (A) CH_4 conversion, (B) CO_2 conversion and (C) H_2/CO ratio obtained during CO_2 reforming of methane versus time, at 700 °C

*Corresponding author email: ftouahra@gmail.com

The EDX (Fig. 7) show amount of carbon deposited on the surface of $NiAl_{600W\text{-}cal}$-R catalyst was relatively low (0.54 wt.%) compared to $NiAl_{900W\text{-}cal}$-R.(6.01 wt.%), $NiAl_{300W\text{-}cal}$-R(6.22 wt.%) and $NiAl_{100W\text{-}cal}$-R (19.55 wt.%). To our expectation, the $NiAl_{600W\text{-}cal}$-R catalyst exhibited a very strong resistance to carbon deposition which was most probably attributed to lower size of nickel particle as shown in the literature [7, 8].

TABLE II
CH_4 AND CO_2 CONVERSION, SURFACE AREA AND NI PARTICLE SIZE

Catalysts	Conversion		Surface	particle size
	CH_4 (%)	CO_2 (%)	area (m^2/g)	[a]Ni^0 (nm)
$NiAl_{100W\text{-}cal}$–R	40,1	46,2	76	10
$NiAl_{300W\text{-}cal}$–R	84,1	89,2	118	7
$NiAl_{600W\text{-}cal}$–R	97,4	98,2	153	5
$NiAl_{900W\text{-}cal}$–R	86,5	91,4	114	7

[a]Calculated from MET

7. *SEM & TEM analyses after reaction*

TEM and SEM analysis of the all catalysts after reaction clearly demonstrate the formation of carbon filaments on the surface of the catalyst, however, no carbon filaments were observed in the case of $NiAl_{600W\text{-}cal}$-R after reaction.

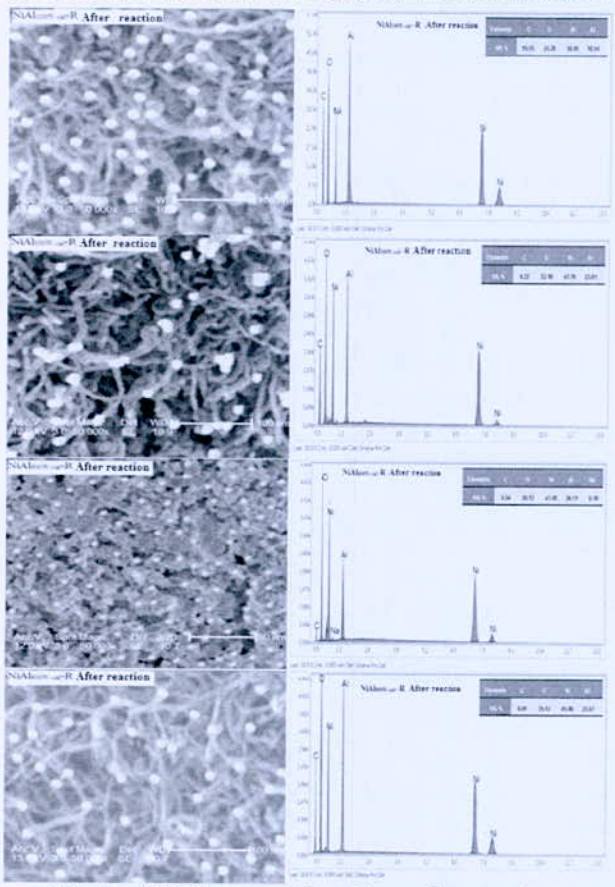

Fig. 7. SEM images of catalysts after reaction

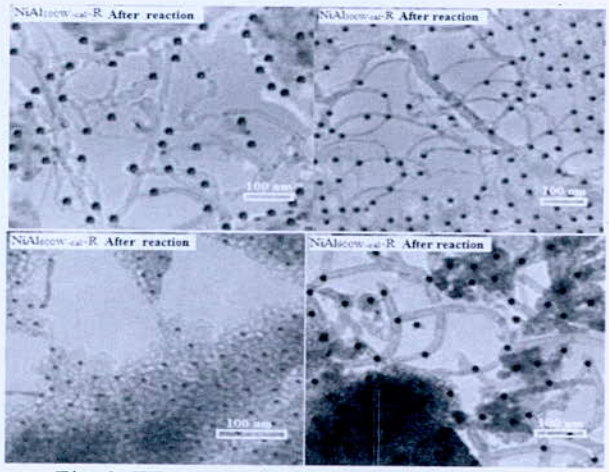

Fig. 8. TEM images for catalysts after reaction

IV. CONCLUSION

Hydrotalcite-like precursors have been successfully synthesized by the microwave method. The decomposition of the precursor at 800°C for 15 h led to the formation of the oxide powder as confirmed by XRD. The $NiAl_{600W\text{-}cal}$-R catalyst, exhibited rather high catalytic activity and stability during the reaction of DRM, compared to some simple catalysts such as $NiAl_{900W\text{-}cal}$-R, $NiAl_{300W\text{-}cal}$-R and $NiAl_{100W\text{-}cal}$-R. This catalyst also possesses essential advantages like resistance to metal sintering and carbon deposition. The CH_4 conversion during steady state was found to decrease in the following order: $NiAl_{600W\text{-}cal}$-R> $NiAl_{900W\text{-}cal}$-R ≈ $NiAl_{300W\text{-}cal}$-R> $NiAl_{100W\text{-}cal}$-R. The high performance of the catalytic process can be explained by: i) a very high specific surface area and iii) lower size of nickel.

REFERENCES

[1] M. Usman, W.W. Daud, H.F. Abbas, "Dry reforming of methane: Influence of process parameters-A review," Renew. Sustainable Energy Rev., vol. 45, pp. 710-744, 2005.

[2] J. Zhang, F. Li, "Coke-resistant Ni@ SiO_2 catalyst for dry reforming of methane," Appl. Catal. B: Environ., vol 176, pp. 513-521, 2015.

[3] O. Muraza, A. Galadima, "A review on coke management during dry reforming of methane," Int. J. Eneg. Res., vol 39, pp. 1196-1216, 2015.

[4] F. Melo, N. Morlanés, "Study of the composition of ternary mixed oxides: Use of these materials on a hydrogen production process," Catal. Today, vol. 133, pp. 374-382, 2008.

[5] F. Touahra, M. Sehailia, W. Ketir, K. Bachari, R. Chebout, M. Trari, O. Cherifi, D. Halliche, "Effect of the Ni/Al ratio of hydrotalcite-type catalysts on their performance in the methane dry reforming process," App. Pet. Res., vol 6, pp. 1-13, 2016.

[6] A.R. González, Y.J. Asencios, E.M. Assaf, J.M. Assaf, "Dry reforming of methane on Ni–Mg–Al nano-spheroid oxide catalysts prepared by the sol–gel method from hydrotalcite-like precursors," Appl. Surf. Sci., vol 280, pp. 876-887, 2013.

[7] F.R. Shamskar, M. Rezaei, F. Meshkani,"The influence of Ni loading on the activity and coke formation of ultrasound-assisted co-precipitated Ni–Al_2O_3 nano-catalyst in dry reforming of methane," int. J Hydrogen Energy, vol 42, pp. 4155-4164, 2017.

[8] J.W. Han, J.S. Park, M.S. Choi, H. Lee, "Uncoupling the size and support effects of Ni catalysts for dry reforming of methane, " Appl. Catal. B: Environ., vol 203, pp. 625-632, 2017.

*Corresponding author email: ftouahra@gmail.com

Characterization of the Combustion of the Mixture Biogas-Syngas Part I: Effect of the Mixture Composition and Radiation

R. Zouagri[1*], A. Mameri[2], F. Tabet[3]

[1*] Département de Physique/FSESNV, Université, Oum el Bouaghi.
[2] Département de Génie Mécanique/FSSA, Université, Oum el Bouaghi.
[3] DBFZ (Deutsche Biomasseforschungszentrumgemeinnützige GmbH), Torgauer Straße 116 D-04347 Leipzig, Germany.

Abstract—**Biogas is a renewable and sustainable energy source, its major problem is its low calorific value and this makes its flame very weak. The idea in this work is to associate the synthesis gas (syngas), containing hydrogen, with biogas to stabilize the flame by consuming two renewable and biodegradable gases. In this context, the effect of the combustion of biogas and synthesis gas on the structure of their flame and emissions has been addressed in many works; but until now, no work has been devoted to the mixture of these two gases. In this work, we are interested to demonstrate the effect of the variation of the composition of the fuel mixture (biogas-syngas), and losses by radiation on the structure of the flame in laminar regime. Many biogas-syngas compositions have been considered in order to know their effects on the structures of the flame and emissions. The results showed that the increase in the volume of methane in the biogas or hydrogen in the syngas increases the low heat value (LHV) of the fuel. It has been demonstrated that the addition of a volume of syngas, exceeding the half of that of biogas, allows the reduction of harmful emissions while maintaining a constant level of operating temperature. Besides to this, compositions studied could be classified according to their ability to radiate, which will allow selecting them in industrial processes requiring thermal radiation.**

Key words—mixture (biogas-syngas), flame opposed jets, polluting emissions-losses by radiation, Chemkin.

I. INTRODUCTION

The most polluting source is the emission of combustion, which is why it is essential to minimize it in all combustion systems. Among optimizing ways, the most promising of combustion systems is the use of biogas. It is later a renewable fuel derived from the degradation of organic matter by microorganisms under anaerobic conditions [1]. Biogas is expected to supply 25% of total renewable energy in Europe by 2020 [2, 3]. This gas consists mainly of methane CH_4 and carbon dioxide CO_2 and hydrogen sulfide H_2S [4]. To show the effects of composition and pressure on the soothing characteristics and on the flame structure in a biogas flame, Marc et al [5] have experimentally and numerically considered three compositions. The first one is the pure methane, the second is composed of 20% CO_2 and 80% CH_4 and the third biogas is composed of 40% CO_2 and 60% CH_4. The flow of methane was 0.55 mg/s and the pressure varies from 1 to 20 atm. The results show that the increase of the pressure reduces the thickness of the flame without changing its height and enhances the soot formation. The dilution of the fuel with CO2 avoids soot formation at any pressure. Mameri et al [6] studied the influence of many conditions of functioning such as the fuel composition and thermal and chemical effects of CO_2 on the flame structure of biogas diffusion and harmful emissions. The results show that the increase in the pressure increases the temperature and reduces the thickness of the flame, the losses by radiation and the amount of dissociation. High pressure deceases the mass fraction of the NO and the addition of CO_2 decreases the temperature of the flame by the chemical and thermal effect. Greco et al [7] conduct a numerical study to show the effects of the composition of biogas on the combustion in a one-dimensional laminar premixed flame. The results showed that the concentration of methane has a significant impact on the combustion process. The major problem with biogas is its low power calorific; in fact, biogas contains carbon dioxide which acts as diluents. In order to overcome these problems, it must be mixed with hydrogen. It's the idea of this work, where a source of renewable hydrogen from the syngas (synthesis gas) is used. The syngas is a combustible gas mixture produced by the pyro-gasification [8]. Its composition varies considerably depending on the type of feedstock used and the gasification process selected, but usually it is predominantly composed of H2 and CO [9]. This gas can be appreciated in many energy-efficient applications, which makes the pyro-gasification process attractive compared to combustion [8]. Park et al. [10] studied numerically the impact of pressure and the gradient of axial velocity on the structure of the counter-diffusion flame of syngas. The study shows that the strength of the flame is globally weakened by the increase in the gradient of the axial velocity but increases by the increase of the pressure. Safer et al [11] studied numerically the effects of turbulence and pressure on counter flow diffusion syngas flame structure and NO emissions. Their analysis is performed on a wide range of H_2/CO ratio (0.4 and 2.0) and the operating pressure (1 to 10atm). The results showed that the maximum temperature of the flame decreases with the addition of H_2 and increases with pressure. The NO levels decline in the hydrogen-rich syngas flames and increase with pressure. Several researches have focused on the biogas and the syngas combustion, including the effect of their composition [12, 13, 14], the pressure [15, 16], the chemical effect of CO_2 [12, 17], and the effect of doping by hydrogen [9, 10, 18, 19]. To this day, no work has been devoted to the study of the mixture of these two low calorific gases.

*Corresponding author: zouagri.ri@gmail.com

II. GEOMETRY AND INJECTION CONDITIONS

1. The geometry

An axisymmetric configuration of two opposing jets was considered. The jets are separated by a distance D = 2 cm. Fuel is injected from the left side, while oxidizer formed by air is injected from the right side. This configuration allows the formation of a diffusion flat stationary flame between the two injectors (Fig. 1). The structure of the flame is supposed to be uniform in the longitudinal direction of the flame (direction r in the Fig.1). This assumption gives a one-dimensional flame with properties depending only on the cross direction (x on the figure). The characterization of the structure of such flame is obtained by making a section perpendicular to the flame (on the figure x direction).

2. Injection and operating conditions

Calculation is achieved for a constant strain rate a = 200 s^{-1}, this latter has allowed us to calculate the velocity of injection from the composition of the gas mixture by the following formula

$$a = \frac{2(-v_O)}{D}\left[1 + \frac{v_F}{(-v_O)}\sqrt{\frac{\rho_F}{\rho_O}}\right] \quad (1)$$

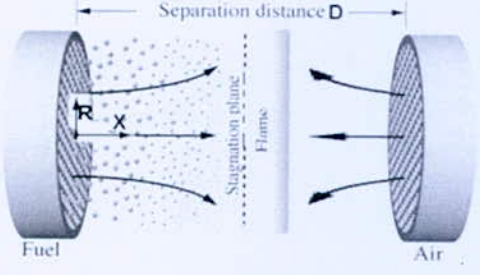

Fig. 1. Geometry of the flame

Where v and ρ are flow velocity at the burner exit and density, respectively. Subscripts F and O denote fuel and oxidizer flows, respectively and D is the distance between the two jets.

The injection temperature of reactants is equal to 300 k, and the pressure P = 1atm.

To illustrate the effect of thermal radiation, we have introduced the relative temperature of the flame defined by [4]:

$$f = \frac{T_{NR} - T_R}{T_{NR}} \quad (2)$$

With T_{NR} and T_R are the temperatures of the flame without and with radiation losses respectively.

For the chemical kinetics, the reaction mechanism Grimech 3.0, which is formed by 53 species and 325 elementary reactions has been adopted. This mechanism has been validated in several works for biogas and syngas [18, 19, 20, 21], and it has been validated for hydrocarbon doped by hydrogen until the rate of 20% [22]. Also, it has been used for pressures up to 20 atm.

*Corresponding author: zouagri.ri@gmail.com

For the calculation tools, the Chemkin code, which includes several reactors (modules) simplifying various calculations, is used.

TABLE I
EXAMPLES OF COMPOSITIONS CONSIDERED IN THE CALCULATION

Mixture	Biogas (B) (%)			Syngas (S) (%)		
	CH_4	CO_2	CH_4/CO_2	H_2	CO	H_2/CO
B_1S_1	25	25	1	25	25	1
B_1S_4	25	25	1	20	30	0.67
B_1S_6	25	25	1	30	20	1.5
B_4S_1	20	30	0.67	25	25	1
B_6S_1	30	20	1.5	25	25	1

III. CALCULATIONS AND RESULTS

1. Effect of the composition on the low heat value

The Fig. 2 shows the low heat value (LHV) which is calculated by varying the molar fraction X_{CH_4} from 0.1 to 0.4 while keeping the value of X_{H_2} and X_{CO} to 0.25, the line S1 on the Fig. 1 is obtained. In this case the low heat value of the mixture increases monotonically from 7920 (kj/kg) to 24710 (kj/kg).

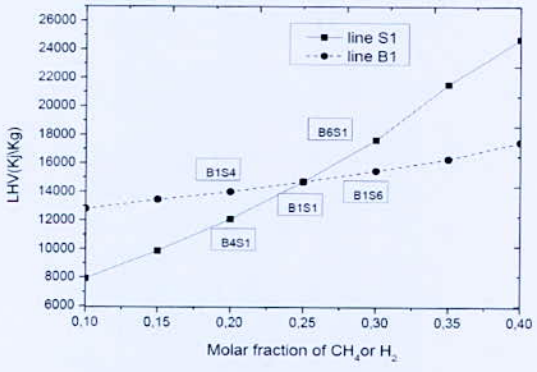

Fig. 2. Variation of LHV with molar fraction of CH_4 and H_2

If the molar fraction $X_{CH_4} = X_{CO_2} = 0.25$ and X_{H_2} is increased from 0.1 to 0.4, the line B1 is obtained, in this case the increase of the LHV is less pronounced. In both cases, the increase is due to the addition of fuel, CH_4 in the first case and H_2 in the second. Moreover, hydrogen with a very low molecular weight (2 g/mol), in front of methane (16 g/mol), has a weak effect on the LHV. Also, it can be noticed that all mixtures studied are classified as LCV fuels compared to methane and hydrogen.

2. Effect of the composition on the stretched flame structure and emissions

The curves presented by Figs. 3 to 6 show the effect of the fuel composition and radiation losses on the maximum variables of the flame, namely: maximum temperature, major species (H_2O) and minor species (OH and NO). The

Fig. 3, shows that for small added amounts of hydrogen and methane, less than 50%, the maximum temperature of the flame is more important in hydrogen mixtures; however, it becomes more important in the mixtures of methane with a volume higher than 50%. It can also be noticed that the radiation losses reduce maximum flame temperature constantly for all studied compositions.

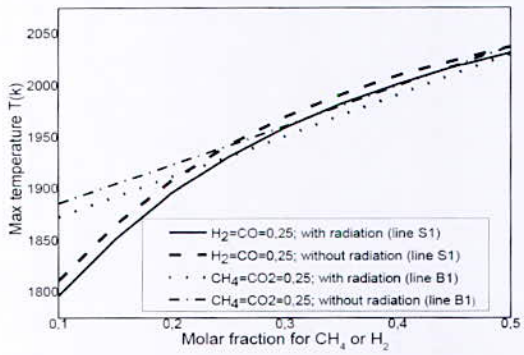

Fig. 3. Variation of the maximum temperature of the flame with CH_4 and H_2 molar fractions

The Fig. 4, shows the maximum H_2O mole fraction. It can be observed that the variation is more important for the hydrogenated mixtures (line B1). The values of H_2O are important for mixtures of methane for added volumes below 50% and they become more significant in the mixtures of hydrogen for added volumes higher than 50%. It is important to stress that radiation losses have no effect on H_2O production for all studied mixtures.

The Fig. 5, shows the maximum OH production for all the mixtues considered. It can be seen that for the added volume of fuels (hydrogen or methane) bellow 50% the OH mole fractions are comparable for both lines B1 and S1. Whereas, for the hight amounts of hydrogen line B1 becomes more important. Moreover, it can be noticed that radiation losses reduces OH production especially for the low volumes of the fuels.

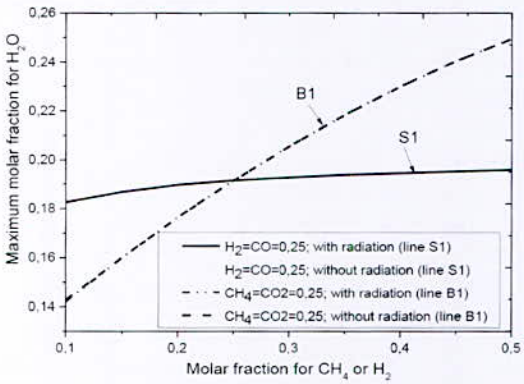

Fig. 4. Variation of the maximum molar fraction of H_2O with CH_4 and H2 molar fractions

The Fig. 6, shows the maximum NO mole fraction produced by the different considered compositions. The values of NO are important for mixtures of hydrogen for added volumes below 50% and they become more significant in the mixtures of methane for added volumes higher than 50%.

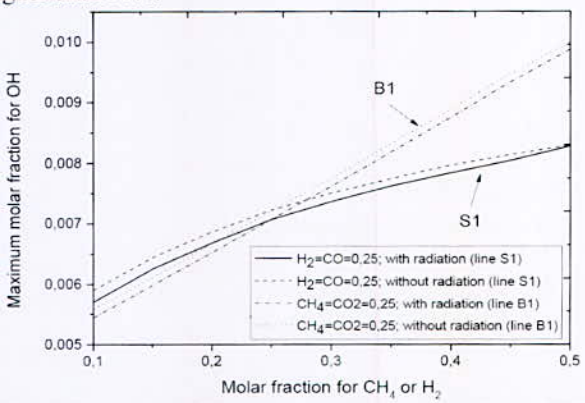

Fig. 5. Variation of the maximum molar fraction of OH with CH_4 and H_2 molar fraction

It is important to stress that radiation losses reduce NO production for all studied mixtures.

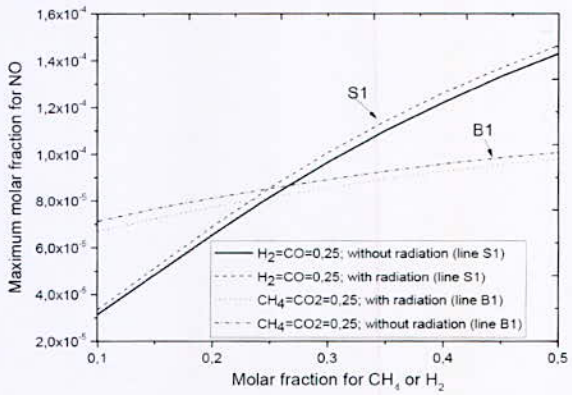

Fig. 6. Variation of the maximum molar fraction of NO with CH_4 and H_2 molar fraction

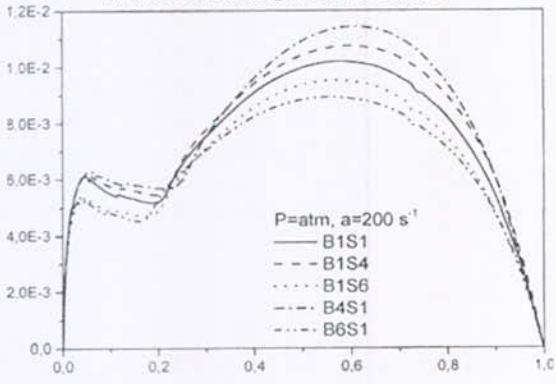

Fig. 7. Effect of the composition of the fuel mixture on the relative temperature

The Fig. 7, shows the variation of the relative temperature based on the fraction of mixture for a few compositions. One can easily notices that the most favorable composition

*Corresponding author: zouagri.ri@gmail.com

for a maximum radiation is B_4S_1 then B_1S_4, the less radiative composition is the B_6S_1.

IV. CONCLUSION

From the above, the following conclusions can be deduced:

- The increase in the volume of methane in biogas or hydrogen in the syngas increases the LHV; this increase is more important in the case of the methane; but mixtures remain low calorific gases comparatively to methane and hydrogen.
- For small added volumes of hydrogen and methane, less than 50%, the maximum temperature of the flame is more important in hydrogen mixtures; however, it becomes more significant, with small differences in mixtures of methane volumes higher than 50%.
- Major and minor species production is more important for mixtures of methane, for added volumes below 50%, and they become significant in the mixtures of hydrogen for added volumes higher than 50%.
- The radiation losses reduce the flame temperature and concentrations of major and minor species except water vapor that shows no variation.
- The most radiative mixture is B_4S_1 then B_1S_4, the less radiant composition is the B_6S_1. Radiant mixtures can be used for example in processes that need heat radiation such as cement and glass factories.

REFERENCES

[1] D. Deublein , A. Steinhauser . "Biogas from waste and renewable resources: an introduction". 2nd, Revised and Expanded Edition. Wiley-VCH Verlag GmbH & Co. KGaA; 2008.

[2] J B . Holm-Nielsen and P. Oleskowicz-Popiel, ''The future of biogas in Europe: visions and targets until 2020. In: Proceedings of the European Biogas Workshop e Intelligent Energy Europe,14e16 June 2007, Esbjerg, Denmark; 2007.

[3] I. Bedoya, S. Saxena S, F.J. Cadavid , R.W. Dibble,M. Wissink, '' Experimental evaluation of strategies to increase the operating range of a biogas-fueled HCCI engine for power Generation '',Appl Energy, Vol 97, pp 618-629, septembre ,2012.

[4] M. Abdelbaki, F. Tabet. "Numerical investigation of counter-flow diffusion flame of biogas–hydrogen blends: Effects of biogas composition, hydrogen enrichment and scalar dissipation rate on flame structure and emissions" International Journal of Hydrogen Energy, Vol. 41, Issue 3, pp. 2011-2022, January. 2016.

[5] R.J.C Marc, Ö. L. Gülder, P.T. G Clinton "Numerical and experimental study of soot formation in laminar diffusion flames burning simulated biogas fuels at elevated pressures'' , Combustion and Flame, Vol. 161, Issue 10, pp 2678-2691, October. 2014.

[6] A. Mameri1, F. Tabet2, A. Hadef1, "Numerical investigation of biogas diffusion flames characteristics under several operation conditions in counter-flow configuration with an emphasis on thermal and chemical effects of CO2 in the fuel mixture", Heat Mass Transfer, Verlag Berlin Heidelberg, 2017.

[7] A. Greco , D. Mira , Xi. Jiang. ''Effects of fuel composition on biogas combustion in premixed laminar flames '' , Energy Procedia, Vol 105, pp 1058-1062 , May, 2017.

[8] H. Maxime, "Valorisation de chars issus de pyrogazéification de biomasse pour la purification de syngas : lien entre propriétés physico-chimiques, procède de fonctionnalisation et efficacité du traitement", Ph D., École Nationale Supérieure des Mines d'Albi-Carmaux, Université de toulouse, 2016.

[9] C. Jean, "Simulation numerique du reformage autothermique du methane", Ph D., Énergétique, École Centrale, Paris , 2013.

[10] J. park,s, kiman lee and euju lee, " effects of ambient pressure on flame structure of CO/H2/N2 counter flow diffusion flame", international journal of energy research NT. J. Energy Res. Pp 187-205, 2001.

[11] K. Safer, F. Tabet, M. Safer ,"A numerical investigation of structure and NO emissions of turbulent syngas diffusion flame in counter-flow configuration", International Journal of Hydrogen Energy, Vol. 41, Issue 4, 30, pp 3208-3221, January. 2016.

[12] Mameri A, F. Tabet, A. Hadef ,"MILD combustion of hydrogenated biogas under several operating conditions in an opposed jet configuration", International Journal of Hydrogen Energy, In press, corrected proof, 2017.

[13] P.Sangwoon , K. Yongmo," Effects of nitrogen dilution on the NOx formation characteristics of CH4/CO/H2 syngas counterflow non-premixed flames". International Journal of Hydrogen Energy, Vol 42, Issue 16,pp 11945-11961, 2017.

[14] L.Guo-Xiu , S.Zuo-Yu ,Z. Zi-Hang ,L. Hong-Meng, y. Ye . Investigation on dilution effect on laminar burning velocity of syngas premixed flames. Energy. Vol 112, pp 146-152, 2016.

[15] J.B. Bhaskor , K. S. Ujjwal, C. Soumya, V. Vijay, "Effect of compression ratio on performance, combustion and emission characteristics of a dual fuel diesel engine run on raw biogas", Energy Conversion and Management, Vol 87, pp 1000-1009 ,2014.

[16] K. Safer, F . Tabet, A . Ouadha, M. Safer, I. Gökalp, "Simulation of a syngas counter-flow diffusion flame structure and NO emissions in the pressure range 1–10 atm", Fuel Processing Technology, Vol 123,pp 149-158, 2014.

[17] C.A. Hoerlle, L. Zimmer, F.M. Pereira, " Numerical study of CO2 effects on laminar non-premixed biogas flames employing a global kinetic mechanism and the Flamelet-Generated Manifold technique",Fuel, Vol 203, pp 671-685 , 2017.

[18] Graeme M.G. Watson, Jeffrey D. Munzar, Jeffrey M. Bergthorson. "NO formation in model syngas and biogas blends", Fuel, Vol 124, pp113-124,2014.

[19] M. Fischer, X. Jiang,"An assessment of chemical kinetics for bio-syngas combustion". Fuel, Vol 137, pp293-305, 2014.

[20] H.O.B. Nonaka, F.M. Pereira. "Experimental and numerical study of CO2 content effects on the laminar burning velocity of biogas". Fuel, Vol 182, pp 382-390 ,2016.

[21] Liu, B. Yan, G. Chen, X.S. Bai. "Structures and burning velocity of biomass derived gas flames. International Journal of Hydrogen Energy", Vol 35, Issue 2, pp 542-555 C,2010.

[22] MAMERI A, ''Etude numérique de la combustion turbulente du prémélange pauvre méthane/air enrichi à l'hydrogène '', Ph D., Université d'Orléans, 2009.

*Corresponding author: zouagri.ri@gmail.com

Characterization of the Combustion of the Mixture Biogas-Syngas Part II: Strain Rate and Ambient Pressure Effect

R. Belalmi[1*], A. Mameri[2] and Z. Aouachria[3]

[1*]Department of physics, University, Batna Algeria.
[2]Department of Mechanical Engineering, University, Oum el Bouaghi, Algeria.
[3]Department of physics, University, Batna Algeria.

Abstract—**The aim of this work is to demonstrate the effect of strain rate (or injection velocity) and ambient pressure on the flame structure (represented by temperature, major and minor species) and extinction limits of the biogas-syngas mixtures flames. The geometry consisted of the one-dimensional laminar diffusion flame in an opposite jets configuration. Chemical kinetics is described by the Gri3.0 reaction mechanism, which involves 53 species and 325 elementary reactions, and the problem is solved by Chemkin program. It was found that the syngas addition enlarges the flame resistance range to stretching. Increasing the pressure increases the temperature and NO production and reduces the other species. The thickness of the flame is constant for all compositions; however, it is reduced by the pressure and by the strain rate.**

Key words—Biogas-syngas mixtures, strain rate, flame under high pressure, flame thickness.

I. INTRODUCTION

The concept of 'sustainable development' can be summarized as three E: Environment, Energy and Economy. This concept has been emerged with the problems of climate change and the depletion of energy resources. According to the refs [1], [2] and since our civilization is heavily depending on hydrocarbons, this concept requires a balance between economic prosperity, energy needs and environmental protection to ensure sustainable development. The combustion produces, at the same time, energy in all useful forms as well as polluting emissions of the environment. Several experimental and numerical works considered this issue. In a numerical investigation of a counter flow diffusion flame of biogas-hydrogen blends, Mameri et al [3] studied the effect of biogas composition, hydrogen enrichment and scalar dissipation on flame structure and emissions. It was shown that the increment of CO_2 decreases flame temperature, mass fraction of chain carrier radicals and NO emissions index. The opposite happens when blending biogas by hydrogen. Hydrogen-rich biogas flame produces less NO at high scalar dissipation rate. The chemical effect of CO_2 is found to be present overall scalar dissipation rate values where it reduces the maxima of temperature and OH mass fraction and increase those of CO and NO mass fraction. H_2 enrichment has a weak influence on CO_2 chemical effects. In other studies from the same author [4] [5], the chemical effect of CO_2 was confirmed in addition to the study of thermal effect one. The authors found that the ambient pressure rise increases temperature and reduces flame thickness, radiation losses and dissociation amount; and at high pressure, recombination reactions coupled with chain carrier radicals diminishes NO mass fraction. The extinction problem in opposed jet diffusion flame with competitive reactions treated by V. K. Jean et al [6]; they developed an efficient numerical procedure for the resolution of the equations describing the chemical kinetics. This study reveals that the mass flow rates at extinction (Apparent Flame Strength) for the mixture (hydrogen-carbon monoxide as a fuel and air as an oxidizer) can be obtained by using a simple mixing rule similar to those used in theories of flame propagation

The emissions issued from syngaz was studied in refs [7], [8] and [9] among these studies, the work of Safer et al [10], they investigate the enhancement of syngas combustion using the promising oxygen-enrichment technology in which the volume of oxygen ranges from 21% to 30%. Two syngaz compositions were considered with H_2/CO rates from 0.25 to 4. The results showed that the oxygen addition increases the flame temperature and intensifies the radiative heat transfer. It also considerably extends flammability limits allowing stable flame at high values of the scalar dissipation rates for lean syngaz.

This work represents the second part which considers the effect of strain rate and ambient pressure on the flame structure of the mixtures Biogas-syngas. To this day, no work has been devoted to the study of the mixture of these two low calorific gases. The idea of this work is to find a source of renewable and biodegradable hydrogen; which is the syngas or synthesis gas or other so-called "city gas". It is mainly composed of carbon monoxide and hydrogen. And then to blend the biogas by the hydrogen contained in the syngas, as hydrogen-hydrocarbon enrichment is known to improve the performance of combustion (increase in reactivity, resistance to stretching, stability, reduction of pollutants, etc.).

II. THEORETICAL STUDY

The opposed jet diffusion flame has been chosen in this study because it constitutes one of the simplest experimental configurations in which extinction of flames

*Corresponding author email: rabab.belalmi@univ-batna.dz

can be measured and it is used to test flammability of various fuel/oxidizer systems [11], and more recently to evaluate fire suppressants.

1. The laminar flamelet model

The physical model considered here is a counter-flow, laminar diffusion flame stabilized near the stagnation plane of two opposing jet flows separated by a distance D = 2cm, as shown schematically Fig. 1. The air composed by oxygen and nitrogen (0.21 O_2 +0.79 N_2) is injected from the first side. The mixture biogas-syngas is injected from the second side. The flame structure is assumed to be uniform in the longitudinal direction of the flame (direction r in the figure); this hypothesis makes it possible to obtain a one-dimensional flame in which the properties depend only in the transverse direction (x in the figure). The characterization of the flame structure is made by producing a section perpendicular to the flame (direction x).

2. *Purpose of the work and operating conditions*

Part 1: demonstrate the effect of strain rate (or injection velocity) on the structure and limits of extinction of the flame, temperature and major and minor species. The strain rate is calculated as a function of the injection velocity and the composition of the gas mixture by:

$$a = \frac{2(-vo)}{D}\left[1 + \frac{v_F}{(-vo)}\sqrt{\frac{\rho_F}{\rho_O}}\right] \quad (1)$$

Five compositions of the biogas-syngas mixture are considered (Table1); the strain rate is varied from ignition to extinction. The ambient pressure and injection temperature in this case are respectively 1 atm and 300K. All calculations are carried out with and without radiative losses from the flames.

TABLE I

COMPOSITIONS OF THE MIXTURE BIOGAS-SYNGAS CONSIDERED IN THE CALCULATION

Mixture	Biogas (B)		Syngas (S)	
	CH_4 (%)	CO_2 (%)	H_2 (%)	CO (%)
B_1S_1	25	25	25	25
B_1S_4	25	25	20	30
$B1S6$	25	25	30	20
B_4S_1	20	30	25	25
B_6S_1	30	20	25	25

Part 2: The interest of this part finds its roots in applications such as internal combustion engines and turbo machinery where the operating pressure is significantly higher than atmospheric. Several studies have considered the effect of ambient pressure variation on the flame structure and harmful emissions [3] [12]. In this work, the ambient pressure is varied from 1 to 10 atm.

Chemical kinetics is described by the Gri3.0 reaction mechanism which is composed by 53 species and 325 elementary reactions. This mechanism is widely validated in the case of hydrocarbons and hydrogen doped hydrocarbons for pressures ranging from 1 to 10 atm. Computations are achieved by the Chemkin code.

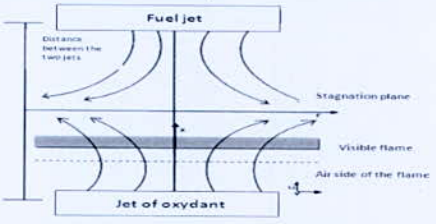

Fig. 1. Configuration of the mixture biogas-syngas counter-flow diffusion flame

III.RESULTS AND DISCUSSION

1. Effect of strain rate (injection velocity)

In Fig. 2, the effect of stretch rate (velocity) on the maximum flame temperature with and without radiation losses is seen. It is observed that at low speeds the effect of radiation is clearly visible, after ignition the maximum temperature of the flame without radiation increases rapidly to reach values close to that adiabatic and then decreases linearly with the velocity. If one considers the losses by radiation, it is clear that the temperature follows a non-monotonic form; it increases rapidly until reaching a maximum and then slowly decreases towards its minimum value. It can be seen that the difference between the two temperatures, with and without radiation, just after the ingestion is maximum, decreases as the speed increases. At low speeds, there is a competition between radiation losses and chemical reactions, when we increase the rates we inject more reagents, the chemical reactions become more active and the temperature increases. At high stretching speeds the residence time of the reactants is reduced, which leaves no time for chemical reactions or radiation losses, that is why the temperature decreases and converges at high speeds.

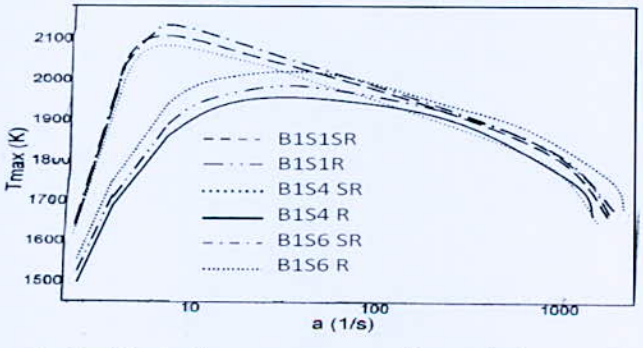

Fig. 2. Maximal temperature profile evolution vs the radiation losses and the rate strain for different composition

*Corresponding author email: rabab.belalmi@univ-batna.dz

Fig. 3, shows the evolution of the maximum of the OH radical as a function of the injection rates for different compositions, this radical being an indicator of the reactivity of the mixture. It is noted that at ignition all the compositions are almost similar; a difference becomes visible when the rate of stretching increases. The evolution of the maximum of the radical OH is done in a non-monotonic manner or it increases until reaching a maximum and then falls towards the high speeds. It is noted that the more fuel and in particular the more hydrogen the OH radical is produced, the combustion system to be optimized to operate at high OH values. One can choose the speed and the appropriate composition

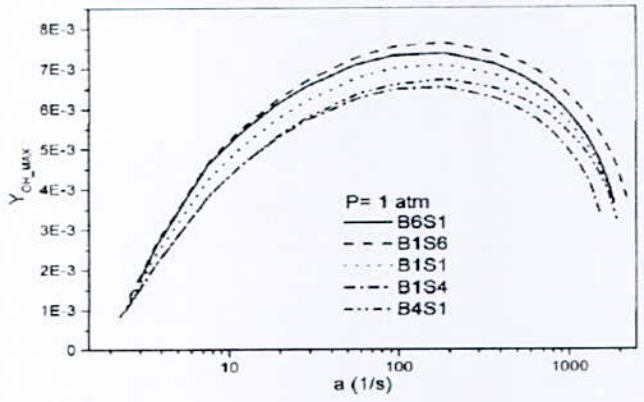

Fig. 3. Maximal OH molar fraction profile evolution vs rate strain for different compositions

The evolution of the maximum of the molar fraction of NO as a function of the velocity (stretching rate) is shown in Fig. 4. We note that at the ignition and extinction we have practically the same weak productions. The maximum is located in the proximity of 30s-1 is an injection speed of 16.17 (cm / s). It is known that the majority of NO is produced by thermal decomposition of nitrogen from air at high temperatures. This is why the NO is directly correlated with the temperatures and especially when it exceeds the 1750k. The stretch rate for which NO is produced is 27.9 (s-1) the latter is to be avoided in applications. The variation of the flame thickness depends on the flame stretching ratio for different compositions at ambient pressure, 1atm. All compositions have practically the same thickness of flame. At low velocities the flame is thick, and exponentially decreases as the rate of stretching increases until extinction

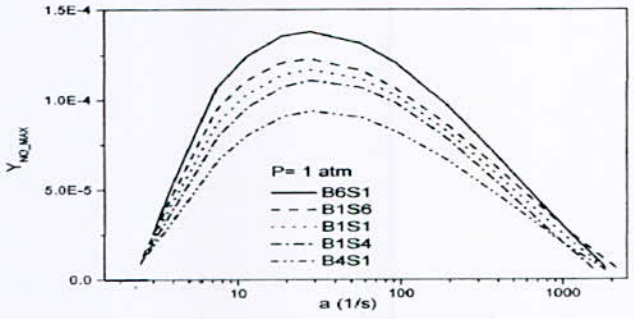

Fig. 4. Variation of the maximum molar fraction of NO as a function of stretching rate for different compositions.

2. ***Effect of pressure***

The maximum of the temperature varied differently on the intervals 1-3atm, 3-5atm and 5-9atm. Indeed, the temperature evolves rapidly over the interval of low pressures 1-3atm and begins to decelerate for the average pressures 3-5atm to arrive at very slow evolution for the high pressures. This phenomenon is also observed in [3] and [10]. Also, it is noticed that maximum temperature evolution depends strongly on the type of fuel used in the flame. For example, in mixtures B_6S_1 (30% methane), the temperature is more influenced by the pressure than the mixture B_4S_1.

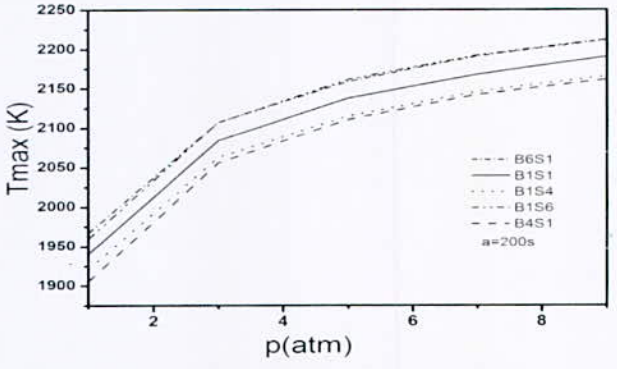

Fig. 5. Maximal temperature profile evolution vs pressure for different composition

The Fig. 6, illustrates the evolution of the OH radical in function of pressure. We observe that when the pressure increases the radical OH decreases from 0.00775 for pressure 1atm to reaches its minimum value 0.00475 for pressure P = 9 atm. It is noticed that the most sensitive composition to pressure in terms of OH is B_1S_6 containing the maximum volume of hydrogen, whereas the least sensitive composition is B_1S_4 and which contains the minimum amount of hydrogen.

*Corresponding author email: rabab.belalmi@univ-batna.dz

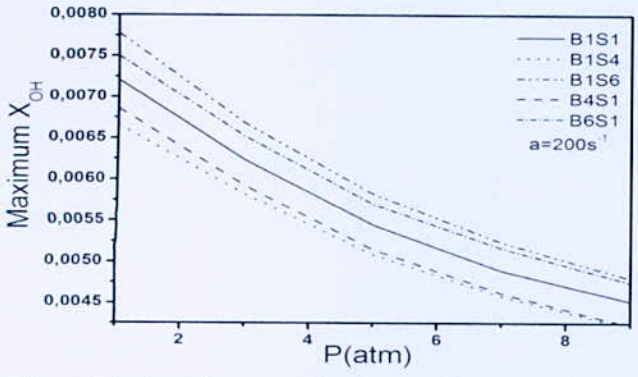

Fig. 6. Maximal OH molar fraction profile evolution vs pressure for different compositions

The variation of the maximum of the molar fraction of NO is presented in the Fig. 7. Globally its evolution is similar that the temperature variation. In fact, the increase in pressure increases the NO especially in the interval 1-3atm as in the temperature case. Similarly, to temperature, the most sensitive composition to pressure in terms of NO production is that which contains more methane and vice versa. It may be noted that the gap of the NO molar faction between B6S1 and B4S1 is higher than the temperature gap when we compare the Fig. 5 and Fig. 7.

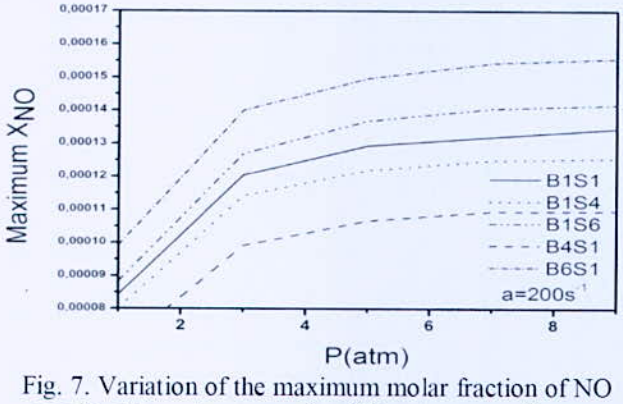

Fig. 7. Variation of the maximum molar fraction of NO as a function of pressure for different compositions

IV. CONCLUSION

The results found showed that the increase in the injection velocity and consequently the strain rate follows a non-monotonic variation where the parameters of the flame increase from the ignition to reach a maximum value then they fall to their values of extinction. At ignition, the minimum values are due to the high residence time due to the low injection speed and the extinction is the reverse.

Concerning the effect of the pressure, the results showed that the increase of the pressure increases the temperature and the production of the NO, on the other hand reduces the other species considered. For the thickness of the flame it is virtually constant for all the compositions considered and it is reduced by the increase in injection velocity and pressure.

REFERENCES

[1] S. Boyer, D. Labrunie, E. Segard, fabrication de biogaz: synthèse de pétrole par fermentation à partir des déchets organiques, 2009/1, (retreved 5/10/2017)

https://www.econologie.com

[2] S. Pacaud, Y. L. Roux, C. Feidt, Projet collectif de méthanisation en milieu rural, 218, 2013/2 pp. 99 – 108. DOI 10.3917/pour.218.0099.

[3] A. Mameri, and F. Tabet, "Numerical investigation of counter-flow diffusion flame of biogas-hydrogen blends: effects of biogas composition, hydrogen enrichment and scalar dissipation rate on flame structure and emissions International journal of hydrogen energy. TR-0200 (2011-22)-3. 2016.

[4] A. Mameri, F. Tabet, A. Hadef, "Numerical investigation of biogas diffusion flames characteristics under several operation conditions in counter-flow configuration with an emphasis on thermal and chemical effects of CO_2 in the fuel mixture," Heat and Mass Transfer.TR-0200(1-10). 2017.

[5] A. Mameri, F. Tabet, A. Hadef, MILD combustion of hydrogenated biogas under several operating conditions in an opposed jet configuration, Int. J. of Hydrogen Energy.TR-0200 (1-11). 2017.

[6]. V. Jain, and H. Mukunda, "The extinction problem in an opposed jet diffusion flame with competitive reactions, " Combustion Science and Technology.TR-0200 (105-17)-1. 1969.

[7] T. Mattisson, et al, "Chemical-looping combustion using syngas as fuel," International journal of greenhouse gas control.TR-0200 (158-69)-1. 2007.

[8] S. Alavandi, A. Agrawal, "Experimental study of combustion of hydrogen-syngas/methane fuel mixtures in a porous burner, Int. J. of Hydrogen Energy. TR-0200, 33, 2008, pp. 1407-1415.

[9] A. Brambilla, et al, "An experimental and numerical investigation of premixed syngas combustion dynamics in mesoscale channels with controlled wall temperature profiles Proc. Combustion Institute, 2015, pp. 3429-3437.

[10] M. Safer, F. Tabet, A. Ouadha, K. Safer, "A numerical investigation of structure and emissions of oxygen-enriched syngas flame in counter-flow configuration Int. J. of hydrogen energy, 40 -6, 2015, pp. 2890-2898.

[11] F. Takahashi, L.P. Goss. "Near-field turbulent structures and the local extinction of jet diffusion flames" in *Proc. International Symposium on Combustion, Elsevier, 1992:*.pp.351-359

[12]K. Safer, et al, "Simulation of a syngas counter-flow diffusion flame structure and NO emissions in the pressure range 1-10atm, " Fuel Process Technol. TR-0200(149-158). 2014.

*Corresponding author email: rabab.belalmi@univ-batna.dz

Simulation Numérique des Transferts de Chaleur et de Masse dans un Réservoir à Hydrure Métallique Equipé d'un Matériau à Changement de Phase

A. Babou[1,2*], Y. K. Ziari[2] and Y.Kerkoub[2]

[1*]Unité de Recherche Appliquée en Energies Renouvelables, URAER, Centre de Développement des Energies Renouvelables, CDER, 47133, Ghardaïa, Algeria.

[2]Laboratoire Thermodynamique et Systèmes Energétiques, Faculté de Physique, Université des Sciences et de la Technologie Houari Boumediene : BP 32 El Alia Bab-Ezzouar, Alger, Algérie.

Résumé— **Le stockage de l'énergie thermique est devenu un des thèmes de recherche très important dans de nombreuses applications industrielles. L'objectif de ce travail est d'analyser numériquement les transferts de chaleur et de masse dans un réservoir à hydrure métallique rempli de l'alliage Lanthane-Nickel, $LaNi_5$ sous forme poudreuse et équipé d'un échangeur plein d'un Matériau à Changement de Phase, "MCP" (Na_2SO_4, $10H_2O$) en tant que "unité de stockage" de la chaleur sous forme latente dégagée lors du processus d'absorption de l'hydrogène et de la restituer pendant le processus de désorption. Dans ce cadre un modèle mathématique a été développé pour prédire les transferts de chaleur et de masse dans le réservoir à hydrure métallique ainsi que dans le MCP. L'amélioration de la conductivité thermique de MCP, facilite les transferts de chaleur et accélère la cinétique de réaction et diminue considérablement le temps de chargement et de déchargement de l'hydrogène. L'insertion de la mousse métallique dans le MCP augmente la conductivité thermique, et favorise la cinétique de la réaction et réduit le temps d'absorption et de désorption de l'hydrogène. Les résultats de la prévision numérique sont en bon accord avec les résultats expérimentaux.**

Mots clés—Stockage de l'hydrogène, Hydrures métalliques, Matériaux à Changement de Phase.

I. INTRODUCTION

Les hydrures métalliques sont formés par réaction solide-gaz, le processus d'absorption de l'hydrogène dans les hydrures est une réaction fortement exothermique et la chaleur produite nécessite d'être évacué, à l'inverse, le processus de désorption est endothermique et nécessite un apport de chaleur. La réaction d'absorption et désorption peut s'écrire sous la forme, (1) :

$$M + n/2\ H_2 \longleftrightarrow MH_n \pm \Delta H \qquad (1)$$

La plupart des études sur le stockage solide de l'hydrogène dans les réservoirs à hydrures métalliques utilisent généralement, un fluide caloporteur pour extraire la chaleur de réaction et la transmettre dans l'environnement, comme chaleur perdue. Cependant, la chaleur dissipée doit être fourni à nouveau au lit d'hydrures pendant le processus de décharge. Les matériaux à changement de phase, (PCM Phase Change Material) ont la particularité de stocker de l'énergie thermique sous forme d'enthalpie de fusion, l'énergie est absorbée lors du passage de l'état solide à l'état liquide du MCP et elle est restituée lors du passage inverse. L'utilisation d'un matériau à changement de phase (MCP) dans le stockage de l'hydrogène dans les hydrures métalliques est une méthode très efficace. Cependant, quelques études ont été réalisées pour enquêter sur le système de stockage solide de l'hydrogène dans des réservoirs à hydrures équipés de MCP, comparé à la multitude des modèles proposés dans la littérature. L'utilisation des MCP dans le stockage solide de l'hydrogène n'est pas nouvelle. Gary Sandrock en 1986 [1], a déposé un brevet d'invention dont l'idée est de stocker la chaleur dégagée du réservoir à hydrures métallique lors de l'absorption de l'hydrogène. Trois configurations ont été choisi dans son travail pour tester la validité de cette invention: sans moyen de stockage de chaleur dégagée, la chaleur dégagée est stockée sous forme sensible dans l'eau et un matériau à changement de phase (sulfate de sodium, (Na_2SO_4, $1OH_2O$)) est utilisé pour stocker la chaleur dégagée sous forme latente, lors de l'absorption de l'hydrogène dans un réservoir à hydrures métalliques de type AB_5 ($Ca_{0.7}$ $M_{0.3}Ni_5$) sous forme poudreuse. L'auteur a constaté que la durée de stockage de la chaleur sous forme sensible ou sous forme latente est comparable et que le stockage de la chaleur sous forme latente peut augmenter la capacité de stockage massique et volumique. Ben Maad et al. [2] ont mené une étude numérique sur les processus d'absorption et de désorption de l'hydrogène dans un réservoir cylindrique à hydrures métalliques rempli de $LaNi_5$ équipé d'un échangeur de chaleur à changement de phase ($LiNO_3$, $3H_2O$). Leurs résultats indiquent que l'absorption se produit beaucoup plus rapidement dans les zones qui sont plus proches de l'échangeur de chaleur à changement de phase. Cependant, le taux d'absorption dépend de la conductivité et l'enthalpie de fusion du MCP. H. Ben Maad et al. [3] ont étendu leurs travaux numériques précédents et ont trouvé que le réservoir peut évacuer jusqu'à 80% d'hydrogène stocké par la mise en œuvre de MCP. R. Darzi et al. [4] ont étudié numériquement les processus de chargement et de déchargement de l'hydrogène dans un réservoir tubulaire d'hydrures métallique contenant $LaNi_5$ et équipé d'une enveloppe annulaire pleine de matériau à changement de phase. Ils ont constaté que l'amélioration la conductivité thermique

*Corresponding author email: allal_babou@yahoo.com

de MCP en ajoutant de la mousse métallique, facilite le transfert de chaleur et le temps de chargement diminue de 28%. Garrier et al. [5] ont mené une étude conjointe expérimentale et numérique afin d'analyser le processus d'absorption et de désorption de l'hydrogène dans un réservoir de MgH_2 équipé d'un matériau de changement de phase, MCP ($Mg_{69}Zn_{28}Al_3$). Ils ont conclu que le réservoir est capable de stocker et de libérer 7050 NL d'hydrogène en 3 h et l'efficacité journalière de stockage est de 70% et que le couplage du réservoir à hydrures métalliques avec une pile à combustion de type PEMFC délivrant une puissance de 1.2 kW s'est révélé concluant. Mellouli et al. [6] ont développé un modèle mathématique en 3D pour simuler quelques nouvelles configurations, pour un réservoir à hydrures métalliques équipé de MCP en tant que échangeur de chaleur à changement de phase. L'alliage de Mg_2Ni est utilisé comme lit d'hydrure et le nitrate de sodium ($NaNO_3$) est choisi comme milieu de stockage de chaleur (MCP). Les auteurs ont analysé, l'effet de la mousse métallique sur l'amélioration du transfert de chaleur et l'influence de quelques paramètres opérationnels sur le taux de stockage ont été aussi présentés.

MODEL DE SIMULATION

On s'intéresse dans ce présent travail aux transferts de chaleur et de masse dans un réservoir à hydrure métallique rempli de l'alliage, $LaNi_5$ et équipé d'un échangeur plein d'un Matériau à Changement de Phase (Na_2SO_4, $10H_2O$).

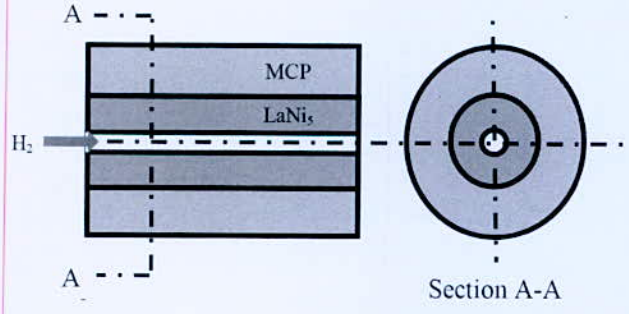

1 Schéma de la géométrie axisymétrique

Le système de stockage est un réservoir cylindrique annulaire, contenant un cylindre intérieur occupé par l'hydrogène gazeux et une région annulaire intermédiaire contenant un hydrure métallique de type AB_5 le $LaNi_5$ et équipé d'un matériau à changement de phase Fig.1. Pour la simulation seulement les variations des paramètres radiales sont considérés, et l'hydrogène se comporte comme un gaz parfait entre les pores de l'hydrure et la température du gaz est localement la même que celle du solide, l'écoulement est laminaire entre les grains de poudre et les transferts radiatifs dans le milieu poreux sont négligés.

II. MATHEMATICAL MODEL

En considérant ces hypothèses, les équations régissant, les transferts couplés de chaleur et de masse dans le lit d'hydrures métalliques sont [7] :

Equation de conservation de l'énergie:

$$(\rho C_p)_e \frac{\partial T}{\partial t} = \frac{1}{r}\frac{\partial}{\partial r}\left(r k_e \frac{\partial T}{\partial t}\right) + \dot{m}\left[\Delta H - T\left(C_{p,g} - C_{p,s}\right)\right] \quad (2)$$

Equation de conservation de la masse de H_2:

$$\varepsilon \frac{\partial \rho_g}{\partial t} = -\dot{m} \quad (3)$$

Equation de conservation de la masse de l'hydrure:

$$(1-\varepsilon)\frac{\partial \rho_s}{\partial t} = \dot{m} \quad (4)$$

Equation de conservation de la quantité de mouvement:

$$\vec{v}_g = \frac{K}{\mu_g}\vec{\nabla}P \quad (5)$$

Cinétique de la réaction (absorption) :

$$\dot{m} = C_a exp\left(-\frac{E_a}{R_g T}\right) ln\left(\frac{P}{P_{eq}}\right)(\rho_{ss} - \rho_s) \quad (6)$$

Pression d'équilibre :

$$P_{eq} = P_{eq}^{ref} exp\left(\frac{\Delta H}{R_g T}\left(\frac{1}{T} - \frac{1}{T_{ref}}\right)\right) \quad (7)$$

Avec : ρ_s la masse molaire du solide et ρ_{ss} la densité de l'hydrure à la saturation; E_a est l'énergie d'activation et C_a constante de la réaction. T est la température absolue ; P est la pression du gaz et R_g est la constante des gaz parfaits. La pression d'équilibre P_{eq} peut être calculée en fonction de la température et en fonction du taux (H/M), hydrogène / Métal. Avec $f(X)$ est la pression d'équilibre à la température de référence $T_{réf} = 25\,°C$. Cette fonction est une fonction polynomiale d'ordre 9, on donne dans le tableau 1 les coefficients de la fonction. ΔH est la variation d'enthalpie de la réaction.

Les équations régissant, le transfert de chaleur dans le MCP sont :

$$\frac{\partial H}{\partial t} = \vec{\nabla}.\left(k_{MCP}\vec{\nabla}T\right) \quad (8)$$

*Corresponding author email: allal_babou@yahoo.com

TABLE I
COEFFICIENTS DE LA FONCTION POLYNOMIALE

a_0	a_1	a_2	a_3	a_4	a_5	a_6	a_7	a_8	a_9
4.00×10^{-1}	2.33×10^{-2}	-2.18×10^{-3}	1.27×10^{-4}	-4.50×10^{-4}	9.91×10^{-4}	-1.36×10^{-5}	1.13×10^{-5}	-5.19×10^{-4}	1.01×10^{-4}

Avec H est l'enthalpie volumique totale du MCP :

$$H = h(T) + \rho_{MCP}.L.g(T) \quad (9)$$

L est la chaleur latente de fusion et $g(T)$ est la fraction liquide de MCP.

$$h(T) = \int_{T_m}^{T} \rho_{MCP} C_{MCP} dT \quad (10)$$

k_{MCP}, ρ_{MCP} *et* C_{MCP} sont la conductivité thermique, la masse volumique et la capacité calorifique du MCP respectivement.

TABLE II
VALEURS DES PARAMETRES UTILISEES DANS LA SIMULATION

Symbol	Métal ($LaNi_5$)	Hydrogène (H_2)
$\rho(kg/m^3)$	8300	0.0838
$K(m^{-2})$	10^{-8}	/
ε	0.5	
$C_p(J/kg.K)$	530	14.500
k_e $(W/m.K)$	1.087	/
$C_a(1/s)$	59.187	/
$E_a(J/mol)$	21170	/

La fraction liquide de MCP est donnée par la relation suivante :

$$g(T) = \begin{cases} 1 & ; si \quad T \geq T_f \\ 0 & ; si \quad T \leq T_s \\ \frac{T-T_s}{T_f-T_s} & ; si \quad T_s < T < T_f \end{cases} \quad (11)$$

T_f et T_s sont les températures de fusion et solidification du MCP. Au temps initial, les valeurs de la pression, et la densité de l'hydrure dans le réservoir sont constantes :

$$T(r,0) = T_0 \; , P(r,0) = P_0 \text{ et } \rho_s(r,0) = \rho_0$$

La résolution du système d'équations est effectuée à l'aide de la méthode des différences finies.

III. RESULTATS

On présente sur la fig. 3 l'évolution temporelle de la capacité de stockage de l'hydrogène moyenne dans le réservoir sans MCP, on observe une bonne concordance des résultats numériques avec les résultats de [7].

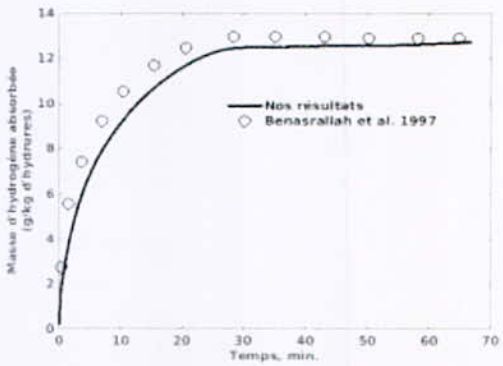

Fig. 2. Comparaison de nos résultats avec [7].

Les figures 3 et 4 montrent l'effet de la conductivité thermique du MCP sur l'évolution temporelle de la capacité de stockage de l'hydrogène et sur la température dans le lit à hydrures métalliques, pour déférentes valeurs de conductivité thermique de MCP (0.6, 5, 15 W/m°K). On observe pour une valeur faible de la conductivité thermique de MCP (0.6 W/m°K), un temps long de chargement de l'hydrogène (fig. 3), qui est expliqué par un mauvais échange de chaleur avec l'hydrure métallique (fig. 4). Et avec l'augmentation de la valeur de la conductivité thermique le temps de chargement de l'hydrogène augmente et la température diminue plus rapidement. Aussi, on constate un faible changement à partir d'une valeur de la conductivité thermique de MCP (5 W/m°K).

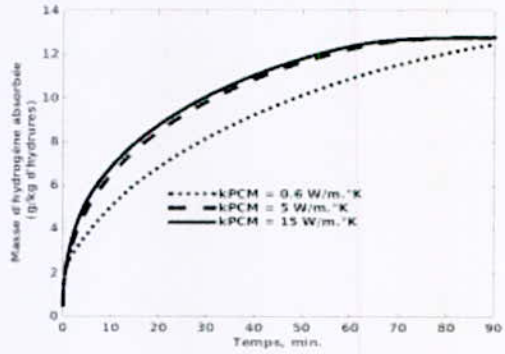

Fig. 3. Effet de la conductivité thermique de MCP sur l'évolution temporelle de la masse d'hydrogène absorbée

Les figures 5 et 6 présentent une comparaison de l'évolution temporelle de la capacité de stockage et de la température moyenne de l'hydrure, avec et sans mousse métallique durant le processus d'absorption.

*Corresponding author email: allal_babou@yahoo.com

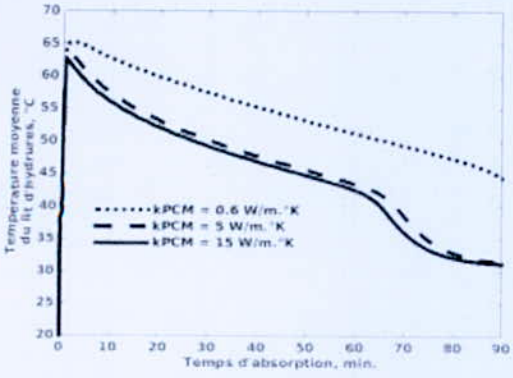

Fig. 4. Effet de la conductivité thermique de MCP sur l'évolution temporelle de la température moyenne du lit d'hydrure métallique

On constate que l'insertion de la mousse métallique dans le MCP réduit significativement le temps total d'absorption de presque de 21%. L'augmentation de la conductivité thermique de MCP favorise bien le transfert de la chaleur de l'hydrure, ainsi la rapidité de la cinétique de la réaction. Aussi, la température d'hydrure diminue de façon rapide comparée au cas sans mousse métallique.

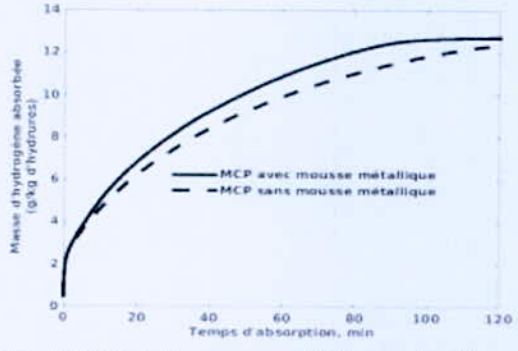

Fig. 5. Effet de la mousse métallique ajoutée au MCP sur l'évolution temporelle de la masse de l'hydrogène absorbée

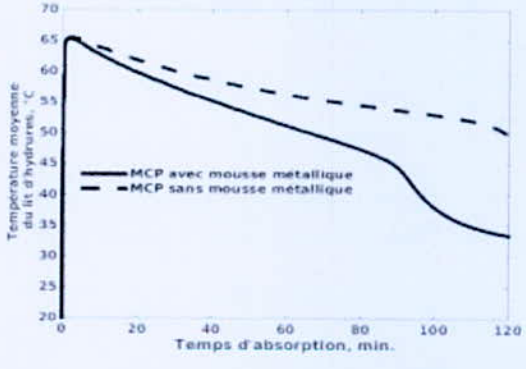

Fig. 6. Effet de la mousse métallique ajoutée au MCP sur l'évolution temporelle de la température moyenne de l'hydrure

VI. CONCLUSION

Dans ce travail nous avons montré la faisabilité et les avantages de l'utilisation des Matériaux à Changement de Phase, MCP dans les hydrures métalliques, aussi nous avons présenté l'influence de quelques paramètres thermiques, à savoir la conductivité thermique de MCP et l'augmentation de la capacité thermique du MCP en utilisant une mousse métallique en Aluminium sur le temps de chargement et sur la quantité d'hydrogène absorbée dans le système de stockage H_2 - $LaNi_5$.

Ce travail ouvre de nombreuses perspectives pour étudier d'autres paramètres tels que l'influence da porosité de MCP sur le temps et le taux de stockage de l'hydrogène et le couplage thermique de réservoir avec les piles à combustible.

REFERENCES

[1] G. D. Sandrock, Edwin Snape, "Reaction heat storage method for hydride tank", WO 4566281, United State Patent

[2] H. B. Ben Mâad HB, F. Askri, S. B. Nasrallah, "Heat and mass transfer in a metal hydrogen reactor equipped with a phase-change heat exchanger", in Int Journal of Thermal Sciences 2016;99:271e8.

[3] H. B. Ben Mâad, A. Miled, F. Askri, S. B. Nasrallah "Numerical simulation of absorption-desorption cyclic processes for metal-hydrogen reactor with heat recovery using phase-change material", in Appl Therm Eng 2016;96:267e76.

[4] A. Ali Rabienataj Darzi, H. Hassanzadeh Afrouzi, A. Moshfegh, M. Farhadi, "Absorption and desorption of hydrogen in long metal hydride tank equipped with phase change material jacket", in International journal of hydrogen energy (2016) 41 9595-9610.

[5] S. Garrier, B. Delhomme, P. De Rango, P Marty, D Fruchart, S Miraglia, "A New MgH_2 tank concept using a phase-change material to store the heat of reaction", in Int J Hydrogen Energy 2013;38:9766e71.

[6] S. Mellouli, E. Abhilash, F. Askri, S. Ben Nasrallah. "Integration of thermal energy storage unit in a metal hydride hydrogen storage tank", in Applied Thermal Engineering, 102 (2016) 1185–1196.

[7] A. Jemni, S. Ben Nasrallah, "Study of two-dimensional heat and mass transfer during adsorption in a metal-hydrogen reactor", in Int J Hydrogen Energy 1995;20(1):43–52.

*Corresponding author email: allal_babou@yahoo.com

Artificial Intelligence Model for Hybrid Renewable Energy System

K. Gairaa[1*], A. Khellaf[2], M. Guermoui[1] and S. Benkaciali[1]

[1*] Unité de Recherche Appliquée en Energies Renouvelables, URAER, Centre de Développement des Energies Renouvelables, CDER, 47133, Ghardaïa, Algeria.

[2] Centre de Développement des Energies Renouvelables, CDER, BP 62 Route de l'Observatoire, Bouzaréah, 16340, Algiers, Algeria.

Abstract— **In some remote areas of our country such as the great Sahara and the highlands, stand-alone (off-grid) systems are an adequate solution for electrical energy supply. However, in the majority of cases, the power generation is usually guaranteed by diesel-powered generators. This type of power supply inevitably includes Co_2 emission and it is not environmental friendly. Otherwise, a small stand-alone system composed by renewable sources (PV modules, wind turbine and hydrogen electrolyzer) can be an alternative way to the diesel generator in term of energy supply. Moreover, by combining these renewable sources to form a hybrid system, we can obtain more economical energy. In this work, an autonomous hybrid system (PV-wind- electrolyzer) is elaborated as mean to provide the electricity power. The optimal design of the mentioned system is based on a simulation model developed under HOMER software. For this purpose, data of Ghardaïa site are used. Thereafter, the obtained simulation values are used as inputs in a neural model (*NAR* and *NARX* architectures), in order to forecast the hourly electrical power supplied by the proposed hybrid system.**

Key words— Hybrid system, neural model, electrical power, HOMER.

I. INTRODUCTION

Renewable energy sources (*RES*) are the subject of a particular interest in recent years. The main cause of this growth lies behind the prognostic depletion of conventional energy resources of the Planet: fuel, natural gas, coal and even uranium. Instead, *RES* can be considered inexhaustible at the human scale, since they use natural energy flows from the sun or biomass [1]. Despite global development, renewable sources cannot be considered as a universal solution to electricity supply problems. This is due to the stochastic nature of the primary solar and wind source. However, the problem with variable power unsecured produced by renewable sources, can be solved by coupling the sources and formatting then so-called hybrid systems. A renewable hybrid system is an electrical system, comprising more than one energy source. This combination makes it possible to optimize electricity production systems as much as possible, both technically and economically. There are several combinations modes, namely: wind-diesel, photovoltaic-diesel and wind-photovoltaic-diesel [2-5]. The hybrid energy system is an excellent solution for the energy problems in the remote areas where grid connection is difficult and not feasible. In the last years, several works have been presented in the literature focused on hybrid systems, aiming to increase the efficiency of systems using a single source. Chavez et al. [6] proposed an ANN based model to predict the performance of a combined power plant (solar- wind-hydrogen) model, for supplying a remote housing in Mexico. The results that were found indicates a good accuracy in term of performance prediction (PV_{MSE}=8.4%, PEM-FC_{MSE}=2.4%, PEM-WE_{MSE}=1.96%, GSR_{MSE}=7.9%, WT_{MSE}=14%). Chatziagorakis et al. [7] designed and intelligence model for the prediction of the daily and the hourly meteorological parameters (global solar radiation and wind speed), for the enhancement of the power management strategies of an autonomous hybrid PV-Wind-FC system. The simulation results indicate that the model thus proposed gives a satisfactory prediction achieving regression coefficient from 0.93 up to 0.99. Kenneth et al. [8] built a hybrid micro-power system for hydrogen production in Oman. This system is constituted by solar PV, wind turbine, electrolyzer, Fuel cell, diesel generator and micro hydropower. The performance and the optimization of the combined system are analyzed with HOMER software. Their findings illustrate an excellent sustainable energy output, even with a high energy cost. This type of micro-power is highly recommended for the remote populations.

The goal of our study is the forecasting of the electrical energy produced by a hybrid renewable system (PV-Wind-Electrolyzer), using an artificial model. Beforehand, the hybrid system which is intended to supply electricity into housing in remote area, is optimized under HOMER software. The mentioned system is tested under Ghardaïa site (Algeria) conditions.

II. METHODS

1. HOMER software

As we noted above, the proposed hybrid power system is optimized under HOMER software [9]. It is developed

*Corresponding author email: kacem_gairaa@uraer.dz

by the National Renewable Energy Laboratory (*NREL*) [10] and performs hourly simulations of every possible combination of components entered and ranks the systems according to user specified criteria such as cost of energy (*COE*) or Capital Costs (*CC*). HOMER has been extensively used as a sizing and optimization software tool.

2. System description and data source

In this study, the hybrid power system consists of PV generators, wind turbine, fuel cells, electrolyzer, and a hydrogen tank, as shown in the following Figure:

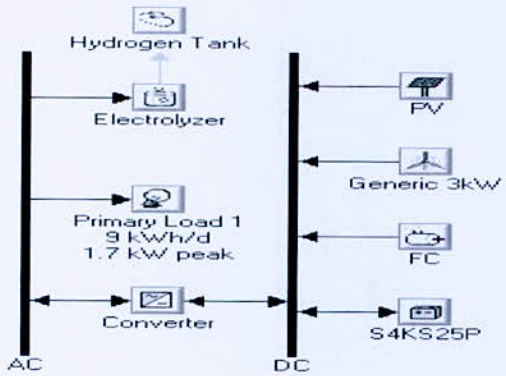

Fig. 1. Considered hybrid power system

This system is tested using the real meteorological data of Ghardaïa area (32.36° N latitude, 3.81° E longitude and 450 m altitude). Figs. 2 and 3 illustrate the global solar radiation profile and wind speed, respectively over a one-year period. The annual average solar radiation for this site is about 5.31 kWh/m²/day, while the annual average wind speed is about 5.13 m/s.

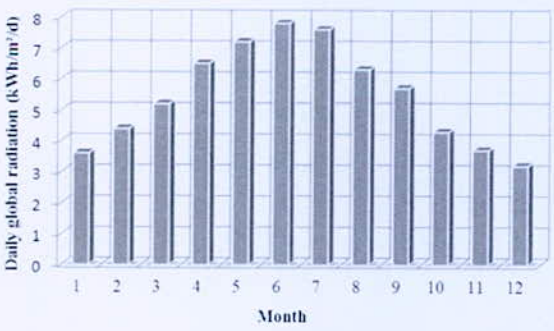

Fig. 2. Monthly mean global solar radiation

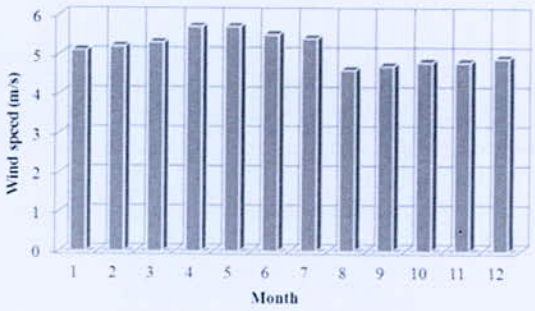

Fig. 3. Monthly mean variation of wind resource

The load of the proposed system is about 9.0 kWh/m^2/day and has 1.7 kW as peak load; Fig. 4 shows the monthly variation of the load entire the year.

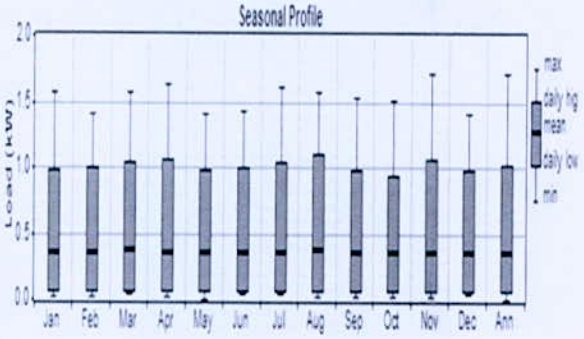

Fig. 4. Monthly average variation of the load

Each wind turbine and solar PV generation unit are rated at 3.5 kW, and 5 kW, respectively. The nominal capacity of the battery is 1900 Ah with the nominal voltage of 6 V. The inverter nominal capacity is 70 kW. The fuel cell and electrolyzer capacity are 10 kW. Hydrogen tank size is 10 kg. Note these capacities are nominal rate for each individual component.

3. Artificial intelligence models

Artificial intelligence (*AI*) techniques have been widely used in recent years in the field of renewable energies, in order to forecast the future values of solar energy conversion devices. We find in the first rank, the artificial neural networks (*ANN*) which are considered as a powerful tool and they are processed by many authors. Due to the nonlinear behavior of the renewable sources (solar radiation and wind speed), the computational paradigm of neural networks was adopted for the design of the forecasting model. In our study, we adopt two kinds of recurrent dynamic neural network, in the goal to forecast the electrical power of the proposed hybrid system. The first model is the nonlinear autoregressive (*NAR*), and second one is the nonlinear autoregressive with exogenous input (*NARX*) model.

*Corresponding author email: kacem_gairaa@uraer.dz

3.1. NAR model

Nonlinear autoregressive (*NAR*) model includes a set of inputs d terms lagged, y (t-1), y (t-2)… y (t-d), one hidden layer with a sigmoid activation function and n neurons, and one output layer with a linear activation function of only one neuron as shown in Fig. 5. The mathematical expression of the NAR model is as:

$$y_{(t+1)} = \sum_{i=1}^{n} \beta_i \phi(\omega_{i0} + \sum_{j=1}^{d} \omega_{ij} y(t-j)) + \beta_0 \quad (1)$$

Where: ϕ is the sigmoid transfer function, the parameters are β_i, ω_{ij} (weight), and β_0, ω_{i0} (bias). The initial conditions are (y (0), y (1)… y (d)).

3.2. NARX model

The *NARX* is a nonlinear model which estimates the future values of the time series based on its last outputs and external data. *NARX* predict series y (t+1) given d past values of series y and another external series x (t), which can be single or multidimensional. So, the *NARX* model is an important class of discrete- time nonlinear systems that can be represented mathematically as follows:

$$y_{(t+1)} = \sum_{i=1}^{n} \beta_i \phi(\omega_{i0} + \sum_{j=1}^{d} \omega_{ij} y(t-j)) + \omega_{ik} \sum_{k=1}^{d} x(t-k)) + \beta_0 \quad (2)$$

Where: ϕ is the sigmoid transfer function, the parameters are β_i, ω_{ij}; ω_{ik}; (weights), a and β_0, ω_{i0} are (bias). Here, four exogenous parameters are considered as inputs, in addition to hybrid system power: PV array power, wind turbine power, global solar radiation and wind speed.

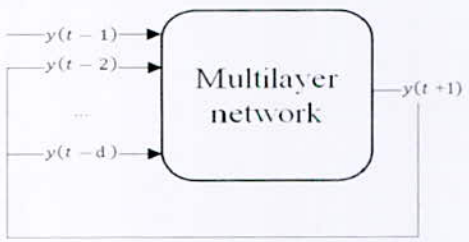

Fig. 5. NAR architecture

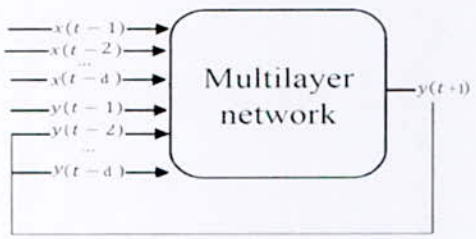

Fig. 6. NARX architecture

III. RESULTS AND DISCUSSION

The different components of the proposed hybrid system have been performed under HOMER software, taking into account the technical characteristics of system operation. The optimal configuration is found after several simulations, considering different PV, wind turbine, FC, electrolyzer, hydrogen tank, and converter capacities. Fig. 7 shows the variation of the monthly average power production. The PV is highly potential during all the year, while a fraction of 34% is produced by the wind. The share of FC is negligible.

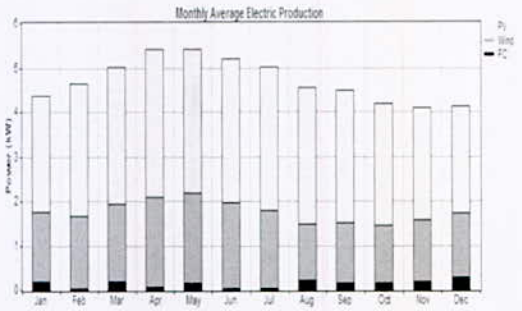

Fig. 7. Monthly average electric production

In addition, Table I summarizes the electricity production by the hybrid system. The biggest contributor in the annual energy production is the PV generator with 63% (25.869 kWh/year) of the total energy produced, followed by the wind turbine with 34% (14.196 kWh/year).

TABLE I
OPERATIONAL CHARACTERISTICS OF THE PROPOSED HYBRID SYSTEM

Annual electricity production	kWh/year	Percent
PV-array	25.86	63
Wind turbine	14.19	34
Fuel cell	1.22	3
Total	41.28	100

The simulation data obtained by HOMER (PV power, wind turbine power, global radiation and wind speed) are used as inputs in the artificial neural network in order to predict the hourly electrical power of the hybrid system thus proposed, intended to supply electricity into housing in a remote area of Ghardaïa. Therefore, two configurations are tested namely *NAR* and *NARX* as indicated above. A statistical test was performed in order to choose the architecture which

*Corresponding author email: kacem_gairaa@uraer.dz

gives the best accuracies. This test includes the root mean square error (*RMSE*), the mean bias error (*MBE*) and the correlation coefficient (R^2). Table II clarifies the statistical comparison between two models. As can be seen, the *NARX* model gives the best accuracy where the R^2 is about 0.941.

TABLE II
STATISTICAL COMPARISON BETWEEN TWO MODELS

Model	RMSE	MBE	R^2
NAR	1.977	0.015	0.919
NARX	1.697	-0.034	0.941

The scatter diagram between observed values and those estimated by *NAR* and *NARX* models shows that the dispersion between forecasted and observed values is strong in the case of *NAR* model, while it lowers in the case of *NARX* model. Measured versus forecasted (*NAR* and *NARX* models) values of the hourly electrical power for a sample of 1000 hours have been plotted in Figs. 8 and 9, respectively. We can notice that, the agreement between the forecasted values and the observed ones is better, especially in the case of the *NARX* model.

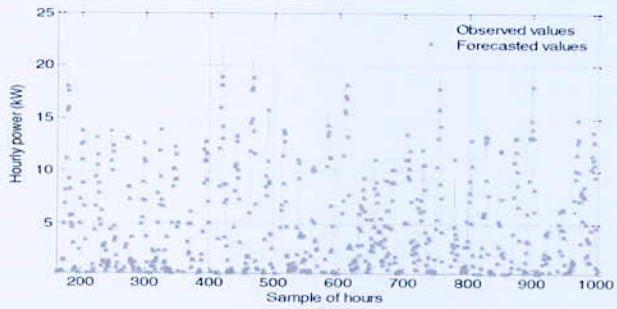

Fig. 8. Experimental and forecasted hourly electrical power of proposed hybrid system (NAR)

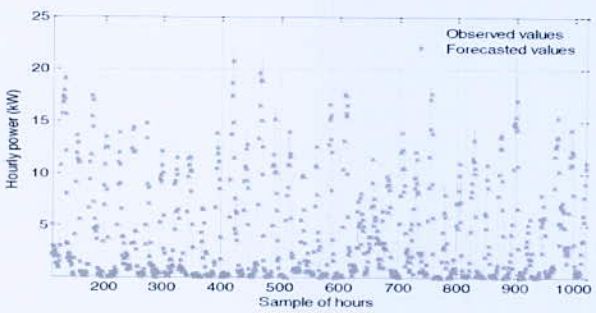

Fig. 9. Experimental and forecasted hourly electrical power of proposed hybrid system (NAR)

IV. CONCLUSION

In this work, HOMER software was used in order to optimize a hybrid renewable system (PV-Wind-electrolyzer) under Ghardaïa climate conditions. The simulation data have been exploited to forecast the hourly electrical power of the proposed system. For thus, two neuronal models were tested. NARX model has proved its effectiveness in the forecasting of electrical energy where a coefficient correlation of 94% has been found.

REFERENCES

[1] E Efstathios, "Alternative energy sources," Ed Springer, 2012.
[2] G Bekele, G Tadesse, "Feasibility study of small Hydro/PV/Wind hybrid system for off-grid rural electrification in Ethiopia," *Appl. Energ.*, Vol. 97, pp. 5-15, 2012.
[3] Y Kalinci, A Hepbasli, I Dincer, "Techno-economic analysis of a stand-alone hybrid renewable energy system with hydrogen production and storage options," *Int. J. Hydrog. Energ.*, Vol. 40, pp. 7652-7664, 2015.
[4] A Busaidi, H Kazem, A Al-Badi, M Khan, "A review of optimum sizing of hybrid PV–Wind renewable energy systems in Oman", *Renew. Sustainable Energy Rev.*, Vol. 53, pp. 185-193, 2016.
[5] T Ma, H Yang, L Lu, "A feasibility study of a stand-alone hybrid solar-wind-battery system for a remote island," *Appl. Energ.*, Vol. 121, pp. 149-158, 2014.
[6] AU Cha´vez-Ramırez, V Vallejo-Becerra, JC Cruz, R Ornelas, G Orozco, et al., "A hybrid power plant (SolareWindeHydrogen) model based in artificial intelligence for a remote-housing application in Mexico," *Int. J. Hydrog. Energ.*, Vol. 38, pp. 2641-2655, 2013.
[7] P Chatziagorakis, C Ziogou, C Elmasides, G Sirakoulis, et al., "Enhancement of hybrid renewable energy systems control with neural networks applied to weather forecasting: the case of Olvio," *Neural Comput Appl.*, Vol. 27, pp. 093-1118, 2016.
[8] EO Kenneth, P Dahramasa, R Uhunmwangho, A Richard, P Madifies, "Hydrogen production in hybrid renewable energy system and power factor improvement," in 3rd International conference on electrical energy system, 2013, pp-201-206.
[9] HOMER Energy LLC. Available from : http://homerenergy.com/index.html
[10] www.nrel.gov

*Corresponding author email: kacem_gairaa@uraer.dz

An Experimental Study of Hydrogen Enrichment on Combustion Performances of Gasoline Wankel Engine

F. Amrouche[1]*, P. A. Erickson[2], J. W. Park[2] and S. Varnhagen[2]

[1] Centre de Développement des Énergies Renouvelables, CDER, 16340, Algiers, Algeria.
[2] Mechanical and Aerospace Engineering Department, UC Davis, CA 95616, USA.

Abstract—**This paper presents the experimental results regarding the effect of hydrogen addition to gasoline in monorotor Wankel engine at wild open throttle position and lean operating regime. This was achieved by investigating the variation effects of hydrogen enrichment levels on the gasoline engine combustion performances. Testing were carried out under constant engine speed of 3000rpm and fixed spark timing of 15 °BTDC. The test results showed that hydrogen enrichment was helpful in improving combustion process through the shortened of the combustion duration. Furthermore, the increase of hydrogen fraction improves the engine economy by reducing the brake-specific energy consumption.**

Key words—Lean burn Wankel rotary engine; Hydrogen enriched gasoline; Reduced combustion duration; Engine economy.

I. INTRODUCTION

The main interest of the Wankel rotary engine is its higher power density as compared to similar conventional engine [1]. This characteristic may offer a benefits if used for extending the range of electric vehicles as well as in hybrid vehicle power [2]. However, the unusual geometry of the Wankel engine affects negatively the engine economy and the exhaust hydrocarbon emissions [1, 3]. This is mainly due to the quenching effect that happen on the large surface area of the combustion chamber walls. Additionally, the squish flow that is moving from the trailing to the leading side of the combustion chamber of the Wankel engine accelerates the flame propagation faster in the leading direction. Consequently, the remaining combustion as the trailing side is squished, is quenched by the cool housing walls, which further reduces combustion efficiency and increases unburnt hydrocarbons emissions [3]. This is the most implicated factor to the low efficiency and higher unburned hydrocarbons emissions of the Wankel rotary engine. In this paper, we have tried to consider the solutions that can help to overcome these problems by using dilute combustion and Hydrogen enrichment technologies.

Hydrogen is a renewable and clean energy sources. That is characterized by a wide flammability and low ignition energy, a high diffusion rate and a significantly faster laminar burning velocity. All of these characteristics are helpful to reduce the combustion duration within the Wankel engine [3, 4]. In addition, hydrogen's combustion characteristics can improve the engine's lean burn capability [4]. Lean combustion help to reduce the emissions of CO, HC, NOx, and is effective for improving thermal efficiency in the reciprocating engine, consequently, this kind of combustion could potentially help to resolve the Wankel engine's drawbacks [4,5].

The purpose of this paper is to investigate experimentally the effect of the addition of hydrogen on the combustion performances and the engine economy of the Wankel engine fueled with gasoline at low lean limit and full load regime.

II. EXPERIMENTAL PROCEDURE

1. Experimental setup

The engine used in this test bench was manufactured by Outboard Marine Corporation, USA. It is a 0.530L single rotor, air cooled Wankel engine, using a single spark plug.

To achieve real time control over the engine air/fuel mixture preparation as well as hydrogen addition, two fuel injection systems were added, one for gasoline and the other for hydrogen. The gasoline fuel flow was metered by a calibrated Micromotion CMF010M Coriolis flow meter with an RFT9739 transmitter with an accuracy of 0.10% of rate for flow rates of 0-23 g/s. The hydrogen used in this study was Bottled industrial hydrogen (99.95% purity) that is regulated and metered via a calibrated Aalborg differential pressure mass flow controller, model GFC 47, with an accuracy of ±3% (0-20% full scale), ±1.5% (20-100% full scale). The air mass flow was metered via a designed orifice plat. The inlet temperature information of air stream was also provided.

The spark timings, injection timings and durations of hydrogen and gasoline were controlled via a hybrid electronic control unit (HECU) developed in the laboratory.

The specific equivalence ratio of the gasoline–hydrogen–air mixture was calculated by Eq. 1 [3]:

$$\lambda = \dot{m}_{air} / \left(\dot{m}_g . AF_{st,g} + \dot{m}_{H_2} . AF_{st,H_2} \right) \quad (1)$$

$\dot{m}_{air}$ $\dot{m}_g$, $\dot{m}_{H_2}$, are respectively the measured air, gasoline and hydrogen mass flow rates (kg/h). $AF_{st,g}$ and AF_{st,H_2} are

*Corresponding author email: f.amrouche@cder.dz

the stoichiometric air-to-fuel ratios of gasoline and Hydrogen, such as $AF_{st,g} = 14.6$ and $AF_{st,H_2} = 34.3$

The energy fraction of hydrogen in the total intake gas is defined as energy fraction, calculated as follow [3]:

$$\%\,H_2 = \left[\frac{(\dot{m}_{H_2} \times LHV_{H_2})}{(\dot{m}_g \times LHV_g) + (\dot{m}_{H_2} \times LHV_{H_2})}\right] \times 100 \quad (2)$$

Where $\dot{m}_{H_2}$, $\dot{m}_g$ are respectively the mass flow rate of Hydrogen and Gasoline (g/s)

LHV_{H_2}, LHV_g are the lower heating value respectively of Hydrogen and Gasoline (MJ/Kg), such as $LHV_{H_2} = 120.1$, $LHV_g = 43.5$

A calibrated Kistler 6051B high temperature piezoelectric pressure transducer was used to capture the In-cylinder pressure data. The signal was amplified using a Kistler 5010B charge amplifier. A trigger wheel and a Hall Effect magnetic sensor system were used to obtain crank angle position data that was synchronized with the pressure trace. Cylinder pressure and crank angle signals for over 300 consecutive cycles were sampled.

A Telma CC100 eddy current dynamometer was coupled to the engine to control and measure the engine speed and torque output.

The schematic of the test bench set up can be found in ref [6]

2. *Tests conditions*

The tests were performed at an engine speed of 3000 rpm and at wide-open throttle. After a warm-up period of the engine on gasoline, the appropriate air to fuel ratio and hydrogen energy fraction was set. The engine was again allowed to come to steady state at each operating conditions and the data was collected. The hydrogen energy fraction in the total fuel energy varies from 0% to 10%. The Lean Operating Limit "LOL"of gasoline that is equal to an equivalence ratio of 0.77 was used during these tests. The spark timing was kept constant at 15 CA BTDC.

III. RESULTS AND DISCUSSION

1. *Combustion analysis*

Mass Fraction Burned (MFB) is the measure of the fraction of heat release during the combustion. This is an important parameter that define the combustion characteristics such as the combustion duration, the flame development "CA0-10", the flame propagation "CA10-90" and the central heat release "CA50". A functional form often used to represent the MFB versus crank angle curve is the Wiebe function [7, 8]:

$$X_b(\theta) = 1 - exp\,[-a*((\theta-\theta s)/\Delta\theta)^{m+1}] \quad (3)$$

Where θ is the crank angle, θ_s is the crank angle of start of ignition, $\Delta\theta$ is the total combustion duration from ($X_b = 0$) to($X_b = 1$). **a** and **m** are adjustable parameters that determine the shape of the curve, where a= 5 and m=2 [9].

Fig. 1, displays the profiles of Mass Fraction Burned (MFB) with respect to crank angle at different hydrogen energy fraction varying from 0% to 10% in air-gasoline mixture, at 3000 rpm, spark timing of 15 °BTDC and full load. As it is shown in fig. 1, the heat release is advanced and accelerated with the rise of hydrogen addition. It can also be seen that the rate of heat release for the addition of hydrogen energy fractions up to 3% are very close. This is because as the engine was running at the LOL of the original engine, the addition of small amount of hydrogen helps to improve significantly the rate of heat release. Consequently, this result indicates that heat release is boosted with hydrogen addition.

The burned fraction rate is improved since more fuel is burned earlier and faster in the cycle. This is due to the increased local laminar flame speed, enhanced flame propagation and shortened combustion durations while hydrogen was added to air- gasoline mixture. In the Wankel engine, this may help faster flame propagation in the trailing side.

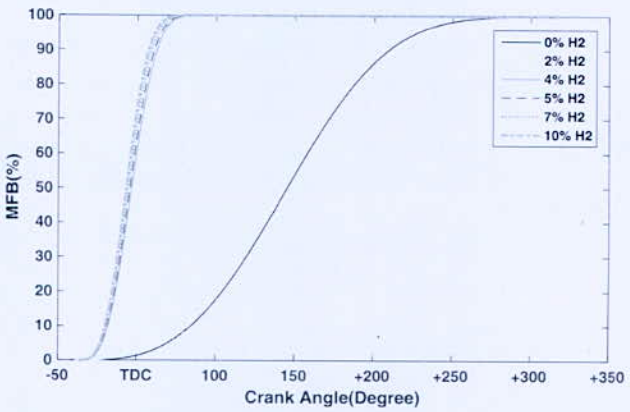

Fig. 1. Mass fraction burnt (MFB) versus crank angle at different hydrogen energy fraction levels

The combustion duration is calculated from the MFB profile. It can be seen from fig. 2 that the combustion duration was reduced as the hydrogen was added to the air-gasoline mixture.

*Corresponding author email: f.amrouche@cder.dz

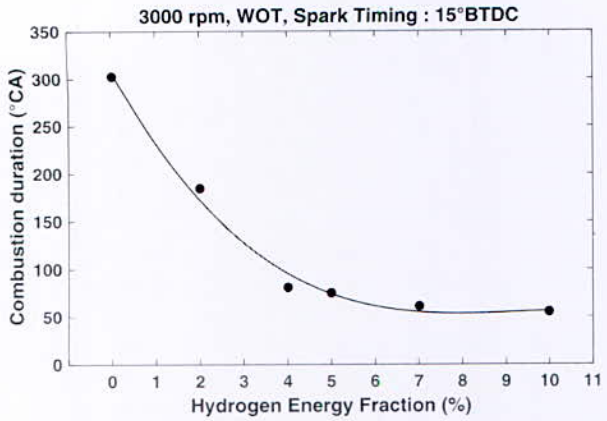

Fig. 2. Combustion duration versus crank angle at different hydrogen energy fraction levels

2. ***Engine economy***

Brake Specific Energy Consumption (BSEC) considers at the same time the flow rate and heating value of fuel. Fig. 3 shows the BSEC for the Wankel engine running with hydrogen-enriched gasoline at different hydrogen energy fraction varying from 0% to 10% in air-gasoline mixture, at 3000 rpm, spark timing of 15 °BTDC, full load and LOL of the original engine.

According to Fig. 3, the BSEC decreases from 21.37MJ/kW h for pure gasoline to 14.51MJ/kW h with an addition of 10% of hydrogen. The improved combustion efficiency and the higher specific energy value with hydrogen addition are the most obvious factors for this result.

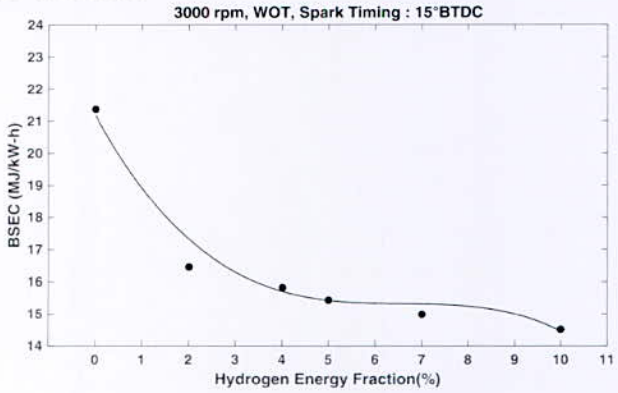

Fig. 3. BSEC versus crank angle at different hydrogen energy fraction levels

IV. CONCLUSTION

The experimental data collected through this experimental work, exhibit the ability of hydrogen enrichment technology to enhance the combustion and economic performances of Wankel engines fueled by gasoline.

ACKNOWLEDGMENTS

The authors thank Moller International for their donation of the Wankel research engines. The University of California, Davis, Green Transportation Laboratory and the Energy Research Laboratory and all their associated members made this work possible.

REFERENCES

[1] K. Yamamoto, "Rotary Engine". Tokyo (Japan): Sankaido Co., Ltd.; 1981.

[2] P. A. Salanki, J. S. Wallace, "Evaluation of the hydrogen fuelled rotary engine for hybrid vehicle application". *SAE Technical Paper* 1996; 960232.

[3] F. Amrouche, P.A. Erickson, S. Varnhagen, J. W. Park. "An experimental study of a hydrogen-enriched ethanol fueled Wankel rotary engine at ultra lean and full load conditions". *Energy Convers Manage* 2016; v 123, pp174-84.

[4] F. Amrouche, P. A. Erickson, J. W. Park, S. Varnhagen, "Extending the lean operation limit of a gasoline Wankel rotary engine using hydrogen enrichment", Int *J Hydrogen Energy* 2016; v 41, pp14261-71.

[5] F. Amrouche, P. A. Erickson, J. W. Park, S. Varnhagen, "An experimental evaluation of ultra-lean burn capability of a hydrogen-enriched ethanol-fuelled Wankel engine at full load condition", Int *J Hydrogen Energy* 2016, v 41 pp 19231 -42.

[6] F. Amrouche, P. A. Erickson, J. W. Park, S. Varnhagen, "An experimental investigation of hydrogen enriched gasoline in a Wankel rotary engine", *Int J Hydrogen Energy* 2014, v 39, pp 8525-8534.

[7] J. B. Heywood, "Internal combustion engine fundamentals", *McGraw Hill International*; 1988. ISBN: 0-07-100499-8.

[8] L. Eriksson, I. Anderson. "An analytical model for cylinder pressure in a four stroke SI engine". *SAE technical paper* 2002-01-0371; 2002.

[9] J. B. Heywood, J. M. Higgins, P. A. Watts, R. J. Tabaczynski, "Development and use of a cycle simulation to predict SI engine efficiency and NOx emissions". *SAE technical paper* 790291; 1979.

*Corresponding author email: f.amrouche@cder.dz

Le Biogaz Dopé par l'Hydrogène, une Approche pour l'Enrichissement du Biogaz au sein de la Chambre de Combustion

S. Benaissa[1*], B. Adouane[1] and C. Ghenai[2]

[1*]Département de Physique/ Laboratoire de recherche LPEA, Université de Batna1, 1 route de biskra Batna 05000 Algérie.
[2]Sustainable and Renewable Energy Engineering Department, College of Engineering, University of Sharjah, Sharjah, UAE.

***Résumé*—Le « Power-to-Gas » (P2G), est une technique nouvelle pour l'enrichissement du biogaz, elle consiste à utiliser l'excès de l'électricité du réseau pour la production de l'hydrogène par l'électrolyse de l'eau. L'hydrogène va réagir avec le CO_2 du biogaz dans un réacteur adéquat pour former du CH_4.**

Dans cette étude, on va approcher cette technique d'une façon un peu différente, et cela en dopant directement le biogaz avec l'hydrogène dans la chambre de combustion elle même.

Dans ce travail, on va présenter une modélisation numérique '3D' de la combustion du biogaz dopé avec de l'hydrogène dans une chambre de combustion d'une turbine à gaz du type cannulaire.

L'objectif principal est d'étudier comment le dopage du biogaz avec de l'hydrogène va affecter le comportement de la combustion ainsi que les émissions.

Le calcul est réalisé à l'aide du code ANSYS FLUENT 17.2, la turbulence est modélisée avec le modèle k-ε standard, et le modèle P-1 pour le rayonnement. Les résultats montrent, que l'hydrogène dans le biogaz joue un rôle important sur la température de combustion, et les émissions.

Mots clés—Power to Gas; Biogaz; Chambre de combustion tourbillonnaire « Swirl »; Émissions.

I. INTRODUCTION

De nos jours, l'un des procédés les plus importants dans la transformation de l'énergie est la combustion; elle est nécessaire pour le chauffage, la génération d'énergie électrique, le transport, les procédés de fabrication,...etc. Malgré les bienfaits de la combustion, elle reste le plus grand pollueur de notre planète. L'utilisation de nouveaux carburants tels que le biogaz pour alimenter les turbines à gaz, peut aider à sauvegarder nos énergies fossiles et réduire ainsi les impacts nocifs sur l'environnement.

Les ressources renouvelables et les nouvelles technologies vertes qui sont développées et améliorées sont un atout pour y répondre. Le biogaz est un gaz combustible renouvelable issu de la dégradation de la matière organique animale ou végétale par des micro-organismes dans des conditions anaérobies (en l'absence d'oxygène). Le biogaz possède les mêmes avantages que le gaz naturel, un transport et un stockage simples, une conversion en d'autre formes d'énergies comme la chaleur et l'électricité, et une combustion également moins polluante que d'autres combustibles fossiles, l'enrichissement du biogaz représente un intérêt pratique à fin de pouvoir l'injecter dans le réseau du gaz naturel ou l'utiliser comme un carburant de transport. Le power-to-gas « P2G », est une nouvelle approche qui gagne de l'ampleur dans le domaine de l'enrichissement du biogaz, cependant dans notre travail, on va l'approcher d'une façon un peu différente, on va doper le biogaz avec l'hydrogène et voir son effet sur la combustion. Afin de réduire davantage les NOx et d'autres polluants nocifs. M.M. Noor *et al.*[1] ont étudié numériquement la combustion du biogaz dopé par l'hydrogène dans une chambre de combustion de forme cylindrique d'extrémité ouverte avec le brûleur monté au fond de la chambre de combustion, et ont conclu de l'importance de l'AFR (rapport air/fuel) pour le biogaz mélangé avec l'hydrogène. Jahangirian *et al.*[2] ont examiné les influences thermiques et chimiques de la teneur en CO_2 du biogaz. Ils démontrent que la présence de CO_2 dans le carburant affecte considérablement les émissions des NO_X. W. Zeng *et al.*[3] a étudié expérimentalement le mélange de méthane / air dilué par N_2 et CO_2, les expériences ont été effectuées sur la température, la pression, le rapport d'équivalence et les coefficients de dilution. Les résultats suggèrent qu'une relation linéaire existe entre la température et le logarithme des temps du retard d'allumage. En outre, une augmentation du coefficient de dilution de N_2 ou de CO_2 entraîne des retards d'allumage croissants, et l'effet d'inhibition du CO_2 sur l'allumage du mélange méthane / air est plus fort que celui de N_2. Schefer *et al.*[4] ont étudié l'amélioration de stabilité de la flamme par le dopage de CH4 en H2. Leung *et al.* [5] ont étudié l'effet de l'ajout de H2 au biogaz sur l'augmentation des limites de stabilité de la flamme.

II. FORMULATION MATHEMATIQUE DU PROBLEME

La modélisation des problèmes de combustion vise la résolution des équations de l'aérothermochimie de manière à calculer, en tout point du système modélisé, les grandeurs caractéristiques du fluide.

-Equation de continuité:

$$\frac{\partial \rho}{\partial t}+\frac{\partial}{\partial x_i}(\rho u_i)=S_m \qquad (1)$$

Equation bilan de quantité de mouvement (pour la direction i):

$$\frac{\partial}{\partial t}(\rho u_i)+\frac{\partial}{\partial x_j}(\rho u_i u_j)=-\frac{\partial p}{\partial x_i}+\frac{\partial \tau_{ij}}{\partial x_j} \qquad (2)$$

Où

$$\tau_{ij}=\left[\mu\left(\frac{\partial u_i}{\partial x_j}+\frac{\partial u_j}{\partial x_i}\right)\right]-\frac{2}{3}\frac{\partial u_l}{\partial x_l}\delta_{ij} \qquad (3)$$

* Courrier électronique: sabrina.benaissa@univ-batna.dz

Équation bilan de l'énergie (pour la direction i):

$$\frac{\partial}{\partial t}(\rho E) + \frac{\partial}{\partial x_i}(u_i(\rho E + p)) = \frac{\partial}{\partial x_i}\left(k_{eff}\frac{\partial T}{\partial x_i} - \sum h_j J_j + u_j(\tau_{ij})_{eff}\right) + S_h \quad (4)$$

$$h_j = \int_{T_{ref}}^{T} c_{p,j}\, dT \quad (5)$$

$$h = \sum_j m_j h_j \text{ et que } E = h - \frac{p}{\rho} + \frac{u_i^2}{2} \quad (6)$$

Equation de conservation des espèces :

$$\frac{\partial p}{\partial t}(\rho m_i) + \frac{\partial}{\partial x_i}(\rho u_j m_i) = -\frac{\partial}{\partial x_i}J_{i,j} + R_i + S_i \quad (7)$$

$$J_{i,j} = -\left(\rho D_{i,m} + \frac{\mu_t}{Sc_t}\right)\frac{\partial m_i}{\partial x_i} \quad (8)$$

$$R_i = M_i \sum_{k=1}^{N_R} \upsilon'_{i,k} M_i AB \rho \frac{\varepsilon}{k} \frac{\sum_p m_p}{\sum_j^N \upsilon'_{j,k} M_j} \quad (9)$$

Dans les équations ci-dessus, S_m est la masse ajoutée à la phase continue, S_h comprend la chaleur de la réaction chimique et S_i est le taux de création par addition de la phase dispersée. Le modèle de turbulence choisi est k-ε. Ces équations sont résolues avec la méthode de volume fini.

III. MODELE GEOMETRIQUE

La géométrie de base de la chambre de combustion de la turbine à gaz est représentée sur la figure 1. Les dimensions de la chambre de combustion sont de 590 mm dans la direction Z, 220 mm dans la direction Y et 250 mm dans la direction X. L'air primaire est guidé par des ailettes pour donner à l'air une composante de vitesse de tourbillonnement. Le diamètre de l'entrée de l'air primaire est de 100 mm. Le carburant est injecté à travers six entrées. Le diamètre de l'injecteur de carburant est de 4.2 mm. L'air secondaire est injecté dans la chambre de combustion à travers six entrées d'air latérales, chacune avec une surface de 33.50 mm^2. La sortie de la chambre de combustion a une forme rectangulaire avec une surface de 15000mm^2.

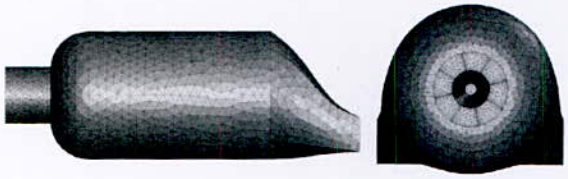

Fig. 1. Modèle de la chambre de combustion: avec le maillage

IV. RÉACTION CHIMIQUE

L'équation générale de la combustion d'hydrocarbure stœchiométrique est :

$$C_nH_m + (n + \frac{m}{4})(O_2 + 3.76N_2) \rightarrow nCO_2 + \frac{m}{2}H_2O + 3.76(n + \frac{m}{4})N_2 \quad (10)$$

Pour le méthane on a :

$$CH_4 + 2O_2 + 7.53N_2 \rightarrow CO_2 + 2H_2O + 7.53N_2 + \text{Chaleur}\left(1.013\ \text{Btu/ft.}^3\right) \quad (11)$$

Réaction chimique du biogaz:

$$(1-\alpha)\left[CH_4 + \frac{1+\varphi}{\varphi}(O_2 + 3.76N_2)\right] + \alpha CO_2 \rightarrow CO_2 + 2(1-\alpha)H_2O + 7.52(1-\alpha)N_2 + \frac{1-\varphi}{\varphi}(1-\alpha)(O_2 + 3.76N_2) \quad (12)$$

α ,φ est la fraction molaire du dioxyde de carbone et le rapport d'équivalence

Pour φ=1 :

$$0.6CH_4 + 0.4CO_2 + 1.2(O_2 + 3.76N_2) \rightarrow CO_2 + 1.2H_2O + 4.512N_2 \quad (13)$$

-Réaction chimique du biogaz dopé par l'hydrogène :

$$(iCH_4 + jH_2 + kCO_2) + (2i + 0.5j)(1.0O_2 + 3.8N_2) \rightarrow (i + k)CO_2 + (2i + j)H_2O + (7.6i + 1.9j)N_2 \quad (14)$$

Où i, j et k sont la fraction molaire du méthane, de l'hydrogène et de dioxyde de carbone. La composition du biogaz dopé par l'hydrogène est présentée dans le tableau 1 pour un pouvoir calorifique fixe.

Pour un biogaz avec une composition typique de 64% méthane de 15%, hydrogène 21% de gaz carbonique on a cette équation de combustion stœchiométriques :

$$(0.64CH_4 + 0.15H_2 + 0.21CO_2) + 1.355(1.0O_2 + 3.8N_2) \rightarrow (0.85CO_2 + 1.43H_2O + 5.149N_2) \quad (15)$$

Cette équation correspond un rapport d'équivalence φ=1

TABLEAU I
COMPOSITIONS DU BIOGAZ DOPE PAR L'HYDROGENE

Compositions	Biogaz	Bio+hyd 1	Bio+hyd 2	Bio+hyd 3	Bio+hyd 4
Ch_4%	60	76	64	52	50
H_2%	0	10	15	20	21
Co_2%	40	14	21	28	29
PCI (MJ/Kg)	30.00	50.00	50.00	50.00	50.00

V. CALCUL DE PUISSANCE

La puissance (W) peut être calculée en multipliant le débit massique (kg / s) du carburant par la valeur de pouvoir calorifique inferieur (kJ / kg).

Le carburant est injecté à travers six petites entrées, chacune avec une surface de 0.14 cm^2 Le gaz est injecté dans la chambre de combustion avec une vitesse de 40 m/s. Le débit massique dépend de la densité du fluide. La densité du carburant est de 0.9034 (kg/m^3)

- Alors le débit massique est 3.0354*10^{-3} (kg/s)

* Courrier électronique: sabrina.benaissa@univ-batna.dz

La Puissance peut être calculée comme ci-dessous. Si on prend le pouvoir calorifique du méthane pur qui est 55.0 MJ / kg.

q = débit massique x pouvoir calorifique du méthane
$=3.0354*10^{-3}$ (kg/s) x 55,0 MJ / kg =166.947 KW

VI. CONDITIONS AUX LIMITES ET LE MAILLAGE

Le domaine de calcul utilisé est en 3D. Concernant les conditions aux limites et initiales traitant d'un solveur d'écoulement totalement compressible. Trois conditions d'entrée et une sortie indiquée dans le tableau 2. Les mailles de forme tétraédrique non structurée avec 31433 nœuds, 106 651 cellules ou éléments et 234368 faces. La méthode du volume fini et la méthode du premier ordre ont été utilisées pour résoudre les équations gouvernantes Les critères de convergence ont été fixés à 10^{-3} pour la continuité, la quantité de mouvement, l'énergie cinétique turbulente, le taux de dissipation de l'énergie cinétique turbulente et la fraction du mélange. Pour les équations d'énergie et de rayonnement, les critères de convergence ont été fixés à 10^{-6}. Les méthodes de modélisation du taux de réaction turbulent moyen peuvent être basées sur les méthodes de moment ou de fonction de densité de probabilité (PDF). ANSYS FLUENT utilise l'approche PDF.

TABLEAU II
CONDITIONS AUX LIMITES D'ENTREE DE CARBURANT

Conditions d'injection de carburant et d'air	Values
Vitesse d'air primaire (m/s)	10
vitesse d'air secondaire (m/s)	40
Vitesse du carburant (m/s)	6
Intensité du Air et carburant%	10
Températures de carburant et d'air (K)	300
Fraction de mélange pour le carburant	1
Fraction de mélange pour l'air	0

VII. RESULTATS ET DISCUSSION

Compte tenu de notre modèle numérique de la combustion de biogaz dopé par l'hydrogène, au premier lieu on a fait une validation avec le biogaz, les résultats du calcul numérique sont en bonne concordance ''figures 1-4''. Le biogaz ($\%CH_4$=64, $\%CO_2$=40) est utilisé comme référence pour les carburants, qui sont indiqué dans le '' ''tableau1'', avec des vitesses de l'air et de fuel constantes. Les résultats de la simulation ont été présentés en termes de température et émissions des polluants NO, CO et CO_2. La Figure 2 montre les résultats numériques concernant la distribution de la température le long de l'axe central de la chambre de combustion. La première remarque est que la température de combustion du mélange biogaz plus H_2 diminue en ajoutant de l'hydrogène davantage. La température maximale de gaz est située dans la zone secondaire (z = 0.25m). Dans la région de l'injection de carburant à z = 0.1m, la température à l'axe central de la chambre de combustion diffère nettement pour les différents carburants. Il y a une augmentation de la température graduellement due à la progression des réactions chimiques à l'intérieur de la chambre de combustion, puis une diminution en raison de l'effet de refroidissement par l'air secondaire.

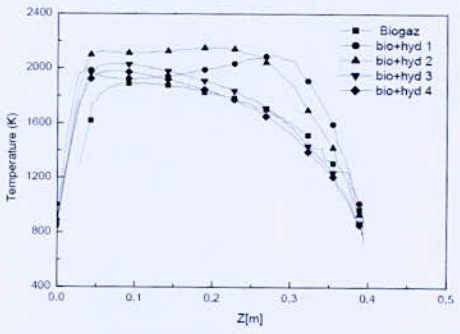

Fig. 2. Distribution de la température

Pour NO ; on a utilisé deux mécanismes de formation à savoir, NO Thermique et NO prompt. Le niveau d'émission de pollution dans une chambre de combustion dépend de l'interaction entre le processus physique et chimique et dépend fortement de la température. Dans le modèle thermique, l'oxydation contrôlée par la température de N_2 conduit à la formation de NO dont le niveau d'émission change avec la distance axiale. La formation du NOx thermique est déterminée pour des températures très élevées au milieu oxydant, utilisant le mécanisme prolongé de Zeldovich[4].

$$N_2 + O \Leftrightarrow NO + N$$
$$N + O_2 \Leftrightarrow NO + O \quad (16)$$

La troisième réaction a été montrée pour contribuer à la formation du NO_x thermique, en particulier aux conditions proches de stœchiométriques et pour les mélanges carburant-riches :

$$N + OH \Leftrightarrow NO + H \quad (17)$$

Le mécanisme du prompt NO est le mécanisme de formation de NO qui fait intervenir les radicaux hydrocarbonés CH et CH_2.

$$CH + N_2 \rightarrow HCN + N$$
$$CH_2 + N_2 \rightarrow HCN + NH \quad (18)$$

HCN est par la suite oxydé en NO en formant également plusieurs autres composés intermédiaires. Ce mécanisme est prépondérant dans les zones riches en combustible. Le carburant ici a eu suffisamment de temps pour permettre à N_2 de réagir avec O_2 et de former NO. À mesure que la température augmente dans la direction axiale, l'oxydation de N_2 augmente, ce qui augmente l'émission de NO. La figure 3 montre la fraction massique de NO pour des différents carburants sur la distance axiale.

* Courrier électronique: sabrina.benaissa@univ-batna.dz

On remarque sur cette figure un phénomène très intéressant, il s'agit de la formation de NO qui commence tôt dans le cas où le taux de H_2 ajouté est élevée, ce qui donne une bonne occasion à l'NO formé de réagir avec un autre NO formé et former ensemble de l'azote moléculaire N_2, ce qui réduira davantage les émissions totales de NO_x à la sortie de la chambre de combustion.

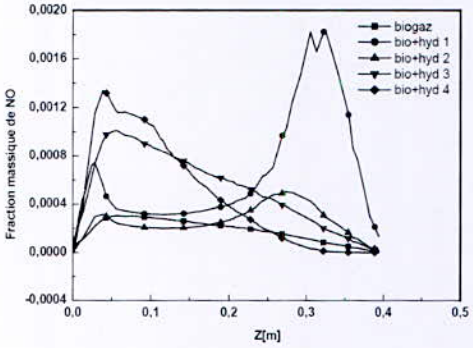

Fig. 3. Distribution de la fraction massique de NO

La figure 4 présente la variation de la fraction massique de CO en fonction de la distance longitudinale de la chambre de combustion. La figure montre le taux élevé de CO pour le mélange carburant à bas H_2, ce qui est logique, car en augmentant le H_2 dans le carburant, une partie de CH_4 est substitutée par le H_2 afin de garder un pouvoir calorifique fixe, après on peut voire clairement que le 'burnout' de CO fait diminuer le CO aux limites acceptables.

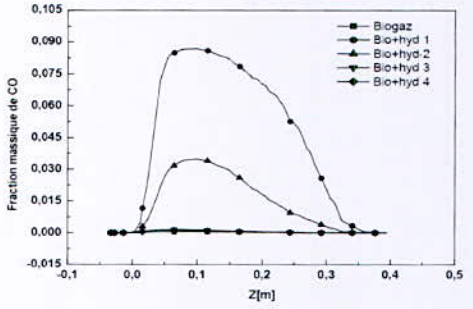

Fig. 4. Distribution de la fraction massique de CO

La distribution du CO_2 dans la chambre de combustion est présentée dans la figure 5. Cette figure montre que La fraction de masse de CO_2 à l'intérieur de la chambre de combustion augmente à partir de Z=0.1m, zone de conversion de CO en CO_2, après il diminue a cause de l'air de dilution

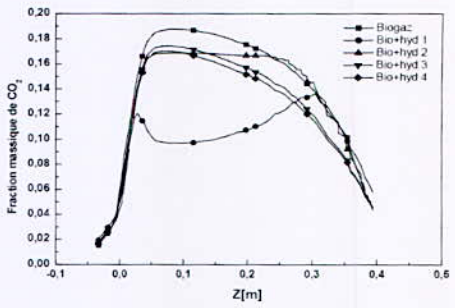

Fig. 5. Distribution de la fraction massique de CO_2

VIII. CONCLUSION

La combustion du biogaz dopé par l'hydrogène dans une chambre de combustion d'une TAG, de type cannulaire est étudiée. La turbulence est modélisée par le modèle standard k-ε. Les analyses ont été effectuées pour la chambre non-prémélangée, en utilisant le logiciel ANSYS Fluent 17.2. les conclusions suivantes sont à noter:

1- L'addition de H_2 dans le biogaz, améliore la stabilité de la flamme ainsi que les émissions.
2- La température de combustion est réduite et l'on diminue ainsi les émissions de NO_x.
3- Les zones de dilution de l'air jouent un rôle important pour la stabilité de la flamme, et pour la formation de NOx.
4- Les effets positifs de l'addition de H_2 commencent à partir d'un seuil minimum.

REFERENCES

[1] M. M. Noor, M. M. Rahman, and J. Ismail, "The air fuel ratio study for the mixture of biogas and hydrogen on mild combustion," presented at Malaysian Postgraduate Conference, Sydney, New South Wales, Australia, 4-5 July2013.

[2] Jahangirian and A. Engeda, "Thermal and Chemical Structure of Biogas Counterflow Diffusion Flames," *Energy&Fuels*, vol. 23, pp. 5312-5321, 2009.

[3] W. Zeng, H. Ma, Y. Liang, and E. Hu, "Experimental and modeling study on effects of N2 and CO2 on ignition characteristics of methane/air mixture," *journal of advanced research*, pp. 189-201, 2015.

[4] Schefer and R. W., "Combustion of Hydrogen-Enriched Methane in a Lean Premixed Swirl-Stabilized Burner," *Proceeding*, pp. 843-851, 2002.

[5] Leung and Wiezba, "The Effect of Hydrogen Addition on Biogas Non-Premixed Jet Flame Stability in a co-Flowing Air Stream," *International Journal of Hydrogen Energy*, vol. 33, pp. 3856-3862, 2008.

[6] Cathonet, *Cinétique chimique de la combustion*, 2002.

* Courrier électronique: sabrina.benaissa@univ-batna.dz

A Stand-alone Power Generation System Based on Wind-Hydrogen Energy Technology

F. Meziane [1, 2*], F. Chellali[3], K. Mohammedi[2], N. Kabouche[1], I. Nouicer[1], R. Boudries[1]

[1] Centre de Développement des Energies Renouvelables, CDER, 16340, Algiers, Algeria
[2]MESOnexus Team / URMPE, University of M'Hamed Bougara, Boumerdès 35000, Algeria
[3]Department of Electrical Engineering, University of Ziane Achour, Djelfa,17000 Algeria

Abstract— **The development of hybrid systems for electricity generation from renewable energies in remote locations, and minimizing environmental risks, is a viable and sustainable solution. The present study deals with the performance and energy analysis of a hybrid wind-hydrogen power system. A dynamic model of Wind-Electrolyzer-fuel cell hybrid system developed under Simulink environment is presented. The proposed configuration is used to supply energy demand of set of ten households and improving the utilization of wind power at the site of Hassi R'mel. Such system consists of wind turbine, electrolyzer, and fuel cell The advantage of this system is a clean production at the location of the consumption (autonomous system) and the pooling of resources. The system optimization is carried out using HOMER software. The optimal system is composed of a wind turbine ENERCON E33 with rated power of 330 KW, an electrolyzer of 4 kW, and a Fuel cell with 4 kW rated power. The electricity delivery cost has been found to be 2.621 $/kWh.**

Key words— Hybrid systems, electricity generation, renewable energies, performance, wind, hydrogen, Hassi R'mel, autonomous system, Homer.

I. INTRODUCTION

Algeria is blessed with an important renewable energy potential, more particularly solar, wind and biomass [1]. One of the most important renewable sources is wind energy. As reported by Chellali et al [2] Algeria is generally quite windy, at 10 m above ground level 78% of the country area is characterized by wind speeds exceeding 3 m/s, with about 40% of these speeds above 5 m/s. This important wind potential allows solving global energy problems. Therefore, wind energy represents an important potential to be exploited, to be a vital source of electric power generation. Because of the intermittent nature of wind energy, a policy of energy development combining wind energy and hydrogen to meet the energy demand is required, especially for remote area in the south of the country. Some studies have been reported in the literature to wind energy conversion systems, Fuel cell power systems (WECS-FC). Among them, Onar et al. [3] designed and modeled a wind-fuel cell-ultra capacitor based hybrid system for grid-independent applications. They developed a detailed dynamic simulation model which allows designing and analyzing any wind-fuel cell-ultra capacitor hybrid system with various parameters and power levels. Leva and Zaninelli [4] designed wind/FCs hybrid power system to produce, distribute, and consume the energy in a remote house with a specific load located in Milano, Italy. Panapakidis et al. [5] suggested wind/Fuel cell hybrid system to meet the load requirements of a typical residence in Greece. Mills and Khan and Iqbal [6] introduced wind/fuel cell hybrid system to meet the typical household electric load requirement in Canada. Korpa et al [7] have shown different possibilities of combining wind and hydrogen in low production networks. They examined the benefits, hydrogen storage limits and its various applications, and presented a logistic simulation model for evaluating the performance of wind-hydrogen plants. The results illustrate the benefits of storing hydrogen and its use for electricity production in periods when the wind speed is low. Ulleberg et al. [8] studied hydrogen production efficiency in an autonomous wind-hydrogen system which located at Utsira, Norway. This system provided all of the energy demand of 10 houses on the island. It is found that it is possible to supply remote area communities with wind power using hydrogen as the energy storage medium. However, further technical improvements and cost reductions need to be made before wind/hydrogen systems can compete with wind/diesel hybrid power systems.

In the present study, we consider the case of providing electricity to the site of Hassi R'mel considered as isolated area. As wind is the most important renewable energy source in the area, electricity is generated using a wind energy conversion system (WECSs) and hydrogen as the storage medium.

The mismatch between load demand and wind generation due to the intermittent nature of the wind source, can be compensated by combining wind generation with fuel cell.

II. WIND DATA AND SITE SELECTION

The site of Hassi R'mel is located in the northern Sahara of Algeria, it is characterized by a hilly topography, and the average altitude is about 750 m above the sea level. In Arabic terminology, the name Hassi-R'mel means the source of sand. The nomads of the region have given this name to this region because it is characterized by heavy sand storms. Located between the region of the continental climates and the Saharan

*Corresponding author email: w_fares2002@yahoo.fr

climate region, it is considered to have a desert climate. This climate is characterized by low rainfall of 140 mm / year, and an average humidity of 19% in summer and 34% in winter. The geographical location of this site is shown in Fig. 1

Fig.1. Location of the wind measurement station

The wind speed data measurement provided by the National Office of Meteorology (N.O.M) were collected at 10 m above ground level; and registered every one hour interval from January 2009 to December 2015 at the site of Hassi R'mel. The wind data measurement station lies in the south of Algeria. The characteristics of the studied site are also shown in Table 1

TABLE I
GEOGRAPHICAL COORDINATES OF THE MEASUREMENT STATION

Location	Long (deg)	Lat (deg)	Alt (m)
H-R'mel	03.26° E	32.93° N	682

III. SYSTEM DESCRIPTION

In this section, the detailed dynamic simulation model is briefly described for Wind-Fuel cell power generation system. The model developed under Simulink environment consists of a wind energy system, an electrolyzer, a Proton Exchange Membrane (PEM) fuel cell, a power control system, and hydrogen storage system. Fig 2 shows the complete block diagram of the stand-alone Wind-Fuel cell system.

The main components of the system are: wind turbine, electrolyzer, and fuel cell.

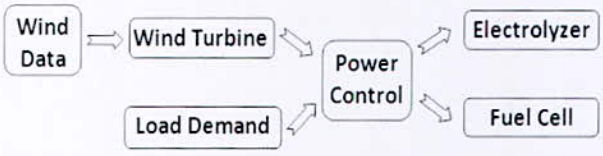

Fig.2.System diagram

When the electrical power produced by the wind generator is greater than the instant load requirement, the excess power is used for the power output is less than the load requirement, the extra power is delivered by the fuel cell consuming the hydrogen previously stored.

1. Wind turbine

The ENERCON E 33 wind turbine is characterized by a "cut-in wind speed" of 2.5 m/s that is inferior to the mean wind speed observed at Hassi R'mel (i.e.; 6 m/s). The rated speed of 12 m/s, and the corresponding rated power of 330 kW for winds attaining the speed of 12 m/s are considered as others criterions added to the raison of our choice. The power output of this machine was evaluated at different hub heights. This evaluation confirms that this wind turbine can be used to supply remote regions with more important electricity demand without conjunction with other energy resources (solar and/or diesel) in order to compensate wind energy output fluctuations. The wind power curve of the ENERCON E33 wind turbine is given in Fig. 4.

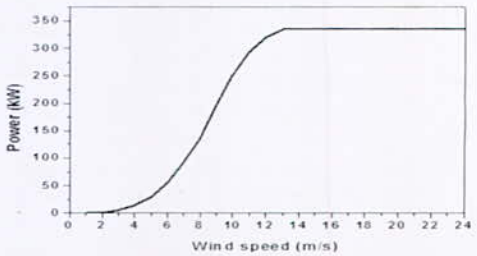

Fig.3.Enercon E33 wind turbine power curve

The Simulink model of the wind turbine is shown in Fig.5

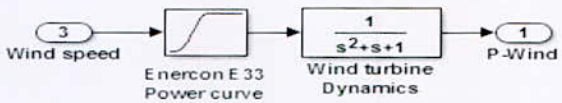

Fig.4.Enercon E33 wind turbine power curve

2. Electrolyzer model

The decomposition of water into hydrogen and oxygen can be achieved by passing an electric current between two electrodes separated by an aqueous electrolyte [25, 26]. The electrochemical reaction of water electrolysis is given by (1):

$$H_2O(l) + Electrical\ energy \Rightarrow H_2(g) + \frac{1}{2}O_2(g) \qquad (1)$$

According to Faraday's law [3], the production rate of hydrogen in an electrolyzer cell is directly proportional to the transfer rate of electrons at the electrodes, i.e., the current flowing through the electrodes.

$$n_{H2} = \frac{\eta_F \times n_c \times i_e}{2 \times F} \qquad (2)$$

Because of charge losses, the actual amount of produced hydrogen is smaller than the theoretical amount of produced hydrogen. The ratio between the actual and the theoretical maximum amount of hydrogen produced in the electrolyzer is known as Faraday efficiency. Assuming that the working temperature of the electrolyzer is 40 °C, Faraday efficiency is given by [6].

*Corresponding author email: w_fares2002@yahoo.fr

$$\eta_F = 96.5 \times \exp\left(\frac{0.09}{i_e} - \frac{75.5}{i_e^2}\right) \quad (3)$$

According to (2) and (3) a simple electrolyzer model is developed using Simulink, which is illustrated in Fig.5.

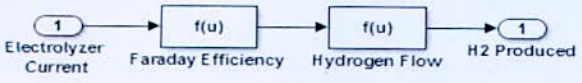

Fig.5.Electrolyzer model developed under Simulink

3. *Fuel Cell model*

The dynamic model of the fuel cell developed under Simulink environment is shown in Fig.6.

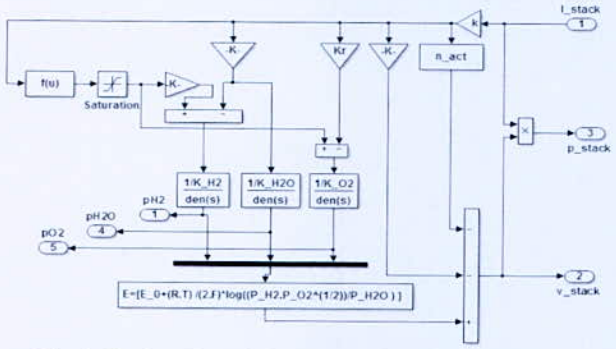

Fig.6. Fuel cell model developed under Simulink

The model input is the Current, and the outputs are stack power and stack voltage respectively.

IV. LOAD DEMAND

The load demand considered is for a set of ten households situated in Hassi R'mel (South of Algeria). The seasonal profile is shown in Fig.7. It shows a relatively constant power demand over all the year except months from June to September where the demand is considered a little less compared to the other months.

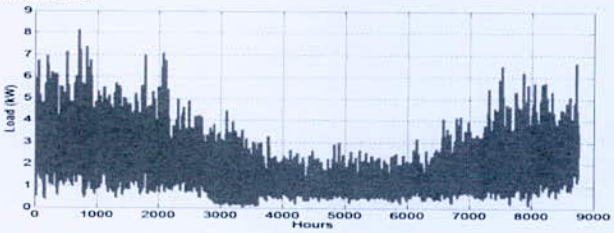

Fig.7. Primary load

V. RESULTS AND DISCUSSION

The hourly wind speed variation at 50 m at the site of Hassi R'mel is shown in Fig 8. The annual mean wind speed at 50 m above the ground level is about 6 m/s. The maximum wind speed is reaching 7 m/s in April, while the minimum wind speed of 5 m/s is occurred during October.

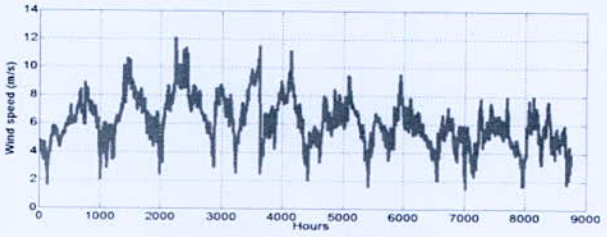

Fig.8.Wind speed at 50 m

The profile of the power electric produced by the ENERCON E33 at 50 m is shown in Fig.9.

The maximum power is occurred in April approximately 200 kW, and the minimum of the production is reached in October 70 kW.

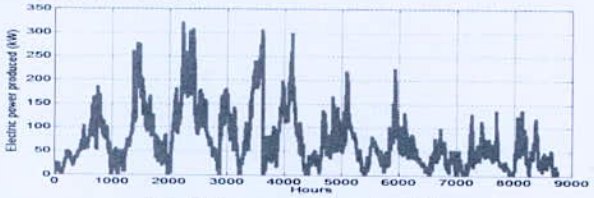

Fig.9.Power produced at 50 m

Fig.10 shows the excess of energy produced that converted to hydrogen for storage.

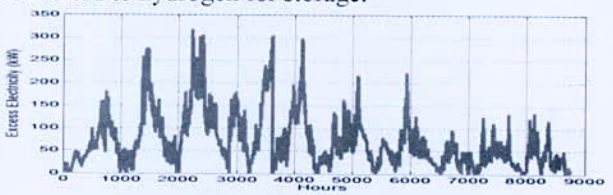

Fig.10.Power excess

The hydrogen flow produced from the excess of electricity is shown in Fig.11.

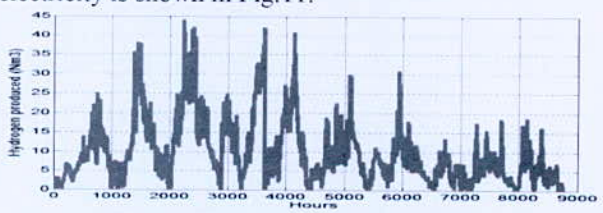

Fig.11. Hydrogen produced at 50 m

The annual average hydrogen production quantity is 7200 Nm^3; while the maximum of production is occurred during April 13230 Nm^3, and the minimum quantity during October about 3575 Nm^3.

VI. OPTIMUM HYBRID SYSTEM

Simulation tools are the most common tools for evaluating the performance of the Hybrid systems. Optimum configuration can be found by using computer simulations, by comparing the performance and energy production cost of different system configurations.

HOMER (Hybrid Optimization Model for Electric Renewable) is user friendly software produced by national renewable energy laboratory. It uses hourly simulations and environmental data for the assessment of the hybrid renewable energy system and performs optimization based on Net Present Cost (NPC).

*Corresponding author email: w_fares2002@yahoo.fr

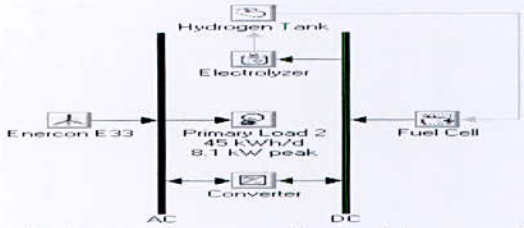

Fig.12. Autonomous system for electricity generation

The considered system Fig.12 consists of an ENERCON E33 wind turbine, which has a rated power of 330 kW AC. It has a lifetime of 20 years with a hub height varying from 37 m to 50 m. The typical power curve of this turbine is shown in Fig.3. The capital cost of this turbine is at 900000 US $ with the replacement assumed at 15000 $ and the operation/maintenance costs at 750$/year.

The electrolyzer has a capital cost of 2000 $ and a lifetime of 20 years. Again the replacement cost is assumed to be 1500 $, with the operation/maintenance costs at 25 $/year.

The system contains a Fuel Cell with a capital cost of 3000 $, the replacement cost is assumed at 1500 $, with the operation/maintenance costs at 175 $/hr, and a life time of 5000 hours.

The hydrogen storage system has a capital cost of 1300 $, with the same replacement cost and operating and maintenance cost of 25 $/year.

The capital cost of the converter is fixed at 800$ at the same replacement price and no operating/maintenance costs. These have 15-year lifetime and 90 % efficiency.

Sensitivity Results | Optimization Results |

Double click on a system below for simulation results

	E33	FC (kW)	Conv (kW)	Elec (kW)	H2 Tank (kg)	Initial Capital	Operating Cost ($/yr)	Total NPC	COE ($/kWh)	Ren. Frac.	FC (hrs)
	1	8	4	4	4	$ 907,213	6,732	$ 1,075,525	2.621	1.00	13
	1	8	4	5	4	$ 907,547	6,750	$ 1,076,300	2.623	1.00	13
	1	8	6	4	4	$ 907,453	6,759	$ 1,076,425	2.623	1.00	13

Fig.13. Optimized system

Fig.13 shows the details of the optimized system.
The optimum system (system with minimum total net present cost (NPC)) for the stand alone power system includes a Wind Turbine (WT) 330 kW, Fuel Cell (FC) 8 kW, converter (CON), 4kW electrolyzer (ELC) and 4kg H2 tank (HT). The initial capital cost (ICC) of the whole system is $ 907.213. The cost of energy (EC) is calculated as 2,621$/kWh.

VII.CONCLUSION

In this study a stand-alone wind-hydrogen based system has been considered; a dynamic model of the system has been developed under Simulink environment for power supplying a set of ten household in the site of Hassi R'mel located in the south of Algeria. When the wind speed is sufficient, the wind turbine meets the load. If the available power from the wind turbine cannot satisfy the load demand, the FC system can meet the excess power demand by converting the stored hydrogen to power electric. The system optimization is carried out using HOMER software. The optimal system is composed of a wind turbine ENERCON E33 with rated power of 330 KW, an electrolyzer of 4 kW, and a Fuel cell with 4 kW rated power. The electricity delivery cost has been found to be 2.621 $/kWh. It has successfully demonstrated that wind energy is another alternative option to adopt in Hassi R'mel which possesses a potential of wind energy in addition to solar energy that can be economically beneficial to Algeria.

APPENDIX

F: Faraday constant [C kmol-1]
HOMER: Hybrid Optimization Model for Electric Renewable
i_e: Electrolyzer current [A]
n_c: number of Electrolyzer cells in series.
η_F: Faraday efficiency.
n_{H2}: produced hydrogen moles per second [mol.s-1].
NPC: Net present cost.

REFERENCES

[1] A. Boudghene Stambouli , Z. Khiat , S. Flazi , Y. Kitamura, " A review on the renewable energy development in Algeria: Current perspective, energy scenario and sustainability issues", Renewable and Sustainable Energy Reviews 16 (2012) 4445–4460.

[2] F. Chellali, A. Khellaf, A. Belouchrani, A. Recioui. "A contribution in the actualization of wind map of Algeria". Renewable and Sustainable Energy Reviews 2011; 15: 993–1002.

[3] O.C. Onar, M. Uzunoglu, M.S. Alam, "Dynamic modeling, design and simulation of a wind/fuel cell/ultra-capacitor-based hybrid power generation system", Department of Electrical and computer Engineering, University of south Alabama, Mobile, AL 36688, USA, May 2006.

[4] S. Leva, D.Zaninelli, "Hybrid renewable energy-fuel cell system: Design and performance evaluation"; Electric Power systems research 79(2), 316-324, 2009.

[5] IP. Panapakidis, Minas C Alexiadis, "Comparative analysis of different grid independent hybrid power generation systems for residential load", Renewable and sustainable energy Reviews, 551-563, (2012).

[6] M. J .Khan, M.T. Iqbal; « Analysis of a small wind-hydrogen stand-alone hybrid energy system. », Applied Energy 86 (2009) 2429–2442.

[7] Magnus Korpa, Christopher J. Greinerb, « Opportunities for hydrogen production in connection with wind power in weak grids », Renewable Energy 33 (2008) 1199–1208.).

[8] Ulleberg Ø, Nakken T, Ete A. The wind/hydrogen demonstration system at Utsira in Norway: Evaluation of system performance using operational data and updatedhydrogen energy system modeling tools. Int J Hydrogen Energ 2010;35:1841-52.

*Corresponding author email: w_fares2002@yahoo.fr

Étude Numérique du Transfert de Chaleur et de Masse Dans un Réacteur D'hydrure Métallique

B. Dadda[1*], A. Babbou[1], R. Zarrit[1], S. Abboudi[2]

[1] Unité de Recherche Appliquée en Energies Renouvelables, URAER, Centre de Développement des Energies Renouvelables, CDER 47133, Ghardaïa, Alegria.
BP : 88 Z.I Bounoura Ghardaïa, Tél : 029 87 01 26 / Fax : 029 87 01 46
[2] UTBM, Laboratoire M3M, site de Sévenans, 90010 Belfort Cedex.

***Résumé*—Dans ce papier, on présente une étude numérique du transfert de chaleur et de masse dans un réacteur d'hydrure métallique. Le transfert est supposé bidimensionnel et transitoire. Le système d'équations régissant les phénomènes de transfert est basé sur le principe de conservation de la masse, de la quantité de mouvement et de l'énergie. La résolution numérique du modèle est basée sur la méthode des volumes finis.**

Les résultats obtenus montrent une bonne cohérence avec ceux de la littérature. Les évolutions de la température et de la densité de l'hydrure au sein du réacteur sont présentées et discutées pour différents instants.

Mots clés—Hydrures métalliques, transfert de chaleur, transfert de masse, volumes finis.

I. INTRODUCTION

Dans le stockage de l'hydrogène, les hydrures métalliques sont considérés comme la nouvelle alternative. En général, les hydrures métalliques sont des combinaisons d'un métal "A" qui peut absorber l'hydrogène indépendamment (La, Ti, Zr, Mg et Ca) avec un métal "B" ne pouvant pas absorber l'hydrogène (tels que Fe, Ni, Mn, Co) [1]. Les exemples d'alliages de stockage d'hydrogène les plus courants sont Fe-Ti, La-Ni, Mg et Ti-Zr [2]. Les hydrures métalliques ont la propriété d'absorber et de désorber l'hydrogène selon la pression appliquée. Plusieurs applications ont été développées pour profiter de ces propriétés, à savoir ; les batteries rechargeables, l'accumulateur d'hydrogène, l'accumulateur de chaleur, les pompes à chaleur, les échangeurs de chaleur, les réfrigérateurs, les compresseurs thermiques et les systèmes de stockage de chaleur et de l'hydrogène. Il est très important de maitriser le transfert de chaleur et de masse dans les réacteurs d'hydrures métalliques durant l'absorption et la désorption de l'hydrogène afin de mieux l'optimiser.

Différentes tentatives ont été faites pour analyser le comportement de l'hydrure durant le phénomène de sorption [3-8] et de désorption [9-11].

Le modèle unidimensionnel utilisé par Mayer *et al.* [9] et les modèles bidimensionnels de Sun et Deng [10] et Pons [11] supposent que les températures du gaz et du solide sont égales et que la pression du gaz dans le réacteur est constante. Dans ce papier on s'intéresse à l'étude théorique du transfert thermique bidimensionnel durant l'absorption dans un réacteur d'hydrure métallique. Pour un premier temps, nous présentons le système d'équation gouvernant le transfert de chaleur et de masse dans le réacteur durant l'absorption. Le système d'équations a été résolu numériquement en utilisant la méthode des volumes finis. La simulation numérique nous a permis de tracer l'évolution spatio-temporelle de différentes variables d'état (température, pression et densité de l'hydrure) dans le réacteur et de déterminer la sensibilité du transfert de chaleur et de masse à quelques-uns de ces paramètres (la pression de sortie, la température du fluide, la conductivité thermique effective du solide et la géométrie du réacteur).

II. FORMULATION MATHEMATIQUE

Le réacteur cylindrique de dimensions (H = 3 cm) × (R = 5 cm) est entouré d'un liquide de refroidissement. Ce refroidissement a pour objectif de garantir efficacement la poursuite de la réaction. Le réacteur cylindrique considéré est muni d'un échangeur de chaleur sur sa surface latérale et sa base (Fig1). La température et le débit d'écoulement dans l'échangeur de chaleur sont considérés constants. Les équations obtenues à partir des lois de la mécanique et de la thermodynamique sont celles des bilans de masse, de chaleur et de quantité de mouvement. Quelques hypothèses sont considérées pour simplifier le modèle :

- Le travail de la compression et la dissipation visqueuse sont négligeables.
- L'hydrogène est un gaz parfait d'un point de vue thermodynamique.
- Les termes de dispersion et de tortuosité sont considérés dans le flux de diffusion.
- Les températures du gaz et du solide sont identiques.

En considérant ces hypothèses, les équations gouvernantes sont :

1. Equation de conservation de l'energie

*Corresponding author email: dadbac@gmail.com

$$(\overline{\rho}Cp_g)_e \partial T/\partial t = (1/r)(\partial(r\lambda_e \partial T/\partial z)/\partial r) + (\partial(\lambda_e \partial T/\partial z)/\partial z) - \overline{\rho}_g^g Cp_g V_{gr}(\partial T/\partial r) - \overline{\rho}_g^g Cp_g V_{gz}(\partial T/\partial z) - m[\Delta H^0 + T(Cp_g - Cp_g)] \quad (1)$$

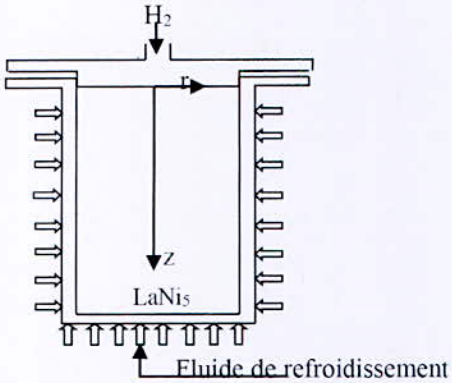

Fig. 1. Réacteur à hydrure métallique

Avec $(\overline{\rho}Cp_g)_e = \varepsilon\rho_g Cp_g + (1-\varepsilon)\rho_s Cp_s$

et $\lambda_e = \varepsilon\lambda_g + (1-\varepsilon)\lambda_s$.

2. Equation de conservation de masse

Pour la phase gazeuse, l'équation de conservation de masse pour l'hydrogène est :

$$\varepsilon\partial\overline{\rho}_g^g/\partial t + div(\overline{\rho}_g^g V_g) = -m \quad (2)$$

En considérant la loi des gaz parfaits et la loi de Darcy l'équation devient :

$$\varepsilon(M_g/RT)(\partial P_g/\partial t) + \varepsilon(M_g P_g/R)(\partial(1/T)/\partial t) - (k/\upsilon_g)(1/r)\partial(r\partial P_g/\partial r)/\partial r - (k/\upsilon_g)(\partial^2 P_g/\partial r^2) = -m \quad (3)$$

Pour la phase solide :

$$(1-\varepsilon)\partial\overline{\rho}_s/\partial t = -m \quad (4)$$

La masse d'hydrogène m, absorbée par unité de temps et de volume est donnée par :

$$m = C_a \exp(-E_a/RT)\ln(P/P_{eq})(\rho_{ss} - \rho_s) \quad (5)$$

Avec C_a comme constante, Ea l'énergie d'activation et ρ_{ss} la densité de l'hydrure à l'état de saturation.

P_{eq} est la pression d'équilibre donnée par :

$$P_{eq} = F(x) \times \exp[-3593.82(1/T - 1/333)]10^5 \quad (6)$$

Avec :

$$F(x) = [84.811x - 402.122x^2 + 908.541x^3 - 972.495x^4 + 395.754x^5] \quad (7)$$

et x représente le rapport de la masse atomique de l'hydrogène à l'hydrure.

3. 3. Conditions initiales et aux limites

A l'état initial, la pression, la température et la densité de l'hydrure sont supposées constantes :

$$T = T_0, P = P_0, \rho_s = \rho_0 \quad (8)$$

En tenant compte de la symétrie par rapport à l'axe z, nous avons :

$$\partial P/\partial r(z,0) = 0,\ \partial T/\partial r(z,0) = 0 \quad (9)$$

Les parois du réacteur sont considérées imperméables :

$$\partial P/\partial r(z,R) = 0,\ \partial P/\partial z(H,r) = 0 \quad (10)$$

A l'entrée, la pression du gaz est supposée constante :

$$P(0,r) = P_0 \quad (11)$$

Sur les parois latérales et sur la base du réacteur l'échange de chaleur est traduit par les expressions suivantes :

$$-\lambda_g \partial T/\partial r(z,R) = h(T - T_f),$$

$$-\lambda_g \partial T/\partial z(H,R) = h(T - T_f) \quad (12)$$

Avec h le coefficient de transfert de chaleur entre le lit hybride et le fluide de refroidissement et T_f *la* température de ce dernier.

La température à l'entrée du réacteur est supposée constante :

$$T(0,r) = T_0 \quad (13)$$

III. METHODE DE RESOLUTION

Les équations de conservation de l'énergie et de la concentration en eau dans la membrane peuvent être écrites sous la forme générale suivante :

$$\partial\phi/\partial t = (1/r)(\partial/\partial r)(rA_r\partial\phi/\partial r) + (\partial/\partial z)(A_z\partial\phi/\partial z) + B_r\partial\phi/\partial r + B_z\partial\phi/\partial z + S \quad (14)$$

Avec comme coefficients :

*Corresponding author email: dadbac@gmail.com

TABLEAU I
LES COEFFICIENTS DES ÉQUATIONS DE CONSERVATION GENERALISEES

	A	Γ	B_r	B_z	S
Equation de conservation de l'énergie	$(\overline{\rho}Cp_g)_e$	λ_e	$-\overline{\rho}_g^g Cp_g V_{gr}$	$-\overline{\rho}_g^g Cp_g V_{gz}$	$-m\Delta H^0 + T(Cp_g - Cp_g)$
Equation de conservation de masse	$\varepsilon M_g / RT$	$\frac{\lambda_e}{\upsilon_s}$	0	0	$-\varepsilon M_g P_g / R \times \frac{\partial}{\partial t} / T - m$

Dans ce travail nous avons utilisé la technique des volumes finis (Patankar [12]) qui consiste à fractionner le domaine physique en un nombre fini de volumes, appelés volumes de contrôle, et d'intégrer ensuite les équations de conservation dans chacun de ces volumes.

Pour déterminer le champ de la variable ϕ dans le domaine d'étude par la méthode des volumes finis, les étapes à suivre sont essentiellement :

- Diviser le domaine d'étude en sous-domaines appelés volumes de contrôle et construire le maillage.
- Intégrer l'équation de transport sur chaque volume de contrôle.
- Discrétiser les différents termes de la forme intégrée de l'équation de transport (transformer l'équation différentielle ponctuelle en un système d'équations algébriques).
- Introduire les conditions initiales et aux limites appropriées.
- Résoudre le système algébrique final pour obtenir enfin un champ approché de ϕ aux points de discrétisation du domaine considéré.

La résolution du système algébrique résultant, représenté par une matrice pentadiagonale, se fait par la méthode dite ADI (Alternating direction implicit). Et la méthode de Thoma pour l'inversion des matrices tridiagonales résultantes.

Le code de calcul a été édité par le logiciel Fortran sur une machine de processeur i5-2310, 2.90 GHz et de 1.90 Go de RAM.

IV. DISCUSSION DES RÉSULTATS

Le réacteur considéré dans notre étude est de volume 235.61 cm². La température et la pression d'entrée sont respectivement T_0=290 K et P_0=10^6 Pa. Le fluide de refroidissement circule autour des parois du cylindre avec une température T_f=293 K.

Le modèle mathématique utilisé dans ce papier, nous a permis de tracer l'évolution spatio-temporelle de la température au sein du réacteur dans différents cas de conditions.

L'évolution de la température dans le réacteur est représentée sur la fig. 2. D'après cette dernière, nous pouvons constater qu'à t=10s la température maximale au sein du réacteur dépasse la valeur de 341 K, et cette température couvre une large surface du réacteur. En avançant dans le temps, l'effet du refroidissement commence à se manifester à travers la diminution de la température qui devient 327 K au point le plus chaud du réacteur à l'instant t=100 s. Les températures diminuent de plus en plus en allant vers les parois, ce qui explique bien que le refroidissement provient des parois du réacteur. Plus le temps avance plus la température diminue jusqu'à l'instant t=500 s, la température maximale prend la valeur 292 K.

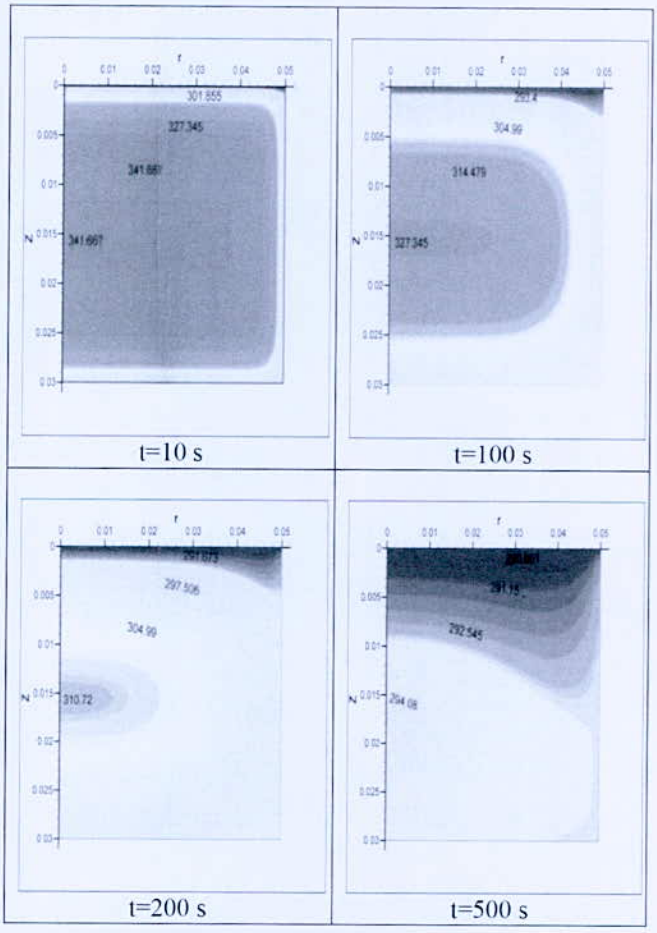

Fig. 2. Evolution des isothermes au cours du temps

Durant cette réaction la densité volumique de l'hydrure au sein du réacteur varie elle aussi. Son évolution au cours du temps est représentée sur la fig. 3. Comme l'expression de la masse d'hydrogène, absorbée par unité de temps et de volume est en fonction de la température, la densité de l'hydrure est fortement liée à cette masse. Nous pouvons constater d'après la fig. 3 que la variation de la densité de l'hydrure est fortement liée à la variation de la température. Donc d'après ces deux figures 2 et 3 on voit

*Corresponding author email: dadbac@gmail.com

bien que là où la température est maximale, la densité de l'hydrure prend sa valeur la plus petite et vice versa. Ce qui veut dire que pour augmenter le taux d'adsorption de l'hydrogène, il faut diminuer la température. Donc on peut dire que le refroidissement appliqué sur les parois du réacteur à visiblement augmenté le taux de création de l'hydrure.

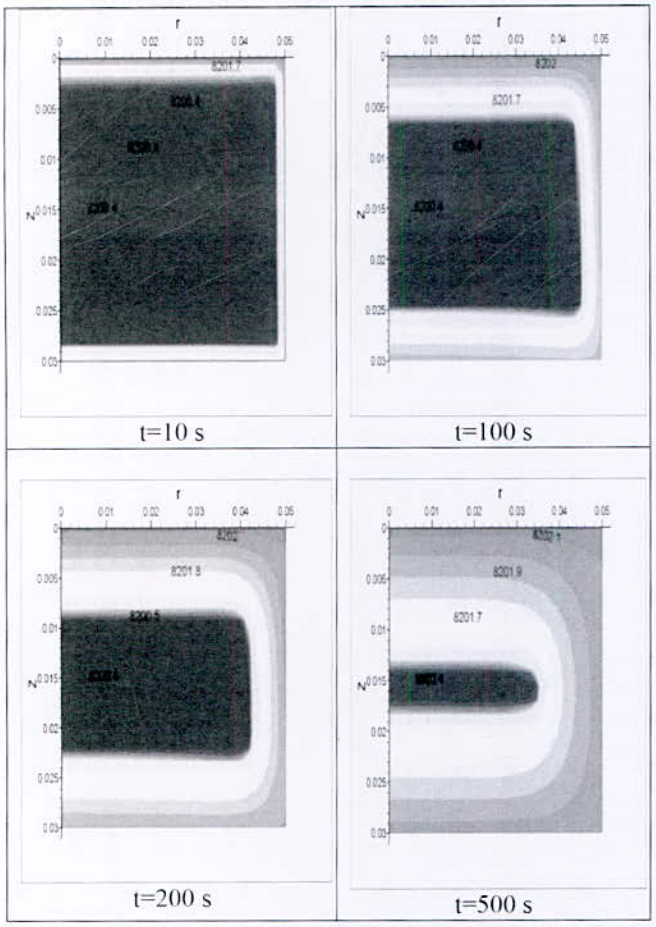

Fig. 2. Evolution des iso valeurs de la densité de l'hydrure au cours du temps

V. CONCLUSION

Dans ce papier une étude numérique du transfert de chaleur et de mass dans un réacteur d'hydrure métallique de forme cylindrique a été menée. Le réacteur est muni d'un système de refroidissement pour optimiser l'absorption de l'hydrogène par le solide.

Le modèle mathématique utilisé est basé sur le principe de conservation de chaleur et de masse. Le domaine d'étude et considéré bidimensionnel en supposant une axisymetrie autour de l'axe z. La résolution du problème mathématique a été faite par la méthode des volumes finis et la méthode ADI a été utilisée pour la résolution du système algébrique résultant. Les résultats de la simulation montrent une bonne cohérence entre les évolutions de la température et de la densité de l'hydrure formé par la réaction de l'hydratation. Les résultats nous montrent aussi la contribution du refroidissement du réacteur à l'augmentation du taux d'absorption de l'hydrogène.

REFERENCES

[1] Anani A. "Alloys for hydrogen storage in nickel/hydrogen and nickel/metal hydride batteries". Int. J. Power Sources, Vol. 47, pp. 261–75. 1994.

[2] T-Raissi A, Banerjee A, Sheinkopf K. "Metal hydride storage requirements for transportation applications". In Proc. IECECI, vol. 4, pp. 2280–2285, 1996.

[3] P. D. Goodell, G. D. Sandrock and E. L. Huston, "Kinetic and dynamic aspects of rechargeable metal hydrides", J. Less-Common Metals Vol. 73, pp. 135-142, Sep.1980.

[4] M. Y. Song and J. Y. Lee, "A study of the hydrating kinetics of Mg-(10-20 w/o) LaNi5" Int. J. Hydrogen Energy Vol. 8, pp. 363-367, 1983.

[5] M. Kawamura, S. Ono and Y. Mizuno, "Dynamic characteristics of a hydride heat storage system", J. Less-Common Metals, Vol. 89, pp. 365, Feb. 1983.

[6] A. Jemni, S. Ben Nasrallah, J. Lamloumi and A. Percheron Guegan, "Study of heat and mass transfer in a metal-hydrogen reactor", in *Proc. Z. Phys. Chem.*, 1992, pp. 197-203

[7] H. Choi and A. F. Mills. "Heat and mass transfer in metal hydride beds for heat pump applications", Int. J. Heat Mass Transfer, Vol. 33. pp. 1281-1288, June 1990.

[8] S. Wakao, M. Sekine. H. Endo, T. Ito and H. Kanazawa, "A heat storage reactor for metal hydrides", J. Less-Common Metals, Vol. 89, pp. 341-350, Feb. 1983.

[9] U. Mayer, M. Groll and W. Supper, "Heat and mass transfer in metal hydride reaction beds: Experimental and theoretical results", J. Less-Common Metals, Vol. 131, pp. 235-244, Mar.1987.

[10] D. W. Sun and S. J. Deng, "Study of the heat and mass transfer characteristics of metal hydride beds: A two-dimensional model", J. Less-Common Metals Vol. 155, pp. 271-279, Nov. 1989.

[11] M. Pons, "Transferts de chaleur dans la poudre de LaNi, et leur couplage avec la réaction d'hydratation", Thèse de Doctorat, Université Paris, 1991.

[12] S. Patankar, "Numerical Heat Transfer and Fluid Flow", McGraw Hill, New York, 1980.

*Corresponding author email: dadbac@gmail.com

Effect of Permeability on the Thermal Field in the DMFC Fuel Cell

S. H. Halitim[1*], B. Zitouni[2], D. Haddad[1] and H. BenMoussa[1]

[1*]Department of Mechanics, University of Hadj Lakhdar. Batna 2. Algeria.
[2]Department of food Technology. Institute of veterinary and agricultural sciences. University of Hadj Lakhdar.Batna1. Algeria.

Abstract—**A two dimensional model for DMFC fuel cell is presented, which considers transit of mass, heat and momentum transfer in the gas channels, diffusers, and catalyzers at both the anode and cathode sides of the DMFC fuel cell. In this study, we visualize the effect of permeability on the field temperature and behavior of the fuel cell with the source terms and compared the effect of parameters like current density and water content.**

The numerical results are obtained by developing a mathematical model in FORTRAN language and the visualization fields are given by the Tecplot software. The results indicate that the high temperatures localization is at the catalyst membrane interface and they show that the permeability has an effect on the thermal fields.

Key words— DMFC, permeability, temperature, concentration, computational, FORTRAN.

I. INTRODUCTION

Extensive research has been carried out to improve the steady state for DMFC. DMFC is device which harnesses electrical energy from electrochemical. The processes that occur within the DMFC are very complex. It has several advantages such; higher energy density, easy liquid fuel storage and the simple structure. The technical issues are related to the transport. This transport not only affects the DMFC operation, but also influences the DMFC energy density. General descriptions of mass and heat transport processes are developed.

In the literature reviewed very few articles have been published in the field of effect of the permeability. A two-dimensional model was developed with the mass transport in two phases for a DMFC [1]. Numerical results show that methanol mass transfer is dominated by the resistance in the porous anode structure, which is affected by the porous medium physical properties, such as porosity, permeability and contacting angle.

Others in paper [2] studied the oxygen starvation. The source terms utilized are those due to; electrochemical reaction, Joule effect, water condensation or evaporation and absorption and desorption of water or methanol.

The results in the study [3] showed that the mass and heat transport affect the DMFC performance and depends strongly on the methanol concentration in the tank. The studied works [4, 5] focuses on the evaporation and condensation effects, water and fuel management in a DMFC. Reference [5] studied the forced air flow effect at the cathode channel. The others of reference [6] considered the effect of diffusion, electro-osmotic drag and convection. Seunghan J. et al [7] study the behavior of CO_2 gas to predict its role in mass transport phenomena in DMFC. The model in [8] presented a two-phase model, multi-components components in three dimensions to a liquid supplying DMFC methanol. The modeling field comprises the membrane, two catalyst layers, two diffusion layers and two channels. For the electrochemical kinetics, the Tafel equation incorporating the effects of the two phases is used both on the side of the cathode and the anode. In the model of [9] they examined heat transfer by natural convection in their study. The heat source term used is composed of the flow resistance, the electrochemical reactions, the over potential, the entropy change due to the electrochemical reaction and the methanol reaction cathode heat loss. A fluid dynamics model (CFD) is developed to study the influence of geometric and operating parameters on DMFC performance. Temperature, methanol concentration and the methanol flow rate are selected as operating parameters in papers [10 and 11].

In this study, a numerical simulation is developed in order to predict the DMFC behavior when the permeability change and how to affect the DMFC. Also temperature, current density and water content are effects studies.

II. THEORETICAL STUDY

The principal reactions in a DMFC are the oxidation reaction mainly occurs at the anode catalyst layer and the reduction reaction occurs at the cathode catalyst layer:

$$\begin{aligned} &Oxidation\,(MOR): CH_3OH + H_2O \rightarrow CO_2 + 6H^+ + 6e^- \\ &\text{Re}duction\,(ORR): \frac{3}{2}O_2 + 6e^- + 6H^+ \rightarrow 3H_2O \\ &Overall: CH_3OH + \frac{3}{2}O_2 \rightarrow CO_2 + 2H_2O \end{aligned} \quad (1)$$

The study focuses on a DMFC elementary cell coupling between the electrochemical and dynamic model. First, appropriate transport and electrochemical parameters geometric and physical parameter are given in Table I-II. Gas channels are considered continuum, while the diffusion layers, catalyst and the membrane are porous media. Physical domain considered is divided into seven regions (Fig. 1):

*Corresponding author email: halitim.siham@yahoo.com

The following hypotheses are considered:

- Stationery model;
- The catalyst layer is treated as an infinitely thin surface;
- Single phase model and homogeneous;
- The reaction of oxidation is supposed total.

TABLE I
PARAMETERS VALUE OF GEOMETRIC AND PHYSICAL USED IN MODEL

Parameter	Symbol	Value
Channel length	L	7.5 x 10-2 m
Channel height	t_{ch}	0.8 x 10-3 m
Diffusion layer thickness	t_a, t_c	0.3 x 10-3 m
Membrane thickness (Nafion 117)	t_m	0.23 x10-3 m
Porosity of anode and cathode Diffusion Layer	ε_a, ε_c	0.3
Porosity of anode and cathode CL	ε_{cla}, ε_{clc}	0.3
Porosity of membrane	ε_m	0.28

TABLE II
INITIALS CONDITIONS

Parameters	Symbols	Values	Refs
Operation temperature	T	350 K, 300K	[8]
Methanol concentration	C_{CH_3OH}	0.032 Kg Kg-1	[7]
Oxygen concentration	C_{O_2}	0. 23 Kg Kg-1	[7]

III. RESOLUTION MATHEMATIQUE

1. Governing equations

- ***Continuity***

$$\nabla(\varepsilon\rho u) = 0 \tag{2}$$

Where 'ε, ρ, u' represent porosity factor of the corresponding region, methanol solution density and fluid velocity vector, respectively.

- ***Momentum***

Based on assumption that we have a steady state:

$$\nabla(\varepsilon\rho uu) = -\varepsilon\nabla p + \nabla(\varepsilon.\mu\nabla u) + S_u \tag{3}$$

Where 'k, μ, p' are the permeability table 3of porous media (m^2), viscosity (kg m^{-1} s^{-1}) and pressure (Pa).

S_u is momentum source term (N m^{-3}), which is caused by porous media and is zero in the channel. Su is defined by Darcy's law:

$$S_u = -\varepsilon\frac{\mu}{k}u \tag{4}$$

- ***Species conservation***

$$\nabla(\rho u C_k) = \nabla(D_k^{eff}\nabla C_k) + S_k \tag{5}$$

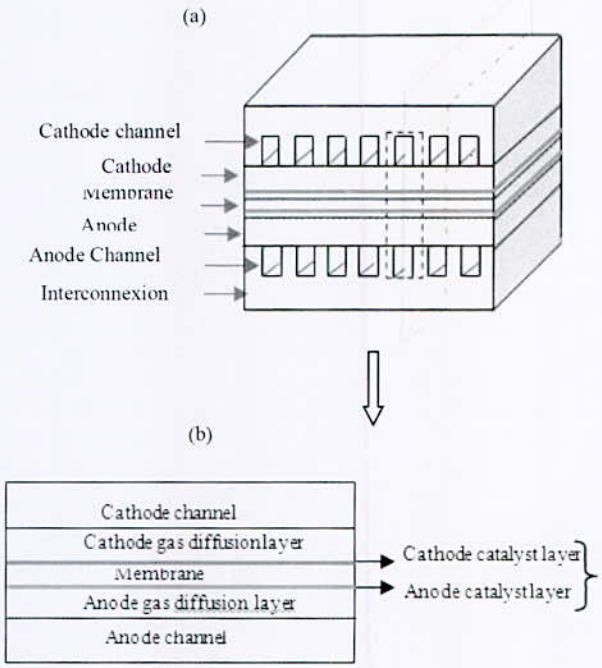

Fig. 1. Physic model; DMFC stack (a), component of unit DMFC (b)

The effective diffusion coefficient D_k^{eff} of species k and is defined by [14]:

$$D_k^{eff} = \begin{cases} D_k & In\ the\ channel \\ \varepsilon^{1.5} D_k & In\ other\ zones \end{cases} \tag{6}$$

- ***Heat Transfer***

$$\nabla(\rho c_p u T) = \nabla(k\nabla T) + S_T \tag{7}$$

For the term source 'S_T', different heat generations are involved in the DMFC, including the generations from anodic and cathode electrochemical reactions in the catalyst layer, and Joule effect.

- ***Electrochemical kinetics***

Tafel equations are used to describe electrochemical reaction in both the anode and cathode catalyst layers.

$$\begin{cases} i_a = i_{a,ref}\dfrac{C_{CH_3OH}}{C_{CH_3OH,ref}}\exp\left(\dfrac{\alpha_a F}{RT}\eta_a\right) \\ i_c = i_{c,ref}\dfrac{C_{O_2}}{C_{O_2,ref}}\exp\left(\dfrac{\alpha_c F}{RT}\eta_c\right) \end{cases} \tag{8}$$

In electrochemical reactions, the dominating kinetic parameter is the exchange current density i, which is a strong function of temperature and reactant concentration. The exchange current density is not an intrinsic parameter

*Corresponding author email: halitim.siham@yahoo.com

of a catalyst and is also a strong function of the morphology of the electrode structure. Where $i_{a,ref}$ and $i_{c,ref}$ denote the exchange current densities for the anode MOR and cathode ORR respectively.

IV. NUMERICAL RESOLUTION

For the governing equations numerical resolution, a discretized by the finite volume method is done. The source terms and physical properties are implemented through the program. While the equations for solid-phase, electrolyte potentials, dissolved water, dissolved methanol and liquid water are implemented also in program.

A program written in FORTRAN language was developed in order to obtain the temperature, water, methanol, oxygen and dioxide of carbon fields. To make the numerical implementation more practical, the single-domain approach is used.

V. RESULTS AND DISCUSSION

The model developed for the cathode and electrolyte parts of a fuel cell is used to examine the dynamic behavior, thermal fields and the velocity profiles for different permeabilities in order to illustrate the transport phenomena that occur in the fuel cell. We solve the model based on the parameters given in table1 and table2, which is defined the base case. It should be noted that under base case, the crossover phenomena is neglected and is not occur.

Effect of permeability

The permeability of a porous medium represents its ability to conduct fluid flow through its open volume.

We perceive a slight variation in the velocity profile due to the temperature rise for different permeability values.

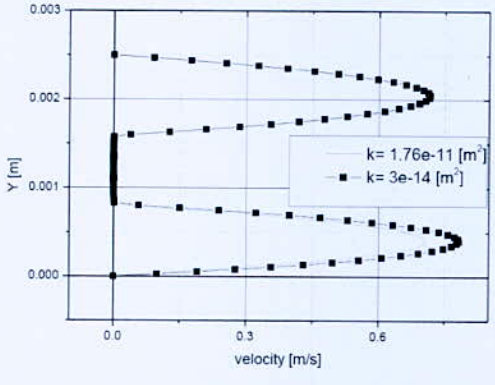

Fig. 2. Velocity profile along the height of the fuel cell for different values of the permeability (T=300[K] and λ=16)

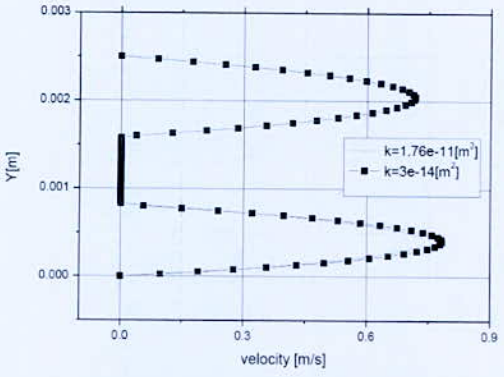

Fig. 3. Velocity profile along the height of the fuel cell for different values of the permeability (T=350[K] and λ=16)

Thermal fields with effect of permeability

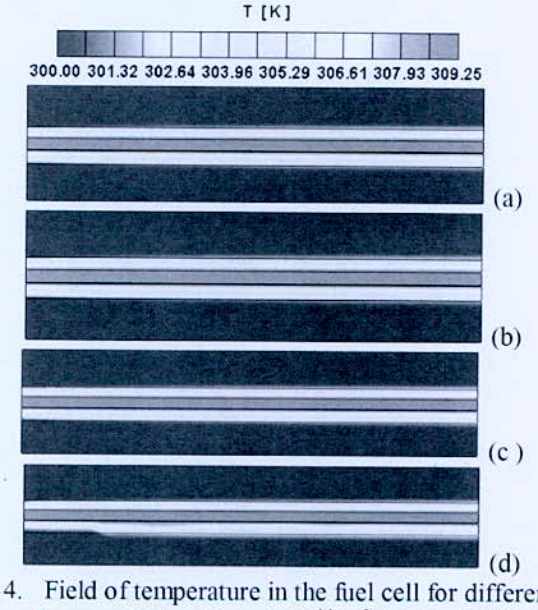

Fig. 4. Field of temperature in the fuel cell for different values of permeability; (a) $k=3.10^{-14}[m^2]$, (b) $k=10^{-13}[m^2]$, (c) $k=2.5.10^{-12}[m^2]$, (d) $k=1.76.10^{-11}[m^2]$

To study the effect of permeability (k) on the thermal behaviour of the DMFC. We select four values of permeability: $k=3.10^{-14}$, 10^{-13}, $2.5.10^{-12}$ and $1.76.10^{-11}[m^2]$.

Effect of water content

For different values of the water content the temperature field shows the effect of the water content.

*Corresponding author email: halitim.siham@yahoo.com

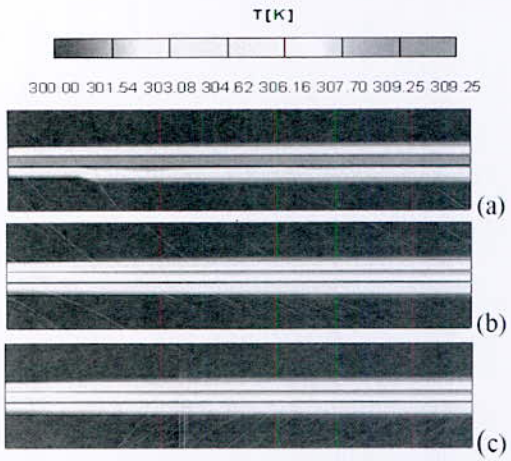

Fig. 5. Field of temperature in the fuel cell for different values of water content; (a) λ=18, (b), λ=20, (c) λ=22

Effect of courant density

The current density of the cell is varied with temperature and cell potential.

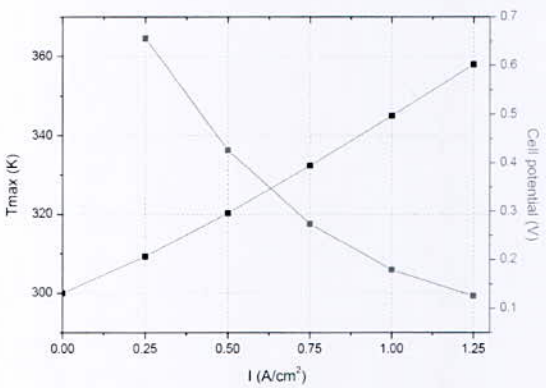

Fig. 6. Current density effects at cell potential and temperature distribution

VI. CONCLUSION

The model is used to investigate the permeability operation conditions (temperature) and at water, methanol, dioxide of carbon and oxygen concentration.

The simulations show that the permeability and water content affect the temperature of cellule. There is proportionality with the temperature.

The DMFC performance can be enhanced by increasing the permeability and water content.

This results show the solution of dehydration problem in the membrane.

The results show that there is a temperature rise at the membrane which involves drying of the membrane. However, for the water content, a dehydration problem solution in the membrane is considered. The current density is the key parameter simulation for temperature and cell potential.

REFERENCES

[1] X. Y. Li, W. W. Yang, Y. L. He, T. S. Zhao and Z. G. Qu, ''Effect of anode micro-porous layer on species crossover through the membrane of the liquid-feed direct methanol fuel cells'' Applied Thermal Engineering 48 (2012) 392-401.

[2] X. G. Yang, Q. Ye and P. Cheng, "Oxygen starvation induced cell potential decline and corresponding operating state transitions of a direct methanol fuel cell in galvanostatic regime''. Electrochimica Acta 117 (2014) 179– 191.

[3] G. Jewett, A. Faghri and B. Xiao, "Optimization of water and air management systems for a passive direct methanol fuel cell''. International Journal of Heat and Mass Transfer 52 (2009) 3564–3575.

[4] J. Rice and A. Faghri,''A transient, multi-phase and multi-component model of a new passive DMFC'' International Journal of Heat and Mass Transfer 49 (2006) 4804–4820.

[5] H. Bahrami and A. Faghri ''Transport phenomena in a semi-passive direct methanol fuel cell'' International Journal of Heat and Mass Transfer 53 (2010) 2563–2578.

[6] C. Xu and A. Faghri, ''Water transport characteristics in a passive liquid-feed DMFC'' International Journal of Heat and Mass Transfer 53 (2010) 1951–1966.

[7] S .Jung, Y. Lengl and Chao-Yang Wang, ''Role of CO2 in Methanol and Water Transport in Direct Methanol Fuel Cells''. Electrochimica Acta 134 (2014) 35–48.

[8] J. Ge and H. Liu, '' A three-dimensional tw o-phase flow model for a liquid-fed direct methanol fuel cell'' Journal of Power Sources 163 (2007) 907–915.

[9] J. Zou, Y. He, Z. Miao and X. Li ''Non-isothermal modeling of direct methanol fuel cell". International journal of hydrogen energy 35 (2010) 7206- 7216.

[10] R. Ghayor, M. Shakeri, K. Sedighi, M. Frefairearhadi, ''experimental and numerical investigation on passive and active μ DMFC". International journal of hydrogen energy 35 (2010) 9329 -9337.

[11] H. Bahrami and A. Faghri, '' Start-up and steady-state operation of a passive vapor-feed direct methanol fuel cell fed with pure methanol '' international journal of hydrogen energy 37 (2012) 86416 - 8658.

*Corresponding author email: halitim.siham@yahoo.com

Biogas-Hydrogen Blends Effect on Emissions in an Internal Combustion Engine: Numerical Simulation

C. Mokrane[1*], B. Adouane[2], A. Benzaoui[1]

[1]Faculty of Physic/fluid mechanics and energy, USTHB University, BP 32 El Alia 16111, Bab Ezzouar, 16111. Algiers, Algeria.

[2]Faculty of Material Sciences/Laboratory (APEL), University of Batna 1, Route de Biskra, 05000. Batna, Algeria.

Abstract—**One of the most important advantages of biogas is that it can easily be adapted as a new fuel for internal combustion engines, but there are several disadvantages concerning the emissions of the pollutants and the combustion itself. One way of avoiding these problems is the addition of hydrogen to the biogas in the combustion chamber in an appropriate manner. The calorific value of biogas can be improved by adding hydrogen, which is known as a clean and reactive fuel, especially when produced from renewable sources. Biogas mixed with hydrogen can overcome flame instability problems, improve combustion properties and significantly reduce emissions.**
This paper present a comparative study using a numerical simulation using (Ansys-Fluent) investigating the effect of doping biogas or not with hydrogen on emissions (NOx and CO) in a spark-ignition internal combustion engine (SI). The results shows that CO emissions decrease drastically with an increase in hydrogen concentration at stoichiometric and fixed power. For NOx emissions, their values generally increase with increasing hydrogen content. For CO emissions, we obtained a general reduction with the addition of hydrogen (more than 10%) because of the reduction of carbon in the fuel. Therefore, the addition of H_2 (up to 20-30% vol.) to biogas may constitute an effective solution for the green-house gases problem.

Key words—Biogas-hydrogen blends, Combustion, NO emissions, CO emissions.

I. INTRODUCTION

Fossil fuels pollute the environment. The focus now is shifting more and more towards the renewable sources of energy, which are essentially, nonpolluting. Biogas is one of the main sources of renewable energy in the world.

The biogas heating value can be upgraded by adding hydrogen which is known as a clean and reactive fuel, especially when it is produced from renewable sources. Hydrogen blended biogas can overcome the flame instability problems and improve combustion properties. In internal combustion engines operating with biogas.

Hydrogen gas is highly reactive and therefore has a very high laminar burning velocity. When added to slower burning fuels the hydrogen will extend the flammability limits and enhance flame propagation. This can result in a more efficient combustion, giving lower emission of hazardous air pollutants and greenhouse gases. It has been shown [1] that hydrogen increase the laminar flame speed through kinetic, thermal and diffusion effects. The kinetic effect is the largest contributor to flame speed enhancement, while diffusion effects are so small they are considered negligible [1].

Porpatham et al. [2] conducted an experimental study on hydrogen addition (5%, 10% and 15% on the energy basis) effect on the performance of spark ignition engine. Small amounts of hydrogen were added to biogas, engine speed was kept constant and equivalence ratio was varied. It was found that hydrogen addition improved combustion rate and extended biogas lean combustion limit. However, beyond 15% of hydrogen enrichment, improvement was not significant at high equivalence ratios.

Park et al. [3] studied the effects of adding H_2 on the behavior of an engine with various excess air ratios and CH4 concentrations in the biogas. They found that adding H2 improved the in-cylinder combustion characteristics and extended the LO while reducing the hydrocarbon emissions.

Lim et al. summarized that, despite enriched biogas has a lower calorific value than the natural gases, NOx emissions were lower for the enriched biogas than for the natural gases and no noteworthy differences were seen in fuel economy between the gases in any of the driving cycle [4].

II. SIMULATION DETAILS

1. Modelling biogas combustion in SI engine

The computational fluid dynamics (CFD) is a tool able to calculate the parameters, which depend on process of combustion and, consequently, of the evolution of the process of combustion. For this reason, this tool was selected in this work to characterize the process of combustion. The software FLUENT®, which is based on the method of finite volumes, is used to carry out the simulation.

For SI engines and some engines of combustion with natural gas, the fuel and the air are mixed before entering

* Corresponding author email: ch.mokrane@gmail.com

the combustion chamber. At the time of the spark, the mixture is supposed to be homogeneous and the process is known as "premixed combustion".

2. Combustion model

In partially premixed combustion, we find the premixed and non-premixed conditions. We employ the method of probability density function (PDF) to detect the mixture fraction and to model chemistry in the system (used for cases of premixed and non-premixed combustion). The Zimont model of the turbulent flame speed is used to enclose the turbulent quantities, typically used for cases of premixed combustion.

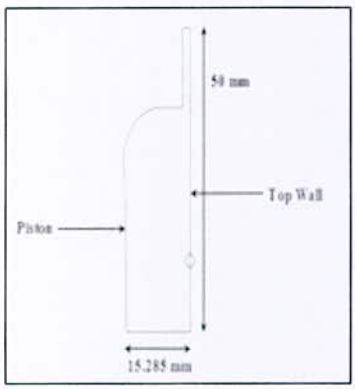

Fig. 1. Computational domain [5]

Combustion is modelled in terms of progress. The progress variable extends from $0<c<1$, where "1" means is burned mixture, "0" means not burned, and in the interval, "c" is a linear combination of burned and not burned. While the flame is introduced into the chamber, progress is placed at "1", and this propagates in all the fuel according to the flame speed.

The flame speed is known for its variation with temperature and pressure, therefore the flame speed should vary clearly during a cycle of combustion. This is explained by using a function "UDF" (User Defined Function) which recomputed the flame speed based on the pressure, the temperature, and the mixture fraction inside the cylinder. The UDF currently used was developed and validate by "©ANSYS, Inc" [5]. The model of turbulence used, is the k-ε model with two equations. Table 2 summarize the combustion model.

3. NOx and CO emissions modeling

For NOx modelling, we have used the ANSYS FLUENT thermal and prompt model. The formation of thermal NOx is determined by a set of highly temperature-dependent chemical reactions known as the extended Zeldovich mechanism. For Prompt NOx formation, it is known that during combustion of hydrocarbon fuels, the NOx formation rate can exceed that produced from direct oxidation of nitrogen molecules (that is, thermal NOx). There is good evidence that prompt NOx can be formed in a significant quantity in some combustion environments, such as in low-temperature, fuel-rich conditions and where residence times are short [6].

Carbon monoxide (CO) emissions from internal combustion engines are controlled primarily by the fuel/air equivalence ratio. For fuel-rich mixtures CO concentrations in the exhaust increase steadily with increasing equivalence ratio, as the amount of excess fuel increases.

For fuel-lean mixtures, CO concentrations in the exhaust vary slightly with equivalence ratio and are of the order 10^{-3} mole fraction [7].We can use for simulation a mechanism with two-steps and three reactions, which allows the calculation of the amount of CO that is generated during the combustion of methane in the SI engine modeled. The considered reactions are:

$$CH_4 + 1.5O_2 \rightarrow CO + 2H_2O \quad (1)$$

$$CO + 0.5O_2 \rightarrow CO_2 \quad (2)$$

$$CO_2 \rightarrow CO + 0.5O_2 \quad (3)$$

Reaction (1) describes the oxidation of methane to form CO and water, reaction (2) shows the formation of CO_2 while the reaction (3) considers the dissociation reaction of the latter specie.

$$H + O_2 \rightarrow O + OH \quad (4)$$

$$OH + CO \rightarrow CO_2 + H \quad (5)$$

Reactions (4) and (5) indicate that hydrogen addition to biogas enhances the reaction, which is the main chain branching step and the overall reaction rate indicator [8]. The OH and H radicals produced by this reaction are the main chain carrier which breakdown CH_4.

III. RESULTS AND DISCUSSION

According to Fig. 2, the temperature increases with increasing H_2 concentration in biogas, and reaches values upper to 1700 K without pics. These conditions lead to the formation of thermal NOx (NO_x formed through high temperature - usually above 1600 °C - oxidation of the diatomic nitrogen found in combustion air).

NOx emissions for varying hydrogen concentrations were illustrated in Fig. 2. As shown, higher NOx emissions were generated for more hydrogen blending due to increase in-cylinder temperature by fast burning speed. In addition, maximum NOx production occurred at a concentration of hydrogen ranging from 15 % to 20 % in the biogas. Increasing further H2 blending (more than 20%), results in decreasing NOx, indication that there is a mechanism competition, between NOx formations. From the oxygen graph below (Fig. 5), we can see that O2 at the

exhaust increases with H2, this explains that less N radicals are oxidized.

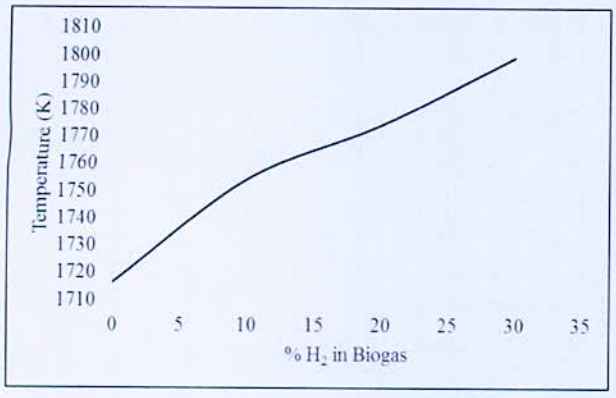

Fig. 2. Temperature versus H_2 concentration in biogas

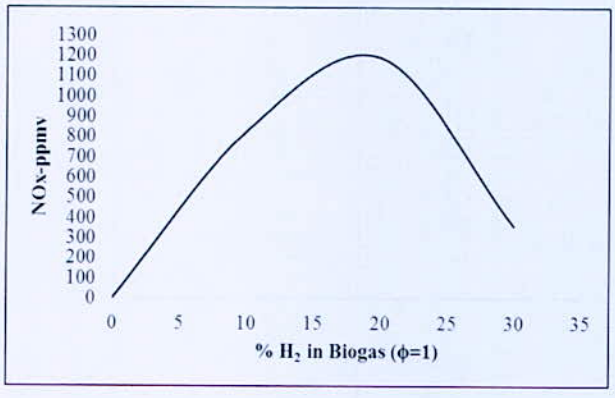

Fig. 3. NOx emissions versus H_2 concentration in biogas

Fig. 4, shows the variation of CO emissions with an increase in hydrogen concentration at stoichiometric and fixed power. CO emissions indicate the completeness of the combustion. It can be observed from Fig. 3, that the CO emissions drastically reduce upon hydrogen enrichment.

We should indicate that CO is lower at H_2 0%, it increases at 10% H_2, due to incomplete combustion, and then decreases again when increasing H_2. This occurs due to the presence of H_2, allowing the formation of OH radical, which has a significant kinetic effect for carbon monoxide oxidation by reacting elemental:

$$OH+CO \rightarrow CO_2+H \qquad (6)$$

Fig. 5, is very important, and it explains what is happening with CO and NOx emissions, at 10% H_2, there is a maximum of oxygen consumption, and therefore emissions of NOx at this level of H_2 increase. It seems that the H_2 conversion to OH, resulting in a rich oxidizer pool, enhancing therefore formation of NOx.

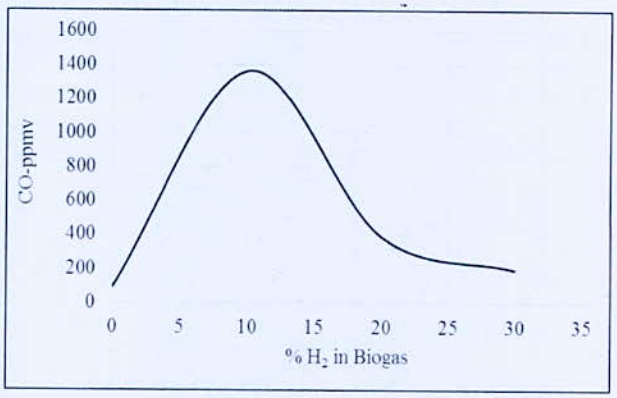

Fig. 4. CO emissions versus H_2 concentration in biogas

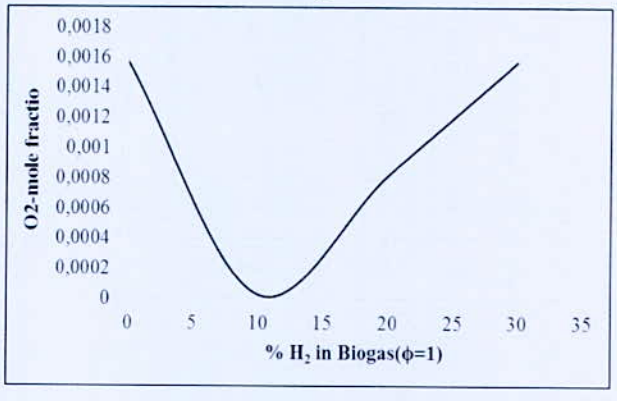

Fig. 5. O_2 mole fraction versus H_2 concentration in biogas

IV. Validation

Concerning NOx emissions, the results found by our simulation can be compared to those found in the experimental investigation conducted by Park et al. [3]. At stoichiometry (ϕ=1), NOx (ppm) values are almost the same of those found in this study.

For CO emissions, Bauer C.G et al [9] and Gómez-Montoya, J. P et al [10] found similar trends.

V. CONCLUSION

In this study, biogas blended with hydrogen simulations were conducted to assess the effects of H_2 concentration variations within biogas on emissions of a spark ignition engine operated at a fixed equivalence ratio ϕ=1.

- The in cylinder temperature rise when the air is enriched with hydrogen. The Oxygen content in biogas further increases the temperature. This results in high NO emissions from the engine NOx emission values generally increase with increasing hydrogen content.
- CO emissions decrease drastically with an increase in hydrogen concentration at stoichiometric and fixed power. We obtained a general reduction in CO with the

addition of hydrogen (more than 10%) because of the reduction of carbon in the fuel.

- The addition of H_2 (up to 20-30% vol.) to biogas may constitute an effective solution for the green-house gases problem and at the same time to introduce H_2 into the fuel market without requiring changes in current engine technology.

APPENDIX

TABLE I
SPECIFICATIONS OF THE SIMULATED ENGINE

Parameter	Value
Crank Shaft Speed (rpm)	1500
Starting Crank Angle (deg)	360
Crank Period (deg)	720
Crank Angle Step Size(deg)	0.25
Piston Stroke (mm)	80
Connecting Rod Length (mm)	140
Compression Ratio CR	6.23 :1

TABLE. II
COMBUSTION MODEL

Partially Premixed Combustion; C-equation
State Relation : Equilibrium
Energy Treatment : Non-Adiabatic
Equilibrium Operating Pressure : 3000000 (Pa)
PDF Options : Inlet Diffusion and Compressibility Effects
Turbulent Flame Speed Constant= 0.6
T= 300°K

TABLE III
BG60-HYDROGEN COMPOSITION

case	Composition (%)			mixture fraction				
	H_2	CH_4	CO_2	Y_{CH4}	Y_{CO2}	Y_{H2}	Y_{O2}	Y_{N2}
1	0	60	40	0.05	0.092	0.0	0.200	0.658
2	10	57.6	32.4	0.048	0.075	0.0011	0.203	0.668
3	20	54	26	0.045	0.062	0.0022	0.206	0.678
4	30	51.6	18.4	0.043	0.045	0.0033	0.210	0.691

REFERENCES

[1] Tang, C. L.; Huang, Z. H.; Law, C. K., "Determination, Correlation, and Mechanistic Interpretation of Effects of Hydrogen Addition on Laminar Flame Speeds of Hydrocarbon-Air Mixtures," Proceedings of the Combustion Institute 2011, vol. 33, pp. 921-928.

[2] Porpatham E, Ramesh A, Nagalingam B., "Effect of Hydrogen Addition on the Performance of A Biogas Fuelled Spark Ignition Engine," Int. J. Hydrogen. Energy, 2007; vol. 32, pp. 2057-65.

[3] Park C, Park S, Lee Y, Kim C, Lee S, Moriyoshi Y., "Performance And Emission Characteristics Of A Si Engine Fueled By Low Calorific Biogas Blended With Hydrogen," Int. J. Hydrogen. Energy, 2011. vol. 36, pp. 10080-10088.

[4] Lim, C., Kim, D., Song, C., Kim, J., Han, J., & Cha, J. S., "Performance and emission characteristics of a vehicle fueled with enriched biogas and natural gases," Applied Energy, vol. 139, pp. 17-29, 2015.

[5] Ansys Fluent Tutorial Guide, Release 14.5, Ansys, Inc., October 2012.

[6] Ansys Fluent Theory Guide, Release 14.5, ANSYS, Inc., October 2012.

[7] J. B. Heywood. "Internal Combustion Engine Fundamentals," New York, McGraw-Hill, 1988, pp. 592-593.

[8] Hwang D-J, Choi J-W, Park J, Keel S-I, Oh C-B, Noh D-S., "Numerical study on NO formation in CH_4-O_2-N_2 diffusion flames diluted with H_2O," Int. J. Energy. Res., vol. 28, pp. 1255-67, 2004.

[9] Bauer C.G., Forest T.W., "Effect of hydrogen addition on the performance of methane fuelled vehicles. Part I: effect on S.I. engine performance," Int. J. Hydrogen .Energy, vol. 26(1), pp. 55–70, 2001.

[10] Gómez-Montoya, J. P., Cacua-Madero, K. P., Iral-Galeano, L. & Amell-Arrieta, A., "Effect of biogas enriched with hydrogen on the operation and performance of a diesel-biogas dual engine," CT&F - Ciencia, Tecnología y Futuro, vol. 5(2), pp. 61-72, 2013.

SiO_2@ NiO Core-Shell Nanoparticles for Efficient Photo-Catalytic Hydrogen Production from Water and Under Visible Light Irradiation

I. Ghiat[1] *, A. Saadi[1], A. Boudjemaa[2], K. Bachari[2]

[1*]Laboratory of Naturel Gas, Faculty of Chemistry, USTHB, Algiers.
[2] Centre de Recherche Scientifique et Technique en Analyses Physico-Chimiques, Bou-Ismail CP 42004, Tipaza, Algeria.

Abstract—**Core@shell nanomaterials with desired morphologies have gained remarkable attention for their potential applications in environmental and energy technology. In this study, SiO_2@xNiO (with x equal to 5 and 10 wt. %) were prepared by hydrothermal method. The samples were characterized by XRD, SEM, FTIR, RDs, Nitrogen adsorption (BET) methods. The photo-catalytic properties were evaluated via hydrogen production through water photo-reduction. The XRD and SEM demonstrate that the synthesized materials composed of SiO_2 shell and NiO nanosheets. RDs study illustrated an indirect band gap energy of 1.58 and 1.18 eV for SiO_2@5NiO and SiO_2@10NiO, respectively. A remarkable surface area lead to a better acceleration of the charge (e^-/h^+) transfer by increasing the number of surface reaction sites. So, under visible light, the photo-catalysts exhibited a good photo-catalytic activity for hydrogen production with a yield of 148.81 and 41.67 µmol /g.min for SiO_2@5NiO and SiO_2@10NiO, respectively after 60 min of irradiation.**

Key words—Photo-catalysis, Hydrogen, Silica, Nickel oxide, Core/shell nanoparticles, Hydrothermal method.

I. INTRODUCTION

Hydrogen is considered as an ideal fuel for the future and an obvious source is water. The photo-reduction of water to hydrogen is an environmentally friendly method that can be achieved using visible light irradiation [1]. Hydrogen produced from water is regarded as a renewable energy source and is a clean fuel which does not generate CO_2 and other pollutants [2]. Several materials with different structures have been investigated for the hydrogen production by water photo-reduction. Recently, the development of a range of photo-catalysts with a semi-conductors (SCs) properties have been attracted a considerable attention. For the efficient hydrogen production by sun light, a sufficiently negative flat band (Vfb) potential and good absorption in the visible region of a material is essential [3].

Nano-sized core@shell materials has recently attracted widespread attention because it can be used in various applications, such as catalysis, photo-catalysis, electrochemical sensing, adsorption...etc [4-6]. Core@shell nanomaterials have a considerable surface area and show a high stability, as well as superior optical and electrical attributes. Template method is one of the most common routes used to prepare core@shell structures. SiO_2 nanoparticles are often used as templates to prepare hollow structures in various types of materials, and the corresponding samples usually have a spherical morphology and possess outstanding porous properties [7-10].

In other hand, nickel oxide (NiO) is a good photo-catalyst owing to its unique magnetic and electrical properties [11]. NiO with nano-structures have been widely investigated [12], which is presented a promising application for photo-reduction of water to hydrogen [13]. In addition, Bej et coauthors and Ali indicated that NiO-SiO_2 composites are a good for hydrogen generation [14, 15].

II. EXPERIMENTAL

1. Materials

Nickel nitrate ($Ni(NO_3)_2$, $6H_2O$), tetraethyl orthosilicate (TEOS), urea ($CO(NH_2)_2$), ethanol, ammonium hydroxide (NH_4OH), hydrochloric acid (HCl) and deionised water were used throughout this study.

2. Preparation of samples

Silica nanoparticles were synthesized according to the well-known Stöber method [16] by hydrolysis and condensation of TEOS in a mixture of ethanol with water, using ammonia as catalyst to initiate the reaction. The SiO_2 nanoparticles were dried at 100 °C. SiO_2@xNiO Core-shell (with x equal to 5 and 10 wt. %) were prepared by hydrothermal method. Silica powder was dispersed in 200 mL of deionised water. Then, $Ni(NO_3)_2 6H_2O$ and $CO(NH_2)_2$ were added to the silica. The obtained suspension was put in a Teflon reactor under magnetic stirring, kept the temperature at 120 °C for 12 h. Then, the precipitates formed were filtrated, and washed with distillated water and finally dried at 80 °C for 12 h.

3. Characterization

The phase composition of the powder samples were characterized with X-ray diffraction (XRD) technique in the 2θ range [5 - 90°] with the use of BRÜKER D8 Diffractometer using CuKα (λ=1.54056 Å) radiation. Scanning Electron Microscopy (SEM) images were performed on a Quanta 250. Chemical composition analysis was carried out using atomic absorption spectroscopy (SAA) and X-ray fluorescence spectrophotometer (XRF, X Phillips MagiX). BET

* Corresponding author email: hamzaouighiat_imane@yahoo.fr

surface area measurements were carried out with micrometrics ASAP2020 equipment using nitrogen at 77 K. Fourier transform infrared (FTIR) spectra were recorded with a PERKIN Elmer model (spectrum one) within the range of 4000 - 400 cm^{-1}. The UV-Vis spectroscopy diffuse reflectance (DR) spectra were performed with Shimadzu model UV-2100 spectrophotometer, equipped with an integrating sphere accessory.

4. Photo-catalytic tests

Photo-catalytic performances of SiO_2@xNiO photo-catalysts were evaluated through the reduction of water to hydrogen under visible light. For each sample, 50 mg was dispersed in 200 mL of KOH electrolyte with a concentration of 0.5 M. The reaction temperature was regulated at (50 ± 1°C) with a thermostated bath. After temperature stabilization, the reaction mixture was stirred with a magnetic stirrer, and irradiated with three tungsten lamps (200 W). Before irradiation, the electrolyte was purged with nitrogen gas bubbling for 30 min with a flow rate of 10 mL min-1. The amount of hydrogen was determined volumetrically by a water manometer with an accuracy DV = ± 0.05 mL.

III. RESULTS AND DISCUSSION

1. Characterization of samples

XRD patterns of SiO_2, SiO_2@5NiO and SiO_2@10NiO are regrouped in Fig. 1. SiO_2 presents a broad peak centered at 2θ = 23°, characteristic of amorphous SiO_2 [17]. The patterns of synthesized SiO_2@5NiO and SiO_2@10NiO are the same and also, the intensities of the diffraction peaks increased when the nickel amount increases, indicating the formation of nickel nanoparticles. For SiO_2@xNiO the diffraction peaks at 2θ = 33° and 60° indexed to the (101) and (110) planes of a-NiO.

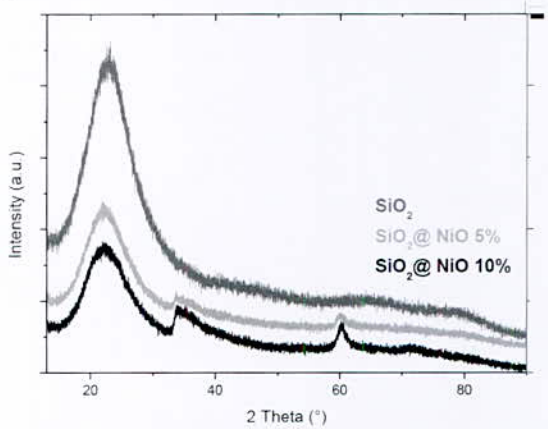

Fig. 1. XRD patterns of SiO_2,SiO_2@5NiO and SiO_2@10NiO

The morphology of the samples observed by SEM show the presence of SiO_2 are evenly distributed microspheres with a diameter around 300 nm and smooth surface, suggesting that an amorphous structure with poor crystallinity is formed (Fig. 2). This observation is in agreement with XRD analysis.

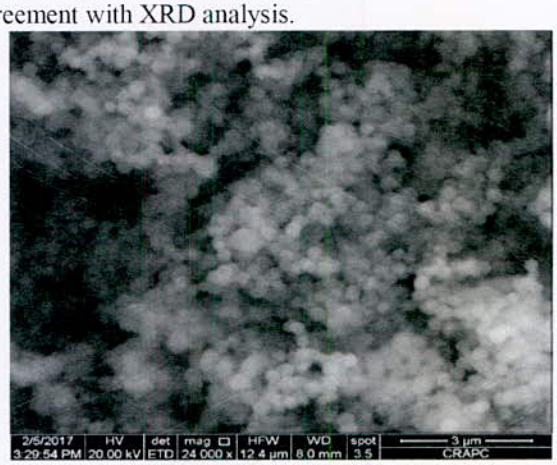

Fig. 2. SEM images of SiO_2

TABLE I
BET AND NICKEL CONTENTS EXAMINED BY SAA AND XRF

Samples	Nickel contents %			Surface area (m^2/g)	Eg (eV)
	Theory content	Experimental results			
		SAA	FRX		
SiO_2	-	-	-	17.2	-
SiO_2@5NiO	5	3.5	4	70.2	1.58
SiO_2@10NiO	10	9.1	9.89	94.9	1.18

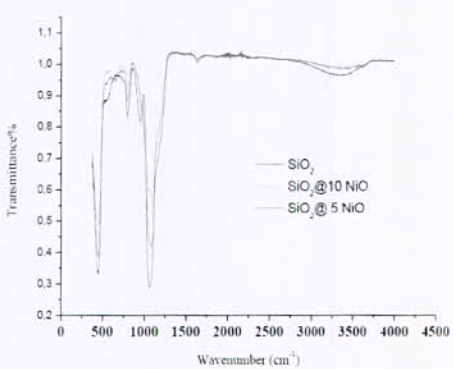

Fig. 3. FTIR spectrum of the SiO_2 and SiO_2@xNiO samples

The BET surface area of SiO_2@xNiO is higher than SiO_2, indicated that the SiO_2@xNiO samples have a relatively high surface-to-volume ratio (table 1). For adsorbent materials, a large surface area generally can provide more adsorption sites. The band gap energy for SiO_2@xNiO is found to be 1.58 and 1.18 eV for 5 and 10 %, respectively. The Eg value of SiO_2@xNiO corresponded to an indirect optical transition. The narrower Eg is responsible for an easier excitation of an electron from the VB to the CB in the materials and thus increased the photo-catalytic activity of these materials.

* Corresponding author email: hamzaouighiat_imane@yahoo.fr

The adsorption band located at 671 and 460 cm^{-1} can be attributed to the Ni-Si and the Ni–O group vibrations, respectively [19, 20].

2. Catalytic hydrogen production

Hydrogen production from water using semiconductors and NiO as photo-catalysts provides a potential way to *obtain hydrogen*. This is a clean, low cost and environmentally friendly production process achieved by irradiation. Preliminary experiments led us to select a basic pH for use in these studies. In the reaction under study the redox couple to produce H_2 involves the oxidation of SO_3^{2-} (hole scavenger) and the reduction of H_2O. When a photon with energy equal to or greater than the Eg is absorbed, an electron from the VB is promoted to the CB leaving a positively charged hole in the VB. The e^-_{CB} and h^+_{VB} are then capable to decompose water into hydrogen:

$$SC + hv \rightarrow e^-_{BC\,(SC)} + t^+_{BV\,(SC)}$$

In solution, hydrogen is produced efficiently by visible irradiation with simultaneous oxidation of the sulfite to sulfate ions.

$$SO_3^{2-} + 2h^+_{VB} + 2OH^- \longrightarrow SO_4^{2-} + H_2O$$

$$2SO_3^{2-} + 2h^+_{VB} \longrightarrow S_2O_6^{2-}$$

$$2H^+ + 2e^-_{CB} \rightarrow H_2$$

It can be seen that, SiO_2@10NiO exhibited an activity less than that of SiO_2@5NiO sample (Fig. 4). So, this material has an ability to absorb light and induce H_2 production and play a crucial role in the photo-catalytic activity.

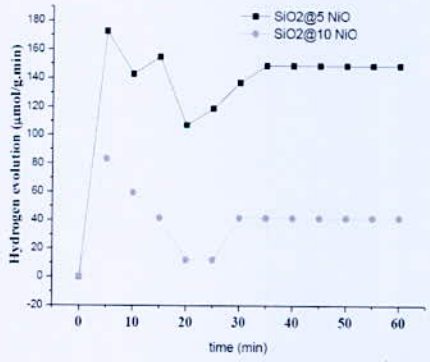

Fig. 4. Hydrogen evolution via photo-catalytic decomposition of water in the presence of the photo-catalysts SiO_2@NiO (5 and 10%) in KOH electrolyte and in the presence of the whole scavengers Na_2SO_3

On the other hand, Fig. 5, illustrates the effect of SiO_2@5NiO catalyst amount varied from 50 to 100 mg. So, the hydrogen evolution is 148.81, 77.38 and 89.29 µmol/g.min for the 50, 100 and 75 mg, respectively.

Using the same conditions, It can observe that the LED lamp show a stability of hydrogen generation during irradiation compared to the Tungesten lamp.

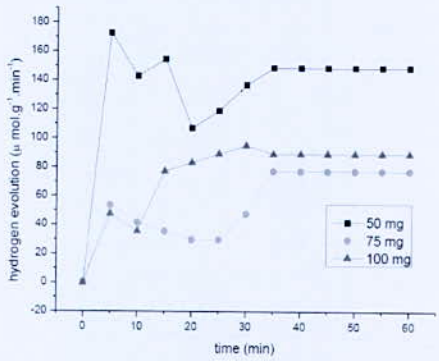

Fig. 5. Hydrogen evolution via photo-catalytic. decomposition of water in the presence of the photo-catalysts SiO_2@5NiO in KOH electrolyte and in the presence of the hole scavengers Na_2SO_3 with different weight of photo-catalysts 50, 75 and 100 mg.

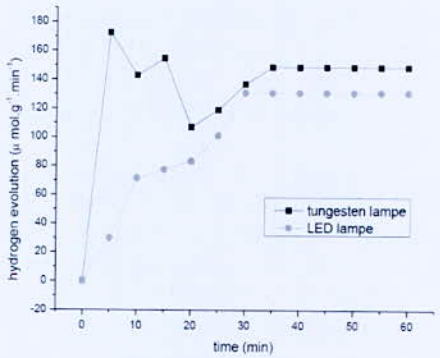

Fig. 6. Hydrogen evolution via photo-catalytic decomposition of water in the presence of the photo-catalyst SiO_2@5NiO in KOH electrolyte and in the presence of the hole scavengers Na_2SO_3 with tungsten lamp and LED lamp

IV. CONCLUSION

This work has focused on the photo-activity of SiO_2@xNiO prepared by hydrothermal method. The performance of this material is assessed for hydrogen evolution under visible light. The best photo-activity is found for the SiO_2@5NiO.

REFERENCES

[1] R.Brahimi, Y.Bessekhouad, A.Bouguelia, M.Trari, $CuAlO_2/TiO_2$ heterojunction applied to visible light H_2 production, J.Photochem. Photobiol.A:Chem.186 (2007) 242–247.

* Corresponding author email: hamzaouighiat_imane@yahoo.fr

[2] S.Saadi, A.Bouguelia, A.Derbal, M.Trari, Hydrogen photo-production over new catalyst $CuLaO_2$, J.Photochem. Photobiol. A: Chem.187 (2007)97–104.

[3] M. Ni, K.H.Leung, Y.C.Dennis, K.Sumathy, A reviewer and recent developments in photocatalytic water-splitting usingTiO_2 for hydrogen, Renew. Sustain. Energy Rev. 11(2005)401–425.

[4] P. Madhusudan, J. Zhang, B. Cheng, J. Yu, Fabrication of $CdMoO_4$@CdS core - shell hollow superstructures as high performance visible-light driven photocatalysts, Phys. Chem. Chem. Phys. 17 (2015) 15339–15347.

[5] J. Wang, S. Wang, Z. Huang, Y. Yu, High-performance $NiCo_2O_4$@Ni_3S_2 core/shell mesoporous nanothorn arrays on Ni foam for supercapacitors, J. Mater. Chem. A 2 (2014) 17595–17601.

[6] J. Zhou, C. Tang, B. Cheng, J. Yu, M. Jaroniec, Rattle-type carbon–alumina core-shell spheres: synthesis and application for adsorption of organic dyes, ACS Appl. Mater. Interf. 4 (2012) 2174–2179.

[7] Q. Guo, Y. Zhou, W. Nie, P. Chen, L. Song, Synthesis of highly monodispersed CdS/SiO_2 core shell nanoparticles and their photocatalytic activities, J. Nanosci. Nanotechnol. 15 (2015) 2364–2370.

[8] M. Ye, H. Zhou, T. Zhang, Y. Zhang, Y. Shao, Preparation of SiO_2@Au@TiO_2 core-shell nanostructures and their photocatalytic activities under visible light irradiation, Chem. Eng. J. 226 (2013) 209–216.

[9] B. Lin, C. Xue, X. Yan, G. Yang, G. Yang, B. Yang, Facile fabrication of novel SiO_2/g-C_3N_4 core–shell nanosphere photocatalysts with enhanced visible light activity, Appl. Surf. Sci. 357 (2015) 346–355.

[10] B. Zhu, J. Zhao, H. Yu, L. Yan, Q. Wei, B. Du, Naphthalimide-functionalized Fe_3O_4@SiO_2 core/shell nanoparticles for selective and sensitive adsorption and detection of Hg^{2+}, Chem. Eng. J. 219 (2013) 411–418.

[11] Y. Zhang, Thermal oxidation fabrication of NiO film for optoelectronic devices, Appl. Surf. Sci. 344 (2015) 33–37.

[12] C. Dong, Q. Li, G. Chen, X. Xiao, Y. Wang, Enhanced formaldehyde sensing performance of 3D hierarchical porous structure Pt-functionalized NiO via a facile solution combustion synthesis, Sens. Actuators B: Chem. 220 (2015) 171–179.

[13] L. Li, B. Cheng, Y. Wang, J. Yu, Enhanced photocatalytic H_2-production activity of bicomponent NiO/TiO_2 composite nanofibers, J. Colloid Interf. Sci. 449 (2015) 115–121.

[14] B. Bej, N.C. Pradhan, S. Neogi, Production of hydrogen by steam reforming ofmethane over alumina supported nano-NiO/SiO_2 catalyst, Catal. Today 207(2013) 28–35.

[15] A.M. Ali, R. Najmy, Structural, optical and photocatalytic properties of NiO-SiO_2 nanocomposites prepared by sol–gel technique, Catal. Today 208 (2013) 2–6.

[16] W. Stöber, A. Fink and E. Bohn. J. Colloid. Interf. Sci. Vol. 26 (1968) 62.

[17] Z. Xu, J. Yu, G. Liu, B. Cheng, P. Zhou, X. Li, Microemulsion-assisted synthesis ofhierarchical porous $Ni(OH)_2/SiO_2$ composites toward efficient removal offormaldehyde in air, Dalton Trans. 42 (2013) 10190–10197.

[18] K. Anandan, V. Rajendran, Morphological and size effects of NiO nanoparticlesvia solvothermal process and their optical properties, Mater. Sci. Semicond.Process. 14 (2011) 43–47.

[19] H. Dalvand, G. Reza Khayati, E. Darezereshki, A. Irannejad, A facile fabricationof NiO nanoparticles from spent Ni–Cd batteries, Mater. Lett. 130 (2014) 54-56.

* Corresponding author email: hamzaouighiat_imane@yahoo.fr

TiO_2@Carbon Spheres as Photo-Catalysts for Hydrogen Generation under Visible Irradiation

A. Boudjemaa[1], I. Beas[2], B. Mutuma[2], B. Motsoso[2], K. Bachari[1], N.J. Coville[2]

[1]Centre de Recherche Scientifique et Technique en Analyses Physico-Chimiques, Bou-Ismail CP 42004, Tipaza, Algeria.
[2] DST-NRF Centre of Excellence in Strong Materials and the Molecular Sciences Institute, School of Chemistry, University of the Witwatersrand, Johannesburg, 2050, South Africa.

Abstract—**Hydrogen production from water using semiconductors based on TiO_2@carbon sphere as photo-catalysts provides a potential way to obtain hydrogen. This is a clean, low cost and environmentally friendly production process achieved by irradiation. In the reaction under study, the redox couple to produce H_2 involves the oxidation of SO_3^{2-} and the reduction of H_2O. These photo-catalysts are an improved photo-activity under visible light irradiation and the enhanced activity is attributed to the light absorption behavior of the carbon spheres, the TiO_2 as well as the intimate contact between TiO_2 and the HCSs.**

Key words—Hydreogen generation, photo-catalysis, visible irradiation, TiO_2, Carbon spheres, nanomaterial.

I. INTRODUCTION

Photo-catalysis is one of the most important fields for renewable and environment friendly green energy research. In effect, catalysts used have semiconductors (SCs) properties with narrow band gap energy (Eg) located between the valence band (VB) and the conduction band (CB). Generally, photo-catalysis is based on the light absorption of SCs, to excite the electrons (e^-) to CB and leave a hole (h^+) in the VB, thus creating photo-generated electron/hole (e^-/h^+) pair, which are contributed to the oxidation and the reduction reactions [1–5]. So, solar energy conversion by photo-catalysis has been attracting much interest as an advantageous technology for a sustainable future in the context to reduce the energy and the environmental problems such as pollution and global warming [6 - 14]. A wide variety of materials have been investigated as photo-catalysts since the discovery of the water splitting photo-catalysis by Fujishima and Honda in 1972 [15]. However, titanium oxide (TiO_2) based materials have been largely investigated in heterogeneous and homogenous catalysts due to its stability, low cost preparation, relatively high efficiency, optical and electronic properties and low toxicity [16]. During the last decade, a considerable number of new photo-catalytic materials have been suggested due to some disadvantages which prevent its performance as larger band gap energy (Eg = 3.2 eV) which limits its use only in UV irradiation (absorption less than 5 % of the total solar irradiance) [15, 17, 18]. It is reported that modification of TiO_2 could make it absorb visible light and improve the efficient utilization of sunlight [19]. To do this, various techniques have been made to develop visible photo-catalysts for extending the absorption of TiO_2 to the visible region include doping, coupling or anchoring with other organic or inorganic elements such as nitrogen, carbon, halogen, or metals oxide.

II. EXPERIMENTAL

1. Materials preparation

1.1. Preparation of the silica materials by Stöber method through the hydrolysis and condensation of Tetraethyl orthosilicate (TEOS) [14].

1.2. Preparation of the core-shell materials based on titanium and iron with different metal weight (2, 5, 10 and 20 wt.%) by hydrothermal method.

1.3. Preparation of hollow carbon material (HCSMs) by CCVD method. The synthesis was carried out at atmospheric pressure in a quartz tube that is inserted vertically into a furnace, using a mixture of a toluene as carbon source and nitrogen as carrier gas. The reactor temperature was set at 900 °C with the flow rate of nitrogen of 100 mL/min.

2. Characterizations

The materials prepared were characterized with X-ray diffraction (XRD), Transmission electron microscopy (TEM) and Raman spectroscopy, thermogravimetric analysis (TGA), Infra-red spectra (FTIR), Raman and diffuse reflectance (DR).

3. Photo-catalytic tests

Photo-catalytic performances of of photo-catalysts were evaluated through the reduction of water to hydrogen under visible light. For each sample, 50 mg was dispersed in 200 mL of KOH electrolyte with a concentration of 0.5 M. The reaction temperature was regulated at 50 °C with a thermostated bath. After temperature stabilization, the reaction mixture was stirred with a magnetic stirrer, and irradiated with three tungsten lamps. Before irradiation, the electrolyte was purged with nitrogen gas bubbling for 35 min with a flow rate of 10 mL min^{-1}. The amount of hydrogen was determined volumetrically.

III. RESULTS AND DISCUSSION

1. Characterization

The TEM images of the HCSTi materials are shown in Fig. 1. As it can be seen that a highly uniform spherical structure with an average size of about 139 nm. A magnified image reveals that the spherical structures of

*Corresponding author email: amel_boudjemaa@yahoo.fr

HCSTi are barely damaged. Also, the materials show the hollow structure of HCSTi with large internal void space and thin nanoshells with not a uniform thickness ranged from 50 to 90 nm. After the leaching, carbon was coated only on the surface of TiO_2, where the dark color is gone out (see Fig. 1).

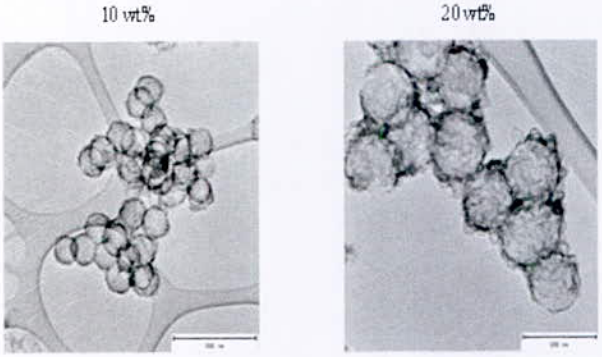

Fig.1. Transmission electron microscopy image of HCS and HCSTi: (a) 10 and (b) 20 %

The characteristic diffraction peaks of HCS located at the 2θ = 26.2 and 44.8°, indexed at (002) and (101), are ascribed to graphitic carbon (see Fig. 2).

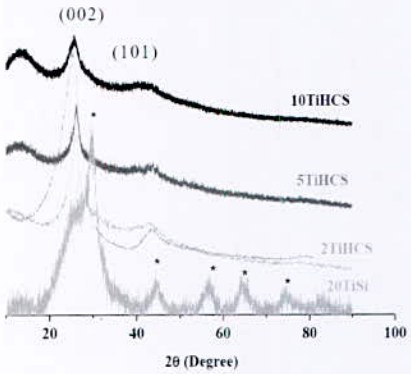

Fig.2. XRD patterns of the CS and xHCSs materials

Raman spectroscopy measurements are conducted to evaluate the graphitization and crystalinity of the prepared materials. All spectra show the presence of two bands; D-band and G-band at 1340 cm^{-1} and 1570 cm^{-1}, respectively (Fig. 3). The D-band is attributed to a disorder-induced feature due to lattice distortion. The G-band originates from the in plane stretching vibration mode, E_{2g}, of single crystal graphite **[19]**. The intensities of these bands give information about structural change characteristics of the carbon materials resulting from a change in morphology **[20]**.

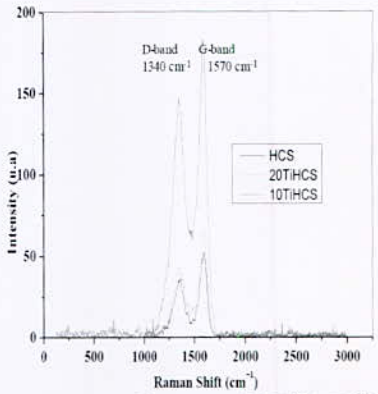

Fig.3. Raman spectra of the x wt. % TiO_2@SiO_2 with x = 5 %, 10 % and 20 %

The BET surface area of CSs is ~ 10 m^2 g^{-1} indicating that the spheres had little or no porosity. Whereas, the BET surfaces of HCS and 10TiHCS is 62 and 144 m^2 g^{-1}.

TABLE I
BET SURFACE DATA

Material	BET Surface (m^2/g)
SiO_2	41
$5TiO_2/SiO_2$	21.7
$20TiO_2/SiO_2$	176.7
TiC	7.4
HCS	62.7
10TiHCS	144.7
CSs	10

The Eg is determined from the absorption spectra using the equation:

$$(\alpha h\upsilon)^n = A(h\upsilon - Eg)$$

where α is the absorption coefficient, hυ is the photon energy, A is a constant depending on the (e^-/h^+) mobility and n depend on type of transition; equal to 2 or 0.5 for direct and indirect transition, respectively. The gap E_g is determined by plotting $(\alpha h\upsilon)^n$ versus (hυ) and extrapolating the linear portion which intercepts the energy axis hυ. The materials have a direct transition with a band gap energy of 1.38 and 1.47 eV which matches the visible spectrum.

2. *Hydrogen generation*

The development of a new photo-catalyst for production of clean and renewable energy is a great technological challenge [20, 21]. The most attractive way is hydrogen generation via photo-catalytic processes [22] which have attracted much interest compared to hydrogen produced from fossil fuel which can result in CO_2 emission [23].

*Corresponding author email: amel_boudjemaa@yahoo.fr

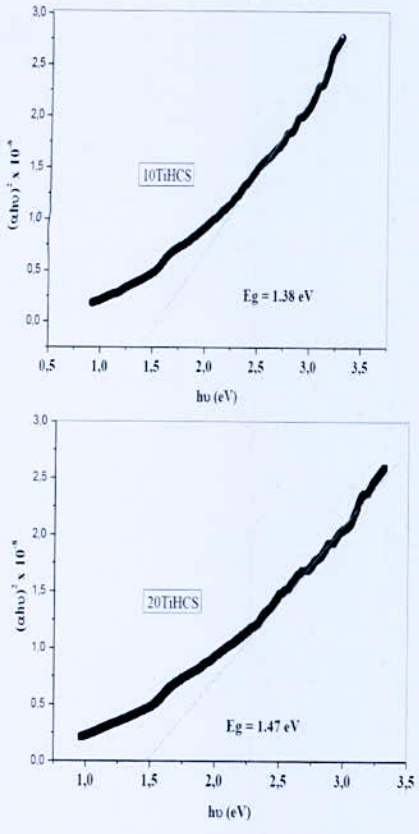

Fig.4. Direct band gap transition of 10TiHCS and 20TiHCS materials

The electrochemical and photo-electrochemical (PEC) measurements were performed with a potentiostat/galvanostat PGZ301. A traditional three electrode cell was used for the PEC characterization including a platinum auxiliary electrode, saturated calomel electrode (SCE) as reference electrode and the working electrode. The current-potential J(V) response upon illumination of the working electrode were recorded in 0.5 M KOH electrolyte.The light source consists of a tungsten lamp (200 W).

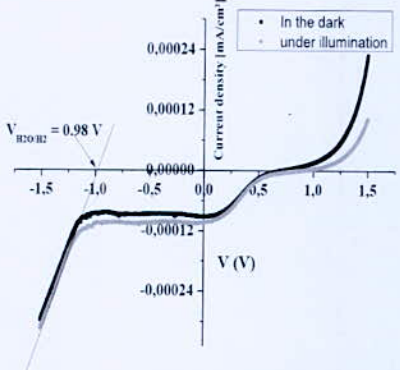

Fig.5. The J(V) plots of 20TiHCS electrode in Na_2SO_4 electrolyte (0.5 M) under N_2-atmosphere, scanning rate 10 mV/s

TABLE II
HYDROGEN GENERATION RESULTS

Material	H_2 evolution (mol/g.s)
TiC	422.85
HCS	262.73
10TiHCS	784.20
CSs	179

It is observed that the difference beteween TiC, HCS, 10ToHCS and CS, prompted an increase in the hydrogen production from 179 to 784 mol $g^{-1}s^{-1}$, for the same catalyst amount (100 mg) following 60 min light irradiation (Table 2). These observations may be due to their large band gap energy in hydrogen generation under visible light irradiation. We can conclude that the performance of carbon spheres based materials catalysis depend on their morphologies and structures.

IV. CONCLUSION

-The best photo-activity is found for the nanoparticles of Ti encapsulate by HCSs.
-Carbon materials are used to improve the electron transport.
- The role of the carbon is to assist in (e^-/h^+) separation at the semiconductor/electrolyte interface.
- The nanosized TiHCSs plays an important role in the process and both the size and the composition of the Ti particles reduce the limitations of a diffusion length.

REFERENCES

[1] L. Yuan, C. Han, M.-Q.Yang, Y.-J. Xu, Int. Rev. Phys. Chem. 2016,35,1.
[2] M.-Q.Yang, Y.-J. Xu, Nanoscale Horiz. 2016, 1, 185.
[3] T. Hisatomi, J. Kubota, K. Domen, Chem. Soc. Rev. 2014,43,7520.
[4] A. Boudjemaa, M. Trari, Intern. J. Hydrogen Energy vol.35, 2010, pp.7684.
[5] P. Reñones , A. Moya, F. Fresno, L. Collado, J. J.Vilatela, V. A.de la Peña O'Shea, J. CO2 Utilization, vol.15, 2016, pp.24
[6] P. Zhang , T. Wang, X. Chang , J. Gong, Acc. Chem. Res. vol.49, 2016, pp;911.
[7] X. Lang, X. Chen, J. Zhao, Chem. Soc. Rev. 2014,43, 473.
[8] M.-Q. Yang, N. Zhang, M.Pagliaro, Y.-J. Xu, Chem. Soc. Rev. Vol. 43, 2014, pp.8240.
[9] N. Zhang, M.-Q. Yang, S. Liu, Y. Sun, Y.-J. Xu, Chem. Rev. Vol. 115, 2015, pp.10307.
[10] S. Liu, Z.-R.Tang, Y. Sun, J.C. Colmenares, Y.-J. Xu, One-dimension-based spatially ordered architectures for solar energy conversion, Chem. Soc. Rev. vol. 44, 2015, pp.5053.
[11] J.C. Colmenares, R. Luque, Heterogeneous photocatalytic nanomaterials: prospects and challenges in selective transformations of biomass-

*Corresponding author email: amel_boudjemaa@yahoo.fr

derived compounds. Chem. Soc. Rev. Vol. 43, 2014, pp.765-778.
[12] A. Kubacka, M.Fernandez-Garcia, G. Colon, "Advanced nanoarchitectures for solar photocatalytic applications". Chem. Rev. Vol. 112, 2011, pp.1555-1614.
[13] L. Yuan, Y.-J. Xu, "Photocatalytic conversion of CO2 into value-added and renewable fuels", Appl. Surf.Sci. vol.342, 2015, pp.154–167.
[14] Y. Zhao, G. Chen, T. Bian, C. Zhou, G.I.N. Waterhouse, L.-Z. Wu, C.-H. Tung, L.J. Smith, D. O'Hare, T. Zhang, Adv. Mater. vol.27, 2015, pp.7824.
[15] A. Fujishima, K. Honda, « Electrochemical photolysis of water at a semiconductor electrode", Nature vol.238, 1972, pp.37.
[16] Du J, Lai X, Yang N, Zhai J, Kisailus D, Su F, et al. Hierarchically ordered macro-mesoporous TiO2-graphene composite fi lms: improved mass transfer, reduced charge recombination, and their enhanced photocatalytic activities. ACS Nano. vol.5, 2011, pp.590.
[17] A. L. Linsebigler, G. Lu, T.Yates J. Chem. Rev. vol.11, 2009, pp.735.
[18] M. Ni, M.K.H. Leung, D.Y.C. Lueng, K. Sumathy, Renew. Sustain. Energy Rev. Vol. 11, 2009, pp.401.
[19] X. Lin, F. Rong, X. Ji, D. Fu, vol.142,2011, pp.276.
[20] H. Zazoua, A. Boudjemaa, R. Chebout and K. Bachari. Enhanced photocatalytichydrogenproduction under visible light over a material based on magnesium ferrite derived from layered double hydroxides (LDHs). Intern. J. Energy Research vol.38, 2014, pp. 2010–2018
[21] A. Boudjemaa, T.Mokrani, K.Bachari, N. J. Coville. Electrochemical and photo-electrochemical properties of carbon spheres prepared via chemical vapor deposition. Mater.Scie.Semicond.Proces., vol.30, 2015, pp. 456-461
[22] A. Boudjemaa, I.Popescu, T.Juzsakova, M.Kebir, N.Helaili, K.Bachari, I.C.Marcu. M-substituted (M = Co, Ni and Cu) zinc ferrite photo-catalysts for hydrogen production by water photo-reduction. Intern.J.Hydrogen Energy, vol.41, 2016, pp. 11108-11118,
[23] F. Touahra, A. Rabahi, R. Chebout, A. Boudjemaa, D. Lerari, M. Sehailia, D. Halliche, K. Bachari. « Enhanced catalytic behaviour of surface dispersed nickel on LaCuO3 perovskite in the production of syngas: An expedient approach to carbon resistance during CO2 reforming of methane". Intern. J. Hydrogen Energy, vol.41 2016 pp.2477-2486

*Corresponding author email: amel_boudjemaa@yahoo.fr

A New Hetero-Junction *p*-CuO/Al_2O_3 for the H_2 Evolution under Visible Light

R. Bagtache[1*], F. Saib[2], K. Abdmeziem[1], M. Trari[2]

[1] Laboratory of Electrochemistry-Corrosion, Metallurgy and Inorganic Chemistry, Faculty of Chemistry, (USTHB), BP 32, 16111, Algiers, Algeria.

[2] Laboratory of Storage and Valorization of Renewable Energies, Faculty of Chemistry, (USTHB), BP 32, 16111, Algiers, Algeria.

Abstract—**This study was undertaken to assess the efficiency of the hetero-junction *p*-CuO x%/Al_2O_3 (x= 0 and 20%) assisted photo-catalytic process for the hydrogen evolution. The catalysts were elaborated by nirate route at 350 °C and characterized by X-ray diffraction, thermal analysis, and photo-electrochemistry. An optical gap of 1.32 eV for CuO was obtained from the diffuse reflectance. The Mott-Schottky plot, measured in neutral solution gave a *p*-type behavior with a flat band of +0.71 V_{SCE}. Hence, the conduction band of -0.52 V_{SCE}, made up of Cu^{2+}: e_g orbital, is more cathodic than the level H_2O/H_2, thus leading to spontaneous H_2 evolution upon visible illumination (2.09×10^{19} photon / s). A liberation rate of 139 µmol (g catalyst)$^{-1}$ min^{-1} and a quantum yield of 0.25% were determined in alkaline solution (NaOH 0.1 M, $S_2O_3^{2-}$ 10^{-2} M).**

Keywords—Hetero-junction *p*-CuO/Al_2O_3, nitrate route, Photoelectrochemical, Hydrogen, Visible light.

I. INTRODUCTION

Energy is essential to life on earth and the depletion of the fossil energy reserves has strongly motivated the research on the solar energy conversion. In this regard, the photocatalysis using colloidal systems is a low cost technique, easy to implement and does not require any special set up. The principle is based on the excitation of a semiconductor material by energetic photons ($h\nu > E_g$), thus generating electron/hole (e^-/h^+) pairs involved in the water reduction. Hydrogen is a friendly energetic vector with a storage capacity of 59.7 kJ kg^{-1} and can be produced cleanly from water and solar energy on low cost catalysts [1, 2].

In this respect, oxides are advantageous and CuO seems promising because of its low cost, friendly environmental characteristics and band gap (~ 1.4 eV), close to the ideal value. It can be synthesized by co-precipitation [3] hydrothermal route [4], microwave [5] and ultrasonic spray pyrolysis [6].

In this work, the hetero-junctions CuO/Al_2O_3 were synthetized from nitrates precursors at low temperature; the method is simple and inexpensive. The prepared oxides were characterized by various physical techniques. The hetero-junctions were successfully used for the hydrogen evolution upon visible illumination. To our knowledge, the hetero-junction *p*-CuO/Al_2O_3 prepared by co-precipitation with no noble metals has not been reported for the photocatalytic H_2 evolution.

II. EXPERIMENTAL

To prepare the hetero-junctions CuO(x%)/Al_2O_3 (x= 0 and 20%), appropriate quantities of $Cu(NO_3)_2.3H_2O$ and $Al(NO_3)_29H_2O$, both of high purity, were dissolved in distilled water and stirred on a hot plate until complete denitrification. Then, the powder was annealed at 400 °C for 3 h in a muffle furnace. The hetero-junctions were identified by X-ray diffraction (Philips PW 1800, using Cu Kα radiation) over the 2θ range (30 - 80°) and diffuse reflectance spectroscopy (Jasco 650).

The activation energy of the sensitizer CuO was determined from the electrical conductivity on sintered disc at 600 °C using the two probe technique. The electrochemical tests were done in a conventional cell under N_2 flow and shielded from external light by a black box. The intensity-potential J(E) characteristics and capacitance measurement were recorded with a PGZ 301 potentiostat (Radiometer), a saturated calomel electrode and Pt-electrode were employed respectively as reference and auxiliary electrodes.

The photocatalysis was realized in a double-walled Pyrex cell (0.2 L capacity), the temperature was maintained at 50 °C using a thermostated bath. The working electrolyte was prepared by dissolving Na_2SO_3 (10^{-2} M) in alkaline solution (NaOH 0.1 M). To preclude the vortex phenomenon and to homogenize the dispersion, a moderate magnetic agitation (250 rpm) was used.

The photo-catalytic activities of the hetero-junctions CuO (x%)/Al_2O_3 were carried out separately. The tests were determined by dispersing 200 mg of powder in alkaline solution for 4 h under visible light (3 × 200 W tungsten lamp, 2.07×10^{19} photons s^{-1}). Hydrogen was identified by gas chromatography (Agilent Technology 7890A) equipped with a thermal conductivity detector and quantified by volumetry in a water manometer. The solution was renewed after each test and distilled water was used for the solutions preparation.

III. RESULTS AND DISCUSSION

The semi conductivity is the main property of the photo-electrochemical device since it has the double role of photoreceptor and reservoir of electrons. The XRD

*Corresponding author email: bagtacheradia@yahoo.fr

patterns of the hetero-junction CuO and Al_2O_3 prepared by chemical route are illustrated in Fig. 1. The patterns indicate mixed oxides system; the peaks are slightly broad and belong to the tenorite CuO (JCPDS N° 45-0937), spread over amorphous alumina Al_2O_3, due to the low synthesis temperature (Fig. 1).

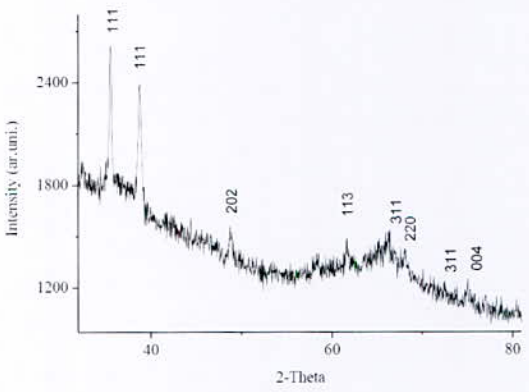

Fig. 1. X-ray pattern of the hetero-junction CuO/Al_2O_3 (20/80) prepared by nitrate route

The photo-catalysis is controlled by the morphology of the powdered catalyst through the specific surface area. Small crystallites should give large active surfaces and consequently better quantum yields are expected because of the decreased path the charge carriers have to diffuse to reach the liquid phase and to contribute to the photocatalytic process. For this reason, the nanosized oxides were prepared by nitrate route for the capture of most incident photons.

The optical transitions are determined from the UV-Visible diffuse reflectance. Fig. 2, relative to the hetero-junction, shows only one transition attributed to CuO, corroborating the XRD analysis. Al_2O_3 is a wide band gap oxide (> 6 eV) and cannot be observed in the diffuse spectrum. The relation between the absorption coefficient (α) and forbidden band (E_g) is given by:

$$\alpha h\nu = A\,(h\nu - E_g)^{1/m} \qquad (1)$$

where hν is the photon energy, the exponent *m* is function of the nature of the optical transition. The E_g value (1.32 eV) in the hetero-junction, determined by extrapolating the straight line $(\alpha h\nu)^2$ indicates a direct transition and agrees with the black color of CuO. Such value comes from the crystal field splitting of the Jahn-Teller ion Cu^{2+} ($3d^9$) in distorted octahedral coordination.

The position of the conduction band is vital in the photo-electrochemical conversion. In this respect, the capacitance^{-2} - potential relation $\{C^{-2} = (2/e\varepsilon\varepsilon_o N_D)\ \{V - V_{fb}\}\}$ provides both the flat band potential (V_{fb}) of 0.60 V, obtained from the extrapolation of the straight line (Fig. 3). The negative slope indicates *p* type behavior of CuO, due probably to Cu^{2+} insertion in octahedral sites.

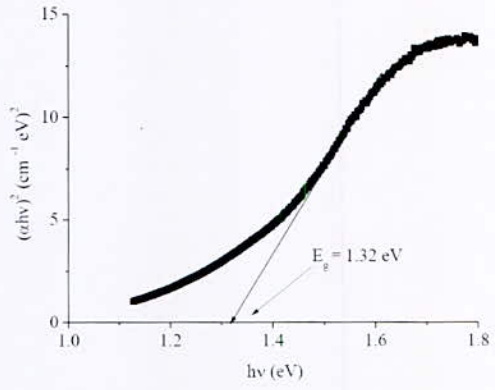

Fig. 2. Optical gap of the hetero-junction CuO/Al_2O_3 (20/80) prepared by nitrate route

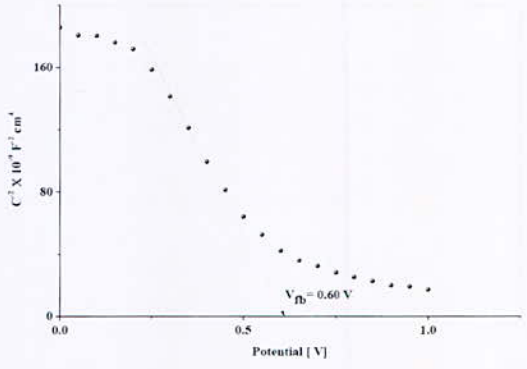

Fig. 3. The Mott-Schottky plot of CuO sintered at 600 °C

In order to test the effect of the hetero-junction, we have taken the best conditions of the hetero-junction CuO/ZnO reported by some of us [7], where the authors investigated the pH effect and found a best performance at alkaline pHs. This can be due to the fact that the potential of the redox couple H_2O/H_2 changes with pH (-0.059 V pH^{-1}) while the electronic bands of CuO, deriving from *3d* orbital, are pH-insensitive, this property was judiciously exploited to get an optimal band bending of ~ 0.5 V at the junction CuO/solution at pH ~ 12.

Fig. 4a, shows that the photo-activity of the hetero-junctions CuO x%/ Al_2O_3 (x= 0 and 20%) is greater than CuO Fig. 4b because of the synergy effect and to the dispersion of the sensitizer CuO on the alumina support.

The hydrogen formation evolves with a rate evolution of 139 µmol (g catalyst)$^{-1}$ min^{-1} at pH ~ 12 require and a conversion yield (η) given by:

$$\eta = 2\ \{\text{number of } H_2 \text{ mol s}^{-1}\} / \{\text{photons flux s}^{-1}\} \qquad (2)$$

*Corresponding author email: bagtacheradia@yahoo.fr

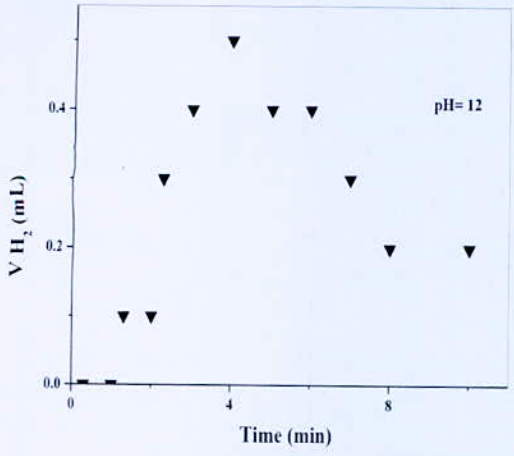

Fig. 4a. Volume of evolved hydrogen vs. illumination time of CuO

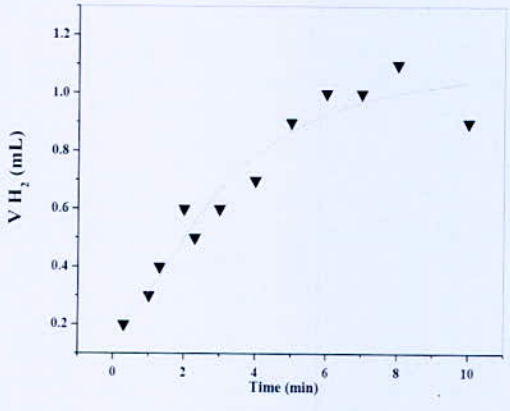

Fig. 4b. Volume of evolved hydrogen vs. illumination time of the hetero-junction CuO/Al_2O_3 (20/80)

A η value of 0.25% is obtained. The photocatalytic hydrogen formation occurs in less than 8 min above which saturation is observed. Hydrogen obtained is not produced according to the following sequences:

$$CuO + h\nu \rightarrow CB\ (e^-) + VB\ (h^+) \quad (3)$$

$$CB\ (2\ e^-) + 2\ H_2O \rightarrow H_2 + 2\ OH^- \quad (4)$$

$$SO_3^{2-} + H_2O + 2\ h^+ \rightarrow SO_4^{2-} + 2\ H^+ \quad (5)$$

The generated holes react with SO_3^{2-} to preclude the photocorrosion and to improve the photoactivity. Indeed, in absence of SO_3^{2-}, the solution turns to blue indicating presence of Cu^{2+}. Al_2O_3 is selected as support because it is chemically stable, non-toxic and inexpensive.

IV. CONCLUSION

The aim of this study was to characterize the hetero-junction *p*-CuO(20%)/Al_2O_3, prepared from nitrate precursors, and to assess its performance for the hydrogen production upon visible illumination. The hetero-junction was characterized photoelectrochemically and the conduction band of CuO, deriving from Cu^{2+}: *3d* orbital is more cathodic than the potential of H_2O/H_2 level, leading to spontaneous hydrogen liberation.

The best activity occurred in alkaline solution because of the optimal band bending.

REFERENCES

[1] D. Meziani, A. Reziga, G. Rekhila, B. Bellal, M. Trari, Hydrogen evolution under visible light over $LaCoO_3$ prepared by chemical route, *Energy Conversion and Management* vol.82, pp 244–249, 2014.

[2] G. Rekhila, Y. Bessekhouad, M. Trari, Hydrogen evolution under visible light over the solid solution $NiFe_{2-X}Mn_XO_4$ prepared by sol gel, *Int J Hydrogen Energy* Vol.40, pp 12611-12618,2015.

[3] S.B. Bagherzadeh, M. Haghighi, Plasma-enhanced comparative hydrothermal and coprecipitation preparation of $CuO/ZnO/Al_2O_3$ nanocatalyst used in hydrogen production via methanol steam reforming. *Energy Conver. Manag.* Vol. 142, pp 452-465, 2017.

[4] S. Bhuvaneshwari, N. Gopalakrishnan, Hydrothermally synthesized Copper Oxide (CuO) superstructures for ammonia sensing. *J. Colloid and Interface Scie.* Vol 480, pp76-84, 2016.

[5] C. Yang, F. Xiao, J. Wang, X. Su, 3D flower- and 2D sheet-like CuO nanostructures: Microwave-assisted synthesis and application in gas sensors. *Sensors and Actuators B: Chemical* Vol. 207, pp 177-185, 2015.

[6] W. Desisto, M. Sosnowski, F. Smith, J. Deluca, A. Wold, Preparation and characterization of copper (II) oxide thin films grown by a novel spray pyrolysis method. Mater. Res. Bull. Vol. 24, pp 753-760, 1989

[7] Y. Belaissa, D. Nibou, A. Assadi, B. Bellal B, M. Trari, a new hetero-junction p-*CuO*/n-*ZnO* for the removal of amoxicillin by photocatalysis under solar irradiation. J. Taiwan Institute of Chem. Eng. Vol. 68, pp254-265, 2016.

*Corresponding author email: bagtacheradia@yahoo.fr

Synthesis and Characterization of 5%Ni/γ-Al_2O_3 Catalyst via Wet Impregnation Method Assisted by Complexes: Primary and Secondary Amines as Ligands.

I. Sebai[1], A. Boulahouache[2] and N. Salhi[1,2*]

[1,*]Laboratoire de Chimie du Gaz Naturel, Faculté de Chimie, USTHB, BP 32 16111, Alger, Algerie.
[2]Laboratoire LCPMM, département de chimie, Faculté des Sciences, B.P 270 Route de Soumâa, U.Blida 1.

Abstract—**Ethylamine (EA) and diethylamine (DEA) were used in the preparation of 5%wtNi/γ-Al_2O_3 catalysts by incipient wetness impregnation (IWI) method. Various techniques including TGA-DTA, XRF, SEM, XRD, particles size, H_2-RTP and BET were used to characterize physico-chemical properties of the mentioned catalysts. The results showed that NiO ions form strongly different complexes with EA and EDA amines. Furthermore, the volume structure size has an effect on both the size and the metal-support interaction (MSI). The secondary amine with the bigger volume structure size achieved smaller NiO particles size highly dispersed and strong MSI due to the stronger steric encumbrance of EDA.**

Key words—Nickel Catalyst, Amine, Complexes, γ-Al_2O_3, Wet Impregnation.

I. INTRODUCTION

Supported Ni catalysts have resulted in being important due to comparative costs with precious metals and to the excellent activity reported in reforming reactions [1, 3]. Also, the support role of either α or γ-Al_2O_3 on the stability of catalyst is well known. However, the particular problem is the strong deactivation by carbon deposition. In order to prevent carbon deposition, chemical and physical structure of supported nickel catalysts have been the subject of many investigations and numerous methods have been used to decrease particles size (enhance the metal dispersion). It's well known that the coke formation behavior of a Ni-based catalyst depends strongly on its surface structure and acidity [4, 5]. It's well known also, that particle size of the active species plays a major role in activity and a stability of catalysts. Otherwise, many researchers showed that organic compounds like polymers and amines are promising agent in nanoparticles powder production and excellent agent for small particles synthesis. Nickel supported catalyst have been synthesized by introducing coordination chemistry in many previous work [6, 7].

For this purpose, we basically aimed to synthesize two supported catalysts using different amines ethylamine and ethyldiamine as ligand to chelate nickel nitrates precursor salt with size controlling and high SMSI of Ni/γ-Al_2O_3 catalysts by incipient wetness impregnation method.

II. EXPERIMENTAL

1. *Catalysts synthesis*

Three catalysts with 5%wtNi loading were prepared by impregnating γ-Al_2O_3 with respectively aqueous nickel nitrates $Ni(NO_3)6H_2O$(98% (Biochem) solution, aqueous nitrates nickel solution mixed with an excess of ethylamine (70% merck) volume forming blue gel and diethylamine (99% merck) volume forming a brown gel. After mixing nickel complexes precursors with support for 1h, the obtained suspensions were evaporated at 80°C, dried at 50°C for 12h and finally calcined at 700°C for 2h under air (5°C.min^{-1}). The achieved powder were crushed and sieved to 0.20-0.63mm particles grain and labeled respectively Ni/Al (conventional catalyst), Ni-EA/Al and Ni-DEA/Al.

2. *Catalysts characterization*

TGA-DTA analyses of non-calcined catalysts were performed on SDT Q600 equipment under Nitrogen flow (100ml min^{-1}) between 20°C and 1000°C at a rate of 20°C.min^{-1}. The chemical compositions of the prepared catalysts were determined by X-ray fluorescence Epsilon3X spectrometer equipement. XRD analyses were performed on Panalytical X'Pert PRO diffractometer using the CuKα radiation over 2θ range from 10 to 80°. The crystallite size was calculated using Scherrer's equation [8]. The morphology was investigated using Scanning Electron Microscopy (SEM) Quanta FEG 250 microscope from FEI with quantitative and qualitative analysis was measured by energy dispersive spectrometry (EDX). Surface area, average pore volume and pore size were determined by N_2 adsorption-desorption at -196°C using BET and BJH method. The measurements were occurred with ASAP 2020 Micromiritics equipment. Temperature-programmed reduction of hydrogen (TPR-H_2) was carried out on an AutoChem II 2920 V4.03 supplied by Micromeritics. 200 mg of calcined catalyst was dehydrated under He flow at 120°C for 1h, then reduced using 10%H_2/Ar (50ml.min^{-1}) at temperature range 50-900°C (10 °C.min^{-1}).

III. RESULTS AND DISCUSSION

TG-TDA analysis profile obtained with conventional catalyst exhibits total weight loss of 18% with three different peaks (Fig. 1a).The first peak at 80°C is

*Corresponding author email: nas.salhi@yahoo.fr

attributed to the removal physisorbed water [3]. The second peak is related to the endothermic dehydration of nickel nitrates between 80 and 230°C [3, 7]. The third weight loss occurring between 230 and 420°C corresponds to the decomposition of nickel nitrates and the formation of nickel oxide [8].

TGA curves of Ni-EA/Al and Ni-DEA/Al (Fig. 1.b and Fig. 1.c) present four weight losses with a total loss respectively of 20% and 23%. EA and DEA decomposition occurred at the temperature range 170-300°C. After eliminating all organic compounds, TGA curves became stable around 500°C forming nickel oxide.

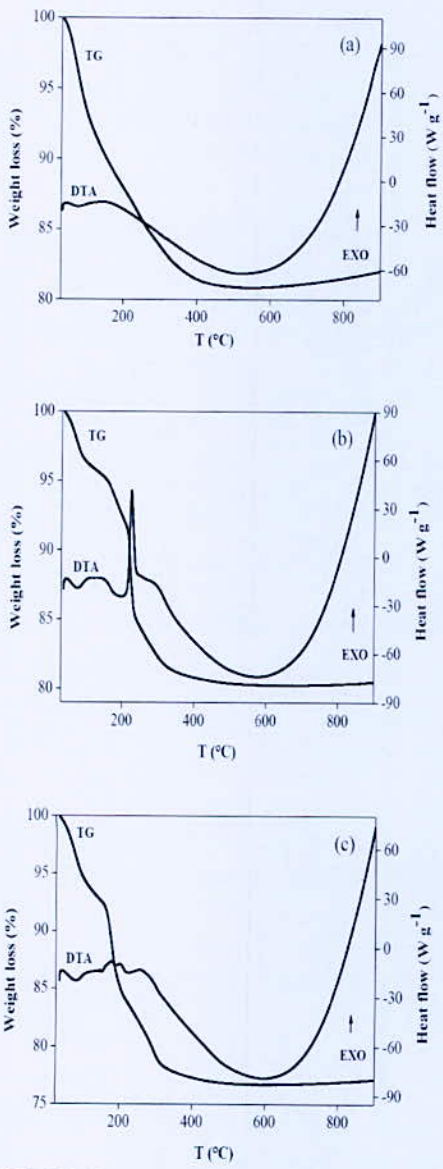

Fig. 1. TGA-DTA curves of non-calcined catalysts: (a) Ni/Al, (b) Ni-EA/Al, (c) Ni-DEA/Al

As expected, XRD patterns (Fig. 2.a) indicate clearly the presence of γ-Al_2O_3 and NiO phases (JCPDS card N°47-1049) for Ni-EA/Al and Ni-DEA/Al catalysts. NiO phase is not detected by XRD for the Ni/Al catalyst. Only spinel $NiAl_2O_4$ phase (JCPDS N°10 0339) is obtained. The diffraction peak of the $NiAl_2O_4$ phase is also observed for Ni-EA/Al sample. These results are in agreement with those obtained with TPR profiles (Fig. 3).

In view of the TPR profiles, different nickel species can be found. Ni/Al catalyst is characterized by one broad and high reduction peak at 735°C, indicating the presence of spinel $NiAl_2O_4$ phase [9, 10].

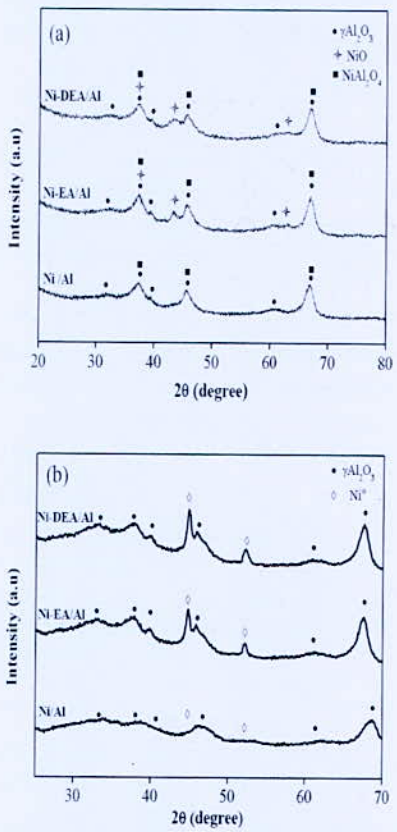

Fig. 2. XRD patterns of the nickel catalysts: (a) calcined, (b) after H_2-TPR.

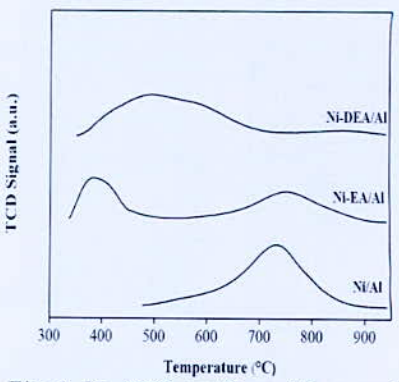

Fig. 3. H_2 -TPR profiles of the samples

Different nickel species can be found according to the TPR profiles. Ni/Al catalyst is characterized by one high and broad reduction peak at 750°C indicating the

*Corresponding author email: nas.salhi@yahoo.fr

reduction of spinel phase [11]. This result in accordance with XRD data.

Ni-EA/Al catalyst presents two main reduction peaks around 380°C and 750°C. These peaks are well described in the literature [12-14]. The large peak at 380°C is ascribed to the reduction of NiO phase interacting weakly with the support and the small peak at 750°C is likely attributed to the presence of spinel phase.

As can be seen, Ni-DEA/Al catalyst presents a large reduction peak shifted into the higher temperature (510°C) with continuous hydrogen consumption from 350°C until 700°C. This result indicates obviously that NiO species strongly interact with support. Ni-DEA complex formation promotes strong metal support interaction (MSI) during calcination step. Ehylenediamine with its larger volume structure size and stronger steric hindrance generates enhanced contact area with alumina support during impregnation step. The large contact area makes geometric distance between all Ni particles more extended preventing consequently their agglomeration.

Smaller Ni particles sizes were achieved when using a larger aliphatic amine.

XRD patterns of the reduced samples at 900°C for 1h given in Fig. 2.b show a narrow peak of Ni° phase (JCPDS, N°04-0850) for only Ni-EA/Al and Ni-DEA/Al materials. The absence of Ni° diffraction peaks in Ni/Al catalyst could be explained by the presence of Ni° in amorphous phase. Crystallite size of NiO and Ni° at 2θ = 46° and 2θ=66° was calculated according to the Scherrer's equation, and presented in Table I.

TABLE I
PARTICLES SIZE OF THE CALCINED AND REDUCED CATALYSTS

Catalyst	Nickel loading(wt %)		particle size (nm)	
	Targeted	Experimental	NiO	Ni°
Ni/Al	5	5.28	-[a]	-[a]
Ni-EA/Al	5	5.81	6.50	13.40
Ni-DEA/Al	5	6.15	3.72	12.64

[a] Non measured due to the XRD pattern showing no deconvoluted peak make it impossible for calculating.

The stronger encumbrance of ehylenediamine prevents NiO agglomeration during calcinations step and reduces sensitively NiO particles size.

Table II, summarizes the textural properties of calcined support catalysts. Samples exhibit pore diameter in the range of 5-78 nm. It's seen that addition of amines has no sensitive change on the surface area. Furthermore, the pore volume and pore size increase by introducing primary and secondary amine as indicated in Table II. The smaller NiO particles and strong MSI generated by addition of DEA avoid the pores obstruction by Nickel particles agglomeration.

TABLE II
TEXTURAL PROPERTIES OF CATALYSTS

Catalyst	BET (m^2/g)	pore volume (cm^3/g)	Average pore size (nm)
Al	111	0.17	4.90
Ni/Al	92	0.19	6.90
Ni-EA/Al	95	0.23	7.56
Ni-DEA/Al	99	0.27	7.70

The morphology of alumina support, Ni/Al, Ni-EA/Al and Ni-DEA/Al catalyst is shown in Fig. 5, γ-Al_2O_3 support presents homogeneous distribution of grain. Better distribution of Ni particles on alumina surface is observed with Ni-EA/Al and Ni-DEA/Al catalysts. Ni particles in conventional catalyst partly agglomerate on the surface and showed non-uniform distribution.

The EDX elemental analysis as shown in Fig. 5, confirms the presence of Ni, Al and O and no other elements were detected.

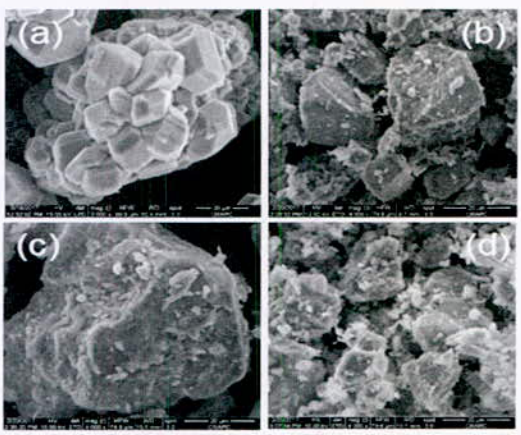

Fig. 4. SEM images a) γ-Al_2O_3, b) Ni/Al, c) Ni-EA/Al, d) Ni-DEA/Al

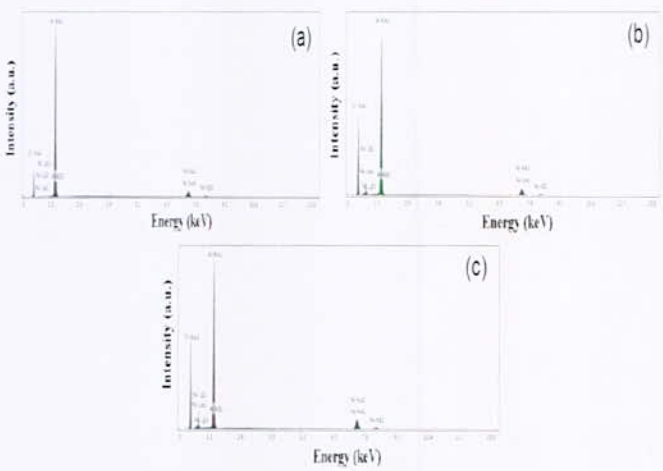

Fig. 5. EDX analysis : a) Ni/Al, b) Ni-EA/Al d) Ni-DEA/Al

*Corresponding author email: nas.salhi@yahoo.fr

IV. CONCLUSION

Our approach showed clearly the benefit of using such preparation method via Ni-Amine complex formation. This method provided a decrease of nickel particle size (enhance of the metal dispersion) and promoting the MSI; whose properties are reported to be *effective in carbon* suppression and preventing the metal sintering during methane reforming reaction. Small Ni particles sizes are achieved when using a larger volume aliphatic amine in preparation.

ACKNOWLEDGMENTS

The authors would like to thank Dr A.Boudjemaa Head of Environmental Chemistry Division Center of scientific and technical research in physicochemical analysis CRAPC, Tipaza, Algeria for her permanent collaboration and technical assistance.

REFERENCES

[1]A.Kambolis, H.Matralis, A.Trovarelli and C.Papadopoulou,"Ni/CeO_2-ZrO_2 catalysts for the dry reforming of methane," *Appl. Catal.* A.,vol. 377, pp. 16-26, Apr.2010.

[2] S.Sayas and A.Chica, "Furfural steam reforming over Ni-based catalysts. Influence of Ni incorporation method,"*Int. J. Hydrogen Energy.*, vol. 39, pp. 5234-5341, Mar.2014.

[3] X.Y.Gao, J.Ashok, S.Widjja, K.Hidajat and S.Kawi, "Ni/SiO_2 catalyst prepared via Ni-aliphatic amine complexation for dry reforming of methane: Effect of carbon chain number and amine concentration," *Appl. Catal.* A., vol. 503, pp. 34-42, Aug.2015.

[4]M.Wiesner and J.Y.Bottero, "Environmental nanotechnology. Applications and impacts of nanomaterials," Nanomaterials fabrication, in: *J.P. Jolivet, A. Barron,* chap. 3, McGraw-Hill, 2007, pp. 29-03.

[5]J.J.Guo, H.Lou, L.y.MO and X.M.Zheng, "The reactivity of surface active carbonaceous species with CO_2 and its role on hydrocarbon conversion reactions," *J. Mol .Catal. A.*vol. 316, pp.1-7, Feb.2010.

[6] F. Negrier, E. Marceau, M. Che and D. De Caro, "Role of ethylenediamine in the preparation of alumina-supported Ni catalysts from [Ni $(en)_2(H_2O)_2](NO_3)_2$:from solution properties to nickel particles," *C. R. Chimie.*, vol. 6, pp. 231-240, Feb.2015.

[7] D.W.Jeong, H.S.Na, J.D.Shim, W.J.Jang, H.S.Roh and U.H.Jung, "Hydrogen production from low temperature WGS reaction on co-precipitated Cu-CeO_2 catalyt: an optimization of cu loading," *Int.J.Hydrogen Energy.*, vol.39, pp. 9135-9142, Jun.2014.

[8] S.Yuvaraj,I.Fan-Yan, C.Tsong-Huei and Y.Chuin-Tih, "Thermal Decomposition of Metal Nitrates in Air and Hydrogen", *J. Phys. Chem.*B.,vol. 107, pp.1044-1047, Jan.2003.

[9] R.Yang, X.Li, J. Wu, X. Zhang and Z. Zhang,"Effects of Copper and Lanthanum Oxides on Nickel/Gamma-Alumina Catalyst in the Hydrotreating of Crude2-Ethylhexanol", *J.Phys.Chem.*,vol.113,pp.17787-17794, Sept.2009.

[10]J.M.Rynkowski, T.Paryjczak and M.Lenik, "Characterization of alumina supported nickel-ruthenium systems", *Appl.Catal. A.*, vol.126, pp.257-271, Jun.1995.

[11] P.Gayan, C.Dueso, A.Abad, J.Adanez, L.F.De Diego, F.de Diego and F.G.Labiano, "NiO/Al_2O_3 oxygen carriers for chemical-looping combustion prepepared by impregnation and deposition-precipitation methods", *Fuel.*, vol.88, pp.1016-1023, Jun.2009.

[12] J.S Lisboa, DCRM. Santos, FB,Passos and F.B. Noronha, "Influence of the addition of promoters to steam reforming catalysts", *Catal.Today.*, vol.101, pp.15-21, Mar.2005.

[13] T.Richardson, M.Lei, B.Turk,K.Forster and Martyn V.Twigg, "Reduction of model steam reforming catalysts:NiO/αAl_2O_3", *Appl.Catal.A.*,vol.110,pp.217-237, Mar.1994.

[14] D.C.R.M.Santos, L.Madeira and F. B.Passos,"The effect of the addition of Y_2O_3 to Ni/α-Al_2O_3 catalysts on the autothermal reforming of methane", *Catal.Today.*, vol.149, pp.401-406, Jan.2010.

*Corresponding author email: nas.salhi@yahoo.fr

Porous Silicon for Electrochemical Hydrogen Storage

S. Merazga* and N. Gabouze

Research Center Semiconductor Technology for Energetic, 02 Bd, Frantz FANON, B.P. 140, Algiers, Algeria.

Abstract—**we have prepared porous silicon (PS) layers by electrochemical anodization.The elaborated (PS) layers were characterized by Infrared Spectroscopy (FTIR), Contact Angle and Scanning Electron Microscopy (SEM).The electrochemical characterization and hydrogen storage were carried out in a three-electrode cell, using sulfuric acid 3M H_2SO_4 as electrolyte by cyclic voltammetry (CV), electrochemical impedance spectroscopy (EIS) and galvanostatic charge/discharge.**

The results indicate the presence of a single oxidation peak at 0.4 V on the anode side corresponding to hydrogen desorption and a reduction peak at -0.2 V corresponding to the adsorption of hydrogen. Moreover, the EIS studies show that the PS electrode behaves electrochemically better than silicon. The considerable hydrogen storage in PS indicated that this material could be a good candidate for hydrogen storage applications.

Keywords—Porous, silicon, hydrogen, storage, Electrochemical.

I. INTRODUCTION

Hydrogen is widely regarded as the most promising alternative to carbon-based fuels. In addition, hydrogen has been called 'the energy carrier of the future'. Different materials have been used for hydrogen storage; porous silicon (PS) is a candidate that could be used as a hydrogen storage material. This material has a large specific surface area (200-600 m^2 /cm^3) and if this zone is covered with a catalyst such as palladium, the hydrogen storage capacity can be improved. Kale et al. obtained a capacity of 2.25 wt% for PS at 9.67 bar and at 120 ° C using the Sievert device [1]. In this study, physicochemical and Electrochemical properties of porous silicon (PS) layers were investigated by Infrared Spectroscopy (FTIR), Contact Angle, Scanning Electron Microscopy (SEM), cyclic voltammetry (CV), electrochemical impedance spectroscopy (EIS)and galvanostatic charge/discharge.

II. EXPERIMENTAL

1. Preparation of PS

The porous silicon layers are obtained by electrochemical anodization of P type Si (100) with thickness of 355-405µm and resistivity of 1-10 Ω.cm^{-1}.The anodization was carried out in a Teflon cell with current density of 20 m A cm^{-2} for 3-10 min by using a potensiostat–galvanostat VMP3 in mi mixture of hydrofluoric acid / ethanol (1/1).The table1 summarizes the porosity and the thickness of the porous silicon layers prepared with a current density of 20 mV / cm 2 at different anodization times from 3 to10 min.

TABLE I
THE POROSITY AND THE THICKNESS OF THE POROUS SILICON LAYERS PREPARED AT DIFFERENT ANODIZATION TIMES

Sample	T anodizing (min)	Thickness (µm)	Porosity (%)
S1	3	2.58	69
S2	5	3.31	59
S3	7	3.58	67
S4	10	5.50	62

3. *Charactization*

The morphology, physico-chemical and hydrophobic properties of the samples were analyzed with scanning electron microscopy (SEM 505 Philips) infrared spectroscopy FTIR (Thermo-Nicolet 'Nexus' 670) and contact angle (Digidrop-GBX).

The electrochemical characterization and measurements were carried out in a three-electrode cell where the Platinum sheet was taken as a counter electrode and the Ag/AgCl was chosen as the reference electrode, the working electrodes were silicon and porous silicon, sulfuric acid 3M H_2SO_4 was used as electrolyte.

III. RESULTS

1. Physicochemical characterization

The FTIR spectra were recorded a resolution of 8 cm^{-1} with 64 scans.

Fig. 1, shows the FTIR spectra of porous silicon and monocrystalline silicon samples. The general appearance shows the interferences due to the pores formed on the surface of the sample; the periodicity of these interferences confirms the homogeneous distribution of the pores on the surface of the sample.

The spectrum of the porous silicon indicates that the PS surface is covered with SiH_x groups (x=1.2 or 3) They appear around 2075, 2116 and 2133 cm^{-1} ,attributed to the stretching modes of the υ (Si-H), υ(Si-H_2) and υ (Si-H_3) bonds, respectively, in agreement with the literature data [2][3]. The scissors mode of the υ(Si-H_2) band is located at 901 cm^{-1}, the wagging modes of the υ(Si-H_2) at 673 cm^{-1}. υ(Si-H) at 623 cm^{-1} are clearly visible in the spectrum [4].

*Corresponding author email: merazgasal@yahoo.fr

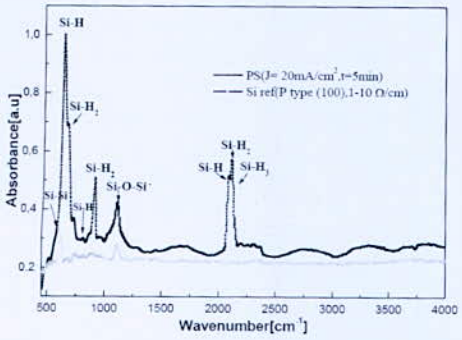

Fig. 1. Infrared spactra of (a)Si substrate, (b) Porous Si (J=20mA/cm^2,t=5 min)

2. Hydrophobic properties

The wettability of the surface was studied by the contact angle. Using 3µL deionized water at a temperature of 20 °C, we measured the contact angle with a controlled geometry system (Visio drop). The contact angle measured for the porous silicon is 111 °, this value being greater than 90 °, which confirms that the freshly prepared hydrogenated PS surface shows a hydrophobic behavior. This indicates that the obtained surface is completely covered with hydride bonds (Si-H_x), these bonds are non-polar functions with very low surface energy, while ultrapure water is a very polar medium with very high surface energy, (Fig. 2) **[5]**.

Fig. 2. The contact angle images of (a) Si substrate, (b) Porous Si

3. SEM microscopy

The SEM micrograph of the PS layers was carried out using a Philips scanning electron microscope. Fig. 3, confirms the formation of nano porous silicon. The surface observation shows a homogeneous and spongy layer which is characteristic of nanoporous silicon.

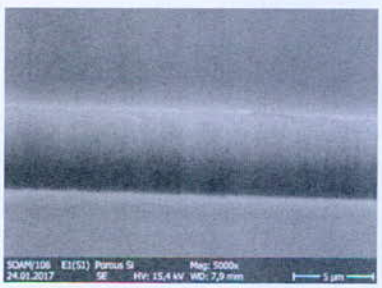

Fig. 3. SEM micrograph of a Porous Si layer

4. Electrochemical measurements

Cyclic voltammetry

This technique allows giving very important information on hydrogen storage performance; such as the potentials of insertion and deinsertion occurring in the material electrode used in the storage of hydrogen.Cyclic voltammetry at a speed of 10 mV / s is carried out on different PS layer, in a sulfuric acid electrolyte 3M H_2SO4; in the ranges of potential -1 to 1 V with respect to Ag / AgCl.

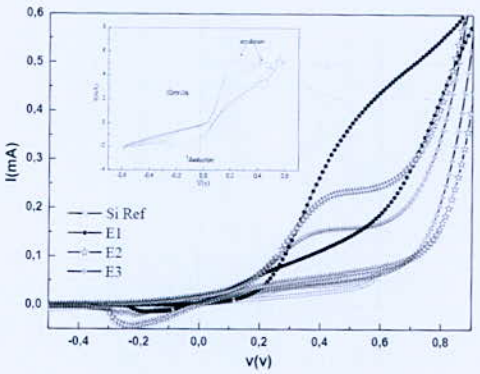

Fig. 4. CV curves of different PS layers in 3M H2SO4

The CV characteristics of the elaborated PS layers shown in Fig. 4 indicate the presence of two oxidation peaks at 0.2 eV and 0.4 eV (desorption of H_2) and a single reduction peak (adsorption of H_2) produced from water decomposition[6,7].

The porous layer with a thickness 3.3 µm (E2) presents a more intense reduction peak, which proves that this layer exhibits better hydrogen adsorption. This result confirms that this material could be a good candidate for use in mobile hydrogen storage applications.

Galvanostatic charge/discharge

Galvanostatic charge/discharge using a potentiostat-Galvanostat Autolab has been performed to evaluate the hydrogen storage capacity in the PS electrode material. Charge/ discharge measurements are recorded at a current density of 0.46 mA.

Although the electrochemical phenomena involved during charging and discharging are complex and imperfectly known, some reactions predominate and can be described. The main phenomena under load and discharge at the two electrodes are therefore:

(1) $H_2SO_4 + H_2O \Longleftrightarrow 2H^+ + SO_4^{-2}$

(2) $3\,H_2O \Longleftrightarrow 2H_3O^+ + 2e^-$

The performance curve of the cyclic life of a PS electrode is shown in Fig. 5. The storage capacity for this electrode shows a maximum of about 86.14 mA h / g and a minimum of 79.93 mA h / g. The results indicate that

*Corresponding author email: merazgasal@yahoo.fr

the storage capacity of PS electrode decreases only by 7% of the initial capacitance, after 40 cycles; this indicated that the electrode has a good stability.

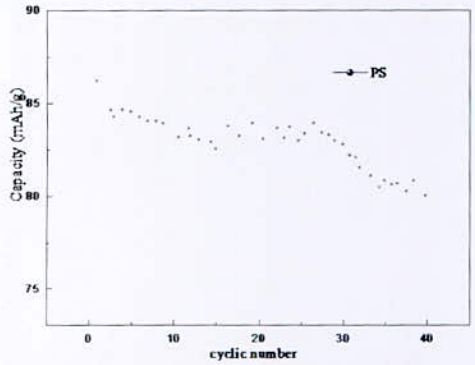

Fig. 5. Cyclic life effect for a PS layer

IV. CONCLUSION

In the present work, physico-chemical and hydrophobic properties of porous silicon layers prepared by electrochemical anodization have been studied.

Electrochemical hydrogen storage has been proved by CV and Galvanostatic charge/discharge measurements. A high hydrogen storage capacity of 86.14 mA h / g is obtained. This value is found to decrease only by 7% after 40 cycles, which can be increased by the addition of a thin layer of MgY.

REFERENCES

[1] P.Kale,C.Aneesh.Gangal,R.Edla,P.Sharma "Investigation of hydrogen storage behavior of silicon nanoparticles" *Int J Hydrogen Energy*, Vol.37, pp.3741-3747, 2010.

[2] V.Lysenko,F.Bidault,S.Alekseev,V.Zaitsev,D.Barbier ,C.H.TurpinF.Geobaldo, P.Rivolo, and E.Garrone "Study of Porous Silicon Nanostructures as Hydrogen Reservoirs" *J. Phys. Chem. B*, Vol.109,pp. 19711 – 19718, 2005.

[3] A.I. Manilov, S.A. Alekseev, V.A. Skryshevsky , S.V. Litvinenko, G.V. Kuznetsov, V. Lysenko "Influence of palladium particles impregnation on hydrogen behavior in meso-porous silicon" *J Alloys Compd*, Vol.492,pp 466–472,2010

[4] V. A., Burrows, Y. J Chabal, G. S.Higashi, K. Raghavachari, S. B. Christman "Infrared spectroscopy of Si(111) surfaces after HF treatment: Hydrogen termination and surface morphology".*J. Appl Phys Lett*,Vol *53*,pp.998-1000, 1988.

[5] K.Khaldi " L'immobilisation d'Acétylcholinestérase sur Silicium/ Silicium poreux fonctionnalisé : Application à la Réalisation de biocapteurs ampérométriques pour la détection des substances" Ph.D, Dept.Phys, Tlamcen Univ, 2016.

[6] Y.Honarpazhouh, F.Razi Astaraei;H.Reza Naderi ; Omid Tavakoli "Electrochemical hydrogen storage in Pd-coated porous silicon/graphene oxide" Int J Hydrogen Energy, Vol.41, pp. 12175-12182, 2016.

[7] GF. Guo, H. Huang, FH. Xue, CJ. Liu, HT. Yu, X. Quan, and al "Electrochemical hydrogen storage of the graphene sheets prepared by DC arc-discharge method", J.SurfCoatTechnol,Vol.228,pp.S120-S125, 2013.

*Corresponding author email: merazgasal@yahoo.fr

Concentration Degradation Effect on Lifetime of PEM Fuel Cell

Y. Kerkoub*, A. Benzaoui, Y. Ziari, F. Haddad and A. Babou

Laboratory of Thermodynamics and Energy Systems, Faculty of Physics, University of Science and Technology Houari Boumediene (USTHB), BP 32 El-Alia Bab Ezzouar, Algiers, Algeria.

Abstract—**Voltage degradation, as PEM fuel cell age is widely observed phenomenon and results in a significant reduction in the electrical power produced by the stack. The most important cause of avoidable serves degradation or failure is contamination electro-catalyst or membrane. Contamination may also be a problem on the cathode side of the fuel cell stack, as the quality of the air is not uniform and in certain urban setting contamination (e.g.CO, CO2, sulphur compounds, volatile compounds) may be considered unavoidable. The aim of this work is to study the effect of masse concentration decrease due to CO and CO2 contamination on the performance of the PEM fuel cell. Thus, causes variation the electrochemical proprieties of catalyst layer with time. These proprieties are described by changing reference current density of cathode catalyst layer. The fresh fuel cell model is validated with the data from the literature. Modifying the model by changing the parameters influenced by degradation, a degraded PEM fuel cell model is used. The degraded fuel cell is parametrically analyzed by using a commercial Computational Fluid Dynamics (CFD) software. The investigated parameters are reference current density the Catalyst Layer (CL) analyzed by using a commercial Computational Fluid Dynamics (CFD).**

It is shown that compared to simulation results for the degraded and the fresh PEM fuel cells for two years of operation, it is concluded that the influence of overall degradation on cell potential is significant.

Key words—PEM fuel cell, Degradation, Porosity, Durability.

I. INTRODUCTION

Proton exchange membrane (PEM) fuel cells have been regarded as one of the most efficient energy conversion engines due to their low to zero emissions, high power density, fast startup, system robustness and high energy conversion efficiency. However, two of most important consideration in electrical power system is reliability and life. Therefore PEM fuel cell lifetime (end of life) is great interest. Voltage degradation, as fuel cell age is widely observed phenomenon and results in a significant reduction in the electrical power produced by the stack. The voltage degradation can be as low as 1-2 µV.h [1]. However, the degradation rates can increase by orders of magnitude when conditions include some of the following, i.e. load cycling, start-stop cycles, low humidification or humidification cycling, temperature of 90°C or higher and fuel starvation.

II. DEGRADATION PHENOMENA DESCRIPTION

The most important cause of avoidable serves degradation or failure is contamination electro-catalyst or membrane. Contamination may also be a problem on the cathode side of the fuel cell stack, as the quality of the air is not uniform and in certain urban setting contamination (e.g.CO, CO2, sulphur compounds, volatile compounds) may be considered unavoidable. Therefore contamination is considered to be predominant degradation cause, and will certainly contribute to lower stability of performance, if not permanent degradation. This factor has been recently investigated in literature. Cheng et al. [2] reported that this type of contamination results in loss of activation in the cell, mainly caused by the impurities in the reactants. According to Taniguchi et al. [3], the durability of PEM fuel cell is affected by corrosion of the carbon support of the catalyst layer, which results in conductivity loss throughout the cell. Also, corrosion of the Platinum catalyst leads to changes in the structure inside the cell, which causes a decrease in electrochemical active surface area of the MEA [4].

The aim of this work is to study the effect of masse concentration decrease in catalysts layers due to CO and CO2 contamination on the performance of the PEM fuel cell. A 3 dimensional CFD model is used to model all transport phenomena in the complete 25 cm2 PEM fuel cell to investigate the effect of non uniform air quality and presence of CO and CO2 on the performance and life time of PEM fuel cell. According to Schmittinger et al [4] the catalyst layer properties, and performance of the cell are negatively influenced by the carbon corrosion of the GDL due to contamination. Also Madden et al. [5] reported that high relative humidity across the cell leads to an increase in the catalyst dissolution rate, which also results in higher rate of radical attack inside the MEA. Catalyst layer reference current density J (A/cm^2) is an important parameter in fuel cell modeling, which directly influenced by contamination.

For anode:

$$J_a = si_{0,H2}^{ref}\left(\frac{C_{H2}}{C_{H2}^{ref}}\right)^{\beta_a}\left[\exp\left(\frac{-\alpha nF\eta_a}{RT}\right) - \exp\left(\frac{(1-\alpha)nF\eta_a}{RT}\right)\right]$$

And for cathode:

$$J_c = si_{0,O2}^{ref}\left(\frac{C_{O2}}{C_{O2}^{ref}}\right)^{\beta_c}\left[\exp\left(\frac{-\alpha nF\eta_c}{RT}\right) - \exp\left(\frac{(1-\alpha)nF\eta_c}{RT}\right)\right]$$

Where

*Corresponding author email: kerkoubyoucef@gmail.com

i_0^{ref} : reference exchange current density (A/m^2)
$[C_{H2}]$,$[C_{O2}]_{ref}$: local species concentration, reference value (kgmol/m3)
s: surface to volume ratio (1/m)
β: concentration dependence (dimensionless)
α : transfer coefficient (dimensionnelles)
F : Faraday constant (9,65×10^7 C/kgmol)
The above equations is the general formulation of the Butler-Volmer function.
The effect of contamination in catalyst layer leads to change in concentration dependence β and α. thus causes a change in the total reference current density J. in this work, three values of reference current density of cathjode catalyst layer have been performed 5.25A/cm^2 (fresh fuel cell), 4.25A/cm^2 , 3.25 A/cm^2 and 2.25.

III. PEM FUEL CELL NUMERICAL MODEL

A complete, single PEM fuel cell model with serpentine design flow channels is analyzed using Fuel Cell Add-on Module of ANSYS Fluent, which is capable of modeling physical and electrochemical phenomena that represent PEM fuel cell operation.

1. *Geometry and operating conditions*

A single serpentine flow channel in bipolar plate for PEM fuel cell is used with 25 channels and active surface area of 25cm^2 includes the anode flow channels, anode gas diffusion layer, anode catalyst layer, proton exchange membrane, cathode catalyst layer, cathode gas diffusion layer, and cathode flow channels which is presented in figure 1. The geometry parameters details and operating conditions are presented in tab 1 and 2 that Corresponding of experimental work of Ferng et al [7]

TABLE I
GEOMETRIC DETAILS FOR SIMULATION

Parameters	Value	Unit
Cell width	50	mm
Cell hieght	50	mm
Channel length	49	mm
Channel height	1.0	mm
Electrode thickness	0.2	mm
Catalyst layer thickness	0.018	mm
Membrane thickness	0.026	mm

2. *Numerical treatment*

The governing transport equations are solved subject to the various boundary conditions presented in below section using Fluent 15 CFD code. Fluent 15 is a parallel code using a finite volume method and an iterative segregated implicit solver.
Second order discretization schemes are used for all transport equations and SIMPLE algorithm for pressure coupled equation. All simulations presented here are performed using a grid of 50 in x direction, 500 in y direction and 100 in z direction. It should be noted that the parallel solver allows the use of a large computational grid total of 2500000 cells.
Discrete solver is used to enhance the convergence of the simulations. Multi-grid cycle is changed to F-cycle with BCGSTAB (biconjugate gradient stabilized method) as the stabilization method for the species and the potential equations. In addition, multi-grid cycle tolerances are decreased to 0.001 for some of the numerical equations, as suggested by Siegel

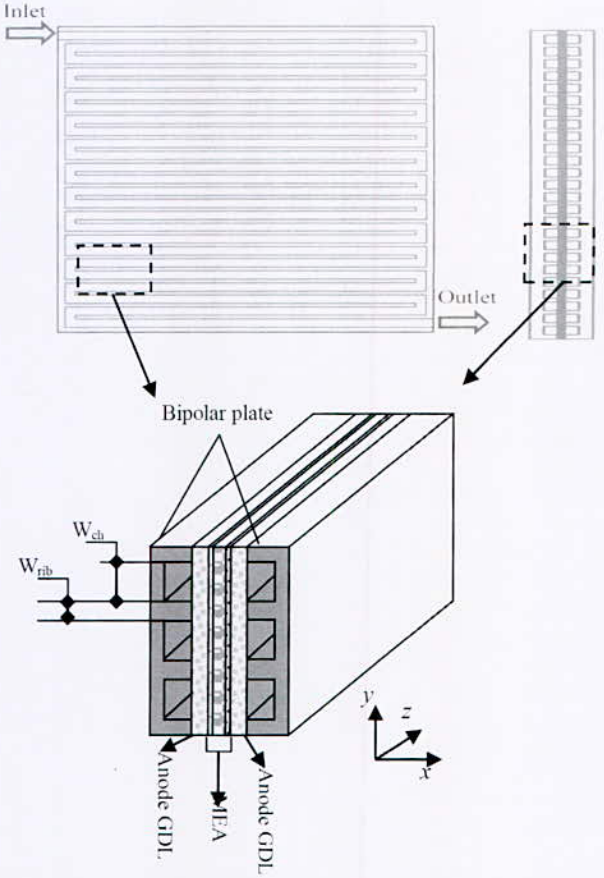

Fig. 1. Schematic of single serpentine PEM fuel cell

TABLE II
OPERATING CONDITIONS USED IN SIMULATION

Operating conditions	value	Unit
Operating temperature	323	°K
Pressure at anode	1	bar
Pressure at cathode	1	bar
Masse flow rate at anode	6.68×10^{-6}	kg/s
Masse flow rate at cathode	1.129×10^{-5}	kg/s
Relative humidity	100	%
Open circuit voltage	0.91	V

IV. RESULTS AND DISCUSSION

In this study a polarization curve for a fresh single serpentine PEM fuel cell is drawn and compared with degraded one. To draw a polarization curve (current density versus cell potential) by using ANSYS Fluent, the

*Corresponding author email: kerkoubyoucef@gmail.com

electric potential for the cathode should be varied begging from a voltage near the open circuit voltage and then, it should be gradually decreased. A degradation phenomenon is investigated by using a variety of reference current density of cathode catalysts layer (from 5.25 to 2.25 A/cm^2). The open circuit voltage of the PEM *fuel cell* varies locally with temperature and the gas composition in the electrodes and is normally around 0.91-1.05 V. In this study, thus lower limit of the open circuit voltage is applied (0.91 V) in CFD simulations.

1. Model validation

First, the fresh PEM fuel cell simulation results are validated to experimental study of Ferng et al [7] shown in fgure2 for geometry and operating parameters mentioned above table 1 and 2. The figure clearly reveal that the performance curves (Polarization curves) predicted by the present CFD model agree with those obtained by the experiments. Discrepancies between the calculations and the experiments are essentially caused by neglecting the liquid water effects and effects of contact resistance, etc.

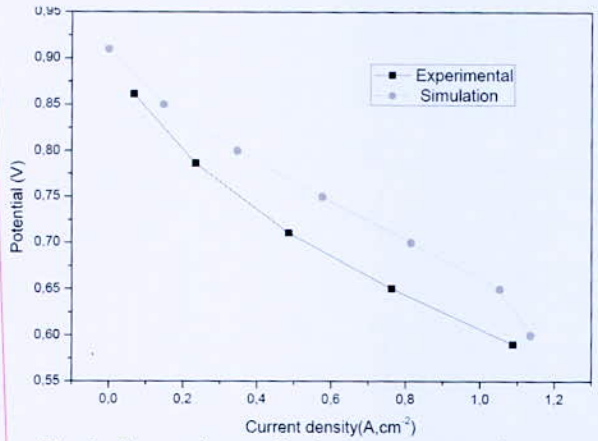

Fig. 2. Comparisons of voltage vs. current density between predictions and experiments for the PEMFC with serpentine flow channels

2. Degraded single cell

The effect of the catalyst layer degradation due to contamination is examined by investigating the effects of the reference current density i_0 (A/cm^2) on the cell performance by assigning three different values for each 4.25,3.25 and 2.25 and compared to the fresh fuel cell. Twenty simulations have been performed, for each current density, the potential of the cell is varying from 0.85 to 0.55V by step of 0.1V.

Figure 3 show the polarization curves for different current density of cathode catalyst layer. It's very clear that decreasing reference current density due to contamination reduces the power density produced by the PEM fuel cell. It's observed that, among the parameters taken into account the effect of contamination on the cell performance loss is below 6.4%. The maximum performance loss is observed for a cell potential value of 0.65 V. However, PEM fuel cells mostly operate above the cell potential value of 0.7 V and below the current density of 700 mA/cm2. The table3 present for details the comparison between fresh and degraded values of the power loss for different operating potential.

After analyzing this figure, it can be observed that the current density magnitude of the degraded cell is lower than that of the fresh cell. Higher reference current density result in drying out of the cell, which considerably limit the performance of fuel cells. Therefore, it can be concluded that the performance of the degraded fuel cell is lower than the fresh cell due to the contamination.

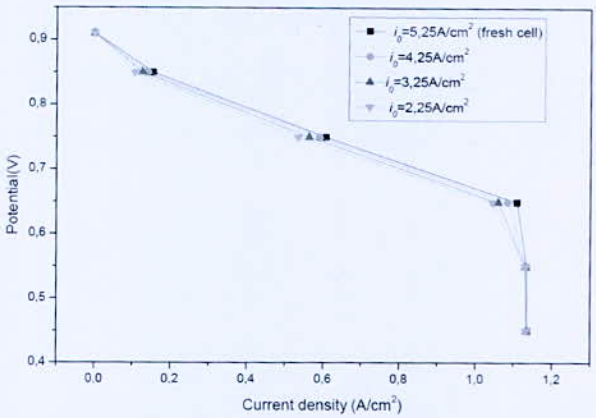

Fig. 3. Comparisons of voltage vs. current density between predictions and experiments for the PEMFC with serpentine flow channels

TABLE III
POWER LOSS FOR DEGRADED CELL

Cell potential	i_0=4.25	i_0=3.25	i_0=2.25
0.85	1.4%	2.8%	4.8%
0.75	1.7%	4.4%	7.3%
0.65	2.4%	4.9%	6.5%
0.55	0.1%	0.3%	0.4%
0.45	0.1%	0.2%	0.5%

V. CONCLUSION

In this work, degradation of a PEM fuel cell has been analyzed by using CFD code to understand the degradation phenomenon in PEM fuel cells.

Also, the effect of various parameters on degradation of cell performance are investigated by performing a parametric analysis on cathode catalyst layer of the PEM fuel cell. It can be concluded that degradation phenomenon due to contamination has great effect on degradation of the cell. It influences electrochemical proprieties of catalysts layer component. It is also observed that degradation has substantial impact on the performance of PEM fuel cells.

Degradation phenomena in PEM fuel cells are complicated. The final results of electrochemical reactions are only observable.

*Corresponding author email: kerkoubyoucef@gmail.com

is possible to extend this work by analyzing some other parameters, which may have effect on fuel cells' performance. The present study may be a beginning point for future numerical investigations of fuel cell power degradation.

REFERENCES

[1] F. A. de Bruijn,V. A. T. Dam, G. J. M. Janssen Review: Durability and Degradation Issues of PEM Fuel Cell Components.

[2] X. Cheng, J. Zhang, Y. Tang, C. Song, J. Shen, D. Song, J. Zhang, Hydrogen crossover in high-temperature PEM fuel cells, J. Power Sources 167 (2007) 25-31.

[3] A. Taniguchi, T. Akita, K. Yasuda, Y. Miyazaki, Analysis of electrocatalyst degradation in PEMFC caused by cell reversal during fuel starvation, J. Power Sources 130 (2007) 42- 49.

[4] W. Schmittinger, A. Vahidi, A review of the main parameters influencing longterm performance and durability of PEM fuel cells, J. Power Sources 180 (2008) 1-14.

[5] T. Madden, D. Weiss, N. Cipollini, D. Condit, M. Gummala, S. Burlatsky, V. Atrazhev, Degradation of polymer-electrolyte membranes in fuel cells: I. Experimental, J. Electrochem. Soc. 156 (5) (2009) B657-B662.

[6] S. Kamarajugadda, S. Mazumder, Cathode catalyst layer model for polymer electrolyte membrane fuel cell, Proc. of the ASME IMECE2012, IMECE2012-85952, 789-798

[7] Y. M. Ferng, A. Su. A three-dimensional full-cell CFD model used to investigate the effects of different flow channel designs on PEMFC performance, International Journal of Hydrogen Energy 32 (2007) 4466 – 4476.

*Corresponding author email: kerkoubyoucef@gmail.com

Hydrogen Production Using Geothermal Power Plant with Binary Cycle

A. Mechid Hadjala[1*] and A. Khellaf[2]

[1*]Compagnie de l'Electricité Et du Gaz (CEEG.SPA), Sonelgaz, Algiers, Algeria.
[2] Centre de Développement des Energies Renouvelables, BP62 Bouzaréah, Algiers, Algeria.

Abstract—Binary cycle power plants play an important role in the world of generating electricity and hydrogen from low and medium temperature, in the case of low temperature the geothermal energy can produce electricity by the technology of Binary cycle. This work describes a thermodynamic model of a binary cycle power plant and its components and hydrogen production with alkaline electrolysis.

Key words—Hydrogen production, binary cycle, geothermal energy.

I. INTRODUCTION

Sustainable hydrogen, as an energy vector and a fuel, is among these energy sources that are attracting a lot of attention.

Algeria is richly endowed with renewable energy resources. The most important renewable energy sources are solar, wind and geothermal energy and to some extend biomass.

Geothermal energy is a very promising renewable energy source. The resources, mainly of hydrothermal nature, are estimated at 460 GWh/year. More than two hundred hot springs have been found in the Northern part of the country. About a third of these hot springs have water temperature above 45 °C, with a temperature of 98 °C at Hammam Meskhoutine (Guelma) [1].

II. DESCRIPTION OF THE STUDY

The main object of this work is to investigate the use of geothermal energy in the hydrogen production. The case of a geothermal energy it used to heat up the water in of electrolyzes and to heat up the Preheater and evaporator of binary cycle power plant, in binary systems, the water from the geothermal source is used to heat a secondary fluid which is vaporized and used to turn the turbine/generator units. The geothermal water and the working fluid are each confined in separate circulating systems and never come in contact with each. The effect of the different system parameters on the production rate will be studies.

III. ASSESSMENT OF HYDROGEN PRODUCTION USING GEOTHERMAL POWER PLANT WITH BINARY CYCLE

1. *Basic geothermal binary cycle power plant* [04]

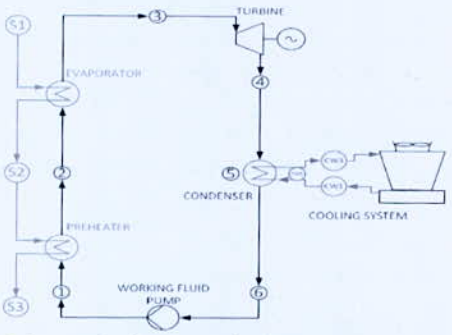

Fig. 1. Schematic diagram of a basic binary power cycle

A simple method for describing a binary power cycle is to follow the T-s diagram shown in Fig. 2. The thermodynamic states of the working fluid in the secondary cycle are shown in the P-h diagram in Fig. 3. Such a diagram helps in understanding the thermodynamic cycle and different states of the working fluid.

The binary cycle (Fig. 1) consists of the following four processes:

- ✓ 6 – 1 Isentropic compression in the working fluid pump;
- ✓ 1–2–3 Constant pressure heat addition in preheater and evaporator;
- ✓ 3 – 4 Isentropic expansion in a turbine;
- ✓ 4 – 5 – 6 Constant pressure heat rejection in a condenser.

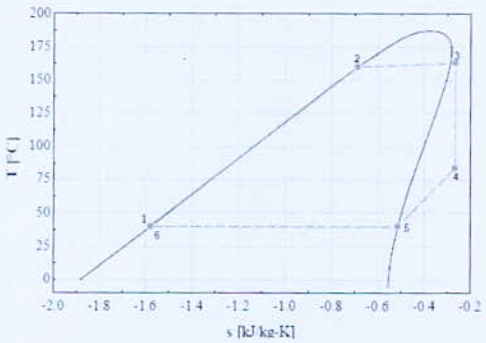

Fig. 2. T-s diagram for a binary cycle using Isopentane as a working fluid [04]

*Corresponding author email: mechidhadjala@hotmail.fr

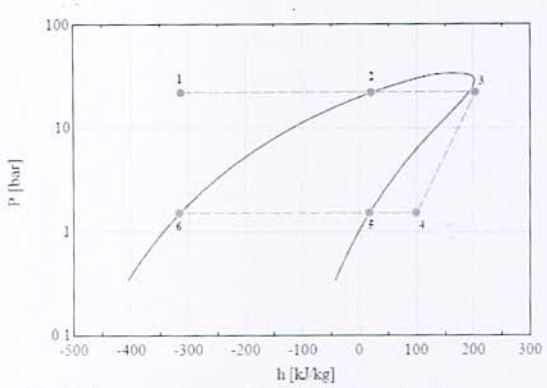

Fig. 3. P-h diagram for a binary cycle using Isopentane as a working fluid [04]

The area under processes 1-2-3 represents the heat transferred to the working fluid in the preheater and evaporator, and the area under the processing curve of states 4-5-6 represents the heat rejected in the condenser. The difference between these two areas is the network produced by the cycle (the area enclosed by the cycle curve).

2. *Binary cycle components and energy analysis* [04]

2-a. Preheater and evaporator

Considering the entire package as a thermodynamic system where the amount of heat transfer to the working fluid is equal to the heat losses from the geothermal fluid, the energy balance equation is given as:

$$\dot{m}_{gf}\,(h_{s1} - h_{s3}) = \dot{m}_{wf}\,(h_3 - h_1) \qquad (1)$$

Where $\dot{m}_{gf}$ = Mass of geothermal fluid;

$\dot{m}_{wf}$ = Mass of working fluid; and

h = Values of enthalpies at each specific point.

If the heat capacity of the geothermal fluid is assumed to be known, in the energy balance the enthalpy difference may be replaced by the difference in temperature:

$$\dot{m}_{gf}\,Cp_{gf}\,(T_{s1} - T_{s3}) = \dot{m}_{wf}\,(h_3 - h_1) \qquad (2)$$

Where Cp_{gf} =Specific heat of geothermal fluid;

and T = Temperatures at each specific point.

The minimum temperature difference in the heat exchanger, between the geothermal fluid and the working fluid, is called the pinch-point, and the value of that difference is designated the pinch-point temperature difference, ΔTpp. In the analysis of this diagram, points 1, 2 and 3 are known from the cycle thermodynamics analysis. Therefore, the preheater and evaporator may be analyzed as follows:

Preheater:

$$\dot{m}_{gf}\,Cp_{gf}\,(T_{s2} - T_{s3}) = \dot{m}_{wf}\,(h_2 - h_1) \qquad (3)$$

Evaporated:

$$\dot{m}_{gf}\,Cp_{gf}\,(T_{s1} - T_{s2}) = \dot{m}_{wf}\,(h_3 - h_1) \qquad (4)$$

The pinch-point temperature difference is generally known from the manufacturer's specifications; this allows TS2 to be found from the known value for T2 as follows:

$$T_{s2} = T_2 + \Delta T_{pp} \qquad (5)$$

where ΔT_{pp} = Pinch-point temperature difference.

2-b. Turbine

The binary cycle turbine converts the vapor thermodynamic energy of the working fluid to mechanical work on the turbine shaft; this shaft is coupled to the generator where electricity is produced. The thermodynamic analysis of the turbine in binary cycles follows the same assumption as for steam turbines. The ideal turbine is isentropic, that means the entropy at the inlet point is the same as at the outlet point.

The vapor enthalpy change in the real turbine is the enthalpy change in the ideal turbine multiplied by the turbine isentropic efficiency. The work output of the real turbine is this enthalpy change multiplied by the working fluid mass flow through the turbine.

$$\dot{W}_T = \dot{m}_{wf}\,(h_3 - h_4) = \dot{m}_{wf}\,\eta_t\,(h_3 - h_{4s}) \qquad (6)$$

where $\dot{W}_T$= Work output of the turbine; and

ηt = Turbine isentropic efficiency.

It is important to note that the selection of the working fluid defines some parameters in the turbine design.

2-c. Condenser

The condenser is another heat exchanger in the binary cycle.

The condenser exchanges heat between the cooling fluid cycle and the working fluid vapor. The turbine exhaust vapor exits the turbine and is led to the condenser where it is condensed by the cooling fluid. The condenser may be water or air cooled. This process occurs at a constant pressure (isobaric condensation).

The calculations for the condenser are roughly the same in both cases as the temperature profile of cooling fluid (air or water) is very close to linear. At point 4, the vapor comes from the turbine. At point 5, the vapor reaches the dew point and it is at this point that the condensation process starts. Point 6 is the condensed fluid, normally saturated liquid, moving towards the working fluid pumps. Point CW3 is the entry of the cooling fluid and CW1 is the outlet of the cooling fluid, to and from the cooling tower.

The condenser heat transfer between the working fluid and the cooling fluid can be expressed as follows:

$$\dot{m}_{CF}(h_{CW3} - h_{CW1}) = \dot{m}_{wf}\,(h_4 - h_6) \qquad (7)$$

where $\dot{m}_{CF}$= Mass of cooling fluid.

The cooling fluid may be taken as having a constant specific heat $C_{P\text{-}CF}$ for the small temperature range from inlet to outlet. To dissipate the required amount of waste heat, a cooling tower with a specified range, TCW3 –

*Corresponding author email: mechidhadjala@hotmail.fr

TCW1, will need a mass flow rate determined by the following equation:

$$\dot{m}_{CF} C_{P-CF} (T_{CW3} - T_{CW1}) = \dot{m}_{wf} (h_4 - h_6) \quad (8)$$

where C_{P-CF} = Specific heat of cooling fluid.

In the thermodynamics analysis of the condenser, the increase in the outlet temperature of the cooling fluid and *the condenser* pinch point temperature are assumed.

3. *Hydrogen production using* geothermal energy

The considered system for hydrogen production is considered in Fig. 5. It is made of a binary cycle power plant for the generation of the electrical energy needed for hydrogen production, an electrolyzer for water dissociation.

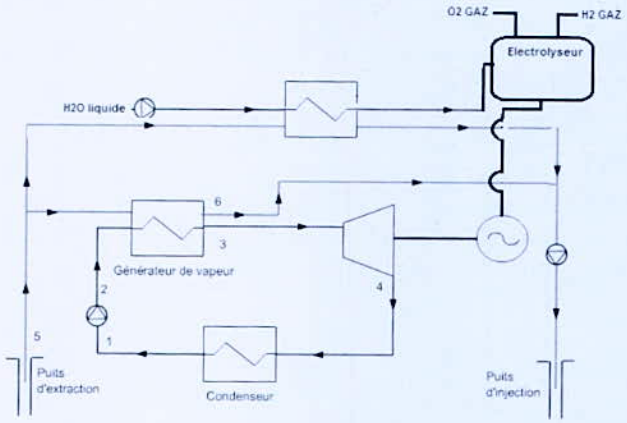

Fig. 5. Schematic diagram of Hydrogen production system using geothermal energy and binary power plant cycle

3-a. *Energy Statement*

The chemical reaction of the electrolysis of water is given by the following reaction:

$$H2O(liq) \Rightarrow H2(g) + \frac{1}{2} O2(g) \quad (9)$$

The required energy for this reaction is equal to the enthalpy variation ΔH

$$\Delta H = \Delta G + T \times \Delta S \quad (10)$$

Such us: ΔH represents the enthalpy of the reaction;

ΔG represents the Gibs enthalpy of the reaction;

ΔS represents the entropy of the reaction.

$$\Delta H_{TP} = \Delta G_{TP} + T \Delta S_{TP} \quad (11)$$

T_{ref} = 298.15 K; P_{ref} = 0.1 MPa;

Enthalpy and Entropy variations of the reaction (9) and the Nernst potential are calculated by the following equation:

$$\begin{cases} \Delta H(T) = \Delta H^{\circ}_{298,15°K} + \int_{298,15°K}^{T} \Delta CP \, dT \\ \Delta S(T) = S^{\circ}_{298,15°K} + \int_{298,15°K}^{T} \frac{\Delta CP}{T} \, dT \\ E(T) = -\frac{\Delta G(T)}{nF} \end{cases} \quad (12)$$

With:

- E (T): The Nernst potential corresponds to the temperature T (equation 4), is considered under the standard pressure for the reactants is produced.

The following table I [3] gives the thermodynamic parameters (standard) for P = 101.325 kPascal and T = 298.15K.

TABLE I
THERMODYNAMIC PARAMETERS STANDARD [03]

	ΔG° $\left(\frac{KJ}{mol}\right)$	ΔH° $\left(\frac{KJ}{mol}\right)$	S° $\left(\frac{KJ}{mol.^{\circ}}\right)$	Lv° $\left(\frac{KJ}{mol}\right)$	Specific heat (Cp) (J / mol / k)
H_2	0	0	0 ,13 1	-	27,28+0, 00326T+5000/T²
O_2	0	0	0,205	-	29,96+0,00418T-16700/T²
H_2O	237,2	285,8	0,07	40,7	75,44
H_2O	-	-	-	-	30,00+0,01071T+3300/T²

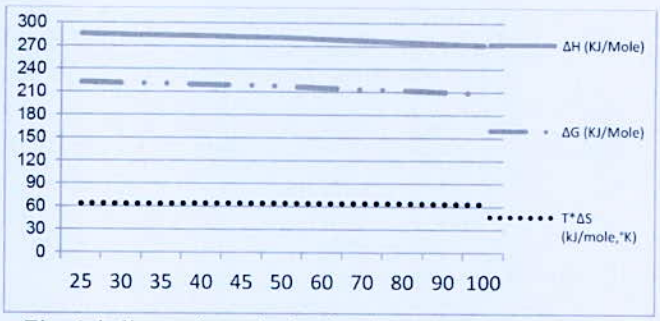

Fig. 6. indicates the reduction in electrical energy with increase in temperature. By increasing the water temperature, the geothermal energy help reduce the need for electricity

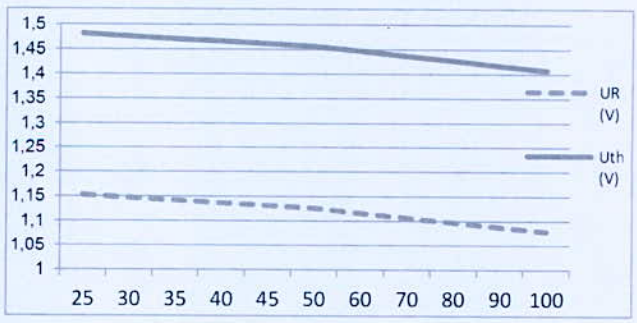

Fig. 7. Thermoneutral and the reverse voltage with temperature

This figure clearly indicates a decrease in the values of these voltages so it is a sign that a higher rate of hydrogen production.

*Corresponding author email: mechidhadjala@hotmail.fr

3-b. Current / voltage curve of an alkaline electrolyzer

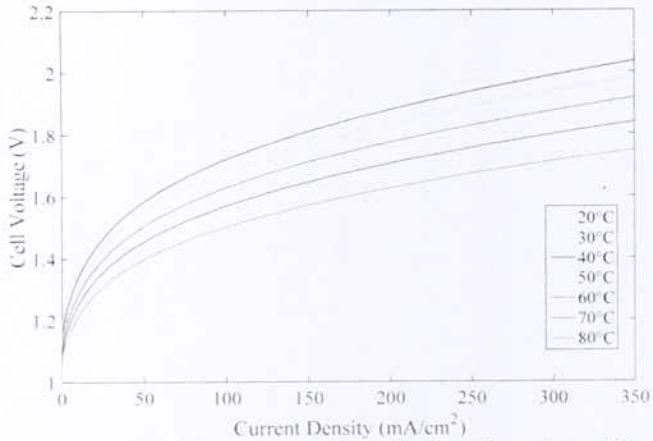

Fig. 8. Current/voltage curve of an alkaline electrolyzer [6]

3-c. Maximal Intensity of Current

For an alkaline electrolyzer [2] having 2 757 000 cells with an area equal to 200 Cm² / cell, it is possible to find the maximal current required to produce a desired hydrogen flow rate.

For temperature range between T=25 to 80°C and the corresponding themoneutral voltage Uth, the current density (J [mA/cm²]) was subject to interpolate from the current curve voltage (Fig. 8), the maximal intensity of current i[a] is defined by: I= J [mA/cm²] x 200 [cm² / Cell] x Number of cell ;

From equation (19), $\dot{m}_{H2} = \frac{1}{F}\frac{M}{N} I\ \eta f$ [kg/s], such as K= FN/M = 96487000 $\rightarrow$ $\dot{m}_{H2} = \frac{I}{K} x\ \eta f$ [kg/s].

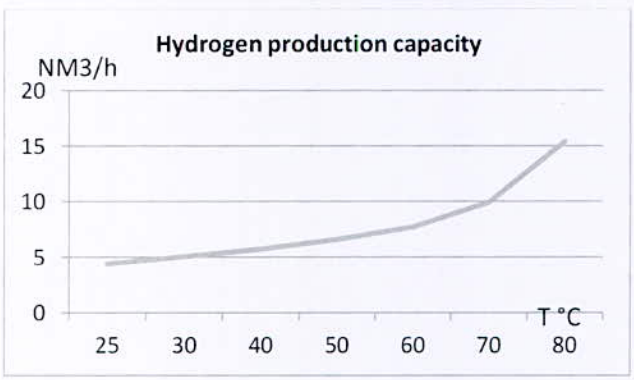

Fig. 4. Maximum of capacity of Hydrogen can be produced with the same unit of alkaline electrolyser for deferent case of temperature

This figure shows the maximum of capacity of Hydrogen can be produced with the same unit of alkaline electrolyser for deferent case of temperature. For the lower température case it is clearely indicate that has a lenear frofile, but after 60°C , the curve change for parabolic forme. , so this is verry important for copling with géothermal heat and energy.

IV. CONCLUSION

A system using geothermal energy to increase the temperature of electrolysis water is considered. The present results indicate that geothermal energy could play an important role in hydrogen production. The use of geothermal energy leads to a reduction in electrical energy needs and in lowering the thermo neutral and reverse voltages. The overall effect in an increase in hydrogen production rate, then higher system efficiency;

REFERENCES

[1] A.Fekraoui et A.Abouriche Ressources Géothermiques du Nord de l'Algérie -Eléments de l'Atlas Géothermique-,Rev. Energ. Ren. : Vaalorisation (1999) 159-162.

[2] Liu Mingy,Yu Bo,Xu Jingming, Chen Jing, Thermodynamic analysis of the efficiency of high-temperature steam electrolysis for hydrogen production; Journal of power sources 177(200_)493-499.

[3] Thermodynamic analysis of the efficiency of high-temperature steam electrolysis for hydrogen production; Journal of power sources 177(200_) 493-499; Liu Mingy,Yu Bo,Xu Jingming, Chen Jing.

[4] Angel Fernando Monroy Parada - Geothermal binary cycle power plant principles, Operation and maintenance - geothermal training programme reports 2013 orkustofnun, grensasvegur 9, Number 20 IS-108 Reykjavik, Iceland.

[5] Etude d'un système de production d'hydrogène par voie solaire, Application sur l'électrolyse de la vapeur d'eau à très hautes température ; Rev.Energ.Ren. Vol.8(2005) 137-156 ; H.Derbal, R.Miri et A .M'Raoui.

[6] Arash Khalilnejad, Aditya Sundararajan, Alireza Abbaspour and Arif Sarwat, "Optimal Operation of Combined Photovoltaic Electrolyzer Systems", Electrical and Computer Engineering Department, Florida International University, Miami, FL 33174, USA.

*Corresponding author email: mechidhadjala@hotmail.fr

Benzylalcohol Production from Benzaldehyde Hydrogenation Using Hydrotalcites as Catalyst: Structural and Textural Properties of Co-M

H. Zazoua[1, 2, *], I. Lounas[2], A. Saadi[2] and K. Bachari[1]

[1]Centre de Recherche Scientifique et Technique en Analyses Physico-chimiques, BP 384-Bou-Ismail-RP 42004, Tipaza-Algérie.

[2]Laboratoire de Chimie du Gaz Naturel, Faculté de Chimie, USTHB, BP32, El Alia, Alger, Algérie.

***Abstract*—The catalytic activity of Co-M (M = Al, Fe) hydrotalcites as heterogeneous catalyst was investigated at atmospheric pressure in the gaseous phase benzaldehyde hydrogenation. Hydrotalcites were prepared by co-precipitation method with M^{2+}/M^{3+} molar ratio of ~ 2 at pH=9-10 using carbonates as an interlayer anions. The chemical composition, structure, morphology and thermal behaviour were investigated using energy-dispersive X-ray (EDX), X-ray diffraction, FTIR spectroscopy, nitrogen adsorption/desorption measurements (BET equation and BJH method) and thermogravimetric analysis (TGA/DTG). The characterization results reveal that hydrotalcite exhibited a type IV isotherm with a H_3-type hysteresis loops characteristic of mesoporous materials and formed with different crystallinity degree depending of cation nature. In the range reaction temperature of 80-200°C under hydrogen flow, benzyl alcohol, toluene and benzene were produced from benzaldehyde hydrogenation. The activities/selectivities of hydrotalcites were significantly different depending on the catalyst composition, nature of active sites and reaction conditions.**

Keywords—Hydrotalcite, Cobalt,Hydrogenation

I. INTRODUCTION

Benzaldehyde hydrogenation is of an industrial importance because benzyl alcohol product reaction is used as intermediate in the synthesis of pharmaceuticals, flavour, fragrances, chemical intermediates and photographic chemicals [1, 2]. It is also used as raw material in the manufacture of various esters, such as benzyl formate, acetate, propionate, and butyrate, which are extensively used in the flavour and fragrance industries [3]. Benzaldehyde hydrogenation can be achieved either through phase transfer catalysis [4], hydrogenation by hydrogen transfer or homogeneous catalysis [5]. At present, heterogeneous catalysts are frequently used in this kind of reaction owing to easy product separation and catalyst recycling. Noble metals (Pd, Pt, Rh and Ru) and transition metals (Cu, Co and Ni) are generally selected as catalysts for hydrogenation because; they have characteristic ability towards hydrogen adsorption [6].

Hydrotalcite-like compounds (HTlcs), representing an important class of layered materials with numerous potential applications as catalysts, catalyst supports, ion exchanger/adsorbents, layered hosts for bio-molecules and precursors for composite materials [7], can be potential candidates to catalyze the reaction of benzaldehyde hydrogenation.

II. EXPERIMENTAL

1. Catalysts preparation

The hydrotalcite-like precursors with both bivalent [M^{2+}: Co^{2+}] and trivalent [M^{3+}: Al^{3+}, Fe^{3+}] metals (M^{2+}/M^{3+} = 2:1) were synthesized by a co-precipitation method [8] at room temperature and constant pH=10. Two aqueous solutions, one containing nitrate salts as such $M^{3+}/[M^{2+}+M^{3+}]$ = 0.33, and the other containing a mixture of $NaOH/Na_2CO_3$, were added dropwise. The suspension thus obtained was kept at 60°C for 15 h. The precipitate was filtered and washed with deionised water until pH= 7 of the filtrate and then dried at 70°C for 24h.

2. Catalytic testing

The catalytic performances were carried out in a fixed-bed glass tubular reactor with 0.1 g samples at atmospheric pressure and the total flow rate of 50 $cm^3.min^{-1}$. The reactant gas feed consisted of 4.8 Torr of benzaldehyde (Aldrich, 99.98%) and 250 Torr of H_2 diluted in N_2. Gaseous benzaldehyde was obtained by bubbling N_2 in liquid benzaldehyde maintained at constant temperature (50°C) in a suitable saturator. Before testing, the catalysts were in-situ reduced for 2 h at 350°C in a current of H_2 with a flow rate of 20 $cm^3.min^{-1}$.

The gaseous reactant and products were heated upstream and out stream and analyzed on line by a FID gas chromatograph (Delsi IGC 121 ML) equipped with a 10% CP-SIL 8 CB/ Chromosorb W column. Each reaction temperature was maintained constant until the corresponding steady-state was reached as indicated by the gas chromatograph analysis of the exit gases samples. For each catalyst the reaction temperature was changed in a crossing order: 200°C, 120°C, 150°C, 80°C and 100°C.

III. RESULTS AND DISCUSSION

1. Characterization of the hydrotalcite precursors

The chemical compositions of the samples, determined by EDX analysis, are reported in Table I. As it can be seen, the M^{2+}/M^{3+} atomic ratio was similar to those expected. This result confirms that the precipitation process is effective, and indicates that HTlcs samples with M^{2+}/M^{3+} atomic

*Corresponding author email: hanene_zazoua@yahoo.fr

ratio of 2:1 are successfully prepared by co-precipitation method.

TABLE I
CHEMICAL COMPOSITION OF LDHS

Catalyst	$M^{3+}/(M^{3+}+M^{2+})$ atomic ratio (%)		M^{2+}/M^{3+} atomic ratio %)	
	theor.	exp.	theor.	exp.
Co-Al-LDH	0.33	0.33	2	1.98
Co-Fe-LDH	0.33	0.34	2	1.94

[a] LDH=layered double hydroxide.
[b] Lattice parameter of the LDH phase calculated by the Scherrer equation.
[c] BET surface area of LDHs degassed at 353 K.

The powder X-ray diffraction patterns (PXRD) of hydrotalcites are shown in Fig. 1. At low values of 2θ (11-23°), the results show that diffractograms exhibited sharp and symmetric reflections of (003) and (006) planes and at higher values of 2θ (34-66°), broad and asymmetric reflections of (012), (015) and (018) planes, characteristic of a highly crystalline layered double hydroxide (LDH) structure were observed in the PXRD patterns (Fig. 1). These reflections are typical characteristics of the hydrotalcite. Presence of CO_3^{2-} anions in the interlayer space of LDHs was confirmed by the characteristic basal spacing of (003) plane of all catalysts (d_{003} = 7.65 A°).

TABLE II
TEXTURAL AND STRUCTURAL CHARACTERISTICS OF LDHS

Catalyst	Lattice parameter[b] (Å)		Specific Surface area[a] (m^2/g^{-1})
	a	c	
Co-Al-LDH	3.05	22.55	23
Co-Fe-LDH	3.02	22.11	38

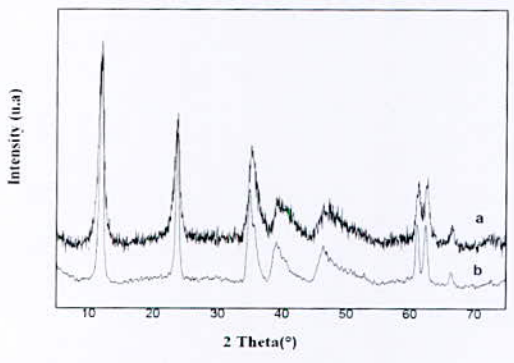

Fig. 1. XRD patterns of hydrotalcites-likes precursors: (a) Co–Al–LDH and (b) Co–Fe–LDH

The values of unit cell parameters (a and c) of LDHs were calculated by the formula: $a=2(d_{110})$ and $c=3(d_{003})$ [9]; where d_{110} and d_{003} are the basal spacing values of (110) and (003) planes respectively (Table II).

Surface areas of the LDH-precursors available to the N_2 molecules were calculated by applying the Brunauer, Emmett and Teller equation (B.E.T.) to the experimental data points obtained in the N_2 adsorption process. The values of the specific surface are in the range 23 to 38 $m^2\ g^{-1}$, values typical of this type of material (Table II).

2. Catalytic Activity/Selectivity

Benzaldehyde, with its aromatic ring, was used as a model molecule to study the hydrogenation of aldehydes. The observed products for the benzaldehyde hydrogenation are benzyl alcohol (BOL), toluene (TOL) and benzene (BENZ).

The data in Table III were recorded in steady-state. The results show that the conversion increases from 1-3% to 20-64% with increase of the reaction temperature from 80 to 200°C, and the highest activity was observed at 200°C for all precursors.

Benzyl alcohol is the only observed product on all catalysts at low reaction temperature (<150°C) and at low benzaldehyde conversion (Table III). The increasing temperature reaction does not promote the benzyl alcohol formation.

Toluene was the principal product resulting from reaction, It was obtained at a moderate reaction temperature (≥120 °C) (Table 2). The maximum of toluene selectivity was obtained at 200°C for Co/Fe (29%) and at 120°C for Co/Al (25 %).

Benzene was formed at rather high reaction temperature, preferentially on the Co-Al-LDH catalyst. The maximum of benzene selectivity was obtained at 200°C for Co/Al (90%) and for Co/Fe (51%).

The presence of easily reducible metals facilitates the reaction between the H_2 pre-treatment and active species for the LDH phase. However, the intervention of the H_2 pre-treatment should also play an important role in the observed yields. In the same way, the increase in the reaction yield after the H_2 pre-treatmentshould be attributed to the increase of the amount of active phase of LDH (Scheme. 1).

The reaction mechanism of the benzyl alcohol formation from benzaldehyde could occur via a 1-2 nucleophilic addition, where the carbonyl function is activated on the active site. Benzaldehyde adsorption, where both the aromatic ring and carbonyl group are co-planar to the surface, can facilitate C=O polarization, rendering the oxygen susceptible to a nucleophilic attack with hydrogen surface species as active intermediates for the direct hydrogenation of benzaldehyde to benzyl alcohol [10,11].

*Corresponding author email: hanene_zazoua@yahoo.fr

TABLE III
CATALYTIC RESULTS FOR GAS PHASE HYDROGENATION OF BENZALDEHYDE OVER THE HYDROTALCITE-LIKE PRECURSORS

Catalysts	Treaction (°C)	Conv[a] (%)	Selectivity[a] (%)		
			AL	TOL	BENZ
Co-Al-LDH	80	1	100	-	-
	100	1	100	-	-
	120	3	45	25	30
	150	6	20	24	56
	200	20	6	4	90
Co-Fe-LDH	80	3	100	-	-
	100	6	100	-	-
	120	6	100	-	-
	150	12	49	24	27
	200	64	20	29	51

BOL benzyl alcohol, TOL toluene, BENZ benzene.
[a]Steady-state conversion and selectivity measured after 5 h of reaction time.

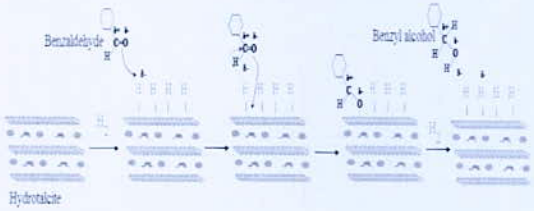

Scheme.1 Reaction pathways of benzaldehyde hydrogenation to benzyl alcohol

IV. CONCLUSION

The hydrotalcites of with M^{2+} = Co^{2+} and M^{3+} = Al^{3+}, Fe^{3+} were synthesized and characterized by different physicochemical methods. It was shown in this work, that hydrotalcites are effective for the benzaldehyde hydrogenation to benzyl alcohol and that the high catalytic performance would be due to the combination of iron and cobalt species that have acid-base and/or redox properties. Toluene formation can result from the subsequent conversion of the alcohol and benzaldehyde hydrogenolysis and benzene from benzaldehyde decarbonylation over the acid sites.

REFERENCES

[1] H. U. Blaser, A. Indolese, A. Schnyder, H. Steiner, M. Studer, "Supporte palladium catalysts for fine chemical synthesis", J. Mol. Catal. A: Chem ., vol. 173, pp. 3-18, 2001.

[2] J. Jenck, J. E. Germain, "High-pressure competitive hydrogenation of aldehydes, ketones, and olefins on copper chromite catalyst", J. Catal., vol. 65, pp. 141-149, 1980.

[3] D. Divakar, D. Manikandan, G. Kalidoss, T. Sivakumar."Hydrogenation of benzaldehyde over palladium intercalated bentonite catalysts: Kinetic studies",Catal. Lett, vol. 125 (3-4), pp. 277-282, 2008.

[4] H. A. Zahalka, H. Alper, "beta.-Cyclodextrin-promoted, rhodium (I)-catalyzed conversion of carbonyl compounds to hydrocarbons under remarkably mild conditions", Organometallics, vol. 5(9), pp. 1909- 1911, 1986.

[5] G. M. Intille, "Hydrogenolysis of alcohols, ketones, aldehydes, esters and ethers", U. S. Patent 4 067 900 A, Jan. 10, 1975.

[6] P. Gallezot, D. Richard, "Characterization and selectivity in cinnamaldehyde hydrogenation of graphitesupported platinum catalysts prepared from a zero-valent platinum complex",Catal. Rev. Sci. Eng., vol. 40, pp. 81-126, 1998.

[7] S. Mandal, , S. K. Ghosh, A. Ghosh, R. Saha, S. Banerjee, B. Saha, "Review of the aldol reaction", Synth. Commun., vol. 46(16), pp. 1327-1342, 2016.

[8] W. T. Reichle, "Catalytic reactions by thermally activated, synthetic, anionic clay minerals", J .Catal., vol. 94(2), pp. 547-557, 1985.

[9] V. Rives, "Characterisation of layered double hydroxides and their decomposition products", Mater. Chem. Phys., vol. 75 (1), pp. 19-25, 2002.

[10] K. Lanasri , A. Saadi , K. Bachari, D. Halliche, O. Cherifi, "Gas phase hydrogenation of benzaldehyde over supported copper catalysts. Effect of copper loading", Stud. Surf. Sci. Catal., vol. 174, pp. 1279-1282, 2008.

[11] N. Haddad, A. Saadi, A. Löfberg , R. N. Vannier, E. Bordes-Richard E, C. Rabia , " Benzaldehyde reduction over Cu–Al–O bimetallic oxide catalyst. Influence of pH during hydrothermal synthesis on the structural and catalytic properties", J. Mol. Catal. A: Chem., vol. 396, pp. 207-215, 2015.

*Corresponding author email: hanene_zazoua@yahoo.fr

A Numerical Study of the Effect of Hydrogen Enrichment on the NO Emissions of a Turbulent Non-Pre-Mixed Combustion of Methane

M. Belacel[1*, 2], F. Amrouche[1], A. Hadef[3], A. Menaa[1] and N. Salhi[2]

[1*]Centre de Développement des Energies Renouvelables, CDER, BP 62 Route de l'Observatoire, Bouzaréah, 16340, Alger.
[2]Laboratoire de Chimie du Gaz Naturel, Faculté de Chimie, USTHB, 109 El-Alia Bab Ezzouar Alger, Algérie.
[3]Faculté des Sciences et Sciences appliquées, Université d'Oum El Bouaghi 04000 Algerie.

Abstract—**In this paper, a numerical simulation of the turbulent non-pre-mixed flame, using ANSYS-Fluent software was done to investigate the effect of adding 10%, 20 % of hydrogen by mass, at pressure of 10 bar, to pure methane on the NO emissions. According to the results, the front of flame temperature is considerably higher with hydrogen addition at high pressure, which increases the NO emissions. Moreover, because the flames temperatures are considerably higher with hydrogen addition, the Zel'dovich mechanism becomes significant in comparison to prompt Fenimore mechanism.**

Key words—CH_4-hydrogen mixture, turbulent non-pre-mixed flame, NO emissions.

I. INTRODUCTION

Nowadays, most of the automotive R&D are focused on reducing the fuel consumption and the pollutant emissions of vehicles. The gaseous alternative fuels such as methane and hydrogen are the most considered in terms of engine application. Moreover, in the last decade, hydrogen-enriched natural gas (HGNC) has received a specific attention and many theoretical and experimental researches have been done in this field. Indeed, in comparison with pure natural gas, the HCNG mixture has many advantages, when it comes to the combustion performances and exhausted emissions. Moreover, when used in an internal combustion engine, even the addition of small amount of hydrogen to natural gas (5-30% by volume) can lead to few polluting emissions, with high thermal efficiency. This is due to the particular physical and chemical properties of hydrogen that improve the combustion quality [2-4].

An overall comparison between the characteristic values of Hydrogen, CNG, 5% HCNG blend and gasoline is given in Table I. As it can be seen, hydrogen has very attractive proprieties that improved the characteristics of the HCNG mixture compared to gasoline or CNG, and this even with a small amount of hydrogen in HCNG mixture. The characteristic values of the HCNG fuel make it remarkably well suited for internal combustion engine.

In Table II, the characteristic value of the HCNG fuel at different hydrogen fractions has been shown. As it can be seen, the improvement of the LHV (Lower Heating Value) of HCNG is increased consistently to the amount of hydrogen added to the fuel mixture. However, because hydrogen has a very low energy density per volume unit, the volumetric heating value of the HCNG mixture decreases as the proportion of hydrogen is increased in the mixture [5].

TABLE I
COMPARISON OF THE CHARACTERISTIC VALUES OF HYDROGEN, CNG, HCNG AND WITH GASOLINE [4]

Properties	H_2	HCNG 5	CH_4	Gasoline
Limits of Flammability in air, vol %	4-75	5-35	5-15	1.0-7.6
Stoichiometric composition in air, vol %	29.53	22.8	9.48	1.76
Minimum energy for ignition in air, mJ	0.02	0.21	0.29	0.24
Auto ignition Temp, K	858	825	813	501-744
Flame Temperature in air, K	2318	2210	2148	2470
Burning Velocity in NTP[a] air, cms^{-1}	325	110	45	37-43
Quenching gap in NTP air, cm	0.064	0.152	0.203	0.2
Normalized Flame Emissivity	1.0	1.5	1.7	1.7
Equivalence ratio flammability limit in NTP air	0.1-7.1	0.5-5.4	0.7-4	0.7-3.8
Methane Number	0	76	80	-
Composition of CNG: CH_4 – 90.2%, C_2H_6 – 8.5%, C_3H_8-0.6%, N_2 -0.6%, Butane- 0.1%				
[a]NTP denotes normal temperature(293.15K) and pressure(1atm)				

TABLE II
PROPERTIES OF CNG AND HCNG BLENDS WITH DIFFERENT HYDROGEN CONTENT [6]

Properties	CNG	HCNG 10	HCNG 20	HCNG 30
H_2[% vol]	0	10	20	30
H_2[% mass]	0	1.21	2.69	4.52
H_2[% energy]	0	3.09	6.68	10.94
LHV[$MJkg^{-1}$]	46.28	47.17	48.26	49.61
LHV[$MJ\ Nm^{-3}$]	37.16	34.50	31.85	29.20
LHV stoich. mixture [$MJNm^{-3}$]	3.376	3.368	3.359	3.349

Through the literature, several numerical and experimental studies that focused on the effect of hydrogen enrichment on combustion performances of a natural gas SI engine have been done. All those studies have concluded that hydrogen enrichment reduces the combustion duration and increases the thermal efficiency of the SI engine [7, 8].

Moreover, as it was shown by Lachaux [9] and Halter [10], the addition of 10% by volume of hydrogen to methane in a turbulent and low-mixture combustion, would not affect the characteristics of the flame. This is to confirm that it is possible to substitute 10% of methane by hydrogen without making any changes in the facility, while getting a fuel economy.

*Corresponding author email: mo.belacel@cder.dz

In virtually every application of combustion processes, the flow in which the chemical reactions are taking place is turbulent. So, in this paper, a numerical simulation using CFD code ANSYS Fluent was used to study the effect of hydrogen enrichment on the NO emissions of turbulent non-pre-mixed flame combustion of methane. To achieve this objective, pure methane and a mixture by mass of [10% and 20% H_2] were used at a high hydrogen injection pressure of 10 bar, and the axial temperature and axial mass fraction of NO were calculated.

II. DESCRIPTION OF NUMERICAL MODEL

1. *Geometrical Configuration*

For this study, a turbulent diffuse flame burner was used. As it can be seen in Fig. 1, the flame consists of two axisymmetric jets of the Fuel and oxidizer (air) that are not pre-mixed.

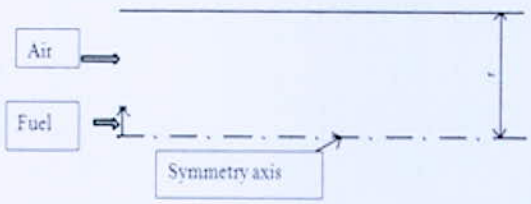

Fig. 1. Scheme of the geometrical configuration

The numerical simulation is performed using a ' Fluent ' commercial calculation code, the configuration used is axisymmetric, the numerical resolution of the system of global equations obtained is performed using a SIMPLE algorithm and using the Standard K-ε turbulence modified model [12] is the most suitable for the numerical simulation of our flame used with the kinetic scheme the GRI 3 for the simulation of a turbulent diffusion flame of the mixtures. The conditions chosen for this study are listed in Table III.

TABLE III
COMBUSTION MODEL

Quantity	Value
Injection diameter (mm)	3.75
Velocity of Air (m/s)	50
Velocity of Air (m/s)	1
Fuel temperature (K)	299
Air temperature (K)	298

III. RESULTS AND DISCUSION

The theoretical results achieved through this study, are presented as axial temperature, and axial mass fraction of NO for pure CH_4 and mixture of 10% H_2 and 20% H_2 by mass, at pressure of hydrogen injection of 10 bar.

The results of the CFD simulation of the flame front temperature of the pure CH_4 and H_2/CH_4 mixtures are illustrated in Fig. 2. It can be observed from this figure that, for high pressure, the temperature increases with increasing the proportion of H_2 added to the air fuel mixture. This can be explained by the hydrogen combustion characteristic that affects the adiabatic temperature and reactivity of the air-fuel mixture.

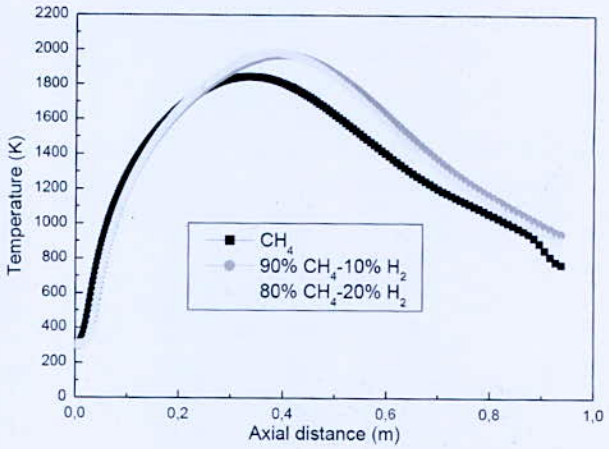

Fig. 2. Axial temperature for P=10bar

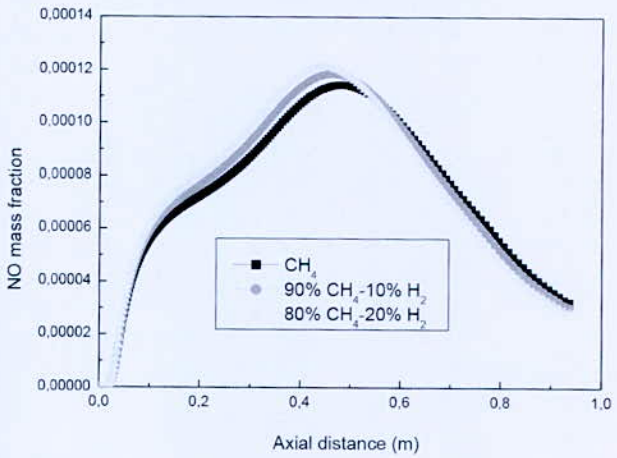

Fig. 3. Axial distribution of NO mass fraction for P=10bar

Fig. 3, shows the axial distribution of the mass fraction of the NO for pure CH_4 and mixture of 10% and 20% H_2, at pressure of hydrogen injection of 10 bar. In the combustion of pure CH_4 and H_2/CH_4 mixtures, the formation of NO can be attributed to two main chemical routes, which are the Zel'dovich thermal and Fenimore prompt NO mechanisms [13]. As it was already seen in Figs. 2, the flame temperatures are considerably higher than 1800°K [16] with hydrogen addition, so the Zel'dovich mechanism becomes more significant in comparison to prompt Fenimore while hydrogen proportion increased.

III. CONCLUSIONS

The simulation results of the turbulent non-pre-mixed hydrogen/methane combustion were obtained using the fluent code. The following results were obtained:

1) The front of flame temperature is considerably higher with hydrogen addition for high pressure, which increases the NO emissions.

*Corresponding author email: mo.belacel@cder.dz

2) With hydrogen addition and at high pressure, the Zel'dovich mechanism becomes more significant in comparison to prompt Fenimore mechanism.

REFERENCES

[1] Raman VJ, Hansel J, Fulton J, Lynch F, Bruderly D. Hythane- an ultraclean transportation fuel. Hydrogen Fuel for Surface Transportation. SAE Publication, 1996. p. 47-56.

[2] Fanhuna Ma, Hanquan Liu, Yu Wang, Yong Li, Junjun Wang and Shuli Zhao, Combustion and Emission Characteristic of a Port Injection HCNG Engine Under Various Ignition Timings.International Journal of Hydrogen Energy, 33(2008), pp. 816-822.

[3] Karner D, Francfort J. Freedom Car and VehicleTechnologies Program – Advanced Vehicle Testing Activity. Arizonal Public Service, Alternative Fuel (Hydrogen) Pilot Plant. US DOE; 2003.

[4] K.P.Kavathekar, S.D.Rairikar and S.S.Thipse., Development of a CNG Injection Engine Compliant to Euro –IV Norms and Development Strategy for HCNG Operation. SAE paper No. 2007-26-029. 2007.

[5] Bell SR, Gupta M., Extension of a Lean Operating Limit For Natural Gas Fuelling of a Spark Ignition Engine Using Hydrogen Blending., Combustion Sciences and Technology, 123(1997), 1-6, pp. 23-48

[6] Jian Xu, Xin Zhang, Jianhua Liu, Longfei Fan., Experimental Study of a Single Cylinder Engine Fueled with Natural gas- Hydrogen Mixtures, International Journal of Hydrogen Energy,35(2010), pp.2909- 2914.

[7] Suzuki T. and Sakurai Y., Effect of Hydrogen Rich Gas and Gasoline Mixed Combustion on Spark Ignition Engine, SAE paper, 2006-01-3379, 2006.

[8] Rakopoulos C.D., Scott M.A., Kyritsis D.C. and Giakoumis E.G., Availability analysis of hydrogen/natural gas blends combustion in internal combustion engines, Energy, 33, pp. 248-255, 2008

[9] Lachaux T., Halter F., Chauveau C., Gokalp I. and Shepherd I.G., Flame front analysis of highpressure turbulent lean premixed methane–air flames, Proc Combust Inst, 30 (2005), pp. 819–826.

[10] Halter F., Caractérisation des effets de l'ajout d'hydrogène et de la haute pression dans les flammes turbulentes de prémélange méthane/air. Thése de doctorat, Université d'Orléans; 2005

[11] N. Syred, M.Abdulsada, A.Griffiths, T.O'Doherty, P.Bowen, «The effect of hydrogen containing fuel blends upon flashback in swirl burners», Journal ofApplied Energy, vol.8, pp.106–110, (2012).

[12] R. Mouangue, M. Obounou. Numerical simulation of turbulent diffusion flames of H2/Air. Phys. Chem. News, 2009, vol. 50, pp. 69–78.

[13] Ilbas M, Yilmaz I, Kaplan Y. Investigation of hydrogen and hydrogen-hydrocarbon composite fuel combustion and NOx emission characteristics in a model combustor. Int J Hydrogen Energy 2005; 30(10):1139–47.

[14] Turns SR. An introduction to combustion: concepts and applications. New York, NY: McGraw-Hill, Inc.; 1996.

*Corresponding author email: mo.belacel@cder.dz

Optimization and Modelization of PV-Electrolyzer System for Sustainable Hydrogen

I. Hadj Mahammed[1, 2], Y. Bakelli[3], A. Mraoui[3], A. Hadj Arab[3] and S. Berrah[1]

[1]Lab/ Faculty of Electronics, A. Mira University, Bejaia, Algeria,
[2]Unité de Recherche Appliquée en Energies Renouvelables URAER Centre de Développement des Energies Renouvelables, CDER, 47133, Ghardaïa, Algeria
[3]Centre de Développement des Energies Renouvelables, CDER, 16340, Algeria

Abstract—**Hydrogen is currently regarded as a potential future clean energy carrier. It can be produced by the electrolysis of water, PV-powered by solar panels. Accordingly, the objective of this paper is to investigate the modeling, optimization and prediction of hydrogen production from photovoltaic sources. In this view, a comprehensive mathematical model has been developed in the goal to predict the performance of a photovoltaic supply source, based upon the combination of the different parts, under the climatic conditions of Ghardaïa site. The obtained results indicate a robust performance in response to external or internal operating variations. The developed approach can be a mathematical tool in the design and analysis of hybrid photovoltaic-hydrogen technical performances.**

Key words—modeling, optimization, hydrogen, hybrid system, electrolysis, photovoltaic

I. INTRODUCTION

Hydrogen is the most plentiful element in the universe, found mainly in water and organic compounds. In the last decades, there is growing use of hydrogen in wide range of industrial applications especially by enabling energy storage through sustainable and non-polluting mechanisms [1, 2]. Hydrogen can be produced from renewable power via water electrolysis, which is environmental benefit by reducing the rising of greenhouse gas (GHG) emissions emitted by the power plants, gas, industry and fuel and mobility sectors. Thus to have a cleaner and more sustainable future energy consumption [3]. The interest in the use of hydrogen has led to the search of various methods to produce and deliver it in a safe and convenient way. One of the most interesting technology for the production of hydrogen based on this electrolysis process is the Proton Exchange Membrane (PEM) electrolyzer, which has attracted a lot of attention over recent years [4, 5]. On another side, solar photovoltaic (PV) energy is an ideal option for renewable hydrogen production using electrolysis process such as MEP. Several studies have been conducted on the PV hydrogen production based on WEP [6]. Through different aspects including design, modelling, simulation, sizing, control strategy, economic and costs estimation, as well as operation performance [7]. Several authors presented an autonomous power system that exploits solar energy for hydrogen production via WEP which is fully assessed in terms of system implementation and optimal operating strategy [8–10].

*Corresponding author email: hmidriss65@yahoo.fr

Within this frame the present work investigates the hydrogen production by water l electrolysis, and evaluates the potential of hydrogen production from solar photovoltaic energy. Accordingly, the paper is organized as follows Section 2 gives a presentation of the mathematical model of the main components of the off-grid PV/Elec system including a semi-empirical model describing the relationship between the hydrogen production rate and power consumption of the electrolyzes cell. Simulation results are discussed in Section 3, including the system behavior over one typical year and the potentialities of Ghardaïa city of PV hydrogen production via MEP. Finally, Section 4 establishes the conclusions

II. MODELING

The used models for estimating the I-V characteristics of the PV modules are described in below.

1. Five Parameters Model

Many models have been employed for estimating the PV module I-V characteristics, among them we found the five parameters models seems to be the best one [11–13]. The photovoltaic generator may be closely represented by the five parameters model based on one diode equivalent circuit of a solar cell; it consists on a diode, a current source (I_L), a series resistance (Rs) , and a parallel resistance (Rsh).The current source generates photocurrent (I_L) which is a function of incident solar irradiation and cell temperature. The diode represents p–n junction of the solar cell. At real solar cells, the voltage loss on the way to the external contacts has been observed, and a series resistance (Rs) expresses it. Furthermore, a shunt resistance (Rsh) describes leakage currents. Using Kirchhoff's first law, the equation for the extended I–V curve is derived as shown by Equation. 1.

$$I = I_L - I_0\left[\exp\left(\frac{V + IR_s}{m\ V_t}\right) - 1\right] - \frac{V + IR_s}{R_{sh}} \qquad (1)$$

Where I is the output current of the PV cell or module. V is the terminal voltage, q is the electric charge ($1.6\ 10^{-19}$ C), K is the Boltzmann constant ($1.38\ 10^{-23}$ J/K), and T is the cell temperature (K), m is the ideality factor and I_0 is the diode saturation current. The five equivalent circuit parameters can be determined using the available operating

points on the I-V curve by analytical equations as mentioned in [13]

2. *ANFIS Model*

Adaptive Neuro Fuzzy Inference System (ANFIS) is a Combining of the advantages of neural networks and the linguistic interpretability of a fuzzy inference system (FIS), ANFISs can be applied to many complicated problems. [14–16]. For modeling the PV modules parameter variations according to the irradiance and temperature, the information provided by the manufacturers is usually insufficient, thus, the modeling can be done in an easy way by making a priori estimation of any parameter model.

The ANFIS architecture programmed in MATLAB is used to develop a model for the PV modules using irradiance (E) as a first input and PV cell temperature (T) as a second input for model parameters estimation. A combination of the least squares and the back-propagation gradient descent methods have been applied for training the FIS membership functions (MFs).

The structure adopted was composed with three layers ANFIS architecture (number of rules 3x2x2). The structure has three inputs namely the irradiance, temperature and the PV module power on multistage. The mentioned

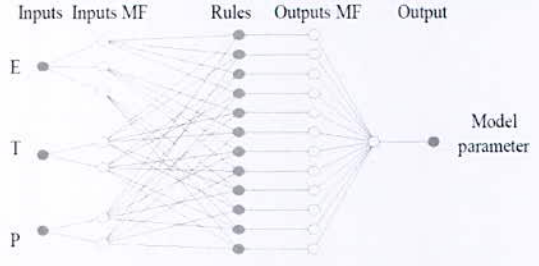

architectures are illustrated in Fig. 1

Fig. 1. Proposed ANFIS architecture applied to PV module model parameters

3. *Electrolyzes Model*

In electrolysis, the operating cell voltage or overpotential is the summation of the reversible overvoltage, the activation overvoltage that is the electrode response and the addition of ohmic overvoltage of electrolyte [17]. Then the equations, applied in the PEM electrolyzer modeling are summarized by "(2) – (4)"

$$V_{cell} = V_{rev} + V_{act} + V_{ohm} \quad (2)$$

At standard conditions V_{rev} = 1.229 V

$$V_{act} = s\log\left(\frac{t_1 + \frac{t_2 + t_3}{T}}{A} I + 1\right) \quad (3)$$

$$V_{ohm} = \frac{r_1 + r_2 T}{A} \quad (4)$$

One way of improving energy transfer efficiency along with hydrogen generation is to couple directly the PV module with the electrolyzer. The main objective of direct coupling is to maximize overall annual energy transfer from the PV system to electrolyzer. There are different algorithms, which are suggested in the optimization problems in various science and engineering areas. The aim of optimization algorithms is to locate an optimal solution in terms of optimal variables. In this case, the optimization problem has four dimensions which are number of electrolyzer cells in series, parallel cells and number of modules PV in series, parallel. In the way to achieve this goal , an empirical model given by "(5)," is used to simulate the IV characteristic of the PEM 50 W StaXX7 electrolyzer manufactured by h-Tec. [18]

$$I=\begin{cases} 0 & \text{for } V<V_{thr} \\ a_3V^3+a_2V^2+a_1V+a_0 & \text{for } V>V_{thr} \end{cases} \quad (5)$$

Where a_3=0.0732506, a_2=2.76617, a_1=33.1587 and a_0=128.118.

The following figure (Fig. 2.) illustrates the characteristic curve (I=f (V)) of the adopted electrolyzer configuration, where Vthr represents the threshold voltage which consists the electrolyzer starting point to produce hydrogen.

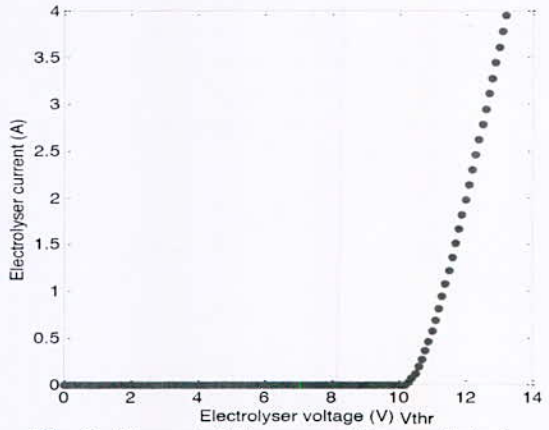

Fig. 2. Characteristic curve of the used stack

III. RESULTS AND DISCUSSION

The recommended models have been applied to analyze the PV-electrolyzer system, which is designed to produce hydrogen at Ghardaïa, Algeria (32°29' N, 3°40'E).

The technical characteristics of the PV module and electrolyzer adopted in the study are listed in Table 1.

Hourly data of solar irradiation on the horizontal plane as well as ambient temperature recorded at Ghardaïa (Algeria), during one year were used in system and the generation was assumed to keep constant value at each interval hour.

Various configurations have been studied in order to show the influence behavior on the system performance.

*Corresponding author email: hmidriss65@yahoo.fr

TABLE1
SPECIFICATIONS OF SYSTEM ELEMENTS

STAXX7 PEM electrolyzer unit	
Electrode area	7 cells of 16 cm^2 each
Power	50 W at 14 V DC
Permissible voltage	10.5 - 14.0 V DC
Permissible current	0 - 4.0 A DC
H2 production	*230 cm^3/min*
PV Module	
Module	*Sharp175*
Technology	*monocrystalline*
Maximum power	*180 W*
Open circuit voltage	*44.4 V*
Short circuit current	*5.48 A*
Voltage at maximum power	*36.8 V*
Current at maximum power	*4.89 A*

The performances of the direct coupling system PV-electrolyzer depend on the adopted configuration; some results are shown in Fig. 3.

Thus, for a selected PV module (Sharp 175), the power absorbed by the electrolyzer, the amount of hydrogen produced, is affected by the number Ns of stacks mounted in series. In fact, for a configuration where Ns*Vthr is higher than NsPV* Voc (NsPV is the number of PV modules in series and Voc is the open circuit voltage of a module), the absorbed energy is insignificant.

However, the effect of the number of parallel PV modules is also felt by the doubling and tripling of the amount of energy absorbed for NpPV =2 and 3 respectively, see Fig. 3, Fig. 4 and see Fig. 5.

For NsPV equal to 2, The production is negligible for Ns equal to or greater than 9. For Ns less than 9, the production increases versus Ns increases until it reaches a maximum value for Ns=5, which corresponds to a configuration whose stack characteristic is closed to the maximum power point of the module at each moment. Then after it begins to decrease. See Fig. 6.

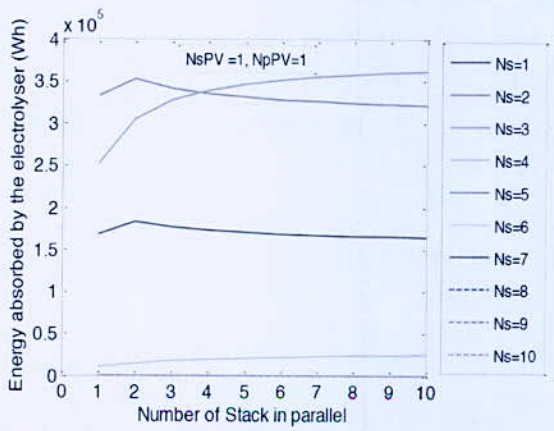

Fig. 3. One-year performance of the system for first configuration

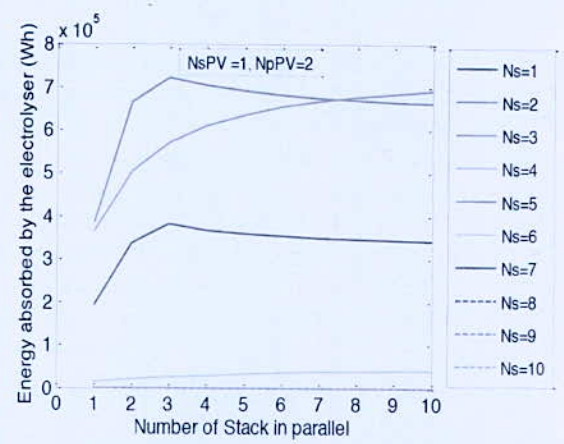

Fig. 4. One-year performance of the system for second configuration

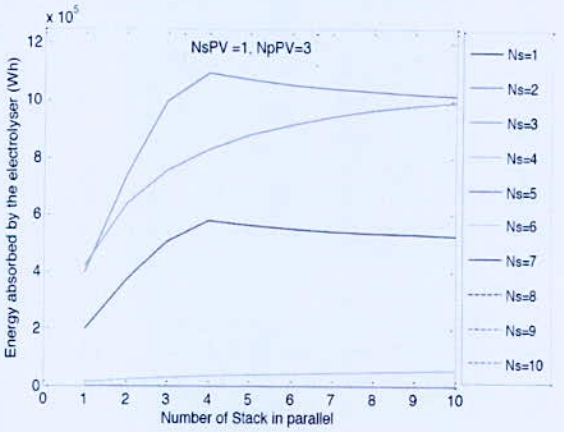

Fig. 5. One-year performance of the system for third configuration

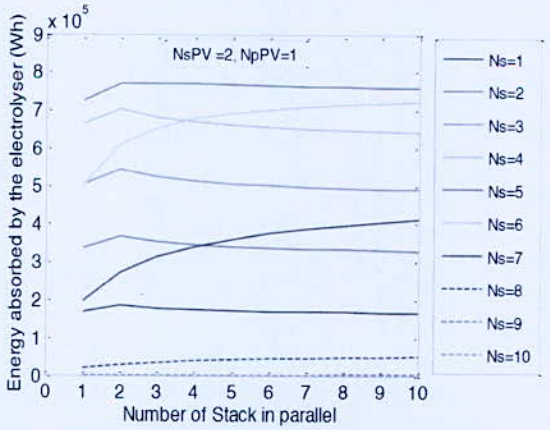

Fig. 6. One-year performance of the system for fourth configuration

*Corresponding author email: hmidriss65@yahoo.fr

IV. CONCLUSION

Hydrogen production via electrolysis process using photovoltaic energy is suitable due to the low energy requirement. Modeling and simulation of a photovoltaic system, as an off-grid used to produce hydrogen through the electrolysis has been proposed. Through experimental measured data of PV module, coupled to semi-empirical model of electrolyzer, describing the variation of the hydrogen rate production by considering the electrolyzer power as input has been developed different combination number of PV module and electrolysis cell are studied for satisfying hydrogen demand by enabling an appropriate operate power output. The strategy is designed for different irradiation and temperature under different range of the electrolyzer power input.

It has been averred that the electrolyzer operates more closed to its rated capacity for specific configurations, such as Ns*Vthr near NsPV*Vm which allows us to produce a maximum amount of hydrogen. In perspective, a simulation study based on mathematical models of all system components, including the PV generator, electrolyzer and hydrogen reservoir is scheduled. The goal is to study the dynamic behavior of the electrolyzer system for hydrogen supply to satisfy various applications with the lowest cost.

REFERENCES

[1] C. A. Martinson, G. van Schoor, K. R. Uren, and D. Bessarabov, « Characterisation of a PEM electrolyser using the current interrupt method », Int. J. Hydrog. Energy, vol. 39, no 36, p. 20865-20878, 2014.

[2] F. Barbir, « PEM electrolysis for production of hydrogen from renewable energy sources », Sol. Energy, vol. 78, no 5, p. 661-669, 2005.

[3] R. E. Clarke, S. Giddey, F. T. Ciacchi, S. P. S. Badwal, B. Paul and J. Andrews, « Direct coupling of an electrolyser to a solar PV system for generating hydrogen », Int. J. Hydrog. Energy, vol. 34, no 6, p. 2531-2542, 2009.

[4] R. García-Valverde, N. Espinosa and A. Urbina, « Simple PEM water electrolyser model and experimental validation », Int. J. Hydrog. Energy, vol. 37, no 2, p. 1927-1938, 2012.

[5] M. Carmo, D. L. Fritz, J. Mergel and D. Stolten, « A comprehensive review on PEM water electrolysis », Int. J. Hydrog. Energy, vol. 38, no 12, p. 4901-4934, 2013.

[6] O. Atlam and M. Kolhe, « Equivalent electrical model for a proton exchange membrane (PEM) electrolyser », Energy Convers. Manag., vol. 52, no 8-9, p. 2952-2957, 2011.

[7] M. Castañeda, A. Cano, F. Jurado, H. Sánchez and L. M. Fernández, « Sizing optimization, dynamic modeling and energy management strategies of a stand-alone PV/hydrogen/battery-based hybrid system », Int. J. Hydrog. Energy, vol. 38, no 10, p. 3830-3845, 2013.

[8] T. L. Gibson and N. A. Kelly, « Predicting efficiency of solar powered hydrogen generation using photovoltaic-electrolysis devices », Int. J. Hydrog. Energy, vol. 35, no 3, p. 900-911, févr. 2010.

[9] O. Atlam, F. Barbir and D. Bezmalinovic, « A method for optimal sizing of an electrolyzer directly connected to a PV module », Int. J. Hydrog. Energy, vol. 36, no 12, p. 7012-7018, 2011.

[10] A. Khalilnejad, A. Abbaspour and A. I. Sarwat, « Multi-level optimization approach for directly coupled photovoltaic-electrolyser system », Int. J. Hydrog. Energy, vol. 41, no 28, p. 11884-11894, 2016.

[11] A. Hadj Arab, F. Chenlo and M. Benghanem, « Loss-of-load probability of photovoltaic water pumping systems », Sol. Energy, vol. 76, no 6, p. 713-723, 2004.

[12] A. N. Celik and N. Acikgoz, « Modelling and experimental verification of the operating current of mono-crystalline photovoltaic modules using four- and five-parameter models », Appl. Energy, vol. 84, no 1, p. 1-15, 2007.

[13] V. Lo Brano, A. Orioli and G. Ciulla, « On the experimental validation of an improved five-parameter model for silicon photovoltaic modules », Sol. Energy Mater. Sol. Cells, vol. 105, p. 27-39, 2012.

[14] A. M. S. Aldobhani and R. John, « Maximum Power Point tracking of PV System Using ANFIS Prediction and Fuzzy Logic Tracking », in Proceedings of the International MultiConference of Engineers and Computer Scientists 2008, Hong Kong, 2008.

[15] A. Mellit and S. A. Kalogirou, « ANFIS-based modelling for photovoltaic power supply system: A case study », Renew. Energy, vol. 36, no 1, p. 250-258, 2011.

[16] Syafaruddin, E. Karatepe and T. Hiyama, « Fuzzy wavelet network identification of optimum operating point of non-crystalline silicon solar cells », Comput. Math. Appl., vol. 63, no 1, p. 68-82, 2012.

[17] Ø. Ulleberg, « Modeling of advanced alkaline electrolyzers: a system simulation approach », Int. J. Hydrog. Energy, vol. 28, no 1, p. 21-33, 2003.

[18] D. Ghribi, A. Khelifa, S. Diaf and M. Belhamel, « Study of hydrogen production system by using PV solar energy and PEM electrolyser in Algeria », Int. J. Hydrog. Energy, vol. 38, no 20, p. 8480-8490, 2013.

*Corresponding author email: hmidriss65@yahoo.fr

L'Effet de la Gestion de l'Eau sur la Performance de Pile à Combustible à Membrane Echangeuse de Protons PEMFC

S. Laribi[1*], K. Mammar[2], K. Koussa[1], Y. Sahli[1], T. Ghaitaoui[1], M. Hamouda[1]

[1]Unité de Recherche en Energies Renouvelables en Milieu Saharien, URERMS, Centre de Développement des Energies Renouvelables, CDER, 01000, ADRAR, Algérie.
[2]Department of Electrical and Computer Engineering, University of Béchar Bp 417, Algeria.

Abstract—**Pour un fonctionnement optimal des piles à combustible, la membrane conductrice de proton doit être correctement hydratée ; c'est-à-dire que la membrane doit avoir une humidité spécifique en fonction de la température, de la pression d'écoulement ... etc., pour éviter toute inondation ou sécher de la membrane et permettre de produire une meilleure puissance. Cet article vise à mettre en évidence l'importance de la gestion de l'eau dans un système à pile à combustible à membrane échangeuse du proton (PEMFC). À l'heure actuelle, plusieurs modèles électrochimiques sont disponibles qui prédisent le comportement à l'état d'équilibre pour un ensemble de conditions de fonctionnement spécifié. Cependant, de tels modèles ont négligé l'effet de la dynamique de gestion de l'eau sur les caractéristiques de polarisation et de performance. Par conséquent, un nouveau modèle dynamique de pile à combustible semi-empirique a été développé dans un environnement MATLAB/SIMULINK qui prédit les phénomènes transitoires et dynamiques complets de la pile qui intègre l'effet des inondations membranaires et de l'hydratation / déshydratation. L'effet de la dynamique de la gestion de l'eau sur le comportement du système est étudié et validé avec les données de référence obtenues à partir d'un système de pile à combustible Nexa 1.2kW de BALLARD. Les résultats obtenus montrent que les réponses au modèle correspondent bien aux résultats expérimentaux. De plus, le modèle peut prédire la réponse dynamique et transitoire de la tension / de la puissance de l'empilage sous un changement brusque du courant de charge. Le modèle développé peut être utilisé pour optimiser les performances de la pile en termes de gestion de l'eau.**

Most clés—Pile à combustible Nexa 1.2kW de BALLARD, Inondations, Déshydratation, Modèle dynamique.

I. INTRODUCTION

Les piles à combustible connaissent actuellement un regain d'intérêt tant sur le plan industriel qu'en recherche. Des industriels de différents secteurs (électronique, automobile, chauffage...etc.) investissent dans le développement de cette technologie à faibles émissions de gaz nocifs et à faibles nuisances sonores [1]. Néanmoins cette technologie doit relever de nombreux défis tant techniques qu'économiques avant d'être commercialisée à grand échelle. Parmi ces défis techniques, la courte durée de vie de produit qui est généralement provoquée par une mauvaise gestion de l'eau au cours du fonctionnement de ce système [2]. La gestion de l'eau est un outil vraiment nécessaire pour l'amélioration des performances et l'augmentation de la durée de vie des piles à combustible à membrane échangeuse de proton (PEMFC), elle assure un fonctionnement plus fiable et plus efficace de la pile.

L'objectif du présent travail est de développer un modèle dynamique de pile à combustible semi-empirique dans l'environnement MATLAB/SIMULINK qui prédit les phénomènes transitoires et dynamiques complets de la pile qui intègre l'effet des inondations membranaires et de l'hydratation / déshydratation. Dans le but d'optimiser les performances de la pile en termes de gestion de l'eau.

II. MODELISATION DE LA PILE A COMBUSTIBLE POUR LA GESTION D'EAU

Les piles à combustible à membrane échangeuse de protons PEMFC est un générateur qui transformé l'énergie chimique d'un combustible en énergie électrique. Le combustible utilise pour les pile PEM est l'hydrogène, il est oxydé à l'anode (en présence de catalyseur), et les protons sont transportés à travers la membrane vers la cathode selon la réaction :

$$H_2 \longrightarrow 2\,H^+ + 2\,e^- \quad (1)$$

A la cathode, l'oxygène est réduit selon la réaction :

$$O_2 + 4\,e^- \longrightarrow 2\,O^{2-} \quad (2)$$

Les électrons générés à l'anode, circule au circuit extérieur durant ces réactions. Une fois que ils arrivent à la cathode, les protons se recombinent avec les ions oxygène pour former de l'eau selon la réaction :

$$H_2 + 1/2\,O_2 \longrightarrow H_2O + \text{chaleur} + \text{énergie électrique} \quad (3)$$

Dans le développement des modèles élémentaires de la pile PEMFC, les transports de matière sont pris en compte via les équations de Maxwell. Les potentiels d'équilibre thermodynamique sont définis en utilisant l'équation de Nernst. Les surtensions d'activation sont calculées par les équations de Tafel [3]. La résistance interne est déterminée par les équations de Nernst-Planck [4]. En utilisant la loi d'Ohm, nous pouvons exprimer la tension de sortie de base produite par une seule pile à combustible :

$$V_{cell} = E_{Nerst} - V_{act} - V_{ohm} - V_{conc} \quad (4)$$

E_{Nerst} ; Potentiel d'équilibre thermodynamique de la cellule donne par :

V_{act} ; Polarisation d'activation ;

*Corresponding author email: laribi.slimane@urerms.dz

V_{ohm} ; Polarisation ohmique ;
V_{conc} ; Polarisation de concentration ;
L'équation de tension de Nernst utilisée pour décrire le potentiel réversible de la cellule est [5]

$$E_{Nerst} = 1{,}229 - 0.85.10^{-3}(T - 298{,}15) + 4{,}31.10^{-5}.T.[\ln(P_{H2}) + \frac{1}{2}\ln(P_{O2})] \quad (5)$$

T ; La température de fonctionnement du système de pile à combustible.
P_{H2}, P_{O2} sont respectivement les pressions partielles d'hydrogène et l'oxygène (atm).
La polarisation d'activation est donnée par la relation de Tafel [6] :

$$V_{act} = -[\xi_1 + \xi_2.T + \xi_3.T.\ln(Co_2) + \xi_4.T.\ln(I_{fc})] \quad (6)$$

Où, les coefficients paramétriques constants ξ_i sont obtenus à partir des données expérimentales [3]. I_{fc} est le courant de fonction de la pile ; Co_2, représente les concentrations de l'oxygène (mol/cm^3) dans l'interface du catalyseur de la cathode donnée par la relation suivante :

$$Co_2 = \frac{Po_2}{5{,}08.10^6.e^{(-498/T)}} \quad (7)$$

La polarisation ohmique se produit en raison de la résistance aux électrolytes, la résistance de contact aux plaques de collecteur et aux électrodes en graphite [7]. Cette perte de polarisation ohmique est linéaire puisqu'elle est constante ; où elle est augmentée avec l'augmentation de la charge. Cela peut être exprimé comme :

$$V_{ohmic} = I_{fc}.R_{ohm} \quad (8)$$

Où R_{ohm} est la résistance électrique interne qui dépend de l'épaisseur de la membrane t_m et la conductivité de la membrane σ_m qui peut être montré comme [8]

$$R_{ohm} = \frac{t_m}{\sigma_m} \quad (9)$$

La conductivité de la membrane est déterminée par la relation suivante :

$$\sigma_m = b_1 \exp\left(b_2\left(\frac{1}{303} - \frac{1}{I_{fc}}\right)\right) \quad (10)$$

Où, b_1 est en fonction de la teneur en eau de membrane λ_m qui varie lorsque la formation d'eau à travers le système varie.

$$b_1 = (b_{11}\lambda_m - b_{12}) \quad (11)$$

Ici, b_2, b_{11} et b_{12} sont des constantes et sont déterminées pour la membrane Nafion 117, dont les valeurs varient en fonction du type de membrane utilisé.

Le calcul de la teneur en eau λ_m dans la membrane et le débit d'eau de la membrane à travers la membrane est essentiel pour le système de gestion de l'eau pour maintenir une bonne hydratation [9].

La teneur en eau de la membrane est calculée à partir de :

$$\lambda_m = \begin{cases} 0.043 + 17.8\,a - 39.85a_i^2 + 36.0a_i^3 & ,0 \le a_i \le 1 \\ 14 + 1.4(a_i - 1) & ,1 \le a_i \le 3 \end{cases} \quad (12)$$

Où a_i représenté l'humidité relative.

1. Calcule de l'humidité relative

Pour un fonctionnement optimal des piles à combustible, la membrane conductrice de proton doit être correctement hydratée ; c'est-à-dire que la membrane doit avoir une humidité spécifique en fonction de la température, de la pression d'écoulement ... etc., pour éviter toute inondation ou sécher de la membrane et permettre de produire une meilleure puissance.

Généralement, l'humidité relative représente la quantité de vapeur d'eau dans l'air, de sorte que ; 0% indique que l'air est totalement sec et 100% indique que l'air est saturé d'eau. L'humidité relative est définie par le rapport entre la pression partielle de l'eau et la pression de vapeur saturée. [10] :

$$RH = \frac{P_{wout}}{P_{sat}(T_{air})} \quad (13)$$

Où P_{wout} est la pression partielle de vapeur d'eau et P_{sat} est la pression de vapeur saturée. La pression de vapeur saturée est liée à la variation de température, elle augmente de manière non linéaire en fonction de l'élévation de la valeur de température. [10].

$$P_{sat} = 10^5 \exp\left(13.7 - \left(\frac{5120}{T_{air} + 273.15}\right)\right) \quad (14)$$

2. Calcule de pression partielle de vapeur d'eau P_{wout}

Dans un mélange gazeux, chaque pression partielle de gaz est donnée par le rapport entre le nombre de molécules de ce gaz et le nombre total de molécules de mélange [11] :

$$\frac{P_{wout}}{p_{exit}} = \frac{\text{number of water molecules}}{\text{total number of molecules}} \quad (15)$$

$$\frac{P_{wout}}{p_{exit}} = \frac{q_{win} + q_{Wprod}}{q_{win} + q_{Wprod} + q_{O2out} + q_{rest}} \quad (16)$$

Où q_{win} est le débit molaire introduit par l'air; q_{Wprod} est le débit molaire d'eau produit (mol.s^{-1}) ; q_{O2out} est le nombre de mole d'oxygène qui laisse la cellule à chaque seconde ; q_{rest} est le nombre de mole des autres composants de l'air, non-oxygène, qui laisse la cellule dans chaque seconde et P_{exit} est la pression de l'air totale à la sortie de la pile à combustible, il est égal à la pression atmosphérique.

$$q_{Wprod} = \frac{I_{fc}}{2F} \quad (17)$$

$$q_{O2in} = \lambda\frac{I_{fc}}{4F} \quad (18)$$

q_{O2in} est défini par le produit d'écoulement molaire d'oxygène consommé.

$$q_{O2out} = (\lambda - 1)\frac{I_{fc}}{4F} \quad (19)$$

Où λ est la stœchiométrie de l'air, I_{fc} est le courant de la pile à combustible (A), et F la constante de Faraday.

$$q_{rest} = \frac{100 - O_{2\%}}{O_{2\%}}\lambda\frac{I_{fc}}{4F} \quad (20)$$

*Corresponding author email: laribi.slimane@urerms.dz

Pour l'air : $\frac{100-O_{2\%}}{O_{2\%}}=\frac{100-21}{21}=3.76$ (21)

$$\frac{P_{win}}{P_{in}}=\frac{q_{win}}{q_{win}+q_{O2in}+q_{rest}} \quad (22)$$

$$q_{win}=\frac{P_{win}}{P_{in}-P_{win}}\left(q_{O2in}+q_{rest}\right) \quad (23)$$

Où P_{in} est la pression d'air d'entrée totale, qui sera généralement un peu plus grande que P_{exit} et P_{win} est la pression de vapeur d'eau à l'entrée de la cellule.

En outre, ψ est défini comme suit :

$$q_{win}=\psi\left(q_{O2in}+q_{rest}\right) \quad (24)$$

L'équation 16 peut être écrite comme :

$$\frac{P_{wout}}{P_{exit}}=\frac{\psi\left(\lambda\frac{I_{fc}}{4F}+\frac{100-O_{2\%}}{O_{2\%}}\lambda\frac{I_{fc}}{4F}\right)+\frac{I_{fc}}{2F}}{\psi\left(\lambda\frac{I_{fc}}{4F}+\frac{100-O_{2\%}}{O_{2\%}}\lambda\frac{I_{fc}}{4F}\right)+\frac{I_{fc}}{2F}+(\lambda-1)\frac{I_{fc}}{4F}+\frac{100-O_{2\%}}{O_{2\%}}\lambda\frac{I_{fc}}{4F}} \quad (25)$$

Pour l'air : $P_{wout}=\frac{(0.420+\lambda\psi)P_{exit}}{\lambda(1+\psi)+0.210}$ (26)

Enfin, l'équation 13 peut être écrite comme :

$$RH=\frac{P_{wout}}{P_{sat}(T_{air})}=\frac{\frac{(0.420+\lambda\psi)P_{exit}}{\lambda(1+\psi)+0.210}}{10^5\exp\left(13.7-\left(\frac{5120}{T_{air}+273.15}\right)\right)} \quad (27)$$

III. RESULTATS ET DISCUSSION

Dans cette section, un modèle mathématique semi empirique pour le système de piles à combustible PEM de Ballard-Mark-V 5kW développé est testé à l'aide de l'environnement MATLAB/SIMULINK. Les paramètres utilisés pour développer le modèle de Ballard sont données dans le Table I ;

TABLE I
LES CONSTANTES ET PARAMETRES PHYSIQUES DE LA PEMFC [2]

Paramètres	Valeurs
T	343K
A	333 cm²
L	178 μm
P_{H2}	1 atm
P_{O2}	1atm
B	0.016 V
Cdl	0.035*232 F
R_C	0.0003 Ω
b_{12}	0.00326
b_{11}	0.005139
ζ_1	-0.948
ζ_2	0.00286+0.0002.ln(A) + (4.3.10-5). ln(CH2)
ζ_3	7.6.10-5
ζ_4	-1.93.10-4
Ψ	23
J_{max}	1500 mA/cm²
J_n	1.2 mA/cm²

Sur la base des caractéristiques électrochimiques et thermodynamiques de la PEMFC discutées précédemment. Nous avons développé un modèle dynamique de la pile à combustible PEMFC (Fig. 1) sous l'environnement du logiciel Matlab/Simulink. Sur cette figure ; nous avons créé un sous-système qu'associe l'ensemble de la pile à combustible et l'unité de calculer des pressions partielles (hydrogène et oxygène), l'unité de calculer le taux d'humidité relative en fonction : du courant demander par la charge et le débit molaire d'eau injecté dans les gazes réactives ainsi que la température de fonctionnement

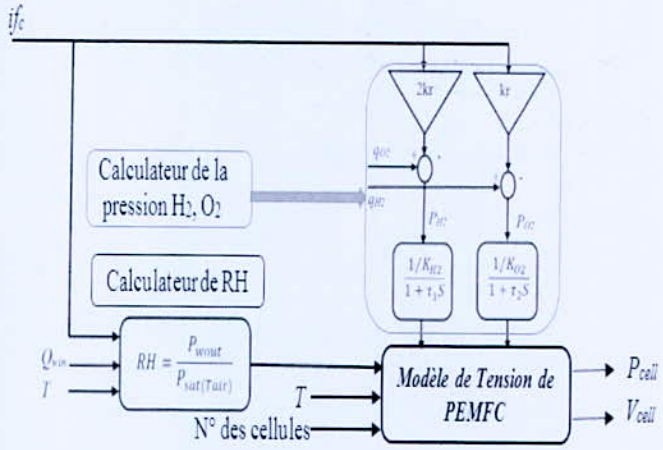

Fig. 1. Schéma synoptique du modèle PEMFC développé

La Fig. 2, représente la variation de l'humidité relative en fonction du temps. Où l'humidité relative est calculée en fonction du débit molaire d'eau.

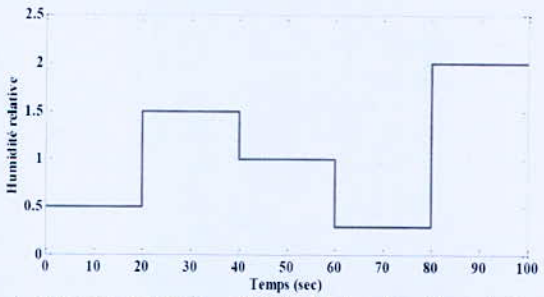

Fig. 2. Variation de l'humidité relative fonction du temps

Fig. 3 et Fig. 4, représentent respectivement les réponses électriques dynamiques de la de pile à combustible (tension, puissance) aux variations abruptes du l'humidité relative (la variation du débit molaire d'eau) en fonction du temps de fonctionnement.

Entre l'intervalle de temps 0s et 20s on a fixé le taux d'humidité relative RH à 0.5 (Fig. 2), on remarque sur les résultats relatifs (Fig. 3 et Fig. 4) et dans le même intervalle, une augmentation exponentielle de la tension et la puissance. Entre l'intervalle de temps 20s et 40s on a effectué un changement brusque du l'humidité RH de 0.5 à 1.5 à l'instant 20s et de 1.5 à 1 à 40s. On observe sur les résultats (Fig. 3 et Fig. 4) une augmentation similaire de

*Corresponding author email: laribi.slimane@urerms.dz

la tension et la puissance ce qu'est expliqué par : La membrane de la pile à combustible conductrice de proton doit être saturée en eau, condition essentielle pour assurer une bonne conductivité ionique et par conséquent le rendement de la pile augmente.

A l'instant 40s, l'humidité relative diminue 1.5 à 1 ce qui provoque une augmentation aussi de la tension et la puissance (Fig. 3 et Fig. 4). A l'instant 60s, l'humidité relative baissait plus de 1 à 0.3, mais dans ce cas, on note à la fois que la tension et la puissance sont également réduits parce que la diminution de RH peut entrainer un assèchement de la membrane, ce qui conduirait à la destruction de la PEMFC, Nous concluons que le meilleur rendement de pile à combustible lorsque l'humidité relative est proche de la valeur 1 .

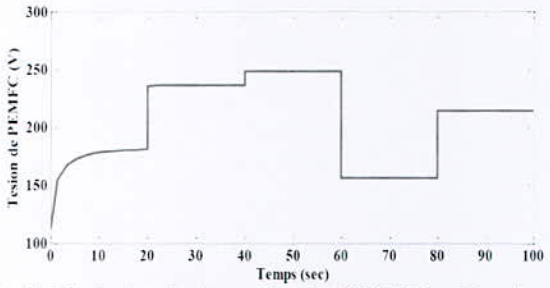

Fig. 3. Variation de la tension de PEMFC en fonction du temps

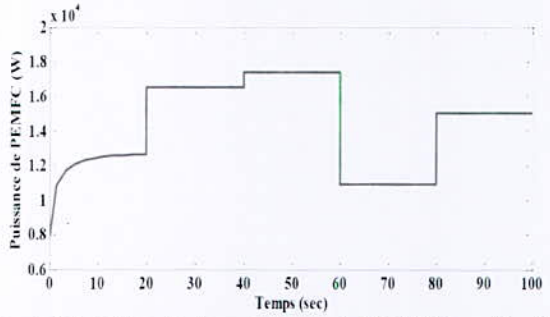

Fig. 4. Variation de la puissance de PEMFC en fonction du temps

IV.CONCLUSION

A la phase finale, le modèle dynamique de la pile à combustible sous l'environnement du logiciel Matlab/Simulink permis nous pour chaque instants et pour n'importe quelle valeur du courant de charge ou bien le débit molaire d'eau introduit dans les gazes réactives ou la température interne, le modèle dynamique de peut calculer la tension et la puissance électrique de la pile à combustible en fonction du ces facteurs.

Les résultats de simulation obtenus montrent que le changement des performances (tension, puissance) de la pile à combustible est lié à la variation du débit molaire d'eau qui introduit dans les gazes réactives parce que la conductivité membranaire de la pile est directement liée à sa teneur en eau. Lorsque l'humidité relative trop augmente, la teneur en eau de la membrane augmente, par conséquent l'eau liquide va gêner le transport des espèces présentes dans le cœur de la pile, et cela provoque la réduction du rendement de la pile.

Nous concluons que :

- Le meilleur rendement de pile à combustible lorsque l'humidité relative est proche de la valeur 1.

- L'augmentation abruptes du courant de charger provoque une augmentation de la température interne de la pile accompagnée d'une diminution de la teneur en eau de la membrane. Et par conséquent la tension électrique de PEMFC diminue.

REFERENCES

[1] G. Dotelli, R. Ferrero, P.G Stampino, S. Latorrata, S. Toscani.: "Diagnosis of PEM fuel Cell drying and flooding based on power converter ripple". IEEE Trans Instrum Meas. 2014;63:2341-8.

[2] K, Murugesan, V, Senniappan.: "Investigation of water management dynamics on the performance of a Ballard-Mark-V proton exchange membrane fuel cell stack system". Int J Electrochem Sci. 2013;8:7885-4.

[3] J. M. Corrêa, F.A. Farret, L.N. Canha, M. Godoy Simões."An electrochemicalbased fuel cell model suitable for electrical engineering automation approach".IEEE T Ind Electron, 2004;51:1103.

[4] J. Hamelin, K. Agbossou, A. Laperri.ere, F. Laurencelle, T.K. Bose.: "Dynamic behavior of a PEM fuel cell stack for stationary applications". Int. J. Hydrogen Energy. 2004;26: 625–629.

[5] Chien-hsing lee and Jian-TingYang. : "Modeling of the Ballard-Mark-V proton exchange membrane fuel cell with power converters for applications in autonomous underwater vehicles". J. Power Sources. 2011;196:3810-3823.

[6] P.R Pathapati, X. Xue, J. TangJ, A new dynamic model for predicting transient phenomena in a PEM fuel cell system, Int. J. Renew. Energy.2005;30 :1-22.

[7] J. Jia, Q. Li, Y.Wang, Y. T. Cham, M. Han .: "Modeling and dynamic characteristic simulation of a Proton Exchange Membrane Fuel Cell". IEEE T Energy Conver., 2009;24:283-291.

[8] B. Dokkar, N. Chennouf, N.Settou, B. Negrou, A. Benmhidi. : "Optimization of PEM Fuel Cell biphasic model". Int J of Chemical, Nuclear, Materials and Metallurgical Engineering, 2013,7 (7).

[9] D. Ali, D. Daniel, D. Aklil-D'Halluin. : "Modeling a proton exchange membrane (PEM) Fuel Cell system as a hybrid power supply for standalone applications". Asia-Pacific Power and Energy Engineering Conference, 2011:1-5.

[10] L. Boulon, K. Agbossou, D. Hissel, A. Hernandez, A. Bouscayrol, P. Sicard, M.C.Pera.: " Energy management of a fuel cell system: Influence of the air supply control on the water issues". IEEE Int Symp Ind Electron 2010;xxx:161-6.

*Corresponding author email: laribi.slimane@urerms.dz

Microorganisms: Biocatalysts Biofilm in Microbial Fuel Cell

I. Tou[1*], Y. M. Azri[1], M. Sadi[1], S. Brahiti[2], R. Rebiai[2] and S. Gana-Kebbouche[2]

[1*]Division Bionergie, Centre de Développement des Energies Renouvelable, Bouzaréah. Algiers, Algeria
[2]Département de Biologie, Université M'Hamed Bougara de Boumerdes, Algeria.

Abstract—**Renewable energies, defined as clean energies that produce little or no pollutants include the Plant Microbial Fuel Cell (PACM), which is a new renewable and sustainable alternative technology for the electricity production from living plants and electroactive soil bacteria. PACMs are capable to convert directly the organic fuels chemical energy into bioelectricity. Electroactive microorganisms forming a biofilm on the electrode surface act as biocatalysts for electrochemical reactions, instead of chemical catalysts in the other fuel cells to carry out the fuel oxidation. This work consists of studying the microbial biofilms effect on the bioelectricity production in a p-MFC from two different environments: agricultural and polluted soils, by directly inoculating bacteria consortium at the p-MFC roots level and to study the resulting electrochemical kinetics through a plant pile electrical circuit.**

Keywords—Electroactive biofilms, Rhizosphere, Microorganisms, Electrochemical System, PEMFC, MFC, p-MFC.

I. INTRODUCTION

The PEMFC (Proton Exchange Membrane Fuel Cell) is one of the most developed renewable energy production systems called hydrogen fuel cells that uses hydrogen as fuel and oxygen as an oxidant; only water is produced as waste. It have high energy yields and low noise emissions (a major factor in the automotive field), with power ranging from 1watt-10kilowatt [1] and current densities of 200-400A/cm² for a voltage approximately 0.7V [2] could be the best alternative energy. However, the PEMFCs development is slow due to two major obstacles, one is the use quite often of a complex and expensive ion exchange membrane (Nafion membrane: 800$/m²), the other is the use of platinum need as an electrochemical reactions catalyst which is a rare and expensive element on our planet. In addition, although hydrogen is an ecofreindly energy carrier, it has some flaws: its flammability, generating regulatory constraints as well as its volatility makes it difficult to store.

In order to replace the expensive platinum catalyst, some researchers are turning to microbial fuel cells (MFCs) using bacteria as electrochemical reactions biocatalysts for bioelectricity production.

Several renewable and sustainable energy sources have been introduced into the market over the last century, including a new biomass energy technology based on solar energy, soil biological activity principles, living plants and microorganisms organized as biofilm to catalyze electrode reactions: "The plant-microbial fuel cell (P-MFC)" [3].

The innovative technologies research are essential to promote bioenergy sectors as credible alternatives energies particularly bioelectrochemical systems using different electroactive biofilms environments (agricultural soils, polluted soils, household and industrial waste, wastewater ...) as an inoculums. The plant biopile constitute a future way that would be a large context part of "p-MFC (plant microbial fuel cell)" energy development sector, by proposing a sustainable management means of agro-energy chains and organic by-products valuation [3].

The p-MFC makes use of electrochemically-active bacteria that catalyze the rhizodeposits anaerobic oxidation at the plants roots. By connecting the plant roots and bacteria directly to an electrical circuit, current will flow because of oxygen reduction at the other end of the circuit. This current can be harvested as electricity.

II. EXPERIMENTAL

1. The P-MFC construction

The plant pile was designed in Bioenergy and Environment-CDER (Renewable Energy Development Center-Bouzareah) laboratory, using a PVC pot (polyvinyl chloride). The pot was filled with CDER garden soil, without adding any organic fertilizer. An anode was set vertically at the rhizospheric medium where the photosynthesis organic products are oxidized, protons H^+ and e^- released are captured by the cathode placed at the soil surface, thus completing the electrical circuit, without using cations exchange membrane. These electrodes were connected via epoxy-capsuled wires and the circuit was closed using an external resister of 66 kΩ [4, 5].

The electrodes are rectangular about 7.5cm² geometric area and 2mm thick each one, they are graphite made which is an ecofriendly material, not expensive and a good current conductor.

2. Electrodes preparation and soil sampling

Graphite electrodes were used as electroactive biofilms supports, are polished, then placed in 5N HCl for 2 hours and rinsed at the end with distilled water.

The microorganisms' electroactive effect of two bacterial inocula (A and B) on the current tension was tested directly in p-MFC. Two soil samples coded A and B were taken according to the standards:

- Sample A (SA): Agricultural soil of a wheat field in the area of Lakhdaria-Bouira.

*Corresponding author email: i.tou@cder.dz

- Sample B (SP): Polluted soil containing vegetation, taken at the edge of Oued El-Harrach.

3. The p-MFC performance study

The p-MFC electrochemical performance was continuously evaluated by following the closed circuit voltage kinetics (U(mV)=(t)) during the period (April-June 2016) everyday at 13:00 AM at room temperature, where the plant was light exposed continually except night.

The current was calculated according to the following equation: $I(mA)=U(mV)/R(\Omega)$ and the current density according to: $d(mA.m^{-2})=I/S$, where U(mV) is the cell voltage, R is the external resistance and S(m^2) is the anode surface (in our case the two anode surfaces are in rhizosphere contact, with total geometric area is 0,0006 m^2.

4. Soil leachates preparation

500ml of each sieved soil was mixed with 750 ml of 60mM KCl solution and stirred for 24 hours and 100ml of 20mM sodium acetate were added as substrate [4]. Measurements of pH, conductivity and temperature of the two leachates were taken at the beginning of the experiments for the samples characterization, and adjusting pH7 approximately, by adding HCl or NaOH and increasing conductivity by adding a KCl 60mM solution, where the physicochemical characteristics of the two samples were:

- Agricultural soil : pH6.86 ; $\varkappa$=47µs/cm ; T=25°C
- Polluted soil: pH 6.9 ; $\varkappa$=47µs/cm ; T=25°C

Graphite electrodes were let in the leachate during 40-45 days at room temperature for biofilm formation on its surface.

5. Biofilms identification

The microorganisms biofilm formed at the electrode surface were isolated by serial dilution method, inoculated on Hectoen and Chapman agar and enumerated on the nutrient agar [7, 8].

The approximate bacteria number per suspension volume was obtained by counting the isolated colonies on agar medium, per dilution and calculated [9, 10, 11].

To identify the isolated bacteria, cell morphology, regrouping, mobility, Gram, oxidase and catalase reactions were studied and other physiological and biochemical properties were carried out using the API galleries Kit (BioMerieux,Marcyl'Etoile, FRANCE), to distinguish species, even closely related ones [12].

6. Bacterial growth kinetics monitoring

The consortia A and B bacterial growth was evaluated by the optical density (OD_{620}) monitoring in standard liquid medium (pH7), at 30°C, stirring at 150 rpm for 5-7 days, at defined times until obtaining growth exponential phase end, using a visible UV spectrophotometer.

7. Monitoring and study of the p-MFC bacterial inocula effect

Exponential phase cells of the samples (PS, AS) were harvested by centrifugation at 1500rpm/15min and washed with sterile distilled water, then suspended in 10ml sterile distilled water for used as p-MFC catalysts by studying their electroactive effect during their inoculation [13].

After the current voltage stabilization produced by the p-MFCs (A and B as well as the control without inoculum), the bacterial suspensions (A and B) were inoculated directly at the p-MFC rhizosphere and follow the voltage produced before and after inoculation, taking daily measurements and recording the data using a Fluke interface Multimeter[14].

III. RESULTS AND DISCUSSION

1. Culture and enumeration of biofilm bacteria

Depending on the dilutions, the dishes contained a large colonies number; we had chosed those containing between 30-300 colonies and enumerated them [15]. Both samples had a large microbial load; so that the bacteria number in the polluted soil sample was approximately (26.10^5 CFU/ml) and the agricultural one had a lower load (15.10^5 CFU/ml).

Microbiological electrode biofilm isolation, revealed the abundance of Gram-negative and mobile bacteria, including 13 species belonging to four (04) different families having common characteristics with electroactive bacteria, which facilitating their self-aggregation on the electrode surface and allowing their electrochemical exchange within biofilm and with the electrode surface [16, 17, 18].

2. Bacterial growth kinetics Monitoring

Fig. 1, shows the bacterial growth kinetics of the consortia: "SA" (four (04) different strains) and "SP" (nine (09) bacterial strains).

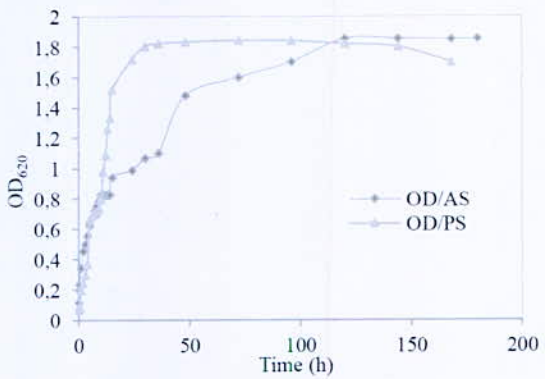

Fig. 1. Bacterial consortia growth kinetics

The growth kinetics showed a bacterial growth curve pattern with exponential and stationary phases. However, we noted almost an absence of the latency phase, which shows that the two consortia bacteria did not require an important acclimatization time to the new environment [5]. The exponential phase cells were thus used as p-MFC catalysts by following the voltage registered before and

*Corresponding author email: i.tou@cder.dz

after their inoculation in the p-MFCs rhizosphere studying directly their electroactive effect.

3. Bacterial inocula influence study on P-MFC (CDER)

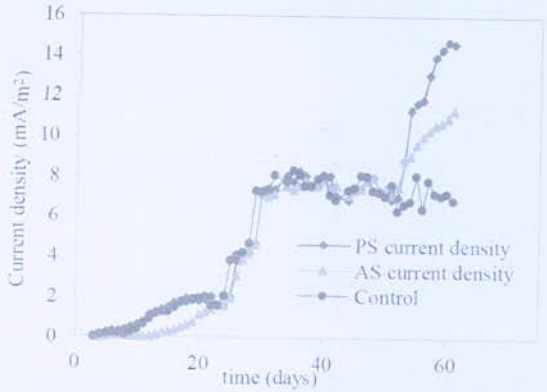

Fig. 2. Current tension yields with bacterial inocula AS and PS

Fig. 2, shows four distinct phases; [0-50th day], current densities are similar between AS, PS and control, they are low in the first 15 days (0.4-0.8 mA/m^2), and a slight increase is registered between 10th and 25th day to reach $2mA/m^2$ this phase characterizes typically the natural biofilm formation on the electrode surface [19]. A gradual increase is noted between 22nd and 35th day to reach approximately $8mA/m^2$ and forms a plateau for the three kinetics. At 50th day and after bacterial inoculation, the current density with PS bacteria increases progressively by 50% to reach $14.8mA/m^2$, and that in the presence of AS inoculum the current density increased by 34% and reaches $11.4mA/m^2$after only 6 days.

The current density with AS inoculum was lower than with PS one, which may be due to the strains number larger in the PS consortium (9 strains) than the agricultural one (4 strains) and thus to the more successive metabolism diversification within the consortium, which can increase the current voltage produced by the p-MFC and thus allows to improve the microbial ecosystem performance and stabilization for the bioelectricity production yield, through the bacteria intervention as biocatalyst in the p-MFC [19,20].

4. Hydrogen production possibility via p-MFC

Nowadays, hydrogen is gaining popularity as alternative renewable energy. The microbial fuel cell is one of the gaseous hydrogen production ways from the organic matter complete conversion in anerobiosis (absence of the oxygen). Thereby, the pure hydrogen gas can be generated with p-MFC since there is an abundant organic matter that is root exudates (carbohydrates, carboxylic acid, amino acid, sugars...). The H_2 thus produced is collected at the cathode as well as at the anode where electrons e^- and protons H^+ from bacterial metabolism recombine and provide external electricity source [3, 21].

Hydrogen is mainly produced from fossil fuels. MFCs have sometimes been boasted as a way of indirectly producing hydrogen from biomass using electricity in a water electrolysis process. [19].

5. Power comparison of three P-MFC and PEMFC

In P-MFC systems, electrochemical units: living plants and microorganisms are able to produce directly clean and sustainable electricity from solar energy, through a natural process around plant roots.

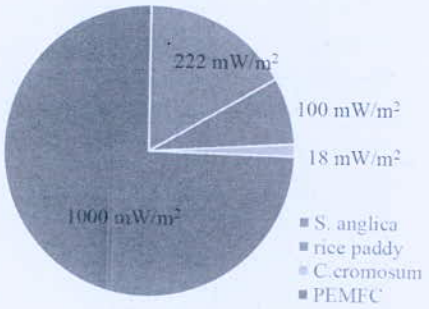

Fig. 3. Power comparison of three P.MFC and PEMFC

Fig.3 shows a power density of ($222mW/m^2$) has been reported from rhizosphere-MFC with *Spartina anglica* (plant inhabiting brackish marsh) in specific cell using membrane and nutrient solution [4]. Experiments in Japan have also been carried in a rice paddy field [22, 23], however, in this case the power output does not exceed 100 mW/m^2 and rice paddy -MFC react as sediment MFC without plants [24]. In the current study, a power density of (18mW/m2) has been reported from rhizosphere-MFCs.

Despite the p-MFCs power is smaller than that hydrogen fuel cells, the p-MFC technology remains non-polluting and in the same time depolluting, discreet and durable and give the possibility to work with a wide plants variety. Researchers estimate that over the next few years, the system's productivity could reach 3.2 W/m^2, and homes could be powered by rooftop crops where a flat roof of $100m^2$ could provide enough electricity year-round to power a home (an average of 2,500 kWh/year) [3,4,25]. P-MFC technology could therefore be an interesting combination, for an innovative application in the energy market using green panels or roofs to produce electricity, so this is a positive point for the development of this sector.

IV. CONCLUSION

The P-MFC current voltage increase after PS and AS consortia inoculation shows that at least one of the bacteria constituting the biofilms is electro-active; or the bacteria within the consortium are electrochemically active.

In fact, the bacterial inoculating made it possible to control the overall microbial consortium metabolism, both in terms of performance and stability. The microbial interactions involved allowed a significant increase in the production of the current voltage (>$14.8mA/m^2$). This highly original mode of interaction therefore makes it possible to envisage a biotic control of microbial ecosystems.

At the anode, bacteria catalyze oxidation reactions of organic molecules to carbon dioxide. These reactions are related to respiratory metabolism. Indeed, the rhizospheric bacteria mainly feed on the photosynthesis products [26].

*Corresponding author email: i.tou@cder.dz

The hydrogen batteries power is higher than that of MFCs and more specifically of p-MFC, however biological catalysts represent an attractive alternative to chemical catalysts conventionally used in fuel cells, which are often expensive, toxic and not stable [4].

REFERENCES

[1] Larminie, J., et Dicks, Aw. Fuel cell systems explained. 2003 deuxième édition. John Wiley & Sons, Ltd.

[2] Hottinen, T., Himanen, O., Lund, P. Effect of cathode structure on planar freebreathing PEMFC. *Journal of Power Sources*, 2004. 138(1), 205-210.

[3] Timmers, RA, DPBTB Strik, HV Hamelers, et CJ Buisman. 2013- Electricity generation by a novel design tubular plant microbial fuel cell. *biomass and bio energy*. 2004- 50 : 60-67.

[4] Helder.M, Strik.D. PBTB, Hubertus VM, Hamelers and Cees JN Buisman. The flat-plate plant-microbial fuel cell: the effect of a new design on internal resistances. *Biotechnology for Biofuels*. 2012- 5:70.

[5] Thomas, Y. R., Picot, M., Carer, A., Berder, O., Sentieys, O., Barrière, F. d.- A single sediment-microbial fuel cell powering a wireless telecommunication system. 2013- 241; 703-708; *Journal of power sources. Elsevier Science B.V.,*

[6] Schaetzle O, Barrier F, Baronian K. Bacteria and yeasts as catalysts in microbial fuel cells: electron transfer from microorganisms to electrodes for green electricity. 2008- 1:607–620.*Energ Environ Sci*

[7] Parot S, Délia ML, Bergel A. Forming electrochemically active biofilms from garden compost under chronoamperometry. *Bioresour Technol*. 2008-99 (11):4809-16.

[8] Pescott.W, Harley.S and Klein.W, Microbiologie.3ème édition. Editions De Boeck, 2010- p.101-125

[9] Marchal (N.), Bourdon (J.L.), Richard (C.). Les milieux de culture pour l'isolement et l'identification biochimique des bactéries. Paris : Doin (éditeur), collection *Biologie appliquée*, 1982-482 p

[10]Dong.F, Cai.X, Makaroff.CA. Cloning and characterization of two Arabidopsis genes that belong to the RAD21/REC8 family of chromosome cohesin proteins.2001- 13; 271(1):99-108.*Gene*

[11]Tortora G.J.,B.R.Funke et C.l.Case, Introduction à la microbiologie. ERPI. 940p. Antibiotiques - les plus couramment utilisés. 2003- pp. 608-613.

[12]B. Tivoli. Guide d'identification des différentes espèces ou variétés de Fusarium rencontrées en France sur la pomme de terre et dans son environnement. Agronomie, EDP Sciences, 1988- 8 (3), pp.211-222.

[13]Régis & Duhem, Bernard. Guide des champignons de France et d'Europe. 1994 Delachaux&Niestlé. Paris.476p

[14]Rabaey.K, Boon.N, Siciliano.SD, Verhaege.M, Verstraete.W. Biofuel cells select for microbial consortia that self-mediate electron transfer. 2004-70:5373–5382.*Appl Environ Microbiol*.

[15] Garrity, G.M., Bell, J.A. &Lilburn, T.G. *Taxonomic Outline of the Prokaryotes. Bergey'sManual of Systematic Bacteriology, 2nd Edition. Release 5.0.* Springer-Verlag, New York. May 2004- 1-399.

[16] Lock M.A.Attached microbial communities in rivers. In: *Aquatic Microbiology*, (Ed. T. E. Ford). Blackwell *Scientific* Publications, Cambridge, 1993- 113-138.

[17] Bieber D, Ramer SW, Wu CY, Murray WJ, Tobe T, *Fernandez* R, Schoolnik GK. Type IV pili, transient bacterial aggregates and virulence of enteropathogenic *Escherichia coli*. *Science*. 1998- 26; 280 (5372):2114-8.

[18] Lovley D. R. Extracellular electron transfer: wires, *capacitors*, iron lungs, and more. *Geobiology*. 2008-6: 225-231.

[19]LoganB.E., Microbial Fuel Cells. John Wiley & Sons, New *Jersey* 2008.

[20] Rafrafi. Y.Impact des facteurs biotiques sur le réseau *métabolique* des écosystèmes producteurs d'hydrogène par voie fermentaire en culture mixte. Thèse de doctorat en Biotechnologie, microbiologie. 2012- Montpelier 2-France

[21]Sekar N, Ramaraja YU and Ramasamy P. photocurrent generation by immobilized Cyanobacteria via direct electron transport in Photo-bioelectrochemical cells. *Phys. Chem*. 2014-16: 7862

[22]N. Kaku, N. Yonezawa, Y. Kodama, K. Watanabe,Plant/microbe cooperationfor electricity generation in a rice paddy field. *Appl. Microbiol. Biotechnol*. 2008- 10, 1007–1014.

[23] K. Takanezawa, K. Nishio, S. Kato, K. Hashimoto, K. Watanabe Factors affecting electric output from rice-paddy microbial fuel cells. *BiosciBiotechnolBiochem*. 2010 - 74 1271–1273.

[24] D.P.B.T.B Strik, R. A. Timmers, M. Helder, K.J.J. Steinbusch, H.V.M. Hamelers, C.J.N. Buisman, Microbial solar cells: applying photosynthetic and electrochemically active organisms, Trends in Biotechnol. 2011- 29:41-49.

[25]Ruud A. Timmers David, PBTB. Strick, HVM. Hamelers HVM, Snel JFH, Buisman CJN.: Long-term performance of a plant microbial fuel cell with *Spartina anglica*. *Appl Microbiol Biotechnol*. 2010-86: 973-981

[26] Chiranjeevi. P. Rhizosphere mediated electro-genesis with the function of anode placement for harnessing bioenergy through CO2 sequestration- Bioressource Tech*nology Journal*. 2012-Vol. 124, pp. 264-370

*Corresponding author email: i.tou@cder.dz

Design and Realization of Hydrogen Bicycle

R.Medjebour[1] and A.Khellaf[1]

[1*]Renewable Energy Development Center, (CDER), B.P. 62, Route de l'Observatoire, 16340, Bouzareah, Algiers, Algeria.

Abstract— **In recent decades, the use of fuel cells in transportation has been the focus of increased attention. Compared with the battery powered electric vehicles, the fuel cell-powered vehicle has the advantages of a longer driving range without a long battery charging time.**

This paper described the development of a hydrogen bicycle, which uses a 300 W fuel cell stack for powering the motor. The hydrogen bicycle use an electric motor for traction, and PEM fuel cell for its energy source. The hydrogen bicycle system mainly consists of a 300 W fuel cell system, a microcontroller, metal hydride canister and brushless motor. This project has been conducted at Development Center of Renewable Energies (CDER).

First the design will be given, then the realization described and the operation reported.

Key words—Hydrogen Bicycle, PEMFC, Transportation.

I. INTRODUCTION

Energy and environmental issues are today part of major international concern. The growing world population and industrial activity in the world have led to an explosion of energy needs. Road transport is one of the main responsible for this pollution. To meet the needs of the future, we need a new generation of electric vehicles whose performance is at least equivalent to that of current thermal vehicles, especially in terms of autonomy. However, said propulsion "zero emission" is possible with electric vehicles. These latter have not experienced a real growth because of their low autonomy and significant recharge time. The production of "clean" energy in sufficient quantity to power an electric motor can be achieved by a hydrogen fuel cell, which is solution to the problem of autonomy and recharge time [1].

Hydrogen technologies and more particularly hydrogen fuel cells (FC) have many advantages to be the energy generators of tomorrow without CO_2 emissions and noises. Hydrogen fuel cells can be deployed in many areas such as automotive transport (public transport, individual transport), stationary applications to generate electricity, e.g. for distributed generation or auxiliary power and portable applications (phones, laptops, etc.) [2].

E-bikes have gained popularity in many countries due to their prices and efficiencies. An electric bike uses a low power source to turn a small motor attached to the wheel core. Generally, e-bikes are powered by either lead-acid or nickel-cadmium batteries, with motor powers between 200 and 400W. Recently, the hydrogen fuel cell has been used to power the motor that propels the bike directly or to charge a battery, which in turn drives the motor.

*Corresponding author email: m-rafik15@hotmail.fr

II. SIZING OF HYDROGEN BIKE

The first step in modeling the bike performances is to produce an equation for traction. This is the driving force of the bike, applied to the rear wheel of the bike.

It is a question of modeling the displacement by bicycle from the parameters of the movement in order to identify the needs in torque and power applied to the hub. As shown in fig.1, we have considered a bicycle proceeding at a speed v on a slope of the angle "α". The total mass of the system (bike + cyclist) is equal to "M". It is assumed that the rolling is without sliding and the moments of inertia of the two wheels are neglected. The resistance to movement is modeled by the displacement "δ" of the point of application of the action of the ground on the wheel, creating an opposing torque independent of the speed brought back on the rear wheel.

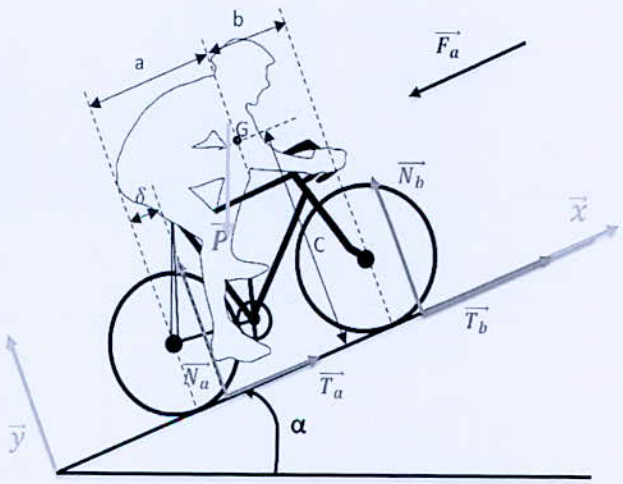

Fig. 1. Representation of the forces applied on the "bike + cyclist" system uphill

In TABLE I, we define the parameters that influence the displacement of "bike + cyclist".

In order to determine the power required to move the cyclist "Pw", it is necessary to identify the torque applied to the rear wheel "Tm":

We apply the Newton's Second Law for translation on the system {Cyclist + Bicycle}

$$\sum \vec{f} = M\frac{d\vec{v}}{dt} \Rightarrow \vec{P} + \vec{F_r} + \vec{F_a} = M\frac{d\vec{v}}{dt} \quad (1)$$

Where:

$\vec{P}$ is the gravity force

$\vec{F_r}$ is the rolling force

$\vec{F_a}$ is the aerodynamic force

By projecting on the "x and y" axes, we obtain:

$$\begin{cases} -P\sin\alpha + T_a + T_b - F_a = M\frac{dv}{dt} \\ -P\cos\alpha + N_a + N_b = 0 \end{cases} \quad (2)$$

Where: $P = M * g$

$$F_a = \frac{1}{2}C_x.S.\rho.v^2$$

By applying the Newton's Second Law for Rotations/G on the system {Cyclist + Bicycle} with projecting on "y" axe we obtain the following equation:

$$N_a.a + T_b.c + T_a.c - N_b.b = 0 \quad (3)$$

TABLE I
PARAMETERS APPLIED TO THE {CYCLIST + BICYCLE} DISPLACEMENT

Symbol	Quantity
M	Mass of the assembly {Cyclist + Bicycle}
g	Gravity acceleration
v	Velocity of the assembly {Cyclist + Bicycle}
S	Normal surface to the direction of displacement
ρ	The density of air
Cx	Coefficient of penetration into the air of the assembly {Cyclist + Bicycle}
α	Angle of road inclination to the horizontal
Dr	Wheel diameter
δ	Rolling resistance coefficient

By applying the Newton's Second Law for Rotations to the rear wheel/wheel center with projecting on "z" axe we obtain the following equation:

$$-C_m + \delta.N_b + T_b.\frac{D_r}{2} = I.\frac{d\Omega}{dt} \quad (4)$$

Where:

C_m is motor torque

By applying the Newton's Second Law for Rotations to the front wheel/wheel center with projecting on "z" axe we obtain the following equation:

$$\delta.N_a + T_a.\frac{D_r}{2} = I.\frac{d\Omega}{dt} \quad (5)$$

In steady state, the terms of acceleration is canceled:

$$\begin{cases} -M.g.\sin\alpha + T_a + T_b - \frac{1}{2}C_x.S.\rho.v^2 = 0 \\ -M.g.\cos\alpha + N_a + N_b = 0 \\ N_a.a + T_b.c + T_a.c = N_b.b \\ -C_m + \delta.N_b + T_b.\frac{D_r}{2} = 0 \\ \delta.N_a + T_a.\frac{D_r}{2} = 0 \end{cases} \quad (6)$$

By resolving the system of equations, we obtain:

$$C_m = \frac{D_r}{2}.M.g.\sin\alpha + \frac{D_r}{4}.C_x.S.\rho.v^2 + M.g.\delta.\cos\alpha \quad (7)$$

The power to be supplied to the rear wheel to obtain a velocity v is then:

$$P_m = F_m.v \quad (8)$$

where: $F_m = 2.\frac{C_m}{D_r}$

By replacing F_m in P_m we obtain the fallowing equation:

$$P_m = M.g.\sin\alpha.v + \frac{1}{2}.C_x.S.\rho.v^3 + \frac{2}{D_r}.M.g.\delta.\cos\alpha.v \quad (9)$$

This relation allow tracing the chart of the power required for a given speed, set according to the slope.

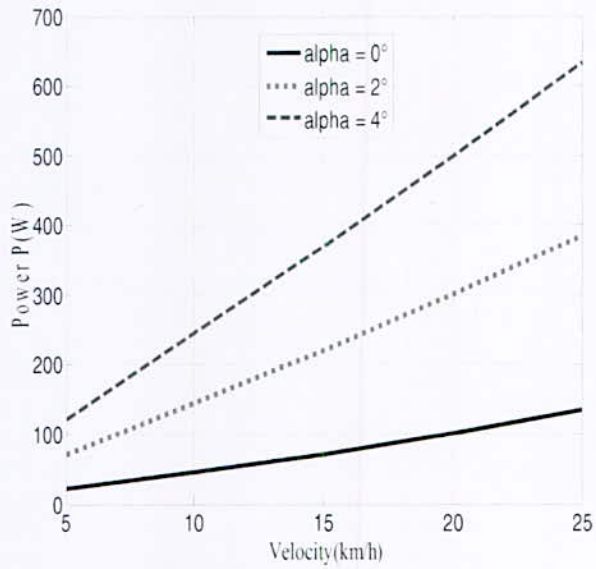

Fig. 1. Power to apply to the rear wheel depending on the inclination of the road and the speed

III.DESIGN AND REALISATION

The hydrogen bicycle is designed and realized by modifying a commercial bicycle. The idea is to introduce an electrical power that the rider can activate any time he/she wishes to. The electrical power is generated by the use of fuel cell that uses the hydrogen carried in a storage tank to generate electrical power. This generated power is used to drive the mounted electrical motor that puts the bicycle in motion.

The bicycle could be used in two ways: either by biking, i.e., using human energy or by using the electrical motor.

The hydrogen bicycle is made of:

- A commercial bicycle that has been acquired. The rear wheel has been modified to be driven by the electrical motor that we have installed. This driving motor has been mounted on the bicycle rear wheel hub.

*Corresponding author email: m-rafik15@hotmail.fr

- The hydrogen fuel cell that is used to produce the necessary electrical power for the drive of the bicycle wheel is of a PEM type.
- A controller is used for the management of the operation of the hydrogen system and the motor control. For a given chosen speed, the hydrogen flow rate is adjusted in such a way as the fuel cell delivers the adequate power for the bicycle to move at the set speed.
- The hydrogen storage tank used to feed the fuel cell is 350nl metal hydride tank.

The characteristics of the different components of the hydrogen bicycle are reported in TABLE II.

The hydrogen electric bicycle system is mounted as shown in Fig. 2.

TABLE II
CHARACTERISTICS OF THE DIFFERENT COMPONENTS OF THE HYDROGEN BICYCLE

Components	Parameters	Type/Value
FUEL CELL	Type of fuel cell	PEM
	Number of cells	60
	Rated power	300W
	Rated performance	36V/8.3A
	Reactants	Hydrogen and Air
	Hydrogen pressure	0.45-0.55Bar
	Stack size	118x262x94mm
	Flow rate at max output	3.9L/min
Electric Motor	Type of motor	Brushless DC
	Rated Power	250W
	Rated performance	36V/7A
	Weight	3.5Kg
Commercial Bicycle	Wheel Diameter	26"
	Weight	25Kg
Storage Tank	Type of Tank	Metal Hydride
	Capacity	350nl

Fig. 2. Hydrogen Electric Bicycle

IV. CONCLUSION

The design and realization of a hydrogen bicycle has been carried out. First the sizing has been made, then the realization of the system has been finalized using a commercial bicycle, a PEM fuel cell, a hydrogen metal hydride storage tank and a motor. Tests are underway. Preliminary results indicate that the performance of the bicycle is close to the value determined by the sizing study. The hydrogen bicycle can reach a speed of 25 km/h.

REFERENCES

[1] Larminie, J., & Lowry, J. Electric Vehicle Technology Explained. Electric Vehicle Technology Explained. John Wiley & Sons Ltd, 2003.
[2] Hoogers G., Fuel Cell Technology Handbook, CRC Press, USA, 2003.

*Corresponding author email: m-rafik15@hotmail.fr

Geothermal Electricity Estimation for Hydrogen Production

M. M. Hadjiat *, S. Ouali

*Centre de Développement des Energies Renouvelables (CDER), B.P. 62 Route de l'Observatoire, 16340, Algiers, Algeria.

Abstract—**Geothermal energy is considered of particular interest for hydrogen production given the calorific and electrical energy that could be ensured from geothermal resource. Indeed, this energy source would lead to reduce relatively the energy needed for hydrogen production process. Hot springs, as a part geothermal potential can be used for power generation. For low geothermal temperature resources, (temperature below 100°C), the Organic Rankine Cycle (ORC) power plant can generate electricity with a low heat source temperature. In fact, the ORC system can provide excellent performance compared with other technologies; in addition, it is flexible, secure and has low maintenance costs.**

In this article is studied the medium temperature geothermal energy use to assist the process of electrolysis for hydrogen production. For this purpose, a system composed of an electrolyzer, combined heat exchanger and condenser in a binary Rankine cycle plant is considered. Thermoptim software package is used to define the optimum parameters of the system when medium geothermal water data (temperature flow rate).

Key words—Geothermal energy, electricity, hydrogen production, electrolysis, hot spring.

I. INTRODUCTION

Dependence on fossil fuel and global warming impact, encourage energy system transition to energy systems based on renewable resources. Hydrogen, as an alternative energy source, is subject of a lot of research work and some consider it as the energy of the future [1]. In addition, hydrogen energy can play a significant role in reducing environmental emissions if it is produced from renewable energy resources references [2]. The hydrogen production process requires cheap and readily available hydrogen sources to convert into pure hydrogen and these criteria are found in water. In electrolysis, water molecule is separated electrochemically into hydrogen and oxygen molecules with the aid of electrical energy. Because of the high energy consumption of water electrolysis (4-5 KWh /m3 of hydrogen) [3], hydrogen production from renewable energies (solar, biomass, geothermal, wind, etc) is attracting increasing attention from researchers for their economic and environmental aspects.

In our case, we consider an average geothermal water temperature of 90°C and rate of 100 kg/s. Under realistic operating conditions, around 4 kW power can be produced in the binary geothermal power plant. The produced power used for the electrolysis process. The electrolysis water can be preheated to 80 °C by the geothermal water.

II. METHODOLOGY

In the considered system, both geothermal electric power and heat are exploited in the electrolysis process, work is produced from a geothermal resource by means of the Organic Rankine cycle; the resulting work is used as a work input and electrolysis water is preheated by the geothermal water at 80°C.

Electricity generation using geothermal hot spring at low temperature is possible with an ORC system as shown in Fig.1. In this design, geothermal hot spring is used as the heat source and the working fluid undergoes an actual closed thermodynamic cycle, called organic Rankine cycle. The working binary fluid has a low boiling temperature.

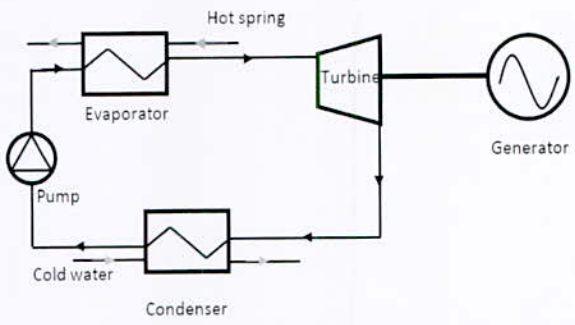

Fig. 1. Schematic diagram of ORC system for electricity generation using hot spring as heat source

Thermoptim is used in the analysis. Thermoptim is a software package, which provide a modeling environment integrating a schematic screen editor in a deeply interconnected way. Its features make Thermoptim a particularly well-suited tool for studying the thermodynamic cycles used in energy technologies, thus enabling it to provide users computing environment enabling them to visually build models of many energy systems, from the simplest to the complex.

III. RESULTS AND DISCUSSION

The organic Rankine cycle operation that is shown on a temperature-entropy diagram in Fig. 2 is used to simplify the simulation.

*Corresponding author email: m.hadjiat@cder.dz

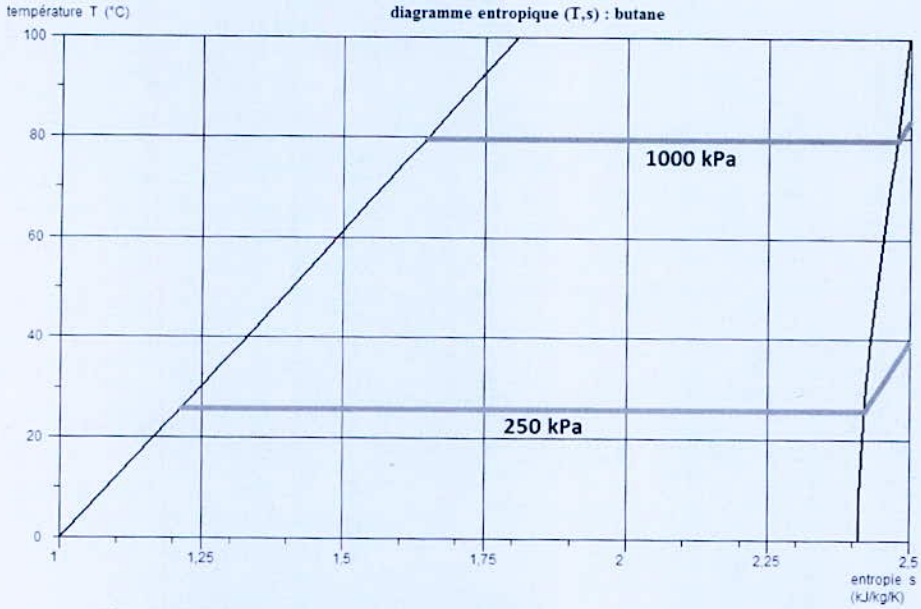

Fig. 2. Temperature entropy (T-s) diagram of organic Rankine cycle

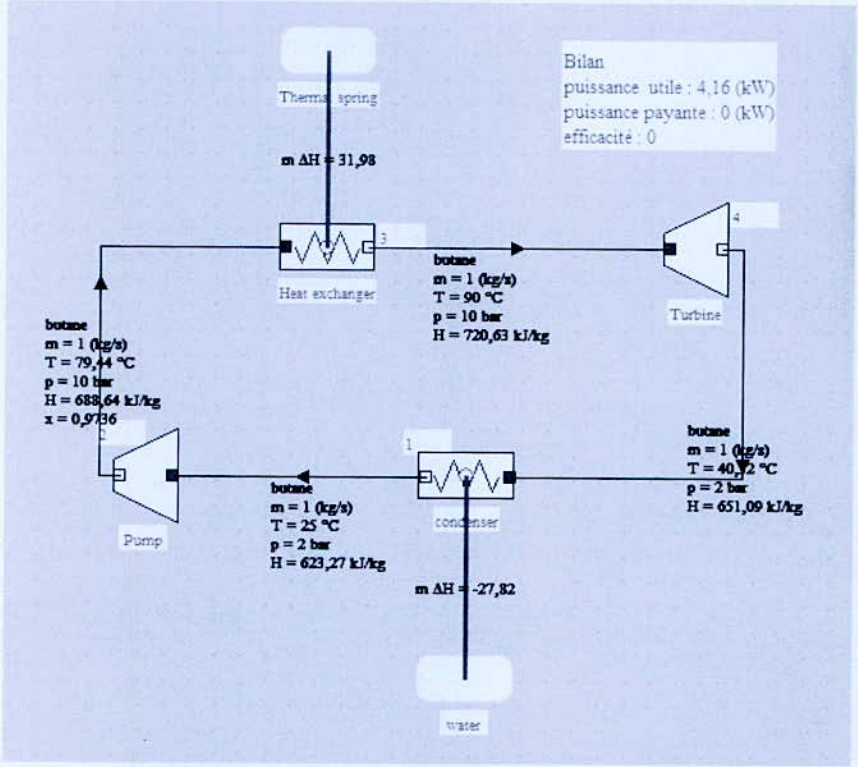

Fig. 3. Model used for synoptic of binary geothermal power plant

Fig. 3 show a synoptic diagram of geothermal power plant, we assume that the heat source for the plant is the flow of geothermal water hot spring entering the plant at 90°C with a total mass flow rate of 50 kg/s.

We take the pressure of hot spring water at 700 kPa. The plant utilizes fresh water to condense the working fluid. Turbine power WT was calculated to estimate the electricity that can be produced at the system WT = 4.16 kW. Considering that 4 kWh can produce 1 m3 of hydrogen, the electrical energy produced by our system could therefore produce an amount of 1 m3 of hydrogen per hour which would be equivalent to 100 g of H2 per hour.

*Corresponding author email: m.hadjiat@cder.dz

IV. CONCLUSION

The medium-temperature geothermal resources can contribute to the hydrogen production process by electrolysis, indeed, the major problems of conventional electrolyzes is their high electricity consumption. The water heated electrolysis by geothermal heat has higher energy efficiency because the energy is supplied in mixed form of electricity and heat and that heat is cheaper than electricity. In addition, the heated- water-temperature accelerates the electrolysis reactions, thus increasing the system efficiency.

REFERENCES

[1] Yilmaz C and Kanoglu M. Thermodynamic evaluation of geothermal energy powered hydrogen production by PEM water electrolysis. Energy 2014; 69:592–602.

[2] Balta MT, Dincer I, Hepbasli A. Geothermal-based hydrogen production using thermochemical and hybrid cycles: A review and analysis, International Journal of Energy Research, 2009, DOI: 10.1002/er.1589.

[3] Zoulias, E., E. Varkaraki, N. Lymberopoulos, C.N. Christodoulou, and G.N. Karagiorgis. 2014. A review on water electrolysis. Center for Renewable Energy Sources (CRES), Pikermi, Greece Frederick Research Center, Kape Publications, section "Hydrogen", pages 1-18.

[4] Kanoglu M, Bolatturk A, Yilmaz C. Thermodynamic analysis of models used in hydrogen production by geothermal energy. Int J Hydrogen Energy 2010; 35:8783-8791.

[5] Yilmaz C, Kanoglu M, Bolatturk A, Gadalla M. Economics of hydrogen production and liquefaction by geothermal energy. Int J Hydrogen Energy 2012; 37: 2058- 2069.

[6] Yilmaz C and Kanoglu M. Thermodynamic evaluation of geothermal energy powered hydrogen production by PEM water electrolysis. Energy 2014; http://dx.doi.org/10.1016/j.energy.2014.03.054.

[7] Pikraa G, Rohmah N, Rakhmad I. Purwanto A. J. The electricity power potency estimation from hot spring in Indonesia with temperature 70-80°C using organic Rankine cycle; Energy Procedia 2015; 68: 12 – 21.

*Corresponding author email: m.hadjiat@cder.dz

New control Strategy with Saturation Management of Standalone Hybrid Photovoltaic/Fuel cells with Battery

H. Assem[1, 2, 3*], T. Azib[2], F. Bouchafaa[3], L. Hamdi[1] and A. Hadj Arab[1]

[1*]Centre de Développement des Energies Renouvelables. CDER PB n°.62, 16340, Bouzaréah, Algiers, Algeria
[2]ESATAC'LAB, S2ET Department 12 rue Paul Delouvrier 78180 Montigny-le-Bretonneux, France.
[3]Laboratory of Renewable Energy and Energy Efficiency, USTHB PB n°. 32, 16111, El Alia Algiers, Algeria.

Abstract—**This paper presents a hybrid system comprise of Photovoltaic (PV), Battery, Fuel Cell (FC) to meet isolated DC load demand. The PV is the primary energy source, whereas battery and SC both are considered for their different power density to supply transient and steady load respectively. To increase the reliability of the system the third source FC has been chosen to keep the battery fully charged. All sources are connected to DC bus by different DC-DC converters. A power flow control strategy adapts their variable DC voltage to Bus voltage by means of these converters. In this work, FC is chosen to work for a limited period. This will avoid the over sizing of the FC and limit the operational cost of the system. The whole energy management principle has been validated in MATLAB/SIMUINK with variable load demand and solar radiation profile.**

Simulation results are presented to check the theoretical analysis, ensure that the system well operates under difference operating conditions and demonstrate the performance of the proposed control strategy.

Key words— Stand-alone photovoltaic generator, maximum power point tracking, energy management strategy, fuzzy control.

I. INTRODUCTION

Due to the fast depletion of fossil fuel and increasing pollution, rate renewable energy sources have become most effective source of energy. However, the major challenge in integration of these renewable sources is its intermittent nature and cost. PV is one of the most effective renewable energy sources. Nevertheless, it is not available at nighttime. However, FC can be available for the whole day, but it increases the system cost. This ensures the requirement of two or more renewable energy sources [1]. Therefore, to make this kind of hybrid system more reliable and cost effective, there must be some energy storage devices to store the available energy as much as possible. Battery is used for storage purposes. The important advantage of battery over SC is its high energy density. They can store at least 3-30 times more charge than SC [2]. Whereas, SCs are able to deliver hundred to thousand time more power than a similar sized Battery [3].

Many researchers have focused their study on control of hybrid system [4]. Glavin *et al.* [5] have studied control of PV-SC-Battery based hybrid energy system. Garcia *et al.* [6] have studied FC-battery-SC based hybrid system to supply hybrid vehicles type load. Thounthong *et al.* [7] and Xue *et al.* [8] have implemented flatness based control strategy and Classical PI controller based control to study PV-FC-SC energy system respectively. Samson *et al.* [9] have taken PVFC –Battery-SC based hybrid system for their study.

II. GLOBAL HYBRYD SYSTEM DESCRIBING

1. System structure

The proposed hybrid Energy system considering PV-FC-Battery is shown in Fig. 1.

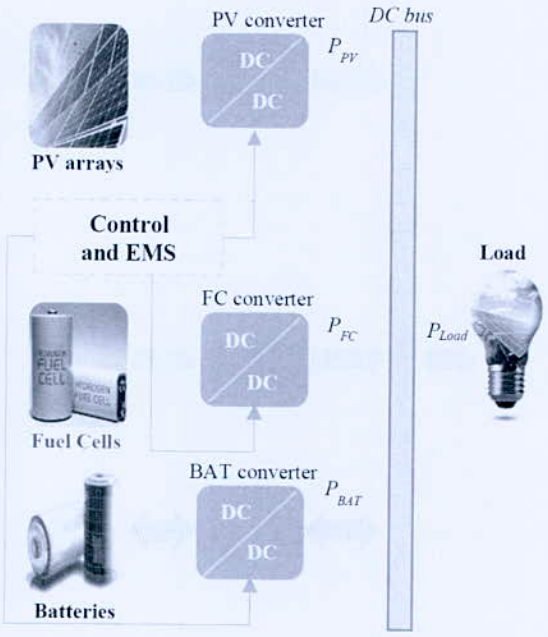

Fig. 1. Parallel structure of a hybrid PV-Bat-FC system

The whole system is used to supply a variable DC load. In this paper, PV and FC are used as the primary and auxiliary sources respectively while Battery is the energy storing elements.

PV arrays are interfaced with the load by means of boost converter including maximum power point tracking to always extract maximum available solar power. Battery is the main energy storing device. It also supplies long term energy when PV is not available. SC is controlled by a cascaded voltage and current control loop to supply the sudden load change and DC bus voltage stabilization. Both Battery is using bidirectional DC/DC converter for their controlling. The main advantage of hybrid system lies in control of FC, which is connected to the DC bus by means of Boost converter. Here FC only uses to charge the battery up to its maximum SOC limit when Battery reaches its minimum State of charge level. So, the power balance in the DC bus must be fulfilled at every time:

$$P_{Load}(t) = \eta_{PV} P_{PV}(t) + \eta_{BAT} P_{BAT}(t) + \eta_{FC} P_{FC}(t) \quad (1)$$

*Corresponding author email: h.assem@cder.dz

Where η_{PV}, η_{BAT} and η_{FC} are the efficiency of the power converters connecting to the different sources. We assume that the converters efficiencies are known and fixed in our case 85%.

2. *Power system modeling*

- PV Generator:

Solar PV systems generate electric power by converting solar photon energy into electrical energy in the form of direct current using solar cell or PV cell. Fig. 2, shows widely used one diode equivalent circuit model for a PV cell [10]. PV cell equivalent circuit model consists of a current source parallel with a diode.

The output terminals of the circuit are connected to the load through the shunt and series resistor.

$$I_{PV} = I_{ph} - I_s\left[exp\left(\frac{q(V_{PV}+R_sI_{PV})}{nkT}\right) - 1\right] - \frac{V_{PV}+R_sI_{PV}}{R_{sh}} \quad (2)$$

I_{PV} is delivered current by PV source, V_{PV} is the voltage across the PV source, k is the Boltzman's constant, T is the temperature on the photovoltaic surface.

- BAT:

Many options are available for the selection of a suitable battery model for a range of applications. These options include the simple voltage source model, the Thevenin model, generic models, and dynamic and more realistic models that consider the nonlinear characteristics of battery parameters [11-14]. However, to avoid excessive complexity with the consideration of the dynamic behavior of the battery cell, this study considered a generic model described in [12]. The model for the lead-acid battery is constructed based on two important parameters, namely, the terminal voltage, V_{BAT}, and state of charge, SOC, which represent the behavior of the battery. They can be calculated as functions of battery current, I_{BAT}, as follows:

$$\begin{cases} V_{bat} = E_{BAT} - R_{int}I_{BAT} \\ SOC = 100\left(1 - \frac{\int I_{BAT}dt}{Q_{BAT}}\right) \end{cases} \quad (3)$$

$$E_{BAT} = E_0 - k\frac{1-SOC}{SOC}Q_{BAT} + Aexp\{-B(1-SOC)Q_{BAT}\} \quad (4)$$

In (3) et (4), R_{int} and Q_{BAT} are the battery internal resistance and capacity, respectively. E_0 represents the battery open circuit voltage that lies between the fully charged voltage and the exponential voltage of the battery discharge curve, K is the polarization voltage, A is the exponential voltage, and B is the exponential capacity. From (4), the model accounts for both the normal voltage part and the exponential part represented by the second and third terms, respectively. Following the parameter extraction procedure provided in [12], all model parameters can be extracted from the manufacturer discharge curves, which are available in the battery datasheet.

3. *Load requirements study*

To evaluate the performance of the proposed approach, standard usage cycles can be considered. As an example, a daily consumption of residential electrical loads (suburban home) can be considered in this paper (Fig. 2), which represents the typical power consumption using primarily of lighting, appliances and plug loads.

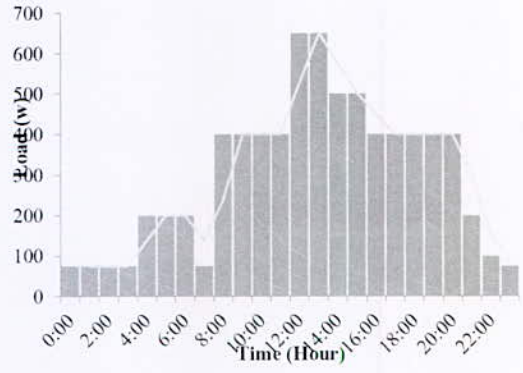

Fig. 2. Daly load profile

III. CONTROLLER DESIGN OF ENERGY MANAGEMENT STRATEGY

To make the system more reliable and efficient for various load condition, operational objectives have been decided. The energy exchange between DC bus and various sources can be established by considering following control parameters:

- Maximum power point tracking of PV power due to the intermittent nature of solar irradiance. This is the main control parameter.
- Load sharing among all the energy sources in energy management strategy.
- Charging-discharging cycle of battery. Battery is allowed to discharge up to a certain limit and then it gets charged by FC.
- DC link voltage stabilization with safe operation of battery by limiting its charging and discharging current limit.

Energy management supervision: it consists on sharing the load power between power sources based on the operating modes according to the local control: MPPT for PV generator and SOC monitoring for BAT. It allows the current reference synthesis for each source (i_{PVref}, i_{BATref}, i_{FCref}). To achieve this, MPPT controller, BAT, FC monitoring and EMS approach are explained more in detail in the following paragraph.

1. *MPPT using FLC approach*

The fuzzy controller proposed MPPT has two inputs and one output. The two input variables of the controller are the error E and the error variation CE sampled at each sampling step k. These two variables are defined as fellow:

$$\begin{cases} E(k) = \frac{P_{PV}(k)-P_{PV}(k-1)}{V_{PV}(k)-V_{PV}(k-1)} \\ CE(k) = E(k) - E(k-1) \end{cases} \quad (5)$$

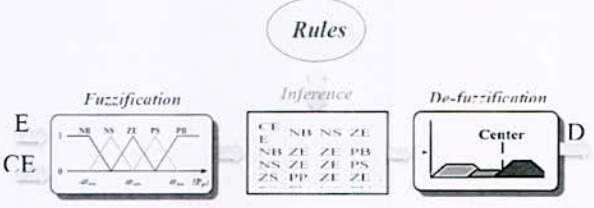

Fig. 3. Structure of MPPT fuzzy controller

*Corresponding author email: h.assem@cder.dz

2. FC, BATcontroller

FC gives direct current at low voltage. Therefore, DC/DC boost converter is connected to *FC*. Due to higher running cost of *FC*, a new control strategy has been proposed with FC to save fuel. Simultaneous operation of all energy sources will cause high system running cost. So a new control strategy has been employed by controlling the *FC running period.*

That a relay decides the ON and OFF state of *FC* and if Battery *SOC* is lower than minimum allowable *SOC* limit of Battery (*SOCmin*), FC current (i_{FC}) will be regulated to its reference value (i_{FCref}) and if it is more than maximum *SOC* limit of Battery (*SOCmax*), *FC* current will be zero. These control parameters can be chosen depending on system requirement and load demand. A current based MPPT technique is applied here to maintain the *FC* current to its maximum value (i_{FCmax}).

3. Energie management supervision

Any power load modification induces a change in the DC bus voltage. Hence its measurement is essential for the supervisor in order to estimate power sources required.

$$\begin{cases} C_{Bus}\dfrac{dv_{BUS}}{dt} = i_{Cbus} = i_{Sources} - i_{Load} \\ i_{Sources} = i_{PV}^{*} + i_{BAT}^{*} = G_1 \cdot i_{PV} + G_2 \cdot i_{BAT} \end{cases} \quad (6)$$

$$G_1 = \frac{v_{BUS}}{v_{PV}} \text{ and } G_2 = \frac{v_{BUS}}{v_{BAT}} \quad (7)$$

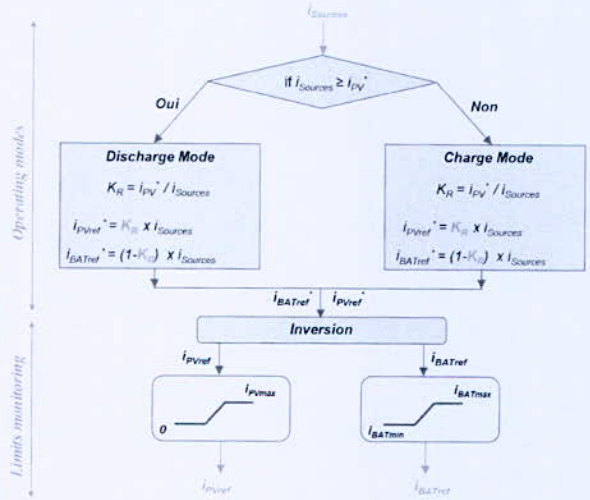

Fig. 4. Energy management strategy

$$\begin{cases} i_{PV}^{*} = k_R \cdot i_{Sources} \\ i_{BAT}^{*} = (1 - k_R) \cdot i_{Sources} \end{cases} \quad (8)$$

Once the required power sources are identified, the proposed EMS remains to be integrated. To implement this strategy, a weighting coefficient k_R can be exploited to manage the power splitting between sources according to the operating modes as depicted in Fig. 4.

IV. SIMULATION RESULTS

To validate the above mentioned control strategy a hybrid system has been taken for study with variable load and variable solar irradiance. The system sizes have been taken such that it should always be able to satisfy the desired load demand. In Table.I, The ratings of the system components including converter specifications are listed.

Table. 1. Electric characteristics of system

PV : Parameter Name	Value
Open circuit voltage	44 V
Rated voltage (Standard conditions)	32 V
Rated current (Standard conditions)	15 A
FC: Parameter Name	Value
Open circuit voltage	24 V
Rated Current	45 A
Rated Current	Value
Internal resistance R_{int}	42 V
Rated Current	15 A
Internal resistance R_{int}	0.2 Ω
Inductors & Capacities: Parameter Name	Value
Inductors LPV /L_{BAT}	100 µH
Rated Currents L_{PV} /L_{BAT}	25 A
Capacities C_{BUS}	4 mF
Optimal DC-Bus Voltage V_{BUSref}	50 V

Three sources are interfaced with standalone DC load by means of three different converters. PV and FC are the main source and auxiliary source respectively. Their sizes have been taken accordingly, so that it can supply the load, as well as keep the storage devices charged. Moreover, Batteries are sized such that they can meet the load demand when PV is unavailable.

Fig. 5 and Fig. 6, present the simulation results obtained using different operational conditions respectively constant and variable solar irradiance.

At first, the investigation will be focused on test with constant solar irradiance (Fig. 5). Thus, the main source PV produces a constant power according to its MPP under constant solar irradiance (Fig. 5-b). When the load power change Fig. 5-a, the BAT power adjusts according to load level. It would indeed have to assist PV in meeting the power demand, because in the proposed strategy, the BAT operates as a buffer to make up the power difference between PV and load required power (Fig. 5-a) depending to the operating mode.

The DC link voltage V_{BUS} is slightly affected by the power load variations (Fig. 5-c). A very low overshoot (less than 1%). These results prove the effectiveness of the regulation voltage and the proposed EMS.

For the second test, meteorological condition is introduced through the variation of solar irradiance (Fig. 6).

V. CONCLUSION

This work presents an optimal energy management control strategy of PV-FC-Battery hybrid system using FC as auxiliary power source which will operate only for a small period. In addition, the inclusion of artificial intelligence as part of the energy management system permits the optimal operation of hybrid energy systems. Fuzzy logic controller was applied to a DC-DC converter device for the maximum power point tracking (MPPT) of a photovoltaic system under variable conditions with a good dynamic performance and without oscillation around

*Corresponding author email: h.assem@cder.dz

maximum power point MPP. The simulation results show the reliability of power supply and reduced fuel usage. This control strategy can be extended to any type of DC load pattern for large-scale and applications.

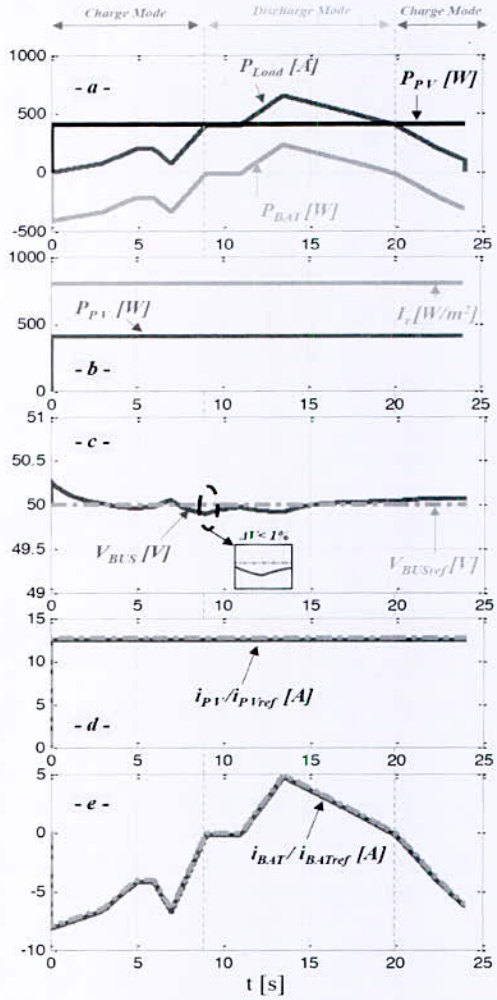

Fig. 5. Simulation results – Constant solar irradiance

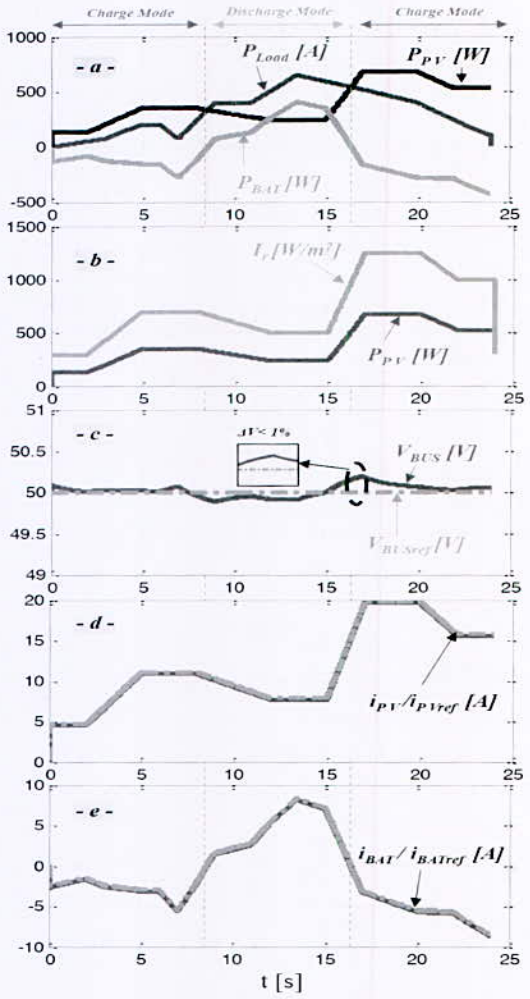

Fig. 6. Simulation results – Variable solar irradiance

REFERENCES

[1] J. Torreglosa, P. Garcia, L. Fernandez, and F. Jurado, "Predictive control forthe energy management of a FC–battery–SC tramway," IEEE Trans. Ind. Inform., vol. 10, no. 1, pp. 276–285, Feb. 2014.

[2] P. Thounthong, S. Rael, and B. Davat, "Energy management of

[3] FC/Battery/SC hybrid power source for vehicle application," J. Power Sources, vol. 190, no. 1, pp. 173–183, May 2009.

[4] A. S. Weddell, G. V. Merrett, T. J. Kazmierski, and B. M. Al-Hashimi, "Accurate supercapacitor modeling for energy harvesting wireless sensor nodes," IEEE Trans. Circuits Syst. II, Exp. Brief, vol. 58, no.12, pp. 911–915, Dec. 2011.

[5] P. Garcia, J. P. Torreglosa, L. M. Fernández, and F. Jurado, "Control strategies for high-power electric vehicles powered by hydrogen FC, battery and SC," Expert Syst. Appl., vol. 40, no. 12, pp. 4791-4804, Sep. 2013.

[6] P. Thounthong, A. Luksanasakul, P. Koseeyaporn, B. Davat, "Intelligent Model-Based Control of a Standalone Photovoltaic/Fuel Cell Power Plant With Supercapacitor Energy Storage," Sustainable Energy, IEEE Transactions, vol. 4, no. 1, pp. 240-249, Jan. 2013.

[7] X.Guiting, Z. Yan and Z. Dakang, " Synthetically Control of a Hybrid PV/FC/SC Power System for Standalone Applications," J. Applied Sciences., vol.5, no. 5, pp.1796-1803, 2013.

[8] M. E. Glavin, P. K. W. Chan, S. Armstrong, and W. G. Hurley, ''A

[9] standalone photovoltaic supercapacitor battery hybrid energy storage system,''in Proc. 13th Power Electron. Motion Control Conf., pp. 1688--1695, Sep. 1--3, 2008.

[10] P. Garcia, J. P. Torreglosa, L. M. Fernández, and F. Jurado, "Control strategies for high-power electric vehicles powered by hydrogen FC, battery and SC," Expert Syst. Appl., vol. 40, no. 12, pp. 4791-4804, Sep. 2013.

[11] B. Prabodh, D. Vaishalee, "Hybrid renewable energy systems for power generation in stand-alone applications: A review," Renewable Sustainable Energy Reviews, vo. 16, no. 5, pp. 2926-2939, 2012. J.M. Kwon, B. H. Kwon, and K. H. Nam, "Grid-connected photovoltaic multistring PCS with PV current variation reduction control," IEEE Transactions on Industrial Electronics, vol. 56, no. 11, pp. 4381–4388, 2009.

[12] H. A. Sher, A. F. Murtaza, A. Noman, K. E. Addoweesh, K. Al-Haddad and M. Chiaberge, "A New Sensorless Hybrid MPPT Algorithm Based on Fractional Short-Circuit Current Measurement and P&O MPPT," in IEEE Transactions on Sustainable Energy, vol. 6, no. 4, pp. 1426-1434, Oct. 2015.

[13] V. Salas, E. Olias, A. Barrado, A. Lazaro, "Review of the Maximum Power Point Tracking Algorithms for Stand-Alone Photovoltaic Systems", Solar Energy Materials & Solar Cells vol:90, n°:11, pp:1555 –1578, 2006.

[14] Lalouni S, Rekioua D, Rekioua T, Matagne E, "Fuzzy logic control of Standalone photovoltaic system with Battery Storage", Journal of Power Sources, vol.193, no.2, pp. 899–907, 2009.

[15] S. Sallem, M.Chaabene, M.B.A.Kamoun, "Energy management algorithm for anoptimum control of a photovoltaic water pumping system". Applied Energy, vol.86, pp.2671-2680, 2009.

*Corresponding author email: h.assem@cder.dz

Two-Dimensional Numerical Modeling of First Stage Hydrogen Magnetic Liquefier Using ANSYS Fluent Code

K. Hamdani and A. Smaili

Laboratoire du Génie Mécanique et Développement, Ecole Nationale Polytechnique, B.P. 182 EL-Harrach, Algiers, 16200, Algeria.

Abstract—**The present paper deals with a numerical study of first stage magnetic liquefier based on the Active Magnetic Regenerator (AMR) cycle principal. For this purpose, two-dimensional numerical modeling has been developed to simulate the operating mode of such hydrogen magnetic liquefier in order to predict and investigate its thermal performances. During transient regime, mass, momentum and energy equations are considered to account for heat transfer that takes place within the Magnetic regenerator bed until reaching a steady-state condition. The numerical model is implanted in ANSYS Fluent software using scheme programs and user defined functions (UDfs) to overcome the complexity of AMR cycle.**

Key words—Hydrogen, magnetic refrigeration, thermal analysis, numerical simulation.

I. INTRODUCTION

Hydrogen is considered as clean and renewable energy. Before hydrogen energy arrives at utilization, three steps are necessary: generation, liquefaction, and storage. Efficient and environmental friendly liquefaction procedures are needed since cryogenic temperature must be achieved to get liquid hydrogen where existing liquefaction systems fails. Magnetic refrigeration is one of the promising techniques and potential candidate to replace conventional liquefaction systems (vapor compression). Using numerical modeling and simulation a feasibility of hydrogen first stage liquefier is demonstrated. Most of the physical problems of AMR cycle are taken into account such as temperature dependent properties (fluid and solid refrigeration physical properties,) viscous dissipation of fluid flow, time, and mass averaging outlet temperature.

II. AMR HYDROGEN FIRST STAGE LIQUEFIER DESCRIPTION

At nearly one atmospheric pressure, hydrogen becomes liquid around 20 K therefore a series of cascades are required to decrease its temperature from 300 K to 20 K. Magnetic refrigeration (MR) based on the magnetocaloric effect (MCE) which was discovered by Warburg in 1881 [1] was firstly used to attain extremely low temperature [2]. The works of Brown [3] open the way for MR near room temperature. In 1983, AMR concept was introduced by Barclay [4]. A practical magnetic hydrogen liquefiers is shown by Fig. 1.

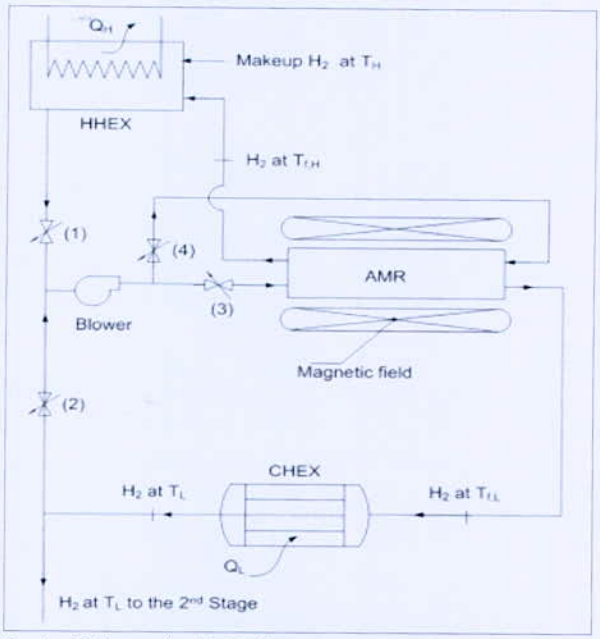

Fig. 1. Schematic AMR first stage hydrogen liquefier [5]

The main components of the liquefier are (i) solid refrigerant that acts both as refrigerant and regenerator (ii) heat transfer fluid (coolant) which is represented by the hydrogen to be liquefied (iii) a blower device to force fluid flow. From thermodynamic point of view, the AMR cycle of the first stage liquefier described above operates according to Bryton cycle [6] which consists of four steps namely magnetization, demagnetization, hot blow, and cold blow as shown in Fig. 2. The solid refrigerant (in this study is Gadolinium) or the magnetic material (MM) is adiabatically magnetized by the application of magnetic induction (B) with no flow resulting in an increase of MM temperature due to the MCE. After the magnetization, a fluid flow (hydrogen in this case) is forced to flow throw the regenerator when the magnetic induction remains applicable from the hot source to the cold source to absorb an amount of heat Q_H which represents the rejected heat to the surrounding . Thus, the MM temperature decreases, this step is called cold blow. During demagnetization, the magnetic induction is removed adiabatically with no fluid flow and thus MM temperature decreases. The final step of AMR Bryton cycle is the cold blow where the fluid is forced to flow from the cold source to the hot source to cool down the working fluid. Thus, the fluid can absorb an amount of

*Corresponding author email: arezki.smaili@g.enp.edu.dz

heat from the hot source, cooling load and denoted by Q_L. To reach steady state conditions AMR cycle must be repeated several times. For multi stage hydrogen liquefier the cold source for a given stage becomes the hot source of the flowing stage and so on.

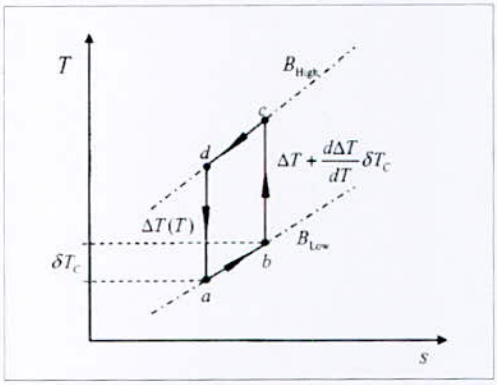

Fig. 2. AMR ideal Bryton cycle [7]

III. NUMERICAL MODELING

1. Approach

The proposed approach consists in modeling the AMR cycle (i.e. four processes) in scheme language files [] to be linked dynamically within ANSYS Fluent solver when it is running. User defined functions (UDFs) [9] are used to initialize the problem, evaluate the outlet fluid temperature, calculate cooling load, compute the coefficient of performance (COP), and define MCE as source term. The automation of the program and repeating cycles is assured by RP-variables defined within scheme files [10]. In general, parallel plane plates (PPP) AMR configuration (Fig. 3) has more advantages comparing to the others configuration therefore the present study is based on it. Symmetry and repetitiveness simplify the configuration.

2. Mathematical model

In AMR system the fluid flow is governed by Navier-Stokes equations given by respectively (1), (2), and (3) for compressible and laminar flow conditions. The heat transfer between fluid and solid mediums are governed by energy equations for fluid and solid given by (4) and (5) for fluid and solid mediums respectively. Perfect gas model is adopted as shown by (6). MCE is implanted as source term using (7) and it takes positive or negative sign depending whether the AMR step is magnetization or demagnetization. Note that hydrogen specific heat is implicitly function of temperature. In the equations cited in this paper t, $\boldsymbol{u}$, u, v, T_f, T_s, ρ_f, ρ_s, μ, p, k_f, k_s, $\dot{S}$, $c_{p,f}$, $c_{p,s}$, Φ, $(\boldsymbol{u}\cdot\nabla)$, τ_1, i, R refer respectively to time, fluid velocity, x-fluid velocity, y-fluid velocity fluid temperature, solid temperature, fluid density, solid density, fluid viscosity, pressure, fluid thermal conductivity, solid thermal conductivity, the solid source term, the fluid specific heat, the solid specific heat,

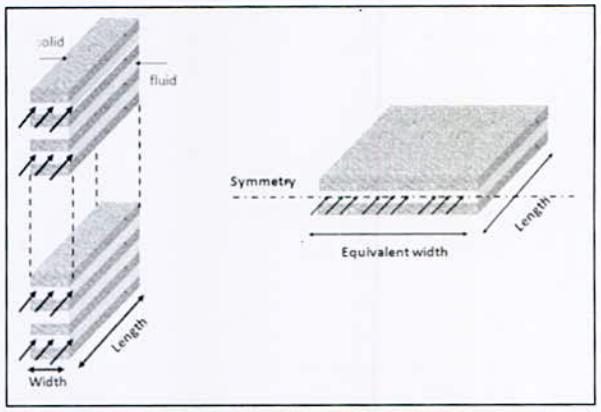

Fig. 3. Parallel plane plates AMR configuration

dissipation function (viscous heat), velocity advection operator, magnetization time, internal energy, and universal gas constant.

$$\frac{\partial \rho_f}{\partial t} + div(\rho_f \boldsymbol{u}) = 0 \quad (1)$$

$$\frac{\partial(\rho_f u)}{\partial t} + div(\rho_f u \boldsymbol{u}) = -\frac{\partial p}{\partial x} + div(\mu\, grad\, u) + S_{Mx} \quad (2)$$

$$\frac{\partial(\rho_f v)}{\partial t} + div(\rho_f v \boldsymbol{u}) = -\frac{\partial p}{\partial x} + div(\mu\, grad v) + S_{My} \quad (3)$$

$$\frac{\partial(\rho_f i)}{\partial t} + div(\rho_f i \boldsymbol{u}) = -p\, div\, \boldsymbol{u} + div(k_f\, grad\, T_f) + \Phi \quad (4)$$

$$\frac{\partial(\rho_s \cdot c_{p,s} T_s)}{\partial t} = div \cdot (k_s\, grad\, T_s) + \dot{S} \quad (5)$$

$$p = \rho_f R T_f \quad (6)$$

$$\dot{S} = \frac{\rho_s . c_{p,s}(B, T_s) . MCE(B, T_s)}{\tau_1} \quad (7)$$

3. Boundary Conditions

As mentioned in the description of AMR cycle, it requires an intermittence of fluid flow. To perform that a scheme program has been considered to attribute the appropriate boundary type for the fluid domain (inlet and outlet). During cold blow process, the cold side will have inlet-velocity type and hot side will have pressure-outlet type and for hot blow this configuration is reversed. This manipulation is done by a scheme file linked dynamically to ANSYS Fluent solver. To accomplish and produce regeneration effect on the magnetic solid the temperature of the entering fluid for each fluid flow (cold/hot blow) steps is the mass-time weighted average temperature of the exiting fluid (bulk temperature of the total amount of leaving fluid) of previous fluid flow step. This is done by a UDFs with RP-variable linked to the solver via a scheme command to be called at the end of each time step during transient calculation. During magnetization and demagnetization steps both cold and hot fluid sides will

*Corresponding author email: arezki.smaili@g.enp.edu.dz

have a wall type (adiabatic) and velocity of fluid domain is fixed to zero (stationary fluid.) With this configuration the stagnated fluid still exchange the heat with the solid while all the system is insulated. The magnetization source term is enabled during magnetization/demagnetization and disabled for cold/hot blow processes using RP-variable and UDFs tools. The solid will have all walls adiabatic. A coupled wall type is attributed to fluid-solid interface shared between them which physically consist on equal heat flux for both sides and one identical temperature value as shown by (8) and (9). Finally the sequencing of the different AMR cycle steps and repeating them is performed by scheme file.

IV. RESULTS AND DISCUSSION

The validity of the numerical model and simulation has been investigated through two dimensions PPP regenerator with geometrical dimensions summarized in Table I. We should note here that the results of the numerical simulation is qualitatively compared to those reported by [5] since experimental tests are not yet available.

TABLE I
GEOMETRICAL DIMENSION OF THE REGENERATOR

Symbol and unit	Quantity	Value
n	plate number	32
$L(m)$	plate length	0.1
$w(m)$	plate width	0.01
$e(m)$	plate thickness	0.0000125

MCE and specific heat of MM material were calculated by molecular field theory (MFT) as shown in Fig. 4 and Fig. 5 using parameters cited in Table II. The computational domain and grid topology of AMR system are composed of a structured mesh with 30000 cells (20000 for fluid and 10000 for solid) refined at inlet/outlet and solid-fluid interface to capture high gradients. The selected mesh is finer which results from mesh sensitivity study where different mesh sizes (coarse, medium, finer, and ultrafine) have been investigated. The time step chosen for temporal discretization is 0.1s. The solver is density based type. SIMPLE algorithm with second order upwind spatial discretization and second order implicit transient formulation which is unconditionally stable has been chosen. In the computing, there are two cases to be considered (i) without load and (ii) with load. In this study the heat losses were neglected (adiabatic AMR system) and the same for losses due the Eddy current, hysteresis, and demagnetizing field.

1. *Without load case*

In order to predict the lower could outlet hydrogen temperatures, simulation without load has been performed under the following conditions: cold source temperature T_H = 298 K, applied magnetic induction B = 5 Tesla, hydrogen mass flow $\dot{m}$ = 32.8 mg/s for frequencies f = 0.1, 0.17, 0.2, and 0.3 Hz.

TABLE II
MAGNETIC AND THERMAL PROPERTIES OF GADOLINIUM

Symbol and unit	Quantity	Value
g	Landé factor	2
θ_c (K)	Curie temperature	293
J_l	total angular momentum	3.5
$\theta_d(K)$	Debye temperature	173
γ(J/kg·K^2)	Sommerfeld constant	6.93E-2
$Cp,s(J/kg·K)$	specific heat	$f(T,B)$
$\rho(kg/m^3)$	density	7900
$K(W/m·K)$	thermal conductivity	10.6

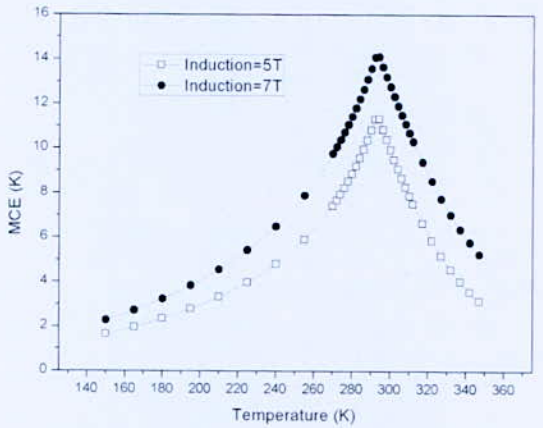

Fig. 4. MCE of Gadolinium as function of magnetic induction (B)

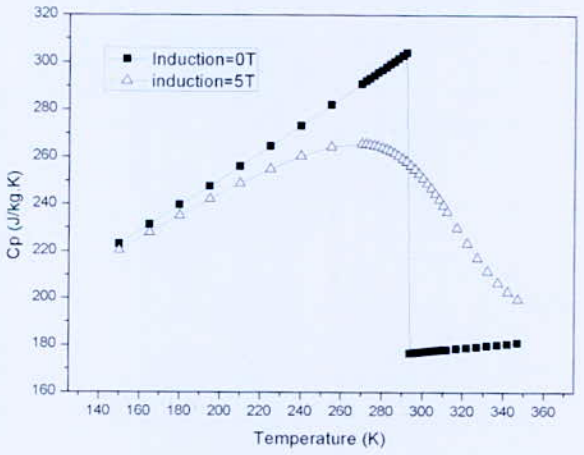

Fig. 5. Specific heat of Gadolinium as function of magnetic induction (B)

As expected, the lower could outlet temperature exhibits decreasing trends as number of AMR cycle increases for all frequencies until reaching a steady state conditions (Fig. 6). It is clear that the lower could temperature increases as frequency goes high and the reason for that is at height frequencies the magnetic work rate which the regenerator is subject to.

*Corresponding author email: arezki.smaili@g.enp.edu.dz

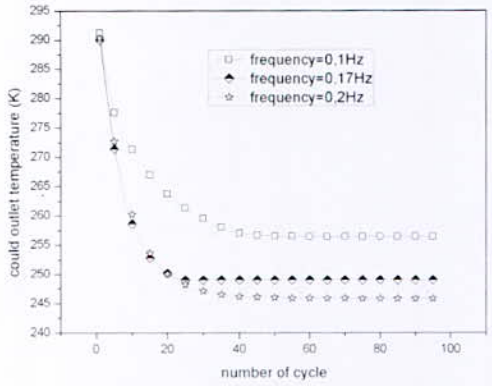

Fig. 6. Cold outlet temperature as function of number of cycle at magnetic induction B = 5 T for different frequencies

2. *With load case*

For an applied load of T_H = 298 K (cold source temperature) and T_C = 260 K (hot source temperature,) hydrogen first stage liquefier performances are investigated. AMR cycle parameter being varied are hydrogen mass flow and frequency since in practical application, these parameters are adjustable. The effect of magnetic induction is also examined. As we can see in Fig. 7, the cooling power increases with mass flow rate to attain a maximum then decreases. Therefore a maximum cooling power can be obtained by adjusting properly mass flow rate. This behavior is due to the amount of utilization of the regenerator defined as the ratio of thermal capacity of fluid by thermal capacity of solid. The effect of magnetic induction on increasing cooling load is clearly visible. When the frequency changed to higher value (Fig. 8), two major observations are noted: the amplification of the cooling power and the operating range of mass flow rate extends.

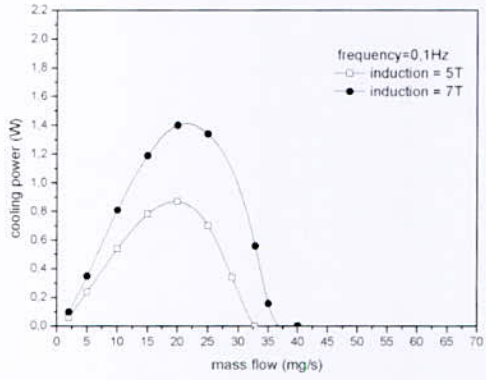

Fig. 7. Cooling load as function of mass flow rate at frequency f = 0.1 Hz for different magnetic inductions (B)

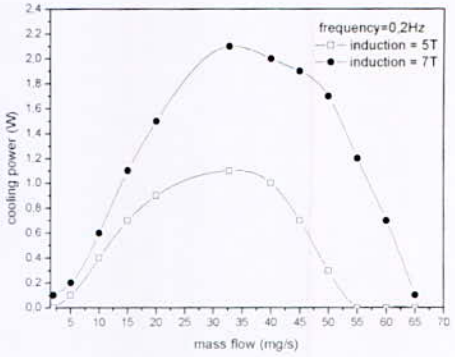

Fig. 8. Cooling load as function of mass flow rate at frequency f = 0.2 Hz for different magnetic inductions (B)

V. CONCLUSION

The present study proves the feasibility of first stage of hydrogen around ambient temperature. The use of multilayer regenerators that have different transition temperatures can achieve more low temperature.

REFERENCES

[1] Emil Warburg, "Magnetische Untersuchungen," Ann. Phys., vol. XIII, pp. 141-164, 1881.

[2] Giauque W. F. and MacDougal D. P., "Attainment of Temperatures Below 1° Absolute by Demagnetization of $Gd_2(SO_4)_3$-$8H_2O$," Physical Review, vol. 43, no. 9, pp. 768-768, 1933.

[3] Brown G.V., "Magnetic heat pumping near room temperature," Applied physics, vol. 47, no. 8, pp. 3673-3680, 1976.

[4] Barclay J.A., "The theory of an active magnetic regenerative refrigerator," in Cryogenic Sensors and Electronic Systems, New mexico, 1983, pp. 375-387.

[5] Smaili A. and al, "Performance predictions of a first stage magnetic hydrogen liquefier," Hydrogen Energy, vol. 36, no. 6, pp. 4169-4177, 2011.

[6] Kitanovski A. and al, Magnetocaloric Energy Conversion: From Theory to Applications, 1st ed.: Springer, 2015.

[7] Rowe A. M. and Barclay J. A., "Ideal magnetocaloric effect for active magnetic regenerators," Journal of Applied Physics, vol. 93, no. 3, 2003.

[8] R Kent Dybvig, The Scheme Programming Language: MIT Press, 1997.

[9] ANSYS, Inc., ANSYS FLUENT UDF Manual., 2011.

[10] Hamdani K. and Smaili A., "Multidimensional numerical method for performance predictions of an AMR cycle using ANSYS Fluent software," in Thermag VII, Torino, 2016, pp. 283-286.

*Corresponding author email: arezki.smaili@g.enp.edu.dz

Ni Catalysts Derived from Hydrotalcite for the Dry Reforming Reaction of Methane. Effect of the Addition of Cerium

B. Djebarri[1, 2], F.Touahra[2, 3], N. Aider[2], F. Bali[2], Z. Abdelsadek[2], V.M. Gonzalez-Delacruz[4], K.Bacharri[3], J.P. Holgado[4], A. Caballero[4], D. Halliche[2].

[1]Department of Chemistry, Faculty of sciences, University of M'hamed Bougara, Independence Avenue, 35000 Boumerdès, Algeria.
[2]Laboratoire de Chimie du Gaz Naturel, Faculté de Chimie, USTHB, BP32, El-Alia, Alger, Algérie.
[3]Centre de Recherches Scientifiques (CRAPC), BP 248, Alger, 16004, Algérie.
[4]Instituto de Ciencia de Materiales de Sevilla and Departamento de Quimica Inorganica, (CSIC-university of Seville), Avda. Americo Vespucio, 49, 41092 Seville, Spain.

Abstract—**A series of mixed oxides (NiMgAl, NiMgAlCe-1, NiMgAlCe-2 and NiMgCe) prepared by thermal decomposition of layered double hydrotalcites (HT) were characterized by XRD, ICP, TPR-H_2, SEM, and N_2 adsorption/desorption technique. The results revealed the formation of periclase-type catalysts with mesoporous structure. The addition of Ce^{+3} lowered the phase crystallization with the formation of oxide particles. The catalysts were tested in dry reforming of methane (CH_4:CO_2: He: 10/10/80). The gas hourly space velocity (GHSV) was 300,000 L/Kgh temperature of reaction 750°C with prior reduction. The increase in the Ce load had a promoter effect in catalytic conversions H_2/CO ratios between 0.8 and 1.0 were obtained. After the catalytic processes, the main formation of nanotubes of coke on the surface of the catalyst was established.**

Key words—Hydrotalcites, Greenhouse effect, CH_4, CO_2, Catalysis.

I. INTRODUCTION

For some years now, CO_2 reforming of methane has been employed for the obtaining of syngas with a H_2/CO ratio suitable for the Fischer Tropsch process [1]. However, the formation of coke has created difficulties for its application on an industrial level due to the deactivation of the catalysts [2].The formation of coke is directly related to the chemical properties of the solid and the particle size of the active phase [1]. Thus, it has been proposed that catalysts with basic characteristics and particle sizes less than 10 nm show lower levels of coke formation [3]. Different types of catalysts have been employed and the Ni catalysts show the greatest potential with regard to economic and availability aspects [4]. Ni is conventionally deposited on catalytic supports of high surface areas by means of techniques such as wet impregnation which do not assure a good distribution of the Ni species and in some cases can lead to the formation of large particle sizes [5].The co-precipitation technique has been widely used to obtain the precursors of oxides with a homogeneous morphological composition in which the strong Ni-surface interactions retard the sintering of the active phase during the catalytic processes. We have synthesized Ni/Ce/Mg/Al catalysts by coprecipitation techniques. In this way, Ce has showed a promoter effect in the activity and selectivity of the solids due to its oxygen storage capacity and redox properties, an aspect which also benefits the reduction of the coke formation on the catalysts. In this work, we will evaluate the effect of the amount of cerium on the chemical, textural, morphological and catalytic properties of Ni-Mg-Al-Ce oxides synthesized by the co-precipitation. The catalysts were evaluated in CO_2 reforming of methane between 750°C with a previous reduction at the same temperature.

II. EXPERIMENTAL

1. Catalysts synthesis

The samples derived hydrotalcites were prepared by continuous coprecipitation method reported by Miyata et al. [6] from two aqueous solutions. The first solution contained nitrates of the metals (Ni^{2+}, $Mg^{2+}$and Al^{3+} or Ce^{3+} cations) and the second solution contained sodium carbonates as precipite. The coprecipitation was carried out under constant agitation at 60°C maintaining the pH constant (12± 0.1) by adjusting the flow rate of solutions. The material was cooled to room temperature, filtered and washed with a large amount of deionised water up to a pH of 7 for complete removal of Na^+ and dried at 80°C for 12h. The resulting precursors were calcined at 800°C for 6 h (4°C/min). The solids obtained were named (NiMgAl, NiMgAlCe-1, NiMgAlCe-2 and NiMgCe).

2. Samples Characterization

The chemical composition of the materials was determined by means of Inductive Coupling Plasma (ICP) analysis Spectroscopy. Specific surface area measurements were performed using a Micromeritics ASAP 2010 apparatus by physical adsorption/desorption of N_2 at the liquid nitrogen using the BET equation. Prior to each experiment, the samples were activated by heating them at 150°C under vacuum.XRD powder analyses were carried out using a Siemens D-501 equipment, with a Bragg- Brentano configuration, using CuKα (λ=1,5418Å). Spectra were collected at room temperature in the range 2Θ = 5°-80°, with a step size of 0.05° and an acquisition time of 1s for each point. Scanning Electron Microscopy (SEM) images were obtained in a Hitachi S-5200 microscopy,

*Corresponding author email: djebaribaya@gmail.com

with a field emission filament, using an accelerating voltage of 5 Kv. FTIR spectra were recorded using the KBr pellet technique on PERKIN-Elmer spectrometer in the range 4000-400cm^{-1} using a resolution of 4 cm^{-1}. The calcined samples were analyzed by temperature programmed reduction (TPR) experiments which were done on a H_2/Ar mixture (5% H_2, 50ml /min flow) from room temperature up to 900°C, with a heating rate of 10°C/min. A thermal conductivity detector (TCD), previously calibrated using CuO, were used to evaluate the H_2 comsuption.

3. Catalytic activity tests

Catalytic Activity Tests were carried out in a fixed-bed tubular reactor, using 20 mg of catalyst between two pompons of quartz wool. The CH_4 and CO_2 reactants were mixed using a 1:1 ratio and diluted in He (10:10:80 in vol.). Before catalytic tests calcined samples were reduced at 750°C for 1hour and cooled down in H_2 to room temperature. After this reduction sample is put in contact with the reaction mixture, and heated from room temperature up to 750°C at 1°C/min rate, holding the samples at 750°C during 8h, and cooled down to room temperature in the same reaction mixture. In all the cases, the experiments have been carried out using a gas hourly space velocity (GHSV) of 300,000 L/kg h (20 mg of sample). Analysis of reactants and products were done by a Gas Chromatograph (Varian CP-3800) equipped with a Thermal Conductivity Detector and a column (Porapak Q).

III. RESULTS AND DISCUSSION

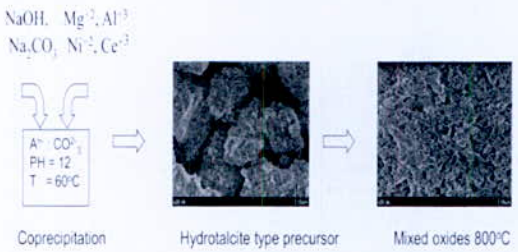

Scheme1. Preparation of the catalysts

Fig. 1, gives the XRD patterns of HT precursors. Due to the completely insertion of metallic cations with comparable ionic radius, Ni/Mg/Al hydrotalcite showed a pure layered double hydroxide structure with sharp and symmetric reflections for (0 0 3), (0 0 6), (1 1 0) and (1 1 3) planes and broad asymmetric peaks for (0 0 9), (0 1 5) and (0 1 8) planes. Diffractograms of the solids synthesized in presence of Ce^{+3} (NiMgAlCe-1, NiMgAlCe-2 and NiMgCe) show the signals of the carbonated phase of hydrotalcite and signals characterizing the $Ce(OH)_3$. A lower cristallinity of the sample which substituted all aluminum by cerium, this lower cristallinity could be due to the large distortions introduced in the layer because of the difference in ionic radius. Fig. 2, presents the XRD for the mixed oxides obtained after calcinations at (800°C, 6h) shows the formation of a solid solution (NiO-MgO) and CeO_2 .

The surface area and pore size distribution were determined from N_2 adsorption/desorption isotherms using BET and BJH methods, respectively. The N_2 adsorption/desorption isotherms of all samples from displayed type IV isotherms with clear hysteresis loops associated with capillary condensation [7] , and their pore sizes were widely distributed around 8 nm, 9 nm, 13 nm and 14 nm, respectively . These results indicated that the mesoporous generally, the preeminent surface area originated from the precursor with high integrated HT structures. Base on the previous XRD analysis, the integrality of pure HT structure for the sample was damaged to a certain extent with the addition of Ce^{3+}, and then the corresponding mixed oxides presented a lower surface area. High surface area for the present samples were formed during calcination. However, due to the introduction of Ce^{3+}, a small decrease on surface area was observed for samples with the following sequence: NiMgAl (101 m^2/g) > NiMgAlCe-1 (98 m^2/g) >NiMgAlCe-2 (76 m^2/g) >NiMgCe (20 m^2/g). The development of porosity and surface area could be attributed to the formation of channels and chimneys through the brucite like layers during removal of carbon dioxide.

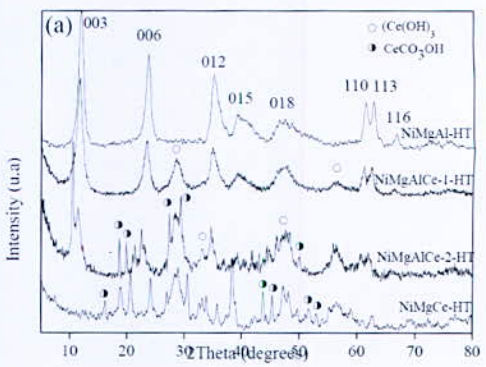

Fig.1. X-ray diffraction diagrams (XRD) of the coprecipitated precursors

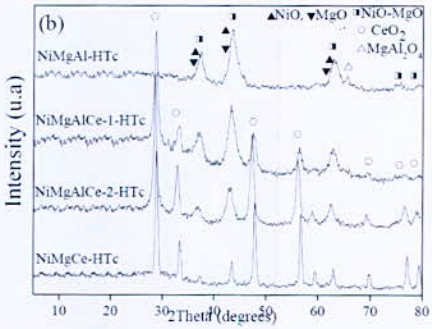

Fig. 2. X-ray diffraction diagrams (XRD) of the corresponding mixed oxides calcined at 800 °C

*Corresponding author email: djebaribaya@gmail.com

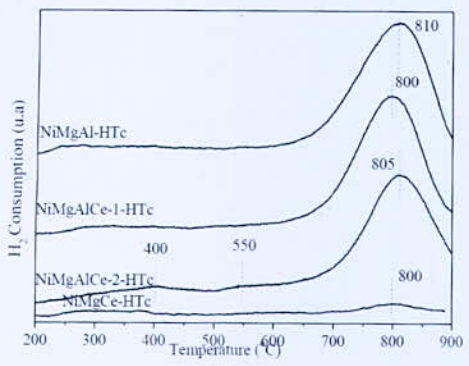

Fig. 3. Temperature programmed reduction (TPR) of the catalysts

The drop of surface area might also be due to that amount of mesopores were blocked by smaller amorphous or ill crystallized materials such as dissociative CeO_2.

Fig. 3, gives the TPR-H_2 profiles of mixed oxides. The Solid NiMgAl and NiMgAlCe-1 showed respectively one strong reduction peak with maximum at around 810°C 800°C and indicating the existence of one single type of reducible species, which corresponds to the reduction of Ni^{2+} in the solid solution. NiMgAlCe-2 had three reduction peaks. The reduction of the CeO_2 surface oxygen catalyst occurs between 400 and 550°C. The total reduction of the CeO_2 bulk into Ce_2O_3 cannot be seen clearly due to the overlapping of the signal coming from the reduction of the solid solution. Al^{3+} replacement by Ce^{3+} to obtain NiMgCe sample, leads to an almost flat profile, with just a small peak at 800°C.

SEM images of all catalysts after reduction at 750°C for 1 hour are shown in Fig. 4. In all samples we can observe the presence of particles of nickel these particles are homogeneously distributed with an average size between 15 nm and 25 nm.

The methane conversion is between 43% and 95%. The catalyst NiMgAl present 95% of methane conversion. Incorporation of cerium in NiMgAl catalyst gives right a lower conversion the activity decrease when increasing of amount of cerium which can be explain by the lower reducibility of nickel particles.

Despite the lower activity of catalysts containing cerium, this element has a beneficial effect in reducing a coke deposition.

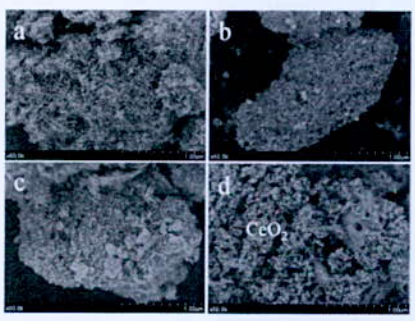

Fig. 4. SEM Image for the reduced samples

Fig. 5, shows H_2/CO ratios obtained at 750°C, in presence of Ni based-catalysts. This figure is a direct consequence of the differences in the conversion levels of CH_4 and CO_2. Once again, the value of the H_2/CO ratio remains approximately constant for all the catalysts after 8 h on stream. For NiMgAl catalyst, the H_2/CO ratio is almost that corresponding to the thermodynamic equilibrium (ca. 1.0). On the other hand, the catalysts (NiMgAlCe-1, NiMgAlCe-2 and NiMgCe) show a H_2/CO ratio smaller than unity. The deviation from the stoichiometric ratio, reflects the occurrence of the reverse water–gas shift reaction [8].

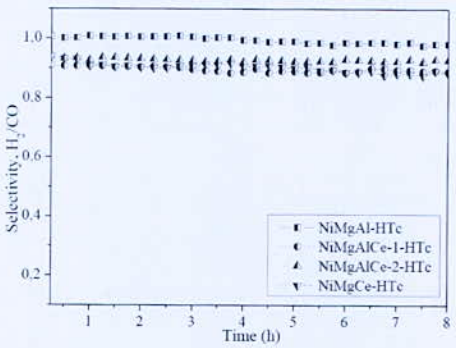

Fig. 5. Selectivity evolution, H_2/CO ratio versus time on stream for Ni-catalysts (750 °C, P = 1 atm, CO_2/CH_4 = 1, GHSV = 300,000 l/kgcat h)

IV. CONCLUSION

(NiMgAl, NiMgAlCe-1, NiMgAlCe-2 and NiMgCe) Catalysts obtained through the thermal decomposition of layered double hydroxide type precursors synthesized by coprecipitation at basic pH. It was shown that the incorporation of cerium by coprecipitation does not involve the isomorphic substitution of Ce^{3+} in the NiMgAl hydrotalcites systems due to the difference in ionic sizes. Theses catalysts are suitable catalysts for selective dry reforming of methane producing high CH_4 conversion and follow approximately the values corresponding to the thermodynamic equilibrium values. There was no significant carbon accumulation.

REFERENCES

[1] Hu, YH, Ruckenstein E, Bruce CG, Helmut K. Catalytic, Adv Catal 2004; 48:297-345.
[2] Rostrup-Nielsen JR. Catal Today1993; 18(4):305-24
[3] Bhattacharyya A, Chang D, Schumacher J. CO_2. Appl Clay Sci 1998; 13(5-6):317-28.
[4] Daza CE, Gallego J, Moreno JA, Mondrago´n F, Moreno S,Molina R. Catal Today 2008; 133-135:357-66.
[5] Zhang J, Wang H, Dalai AK. J Catal 2007; 249(2):300-10.
[6] Miyata, M., Okada, A., Clays Clay Miner., vol.25, 1977, p. 14.
[7] Wu. GD, Wang XL, Chen B, Li JP, Zhao N, Wei W, et al. Appl Catal A General 2007; 329:106-11.39.
[8] Montoya JA, Romero-Pascal E, Gimon C, Del Angel P, Monzon A (2000) Catal Today 63:71.

*Corresponding author email: djebaribaya@gmail.com

Effect of Operating Parameters on the Dynamic Behavior of a Metal Hydride Pump Equipped with a Phase Change Material

A. Miled[1*], F. Bouzgarou[1], F. Askri[1, 2]

[1*] Laboratory of Thermal and Energetic Systems Studies (LESTE) at the National School of Engineering of Monastir, University of Monastir, Tunisia.

[2] Mechanical Department, Faculty of Engineering, King Khalid University, Abha, Saudi Arabia.

Abstract—**Metal hydride water pumping system uses hydrogen as a working fluid to convert thermal energy into mechanical energy in order to pump water for a low head and high discharge [1]. The principal operation of this pump is based on the absorption and desorption of hydrogen by a metal hydride. However, an important quantity of heat released during absorption is lost, thereby reducing the pump efficiency. Therefore, the objective of this study is to discuss a new concept of a metal hydride pump (MHP) equipped with Ba(OH)2-8H2O as a phase change material (PCM). This system is enable to store the heat released during the absorption of hydrogen (suction of water) and to reused it during desorption stage (water pumping) using a phase change material. A mathematical model of the dynamic behavior of MHP-PCM is presented and a numerical simulation was performed to study the effect the mass of Ba(OH)2-8H2O and the effect of the heat transfer coefficient on the performance of the pump (specific water discharge, pump efficiency and pumping time).**

Key words—Metal hydride pump, phase change material, Ba(OH)2-8H2O, pumping time, pump efficiency

I. INTRODUCTION

Metal hydride pump is one of the unconventional pump systems which operate in an autonomous mode without the consumption of electric power and fossil energies. A study performed by Prasad et al. [2] on the performance of MHP using $LaNi_5$ as hydriding alloy, shown that the pump efficiency is about 6%. Also, a recent study by the same authors [3] shown that with Mg_2Ni, the metal hydride pump has a low pump efficiency that does not exceed 7.6% depending on the operating conditions. Debashiu Das and M.Ram Gopal [4] shown that depending on the design and operating condition, the overall thermal efficiency was found to be about 1.5%. Through these studies, it is seen that metal hydride pump has a low efficiency, this is due to the lost of an important quantity of thermal energy released during absorption. Then, to improve the pump efficiency, this paper discusses the dynamic behavior of metal hydride pump equipped with a phase change material. In fact the heat released during absorption is stored and reused during desorption using Ba(OH)2-8H2O as a phase change material. First, a mathematical model of a MHP-PCM is presented. Then, simulations were performed to study the effect of the mass of Ba(OH)2-8H2O and the effect of heat transfer coefficient on the specific water discharge, pump efficiency and pumping time.

II. OPERATING CONCEPT OF MHP-PCM

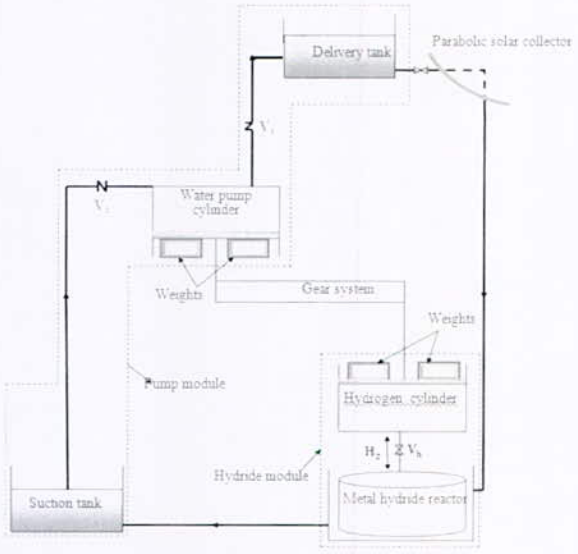

Fig. 1. Schematic diagram of MHP-PCM

The MHP-PCM is composed of two modules:

- Hydride module which is composed of a metal hydride reactor equipped with a phase change material (Ba(OH)2-8H2O) and a frictionless piston cylinder arrangement with dead weights.

- A pumping module which consist of a frictionless piston cylinder arrangement with dead weights and two tanks: one for suction and the other for delivery.

These two modules are connected by a gear system. During the desorption of hydrogen, heat is supplied through the concentric heat exchanger and by the latent heat of solidification of the PCM, which causes the increase of hydrogen concentration, average temperature and pressure inside the reactor. Then, the hydrogen piston moves outwards, the gear system transfers this displacement to the pump piston causing the pump of water. At the end of desorption, heat is no longer provided and the gear ratio is reset to a lower ratio (G_e). Then, hydrogen expands adiabatically moving the hydrogen and pump piston further outwards and inwards. Thus,

*Corresponding author email: amelmiled10@yahoo.fr

pumping more water. During the absorption process the interior pressure of the cylinder decreases and dead weight on the piston pushes it inwards. Then, dead weight pulls the pumping piston outwards to suck water from suction tank. During the hydrogen absorption, the heat generated by the hydride bed is stored in the PCM. At the end of this process, the reactor reaches the saturated state, the total heat is stored, the PCM is completely melted and the gear system is reset to the higher ratio.

III. MATHEMATICAL MODEL

The metal hydride reactors considered in this work is presented in Fig. 2. It is composed of three coaxial cylinders. The inner one (R1), represents a heat exchanger. The second cylinder (R2), is filled with one kg of LaNi5 powder and the external cylinder (R3) is filled with Ba(OH)2-8H2O as phase change material.

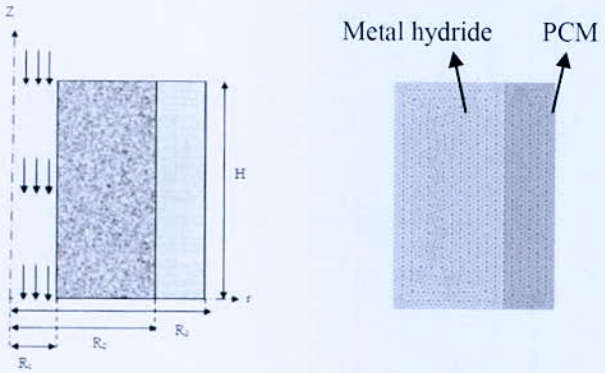

Fig. 2. Schematic diagram of metal hydride reactor

During the Hydrogen absorption, the heat released is stored by the PCM, then, this heat will be reused to desorb hydrogen during pumping process (During hydrogen absorption and desorption PCM changes from solid to liquid and vice versa).

1. Metal hydride reactor

• The energy equation is given by:

$$\left(\rho C_p\right)_e \frac{\partial T}{\partial t} = \lambda_e \frac{1}{r}\frac{\partial}{\partial r}\left(r\frac{\partial T}{\partial r}\right) + \lambda_e \frac{\partial}{\partial z}\left(\frac{\partial T}{\partial z}\right) + \dot{m}\left[\Delta H + T\left(C_{pg} - C_{ps}\right)\right] \quad (1)$$

Where

λ_e, C_{pe} and ρ_e are respectively the effective thermal conductivity, the specific heat and the effective density.

•Hydrogen desorbed per unit volume and unit time is given by [5]:

$$\dot{m} = \rho_s C_d \exp\left(-\frac{E_d}{RT}\right)\left(\frac{P_g - P_{d,eq}}{P_{d,eq}}\right) \quad (2)$$

Where $P_{d,eq}$, C_d and Ed are, respectively, the equilibrium pressure during desorption, the desorption rate constant (Cd = 9.57) and the desorption activation energy (Ed = 16473.59 J/mol) [6].

•The energy equation of the phase change material can be expressed as follows [7]:

$$\frac{\partial H}{\partial t} = \nabla.\left(\lambda_{PCM}\nabla(T)\right) \quad (3)$$

Where H is the total volumetric enthalpy of the PCM:

$$H(T) = h(T) + \rho_{PCM} L f(T) = \int_{T_m}^{T} \rho_{PCM} C_{P,PCM}\, dT + \rho_{PCM} L f(T) \quad (4)$$

Where $\lambda_{p,PCM}$, $\rho_{p,PCM}$, $C_{p,PCM}$ L and f (T) are respectively the thermal conductivity, the density, the specific, the latent heat and the liquid fraction of the PCM.

•The liquid fraction is as follow:

$$f(T) = \frac{1}{1 + e^{-2K(T - T_m)}} \quad (5)$$

Tm is the melting temperature

K is the sharper transition at T = Tm.

2. Pumping system

The bed pressure is given as follows:

$$P(T) = \frac{\left(n(t) + n_0\right) R_g T_{moy}}{V_0} \quad (6)$$

Where T_{moy} is the average temperature in the metal hydride reactor (MHR-PCM), V0 is the initial volume of the hydrogen cylinder and n_{H_2} is the number of moles of hydrogen desorbed, per kilogram of metal hydride:

$$n_{H_2} = \frac{HM_{\max}\left(X_i - X(t)\right) m_{LaNi5}}{2M_H} \quad (7)$$

The average temperature and the hydrogen concentration X(t) are determined by solving the governing equations of heat and mass transfer within the MHR-PCM

There exists a unique desorption pressure for a given set gear ratio (G_{de}) and for the given parameters. It is given by:

$$P_{de} = P_i + \rho g h_t G_{de} \frac{A_p}{A_h} \quad (8)$$

During desorption, heat is supplied by the latent heat of solidification of the PCM and through the concentric heat

*Corresponding author email: amelmiled10@yahoo.fr

exchanger. Total heat supplied causes the increase of hydrogen concentration, average temperature and pressure within the reactor. When, this pressure P(t) tends to exceed the pressure set by the gear ratio (P_{de}), the pump process is triggered. Then, the volume of water pumped as a function of time during desorption is as follows:

$$V_{pd}(t) = G_{de} V_{hde}(t) \frac{A_p}{A_h} \quad (9)$$

Where:

$$V_{hde}(t) = \frac{n(t) R_g T_{moy}}{P_{de}} \quad (10)$$

During expansion process, a further volume is pumped.

$$V_{pe}(t) = G_e \left(V_{he}(t) - V_{hde}(t)\right) \frac{A_p}{A_h} \quad (11)$$

Where:

$$V_{he} = \left(\frac{P_{de}}{P_{he}}\right)^{\frac{1}{\gamma}} V_{hde}(t) \quad (12)$$

The total volume of water pumped during desorption and expansion is given by:

$$V_t(t) = V_{pd}(t) + V_{pe}(t) \quad (13)$$

The efficiency of the pump is the ratio of energy required to pump water to the heat, Q_e supplied to the system by convection.

$$\eta = \frac{\rho g V_t(t) h_t}{Q_e} \quad (14)$$

IV. RESULTS AND DISCUSSION

In this paper, the effects of PCM mass and the heat transfer coefficient on the performance of the metal hydride pump are evaluated.

1. Effect of PCM mass

The mass of Ba(OH)2-8H2O should be carefully chosen. In the present study, the mass of LaNi5 powder is keeping unchanged and the radius of the hydride cylinder is fixed at R2=3.73 cm. But, the radius R3 is variable in function of PCM mass. Table 1 presents the different scenarios tested. To compare these different scenarios, the heat transfer coefficient is equal to 100 W/m2.K and the other parameters are kept constant (Pde= 8 bar, Tf= 353 K, ht=5m, Ge=4, $T_{PCM,\ solidfraction}$=351, ΔH_{PCM}= 265 KJ/kg.

Fig. 3, presents the time evolution of the hydrogen desorbed, the specific water discharge and the liquid fraction for different masses of Ba(OH)2-8H2O as phase change material. It is observed that For a Ba(OH)2-8H2O mass equal or less than 0.5 kg, the PCM is solidified rapidly, but hydrogen is not completely desorbed. Then, the specific water discharge is not very important. That is to say, the PCM quantity is insufficient to release all the hydrogen stored during the desorption process.

TABLE I
DIFFERENT MASS TESTED

Scenario	PCM mass (Kg)	R3(cm)
1	0.4	4.9
2	0.5	5.1
3	0.6	5.45
4	0.65	5.5
5	0.8	5.9
6	0.91	6.1
7	1	6.3

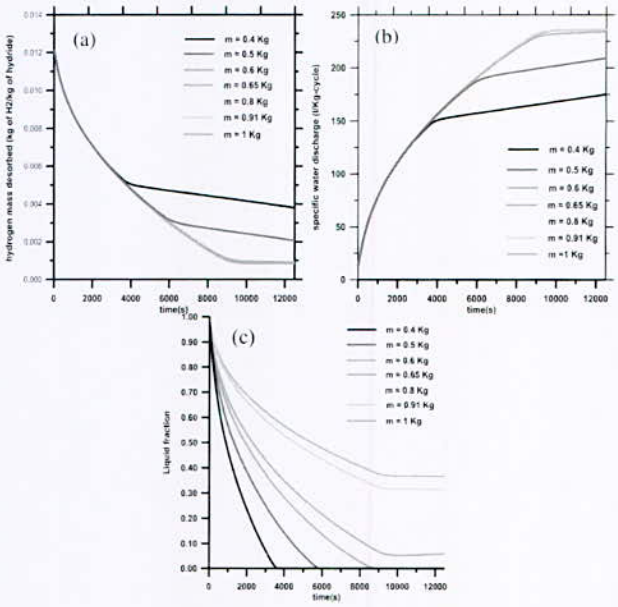

Fig. 3. Time evolution of (a) hydrogen mass desorbed, (b) specific water discharge and (c) liquid fraction, for different masses of Ba(OH)2-8H2O

It is found also according to the Fig. 3, that for a PCM mass equal or greater than 0.65 kg, the hydrogen is completely desorbed and the curves showing the desorbed hydrogen mass are confused. Thus, a large quantity of water is pumped (Fig. 3b). However, the PCM is not completely solidified (Fig. 3c). Then, a large quantity of energy is still stored in the PCM, without being released and used during the pumping process. Then, it can be conclude that a mass of Ba(OH)2-8H2O equal to 0.6 kg represents the optimal mass which permits to get a high desorption rate (93 %) so, an important specific water discharge. Also, with 0.6 kg of Ba(OH)2-8H2O, the total heat stored is released and the PCM is completely

*Corresponding author email: amelmiled10@yahoo.fr

solidified. Then, a mass of Ba(OH)2-8H2O equal to 0.6 kg should be considered.

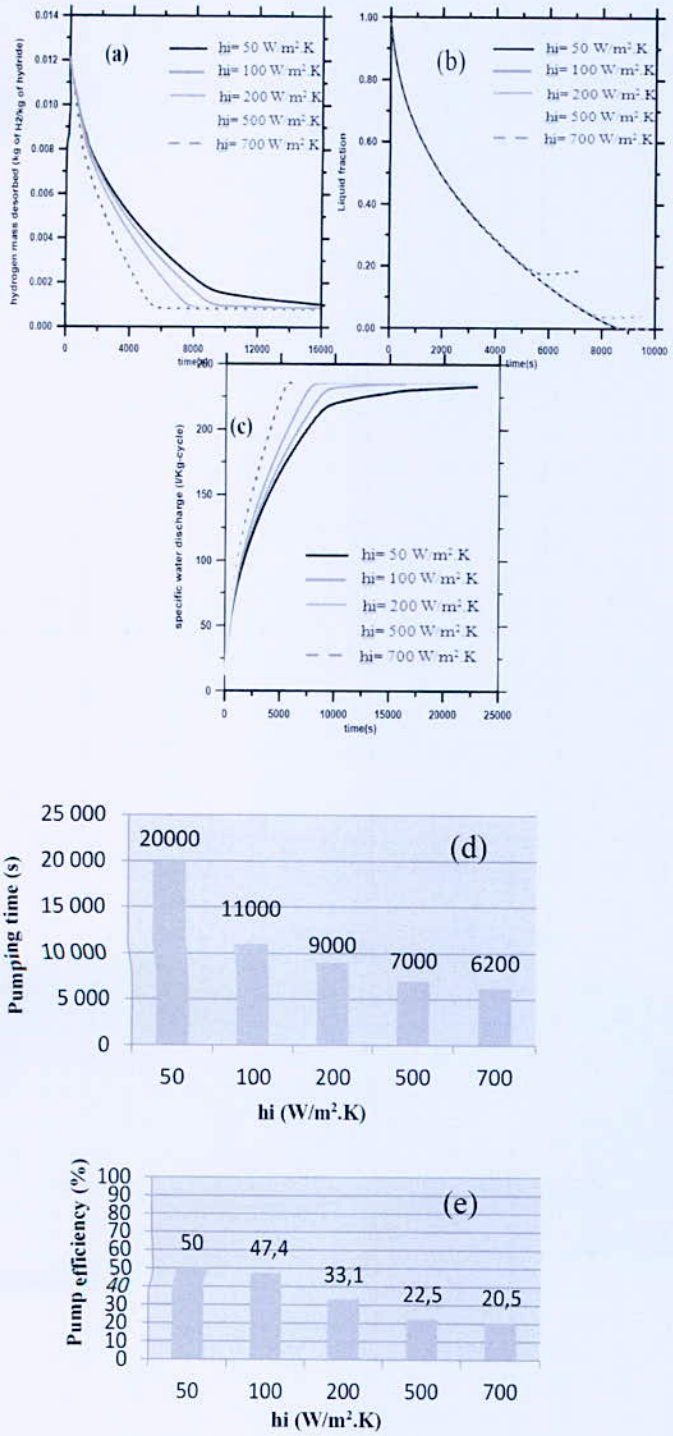

Fig. 4. Effect on heat transfer coefficient on (a) hydrogen mass desorbed, (b) liquid fraction (c), specific water discharge, (d) pumping time and (e) pump efficiency

2. *Effect of heat transfer coefficient*

Fig. 4, shows that the heat transfer coefficient has no effect on the hydrogen mass desorbed (Fig. 4a) and on the same specific water discharge. Also, from Fig. 4-b, it is seen that the increase of the heat transfer coefficient (hi) leads to an important reduction of the pumping time.

Fig. 4b, shows that for a heat transfer coefficient higher than 100 W/m2.K, Ba(OH)2-8H2O is not completely solidified. However, for a heat transfer coefficient less than 100 W/m2.K, a total solidification of the PCM can be noticed. Hence, the material has released the entire heat stored to desorb hydrogen. It is observed from Fig. 4e that the decrease of the heat transfer coefficient improves the pumping efficiency. According to the obtained results, it can be concluded that a convective heat coefficient of 100 W/m2.K allows to pump 236 l/K-cycle with a good pump efficiency and an acceptable pumping time.

V. CONCLUSION

A metal hydride pump equipped with Ba(OH)2-8H2O as a phase change material (MHP-PCM) was numerically investigated. A computer code is developed to predict the effect of the PCM mass and the effect of the convective heat coefficient on the performance of MHP-PCM. Results have shown that a suitable choice of the PCM mass (m=0.6 kg) allows the optimization of the MHP-PCM performance. Also, it is seen that the convective heat coefficient must be carefully selected. It is found that hi=100 W/m2.K allows to pump 236 l/.kg-cycle with a good efficiency (47.4%) during an acceptable pumping time.

REFERENCES

[1] AI. Solovey, VP. Frovol. Metal hydride heat pump for watering systems. International Journal of Hydrogen Energy 26 (2001) 707–709.

[2] U.A. Rajendra Prasad, M. Prakash Maiya, S. Srinivasa Murthy. Metal hydride water pumping system for low head-high discharge applications, International Journal of Hydrogen Energy 29 (2004) 501 – 508.

[3] A. Miled, F. Askri, S. Ben Nasrallah. Numerical study of the dynamic behavior of a metal hydride pump. International Journal of Hydrogen Energy, 40 (2015) 1083-1095.

[4] Das. Debashis, M. Ram Gopal. Studies on a *metal* hydride based solar water pump. International Journal of Hydrogen Energy 29 (2004) 103 – 112.

[5] U. Mayer, M. Groll, W. Supper. Heat and mass transfer in metal hydride reaction beds: experimental and theoretical results Journal of the Less Common Metals 131 (1987) 235–244.

[6] S. Suda, N. Kobayashi. Reaction kinetics of metal hydrides and their mixtures, Journal of the Less Common Metals 73 (1980) 119–126.

[7] V.R. Voller. An overview of numerical methods for solving phase change problems, Adv. Numer. Heat Transf. 1 (1996)

*Corresponding author email: amelmiled10@yahoo.fr

Photocatalytic Hydrogen Production under Visible Light over the Perovskite $LaFeO_3$ Synthesized by Citrates Sol-Gel method

S. Boumaza[1*], K. Benhenni[1], A. Benaissi[1], M. Mendil[1], M. Ezzouaoui[1], L. Boudjellal[1], A. Belhadi[1] and M. Trari[2]

[1*]Laboratory of Chemistry of Natural Gas, Faculty of Chemistry (USTHB), BP 32, 16111 Algiers, Algeria.
[2]Laboratory of Storage and Valorization of Renewable Energies, Faculty of Chemistry (USTHB), BP 32, 16111 Algiers, Algeria.

Abstract—**In this work, we have synthesized the perovskite $LaFeO_3$ by sol-gel method. The powder is characterized by (TG-ATD/DSC) analysis, X-ray diffraction, BET surface area, SEM analysis, laser granulometry and electrical conductivity. The XRD patterns at different temperatures show that the pure perovskite $LaFeO_3$ is obtained beyond 850 °C. The BET measurements give relatively a small surface area (7 m^2 g^{-1}). The elemental chemical analysis by laser granulometry, confirmed the agglomerated nature of the synthesized powder observed by SEM analysis and attributed to the fine powder obtained by sol-gel method. The diffuse reflectance gives an optical gap of 2.22 eV, in agreement with the brown color. The transport properties show a semi-conductor behavior with *n*-type conductivity and activation energy of 0.20 eV. $LaFeO_3$ exhibits an excellent chemical stability in the pH range (5-14); a corrosion potential of 0.515 VSCE and an exchange current density of 35 µA cm^{-2} have been determined from the semi-logarithm plot. The capacitance measurement (C^{-2}-E) in basic electrolyte reveals a linear behaviour from which a flat band potential of 0.62 V_{SCE} is obtained. $LaFeO_3$ is tested successfully as photocatalyst for the hydrogen production upon visible light and the best performance is obtained in alkaline solution (NaOH 0.1 M, $Na_2S_2O_3$ 10^{-3} M) with an average rate of 0,026 cm^3 h^{-1} (mg catalyst)$^{-1}$. The system shows a tendency toward saturation whose deceleration is the result of the competitive reduction of the end product $S_4O_6^{2-}$.**

Key words—$LaFeO_3$, Perovskite, Sol-gel, Hydrogen, Visible light.

I. INTRODUCTION

Hydrogen is considered as energetic vector of the future envisaged for the storage of electricity, via its electrochemical conversion in fuel cells. However, its production, storage and distribution remain major issues for its industrial development [1]. Most hydrogen production methods are based on the fossil fuels which liberate greenhouse gases. So, developing methods to convert solar energy directly into hydrogen is the challenge of the recent research. In this respect, the photocatalysis is used for the energy supply as well as the decontamination of liquid or gaseous effluents. However, the possibility of converting these effluents into an energy source, especially in the form of hydrogen, remains an interesting alternative [1, 2]. Various strategies employed for enhancing the photocatalytic performance have been discussed, emphasizing the specific advantages and challenges offered by ternary oxides. they constitute the most attractive class of materials with a variety of structures and properties. The perovskite ABO_3 are of significant interest in the field of photocatalysis [3]. They exhibit a good chemical stability in aqueous medium; a small gap allows them to absorb the maximum of the solar spectrum. In addition, their method of synthesis is simple and requires only cheap products. In this work, the properties of the perovskite $LaFeO_3$ synthesized by sol-gel method has been developed and their applications for the hydrogen production under visible light are studied. The presence of lanthanum decreases the electroaffinity of $LaFeO_3$ and shifts the flat band potential (E_{fb}) and increase the band bending, an advantageous property for the charges separation.

II. EXPERIMENTAL/THEORETICAL STUDY

$LaFeO_3$ is synthesized by the citrates sol-gel method. In the first step, stoichiometric amounts of $La(NO_3)_3$, $6H_2O$; $Fe(NO_3)_3$,$9H_2O$ and citric acid ($C_6H_7O_6$) were dissolved in a minimum of distilled water to obtain a homogeneous solution. Then, the solutions of nitrates were mixed and the complexion agent (citric acid solution) was added. After homogenization of the mixture, the final solution was evaporated under vacuum in a rotary evaporator at 50 °C until getting to obtain a gel. The gel was dried at 110 °C overnight. Before calcination, the nitrates present in the powder obtained were decomposed at ~250 °C. Then, the powder was crushed and calcined at 850 °C with a heating rate of 3 °C min^{-1}.

After the synthesis, the powder was characterized by Attenuated total reflection (ATR), X-ray diffraction (XRD), thermo gravimetric (TG), differential thermal analysis (DTA) and differential scanning calorimetry (DSC), BET surface area, Scanning electron microscopy (SEM), laser granolumetry, Electrical conductivity, thermoelectric power and photoelectrochemical characterization.

Combined (TG-ATD/DSC) were carried out, thanks to a Setaram thermobalance (Set Sys 16/18, DSC 111), in air with a heating rate of 3 K min^{-1}.The XRD patterns were recorded with a *XPERT-PRO* diffractometer using $Cu_{K\alpha}$ radiation ($\lambda_{Cu\ K\alpha}$= 1.5406 Å). The diffuse reflection spectrum is plotted with a double beam spectrophotometer type *Shimadzu 1800* equipped with an

*Corresponding author email: boumazasouhila@gmail.com

integrating sphere. The attenuated total reflection (ATR) allows to examine the samples directly without further preparation; the ATR analysis of the powder was carried using a spectrometer type *Perkin Elmer spectrometer-SPECRTRUM TWO*. The surface area was determined by the BET method using nitrogen gas as adsorbent on *ASAP2010 micromeritics* apparatus. The micro-morphology was realized by SEM microscope type *JSM Jeol 6360L*.

The corrosion was determined by analyzing Fe^{3+} by atomic absorption (*Parkin Elme-AAnalyst 700*). 30 mg of the powder $LaFeO_3$ was immersed during 10 months in three solutions: NaOH, HCl and Na_2SO_4 (0.1 M).

Dense pellets were obtained by sintering pressed pellets at 850 °C. The electrical conductivity (σ) was measured by the d.c. two probe method. The thermoelectric power (type of conductivity) was performed by the differential technique.

The intensity-potential (J-E) curves and the Mott Schottky characteristic were plotted in alkaline solution (NaOH, 0.1 M) in a standard electrochemical cell using Pt emergency electrode and a saturated calomel electrode (SCE).

The photoactivity was determined by measuring the volume of evolved hydrogen. The experiments were carried out in a double walled Pyrex reactor (600 cm^3); the temperature was regulated at 50 °C with a thermostated bath. The powder (250 mg) was dispersed under constant magnetic agitation (210 rpm) in 200 mL of freshly prepared solution ($Na_2S_2O_3$ or Na_2SO_3 10^{-3} M) and deoxygenated by N_2 bubbling for 30 mn. The light source consisted of three tungsten lamps (200 W, Osram) providing an intensity of 29 mW cm^{-2}. The H_2 volume was measured through water displacement in an inverted graduated burette. Hydrogen was identified by *Agilent Technologies 7890A GC System*. The solutions were prepared from reagents of analytical grade quality and distilled water.

III. RESULTS AND DISCUSSION

1. Characterizations

In order to estimate the temperature of calcination and to obtain a well crystallized oxide, the precursor of the dried gel of $LaFeO_3$ was analyzed by TG, DTA and DSC under air flow up to 1000 °C. The curves (TG-ATD/DSC) of $LaFeO_3$ were carried out before calcination. The TGA plot shows five weight loss segments:

The first weight loss (5%) up to 150 °C accompanied by a low endothermic peak and a large exothermic peak are attributed to the removal of the residual water and a partial decomposition of the citric acid chain. The second weight loss step (33%) in the region (150-270 °C) with a large exothermic peak corresponds to the decomposition of the citrates and some of nitrates. The third part between 270 and 340 °C (12%) is associated with a high exothermic peak observed at about 315 °C, due to the decomposition of the remaining organic matter and the formation of La_2O_3 disorder. A fourth part of weight loss (13%) in the range (340-547 °C) is detected, accompanied by an exothermic peak corresponding to the combustion of residual carbon and nitrates. A final weight loss (~ 7%) in the region (547 - 650 °C) with an exothermic peak is assigned to the loss of oxygen resulting in the formation and crystallization of the perovskite phase $LaFeO_3$. These results agree with the XRD analysis of the perovskite $LaFeO_3$ obtained above 850 °C. Such results are corroborated by the DSC plot.

The XRD pattern of the powder $LaFeO_3$ calcined at 850 °C is presented in Fig. 1. It reveals a single pure perovskite phase "$LaFeO_3$" crystallizing in the orthorhombic system (JCPDS file N° 88-0641, SG: Pnma). The lattice parameters a= 5.5632 Å; b= 7.8633 Å; c= 5.5572 Å while the particle size (75 nm) is determined from the full width at half maximum. $LaFeO_3$ has relatively a small specific surface area (7 $m^2 g^{-1}$); a value closes to other perovskite oxides, of the order 15 m^2g^{-1} [4]. Such values can be explained by the high synthesis temperature used (>800 °C) and the agglomeration of the particles.

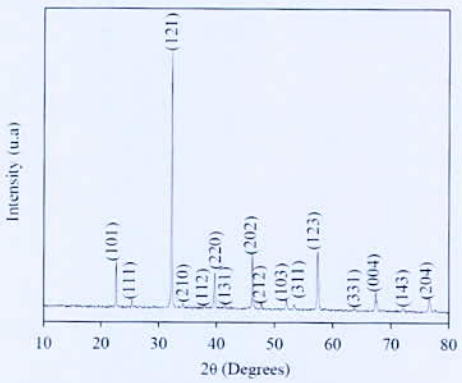

Fig. 1. Powder X-ray diffraction pattern of $LaFeO_3$ calcined at 850 °C

In this study, the ATR spectrum of $LaFeO_3$ is similar to that obtained in the literature. It shows an intense fine peak at 533 cm^{-1} attributed to Fe-O bond vibrations. The vibration band characteristic of Fe-O bond is observed between 500 and 700 cm^{-1}. Moreover, it is noted the absence of peaks characteristic of OH- groups, water and nitrates, confirming that their complete disappearance.

The SEM images of $LaFeO_3$, is given with three magnifications. They show that the solid exhibits a porous surface due probably to the evolution of CO_2 and NO_2 during the combustion of the gel; Gaseous products, escaping from the gel, result in spraying of the grains and formation of pores. The micrographs present a homogeneous surface and grains with poorly defined shape and large sizes, due probably due to the agglomeration of the fine powder of $LaFeO_3$ obtained by sol-gel method, in agreement with the low surface area obtained by BET analysis.

*Corresponding author email: boumazasouhila@gmail.com

The analysis of the grain size distribution of $LaFeO_3$ performed by laser granulometry analysis to determine the grain size in a range between 0.01 and 3000 µm. $LaFeO_3$ has a grain diameter distribution between 200 and 1000 µm. The average grain size obtained by laser particle size is ~ 559 µm. The large size obtained confirms the agglomerated nature of the fine powder $LaFeO_3$ observed by SEM analysis. Moreover, we noted the total absence of grains smaller than 200 nm.

The gap E_g of $LaFeO_3$ has been determined from the plot of $(\alpha h\nu)^n$ as a function of $(h\nu)$. For n= 2, a linear part of the curve is observed and its extrapolation cuts the axis of the energies to a value equal to 2.22 eV (Fig. 2). So, the gap of $LaFeO_3$ is 2.22 eV and is due to a direct optical transition. This result is in good agreement with those obtained by Sumalin Phokha et al. [5] which report a direct transition gap for $LaFeO_3$.

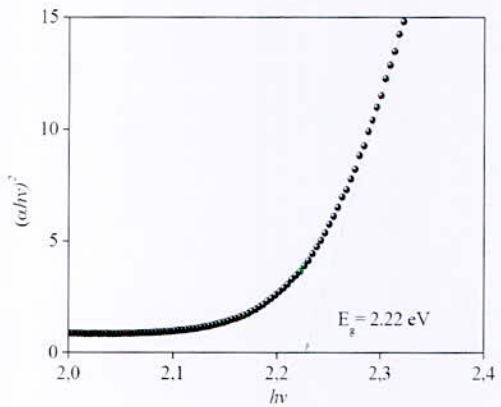

Fig. 2. Direct optical transition of $LaFeO_3$

The variation of the electrical conductivity (σ) of $LaFeO_3$ as a function of the temperature, indicates that the conductivity increases with the temperature; which shows a semiconductor character of the oxide throughout the temperature range studied. An activation energy (ΔE) of 0.20 eV, is determined from the slope of log (σ) vs. reciprocal absolute temperature. S is negative and decreases monotonically with temperature up to 390 K above which it remains almost constant. So, one can conclude that the material exhibits *n*-type conductivity. The convergence of S to a fixed value may be due to the presence of crystal defects or to the existence of a recombination center in the direction of the charge flow.

2. *Photoelectrochemistry*

$LaFeO_3$ is an interesting material for PEC characterization. The representation (C^{-2}) as a function of the applied potential reveals the existence of a single cathodic region (> 0.5 V), confirming the *n*-type behavior of $LaFeO_3$ where the electrons are the majority carriers (Fig. 3). The potential V_{fb} (+0.62 V) is determined from the abscissa at the origin of the curve. The obtained value V_{fb} is different from that of V_{on} indicating the existence of the surface states within the band gap.

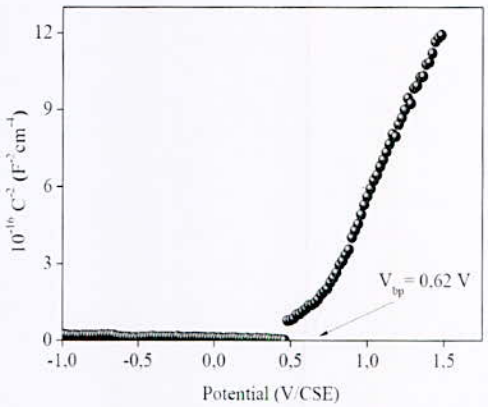

Fig. 3. The Mott-Schottky characteristic of $LaFeO_3$ in NaOH solution (0.1 M) at frequency of 10 kHz

Because of our interest in using $LaFeO_3$ for the energy storage, the resistance to corrosion is a crucial parameter to determine for the practical application. The oxide exhibits a good chemical stability in both neutral and alkaline electrolytes. From the results of the table I, the rates dissolution measured in basic (pH~ 13) and neutral (pH~ 7) solutions, after 10 months of immersion, exhibit excellent chemical stability. As pH decreases (pH~ 1), the corrosion rate increases indicating that $LaFeO_3$ is not stable in acidic medium. Note that, we have observed the total dissolution of $LaFeO_3$ in acidic medium. The electrokinetic parameters i.e. the exchange current density (35 µA cm^{-2}), the corrosion potential (0.515 V) and the polarization resistance (1.28 kΩ cm^2) determined from the semi-logarithmic plot, corroborate such result.

TABLE I
CORROSION RATES OF LAFEO3 IN DIFFERENT SOLUTIONS

Solutions	$[Fe^{3+}]$ (mg L^{-1})	Corrosion rate (µmol $m^{-2}jour^{-1}$)
HCl	41.27	0.4690
Na_2SO_4	0.081	0.00092
NaOH	0.342	0.0038

3. *Photocatalysis*

The photocatalytic activities of $LaFeO_3$ were measured via the photoreaction of water decomposition to product the hydrogen. The photoactivity is thermally activated and the experiments were carried out at 50 °C. Fig. 4 shows the variation of the volume of the hydrogen over $LaFeO_3$ in alkaline and neutral solutions. The photoelectrons reducing power increases with pH; the greatest volume of H_2 is obtained in basic medium (pH ~ 13) and decreases progressively in neutral medium (pH ~ 7).

*Corresponding author email: boumazasouhila@gmail.com

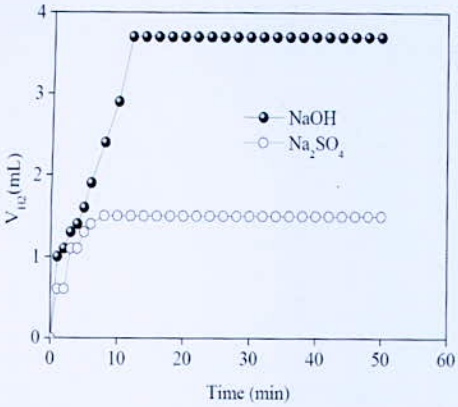

Fig. 4. Volume of evolved H_2 vs. illumination time over $LaFeO_3$ in $S_2O_3^{2-}$, pH~ 13 and pH~ 7; $S_2O_3^{2-}$ (10^{-3} M)

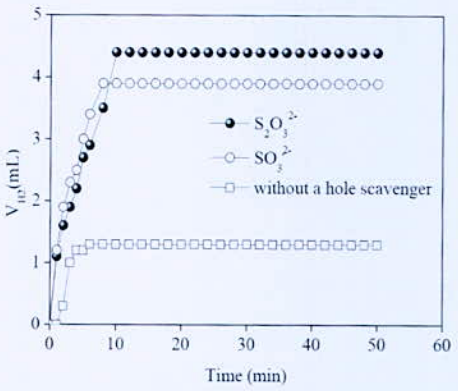

Fig. 5. Volume of evolved H_2 vs. illumination time over $LaFeO_3$ in presence and absence of holes scavenger NaOH: (10^{-3} M); X^{2-} (10^{-3} M)

Fig. 5. shows the volume of the evolved hydrogen released as a function of time for $LaFeO_3$ in NaOH solution in presence and absence of reducing species X^{2-} ($X^{2-} = S_2O_3^{2-}$ and SO_3^{2-}). The largest volume obtained is in the case of $S_2O_3^{2-}$ and the volume of hydrogen increases over illumination time. The presence of $S_2O_3^{2-}$and SO_3^{2-} increases the production rate of H_2 which improved the photoactivity. The excitation of $LaFeO_3$ by visible light produces pairs (e^-, h^+).The photoelectrons are responsible of the water reduction to hydrogen. While the holes oxidize the reducing species ($X^{2-} = S_2O_3^{2-}$ or SO_3^{2-}). In the absence of X^{2-}, $LaFeO_3$ undergoes photocorrosion by holes attack. The hydrogen evolution depends on the separation of the pairs (e^-, h^+) by the electric field junction which is a function of the potential of the flat band V_{fb} and the potential $E^0_{ox/red}$ of the redox couple: $B = | E^0_{ox/red} - V_{fb}|$. The high volumes of H_2 obtained with $S_2O_3^{2-}$ is attributed to a larger band bending, where the pairs (e^-,h^+) are separated more efficiently. The evolved volume of hydrogen tends towards saturation due to the concurrent reduction of the final products $S_2O_6^{2-}$ and $S_2O_4^{2-}$ by consuming electrons destined for the reduction of water.

IV. CONCLUSION

In the present work, we have successfully synthesized the perovskite $LaFeO_3$ by the citrates sol-gel method. The thermal and XRD analysis showed single phase obtained at 850 °C with a particle size ~ 75 nm. The capacitance measurement indicated *n*-type conductivity. The optical gap (E_g= 2.22 eV) and the chemical stability make $LaFeO_3$ attractive for the solar conversion. At basic pH, the conduction band is suitably positioned and the oxide has been successfully tested for the hydrogen evolution under visible light and ensures chemical storage.

ACKNOWLEDGMENTS

The authors would like to thank Drs. B. Bellal, Azzaz and A. Lounis for their helpful discussion and technical assistance. The *CRD (SONATRACH)* group of Boumerdès for the X-ray diffraction.

REFERENCES

[1] S. Boumaza, H. Kabir, I. Gharbi, A. Belhadi, M. Trari, "Preparation and photocatalytic H_2-production on α-Fe_2O_3 prepared by sol-gel," Int. J. Hydrogen Energy 2017, pp. 1-7, In Press.

[2] I. Dincer, C. Acar, "Innovation in hydrogen production, Int. J. Hydrogen Energy," Vol. 42, Issue 22, 2017, pp. 14843-14864.

[3] P. Kanhere, Z. Chen, "A Review on Visible Light Active Perovskite-Based Photocatalysts," Molecules Vol. 19, 2014, pp. 19995-20022.

[4] F. Touahra, A. Rabahi, R. Chebout, A. Boudjemaa, D. Lerari, M. Sehailia, D. Halliche, K. Bachari, "Enhanced catalytic behaviour of surface dispersed nickel on $LaCuO_3$ perovskite in the production of syngas: An expedient approach to carbon resistance during CO_2 reforming of methane, " Int. J. Hydrogen Energy, Vol. 41, 2016, pp. 2477-2486.

[5] S. Phokha, S. Pinitsoontorn, S. Maensiri, S. Rujirawat, "Structure, optical and magnetic properties of $LaFeO_3$ nanoparticles prepared by polymerized complex method," J. Sol-Gel Sci. Technol., Vol. 71, 2014, pp. 333-341.

*Corresponding author email: boumazasouhila@gmail.com

Visible Light Hydrogen Evolution over α-MoO_3 and α-MoO_3/ZnO Hetero-junction

K. Bounache[1], W. Tallas[1], S. Boumaza[1]; A. Belhadi[1*] and M. Trari[2]

[1*]Laboratory of chemistry of Natural gas, Faculty of Chemistry, (USTHB) BP 32, 1611, Algiers, Algeria.
[2] Laboratory of Storage and Valorization of Renewable Energies, Faculty of Chemistry (USTHB) BP 32, 16111, Algiers, Algeria.

Abstract—**Hydrogen is a clean energy which can be produced from water and sunlight on semiconductor oxides. Unlike primary energy sources, hydrogen must be manufactured before being stored and used. MoO_3 has received a considerable attention over the last years because of its applications in various fields and mainly in catalysis. The supported catalyst (5% MoO_3/ZnO) was synthesized by impregnation using $(NH_4)_6Mo_7O_{24}$, $4H_2O$ as precursor and ZnO as support. α-MoO_3 prepared by calcination of ammonium heptamolybdate at 700°C for 6 h, was photo-electrochemically characterized to assess its feasibility for hydrogen production under visible light, an issue of energy concern. The morphology was analyzed by scanning electronic microscopy (SEM) and Fourier transform infrared spectroscopy (FTIR). The X-ray diffraction (XRD) showed that the MoO_3 powder treated in the range (500-700 °C) crystallizes in an orthorhombic structure. MoO_3 exhibits a direct optical transition at 2.90 eV. The Mott-Schottky characteristic plotted in (Na_2SO_4, 0.1 M) solution indicates *n* type conduction with a flat band potential of 0.61V_{SCE}. As application, hydrogen evolution is successfully realized under visible light; the best performance occurs on MoO_3 at pH ~ 7.**

Keywords—MoO_3, MoO_3/ZnO, Hetero-junction, Impregnation way.

I. INTRODUCTION

Today, the energy becomes a major problem which stands face to face against our civilization: the energy growing demand leads to the exhaustion of natural resources (coal, oil, gas etc.), whereas we are more dependent than ever. For this reason, we must find friendly alternatives for the coming years. So, we have been seeing novel clean strategies of production known. The renewable energies have many advantages due to their availability, cleanness and power.

In this perspective, hydrogen is regarded as a promising energetic vector because of its clean status; it is used fuel cells, transport and industrial sector. However, hydrogen differs from other primary energetic sources in that it must be manufactured just before its use because it is difficult storage or liquefaction. Its in-situ production is necessary and even if it seems to be a promising solution, it remains difficult to put into practice. However, in view of the importance of this strategic product, both scientific and technological advances are being made, as it has become essential to control the new technologies producing renewable and sustainable energy. The latter is produced by various methods such as water electrolysis [1-4], coal gasification and essentially by reforming methane (steam reforming [5], oxidation and dry reforming [6]).

The aim of the present work is focused on the preparation of α-MoO_3 and hetero-junction α-5% MoO_3/ZnO prepared by impregnation method and their applications for the photochemical hydrogen evolution upon visible light. The hetero-junction is characterized by X-ray diffraction (XRD), Fourier transform infrared (FTIR), chemical analysis, diffuse reflectance spectra, scanning electronic microscopy (SEM) and photoelectrochemistry.

II. EXPERIMENTAL/THEORETICAL STUDY

The supported catalyst (5% MoO_3/ZnO) was synthesized by impregnation using $(NH_4)_6Mo_7O_{24}$, $4H_2O$ as precursor and ZnO as support.

The solides MoO_3 and (5% MoO_3/ZnO) were identified by X ray diffraction (XRD) using INEL XRG 3000 diffractometer with Cu Kα anticathode (λ= 0.15405 nm). The morphology was analyzed by scanning electronic microscopy (SEM) taken with apparatus of the type PHILIPS XL30-FEG. The Fourier transform infrared (FTIR) spectra were recorded with a FTIR ALPHA Bruckers spectrometer. The diffuse reflectance sprectrum of MoO_3 was plotted with a Specord 200 Plus spectrophotomoter. The solution was deaerated before and during the electrochemical test. The intensity potential J (V) characteristics were plotted Na_2SO_4, 0.1 M solution with a PGZ301 potentiostat (Radiometer analytical). The capacitance measurements were performed at a frequency of 10 kHz.

The photocatalysis was performed in a Pyrex reactor equipped with a cooling system; the temperature was regulated at 50 ± 1 °C.

Three stabilized tungsten lamps (200 W, Osram) were used for the illumination. The hydrogen was quantified volumetrically by water displacement caused by the pressure developed in the reactor.

*Corresponding author email: sarakila@yahoo.fr

After this step, the passivity command called IDA (Interconnection and Damping Assignment) is used. Consider the system (1), assumes that matrices $J_d(x) = -J_d^T(x)$, $R_d(x) = R_d^T(x) \geq 0$ are the desired matrices, $g^{\perp}(x)$ and function $H_d(x)$: $\mathcal{R}^n \longrightarrow \mathcal{R}$ that verify the partial differential equation.

$$g^{\perp}(x)f(x) = g^{\perp}(x)[J_d(x) - R_d(x)]\nabla H_d \quad (4)$$

∇H_d is such that

$$\bar{x} = argmin(H_d(x)) \quad (5)$$

Where $\bar{x}$ is a desired equilibrium to be stabilized, taking the control u as:

$$u = [g^T(x)g(x)]^{-1}g^T(x)\{[J_d(x) - R_d(x)]\nabla H_d - f(x)\} \quad (6)$$

Then the closed-loop dynamic takes the form:

$$\dot{x} = [J_d(x) - R_d(x)]\nabla H_d \quad (7)$$

$\bar{x}$ is then a stable equilibrium. It will be asymptotically stable if in addition, $\bar{x}$ is an isolated minimum of H_d(x) and the largest invariant set under the closed-loop dynamics (7) contained in
$\{x \in \mathcal{R}^n, \nabla H_d^T R_d(x) \nabla H_d = 0\}$

III. HYBRID FC SYSTEM STRUCTURE

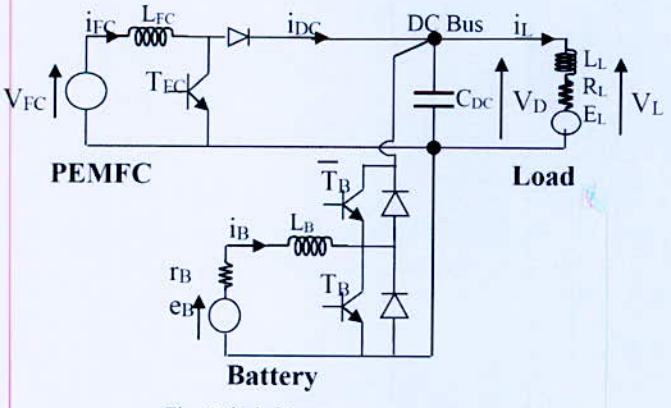

Fig. 1. hybrid system structure

The complete model of the hybrid system can be written by the following state space equations:

$$\begin{aligned}
\dot{x}_1 &= \frac{1}{L_{FC}}[V_{FC} - \mu_1 x_2] \\
\dot{x}_2 &= \frac{1}{C_{DC}}[\mu_1 x_1 - x_4 + \mu_2 x_3] \\
\dot{x}_3 &= \frac{1}{L_B}[e_B - r_B x_3 - \mu_2 x_2] \\
\dot{x}_4 &= \frac{1}{L_L}[E_L - R_L x_4 + x_2]
\end{aligned} \quad (8)$$

Where:

$x = [x_1, x_2, x_3, x_4]^T = [i_{FC}, V_{DC}, i_B, i_L]^T$

μ_1, μ_2 are the control of the FC boost converter, and the battery control of the buck-boost converter, respectively.

The natural energy function is:

$$H = \frac{1}{2}x^T Q x \quad (9)$$

With matrix Q= diag(L_{FC}, C_{DC}, L_B, L_L).

$\bar{x} = [\bar{x}_1, \bar{x}_2, \bar{x}_3, \bar{x}_4] = [\bar{x}_1, V_d, I_{ref}, \bar{\imath}_L]$

- If $I_{ref} = 0$, the controls law at the equilibrium are:

$$\bar{\mu}_1 = \frac{V_{fc}}{\bar{x}_2} \quad ; \quad \bar{\mu}_2 = \frac{e_B}{\bar{x}_2} \quad (10)$$

- If $I_{ref} \neq 0$, the controls law are:

$$\bar{\mu}_1 = \frac{V_{fc}}{\bar{x}_2} \quad ; \quad \bar{\mu}_2 = \frac{e_B - r_b I_{ref}}{\bar{x}_2} \quad (11)$$

In the following, the model is written using the new state space $\tilde{x}$, which is defined as the error between the state and its equilibrium value

$\tilde{x} = x - \bar{x}$.

The desired closed loop energy function is given by:

$$H_d = \frac{1}{2}\tilde{x}^T Q \tilde{x} \quad (12)$$

The error dynamic equations are expressed using the gradient of the desired energy as follows:

$$\dot{\tilde{x}} = [J - R]\nabla H_d + \xi \quad (13)$$

The desired equilibrium are noted as following:

*Corresponding author email: amel.benmouna@utbm.fr

$$\begin{bmatrix} 0 & \frac{-\mu_1}{L_{fc}C_{DC}} & 0 & 0 \\ \frac{\mu_1}{L_{fc}C_{DC}} & 0 & \frac{\mu_2}{L_BC_{DC}} & \frac{-1}{L_LC_{DC}} \\ 0 & \frac{-\mu_2}{L_BC_{DC}} & \frac{-r_B}{L_B^2} & 0 \\ 0 & \frac{1}{L_LC_{DC}} & 0 & \frac{-R_L}{L_L^2} \end{bmatrix} \begin{bmatrix} L_{fc}\tilde{x}_1 \\ C_{DC}\tilde{x}_2 \\ L_B\tilde{x}_3 \\ L_L\tilde{x}_4 \end{bmatrix} + \begin{bmatrix} \frac{1}{L_{fc}}(\tilde{\mu}_1 - \mu_1)\tilde{x}_2 \\ \frac{1}{C_{DC}}[(\mu_1 - \tilde{\mu}_1)\tilde{x}_1 - (\mu_2 - \tilde{\mu}_2)\tilde{x}_3] \\ \frac{1}{L_B}(\tilde{\mu}_2 - \mu_2)\tilde{x}_2 \\ 0 \end{bmatrix}$$

$J-R$ $\quad \nabla H_d$ $\quad \zeta$

$\nabla H_d = [L_{FC}\tilde{x}_1, C_{DC}\tilde{x}_2, L_B\tilde{x}_3, L_L\tilde{x}_4]^T$

$J(\mu) = -J^T(\mu)$ is a skew symmetric matrix defining the interconnection between the variables and $R = R^T \geq 0$ is symmetric positive semi definite matrix defining the damping of the system.

With control laws which are chosen as:

$$\begin{cases} \mu_1 = \bar{\mu}_1 \\ \mu_2 = \bar{\mu}_2 - r\tilde{x}_3 \end{cases} \quad (15)$$

Where r is a positive design parameter.

IV. PROPOSED SCENARIO

The major objectives to achieve are:

- Voltage control of the load and therefore the voltage of DC bus through the command of the two DC-DC converters.
- Ensure that the battery provides the power required during the transient phases.
- Supply the load by the battery when the FC is not able, for example in the system start up or under limitation.
- The energy management strategy is based on the control of the battery current to a desired battery current reference.
- This reference can be imposed regarding different criteria (battery SOC, FC state of heath, hydrogen level, start-up, load transient power,...).

The control objective is to control the battery current to its reference. In this work, a power source is used to emulate the FC role.

V. SIMULATION RESULT

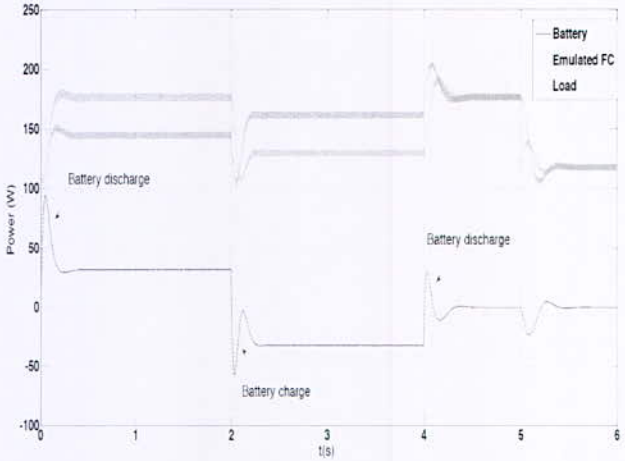

Fig. 2. Powers of different HEV source

VI. EXPERIMENTAL RESULT

The test bench is developed at State Key Laboratory of Industrial Control Technology, Zhejiang University (Hangzhou, China). The experimental is illustrated in the Fig.3 and the objective is to valid the correct operation of the chosen control strategy, study the role of used sources and the distribution control of the power between different elements.

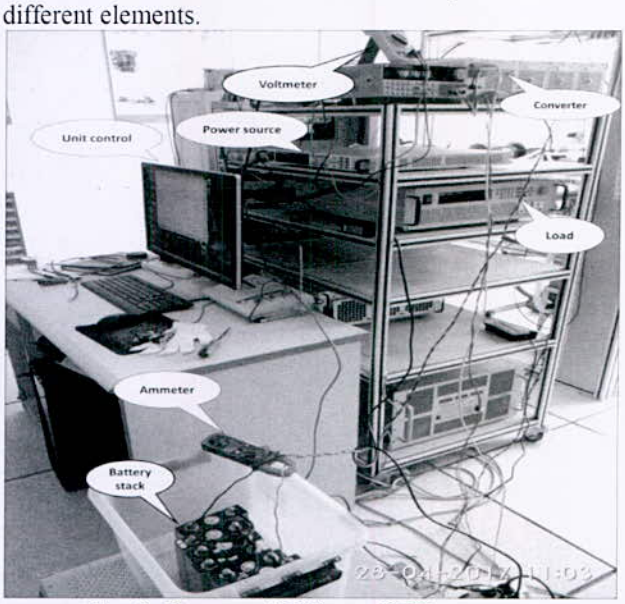

Fig. 3. Powers of different HEV source

The used test bench in this study has been built by authors (see Fig.5).

This test bench makes it possible to emulate energy exchanges within a vehicle on a reduced scale. The test bench is composed of:

- Power source emulating a FC role.
- Battery stack consists of 6 cells of 3.2 V connected in series (36Ah each).

*Corresponding author email: amel.benmouna@utbm.fr

- An electrical charge emulating the power demand.
- Two DC / DC converters for the power source and the battery.
- Ammeters to measure the current
- Voltmeters to measure the voltage.
- Labview software with DAQ MAX Acquisition system.

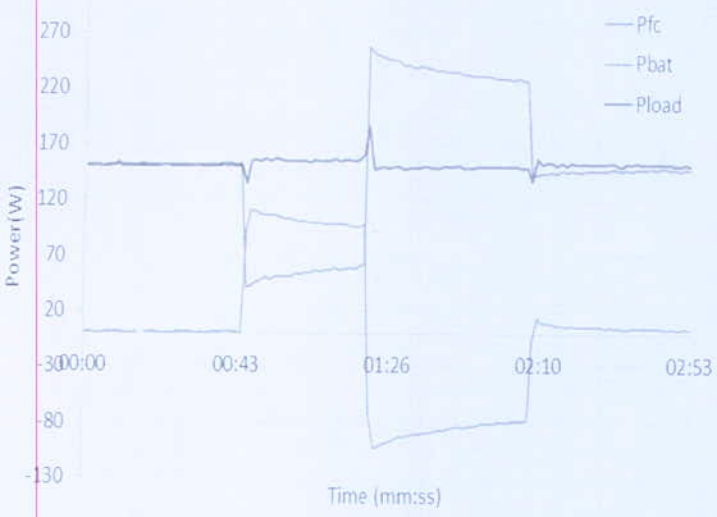

Fig. 4. Experimental results of powers using IDA-PBC technique

VII. CONCLUSION

A studied hybrid system is composed of a power source emulating the FC as primary source and battery. A control strategy along with the energy management is developed using the passivity control. For this purpose, this paper introduces the system mathematical modeling. The IDA-PBC is used to design a smart nonlinear energy management control. The experimental and simulation results show the correct and the efficacy of the proposed control. This is clearly demonstrated in the obtained curve through the simulation and practical results. The obtained results reflect exactly the proposed scenario. The other results will be given in an extended journal version.

ACKNOWLEDGMENTS

The authors gratefully acknowledge the College of Control Science and Engineering, Zhejiang University (Hangzhou, China), where the practical work has been carried.

Parameters	Definition
L_{FC}	FC inductance
V_{FC}	FC voltage
V_d	Desired DC bus voltage
C_{DC}	Converter capacity
L_B	Battery inductance
I_{ref}	Battery current reference
e_B	f.e.m of battery
r_B	internal resistance of battery
L_L	load inductance
E_L	f.e.m of load
R_L	resistance of load
r	damping parameter
P_{FC}	FC power
P_{Batt}	battery power
P_{load}	load power

REFERENCES

[1] X. Zeng and J. Wang, "A Parallel Hybrid Electric Vehicle Energy Management Strategy Using Stochastic Model Predictive Control With Road Grade Preview," *IEEE Trans. Control Syst. Technol.*, vol. 23, no. 6, 2015.

[2] A. Benmouna, M. Becherif, D. Depernet, F. Gustin, H. S. Ramadan, and S. Fukuhara, "Fault diagnosis methods for Proton Exchange Membrane Fuel Cell system," *Int. j ournal Hydrog. energy*, vol. 42, pp. 1534–1543, 2017.

[3] C. Xia and C. Zhang, "Power management strategy of hybrid electric vehicles based on quadratic performance index," *Energies*, 2015.

[4] O. Kraa *et al.*, "Energy Management of Fuel Cell/ Supercapacitor Hybrid Source Based on linear and sliding mode control," *Energy Procedia*, vol. 74, pp. 1258–1264, 2015.

[5] A. Kraa, O. Ghodbane, H. Saadi, R. Ayad, M. Y. Becherif, M. Bahri, M. Aboubou, "Experimental validation of a dual loop control of two phases interleaved boost converter for fuel cell applications," *J. Fundam. Appl. Sci.*, vol. 8, no. 2, pp. 327–345, 2016.

[6] M. Becherif, *Passivity-Based Control of Hybrid Sources: Fuel Cell and Battery*, vol. 39, no. 12. IFAC, 2006.

*Corresponding author email: amel.benmouna@utbm.fr

L'Effet Physique et Chimique de Remplacement de N_2 de l'Air par le CO_2 d'une Flamme de Diffusion à Contre-Courant d'un Biogaz Hydrogéné dans un Régime sans Flamme

A. Hadef[1,*], A. Mameri[1], F. Tabet[2] and Z. Aouachria[3]

[1]Faculté des Sciences et Sciences appliquées, Université d'Oum El Bouaghi 04000 Algerie.
[2]DBFZ, Torgauer Straße 116, D-04347 Leipzig, Germany.
[3]Laboratoire de Physique Energétique Appliquée, Université de Batna1 05000 Algerie.

Résumé—**Lorsqu'on remplace une quantité d'azote de l'air par le CO_2, la structure interne d'une flamme de diffusion laminaire est affectée par trois mécanismes : la variation du transport des propriétés thermiques du mélange, l'effet chimique de CO_2, ainsi que le transfert par rayonnement qui est amélioré par le CO_2. Le présent papier consiste à une analyse numérique de l'effet d'addition de H_2 dans le combustible et le CO_2 dans l'air.**
Une attention particulière est portée aux effets thermiques et chimiques de CO_2 dans un régime sans flamme, sur la structure interne d'une flamme de diffusion laminaire à contre-courant d'un biogaz et le comportement des émissions polluantes telles que le CO, le CO_2 et le NO, ainsi que le précurseur de particule de suie C_2H_2, sont numériquement étudiés avec un taux d'étirement de flamme a=200 s^{-1}.
Le programme Oppdiff de Chemkin avec une cinétique de la combustion décrite par le mécanisme Grimech 3.0 est adopté.

Mots clés—Effets physiques et chimiques de CO_2, combustion sans flamme, addition du CO_2.

I. INTRODUCTION

L'utilisation du régime pauvre conduit à une faible production des espèces polluantes mais avec une flamme instable qui est néfaste pour les applications industrielles, pour remédier à ce problème, l'hydrogène connu par son grand pouvoir calorifique et sa réactivité est ajoutée aux mélanges pauvres. Une autre approche utilise un combustible à faible pouvoir calorifique qui est le biogaz, pour augmenter son efficacité énergétique. Des études récentes ont montré que l'ajout de l'hydrogène au biogaz est aussi bénéfique que son ajout aux mélanges pauvres d'hydrocarbures [1]. Sur le plan environnemental la volonté de réduction des polluants amène les spécialistes dans la conversion d'énergie à minimiser la production des espèces polluantes par la dilution de l'oxydant par les produits de combustion ré circulant parmi lesquels CO_2 et H_2O [2], qui jouent un rôle dominant, en matière de quantité et de propriétés physico-chimiques sur la stabilisation de la flamme et la qualité de la combustion dans les foyers.

Un biogaz BG75(75% CH_4+25% CO_2) enrichis par l'hydrogène de 20% , sous une température de 300 K, mélangé avec de l'air préchauffé de 1200K et dilué par le dioxyde de carbone 0% à 30% qui est substitué de la quantité d'azote de l'air qui se réduit de 79% à 49% (en volume) suivant un régime de combustion à faible teneur en oxygène 02% à 10% (en volume), dans une configuration géométrique à jet opposé d'une flamme de diffusion laminaire est inscrit ce travail pour étudier l'impact de tous ces paramètres sur la structure de la flamme et les espèces polluantes.

II. CONFIGURATION GEOMETRIQUE ET STRATEGIE DE CALCUL

La géométrie utilisée se compose par deux jets opposés d'une distance D=1.4cm, l'un injectant le combustible et l'autre le comburant. Cette configuration permet de simplifier d'une part les équations du phénomène qui deviennent unidimensionnelles et d'autre part d'obtenir une flamme plane permettant la caractérisation de sa structure.

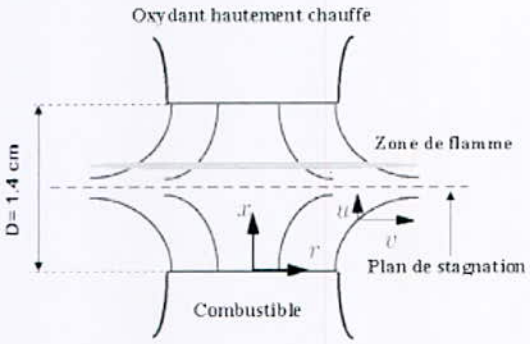

Fig. 1. Configuration géométrique d'un jet opposé

Le programme Oppdiff de Chemkin établit par Kee et al. [3] est utilisé pour la résolution de l'équation de conservation de la quantité de mouvement ''Eq.1'' et l'équation de la conservation d'énergie ''Eq.2'' et d'espèce ''Eq.3''.

$$H - 2\frac{d}{dx}\left(\frac{FG}{\rho}\right) + \frac{3G^2}{\rho} + \frac{d}{dx}\left[\mu\frac{d}{dx}\left(\frac{G}{\rho}\right)\right] = 0 \qquad (1)$$

$$\rho u\frac{dT}{dx} - \frac{1}{c_p}\frac{d}{dx}\left(\lambda\frac{dT}{dx}\right) + \frac{\rho}{c_p}\sum_k c_p V_k Y_k\frac{dT}{dx} + \frac{1}{c_p}\sum_k h_k\dot{\omega}_k - \frac{\dot{q}_r}{c_p} = 0 \qquad (2)$$

$$\rho u\frac{dY_k}{dx} + \frac{d}{dx}\left(\rho Y_k V_k\right) - \dot{\omega}_k W_k = 0 \ ; \text{k=1,.....K} \qquad (3)$$

*Corresponding author email: hadef_am@yahoo.fr

Avec $$G(x) = \frac{dF(x)}{dx} \quad (4)$$

L'équation d'état de gaz parfait s'écrit :

$$P = \rho R_u T \sum_k \frac{Y_k}{W_k} \quad (5)$$

$\dot{\omega}$ et W_k sont respectivement le taux de production et la masse molaire des espèces k, dans l'équation (2)

Les conditions aux limites pour le fuel (F) et l'oxydant (O) sont:

$$x = 0 : F = \frac{\rho_F u_F}{2}, G = 0, T = T_F, \rho u Y_k + \rho Y_k V_k = (\rho u Y_k)_F$$
$$x = +L : F = \frac{\rho_O u_O}{2}, G = 0, T = T_O, \rho u Y_k + \rho Y_k V_k = (\rho u Y_k)_O \quad (6)$$

Les pertes par rayonnement thermique des espèces CO_2, H_2O, CO, et CH_4 sont modélisés comme un corps optique mince sont pris en compte [4]:

$$\dot{q} = -4\sigma K_P (T^4 - T_\infty^4) \quad (7)$$

$$K_P = \sum_{i=1}^{4} P_i K_i \quad i = CO_2, H_2O, CO, CH_4 \quad (8)$$

où σ est la constante de Stefan-Boltzmann, T et T_∞ sont respectivement la température de la substance rayonnante et celle milieu ambiant, P_i pression partielle, K_i coefficient moyen d'absorption de l'espèce i.

La cinétique de la combustion est décrite par le mécanisme GRI Mec 3.0 [5], qui est composé de 325 réactions impliquant 53 espèces.

III. RESULTATS ET DISCUSSION

1. *Temperature relative de flamme*

La température relative de la flamme [6] est introduite pour illustrer le rayonnement de la zone de combustion:

$$f = \frac{T_{nonad} - T_{ad}}{T_{nonad}} \quad (9)$$

où, $T_{non\ ad}$ et T_{ad} sont les températures de flamme sans et avec rayonnement respectivement.

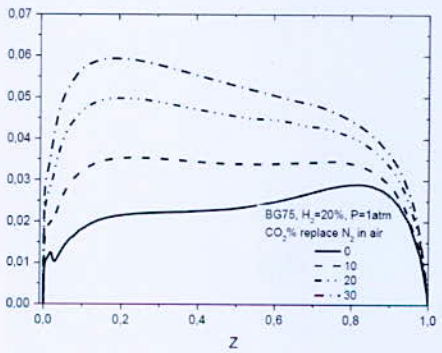

Fig. 2. Effet de CO_2 su la température relative de flamme

La Fig. 2, montre le profil de la température relative de combustion d'un biogaz BG75 dopé avec 20% d'hydrogène à la pression atmosphérique de 1 atm, avec une teneur d'oxygène égale à 4 % et une quantité de CO_2 qui remplace le N2 de l'air le CO_2 , où cette dernière varie de 0% à 30%, on constate que l'ajout du dioxyde de carbone augmente la température relative puisqu'il substitue le CO_2, ce qui est une bonne espèce rayonnante.

2. *Structure de la région de combustion*

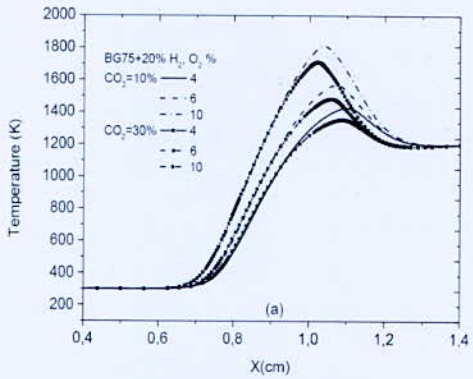

Fig. 3. Effet de l'O_2 et le CO_2 sur la variation de la température de flamme

La Fig. 3, illustre l'évolution de la température à la pression P=1atm, pour le biogaz BG75 avec 20% d'hydrogène et plusieurs concentrations d'oxygène et de l'azote remplacé par le CO_2 dans l'air. On voit que la température de la flamme est fortement dépendante de la teneur d'oxygène et de l'ajout du CO_2 dans l'oxydant, pour une fraction molaire d'oxygène $Y_{O2} = 4\%$ la température atteint son maximum T = 1400 K à la distance X= 1.10 cm et pour $Y_{O2} = 10\%$; la température augmente pour atteindre une valeur de 1800 K avec un déplacement X= 1.00 cm vers le côté de combustible. Pour e remplacement de N_2 par le CO_2, la température diminue d'une manière constante pour les deux concentrations de CO_2 (10% et 30%).

La fraction molaire de l'espèce OH est représentée dans la Fig. 4(a), cette espèce est très affectée par la réduction de la quantité d'oxygène, ainsi que la dilution par le CO_2 qui remplace la teneur d'azote dans l'oxydant qui déplace le pic maximal de l'espèce sur le côté de combustible relativement à la température. L'effet de CO_2 dans un régime sans flamme (avec 4% O_2) est moins important que dans un régime conventionnel (avec 10% O_2). La fraction molaire de NO, Fig. 4(b), est considérablement réduite suivant la diminution d'oxygène et l'augmentation de CO_2 dans le flux de l'oxydant, elle passe de $3.10E^{-6}$ (10% d'O_2) à $1.25E^{-5}$ (4% d'O_2) pour une teneur de 10 % de CO_2, et pour 30% de CO_2 la réduction passe de $5.75E^{-5}$ à $1.25E^{-6}$.

*Corresponding author email: hadef_am@yahoo.fr

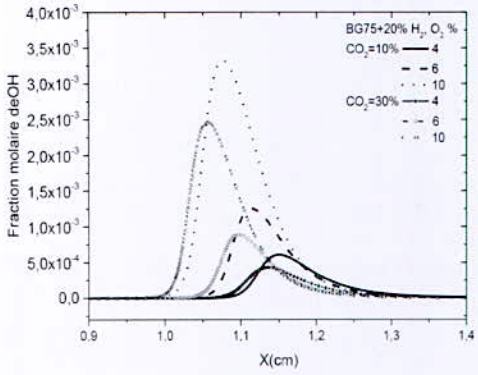

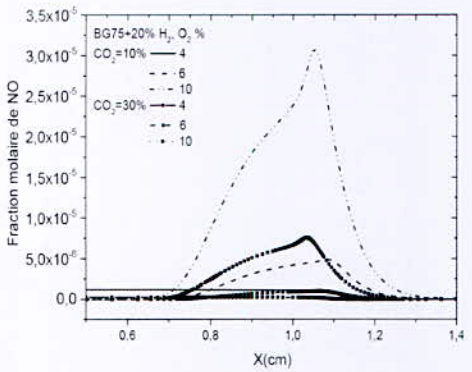

Fig. 4. Effet de l'O_2 et le CO_2 sur la variation de des espèces OH et NO

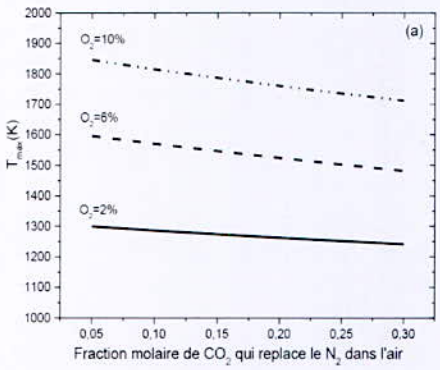

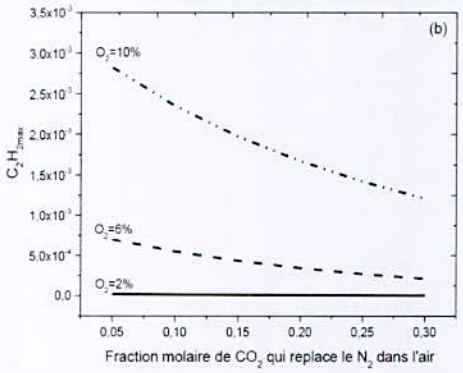

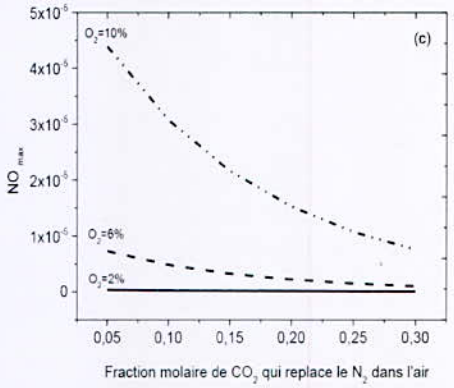

Fig. 5. Variation de Température et fraction molaire maximales des espèces en fonction de N_2 remplacé par le CO_2 dans l'oxydant

La Fig. 5(a), illustre la variation de maximum de température pour trois teneurs d'oxygène en fonction de la quantité de CO_2 remplacé dans l'oxydant qui est substitué de la quantité de N_2 contenue dans l'air, on remarque la température est très affecté par la réduction de la teneur d'oxygène, mais elle est moins induite par la quantité de CO_2 ajouté.

L'espèce C_2H_2 est un précurseur de production de suie alors que les radicaux OH et O peuvent favoriser l'oxydation des suies et de réduire leur formation suivant les réactions élémentaires suivantes :

$C_2H_2 + O \Leftrightarrow H + HCCO$ et $O + C_2H_2 \Leftrightarrow CO + CH_2$,

l'augmentation du taux de C_2H_2 est très significative par l'augmentation de l'oxygène, mais sa réduction est très affecté par la dilution par le CO_2 Fig. 5(b) d'un taux de 54% pour une teneur de 6% d'O_2 et 69% pour 10% d'O_2.

Lorsque la quantité d'oxygène démunie dans l'oxydant le monoxyde d'azote chute d'une manière remarquable, il est complètement absent pour une teneur de 2% d'O_2, alors que le remplacement de N_2 par le CO_2, la réduction d'une teneur de 6% d'O_2 est moins importante que 10% d'O_2 Fig. 5(c).

3. *Effet thermique et chimique du CO2 ajouté dans le flux d'air*

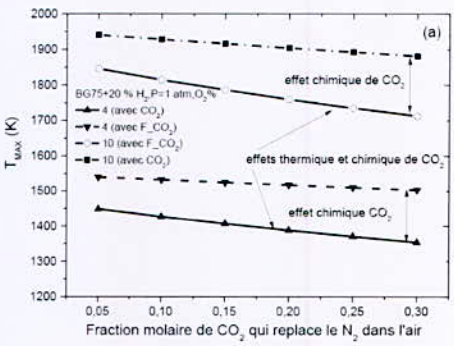

*Corresponding author email: hadef_am@yahoo.fr

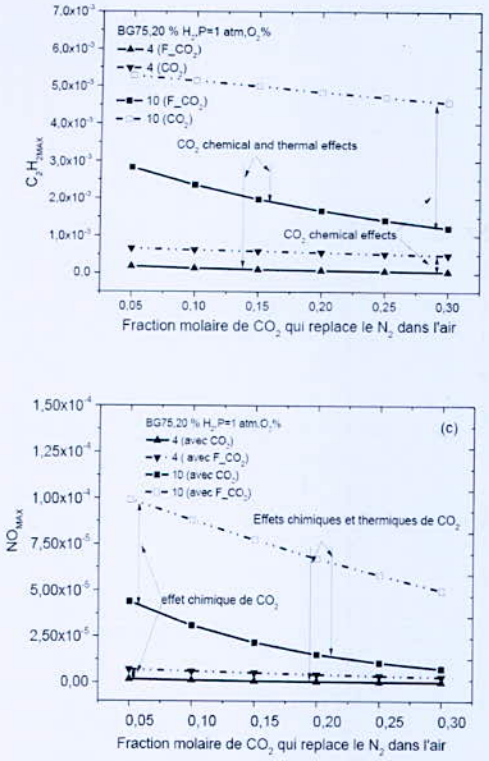

Fig. 6. L'effet chimique et thermique de CO_2 sur la variation de température de flamme et la fraction molaire maximales de CO, C_2H_2 et NO en fonction de CO_2 dans l'oxydant

La Fig. 6, montre que les effets thermiques et chimiques de l'addition de CO_2 au flux d'oxydant réduisent la température maximale. Les effets chimiques de l'addition de CO_2 augmentent d'un taux de 10 % dans une teneur de 4% d'oxygène, alors que le taux est 6 % pour une teneur de 10% d'O_2.

Le taux de production de la fraction molaire maximale de C_2H_2 est très affecté par l'augmentation de la quantité d'oxygène dans l'oxydant, donc le régime de combustion sans flamme réduit la production de C_2H_2 d'une manière très importante, où les effets chimiques et thermiques n'influe pas sur la formation de l'espèce, alors que dans une teneur de 10% d'O_2 l'effet chimique augmente relativement à l'ajout du CO_2 dans l'air, Fig. 6(b).

L'effet chimique du CO_2 sur le maximum de la fraction molaire de NO est représenté par la Fig. 6(c) pour les deux teneurs en oxygène, 4% et 10%. Les effets chimiques et thermiques de CO_2 ne réduisent pas le maximum de la fraction molaire de NO avec une teneur d'oxygène égale à 4%, puisque que cette dernière est très négligeable, c'est l'avantage du régime de combustion sans flamme, mais avec la teneur de 10% en oxygène les effets combinés de l'addition de CO_2 réduisent le maximum de fraction molaire de NO progressivement et relativement au pourcentage de dilution par l'addition du CO_2 dans l'oxydant.

III. CONCLUSION

L'augmentation de l'oxygène induit des augmentations importantes de température et des espèces, La température de la flamme se réduit par la quantité de CO_2 ajouté à coté de l'air $CO_2 + H = CO + OH$, l'effet chimique de CO_2 supprime l'étape de réaction $H + O_2 = O + OH$ pour la consommation d'atome H, en conséquence, le taux de réaction de ramification de la chaîne principale est supprimé.

REFERENCES

[1] T. Leung and I. Wierzba, 'The Effect of Hydrogen Addition on Biogas Non-Premixed Jet Flame Stability in a Co-Flowing Air Stream', International Journal of Hydrogen Energy, Vol. 33, N°14, pp. 3856 – 3862, 2008.

[2] J.Park, SG.Kim, KM.Lee, TK.Kim. 'Chemical effect of diluents on flame structure and NO emission characteristic in methane–air counter flow diffusion flame. International Journal of Energy Research, Vol.26, pp.1141-1160; 2002.

[3] R.J. Kee J, J.A.Miller, G.H. Evans and G.A.Dixon-Lewis.' Computational model of the structure and extinction of strain, opposed flow, premixed methane-air flames', Twenty-Second Symposium (International) on Combustion, The Combustion Institute,pp1479-1494,1988.

[4] A.Mameri , F.Tabet and A.Hadef,'MILD combustion of hydrogenated biogas under several operating conditions in an opposed jet configuration' article in press,International Journal of Hydrogen Energy, http://dx.doi.org/10.1016/j.ijhydene.2017.04.273 (2017).

[5] Gregory P. Smith, David M. Golden, Michael Frenklach, Nigel W. Moriarty, Boris Eiteneer, Mikhail Goldenberg, C. Thomas Bowman, Ronald K. Hanson, Soonho Song, William C. Gardiner, Jr., Vitali V. Lissianski, and Zhiwei Qin http://www.me.berkeley.edu/gri_mech/ ...

[6] J.Park, DS. Bae, MS. Cha, JH. Yun, Keel.SI, HC.Cho, et al. 'Flame characteristics in H2/CO synthetic gas diffusion flames diluted with CO2: effects of radiative heat loss and mixture composition', International Journal of Hydrogen Energy, Vol.33, N° 23, pp 7256-7264.2008.

[7] V.Chernov, M.J. Thomson, S.B.Dworkin,N.A Slavinskaya and U.Riedel, 'Soot formation with C1 and C2 fuels using an improved chemical mechanism for PAH growth'. Combust and Flame Vol.161, N°2, pp, 592-601. 2014.

*Corresponding author email: hadef_am@yahoo.fr

La Transition Vers une Economie de l'Hydrogène

S. Cherifi[1*] and M. Haddad[2]

[1*] Faculté des sciences économiques, Université d'Alger3, Alger, Algérie.
[2]Faculté des sciences de gestion, Université d'Alger3, Alger, Algérie.

Résumé—**Depuis peu, l'hydrogène s'invite dans le grand débat de la transition énergétique, les combustibles fossiles origines de cette transition sont par nature épuisable et la principale cause du réchauffement climatique de la planète. Aujourd'hui ce combustible provenant des énergies renouvelables apparait comme étant la solution du futur d'où vient l'internet de l'abordé de tous les côtés (technique, économique, environnemental..).**
L'objectif de la présente étude consiste à analyser et démontrer les défis et les avantages économiques vers une transition d'hydrogène. Par conséquent, notre étude parvenu au résultat que la transition vers une économie de l'hydrogène repose sur la création d'un cadre propice à la recherche et le développement des technologies de l'hydrogène, laissant celui-ci concurrencé les combustibles fossiles essentiellement en matière de coût et de risque. Seule donc les pays arrivant à déterminer la technologie appropriée, auront une avance considérable qui leur garantira un développement durable.

Mot clés—Hydrogène, Combustibles Fossiles, Transition Energétique, Energies Renouvelables, Développement Durable.

I. INTRODUCTION

La transition énergétique s'avère aujourd'hui une nécessité absolue cela afin de satisfaire les besoins croissant en énergie d'un coté, mais aussi de participer à la préservation de la planète. En effet, la dépendance de la société moderne en vers les énergies fossiles dont les réserves sont limité, ne cesse d'augmenter, causant ainsi un problème environnemental majeur celui d'augmentation massive d'émission du gaz de dioxyde de carbone(Co_2), ce dernier à contribuer à l'effet de serre et par conséquent au réchauffement global de la terre.

Pour y parvenir au challenge de la transition énergétique, il parvient de mettre en œuvre des efforts de façon concertée. Dans ce contexte, l'hydrogène offre un important potentiel pour surmonter les nombreux obstacles sur le chemin d'une économie bas-carbone résiliente.

Fut reconnu comme une substance distincte en 1766 par Henry Cavendish. Antoine Lavoisier et nommé par la suite de la part du chimiste français Antoine Laurent de Lavoisier [1]. L'hydrogène est Défini comme étant l'élément le plus simple, le plus léger et le plus abondant de l'univers, et est composé uniquement d'un électron et d'un proton, il s'agit donc du premier élément du tableau périodique [2].

À l'état normal, c'est-à-dire gazeux, l'hydrogène est inodore, insipide, incolore et non toxique, élément se présente rarement à l'état isolé c'est pourquoi il est appelé un vecteur énergétique et non pas une source, car il est toujours fortement lié, principalement à l'oxygène et au carbone. Il faut rompre l'une ou l'autre de ces liaisons si l'on veut disposer d'hydrogène en tant que matière première ou combustible.

Environ 96% de l'hydrogène est actuellement produit a partir des hydrocarbures (charbon, pétrole, gaz naturelle d'une part dominante) se qui laisse la problématique du rejet de gaz carbonique dans l'atmosphère omniprésente. Tant dis que 4% d'hydrogène est produit à travers la technique de l'électrolyse de l'eau qui consiste à décomposé l'eau en hydrogène et en oxygène en appliquant un courant électrique. Pour que cette technique ne soit pas polluante l'électricité consommée, doit être produite à partir d'énergies renouvelables [3]. (Fig. 1)

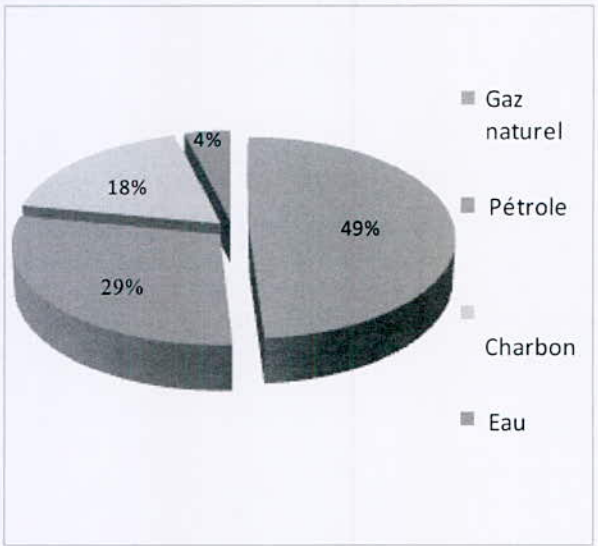

Fig. 1. Répartition des modes de production d'hydrogène [3]

Bien que l'hydrogène se présente comme étant le combustible du futur, on la déjà utilisé au passé, À la fin du XIXe siècle, l'hydrogène était le combustible indispensable employé à la fois pour l'éclairage dans les lampes et comme gaz de ville, et même pour faire rouler certaine voiture, mélangé à l'oxyde de carbone. Avec l'avènement de l'industrie du pétrole au XXe siècle, il n'est plus utilisé pour la production d'énergie (sauf dans

* Email: cherifisarah9393@gmail.com

la propulsion des fusées). Mais depuis quelques années l'hydrogène fait un retour en force, cela en l'expérimentant sur des voitures, des bus, afin de parvenir, au futur à l'utiliser dans des moteurs, type moteur à explosion, et permettra de fournir de l'électricité grâce à la pile à combustible. L'hydrogène présente ainsi un double intérêt :

- être un carburant.

- être un moyen de stocker l'électricité. En effet, si l'on ne sait pas stocker efficacement l'électricité, l'hydrogène par contre peut être stocké et utilisé dans la pile à combustible où il permet de produire de l'électricité n'importe où, n'importe quand. Cette propriété ouvre de multiples possibilités d'application :

- Secteur du transport : les véhicules électriques alimentés par une pile à combustible n'émettront plus de gaz à effet de serre ; il est a noté aussi que Leur autonomie dépasse actuellement 500 km et ils ont un temps de rechargement de l'ordre de 3 à 5 minutes [4], équivalent à celui d'un véhicule à moteur thermique. Aujourd'hui, de grands constructeurs automobiles (Daimler, Hyundai, Nissan, Ford, ...) sont sur le point de proposer des automobiles à hydrogène sur le segment haut de gamme avant peut-être de descendre sur l'échelle des segments ; ils tirent ainsi parti des travaux réalisés depuis plusieurs années et du retour d'expérience des premières réalisations

- dans le domaine des appareils portables (téléphone, ordinateur...) la pile augmentera leur autonomie ;

- dans le secteur de l'habitat comme source de chaleur et d'électricité ;

- dans le domaine des énergies renouvelables, sur les sites isolés, en complément du solaire ou de l'éolien dont le fonctionnement est forcément intermittent ;

- dans la fourniture de l'énergie par combustion (propulsion des fusées) et en entrant dans la composition de gaz de synthèse pour obtenir des carburants plus performants.

Le principal frein à l'investissement en hydrogène est les coûts élevés. Aucune entreprise privée n'investira dans une initiative commerciale portant sur l'hydrogène à moins d'être convaincu qu'il pourra concurrencer les combustibles existants et engendrer des bénéfices. Mais l'hydrogène est encore loin d'être compétitif dans la plupart de ses applications [2], cependant cela pourrait changer avec des mesures d'incitations gouvernementales émise à ce niveau consistant essentiellement :

- Incitation à la Recherche ET développement (R&D) dans le domaine des technologies de l'hydrogène qui pourrait être bénéfique à l'accomplissement des progrès technologiques nécéssaire.

- encourager l'investissement en infrastructure hydrogène et l'adoption de ce combustible une fois les technologies jugées économiques.

Le coût n'est toutefois pas la seule entrave à l'investissement. Comme pour toute technologie nouvelle, l'hydrogène pourrait se retrouver confronté à l'absence d'un marché dissuade l'investissement, ce qui empêche le marché de se développer. En d'autres termes, pourquoi concevoir des voitures à hydrogène alors qu'il n'existe aucun réseau de distribution et pourquoi concevoir un réseau de distribution alors qu'il n'existe aucune voiture à hydrogène ? Le développement de l'hydrogène sur le marché est donc freiné par un attentisme simultané de la demande et de l'offre. Les investisseurs potentiels dans l'infrastructure ne sont pas incités à engager des sommes considérables en capital avant la formation de la demande pour l'hydrogène ; et les consommateurs n'adhèrent pas à la nouvelle technologie sans avoir la garantie d'un confort identique à celui de la technologie conventionnelle. Il s'agit du dilemme de «L'œuf et de la poule» [5]. Ce dilemme est connu dans la littérature anglo-saxonne sous le terme « chicken-or-egg stasis» et se caractérise par : l'incompatibilité entre la nouvelle technologie et l'infrastructure existante, ce qui empêche la formation du marché, L'utilisation de l'hydrogène ne connaîtra par conséquent d'essor qu'une fois atteint le seuil minimum pour réaliser des économies d'échelle. Le marché doit être suffisamment important pour démontrer aux usagers et fournisseurs de combustibles potentiels que l'hydrogène constitue une alternative sûre, fiable et économique aux combustibles conventionnels. C'est-à-dire plus il y aura de véhicules à pile à combustible sur les routes, plus les autres propriétaires de véhicules seront confiants à l'idée de changer de carburant.

La mise en place donc de l'infrastructure légèrement en avance par rapport à la demande peut être la clé du dilemme de « l'œuf et de la poule », Il faudrait par la suite, développer rapidement le réseau de ravitaillement en hydrogène, Auprès des propriétaires de véhicules, un manque de stations constituerait un frein considérable à l'adhésion au passage à L'hydrogène, même en cas d'incitation financière en ce sens.

Une fois les obstacles précédents seront levés, L'hydrogène étant produit localement grâce à l'énergie renouvelable, aiderait à réduire les importations de combustibles fossiles et par la même permettra d'améliorer la balance commerciale. Toute en Permettant d'assurer le stockage de l'électricité excédentaire, et favorisant par conséquent le développement des productions électriques renouvelables nationales.

C'est ainsi que le développement des technologies liées à l'hydrogène, la construction et l'exploitation d'installations utilisant ces procédés, créera un nombre d'emplois important et procurera des opportunités intéressantes d'exportation de ces technologies.

* Email: cherifisarah9393@gmail.com

De nombreux pays ont compris l'importance de l'hydrogène comme vecteur énergétique, tels que le Japon, l'Allemagne ou les Etats-Unis qui investissent aujourd'hui massivement dans son développement : mise en service de plus de 100 000 piles à combustible pour cogénération résidentielle au Japon, plus de 5 000 chariots élévateurs en service aux Etats-Unis, 50 stations hydrogène pour véhicules en cours de déploiement en Allemagne, mais également au Danemark, en Suède, au Royaume-Uni, aux Pays-Bas, au Canada... De même les vecteurs hydrogène et méthane de synthèse (Power to Gas), font l'objet de plusieurs projets de démonstration à échelle industrielle en Allemagne et en Italie [6].

Les économies en voie de développement compte à elles, ont autant à gagner d'une transition vers l'économie de l'hydrogène que les économies industrialisées, car ces pays ont tendance à souffrir d'avantage de la pollution et à consommé l'énergie d'une manière inefficace et excessive généralement généré de sources fossiles. Pourtant, la transition commencera probablement plus tard dans la plupart des nations en développement, car elles sont moins à même de participer à la recherche et développement et de financer les aides nécessaires au lancement du processus. Alors c'est au pays riche et développé donc d'être prêt à soutenir les économies en développement dès que l'hydrogène deviendra une solution énergétique viable, dans l'intérêt général. Les organisations internationales et non gouvernementales ont un rôle important à jouer afin d'aider les pays à créer un cadre basé sur le marché au sein duquel l'hydrogène et les autres technologies énergétiques émergentes pourraient rivaliser avec les systèmes énergétiques conventionnels.

II. CONCLUSION

A la fin on peut dire que la transition vers l'économie de l'hydrogène repose sur la création des pays, d'un cadre propice à la recherche et le développement des technologies d'hydrogène laissant celui-ci concurrencé les énergétiques fossiles essentiellement en matière de coût et de risque. Il est donc probable que les pays qui arriveront en premier à des bons choix technologiques auront une avance considérable qui leur garantira un développement économique durable et non rattrapable à court terme.

REFERENCES

[1] C. Nacerddine, Perspectives de Développement de la Production Industrielle de L'hydrogène dans le Sud Algérien A Partir des Energies Renouvelables, Thèse de Doctorat, Département de Génie des Procèdes, Université KASDI MERBAH Ouargla, juin, 2014.

[2] Report Of United Nations Environnent Programme, "L'Economie de l'Hydrogène : Une Etude Générale," France, 92-807-2685-4, 2006. disponible sur le site : http://www.unep.fr

[3] P. BOUCLY, L'hydrogène, vecteur de la transition énergétique, Rapport de l'Association Française d'hydrogène et de Piles A Combustible, Nov.2016.

[4] Hydrogen council disponible sur le site : http://hydrogencouncil.com/

[5] N. Bento, La Transition Vers Une Economie de l'Hydrogène : Infrastructures Et Changement Technique, Thèse de Doctorat, Dept. Economie, Stratégies, Entreprise, Université de Grenoble, Mars, 2010.

[6] P. Mauberger, et autres, l'hydrogène, essentiel aujourd'hui, indispensable demain, Bulletin du Droit de l'Environnement Industriel, Lamy Revue, Vol : 60, Déc.2015.

* Email: cherifisarah9393@gmail.com

Electrodeposited Cobalt Sulfide for the Production of Hydrogen

H. Cherfouh[1*], A. Khellaf[2] and B. Marsan[1*]

[1*]Département de chimie, Université du Québec à Montréal, C.P.8888, Succ. Centre-ville, H3C 3P8, Montréal, Québec, Canada.

[2]Centre de Développement des Energies Renouvelables, CDER, BP. 62 Route de l'Observatoire Bouzaréah, 16340, Alger, Algérie.

Abstract—This work aims at studying cobalt sulfide (CoS) as a (photo)catalyst for the production of hydrogen from an aqueous medium. CoS possesses remarkable electrocatalytic properties and this material is much less expensive than platinum which has a limited earth abundance. CoS films were prepared by electrodeposition on a conductive glass substrate (FTO: fluorine-doped tin oxide)/glass) combining several experimental conditions[1], including the deposition method (pulse, galvanostatic and potentiostatic deposition). Scanning electron microscopy (SEM) analysis was used not only to evaluate the film morphology and porosity, but also to appreciate its homogeneity onto the FTO surface. Chemical analysis of the CoS films was determined by energy-dispersive X-ray spectroscopy (EDX), and the presence of oxygen was also verified. Absorbance and transmission properties of CoS films were determined by UV-Visible spectroscopy and transmission measurements, respectively. The electrochemical behavior of CoS electrodes in aqueous medium containing K_2SO_4 was studied by carrying out potentiodynamic (from -0.5 V to -2.5 V vs. Ag/AgCl) and electrochemical impedance spectroscopy measurements. Platinum was used as the counter-electrode and the resulting current was measured. The next step will consist in quantifying the volume of hydrogen produced, and in carrying out numerical simulation studies in order to evaluate the potentiality of cobalt sulfide for the production of H_2.

Key words—(photo)catalyst material, CoS film, electro-deposition, production of H_2.

I. INTRODUCTION

The hydrogen molecule, commonly called "hydrogen", is considered an energy carrier (which carries energy) and today it is produced from a source of energy; its combustion generates a large amount of energy (about 3 times more than gasoline at constant weight) [1]. Hydrogen does not exist in the natural state but

is very abundant on earth in atomic form (water, hydrocarbons "oil and gas", etc.); its combustion is non-carbon (no CO_2 emission when it comes from renewable sources). Hydrogen is storable and can be an effective way of storing electricity over long periods of time. Hydrogen production requires a source of hydrogen (hydrocarbons or water) and a source of energy; several techniques exist such as the catalytic decomposition of natural gas, the partial oxidation of heavy oils, the gasification of coal and the electrolysis of water. Today, 96 % of hydrogen is produced from fossil fuels (petroleum, natural gas and coal) and 4 % from the electrolysis of water because of the high cost [1]. The most common process for producing hydrogen is the reforming of natural gas by superheated steam. In the presence of this water vapor and heat, the carbon atoms (C) of methane (CH_4) dissociate. After two successive reactions, they reform separately to obtain, dihydrogen (H_2) and carbon dioxide (CO_2). The other method is the gasification of charcoal, composed mainly of carbon and water. When burned in a reactor at a very high temperature (around 1500 °C), the wood releases gases that will then separate and reform to obtain hydrogen (H_2) and carbon monoxide (CO). The electrolysis of water consists to decompose water (H_2O) into dioxygen (O_2) and dihydrogen (H_2). The latter process uses electricity to decompose the water molecules and thus forms hydrogen and oxygen gases. This process corresponds to the reverse reaction used in H_2/O_2 fuel cells. The decomposition of water by the photoelectrochemical process uses a semiconductor electrode material (usually the photoanode) and a conductive catalytic material (cathode) immersed in an aqueous electrolyte. The semiconductor acts as a catalyst on the surface of which the electrons and photogenerated holes participate, respectively, in reduction and oxidation reactions.

The main electrode materials studied in the literature for hydrogen generation by the photoelectrochemical process are metal oxide materials [2], such as ZrO_2, $KTaO_3$, $SrTiO_3$ and TiO_2. These materials possess a suitable strip structure for the decomposition of water, in addition to being stable. They absorb a small fraction of the solar spectrum (ultraviolet) and are active to decompose water when modified with suitable co-catalyst materials. On the other hand, the cadmium compounds (CdS and CdSe) possess an appropriate bandgap energy and their conduction and valence band levels are compatible for the H_2 and O_2 reaction: E_c more positive than the $E_{H+/H2}$ level, to promote the release of H_2, and E_v more negative than $E_{O2/H2O}$ level, to favour the release of O_2, at selected pH values of the electrolyte. However, these materials are not stable in aqueous media because photogenerated holes (h^+) interact with CdS and CdSe to generate Cd^{2+} ions that pass into solution (photocorrosion process) [3]. In addition, these cadmium-based materials have a high toxicity in aqueous solution. Moreover, zinc oxide (ZnO, E_g = 3.3 eV) is a photocatalyst material, but it also undergoes the photocorrosion process under light

*Corresponding author email: cherfouh.hayet@courrier.uqam.ca; marsan.benoit@uqam.ca

excitation, in addition to absorbing only a small proportion of visible light. Although tungsten oxide (WO_3, E_g = 2.8 eV) is a good photocatalyst for the O_2 evolution reaction under visible light irradiation, this material is unable to produce H_2 because of its too negative conduction band level [2].

The aim of this work is to develop a new (photo) catalyst material based on cobalt sulphide (CoS) for the release of hydrogen. The choice of this material is based on its exceptional electrocatalytic properties [4-5]: better catalytic activity and better stability than platinum (Pt) in dye-sensitized solar cells, with comparable energy conversion efficiency, in addition to being much less expensive than platinum which has a limited earth abundance. According to the work of *Sun et al.* [6], a cobalt sulphide (CoS) film prepared by electrochemical deposition (potentiostatic method) onto conductive substrates proves to be an efficient and robust catalyst for the production of electrochemical and photo-electrochemical hydrogen in aqueous medium. The electrochemical experiments demonstrate that the current densities can reach 50 mA/cm^2 and that the activity is maintained for at least 40 h. The catalyst can also be electrochemically coated on silicon, thus providing a water-compatible photoelectrochemical system for the production of hydrogen under simulated sunlight. Furthermore, the methods for preparing the CoS films are easy and effective, and this material has a long-term stability in aqueous medium. Several electrodeposition methods of CoS were developed by *Marsan et al.* [4-5, 7-8]: electrodeposition by galvanostatic, potentiostatic and pulse methods. The CoS films obtained onto conductive glass or plastic substrates are homogeneous, mechanically stable and quasi-transparent, and show excellent cathodic electrocatalytic activities. In this study, CoS was first used as a cathode material in a cell containing an aqueous medium for the production of hydrogen.

II. EXPERIMENTAL

The CoS films were prepared by electrodeposition onto conductive glass substrates (FTO: fluorine-doped tin oxide)/glass: 8.0 ohms/square, 1 cm^2) using several experimental conditions, including the deposition method (pulse, galvanostatic and potentiostatic deposition) and the deposition parameters (such as the deposition time). Only the results regarding the galvanostatic method will be presented. Informations regarding the morphology of the CoS films were obtained using scanning electron microscopy (SEM). The instrument employed was a Hitachi, model S-4300SE/N, with different magnifications, through detection of the secondary electrons. An acceleration voltage of 20 keV was used for the analyses, with a range of amplification between 10 000 × and 500 000 ×. Stoichiometry of the samples was determined by energy dispersive X-ray analysis (EDX) using an X-ray detector integrated in the scanning electron microscope (SEM, Hitachi S-4300). The transmission measurements were carried out on thin CoS films, using a UV-Visible-NIR 100 spectrophotometer, Perkin Elmer, Lambda 750. The spectra were recorded in the wavelength range between 200 and 900 nm, in transmission mode. For the potentiostatic measurements, platinum (6.25 cm^2) was used as the counter-electrode and Ag/AgCl (3 M, 0.21 V vs. N.H.E. served as the reference electrode. The aqueous electrolyte was 1 M potassium sulphate (K_2SO_4, ACS). The measurements were carried out using a multi-channel potentiostat, Solartron 1470E (8 optimized channels, 10 V and 4 A per channel) controlled by *CorrWare* data acquisition and processing software (version 2.80, Scribner Associates, Inc.) and *CorrView* (version 2.70). Electrochemical impedance spectroscopy measurements were performed with a Solartron 1470E multi-channel coupled with a Solartron 1255B frequency analyzer, controlled by the *ZPlot* software (version 2.80). Acquisition and processing of data were done using *ZView* software (version 2.70). Impedance spectroscopy was used in a range of frequencies between 10^6 Hz and 1 Hz.

III. RESULTS AND DISCUSSION

SEM analysis shows that the morphology of CoS films (obtained via galvanostatic electrodeposition on FTO/glass) is very uniform (Fig. 1), and that the galvanostatic electrodeposition has allowed the catalyst particles of CoS to adhere to the FTO/glass substrate. The thickness of the film depends essentially on the deposition time and deposition method. According to Alina's work [9], the thickness of CoS film obtained by chemical deposition from a solution containing a source of CO^{2+} ions ($CoCl_2$) to which a source of S^{2-} (Na_2S) ions is subsequently added.) was estimated at about one micrometer. The EDX chemical analysis confirms the presence of the expected elements, composed of cobalt and sulphur for CoS, with signature of tin and oxygen ascribed to the underlying SnO_2-based substrate, and traces of carbon (Fig. 2). The estimated atomic ratio of Co/S is about 2 (calculated from weight percentage and atomic mass of Co and S), which means an excess of cobalt over sulfide. This result suggests that the composition of film is not pure with CoS but could contain cobalt hydroxide (providing from electrodeposition solution) and/or cobalt oxide (presence of oxygen in atmosphere). This result is in a good agreement with that obtained y *Sun et al.* [6]. The CoS film prepared by potentiostatic electrodeposition give an excess of Co compared to the S, which is related to the presence of CoO and $Co(OH)_2$ with CoS. The transmission measurements of CoS films obtained using the galvanostatic deposition method suggest quasi-transparent properties (~ 75 % to 80 %). The thickness and transmittance of cobalt sulphide films strongly depend on the deposition parameters, inter alia, the deposition time. Indeed, for deposition times of 1 s, 2 s, 5 s and 10 s the films will be thin and transparent. On the other hand, thick and opaque films will be obtained for

*Corresponding author email: cherfouh.hayet@courrier.uqam.ca; marsan.benoit@uqam.ca

higher deposition times (30 s, 60 s and 90 s). Electrochemical impedance spectroscopy measurement show that the CoS films possess a low resistivity (~11 Ω).

The electrochemical behavior of CoS electrodes in an aqueous medium containing 1 M K_2SO_4 was studied by carrying out potentiostatic measurements (from -0.5 V to -2.5 V vs Ag/AgCl). Fig. 3, shows the variation of the current with the applied potential. As the potential becomes more cathodic, the current increases due to the production of more hydrogen gas.

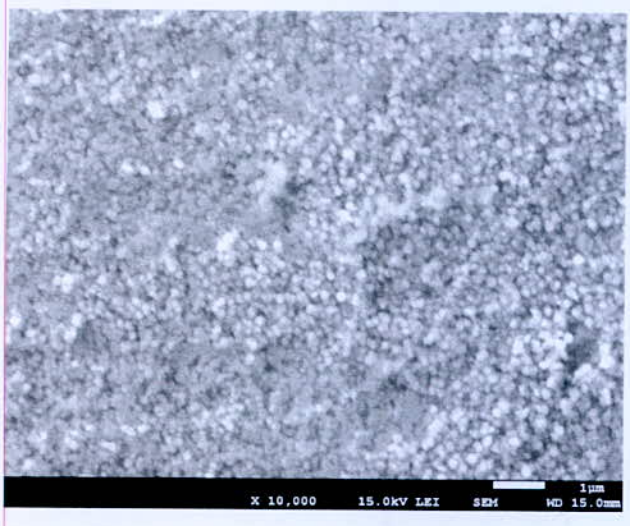

Fig. 1. SEM image of CoS film obtained by galvanostatic deposition onto a FTO/glass substrate with magnification of ×10 000

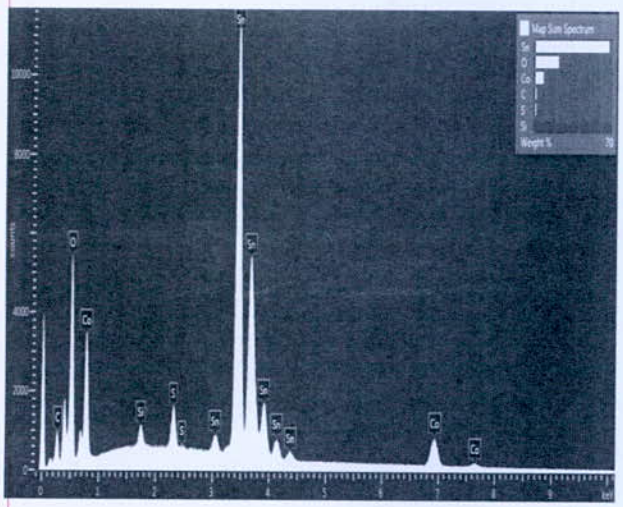

Fig. 2. EDX spectrum of CoS film obtained by galvanostatic deposition onto a FTO/glass substrate

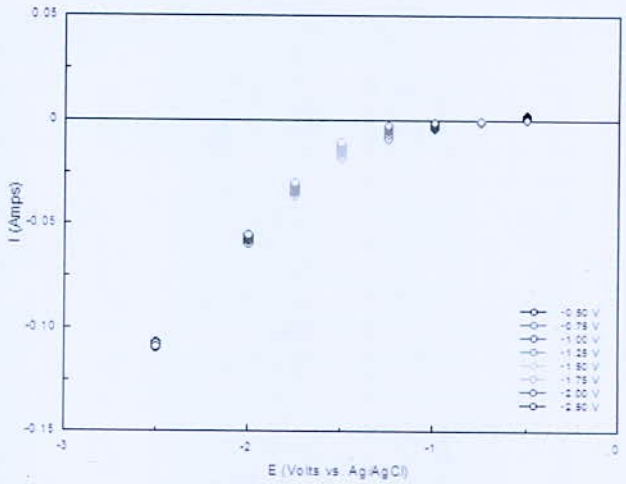

Fig. 3. Potentiostatic curves (current versus potential) measured between -0.5 V and -2.5 V vs. Ag/AgCl, using a CoS working electrode, a Pt counter electrode and an Ag/AgCl reference electrode. Electrolyte: aqueous 1 M K_2SO_4

IV. CONCLUSION

The new CoS catalyst material presents interesting properties. SEM analysis shows that the morphology of CoS films is very uniform, and the EDX analysis confirms the formation of CoS. The optical and electrochemical properties of CoS films obtained using the galvanostatic deposition method show quasi-transparent (~75%) films with a low resistivity (~11 Ω). Current-potential measurements show an increase in the current when the potential becomes more negative with significant evolution of H_2.

ACKNOWLEDGMENTS

The authors acknowledge NanoQAM for DRX, SEM and EDX analyses. Natural Sciences and Engineering Research Council of Canada (NSERC) is acknowledged for the financial support.

REFERENCES

[1] H. Cherfouh, O. Fellahi, T. Hadjersi and B. Marsan, "Preparation and characterization of a new $CuInS_2$/SiNWs/Si composite material for photovoltaic and photo-catalytic applications," *International Journal of Hydrogen*, accepted, September 2017.

[2] K. Akihiko and M. Yugo, "Heterogenous photocatalyst materials for water splitting," *Chem. Soc. Rev.*, vol. 38, pp. 253-278, 2009.

[3] Y.V. Pleskov and Y.Y. Gurevich, "In Semiconductor Photoelectrochemistry," *Ed. P. N. Bartlett, Plenum, New York*, 1986.

[4] B. Marsan and B. Bourguignon, "Electrode having a CoS layer thereon, process of preparation and uses

*Corresponding author email: cherfouh.hayet@courrier.uqam.ca; marsan.benoit@uqam.ca

thereof," *Patent:WO/2005/040458,* CA 2,544,073 , US 2005/0089681 and EP 1680531, 2005.

[5] M. Wang, A. M. Anghel, B. Marsan, N. Le Cevey Ha, N. Pootrakulchote, S. M. Zakeeruddin and M. Gratzel, "CoS Supersedes Pt as Efficient Electrocatalyst for Triiodide Reduction in Dye-Sensitized Solar Cells," *J. Am. Chem. Soc.*, vol. 131, pp. 15976–15977, 2009.

[6] Y. Sun, C. Liu, D. C. Grauer, J. Yano, J. R. Long, P. Yang and C. J. Chang, "Electrodeposited Cobalt-Sulfide Catalyst for Electrochemical and Photoelectrochemical Hydrogen Generation from Water," *J. Am. Chem. Soc.*, vol. 47, pp. 17699–17702, 2013.

[7] C. Sauvé, H. Cherfouh, N. P. Benehkohal, G. Demopoulos and B. Marsan, "Development and characterization of CoS catalytic film for DSSCs counter electrode," submitted.

[8] H. Cherfouh, L. Breau and B. Marsan, "Cobalt sulphide as a counter electrode for electrochemical photovoltaic cells: effect of the electrodeposition method," *7th ECS Montreal Student Symposium of the Montreal Student Chapter*, Montréal, May 26, 2017.

[9] A. M. Anghel, "Nouvelle méthodes d 'électrodéposition d 'un catalyseur employé dans une cellule photovoltaïque électrochimique," Mémoire, département de chimie, UQAM, 2009.

*Corresponding author email: cherfouh.hayet@courrier.uqam.ca; marsan.benoit@uqam.ca

Aqueous Biomass Gasification in Supercritical Water Process for Hydrogen Production: A Stoichiometric Thermodynamic Model

L. Hamdi[1,2*], A. Khellaf[1]

[1]Centre de Développement des Énergies Renouvelables, CDER, 16340, Alger, Algérie.
[2]Laboratoire des Sciences du Génie des Procédés Industriels (LSGPI) FGMGP, USTHB, BP 32 El-Alia Bab -Ezzouar, 1611 Alger, Algérie.

***Abstract*—Supercritical water gasification is a promising reforming process for the direct production of hydrogen at high pressures with a short reaction time which avoid energy expenses associated with its compression. The aim of this work is to give insights of the gasification of aqueous biomass in supercritical water. A mathematical model based on the hypothesis of thermodynamic equilibrium is used. The model was validated against literature experimental data for corn starch and sawdust feedstocks.**
The calculations were carried out by using equation of state (EOS) for ideal gas. Theoretical model predictions are compared with literature data and the agreement was satisfying.

Key words—Biomass, Hydrogen, Supercritical water gasification, Thermodynamic modeling.

I. INTRODUCTION

Concerns about exhaustion of fossil fuels, atmospheric pollution, greenhouse effect, and energy security have awakened increasingly interest in developing new alternative routes to manage the energy demand with more effectively and more eco-friendly manner.

Hydrogen has the highest energy content (120 MJ/Kg) compared to conventional fuels and its sole combustion product is water, consequently hydrogen is a powerful and clean energy carrier [1].

Biomass has been widely proposed as a valuable alternative to fossil fuels. Differently from fossil resources, biomass is fully renewable since it is continuously generated through the life cycle of the living beings [2]. The conversion of waste biomass and high concentrated organic wastewaters to hydrogen could simultaneously recover resources and reduce pollution [3].

Recently, there has been increasing attention toward the "hydrothermal technologies". Such class of technologies includes different types of treatments whose common point is the involvement of hot pressurized water, which can be found at liquid or supercritical state. This way of processing biomass is very interesting, since it does not require harmful and polluting solvents or chemicals and allows converting a number of low-value biomass. Also, we note that these hydrothermal processes become more appropriate when the feedstock presents high water content (i.e. moisture higher than 60%), [4]. In this process biomass is gasified using the supercritical conditions of water at temperature above than 374°C and pressures above than 22.1 MPa. The product gases consist mostly of hydrogen (H_2), carbon dioxide (CO_2), methane (CH_4) and carbone monoxide (CO). Also, hydrogen sulphide (H_2S) is formed when sulphur-containing biomass is used as raw material. As the water acts as solvent, catalyst and reaction media in SCWG there is no need for drying, and in this way the energy efficiency is increased [5].

Supercritical water gasification (SCWG) is very interesting because the water is used as reacting media. Indeed, water above its critical point (T = 374 °C, P = 22.1 MPa) has thermo-physical properties that are intermediate between gas and liquid. Water is much less polar in this state and becomes a good solvent for nonpolar compounds and gases [6]. Another advantage of SCWG is that the H_2 is produced at a high pressure, which can be stored directly, avoiding the large energy expenditures associated with its compression [7]. The scheme 1 explains the concept of SCWG:

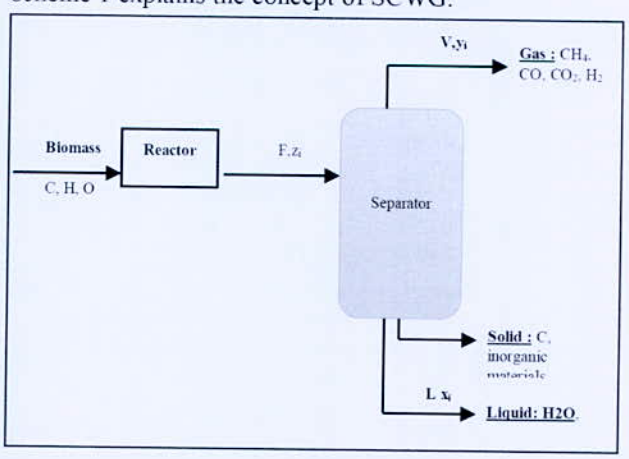

Fig. 1. Scheme of the SCWG process

Gasification of biomass and other effluents in supercritical water was the scope of several experimental and numerical studies in the literature: fruit pulp [8], grape marc [4], eucalyptus grandis [9], maize silage [2], oily wastewater [10], fruit wastes and agro-food residues [11]. Numerical studies have focused on thermodynamic modeling [10] which is considered as an important way to understand several aspects of the process [12].

*Corresponding author email: l.hamdi@cder.dz

Also, the composition of the product gas and the influence of the operating conditions are among the issues that can be answered through thermodynamics modeling.

In the present work, the predictions of this mathematical model are compared to experimental results obtained in the case of gasification of cornstarch and a mix of cornstarch with sawdust in supercritical water.

II. THEORETICAL STUDY

The stoichiometric model proposed by Daniele Castello et al. [2] was adopted. This model is based on a reduced number of chemical reactions.

1. *Model description*

The later model is based on the assumptions that at equilibrium:

a) the entire biomass flow at the inlet is converted, so no biomass remains after the reaction;
b) the products of reaction prevailing are water (H_2O), hydrogen (H_2), methane (CH_4), carbon monoxide (CO) and carbon dioxide (CO_2).

At first the biomass is converted into carbon monoxide and hydrogen through the presence of water:

$$CH_yO_z + (1-z)H_2O \rightarrow CO + \left(1 - z + \frac{y}{2}\right)H_2 \quad (1)$$

After this reaction, the system is only composed of H_2O, CO and H_2. Other two stoichiometric independent reactions can be written to express the amount of CO_2 and CH_4. The first reaction is the water-gas shift (WGS) reaction which expresses the equilibrium between CO and CO_2:

$$CO + H_2O \rightarrow CO_2 + H_2 \quad (2)$$

The CO Methanation reaction is produced after:

$$CO + 3H_2 \rightarrow CH_4 + H_2O \quad (3)$$

For both reactions 2 and 3, an equilibrium constant K_i can be defined, which is calculated by means of purely thermodynamic data:

$$K_i = \exp\left(-\frac{\Delta G}{RT}\right) \quad (4)$$

The same equilibrium constant can be related to the equilibrium composition of the system through equation (5):

$$K_i = \prod_{j=1}^{N} a_j^{\gamma j} \quad (5)$$

Where a_j is the activity of the j^{th} species, to the power of its own stoichiometric coefficient (negative for the reactants). The activity is defined as:

$$a_j = \frac{f_j}{f_j^0} = \frac{\varphi_j P x_j}{P^0} \quad (6)$$

Where x_j is the molar fraction of the j^{th} species and Φ_j is its fugacity coefficient, which accounts for the non-ideality of the gaseous mixture.

For simplification reasons, the model was used using the ideal gas EoS. In this case, the fugacity coefficients are all equal to 1.

The problem is composed of 6 unknowns which correspond to the molar fractions of the 5 gaseous species involved in the model, plus the total number of gas moles M_{tot}. In addition, the chemical equilibria of reactions 2 and 3 are included. The model also contains three equations for the elementary equilibrium of carbon, hydrogen and oxygen and a congruence equation which states that the sum of the molar fractions x_j must be equal to 1.

The system can be written in the following way:

$$\begin{cases} K_2 = \frac{(\varphi x)_{CO_2}(\varphi x)_{H_2}}{(\varphi x)_{CO}(\varphi x)_{H_2O}} \\ K_3 = \left(\frac{P}{P_0}\right)^{-2}\frac{(\varphi x)_{CH_4}(\varphi x)_{H_2O}}{(\varphi x)_{CO}[\varphi x]_{H_2}^3} \\ M_{tot}\left(x_{CO} + x_{CO_2} + x_{CH_4}\right) = M_C \\ M_{tot}\left(2x_{H_2} + 4x_{CH_4} + 2x_{H_2O}\right) = M_H \\ M_{tot}\left(x_{CO} + 2x_{CO_2} + x_{H_2O}\right) = M_O \\ x_{CO} + x_{CO_2} + x_{CH_4} + x_{H_2O} + x_{H_2} = 1 \end{cases} \quad (7)$$

Where M_C, M_H and M_O are the total number of moles of carbon, hydrogen and oxygen present in the system. The non-linear algebraic system was solved by using the Excel solver.

III. RESULTS AND DISCUSSION

The model is validated against experimental data provided by Calzavara et al. [13] who evaluated the biomass gasification in supercritical water process for hydrogen production, the biomass used was the cornstarch and a mix of cornstarch with sawdust.

1. *Model validation*

In the present section, the model is validated against experimental literature data and then a graphical interpretation of the results is provided, which is useful to highlight the difference between experimental and thermodynamic results for the two different biomasses used.

The model was run with equation of state (EoS) for ideal gas. The results are presented in Figures 2 and 3.

As it can be seen from figures 2 and 3, the production of all major permanent gases (H_2, CO_2, CO, CH_4) for the two feedstocks used (cornstarch and a mix of cornstarch+sawdust) was properly estimated. So, the proposed mathematical model is qualified to predict the experimental results in a satisfactory manner. We note also, that the estimation of CO and CH_4 gases is more accurate than that for H_2 and CO_2.

*Corresponding author email: l.hamdi@cder.dz

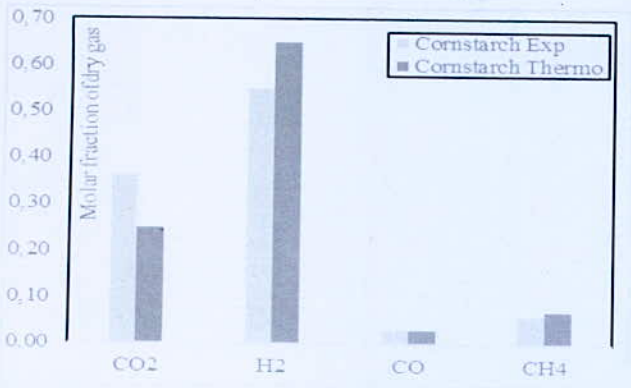

Fig. 2. Comparison between experimental and thermodynamic results obtained by the present model developed by Castello et al. (Cornstarch: F0=0.12 kg/h, T=745°C, P=280 bar, wt (%)=15)

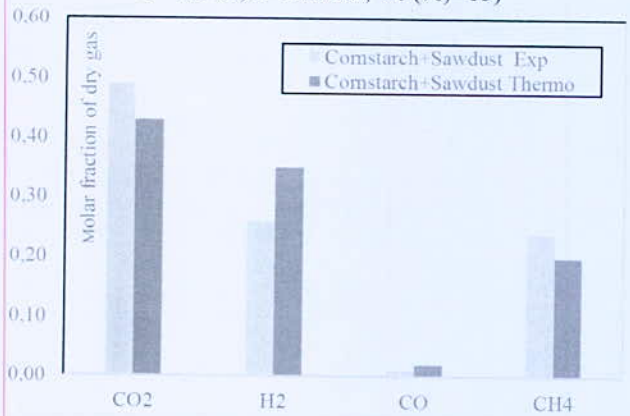

Fig. 3. Comparison between experimental and thermodynamic results obtained by the present model developped by castello et al. (cornstarch+sawdust: F_0=0.12 kg/h, T=745°C, P=280 bar, wt (%) =15)

IV. CONCLUSION

SCWG is a technology in the early stages of technical development. A better understanding of the fundamental phenomena is essential for an adequate improvement of such process.

In this work, a stoichiometric model proposed by castello et al. for the SCWG of biomass was presented and tested for two new feedstocks. The model was validated with experimental literature data during the SCW gasification of cornstarch and a mix of cornstarch and sawdust. The results showed a good agreement between experimental and predicted values for both biomasses.

REFERENCES

[1] S. Seif, S. Fatemi, O. Tavakoli, H. Bahmanyar,"Hydrogen Production through Hydrothermal Gasification of Industrial Wastewaters using Transition Metal Oxide Catalysts", Supercritical Fluids,http://dx.doi.org/doi:10.1016/j.supflu.2016.03.028.

[2] D. Castello, A. Kruse, L. Fiori," Supercritical water gasification of hydrochar", Chemical engineering research and design, vol.92, 2014, pp.1864–1875.

[3] Y. Wang, S. Wang, G. Zhao, Y. Guo, Y. Guo," Hydrogen production by partial oxidation gasification of a phenol, naphthalene, and acetic acid mixture in supercritical water", International Journal of Hydrogen Energy, 2016, vol. 41, pp. 2238- 2246.

[4] D. Basso, F. Patuzzi, D. Castello, M. Baratieri, E. C. Rada, E. Weiss-Hortala, L. Fiori, "Agro-industrial waste to solid biofuel through hydrothermal carbonization", Waste Management,2015, vol. 92, pp. 1864–1875.

[5] I.RonnIund, L.Myréen, K.Lundqvist, J.Ahlbeck, T.Westerlund, "Wadte to energy by industrially integrated supercritical water gasification- Effects of alkali salts in residual byproducts from the pulp and paper industry", Energy, 2011, vol.36, pp.2151-2163.

[6] S. Letellier, F. Marias, P. Cezac, J.P. Serin, "Gasification of aqueous biomass in supercritical water: A thermodynamic equilibrium analysis", J. of Supercritical Fluids, 2010, vol.51, pp.353–361.

[7] A. J. Byrd, K.K. Pant, R.B. Gupta, "Hydrogen production from glycerol by reforming in supercritical water over Ru/Al_2O_3catalyst", Fuel, 2008, vol.87, pp. 2956–2960.

[8] D.Elif, A. Nezihe, "Hydrogen production by supercritical water gasification of fruit pulp in the presence of Ru/C", International Journal of Hydrogen Energy, 2016, vol.41, pp. 8073-8083.

[9] J. Louw, C.E. Schwarz, A.J. Burger, "Supercritical water gasification of Eucalyptus grandis and related pyrolysis char: Effect of feedstock composition", Bioresource Technology, 2016, vol.216, pp.1030–1039.

[10] Y. Zhiyong and T.Xiuyi, "Hydrogen generation from oily wastewater via supercritical water gasification (SCWG) ", Journal of Industrial and Engineering Chemistry, 2015, vol. 23, pp. 44–49.

[11] S. Nanda, J. Isen, A.K. Dalai, J.A. Kozinsk, "Gasification of fruit wastes and agro-food residues in supercritical water ", Energy Conversion and Management, 2016, vol. 110, pp. 296–306.

[12] D. Castello, L. Fiori, "Supercritical water gasification of biomass: A stoichiometric thermodynamic model", International Journal of Hydrogen Energy, 2015, vol.40, pp.6771-6781.

[13] Y. Calzavara, C. Joussot-Dubien, G. Boissonnet, S. Sarrade, "Evaluation of biomass gasification in supercritical water process for hydrogen production ", Energy Conversion and Management, 2005, vol.46, pp.615–631.

*Corresponding author email: l.hamdi@cder.dz

Thermochemical Decomposition Study of SO_3 in Tubular Reactor for Hydrogen Production

F. Lassouane[1*] and A. Khellaf[2]

[1*]Centre de Développement des Energies Renouvelables, CDER, B.P. 62, Route de l'Observatoire, 16340, Bouzaréah, Alger, Algérie.

Abstract—**The reduction of sulfuric acid to sulfur dioxide plays an important role in sulfur-based thermochemical cycles for hydrogen production from water. Thus, the reaction produces oxygen and generates SO_2 which is the key compound used in other reaction steps to complete the cycle. The thermodynamic aspect is presented in this paper to estimate the possible equilibrium conversion of SO_3 to SO_2 (X) that can be obtained in the tubular reactor fed by concentrated solar radiation. The effect of temperature and pressure on the equilibrium conversion of sulfur trioxide to sulfur dioxide was studied.**

Results show that the higher conversion was obtained at low pressure and high temperature.

Key words—Hydrogen, thermochemical cycle, SO_3 decomposition, solar energy, tubular reactor

I. INTRODUCTION

Hydrogen produced from solar energy is one of the most promising energy technologies that can considerably contribute to a sustainable energy supply in the future. Thermochemical water splitting cycles represents an appealing carbon-free option for hydrogen production powered by solar energy source. Among them, sulfur thermochemical cycles have attracted a great deal of international interest over the past few decades.

In these processes, the water and heat are the inputs, and hydrogen and oxygen are the only outputs. The other chemicals and reagents are recycled in a closed cycle [1, 2].

The decomposition of the sulfuric acid is a well-known process proposed in the first half of the twentieth century [3]. These cycles have in common the decomposition of sulfuric acid session, which is the crucial step in the process. Indeed, the SO_2 obtained from this step will supply the electrolyzer in Westinghouse cycle to produce hydrogen [4]. Thus, the most energy intensive step of the above cycles is the reduction of SO_3 to SO_2. This reaction requires the presence of catalysts and due to its endothermicity, it takes place at temperatures higher than 1000 K.

Banerjee et al. [5] describe the decomposition of sulfuric acid as the "most endothermic step" of researched sulfur-based cycles for hydrogen production, which is also observed in the standard heats of the reactions.

Kondamudi et al. [6] states that two reactions can take place simultaneously, wherein sulfur trioxide that forms will consecutively decompose into sulfur dioxide and oxygen, the sulfuric acid is first vaporized and decomposed into sulfur trioxide and water, followed by a second stage where the sulfur trioxide is decomposed into sulfur dioxide and oxygen, is used.

In this paper, the sulfur family thermochemical cycles concept are described by focusing on the decomposition of sulfur acid with the solar energy in the tubular reactor. This work is focused on thermodynamic study in the plug flow tubular reactor fed by concentrated solar radiation. The objective of this study is to determine the influence of temperature and pressure parameters on the reduction SO_3 to SO_2 to achieve a maximum conversion.

II. THEORETICAL STUDY

1. *SO_3 decomposition in tubular reactor*

The first step in the decomposition of pure sulfuric acid is its evaporation and conversion to SO_2 and H_2O. These two steps take place at the same temperature interval and lead to a gas mixture H_2SO_4, SO_3 and H_2O.

Sulfur trioxide is not stable at high temperature and its decomposition leads to the formation of SO_2. Indeed, the conversion of SO_3 occurs in excess of 700 K and becomes complete at 1200 K.

$$SO_3 \longrightarrow SO_2 + \tfrac{1}{2} O_2$$

The conversion of SO_3 to SO_2 (X) can be obtained in plug flow tubular reactor fed (Fig. 1) by concentrated solar radiation.

2. *Standard Gibbs Energy* ΔG_r^0 of the reaction

The relation of the standard Gibbs energy ($J.mol.^{-1}.K^{-1}$) for the reaction is given by:

$$\Delta G_r^\circ = \Delta H_r^\circ - T\Delta S_r^\circ \qquad (1)$$

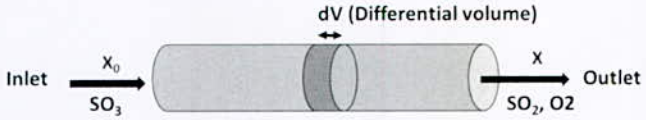

Fig. 1. Schematic of plug flow tubular reactor

*Corresponding author email: f.lassouane@cder.dz

To evaluate the enthalpy of the reaction, first the change in the enthalpy, entropy of the individual species entering in the reaction are estimated using the following equations:

$$\Delta H_r^\circ = \Delta H_{298}^\circ + \int_{298}^{T} \Delta C_p^\circ dT \qquad (2)$$

$$\Delta S_r^\circ = \Delta S_{298}^\circ + \int_{298}^{T} \frac{\Delta C_p^\circ}{T} dT \qquad (3)$$

The thermodynamics data for each compound (SO_3, SO_2 and O_2) are given in the literature [7]. C_p° is the specific heat at constant pressure of each species.

The reference temperature is taken as the room temperature (298 K).

3. Equilibrium constant K calculation

The equilibrium constant is calculated from the standard Gibbs energy method (Equation 2):

$$-\ln K = \frac{\Delta G_T^\circ}{RT} \qquad (4)$$

K is the equilibrium constant and R is the gas constant (8.314 $J.K^{-1}.mol^{-1}$)

The parameters are calculated in the temperature range of 300 K and 1200 K with the different at Gibbs energies for each compounds involved in the composition reaction.

4. Estimation of equilibrium conversion

The relationship between the equilibrium constant K and the composition of SO_3, SO_2 and O_2 is given by the following equation [8]:

$$\left(\frac{P}{P^\circ}\right)^{\gamma} K = \prod (Y_i \varphi_i)^{\gamma_i} \qquad (5)$$

P is the operating pressure (bar), P° is the pressure in standard state taken for one bar and Yi is the molar fraction (%) of each chemicals.

φi, γ, γ_i are the fugacity coefficient for each compounds (SO_3, SO_2 and O_2), global stoichiometric Coefficient and stoichiometric Coefficient for each element, respectively.

Equation 5 relates K to fugacities of the reacting species, as they exist in the real equilibrium mixture. These fugacities reflect the nonidealities of the equilibrium mixture and are functions of temperature, pressure, and composition.

$$\left(\frac{P}{P^\circ}\right)^{0.5} K \frac{\varphi_{SO_3}}{\varphi_{SO_2} \varphi_{O_2}^{0.5}} = \frac{Y_{SO_2} Y_{O_2}^{0.5}}{Y_{SO_3}} \qquad (6)$$

The fugacity coefficients φ_{SO3}, φ_{SO2} and φ_{O2} have been calculated from the data given in the literature [8].

The standard pressure was set at 1 bar while the operating pressure was set at values of 1 bar, 3 bar, 6 bar, 9 bars, 12 bar and 20 bar.

The molar fractions for each component (Y_{SO3}, Y_{SO2}, and YO_2) were determined with the following equations:

$$Y_{SO_3} = \frac{1 - X}{1 + 0.5X} \qquad (7)$$

$$Y_{SO2} = \frac{X}{1 + 0.5X} \qquad (8)$$

$$Y_{O_2} = \frac{0.5X}{1 + 0.5X} \qquad (9)$$

By solving the Equation 6, the fractional conversion (x) and the equilibrium composition of the gas mixture (SO_2, O_2, SO_3) was determined.

III. RESULTS

The molar fractions of SO_3, SO_2 and O_2 at 1200 K were presented in Fig. 2. In this temperature of the SO_3 decomposition, the highest molar fraction of SO_2 was obtained at 1 bar.

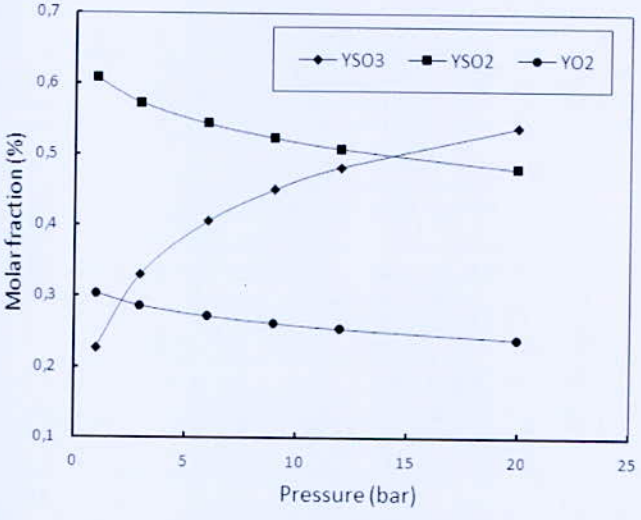

Fig. 2. Molar fraction variation of SO_3 to SO_2 and O_2 at different pressures

The equilibrium constant values for the temperature interval between 300 K and 1200 K at different operating pressure are presented in Fig. 3. The plot clearly shows the significant influence of pressure on the equilibrium conversion. Indeed the lowest operating pressure increase the equilibrium conversions of SO_3 to SO_2.

The study of Coetzee [9] was compared with conversions obtained at the same conditions in order to validate the calculations that were done. It can be seen that the results were almost identical.

*Corresponding author email: f.lassouane@cder.dz

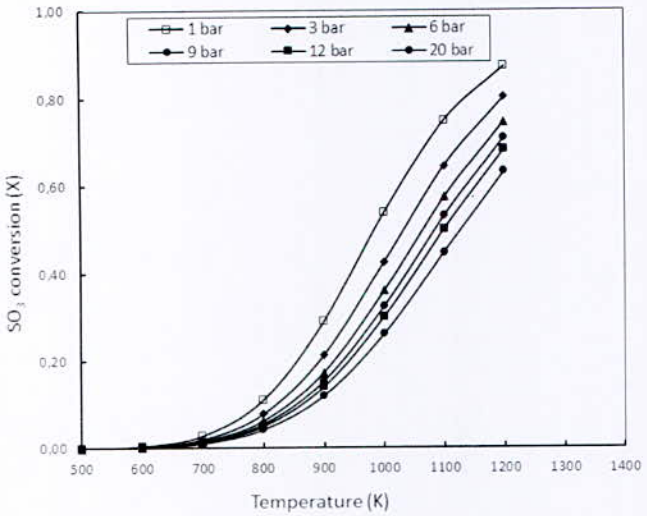

Fig. 3. Estimation of equilibrium conversion of SO_3 to SO_2 as function of temperature at different pressure

The pressure of 1 bar allows for conversion of 87.17 % at temperature of 1200 K.

IV.CONCLUSION

We have presented the thermodynamics of sulfuric trioxide SO_3 decomposition reaction and given a parametric study showing the effects of temperature, pressure on the SO_3 conversion. Thermodynamic results show that the conversions on SO_2 decrease with increasing pressure.

Thermodynamic data of SO_3 reduction to SO_2 in the calculated temperature range of 300 - 1200°C shows that the reaction is favored by increasing the temperature.

REFERENCES

[1] S.P. Abanades,G. Charvin, G. Flamant and P. Neveu.,"Screening of water-splitting thermochemical cycles potentially attractive for hydrogen production by concentrated solar energy". *Energy* , vol 31: 2805-2822, 2006.

[2] Hydrogen Program, Hydrogen & our Enerrgy future, US Department of Energy,
Website:
https://www1.eere.energy.gov/hydrogenandfuelcells/pdfs/hydrogenenergyfuture_web.pdf

[3] L. M. Gandia, G. Arzamedi, and P. M. Dieguez, "Renewable hydrogen technologies: production, purification, storage, applications and safety". USA: Elsevier. 2013.

[4] A. M. Banerjee, A. R. Shirole, M.R. Pai, A. K. Tripathi, S. R. Bharadwaj, D. Das, P. K. Sinha, "Catalytic activities of Fe_2O_3 and chromium doped Fe_2O_3 for sulfuric acid decomposition reaction in an integrated boiler, preheater, and catalytic decomposer", Appl. Catal, B-ENVIRON, vol 127, pp. 36-46, 2012.

[5] Banerjee A.M., Pai M.R., Meena S.S., Tripathi A.K. & Bharadwaj S.R. 2011. Catalytic activities of cobalt, nickel and copper ferrospinels for sulfuric acid decomposition: The high temperature step in the sulphur based thermochemical water splitting cycles. International Journal of Hydrogen Energy, 36(2011):1-13.

[6] K. Kondamudi & S. Upadhyayula, "Kinetic studies of sulfuric acid decomposition over Al-Fe 2 O 3 catalyst in the sulfur-iodine cycle for hydrogen production", Int. J. Hydrogen Energy, vol 37, pp.3586-3594, 2012.

[7] J.C.Kotz, P.M. Treichel and J.R. Townsend, "Chemistry and chemical reactivity", 8th ed., USA: Brooks/Cole, Cengage learning, 2012, Appendix L, A-31.

[8] J.M.Smith, H.C.VanNess,M.M.Abbott, "Introduction to Chemical Engineering Thermodynamics", 6th ed., New York: Mc Graw Hill, 2001, 749 p.

[9] M.D. Coetzee, "The chemical reactor for the decomposition of sulphuric acid for the hybrid sulphur process", PhD. dissertation, North west University, 2008.

*Corresponding author email: f.lassouane@cder.dz

Effects of the Introduction of Alternative Fuels and Hydrogen Based Fuel on Vehicles Pollutants Emissions

R. Boudries[1*], H. Kendil[2], M.Boughrara[2], N. Kabouche[1], F. Meziane[1]

[1*]Centre de Développement des Energies Renouvelables, Bouzaréah, Algiers, Algeria.
[2]Département Génie des Procédés, USTHB, Bab Ezzouar, Alger.

Abstract—**The use of conventional fuel in the transport sector has led to serious environmental problems, more particularly to greenhouse gases emissions. Strict laws, improvement in engine technology and use of alternative vehicles has led to an improvement in the situation. But it is only by using alternative fuels such as hydrogen that the problem of greenhouse gases emissions could be seriously addressed.**

The aim of the present work is to study the effect of the alternative fuels, such as LPG and Hythane on the greenhouse gases emission. We consider the case of Algeria. We have then investigated the evolution of the vehicle emission of greenhouse gases, such as CO.

Key words—Conventional fuel, transport sector, environmental problems, greenhouse gases emissions, alternative fuel.

I. INTRODUCTION

As the transportation sector is powered mainly by hydrocarbon-based fuels, its contribution to environment degradation is important. This degradation is a result of the emissions of not only greenhouse gases but also of fine particulate matters, volatile organic compounds and nitrogen oxides. The negative impacts of these emissions on the global warming and air and land pollution are well documented [1]. With increase in population and growth in economy, there is an increase in environment pollution and greenhouse gases emissions.

To effectively deal with these environmental issues, different initiatives have been undertaken. These initiatives include the issuing of stringent regulations, the improvement in engine technology and its efficiency and the introduction of low emission fuels. In the long run, clean alternative fuels should replace the hydrocarbon-based fuel.

Actually, there are various competing vehicle technologies and competing alternative fuels that are under consideration as sustainable clean transport systems and fuels of the future [2].

In the present work, the issue of alternative fuels is dealt with alternative fuels include hydrogen, natural gas, methanol, ethanol, LGP, biodiesel and electricity both plug-in and fuel cell [3]. Of all the alternative fuels, hydrogen produced from renewable energy is considered as the best contender as it is the cleanest and the most sustainable. It is also versatile in its use and can be used as a sole fuel or mixed with other fuels such as gasoline or natural gas. Different scenarios for environment pollution mitigation in the transport sector have been considered [1, 4, 5].

In the present study, the effect of the introduction of alternative fuels on the mitigation of environmental degradation is evaluated. First, the evolution of the vehicle park is investigated. The alternative fuel driven vehicles are introduced. Then the number of these vehicles is increased until the conventional fuel vehicles are completely replaced. Three scenarios are considered. In scenario 0, it is business as usual, i.e., no change to alternative fuel vehicles. In Scenario 1, we assume that there is a gradual switch to vehicles running on cleaner fuel, i.e., LPG fueled vehicles. Finally and in scenario 2, we consider the case of introduction of hydrogen in the fuel system. In this scenario, vehicles running on Hythane, which is a mixture of natural gas and hydrogen, are introduced gradually. The evolution of the emissions of CO, NOx and VOC are investigating in each scenario.

1. Evaluation method

In this scenario [4], it is assumed that the vehicle park increases exponentially at the rate α. The vehicle park size Nc is then given as function of the year t by

$$N_c = N_{co} e^{\alpha(t-2012)} \quad (1)$$

N_{co} is the vehicle park size at year 2012.

We assume that only the vehicles using gasoline are going to be replaced and that the initial number of vehicles powered by alternative fuel represents 5 % of the total gasoline fuel vehicles. The number of vehicles introduced each year increases then at a rate of 8 % until all the gasoline fueled vehicles are replaced. The properties of the fuels under consideration are reported in Table I.

TABLE I
PROPERTIES OF SELECTED FUELS

Fuel	Mass energy density (MJ/kg)	Fuel economy (l/100 km)
Gasoline	44.5	9.04
LPG	20.70	9.7
Hythane	53.67	7.8

*Corresponding author email: email corresponding author

The amount of a pollutant i emitted per km in the year t, where the number of conventional vehicle is N_c and the number of alternative fuel vehicle is N_A, is given by

$$E_i = P_{i,A} N_A + P_{i,G}(N_c - N_A) \quad (2)$$

$P_{i,A}$ et $P_{i,G}$ are the specific pollutant i emissions respectively of alternative fuel and conventional fuel. The specific pollutants emissions of the different fuels are reported in Table II.

TABLE II
SPECIFIC POLLUTANTS EMISSIONS OF SOME FUELS

Fuel	NOx (g/km)	CO (g/km)
Gasoline	0.42	5.2
LPG	0.17	1.44
Hythane	0.02	0.115

II. RESULTS

1. *Evolution of CO emissions*

The evolution of CO emissions for the scenarios under consideration is reported in Fig. 1.

From this Figure, it can be seen that in the case of scenario 0, which is the case of business as usual, the increase of CO emission at the steady rate of the actual increase in the vehicle park is more than twelve times what it is actually. This Figure shows that switching to cleaner fuels drastically reduces CO emission.

The increase of NOx emission at the actual steady rate of increase in the vehicle park is more than sixteen times what it is actually. This Figure shows that switching to cleaner fuels drastically reduces NOx emission.

In scenario 1, corresponding to the gradual switching to LPG fueled vehicles, the NOx emission increases until it reaches a peak around the year 2095. At this peak, NOx emission is about eight times what it is actually. But it is 49 % lower than in the case of business as usual of this peak year.

For the case of Hythane, the reduction in NOx emission is even greater. The NOx emission peaks earlier, i.e., around the year 2080. At this peak, NOx emission is about four times what it is actually.

In scenario 1, corresponding to the gradual switching to LPG fueled vehicles, the CO emission increases until it reaches a peak around the year 2090. At this peak, CO emission is about six times what it is actually but 50 % lower than in the case of business as usual.

For the case of Hythane, the reduction in CO emission is even greater. The CO emission peaks earlier, i.e., around the year 2085. At this peak, CO emission is about four times what it is actually with roughly 57 % reduction by comparison to the case of business as usual.

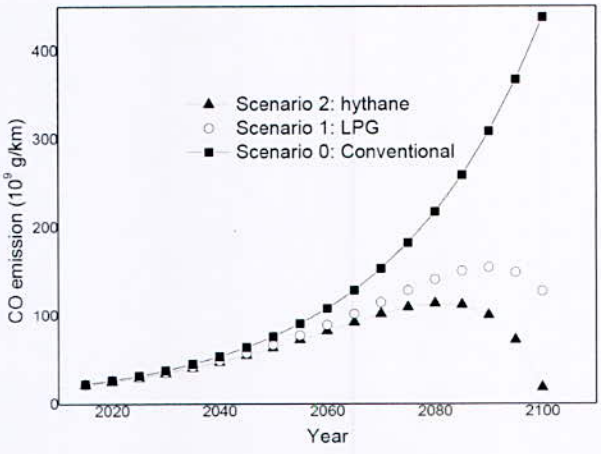

Fig. 1. Evolution of CO emission

2. *Evolution of NOX emissions*

The evolution of NOx emission for the scenarios under consideration is reported in Fig. 2. With roughly 57 % reduction by comparison to the case of business as usual at this peak year.

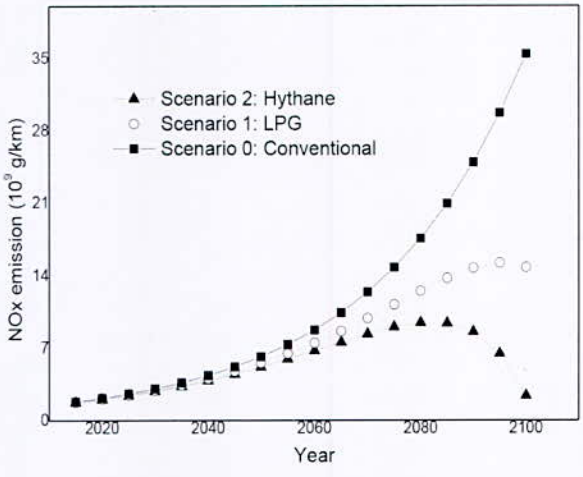

Fig. 2. Evolution of NO_X emission

3. *Evolution of VOC emissions*

The evolution of VOC emission for the scenarios under consideration is reported in Fig. 3. From this Figure, it can be seen that in the case of scenario 0, which is the case of business as usual. The increase of VOC emission at the actual steady rate of increase in the vehicle park is more than thirteen times what it is actually. This Figure shows that switching to cleaner fuels drastically reduces VOC emission.

In scenario 1, corresponding to the gradual switching to LPG fueled vehicles, the VOC emission increases until it reaches a peak around the year 2090. At this peak, VOC emission is about six times what it is actually. But it is 50 % lower than in the case of business as usual of this peak year.

*Corresponding author email: email corresponding author

For the case of Hythane, the reduction in VOC emission is even greater. The VOC emission peaks earlier, i.e., around the year 2085. At this peak, VOC emission is about five times what it is actually with roughly 53 % reduction by comparison to the case of business as usual at this peak year.

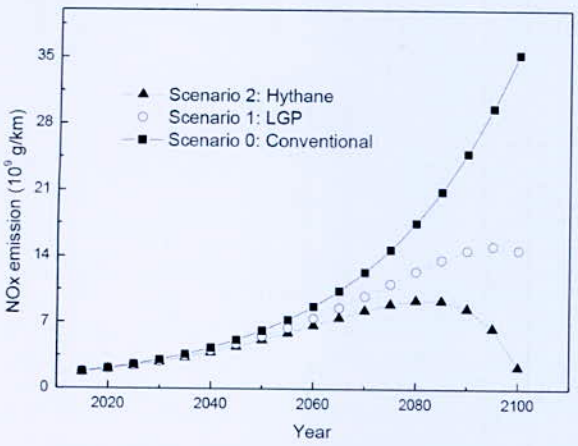

Fig. 3. Evolution of VOC emission

III. CONCLUSION

In this work we are interested in evaluating the influence of the introduction of alternative fuels in the transport sector. For this assessment, the evolution of the vehicle park is investigated. It can be seen that in recent years the evolution of the car fleet is increasingly increasing, which has led to a high consumption of conventional fuels. This high consumption has led to increasing air pollution, which is undoubtedly one of the major problems of our time. The need to replace these fuels with alternative and clean fuels is becoming more and more necessary. It is in this perspective the alternative fuel driven vehicles are introduced. Then the number of these vehicles is increased until the conventional fuel vehicles are completely replaced. Three scenarios are considered. In scenario 0, it is business as usual, i.e., no change to alternative fuel vehicles. In Scenario 1, we assume that there is a gradual switch to vehicles running on cleaner fuel, i.e., LPG fueled vehicles. Finally and in scenario 2, we consider the case of introduction of hydrogen in the fuel system .The evolution of the emissions of CO, NOx and VOC are investigating in each scenario.

In scenario 1, corresponding to the gradual switching to LPG fueled vehicles, the CO emission increases until it reaches a peak around the year 2090. At this peak, CO emission is 50 % lower than in the case of business as usual.

For the case of Hythane, the reduction in CO emission is even greater. The CO emission peaks earlier, i.e., around the year 2085. At this peak, CO emission is is with roughly 57 % reduction by comparison to the case of business as usual

For the case of Hythane, the reduction in NOx emission is even greater. The NOx emission peaks earlier, i.e., around the year 2080. At this peak, NOx emission is about roughly 57 % reduction by comparison to the case of business as usual at this peak year.

For the case of Hythane, the reduction in VOC emission is even greater. The VOC emission peaks earlier, i.e., around the year 2085. At this peak, VOC emission is with roughly 53 % reduction by comparison to the case of business as usual at this peak year.

REFERENCES

[1] Mikhail Granovskii, Ibrahim Dincer_, Marc A. Rosen, " Air pollution reduction via use of green energy sources for electricity and hydrogen production" Atmospheric Environment 41 (2007) 1777–1783

[2] Boudries R., "Comparative economic competitiveness assessment of hydrogen as a fuel in the transport sector in Algeria", Chemical Engineering Transactions, 42 (2014) 61-66 DOI:10.3303/CET1442011

[3] Brenda Johnston, Mayo Michael C, Khare Anshuman. Hydrogen: the energy source for the 21st century. Technovation 25(2005)569-585.

[4] Ayoub Kazim, "Introduction of PEM fuel-cell vehicles in the transportation sector of the United Arab Emirates" Applied Energy 74 (2003) 125–133.

[5] Sungjun Hong, Yanghon Chung, Jongwook Kim, Dongphil Chun, "Analysis on the level of contribution to the national greenhouse gas reduction target in Korean transportation sector using LEAP model "Renewable and Sustainable Energy Review 60(2016) 549-559.

*Corresponding author email: email corresponding author

Chalumeau à Hydrogen Renouvelable

M. Medjouti, S. Zitouni, R. Medjebour, Z. Mouhoub and A. Khellaf

Centre de développement des énergies renouvelables, CDER, 16340, Algiers, Algeria.

Résumé—Ce travail présente 'le chalumeau à hydrogène renouvelable', c'est un dispositif écologique à usage divers, il est caractérisé par la génération d'une flamme de haute température en utilisant principalement un électrolyseur alcalin avec six (06) cellules.
En premier lieu, nous avons commencé par la conception du chalumeau à hydrogène renouvelable
L'électrolyseur et le boitier sont conçus en utilisant le logiciel Solide Works pour la conception et l'assemblage des pièces.
En deuxième lieu, nous avons menu une étude thermique sur la caractérisation du générateur d'hydrogène,
Les résultats montrent que la température de la réaction influe sur la production d'hydrogène.

Mots clés—éléctrolyseur, chalumeau, hydrogène renouvelable.

I. INTRODUCTION

L'utilisation excessive de ressources énergétiques fossiles, dans pratiquement tous les secteurs industriels, a une influence nuisible sur l'environnement. De ce fait, résulte le problème de la pollution qui présente de nos jours un grand souci au monde.
Dans ce contexte et en vue de préserver l'environnement, ainsi que de chercher la possibilité d'avoir des énergies non polluantes.
Dans l'industrie des matériaux plusieurs opérations délicates nécessitant des mesures de sécurité très élevées, telles que le soudage et le découpage. Ces dernières sont manipulées par le chalumeau.
Pour faire face aux trois problématiques, à savoir : les ressources énergétiques non renouvelables, la pollution et le facteur de sécurité. Ce qui a mené à développer l'idée de l'électrolyse de l'eau afin de réaliser un prototype d'un chalumeau à hydrogène renouvelable basé essentiellement sur la production et la combustion de l'hydrogène et qui peut répondre aux problématiques citées précédemment. Ce prototype fonctionne par l'hydrogène renouvelable, non polluant et sécurisé. Ce nouveau chalumeau a été réalisé selon les étapes décrites ci-dessous.

II. CONCEPTION ET REALISATION DU CHALUMEAU A HYDROGENE RENOUVELABLE

Ce chalumeau est complètement conçu et réalisé au sein de la division hydrogène énergie renouvelable du centre de développement des énergies renouvelables. Le chalumeau à hydrogène renouvelable comprend plusieurs éléments ou pièces. Il y a ceux qui ont été réalisés, modifiés ou places directement tels qu'ils sont. Les parties les plus importantes sont :

1. Boitier

C'est le support qui porte les différentes parties du chalumeau, le boitier est conçu de manière à contenir toutes les composantes du chalumeau, a savoir : le Générateur d'hydrogène, la batterie, la bouteille, le filtre, les deux anti-retours de flamme, les deux ventilateurs, la pompe à eau, la boite électronique, le régulateur de charge, l'afficheur, le capteur de température, le capteur de puissance, le capteur du niveau de charge, la prise d'alimentation et le bouton ON/OFF.
La matière première pour la construction du boitier est le plexiglas. Le choix est porté sur le plexiglas car ce matériau est de faible densité, assurant ainsi un boitier léger. Comme le montre la Fig. 1, ce boitier est de forme parallélépipédique avec comme dimensions 520mm*470mm*190mm.

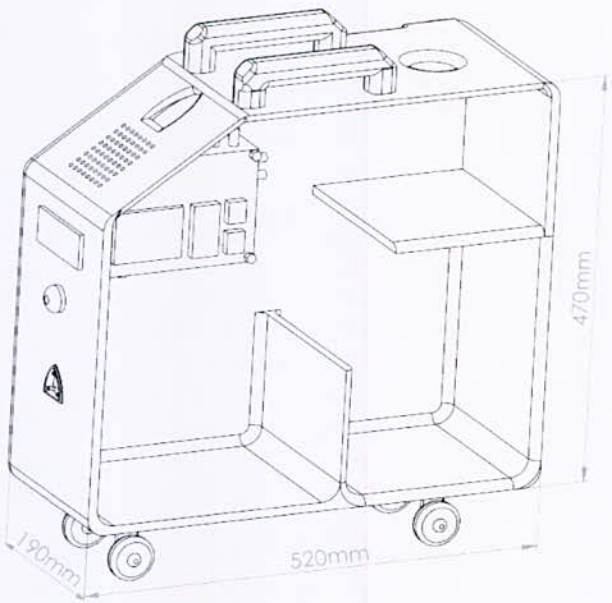

Fig. 1. Vue perspective du boitier

Ce boitier est muni d'un poignet pour porter le chalumeau et quatre roues pour le déplacer.
Il y a aussi des ouvertures pour l'aération, la commande de l'instrumentation et une ouverture pour le passage du tuyau menant vers le bruleur.

2. Générateur d'hydrogène

La partie essentielle du chalumeau, l'électrolyseur de type alcalin comportant 06 cellules, a été conçue et réalisée principalement avec deux matériaux, le plexiglas

*Corresponding author email: medjouti.mohamed@gmail.com

pour les plaque de serrages et l'acier inoxydable pour les plaques neutres, l'anode et la cathode.

La matière première pour la réalisation des cellules est l'acier inoxydable 316 L avec une conductivité électrique de $1.32*10^6$ Siemens/m aux conditions normales. Chaque cellule est composée de trois plaques neutres.

La surface active totale des 06 cellules du générateur sera 0.13916 m^2. La Fig. 2 représente l'électrolyseur avec une vue détaillé d'une cellule.

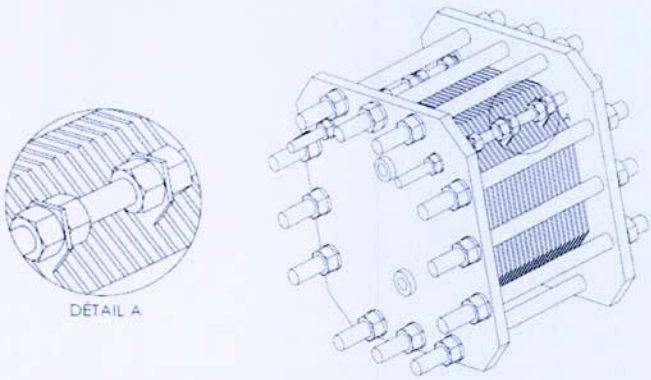

Fig. 2. Vue détaillé d'une cellule (A) et vue perspective du générateur d'hydrogène

En Détail A, on montre le détail d'une cellule. On peut voir la tige fileté qui traverse les plaque anodes ou cathode. Cette tige, avec deux écrous de serrage pour chaque plaque, assure un meilleur contacte d'une part entre le pôle positif et les anodes et d'un autre part le pôle négatif et les cathodes.

Entre deux plaques consécutives, un joint est placé pour assurer l'étanchéité du système. Le joint d'étanchéité, la plaque neutre, l'anode et la cathode sont représentés aux Fig. 3 et Fig. 4. Les formes de différentes parties sont comme les montrés sur les Figures.

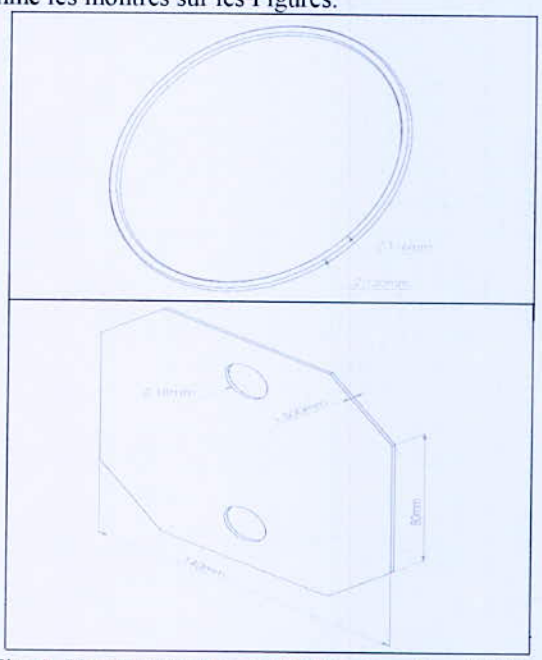

Fig. 3. Vue perspective de la plaque neutre et joint d'étanchéité

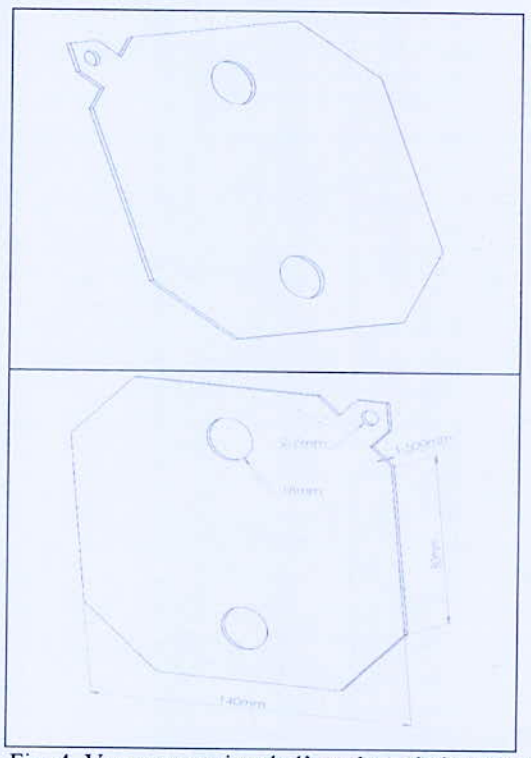

Fig. 4. Vue perspective de l'anode et de la cathode

Les plaques de serrages ont été réalisées en plexiglas avec les dimensions 200mm*200mm*10mm. Ces deux plaques permettent d'assembler toutes les pièces du générateur d'hydrogène, à savoir les anodes, cathodes, plaques neutres, joints d'étanchéités, les vis, écrous et les rondelles. Les deux plaques sont représentées en Fig. 5.

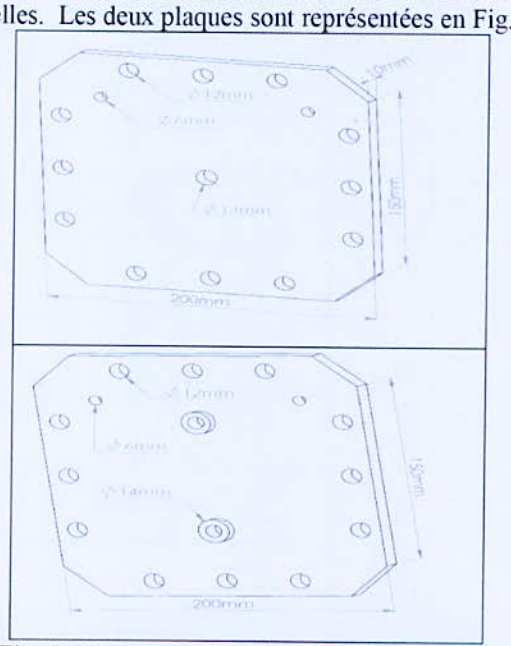

Fig. 5. Vue perspective des plaques de serrage

Les plaques de serrage sont caractérisées par quatre ouvertures sous forme de perçage.

*Corresponding author email: medjouti.mohamed@gmail.com

Les trous du diamètre de 12mm sert a assuré l'assemblage et le serrage du générateur par des tiges qui traversant les deus plaques.
Les trous du diamètre de 6mm sert à assurer le circulation de l'électricité de l'anode vers la cathode.
Les trous du diamètre de 14mm sert à assurer la circulation de la solution aqueuse et la récupération des gaz.
Le trou du diamètre 13mm sert à purger le circuit de la solution aqueuse.

3. Batterie

Une batterie rechargeable (par un panneau photovoltaïque) avec une puissance de 900W sert à fournir l'énergie électrique nécessaire pour le fonctionnement du générateur d'hydrogène.

4. Bouteille

Ce réservoir, d'une capacité de 2 litres muni d'une soupape de sécurité, est conçu pour contenir une solution aqueuse qui est la matière première pour la génération d'hydrogène. Cette bouteille est caractérisée par trois ouvertures, deux en bas pour assurer une meilleure circulation de la solution aqueuse ainsi que la récupération des gaz, la troisième ouverture en haut pour transmettre le gaz à travers un tuyau vers le bruleur.

5. Bruleur

C'est là où la combustion de gaz a lieu. Ce bruleur a été modifié pour le rendre compatible avec la flamme d'hydrogène.

6. Filtre

Un filtre, placé entre la bouteille de stockage et le bruleur, permet de filtrer les gaz produits par l'électrolyseur. Ceci mène à une meilleure flamme.

7. Anti-retour de flamme

Placés le long du tuyau entre le filtre et le bruleur, les anti- retours de flamme permettent d'assurer la sécurité du système lors d'utilisation du chalumeau.

8. Ventilateur

Pour l'aération.

Le chalumeau à hydrogène renouvelable est composé de l'ensemble de tous les éléments mentionnés précédemment.
L'étape de la réalisation a été menée avec succès. La Fig. 6 représente le chalumeau à hydrogène renouvelable qui à été réalisé.

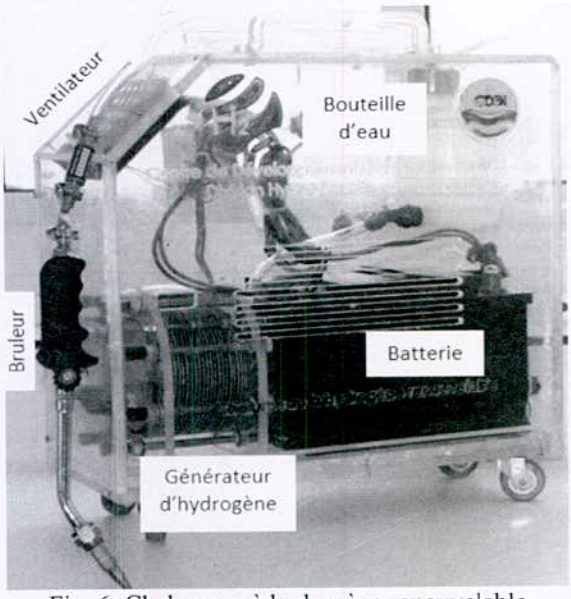

Fig. 6. Chalumeau à hydrogène renouvelable

Beaucoup de tests de fonctionnement ont été faits. Ceci inclus des tests de soudage et de découpage. La prochaine étape est de déterminer les limites de ce dispositif et comment on peut l'utiliser avec une fiabilité maximale.

III. CARACTERISATION DU CHALUMEAU A HYDROGENE RENOUVELABLE

La température du générateur à une influence directe sur la quantité d'hydrogène produite, l'augmentation de cette température facilite la décomposition de la molécule H_2O en présence d'un catalyseur KOH, cependant une température très élevée peut endommager le générateur d'hydrogène et même diminuer la température de la flamme.
Pour cette raison nous avons menu une étude thermique sur l'électrolyseur dans le but de suivre le comportement du générateur d'hydrogène afin de développer ce dernier et l'obtention d'une meilleure flamme.
Nous avons utilisé une caméra thermique qui enregistre les différents rayonnements infrarouges (ondes de chaleurs) émis par le générateur et qui varient en fonction de leurs températures.
Après une série des tests préliminaires nous avons choisi les paramètres suivants :

- Alimentation : Tension 12V et courant 60A.
- Solution aqueuse : Concentration du KOH 56.1g/l.
- Température ambiante : 18C°.

Fig. 7 représente une image thermique globale du générateur en fonctionnement.

*Corresponding author email: medjouti.mohamed@gmail.com

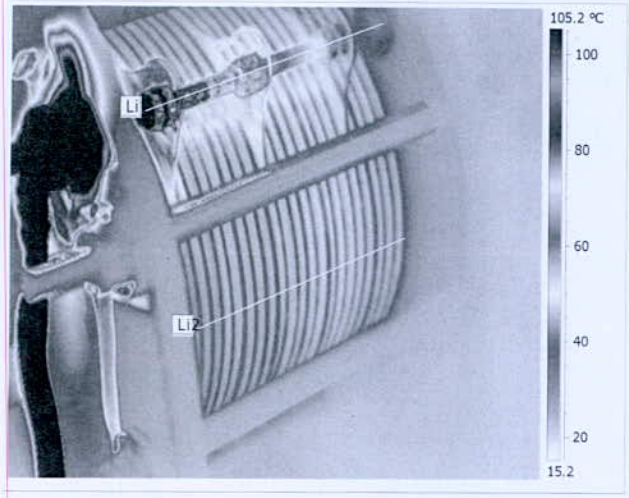

Fig. 7. Image thermique globale du générateur

Cette image thermique montre la température des différentes parties du générateur. On remarque qu'il y a une grande différence de température entre les pièces du générateur.

On voit qu'on a une température minimum de 21°C au niveau des plaques en plexiglas et des tiges de serrage ; par contre la température maximale est de 90°C au niveau des tiges de contacte.

On voit aussi que la température des plaques neutres, les anodes et les cathodes varient entre 40 et 50°C.

Fig. 8 représente une image thermique focalisée sur la zone active du générateur en fonctionnement. Fig. 9 représente l'évolution de la température de la section Li1 de la Fig. 8.

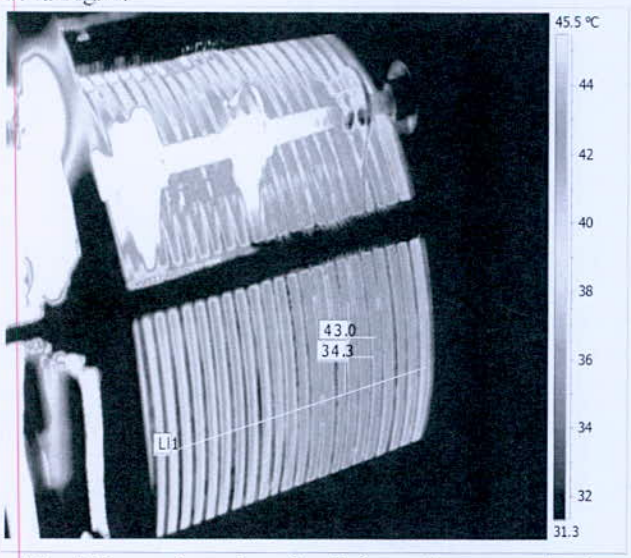

Fig. 8. Image thermique focalisée sur la zone active du générateur

Sur cette image focalisée, on remarque qu'il n'y a pas une grande différence de température entre les différents éléments de la zone active. Elle montre aussi les deux valeurs maximale et minimale de température et qui sont de l'ordre de 43°C et 34.8°C respectivement. Ces températures sont celles respectivement de la plaque d'acier et du joint d'étanchéité.

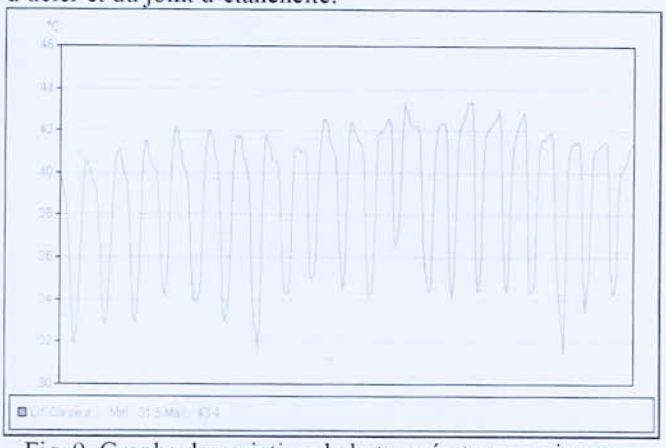

Fig. 9. Graphe de variation de la température au niveau de la zone active

De la Fig. 9, on observe des pics supérieurs qui correspondent aux températures des plaques d'acier et des pics inférieurs qui correspondent aux températures des joints d'étanchéité. La température moyenne de cette zone est de 38°C.

IV. DISCUSSIONS ET RESULTATS

La température basse des plaques en plexiglas et des tiges de serrage est due au fait que :

- Ces plaques ne rentrent pas dans la réaction de l'électrolyse.
- L'utilisation des rondelles ne permet pas le transfert de chaleur vers les plaques en plexiglas et les tiges de serrage.

La température élevé des tiges de contacte est due au fait que :

- La puissance est fournie par l'alimentation.
- Le point de contacte tige-anode et tige-cathode permet un transfert élevé de chaleur.

La stabilité de température sur toutes les plaques en acier est due à la circulation de la solution aqueuse.

V. CONCLUSION ET PERSPECTIVE

Le chalumeau à hydrogène renouvelable c'est un dispositif pour génération de flamme à usage divers utilisé essentiellement dans industrie métallurgique.

D'après les tests de caractérisations du générateur par la caméra thermique qui permet d'effectuer un contrôle non destructive, on peut déduire l'efficacité de ce dernier. La stabilité de la température au niveau des plaques en acier montre que la conception du générateur est bien réussite.

La capacité de production de gaz (60 l/h), peut être améliorée par un bon contrôle de température surtout aux zones chaudes comme montre les images thermiques.

Ce travail entre dans le projet de l'équipe « technologie » :
M. Medjouti ; S. Zitouni; M. Kedaid; R. Medjour ;Z. Mouhoub.

*Corresponding author email: medjouti.mohamed@gmail.com

Simulation de la Production d'Hydrogène par une Centrale Hybride Solaire/Cycle Combiné dans le Sahara Algérien

H. Derbal-Mokrane[1*], F. Amrouche[2] , A. Benzaoui[1]

[1*] Université des Sciences et de la technologie Houari Boumedienne, Algeria.
[2] Renewable Energy Development Centre, CDER, PO Box 62, Route de L'Observatoire, Celeste Valley, Bouzareah, 16340, Algiers, Algeria.

***Résumé*—Ce travail porte sur la simulation de la production d'hydrogène par voie électrolytique moyennant une centrale solaire intégrée à un cycle combiné ISCCS. Les ressources énergétiques en vapeur et en électricité de l'électrolyse sont assurées par le cycle ISCCS dont le champ solaire contribue dans la production de vapeur pour alimenter la chaudière de récupération. Pour ce travail, les différents modèles mathématiques des éléments de la centrale ont été établis, et les simulations de la production d'électricité, de vapeur ainsi que de la production d'hydrogène par électrolyse ont été faite. Ce travail fut finalisé par une étude paramétrique et financière. Les résultats obtenus grâce à cette étude ont pu démontrer la faisabilité de la production d'hydrogène par cette technologie en Algérie, qui est un pays fortement ensoleillé.**

Mots clés—cycle combiné, centrale cylindro parabolique, électricité, vapeur, chaudière de récupération, électrolyse à haute température, hydrogène.

I. INTRODUCTION

L'hydrogène est considéré aujourd'hui par les instances scientifique et politique comme étant le vecteur énergétique renouvelable de substitution aux ressources énergétiques fossiles. Il existe divers technologies permettant la production de l'hydrogène. De ce fait, cet article sera consacré à la production d'hydrogène par électrolyse de vapeur d'eau à haute température dont les besoins énergétiques en électricité et en vapeur sont assurées par une centrale hybride solaire à concentration cylindroparabolique/ cycle combiné. Pour cela l'étude de l'ensemble des centrales à cycle combiné [1, 2] ainsi que la technologie des concentrateurs cylindro-paraboliques [3, 4] a été traitée avec attention. Pour la réalisation de cette étude, des simulations sur la production d'électricité et de vapeur par la centrale ainsi que de la production d'hydrogène a dû être faite.

II. MODELISATION MATHEMATIQUE

1. Modèle de la centrale hybride

La centrale hybride (ISCCS) (Integrated Solar Combined Cycle System) a comme principe, d'intégrer l'énergie solaire thermique issue d'un champ solaire à concentration dans une centrale à cycle combiné. Cette dernière réalise la combinaison d'un cycle de turbine à combustion et d'un cycle de turbine à vapeur, via une chaudière de récupération qui utilise les gaz d'échappement du générateur électrique de la turbine à combustion [5].

La chaudière de récupération sert d'une part, à surchauffer et/ou générer la vapeur qui alimente la turbine à vapeur tout en utilisant le champ solaire à concentrateurs cylindroparaboliques, et d'autre part, à alimenter en vapeur l'électrolyseur a haute température. Cette configuration a été choisie pour son avenir attrayant, sa simplicité de réalisation, son bas coût et surtout ses faibles émissions des gaz à effet de serre. L'association des deux cycles permet de tirer deux travaux utiles à partir de la chaleur produite par une seule source [5]. L'installation hybride ainsi obtenue (Fig. 1) est un mariage particulièrement réussi permettant d'atteindre une efficacité électrique qui dépasse les 55 % [6].

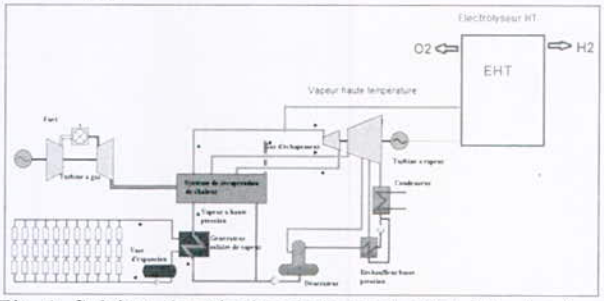

Fig. 1. Schéma de principe de la production d'hydrogène par le cycle ISCCS

Les échanges enthalpiques au sein d'un cycle combiné peuvent être résumés par le schéma de la Fig. 2.

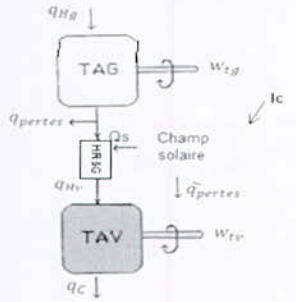

Fig. 2. Les échanges enthalpiques au niveau d'un cycle ISCCS

On peut déduire les relations suivantes [5, 6] :

Le rendement du cycle à combustion η_{thg} :

$$\eta_{thg} = \frac{w_{tg}}{q_{Hg}} \quad (1)$$

Où w_{tg} est le travail fourni par la turbine à gaz et q_{Hg} est la chaleur reçue par le cycle à combustion.

Le rendement du cycle à vapeur η_{thv} :

$$\eta_{thv} = \frac{w_{tv}}{q_{Hv}} \quad (2)$$

*Corresponding author email: hderbal@gmail.com

Où w_{tv}est le travail fourni par la turbine à vapeur et q_{Hv} est la chaleur reçue par le cycle à vapeur par l'intermédiaire du récupérateur HRSG (Heat Recovery Steam Generator).

L'efficacité du HRSG $\varepsilon_{\text{HRSG}}$:

$$\varepsilon_{\text{HRSG}} = \frac{q_{Hv}}{q_{pertes} + q_{Hv} + Q_S} \quad (3)$$

Où Q_S représente la chaleur fournie par les champs solaires.

Le rendement du champ solaire :

$$\eta_S = \frac{Q_S}{I_C . A} \quad (4)$$

Le rendement du cycle ISCCS s'écrit alors :

$$\eta_{cc} = \frac{w_{tg} + w_{tv}}{q_{Hg}} = \eta_{tg} + \eta_{tv}\frac{q_{Hv}}{q_{Hg}} \quad (5)$$

$$\eta_{cc} = \eta_{thg} + \varepsilon_{\text{HRSG}}(1 - \eta_{thg})\eta_{thv} \quad (6)$$

$$\eta_{ISCCS} = \frac{w_{tg} + w_{tv}}{q_{Hg} + I_C . A} \quad (7)$$

2. *Modèle pour le champ solaire*

Il est basé sur l'établissement d'un bilan énergétique du concentrateur qui inclut le rayonnement solaire direct, les pertes optiques et thermiques dont le but est de déterminer l'énergie utile délivrée par le fluide caloporteur. On peut exprimer cette énergie par

$$Q_u = Q_{abs} - Q_{perdue} \quad (8)$$

Q_u : Énergie utile délivrée $[W/m^2]$

Q_{abs} : Rayonnement incident avant d'atteindre le récepteur, peut subir différents affaiblissements à cause des pertes optiques du champ d'héliostats et les pertes liées à l'atténuation atmosphérique $[W/m^2]$

Q_{perdue} : Énergie thermique perdue au niveau du récepteur $[W/m^2]$

L'expression du rayonnement solaire absorbé est [7, 8, 9] :

$$Q_{abs} = I_b\, IAM\, \eta_o\, K_{ombre}\, K_{extr}\, K_{opér} \quad (9)$$

Q_{abs} : Rayonnement solaire absorbé par le collecteur thermique $[W/m^2]$

I_b : Rayonnement solaire direct capté ;

IAM : Facteur de correction d'angle d'incidence ;

η_o : Rendement optique du capteur ;

K_{ombre} : Facteur de performance qui tient compte de l'effet d'ombre causé par les rangés des concentrateurs disposés en parallèle ;

K_{extr} : Facteur de performance qui tient compte des pertes aux extrémités du HCE ;

$K_{opér}$: Fraction du champ solaire opérationnel et correctement pointé vers le soleil.

$$Q_{perdue} = U_L(T_c - T_a)a \quad (10)$$

U_L : Conductance globale des pertes thermiques au niveau de l'absorbeur ;

T_c : Température moyenne du fluide caloporteur ;

T_a : Température ambiante.

a: Surface de l'absorbeur

3. *Modèle pour l'électrolyse de la vapeur d'eau*

L'utilisation future de l'hydrogène comme vecteur énergétique impose le développement d'un procédé qui assure une production massive à faible coût. Le procédé « haute température -vapeur » (EHT), bénéficie d'une double action de chaleur et de potentiel électrique pour la dissociation de la molécule d'eau. La haute température du système accélère la cinétique de réaction, réduisant la perte d'énergie due à la polarisation de l'électrode et donc augmente les performances globales du système [10, 11].

Il présente, par rapport à l'électrolyse conventionnelle en milieu liquide, des avantages théoriques incontestables sur trois niveaux :

-Au niveau énergétique d'abord : L'électrolyse à haute température permet de réduire la consommation électrique d'environ 35% pour la production d'hydrogène, par rapport au procédé courant d'électrolyse.

La consommation électrique requise est estimé au environ de 2,6 à $3kWh/Nm^3\ H_2$ pour un électrolyseur fonctionnant à 900°C et à pression atmosphérique. Les recherches sont en cours pour rendre l'hydrogène produit par cette méthode compétitif avec le reforming catalytique [12].

-en matière de compacité, l'EHT permet de travailler à forte densité de courant, d'où une forte capacité de production dans un volume réduit (de moitié).

-Au niveau économique enfin : l'apport d'une partie significative de l'énergie sous forme de chaleur au lieu d'électricité, ce qui permet de diminuer le cout d'exploitation, la chaleur étant une source d'énergie nettement moins chère que l'électricité.

Le principe de l'électrolyse à haute température repose sur la décomposition des molécules d'eau sous forme vapeur au niveau de la cathode. Cette décomposition dépend alors de la nature de l'électrolyte.

Deux types d'électrolyses existent (Fig. 3) [13, 14, 15]:

-l'électrolyse utilisant un électrolyte à conduction anionique (800-100°C) ;

-l'électrolyse utilisant un électrolyte à conduction protonique à plus basse température de fonctionnement (300°C à 600°C). C'est le type adopté dans notre travail puisque l'hydrogène produit est sec contrairement à celui obtenu dans le cas de la conduction anionique, le traitement de séchage n'est donc pas nécessaire pour purifier l'hydrogène, abaissant ainsi les coûts de production[16]. De plus, la gamme de température utilisée est celle fournie par le cycle ISCCS.

La tension U appliquée aux bornes de la cellule est égale à la somme de cette tension minimale U_R auquel s'ajoute le rapport des concentrations des espèces chimiques qui interviennent dans la réaction (FS – deuxième terme de l'Equation de Nernst) et les surtensions qui sont provoquées par l'activation des électrodes(ΔU_{act}), la

*Corresponding author email: hderbal @gmail.com

différence de concentration des gaz au sein des électrodes (ΔU_{conc}) et la résistance ohmique des matériaux dont la cellule est fabriquée(ΔU_{ohm}).

L'équation (11) inclut ces différents termes [5].

$$U = U_R + FS + \Delta U_{act} + \Delta U_{conc} + \Delta U_{ohm} \quad (11)$$

$$U_R = -\Delta G / Z'F \quad (12)$$

Où ΔG la est la variation d'énergie libre, F la constante de Faraday et Z' le nombre d'électrons mis en jeu (= 2)

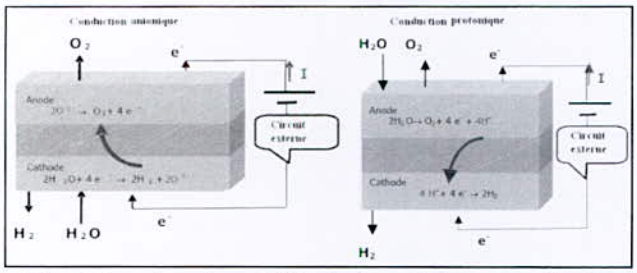

Fig. 3. Les deux types d'électrolyse de la vapeur haute température

III. RESULTATS ET INTERPRETATIONS

La première partie concerne la simulation de la production d'électricité et de la vapeur par la centrale ISCCS.

La configuration de la centrale choisie est du type ISCCS hassi R'mel de puissance 150MW avec une contribution solaire de 30MW.Dans cette partie, nous avons traité d'abord la simulation de production de la centrale adoptée dans le site de Hassi R'mel. Puis, nous avons fait l'étude paramétrique et la simulation de la production dans quelques sites du territoire algérien, favorables à cette technologie. Nous avons étudié aussi les différentes possibilités de contribution énergétique solaire au niveau du cycle combiné. La deuxième partie, a ete consacrée à l'étude de faisabilité de la production d'hydrogène par électrolyse. Cette production est liée directement à l'électricité produite. Cette étude a montré aussi que pour les différentes configuration les quantités d'hydrogène produites sont plus grandes en utilisant l'électrolyse de vapeur d'eau à haute température. Nous avons pu affirmer que la consommation d'eau est un point à ne pas négliger dans la production d'hydrogène par voie électrolytique.

Les figures 4 et 5 présentent les moyennes mensuelles du rayonnement direct et de la durée d'ensoleillement.

La figure 4 montre que le site de Tamanrasset présente le meilleur DNI moyen qui dépasse les 250W/m² dans la majorité des mois. Les durées maximales sont enregistrées pour le site de Tamanrasset où la durée de 11h a été enregistrée pour sept mois de l'année, les autres sites possèdent aussi des durées satisfaisantes qui varient entre 12 et 8h.

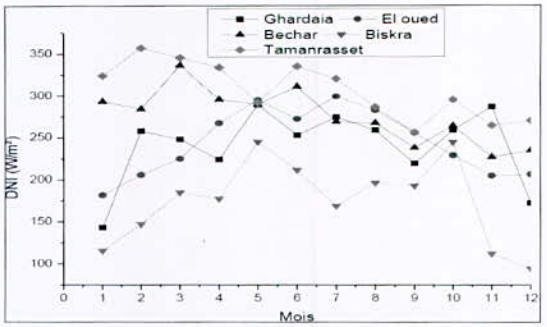

Fig. 4. Moyennes mensuelles des DNI

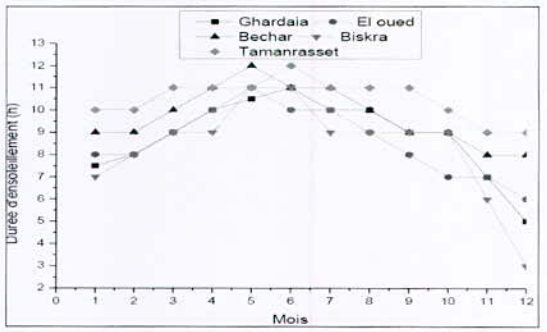

Fig. 5. Moyennes mensuelles des durées d'ensoleillement

La Fig. 6 donne la chaleur fournie par le champ solaire pour les journées des solstices d'été et d'hiver pour le site de Ghardaïa. Cette chaleur est proportionnelle au rayonnement direct normal DNI, elle varie entre 80 et 100 MW pour le 21 juin, elle représente ainsi (avec un rendement de 40%) 100% de la chaleur nécessaire pour entraîner une turbine de 30MW de capacité.

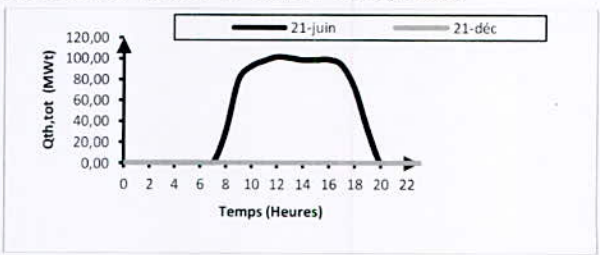

Fig. 6. Variation journalière de la puissance thermique totale du champ solaire

La Fig. 7 exprime, pour le site de Ghardaïa la puissance électrique nette issue de la centrale ISCCS qui est de valeur constante de 150 MW. Cette figure présente aussi la contribution du champ solaire qui peut atteindre une valeur maximale de 30MW, qui correspond à une contribution remarquable au lissage de la production d'électricité.

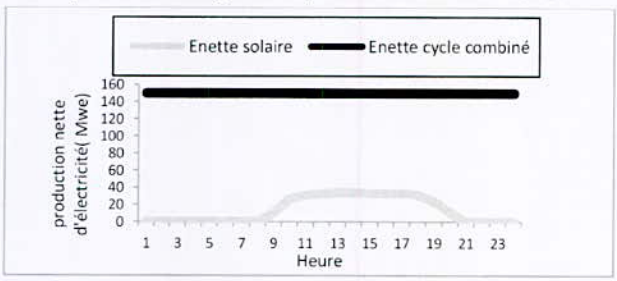

Fig. 7. Variation journalière de la puissance électrique issue de la centrale ISCCS et du champ solaire

*Corresponding author email: hderbal @gmail.com

Dans la Fig. 8, les meilleures productions mensuelles du champ solaire sont repérées dans la période estivale, et cela proportionnellement au DNI et à la durée d'ensoleillement. Le site de Tamanrasset présente les meilleures productions mensuelles suivi par les sites de Bechar, El Oued et Ghardaïa. Le site de Biskra présente les productions les plus faibles.

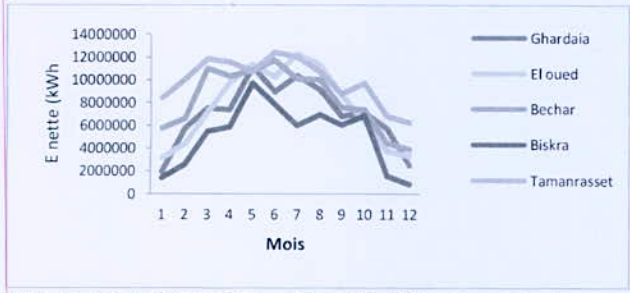

Fig. 8. Production mensuelle nette délivrée par le champ solaire pour différent sites

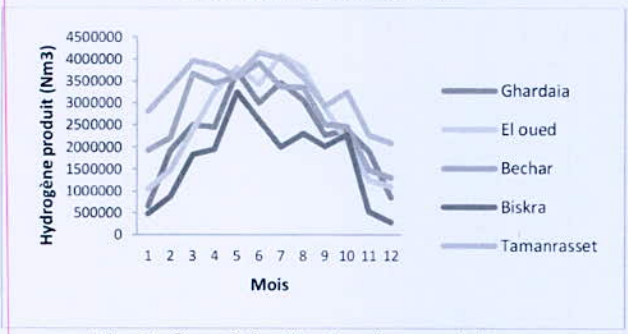

Fig. 9. Quantités d'hydrogène produites

La Fig. 9 exprime les quantités d'hydrogène produit par l'électrolyseur à haute température pour les différents sites. Les quantités produites sont étroitement liées à l'énergie électrique disponible qui est plus importante dans le site de Tamanrasset.

III. CONCLUSION

Grace à cette étude, nous avons pu démontrer la faisabilité de la production d'hydrogène par électrolyse moyennant une centrale ISCCS en Algérie. L'Algérie dont les ressources météorologiques et matérielles sont largement disponibles, favorisant le succès d'une centrale ISCCS. En effet, avec un rayonnement direct normal (DNI) qui dépasse les 2000kWh/m²/an, une durée d'ensoleillement journalière moyenne qui dépasse les 10h et une réserve considérable du gaz naturel, ce pays dispose des éléments clés pour la réussite de ce type de projet. Les résultats obtenus durant cette étude, ont prouvé la possibilité d'assurer les besoins énergétiques de l'électrolyse en électricité et en vapeur d'eau. La contribution solaire est présente dans ce travail comme solution partielle pour la transition vers un système à énergie propre et économique.

REFERENCES

[1] La sous-commission offre et demande de gaz de l'ATG. Gaz naturel et production d'électricité : Les centrales à cycle combiné et leurs performances. Revue Gaz d'aujourd'Hui N° 7-8-9. Sep 1992.

[2] J. Mariyappan, D. Anderson. Thematic Review of GEF-Financed Solar Thermal Projects. Monitoring and Evaluation Working. Paper 7 .October 2001.

[3] M. Romero-Alvarez and E. Zarza. Concentrating Solar Thermal Power. Energy conversion. D. Yogi Goswami, Frank Kreith: Taylor&Francis Group, LLC. CRP Press 2008.

[4] J-P. Py. A. Capitaine. Hydrogen production by high temperature electrolysis of water vapour and nuclear reactors. (AREVA NP & EDF).

[5] H. Mokrane-Derbal. Contribution à l'étude des centrales de puissance à concentration solaire pour la production d'énergie. Etude des perspectives de production d'hydrogène pour les piles à combustible. Thèse de Doctorat.USTHB.2012

[6] R.Gicquel, Systèmes énergétiques Tome 2 : Applications classiques. Edition: école polytechnique. 02/2009.

[7] A. Patnode, (2006). Simulation and Performance Evaluation of Parabolic Trough Solar Power Plants. (Master's Thesis, University of Wisconsin – Madison, 2006).

[8] M. G. Elsaket. Simulating the Integrated Solar Combined Cycle for Power Plants Application in Libya. Thèse de Master. Cranfield University. Sep 2007.

[9]J. A. Duffie, and W. A. Beckman. Solar Engineering of Thermal Processes. 2nd edition. New York: John Wiley and Sons, Inc., 1991

[10] Office of Power Delivery, Office of Power Technologies, Energy Efficiency and Renewable Energy, U.S. Department of Energy. A Multiyear Plan for the hydrogen R&D Program Rationale, Structure and Technology Roadmaps, August 1999.

[11] D. Gallet et R. Grastien. L'électrolyse haute température. CLEFS CEA- N°50/51-Hiver 2004-2005.

[12] N. Muradov "Thermocatalitic CO_2 free production of hydrogen from hydrocarbon fuels" final cooperative agreement report N° DE-FC39-99GO10456. 1995.

[13] J. Labbé. L'hydrogène électrolytique comme moyen de stockage d'électricité pour systèmes photovoltaïques isolés .Ecole des Mines de Paris .décembre 2006.

[14] B. Sala. Etude et développement d'un assemblage électrode -électrolyte à conduction protonique avec réalisation d'une cellule d'électrolyse de la vapeur. Programme ANR: CELEVA .Octobre 2009.

[15] J-P. Py. A. Capitaine. Hydrogen production by high temperature electrolysis of water vapour and nuclear reactors. (AREVA NP & EDF).

[16]Grégory GOUPIL. Elaboration et caractérisation de matériaux d'anode à conduction mixte protonique/électronique pour l'électrolyse de la vapeur d'eau à haute température. Thèse de doctorat. Université de Grenoble. Janvier 2011.

*Corresponding author email: hderbal @gmail.com

Author Index